



**GDAŃSK UNIVERSITY  
OF TECHNOLOGY**  
FACULTY OF CHEMISTRY



The author of the PhD dissertation: **Natalia Maciejewska**  
Scientific discipline: **Chemistry**

## DOCTORAL DISSERTATION

Title of Ph.D. dissertation: Telomerase inhibition - unfulfilled hopes in the perfect molecular target

Title of Ph.D. dissertation (in Polish): Inhibicja telomerazy – niespełnione nadzieje idealnego celu molekularnego

Supervisor

*signature*

Prof. Dr Eng. Maciej Bagiński

Gdansk, year 2022



## STATEMENT

The author of the PhD dissertation: Natalia Maciejewska

I, the undersigned, agree that my PhD dissertation entitled:  
Telomerase inhibition - unfulfilled hopes in the perfect molecular target  
may be used for scientific or didactic purposes.<sup>1</sup>

Gdańsk, 17.10.2020

.....  
*signature of the PhD student*

Aware of criminal liability for violations of the Act of 4<sup>th</sup> February 1994 on Copyright and Related Rights (Journal of Laws 2006, No. 90, item 631) and disciplinary actions set out in the Law on Higher Education (Journal of Laws 2012, item 572 with later amendments),<sup>2</sup> as well as civil liability, I declare, that the submitted PhD dissertation is my own work.

I declare, that the submitted PhD dissertation is my own work performed under and in cooperation with the supervision of Professor Maciej Baginski.

This submitted PhD dissertation has never before been the basis of an official procedure associated with the awarding of a PhD degree.

All the information contained in the above thesis which is derived from written and electronic sources is documented in a list of relevant literature in accordance with art. 34 of the Copyright and Related Rights Act.

I confirm that this PhD dissertation is identical to the attached electronic version.

Gdańsk, 17.10.2020

.....  
*signature of the PhD student*

I, the undersigned, agree to include an electronic version of the above PhD dissertation in the open, institutional, digital repository of Gdańsk University of Technology, Pomeranian Digital Library, and for it to be submitted to the processes of verification and protection against misappropriation of authorship.

Gdańsk, 17.10.2020

.....  
*signature of the PhD student*

---

<sup>1</sup> Decree of Rector of Gdansk University of Technology No. 34/2009 of 9<sup>th</sup> November 2009, TUG archive instruction addendum No. 8.

<sup>2</sup> Act of 27<sup>th</sup> July 2005, Law on Higher Education: Chapter 7, Criminal responsibility of PhD students, Article 226.





## DESCRIPTION OF DOCTORAL DISSERTATION

**The Author of the PhD dissertation:** Natalia Maciejewska

**Title of PhD dissertation:** Telomerase inhibition - unfulfilled hopes in the perfect molecular target

**Title of PhD dissertation in Polish:** Inhibicja telomerazy – niespełnione nadzieje idealnego celu molekularnego

**Language of PhD dissertation:** English

**Supervision:** Prof. Dr Eng Maciej Bagiński

**Date of doctoral defense:**

**Keywords of PhD dissertation in Polish:** Antrachinony, nowotwór, telomeraza, telomery

**Keywords of PhD dissertation in English:** Anthraquinones, cancer, telomerase, telomeres

**Summary of PhD dissertation in Polish:**

Telomeraza odgrywa kluczową rolę w procesie proliferacji komórek, homeostazy oraz transformacji nowotworowej, co czyni ją obiecującym celem molekularnym w chemioterapii przeciwnowotworowej. Co ważne, mimo że enzym ten został dobrze zbadany jako cel, to do tej pory żadna z obiecujących cząsteczek nie została zarejestrowana jako lek.

Przedmiotem badań prowadzonych w ramach mojej dysertacji doktorskiej jest określenie komórkowego i molekularnego mechanizmu działania nowych związków heterocyklicznych wywodzących się z klasy karbazoli, pirazoli oraz antrachinonów. Z wszystkich przebadanych kandydatów, jedynie pochodne antrachinonów wykazywały aktywność względem telomerazy. Wykazałam, że najbardziej aktywny związek (TXT4) preferencyjnie uszkadza DNA na telomerach. Co więcej ustaliłam, że TXT4 hamuje również aktywność wielu kinaz tyrozynowych. Spośród karbazoli, wyselekcjonowałam związki 5aa oraz 8, których mechanizm działania polega na produkcji reaktywnych form tlenu. Natomiast najbardziej obiecującym związkiem z klasy pirazoli jest PCH-1, którego aktywność opiera się na stabilizacji dynamiki polimeryzacji tubuliny - białka wchodzącego w skład cytoszkieletu.

Na podstawie przeprowadzonych badań ustaliłam główne mechanizmy działania nowych związków przeciwnowotworowych, które w przyszłości mogą stanowić podstawę do projektowania i syntezy nowych potencjalnych środków farmaceutycznych.

**Summary of PhD dissertation in English:**

Telomerase plays a pivotal role in cell proliferation, homeostasis, and neoplastic transformation, making it a promising molecular target for cancer chemotherapy. Of note, although hTERT has been explored thoroughly as a target, none of the promising molecules has been approved as a drug until now.

The subject of research conducted as part of my doctoral dissertation is explaining the cellular and molecular mechanism of action of new heterocyclic compounds derived from the class of carbazole, pyrazole, and anthraquinone. Of all the candidates tested, only anthraquinones inhibited telomerase





activity. I have shown that the most active compound (TXT4), apart from the typical features of telomerase targeting molecules, also preferentially damages DNA on telomeres. Furthermore, I have found that TXT4 has an additional mechanism of action, consisting of multidirectional inhibition of tyrosine kinases. From among carbazoles, I selected compounds 5aa and 8, whose primary mechanism of action is reactive oxygen species production. In addition, I showed that the most promising compound from the pyrazole class is PCH-1, whose anticancer activity is based on the stabilization of tubulin polymerization - the cytoskeleton-forming protein.

On the basis of the conducted research, I determined the main mechanisms of action of new anti-cancer compounds, which in the future may employ as the basis for the design and synthesis of new potential pharmaceutical agents.



## TABLE OF CONTENTS

Abbreviations.....	8
1. Introduction .....	13
1.1. The outline of the cancer problem and drug discovery process.....	13
1.2. Telomeres – structure, and function .....	14
1.3. The role of telomeres in cellular senescence and carcinogenesis .....	16
1.4. Structure of telomerase .....	17
1.5. hTERT promoter mutations and activation of telomerase .....	19
1.6. Non-canonical functions of telomerase .....	21
1.6.1. Mitochondrial hTERT.....	22
1.6.2. Telomerase as a regulator of gene expression - Wnt/ $\beta$ -catenin complex.....	22
1.6.3. Telomerase as a regulator of gene expression - NF- $\kappa$ B transcription factor.....	23
1.6.4. hTERT in angiogenesis .....	24
1.6.5. hTERT in the tumour microenvironment .....	24
1.6.6. hTERT in the nervous system .....	24
1.7. Approaches to inhibit telomerase .....	25
1.7.1. Antisense oligonucleotides .....	25
1.7.2. Stabilization of the G-quadruplex structure .....	26
1.7.3. Direct telomerase inhibitors - synthetic compounds.....	28
1.7.4. Natural compounds and derivatives .....	28
1.7.5. Nucleoside analogues .....	29
1.7.6. RNA interference-based therapy.....	30
1.7.7. CRISPR Cas9-mediated gene therapy .....	30
1.7.8. hTERT promoter-driven oncolytic adenovirus .....	31
1.7.9. TAGE system .....	31
1.7.10. Cancer immunotherapy .....	32
1.7.11. Suicide gene therapy.....	32
2. Object of Research .....	34
3. Results .....	37
3.1. Selection of cancer cell lines .....	37
3.2. Compounds screening - determination of the inhibitory effect of the compounds against telomerase .....	37
3.3. Project I – anthraquinone derivatives as telomerase inhibitors .....	40
3.3.1. Determination effect of the anthraquinones on cell viability.....	40
3.3.2. The antiproliferative potential of anthraquinones .....	41
3.3.3. Study of proapoptotic properties - changes in the plasma membrane.....	48
3.3.4. Detection of caspase-3 and caspase-7 activity .....	52
3.3.5. Analyses of expression apoptosis-related proteins.....	55
3.3.6. Impact of anthraquinones on calcium homeostasis .....	56
3.3.7. Study changes in mitochondria structure .....	57
3.3.8. Effect of anthraquinones on stress-induced senescence.....	60
3.3.9. Study of prooxidative properties.....	61
3.3.10. Impact of anthraquinones on DNA damage .....	64
3.3.11. Assessment of the DDR protein network .....	71
3.3.12. Genotoxicity evaluation using comet assay .....	71
3.3.13. Analysing G-4 stabilizing properties of anthraquinones .....	72
3.3.14. Analysis of TXT4 to interact with hTERT.....	73
3.3.15. Analyses of hTERT mRNA expression .....	74
3.3.16. Effect of TXT2 and TXT4 on cytoskeleton structure .....	75
3.3.17. Analyses of anti-migratory properties of TXT2 and TXT4.....	77
3.3.18. Impact of TXT4 on the expression of autophagy-related proteins .....	79
3.3.19. Effect of TXT4 on cancers with overexpression ABC transporters .....	82
3.3.20. Impact of long-term treatment of TXT4 .....	84
3.3.21. Analysis of changes in phosphorylation of protein tyrosine kinases .....	87

3.3.22.	Study of anthraquinones and carbazoles as DNA intercalators and topoisomerase inhibitors .....	94
3.3.23.	Structure-activity relationship analysis .....	95
3.4.	Project II - carbazole derivatives .....	96
3.4.1.	Scientific problem addressed.....	96
3.4.2.	Role of reactive oxygen species in carbazole-induced cancer cell death .....	97
3.4.3.	Determination impact 5aa and 8 on PTK activity.....	102
3.5.	Project III – pyrazole derivatives .....	103
3.5.1.	Scientific problem addressed.....	103
4.	Discussion .....	105
5.	Conclusion.....	111
6.	Materials and Methods .....	113
6.1.	Materials.....	113
6.1.1.	Antibodies .....	113
6.1.2.	Oligonucleotides .....	114
6.2.	Methods .....	114
6.2.1.	Cell lines cultivation .....	114
6.2.2.	TRAP assay .....	115
6.2.3.	Cell viability assay .....	115
6.2.4.	Analysis of cell cycle distribution .....	116
6.2.5.	Colony formation assay .....	116
6.2.6.	Apoptosis and caspase 3/7 assay .....	116
6.2.7.	Calcium efflux assay .....	116
6.2.8.	Quantification of lysosomal and mitochondrial cellular content.....	117
6.2.9.	Live cell imaging .....	117
6.2.10.	Mitochondrial morphometric analyses .....	117
6.2.11.	$\beta$ -Galactosidase in situ assay for cellular senescence .....	117
6.2.12.	Intracellular ROS measurement .....	118
6.2.13.	H2AX phosphorylation assay.....	118
6.2.14.	Immunofluorescence .....	118
6.2.15.	Combined immunofluorescence and telomere FISH.....	119
6.2.16.	Western blot.....	119
6.2.17.	Genotoxic activity (comet assay) .....	120
6.2.18.	FRET.....	120
6.2.19.	CETSA .....	120
6.2.20.	DNA extraction.....	121
6.2.21.	RNA extraction.....	121
6.2.22.	Analysis expression of hTERT by RT-PCR .....	121
6.2.23.	Wound healing migration assay.....	121
6.2.24.	HPLC-MS analysis.....	122
6.2.25.	TXT4 accumulation studies .....	122
6.2.26.	TXT4 efflux studies .....	123
6.2.27.	Impact of long-term treatment of TXT4.....	123
6.2.28.	Quantification of relative telomere length by real-time PCR.....	123
6.2.29.	Universal tyrosine kinase assay .....	123
6.2.30.	Phospho-flow cytometry .....	124
6.2.31.	RTK phosphorylation array .....	124
6.2.32.	DNA unwinding assay.....	125
6.2.33.	Human topoisomerase I relaxation assay .....	125
6.2.34.	Determination of the role of ROS in carbazole derivatives-related cell death .....	125
6.2.35.	Statistical analyses .....	125
7.	References .....	126
8.	Authors Contribution.....	157
8.1.	Project II - From tryptophan to novel mitochondria-disruptive agent, synthesis and biological evaluation of 1,2,3,6-tetrasubstituted carbazoles .....	157

8.2. Project III - Novel chalcone-derived pyrazoles as potential therapeutic agents for the treatment of non-small cell lung cancer.....	160
Professional Experience .....	164
Scientific achievements.....	165
Annexes .....	167

## ABBREVIATIONS

<i>2'MOE</i>	- <u>2</u> '-O-(2- <u>m</u> ethoxy <u>e</u> thyl)
<i>2'OMe</i>	- <u>2</u> '-O- <u>m</u> ethyl
<i>DAPI</i>	- 4',6- <u>d</u> iamidino-2- <u>p</u> henyl <u>i</u> ndole
<i>5-FU</i>	- <u>5</u> - <u>f</u> luoro <u>u</u> racil
<i>7-AAD</i>	- <u>7</u> - <u>a</u> mino <u>a</u> ctinomy <u>c</u> in <u>D</u>
<i>8-oxoG</i>	- <u>8</u> - <u>o</u> xo <u>g</u> uanine
<i>ABC</i>	- <u>A</u> TP- <u>b</u> inding <u>c</u> assette
<i>ADMET</i>	- <u>a</u> bsorption, <u>d</u> istribution, <u>m</u> etabolism, <u>e</u> xcretion, and <u>t</u> oxicity
<i>ALT</i>	- <u>a</u> lternative <u>l</u> ength <u>t</u> elomere
<i>ALS</i>	- <u>a</u> myotrophic <u>l</u> ateral <u>s</u> clerosis
<i>AMPK</i>	- <u>A</u> MP- <u>a</u> ctivated protein <u>k</u> inase
<i>AP-2</i>	- <u>a</u> dipocyte <u>p</u> rotein <u>2</u>
<i>ASOs</i>	- <u>a</u> ntisense <u>o</u> ligodeoxynucleotides
<i>ATR</i>	- <u>a</u> taxia <u>t</u> elangiectasia mutated and <u>r</u> ad3-related kinase
<i>ATP</i>	- <u>a</u> denosine <u>t</u> riphosphate
<i>ATRX</i>	- <u>a</u> lpha- <u>t</u> halassemia/mental <u>r</u> etardation, <u>X</u> -linked
<i>ATM</i>	- <u>a</u> taxia <u>t</u> elangiectasia <u>m</u> utated kinase
<i>AZT</i>	- 3'- <u>A</u> zido-2',3'-dideoxy <u>t</u> hymidine
<i>Bad</i>	- <u>B</u> cl2 associated <u>a</u> gonist of cell <u>d</u> eath
<i>BafA1</i>	- <u>b</u> afilomycin <u>A</u> 1
<i>Bax</i>	- <u>B</u> cl2 <u>a</u> ssociated <u>X</u> protein
<i>Bcl-2</i>	- <u>B</u> -cell lymphoma <u>2</u>
<i>Bid</i>	- <u>B</u> H3 <u>i</u> nteracting- <u>d</u> omain death agonis
<i>bi-shRNA</i>	- <u>b</u> ifunctional <u>s</u> hort <u>h</u> airpin <u>R</u> NA
<i>CAB-box</i>	- <u>C</u> ajal <u>b</u> ody <u>b</u> ox sequence
<i>CADD</i>	- <u>c</u> omputer- <u>a</u> ided <u>d</u> rug <u>d</u> esign
<i>Cas</i>	- <u>C</u> RISPR- <u>a</u> ssociated
<i>CETSA</i>	- <u>c</u> ellular <u>t</u> hermal <u>s</u> hift <u>a</u> ssay





<i>Chk1</i>	- <u>check</u> point <u>kin</u> ase <u>1</u>
<i>Chk2</i>	- <u>check</u> point <u>kin</u> ase <u>2</u>
<i>CPT</i>	- <u>campto</u> <u>thec</u> in
<i>CRISPR</i>	- <u>cl</u> ustered <u>reg</u> ularly <u>int</u> erspaced <u>sh</u> ort <u>pal</u> indromic <u>rep</u> eat
<i>CTTN</i>	- <u>co</u> rtact <u>in</u>
<i>CQ</i>	- <u>ch</u> loro <u>qu</u> ine
<i>DABCO</i>	- 1,4- <u>dia</u> zab <u>icy</u> clo[2.2.2] <u>oc</u> tane
<i>DAT</i>	- <u>do</u> ma <u>in</u> of h <u>T</u> ERT
<i>DAXX</i>	- <u>de</u> ath domain <u>as</u> sociated protein
<i>DDR</i>	- <u>D</u> NA <u>da</u> mage <u>re</u> sponse
<i>DKC1</i>	- <u>dy</u> s <u>ker</u> in pseudouridine synthase <u>1</u>
<i>DOX</i>	- <u>do</u> xorubicin
<i>DSB</i>	- <u>do</u> uble- <u>st</u> randed <u>br</u> eak
<i>dsRNA</i>	- <u>do</u> uble- <u>st</u> randed <u>R</u> NA
<i>EGF</i>	- <u>ep</u> idermal <u>gr</u> owth <u>fa</u> ctor
<i>ELISA</i>	- <u>en</u> zyme- <u>li</u> nked <u>im</u> munosorbent <u>as</u> say
<i>EMA</i>	- <u>E</u> uropean <u>M</u> edicines <u>A</u> gency
<i>EMT</i>	- <u>ep</u> ithelial- <u>me</u> senchymal <u>tr</u> ansition
<i>ER</i>	- <u>en</u> doplasmic <u>re</u> ticulum
<i>ETP</i>	- <u>et</u> oposide
<i>ETS</i>	- <u>E</u> - <u>tw</u> enty- <u>s</u> ix
<i>FADD</i>	- <u>F</u> AS- <u>as</u> sociated <u>de</u> ath <u>do</u> main protein
<i>GAR1</i>	- <u>gl</u> ycine <u>ar</u> ginine <u>ri</u> ch <u>1</u>
<i>GLB1</i>	- <u>ga</u> lactosidase <u>be</u> ta <u>1</u>
<i>G-4</i>	- <u>G</u> -quadruplex
<i>gRNA</i>	- <u>gu</u> ide <u>R</u> NA
<i>HDR</i>	- <u>h</u> omology- <u>di</u> rected <u>re</u> pair
<i>hTERT</i>	- <u>h</u> uman <u>te</u> lomerase <u>re</u> verse <u>tr</u> anscriptase
<i>HPLC-MS</i>	- <u>h</u> igh- <u>pe</u> formance <u>li</u> quid <u>ch</u> romatography - <u>ma</u> ss <u>sp</u> ectrometry



<i>HRP</i>	- <u>h</u> orse <u>r</u> adish <u>p</u> eroxidase
<i>HUVEC</i>	- <u>h</u> uman <u>u</u> mbilical <u>v</u> ein <u>e</u> ndothelial <u>c</u> ells
<i>LC3</i>	- microtubule-associated protein <u>l</u> ight <u>c</u> hain <u>3</u>
<i>LNA</i>	- <u>l</u> ocked <u>n</u> ucleic <u>a</u> cid
<i>LS</i>	- <u>l</u> ow <u>s</u> erum
<i>MAD1</i>	- <u>m</u> itotic <u>a</u> rrest <u>d</u> eficient <u>1</u>
<i>MCC</i>	- <u>M</u> ander's <u>c</u> orrelation <u>c</u> oefficient
<i>MDR</i>	- <u>m</u> ultidrug <u>r</u> esistance
<i>MCP-1</i>	- <u>m</u> onocyte <u>c</u> hemoattractant <u>p</u> rotein <u>1</u>
<i>MHC</i>	- <u>m</u> ajor <u>h</u> istocompatibility <u>c</u> omplex
<i>miRNA</i>	- <u>m</u> icro <u>R</u> NA
<i>MMP</i>	- <u>m</u> atrix <u>m</u> etalloproteinases
<i>MOMP</i>	- <u>m</u> itochondrial <u>o</u> uter <u>m</u> embrane <u>p</u> ermeabilization
<i>mPTP</i>	- <u>m</u> itochondrial <u>p</u> ermeability <u>t</u> ransition <u>p</u> ore
<i>MTT</i>	- 3-(4,5-Di <u>m</u> ethylthiazol-2-yl)-2,5-Diphenyl <u>t</u> etrazolium Bromide
<i>MTX</i>	- <u>m</u> itox <u>a</u> ntrone
<i>MZT</i>	- <u>m</u> yeloid <u>z</u> inc <u>f</u> inger protein
<i>NAC</i>	- <u>N</u> - <u>a</u> cetyl <u>c</u> ysteine
<i>NAF1</i>	- <u>n</u> uclear <u>a</u> ssembly <u>f</u> actor <u>1</u> ribonucleoprotein
<i>ND1</i>	- <u>N</u> <u>A</u> <u>D</u> H:ubiquinone oxidoreductase subunit <u>1</u>
<i>ND2</i>	- <u>N</u> <u>A</u> <u>D</u> H:ubiquinone oxidoreductase subunit <u>2</u>
<i>NF-κB</i>	- <u>n</u> uclear <u>f</u> actor <u>κ</u> appa-light-chain-enhancer of activated <u>B</u> cells
<i>NHBE</i>	- <u>n</u> ormal <u>b</u> ronchial <u>e</u> pithelial cells
<i>NHEJ</i>	- <u>n</u> on- <u>h</u> omology <u>e</u> nd joining
<i>NHP2</i>	- <u>n</u> on- <u>h</u> istone chromosome <u>p</u> rotein <u>2</u>
<i>NOP10</i>	- <u>n</u> ucleolar <u>p</u> rotein <u>10</u>
<i>NSCLC</i>	- <u>n</u> on- <u>s</u> mall <u>c</u> ell <u>l</u> ung <u>c</u> arcinoma
<i>LAMP1</i>	- lysosomal <u>a</u> ssociated <u>m</u> embrane <u>p</u> rotein <u>1</u>
<i>PARP</i>	- poly( <u>A</u> PD- <u>r</u> ibose) <u>p</u> olymerase



<i>PCC</i>	- <u>P</u> earson's <u>c</u> orrelation <u>c</u> oefficient
<i>PE</i>	- <u>p</u> hosphatidylethanolamine
<i>PFA</i>	- <u>p</u> ara <u>f</u> ormal <u>d</u> e <u>h</u> yd <u>e</u>
<i>PI</i>	- <u>p</u> ropidium <u>i</u> odide
<i>PN</i>	- <u>p</u> hosphoramidates
<i>PNA</i>	- <u>p</u> eptide <u>n</u> ucleic <u>a</u> cids
<i>POT1</i>	- <u>p</u> rotection <u>o</u> f <u>t</u> elomeres <u>1</u>
<i>PS</i>	- <u>p</u> hosphorothioate
<i>PTK</i>	- <u>p</u> rotein tyrosine <u>k</u> inase
<i>RAP1</i>	- <u>r</u> epressor- <u>a</u> ctivator <u>p</u> rotein <u>1</u>
<i>RISC</i>	- <u>R</u> NA- <u>i</u> nduced <u>s</u> ilencing <u>c</u> omplex
<i>ROS</i>	- <u>r</u> eactive <u>o</u> xygen <u>s</u> pecies
<i>RNAi</i>	- <u>R</u> NA <u>i</u> nterference
<i>RT</i>	- <u>r</u> oom <u>t</u> emperature
<i>RT-PCR</i>	- <u>r</u> everse- <u>t</u> ranscription <u>p</u> olymerase <u>c</u> hain <u>r</u> eaction
<i>SA-β-gal</i>	- <u>s</u> enescence- <u>a</u> ssoiated <u>β</u> - <u>g</u> alactosidase
<i>SIPS</i>	- <u>s</u> tress- <u>i</u> nduced <u>p</u> remature <u>s</u> enescence
<i>siRNA</i>	- <u>s</u> hort <u>i</u> nterference <u>R</u> NA
<i>shRNA</i>	- <u>s</u> hort <u>h</u> airpin <u>R</u> NA
<i>SRSF11</i>	- <u>s</u> erine and <u>a</u> rginine-rich <u>s</u> plicing <u>f</u> actor <u>11</u>
<i>STAT</i>	- <u>s</u> ignal <u>t</u> ransducer and <u>a</u> ctivator of <u>t</u> ranscription
<i>SWI/SNF</i>	- <u>S</u> W <u>I</u> tch/ <u>s</u> ucrose <u>n</u> on-fermentable
<i>TAGE</i>	- <u>t</u> elomerase- <u>a</u> ctivating <u>g</u> ene <u>e</u> xpression
<i>TBE</i>	- <u>t</u> emplate <u>b</u> oundary <u>e</u> lement
<i>TCAB1</i>	- <u>t</u> elomerase <u>C</u> ajal <u>b</u> ody protein <u>1</u>
<i>TERRA</i>	- <u>t</u> elomeric <u>r</u> epeat-containing <u>R</u> NA
<i>THOR</i>	- <u>h</u> TERT <u>h</u> ypermethylated <u>o</u> ncological <u>r</u> egion
<i>TIN2</i>	- <u>T</u> RF1- <u>i</u> nteracting <u>n</u> uclear protein <u>2</u>
<i>TME</i>	- <u>t</u> umour <u>m</u> icro <u>e</u> nvironment



- TPP1* - TIN2- and POT1-organizing protein
- TRF1* - telomeric repeat-binding factor 1
- TRF2* - telomeric repeat-binding factor 2
- VINC* - vincristine
- VEGF* - vascular endothelial growth factor
- WHO* - World Health Organization
- WT1* - Wilms' tumour 1

# 1. INTRODUCTION

## 1.1. *The outline of the cancer problem and drug discovery process*

Cancer is characterized by rapid, uncontrolled growth of cells that can invade surrounding tissues and may spread from its site of origin to other parts of the body, serving serious health consequences including death. The World Health Organization (WHO) states that in 2020 cancer was the second leading cause of death behind cardiovascular diseases which caused over 9.96 million deaths globally.<sup>1</sup> The estimated increase in the number of cancer-related deaths is even larger and is expected to be about 16.3 million deaths worldwide in 2040. The most diagnosed cancers are those of the breast (2.3 million, 11.7% of the total number), lung (2.2 million, 11.4%), colorectal (1.9 million, 10%), and prostate (1.4 million, 7.3%).<sup>2</sup> The continuous increase in cancer incidence in developed countries is associated with ageing and the growth of the world's population as well as pollution. Several major factors have been associated with carcinogenesis such as certain chemicals in the environment, sunlight, lifestyle, and genetic predispositions.<sup>3</sup> Along with surgical operation and radiation therapy, chemotherapy remains the main approach to cancer treatment.<sup>4</sup>

The development of cancer chemotherapy began in the 1940s with the discovery of mustine hydrochloride, as an alkylating agent.<sup>5</sup> Since then, the use of chemotherapy in both advanced and early stages of cancer has made significant progress in the last decades. According to the cancer drugs database, 259 anticancer drugs have been approved by the European Medicines Agency (EMA) for treating various types of cancer.<sup>6</sup> Accomplishing an ideal drug development is still demanding and requires an analysis of different aspects because the therapeutic efficacy of the drug is affected by its biological activity, bioavailability, toxicity, and many other factors. The effective drug should target differences between cancer and normal cell; however, elaborating on new anticancer agents based on the discovery of new targets is relatively rare, especially nowadays. This is because many anticancer targets have already been discovered and explored.<sup>7,8</sup> It is also worth underlining that classical methods of searching for new drugs effective against new or old targets are often insufficient due to their side effects and induction of resistance. Furthermore, these approaches are associated with high costs and a very long process of implementation in treatment (clinical studies).<sup>9</sup>

The availability of crystallographic data for many proteins essential for disease development and documented as molecular targets have led to the emergence of a new approach to designing drugs tailored for the structure of particular receptor (target) binding sites.<sup>10</sup> Therefore, the pharmaceutical industry has seen a clear upward trend in the process of discovery of new drug substances over the past decade through rationalized drug design. The dynamic growth of computing power, the efficiency of new and fast algorithms, as well as application of specialized programming technology, have contributed to the development of computer-aided drug design (CADD) technology based on molecular modelling, bioinformatics, and cheminformatics techniques.<sup>11</sup>

Molecular modelling of small molecules binding protein sites was pioneered during the early 1980s and has been used to predict the intermolecular framework to the present day.<sup>12,13</sup> It encompasses all theoretical and computational techniques used to predict drug efficacy. Molecular docking, molecular dynamic simulation, and ADMET (absorption, distribution, metabolism, excretion, and toxicity) prediction represent the most widely used approaches of computational modelling used in the drug discovery and design process.<sup>14</sup> The typical approach involves structure-based virtual screening through docking in order to identify potential hit candidates with the highest binding affinity and correct binding mode.<sup>15</sup> Starting from a compound with a known mechanism of action and biological activity (discovered in the screening process and called “hit molecule”), it is possible to design related molecules as drug candidates with better efficacy and fewer side effects (lead optimization). Another approach is based on the *de novo* design of a new molecule interacting with a particular target.<sup>16</sup> In this approach, a broader chemical space can be explored, applying scaffold hopping or fragment-based design.<sup>16</sup> Molecular modelling is crucial to preselect and help lead experimental *in vitro* and *in vivo* studies, reducing the cost and time required for the development of effective drugs.<sup>17</sup>

The ideal molecular drug target should exhibit high specificity to cancer cells, which minimalizes adverse effects on normal cells after treatment. According to many previous studies as well as expectations, the target that fulfils this requirement is telomerase, which is expressed and activated in almost all types of tumours but is silent in the majority of human tissue.<sup>18</sup> However, although several strategies of telomerase inhibition have been already developed and explored, there are not enough successful results, and therefore there is still a need and a place for new strategies and new molecules – directed as telomerase inhibitors. It is particularly important as until now none of the initially promising molecules acting at this target has been developed up to the drug stage.<sup>19–22</sup>

### **1.2. Telomeres – structure, and function**

Telomeres are nucleoprotein complexes composed of tandem repeating DNA sequences, and specialized proteins essential for protection and genomic stability. In humans, the DNA telomeric sequence is (TTAGGG)*n*, and is highly conserved among vertebrates.<sup>23</sup> Telomeric DNA structure is protected by a six-subunit protein complex called shelters – comprised of telomeric repeat-binding factor 1 (TRF1), telomeric repeat-binding factor 2 (TRF2), repressor-activator protein 1 (RAP1), TRF1-interacting nuclear protein 2 (TIN2), TIN2- and POT1-organizing protein (TPP1), and protection of telomeres 1 (POT1). TRF1 and TRF2 are homodimers that directly bind to the double-stranded telomeric DNA, whereas POT1 is associated with single-stranded telomeric DNA. POT1 is linked to TRF1 and TRF2 through an interaction between the TPP1 and TIN2, which binds both TRF1 and TRF2. The sixth shelterin subunit, RAP1 is recruited to telomeres via interaction with TRF2. The spatial arrangement of shelterin proteins is presented in **Figure 1**.<sup>24,25</sup>

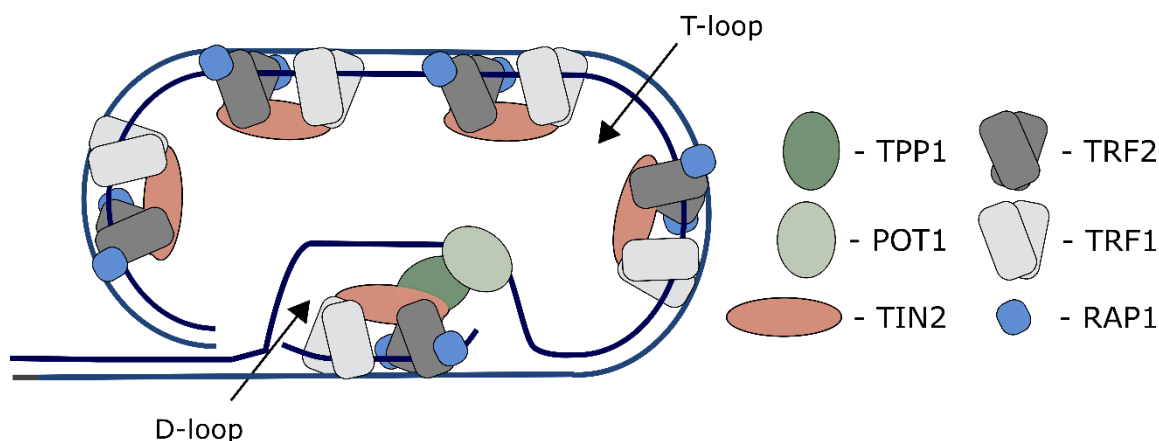


**Figure 1** The spatial arrangement of shelterin.<sup>24,25</sup>

Each shelterin subunit has essential functions contributing to the genome's stability and end-of-chromosome protection but also displays roles aside from their role as telomeric subunit, like regulating the DNA damage response, metabolism, inflammation, oxidative stress, and many others.<sup>26</sup>

TRF1 precipitates in sister telomere cohesion, chromosome end protection, DNA damage response, telomere transcription, and replication.<sup>27</sup> The activity of the TRF2 blocks ataxia telangiectasia mutated (ATM) DNA-damage signalling pathway and non-homology end joining (NHEJ) repair pathway, protecting telomeres from recognition as double-stranded DNA breaks. In addition, TRF2 influences the folding of telomeric DNA into a telomere loop structure called a t-loop.<sup>28</sup> T-loops are formed by the invasion of the single-stranded 3' DNA telomeric overhangs into duplex strands, forming a d-loop. Such spatial displacement prevents DNA damage response machinery from recognizing DNA ends as damage.<sup>29,30</sup>

The telomere G-rich strand binding protein POT1 interacts with TPP1 forming a stable heterodimer that represses the response to ATR kinase-mediated DNA damage and inhibits telomerase-dependent telomere extension.<sup>31</sup> The ATR DNA repair pathway also could be blocked by TRF2 but independently of POT1 activity.<sup>32</sup>

The TIN2 subunit promotes TPP1/POT1 localization and stabilizes bindings of TRF1 and TRF2 with telomeric DNA. It is essential for the overall integrity of the shelterin complex because of creating a molecular bridge or platform by simultaneous interaction with TRF1, TRF2, and TPP1.<sup>33</sup> Moreover, TIN2 facilitates TRF2-mediated higher-order DNA structures, such as telomeric DNA compaction, t-loop formation, and bridging of dsDNA, ssDNA, and ssRNA (TERRA) to dsDNA.<sup>34</sup>

Among telomeric proteins, RAP1 is the most conserved. Its function is repressing homologous recombination in cooperation with TRF2 and is particularly important in senescent cells protecting critically short telomeres from DNA damage.<sup>35</sup>

### 1.3. The role of telomeres in cellular senescence and carcinogenesis

In humans, the chromosome length distribution in different cells is heterogeneous and ranges from 5 to 15 kbp.<sup>36</sup> Telomere shortening is a dynamic process and depends on the mechanisms involved in the DNA replication process known as the end replication problem (**Figure 2**). DNA polymerase synthesizes the leading strand only in the 5' to 3' direction and requires the presence of a polynucleotide primer to initiate the synthesis of a new DNA strand. The process is semi-conservative, which means that one of the leading strands is synthesized continuously (5'→ 3'), and the other is delayed (3'→ 5'). In the case of the lagging strand, the polymerase synthesizes short sections, called Okazaki fragments, each with its primer. During replication termination, primers are removed, and the resulting fragments are ligated.<sup>37</sup> However, the polymerase cannot fill the gap at the 3' end, making the newly synthesized daughter strand shorter than the parent strand, causing the chromosome to shorten by 50 - 150 bp with each cell division.<sup>38</sup>

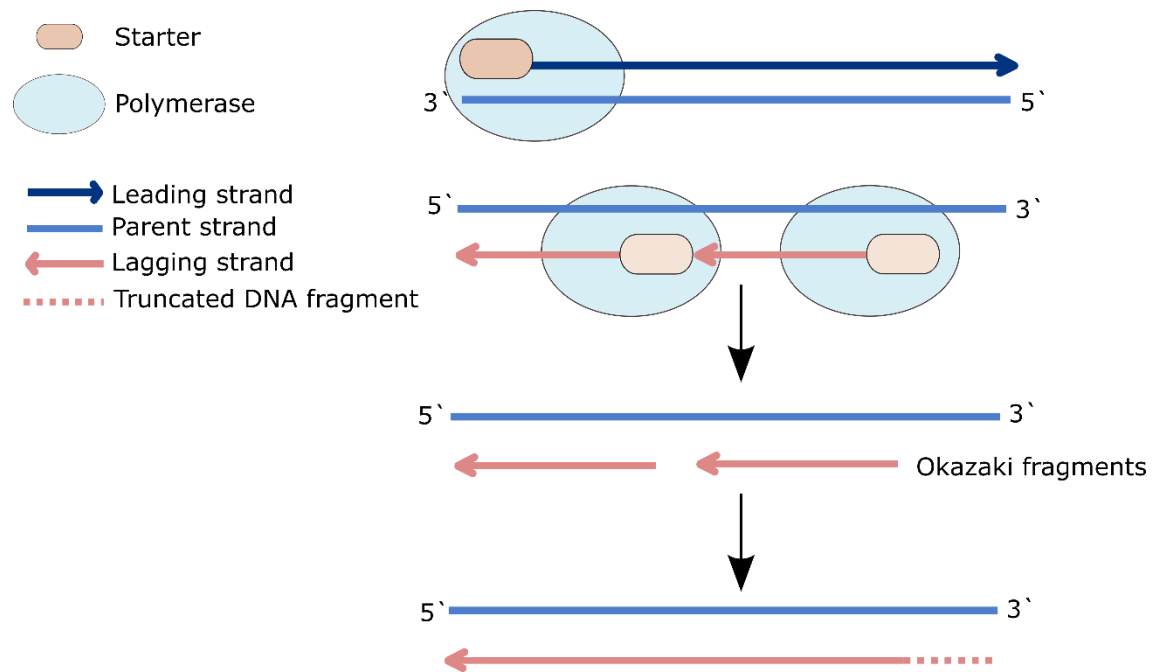


**Figure 2** The end replication problem.

Telomere shortening eventually promotes genome instability, potentially stimulating the initiation of the early stages of cancer.<sup>39</sup> The natural barrier that prevents cells from entering neoplastic transformation is replicative senescence, the so-called Hayflick limit. The Hayflick phenomenon refers to the maximum number of divisions that a somatic cell can undergo during its lifespan.<sup>38</sup> Upon reaching a sub-threshold number of repeats, cells enter the M2 stage, characterized by uncapped telomeres, chromosome breakage fusion–bridge cycles, end-to-end chromosome fusions, mitotic catastrophe, and apoptosis.<sup>40,41</sup>

In the case of aberrations, the accumulation of chromosomal rearrangements and mutations may lead to cell immortalization.<sup>42</sup> Maintenance of telomere length in cancer requires activation of a telomerase enzyme or activation of an alternative length telomere (ALT) independent of telomerase.<sup>43</sup> Telomerase and specifically its catalytic subunit hTERT is expressed and



activated in 85-90% of cancers; whereas other tumours promote telomere DNA synthesis via the ALT pathway based on a recombination-based mechanism.<sup>44-46</sup> ALT phenotype is characterized by a reduced nucleosome density caused by alterations in chromatin remodelling factors, such as alpha-thalassemia X-linked syndrome protein (ATRX) and deletion of death-associated protein (DAXX).<sup>47,48</sup> One of the hallmarks of ALT cells is excessively clustered telomeres caused by DNA damage response (DDR) which promotes homology-directed telomere synthesis to gain an unlimited proliferation potential for cancers.<sup>49</sup>

#### **1.4. Structure of telomerase**

Telomerase is a large ribonucleoprotein complex responsible for the synthesis of TTAGGG repeats at the 3' ends of linear chromosomes by reverse transcription. This enzyme is composed of the reverse transcriptase subunit hTERT, the template containing non-coding RNA hTERC, and accessory proteins.<sup>50</sup> Additional processive extension of telomeres requires binding telomerase to telomeric DNA which is properly maintained through the shelterin complex. The hTERT gene is located at chromosome 5p15.33 and encodes the catalytic subunit of the hTERT holoenzyme. The hTERC gene is mapped at chromosome 3q26 and acts as a template for the synthesis of telomeric DNA. Moreover, it participates in the catalysis, localization, and assembly of the telomerase holoenzyme.<sup>38</sup> The hTERC is expressed in all tissues, while hTERT is generally repressed in normal cells and upregulated in cancer cells. Therefore, hTERT is a critical determinant of telomerase activity, responsible for the synthesis of telomeric DNA repeats.<sup>51</sup>

Human TERC contains several structural regions: template boundary element (TBE) pseudoknot domain, a CR4/CR5 domain, and H/ACA box; however, only the pseudoknot and CR4-CR5 domains are necessary for telomerase activity.<sup>52</sup> The H/ACA RNAs associate with a set of proteins, together acting as ribonucleoprotein (RNP) enzymes mainly in the site-specific pseudouridylation reside in the small Cajal body and small nuclear RNAs.<sup>53</sup> In addition, the H/ACA box at the TERC 3' end contains a Cajal body box sequence (CAB-box) which binds a telomerase Cajal body protein 1 (TCAB1) and facilitates telomerase trafficking to Cajal bodies (**Figure 3**).<sup>54</sup> Despite telomerase accumulating in Cajal bodies for most of the cell cycle, their function concerning telomerase remains unexplained. The H/ACA box binds accessory proteins, including dyskerin (DKC1), non-histone chromosome protein 2 (NHP2), nucleolar protein 10 (NOP10), and glycine arginine rich 1 (GAR1) which are essential for maturation, stability, and cellular localization of the enzyme.<sup>55</sup> Other proteins, such as heat shock proteins HSP90 and HSP23, as well as ATPases pontin and reptin, also bind to the two major telomerase subunits and are believed to be involved in the formation of a functional telomerase holoenzyme, but the exact mechanism of their action remains poorly understood.<sup>56</sup> Dyskerin, pontin, and reptin serve as the scaffold for assembling the nascent hTERT transcripts through interaction with the H/ACA motif-binding complex of dyskerin, NHP2, NOP10, a nuclear assembly factor 1 ribonucleoprotein (NAF1), and the telomerase RNP.<sup>57</sup> Next, hTERT undergoes maturation accompanied by an exchange of NAF1 for GAR1, leading to the formation of physiologically stable hTERT H/ACA RNP.

Then, the hTERT 3' -hairpin CAB-box motif binds TCAB1, and hTERT interacts with CR4/CR5 domains generating a catalytically active RNP telomerase.<sup>58</sup>

Telomerase is recruited to telomeres during the S phase of the cell cycle, and involves interactions between TPP1, POT1, and dissociates the activities of the telomerase domain of hTERT (DAT).<sup>41</sup> TPP1 contains the oligosaccharide binding (OB)-fold domain that includes a group of amino acids, defined as the TEL-patch, which interacts with the DAT region.<sup>57</sup> The central domain of TPP1 binds to POT1, whereas the C-terminal motif interacts with TIN2. Interaction between shelterin subunits and the DAT domain of hTERT assures proper positioning of telomerase at the 3' ends of DNA for the synthesis of telomeric DNA. Moreover, a TERC-binding protein (SRSF11) is associated with telomeres through the interaction with TRF2 stabilizing the telomerase with the telomere overhang for DNA synthesis.<sup>59</sup>

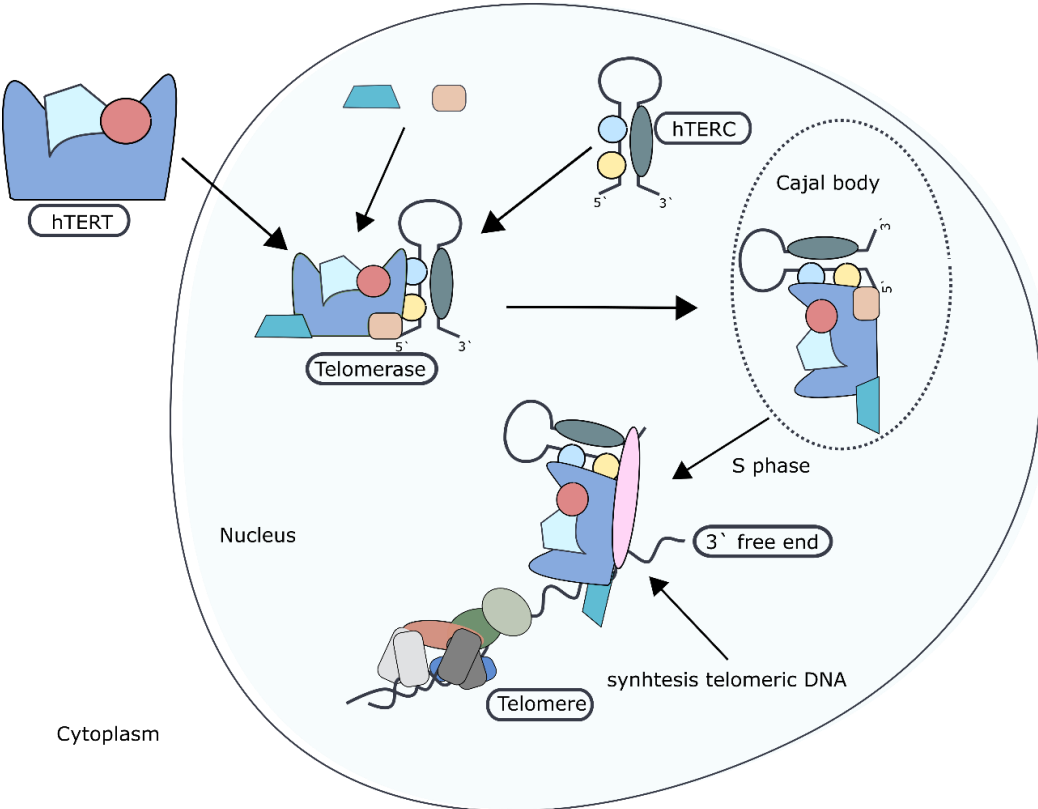
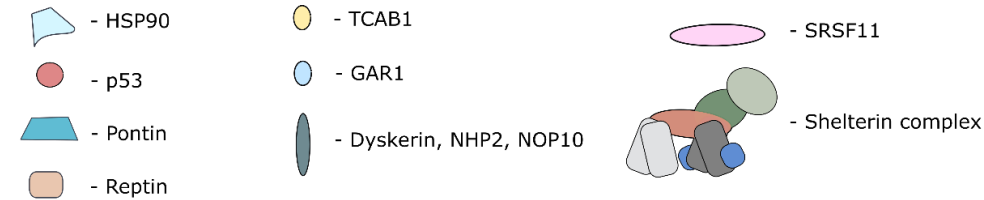


**Figure 3** Telomerase assembly and recruitment to the telomere.<sup>54</sup>

### 1.5. *hTERT* promoter mutations and activation of telomerase

*hTERT* is a 42 kb gene located on the short arm of the human chromosome 5 (5 p15.33) and spans 15 introns and 16 exons.<sup>60</sup> The *hTERT* promoter is rich in GC pair, lacks CAAT and TATA boxes, but contains binding sites for many transcription factors including the MYC oncogene (E-box) and Sp1 (GC box). Most of the transcriptional activity is related to the proximal region of the *hTERT* promoter and contains GC-boxes (GGGCGG), which are binding sites for the zinc finger transcription factor Sp1 and are important for *hTERT* promoter activity.<sup>61</sup>

The *hTERT* promoter contains two E-box motifs (5'-CACGTG-3') located at positions -165 and +44 which are required for binding several proteins like Myc/Mac/Mad and USF1/2. C-myc expression triggers a switch from Mas1/Max to c-Myc/Max binding to E-boxes on an *hTERT* promoter, inducing *hTERT* expression and telomerase activation. Interestingly, the promoter also contains repressor binding sites.<sup>62</sup> Another unique feature is that the *hTERT* promoter is unmethylated in normal cells, while its methylation is required for *hTERT* expression and telomerase activation in malignant cells.<sup>63</sup> Lee et al. reported that the *hTERT* Hypermethylated Oncological Region (THOR) is composed of 52 CpG sites, located further away from the core promoter, suggesting an epigenetic-based *hTERT* upregulation.<sup>64</sup> Interestingly, several reports evidenced that the unmethylated promoter sequence favours a repressor-binding in several cell lines.<sup>59,65</sup>

The transcription of the *hTERT* promoter is regulated by the interplay of many transcription factors and chromatin remodelling, leading to either activating or downregulating *hTERT* transcription. Transcription factors such as c-MYC, nuclear factor  $\kappa$ -light-chain-enhancer of activated B cells (NF- $\kappa$ B), specificity protein 1, the adipocyte protein 2 (AP-2) family, E-twenty-six (ETS) family members, and signal transducer and activator of transcription (STAT) family upregulate *hTERT* expression, whereas p53, Wilms' tumour 1 (WT1), mitotic arrest deficient 1 (MAD1), myeloid zinc finger protein (MZF)-2, and menin have been shown to repress *hTERT* transcription (**Figure 4**).<sup>66</sup> Most of the activator transcription factors regulate *hTERT* expression in tumours and normal cells and thus cannot fully account for *hTERT* upregulation and telomerase activation during carcinogenesis.<sup>67</sup>

One possible mechanism of telomerase activation involves mutations in the core promoter region of *hTERT*. These mutations occur predominantly at two hotspots of chromosome 5 at positions -124 and -146, known as 1 295 228 C>T (C228T), and 1 295 250 C>T (C250T9), respectively.<sup>68</sup> Both mutations create an 11 bp nucleotide stretch harbouring a consensus binding motif for ETS transcription family members, such as the GA-binding protein (GABP).<sup>69</sup> These ETS-binding sites are functionally distinct and required for transactivation *hTERT*, dimer formation with other transcription factors, like p52. Although the C250T mutation, unlike the C228T mutation, is driven by non-canonical NF- $\kappa$ B signalling, the exact mechanism of *hTERT* activation has not been fully understood.<sup>68</sup> Hsu et al. demonstrated that epidermal growth factor (EGF) in lung cancer activates telomerase by direct binding transcription factor ETS-2 to the *hTERT* promoter.<sup>70</sup>

These mutations were found in 60% of bladder cancers, 80–90% of glioblastomas, 50% of cutaneous squamous cell carcinomas, 70% of melanomas, 60% of hepatocellular carcinomas, 70% of oligodendrogliomas, and approximately 30% of thyroid cancers.<sup>71–73</sup> Additionally, on chromosome 5, there is a rarer mutation in the *hTERT* promoter, -57 bp upstream of the ATG start site, causing the A>C transition.<sup>72</sup>

Noncoding mutations of *hTERT* are the most prevalent in cancers, but their frequency and level are different depending on the tumour type. Some cancers, such as glioma, pleomorphic dermal sarcoma, liver cancer, myxoid liposarcoma, urothelial cell carcinoma, and melanoma are characterized by relatively frequent mutations in the *hTERT* promoter, while the low frequency was observed in small cell lung carcinoma, pancreatic cancer, gastric cancer, and gastrointestinal stromal tumours.<sup>72,74,75</sup> One possible explanation for these observations may be that incipient cancer cells, derived from renewing self-renewing telomerase-competent cells, do not require mutation in the *hTERT* promoter to regulate telomere length. Thus, tumours arising from rapidly proliferating cells tend to just upregulate enzyme activity with fewer mutations in the *hTERT* promoter.<sup>76</sup> Considering whether these mutations occur most frequently at the time cells undergo a "crisis" will help establish the role of these mutations as early events in the process of neoplastic transformation.

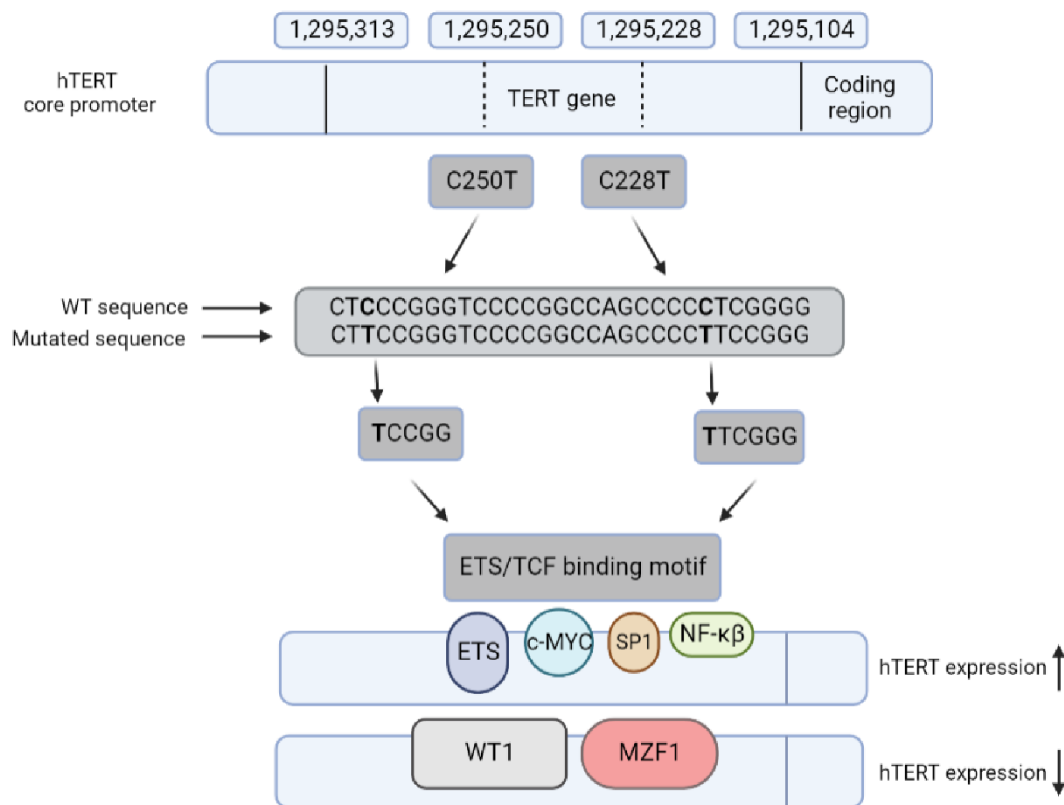


**Figure 4** Transcription and mutations of *hTERT* promoter.<sup>77</sup>

Regulation of telomerase expression occurs through the control transcriptional, post-transcriptional, and epigenetic levels in various processes, like mRNA splicing, telomerase nuclear localization, recruitment to telomeres, *hTERT*, and *hTERT* synthesis and maturation,

and post-translational modification.<sup>78</sup> Epigenetic regulation of *hTERT* transcription includes chromatin remodelling, DNA methylation, and histone modification.<sup>79,80</sup> Alternative *hTERT* mRNA splicing is a key mechanism of post-transcriptional regulation, but it remains unclear whether telomerase activity is directly related to *hTERT* splicing.<sup>81</sup>

### 1.6. Non-canonical functions of telomerase

The main, canonical function of telomerase is to maintain a constant telomere length in tumour cells during mitotic divisions to overcome the Hayflick limit. Therefore, this enzyme plays a key role in cancer metabolism, senescence, and degenerative disease. However, several studies report other, non-canonical functions beyond telomere lengthening. These extra-telomeric functions of *hTERT* include cell survival, chromatin modulation, transcriptional regulation of gene expression, mitochondrial metabolism, and stress response (**Figure 5**).<sup>82,83</sup> It has been shown that the catalytic subunit of *hTERT* telomerase, apart from its nuclear location, is also present in the cytoplasm and mitochondria, which is related to its extra-telomeric functions.<sup>57</sup> In mitochondria, the enzyme is responsible for reducing the level of reactive oxygen species (ROS), binding mitochondrial DNA and tRNA, and is associated with the increased potential of the mitochondrial membrane and the activity of the respiratory chain.<sup>84</sup> Understanding the non-canonical functions of telomerase may have important implications for the rational design of anti-cancer agents.

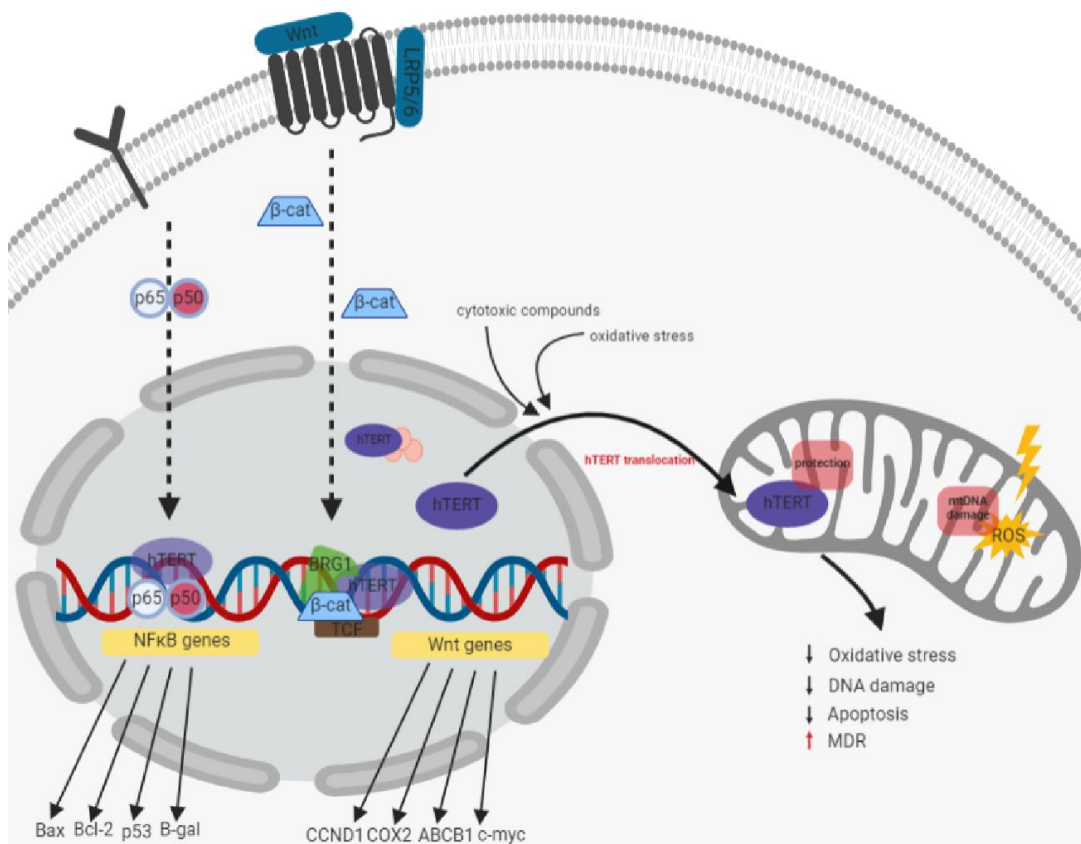


**Figure 5** Mitochondrial *hTERT*.<sup>85</sup>

### 1.6.1. Mitochondrial hTERT

Telomere shortening can directly lead to senescence, but this process could be triggered by other factors such as oxidative stress or inflammation.<sup>86</sup> This suggests a correlation between these processes, but the function of telomerase in reducing the effects of oxidative stress remains unclear. One possible hypothesis is that telomeres are the preferred targets for oxidative damage due to the presence of many guanine residues in DNA sequences. High guanine content is associated with the production of 8-oxoguanine (8-oxoG), which, if left unrepaired, leads to mutations, and thus genome instability.<sup>87</sup> It has been demonstrated that mitochondria in normal and cancer cells contain telomerase enzymatic activity.<sup>88</sup> hTERT interacts with two regions of circular mtDNA containing coding sequences for NADH: ubiquinone oxidoreductase (complex I) subunits 1 and 2 (ND1, ND2); however it remains unclear whether protection of ND1 and ND2 subunit genes by hTERT is sufficient for reducing complex I produced ROS.<sup>89</sup> Miao et al. reported that tumour cells with dysfunctional telomerase were more sensitive after radiation exposure.<sup>90</sup> hTERT suppression induced mitochondrial dysfunction, which was evidenced by decreased membrane potential, changes in mitochondrial mass, mtDNA copy number, total ATP levels, and an increase in ROS.<sup>90</sup> Muzza et al. reported that high oxidative stress (H<sub>2</sub>O<sub>2</sub>) triggers the translocation of hTERT to mitochondria.<sup>91</sup> Similarly, Singhapol et al. showed that telomerase reduces mtDNA damage induced by UV and ethidium bromide.<sup>92</sup> Interestingly, cells with mutated, dysfunctional hTERT displayed increased levels of ROS and disruption in mitochondrial functions.<sup>93</sup>

The protective effect of the mitochondrial translocation of hTERT has a particularly important role in the multi-drug resistance (MDR) of cancer cells.<sup>94</sup> Ling et al. reported that mitochondrial translocation of hTERT led to chemotherapeutic resistance in hepatocellular carcinoma.<sup>95</sup> The drug-resistance cells have lower mitochondrial membrane potential, a reduced ROS level, and are less prone to oxidative damage to mtDNA.<sup>95</sup> Another study demonstrated that mitochondrial hTERT exerts a neuroprotective role due to the induction of cell proliferation, antioxidant properties, and inhibiting apoptosis and senescence.<sup>96</sup> The catalytic subunit of telomerase may also protect the neonatal mitochondrial DNA from oxidative damage during pregnancy.<sup>97</sup> However, there is still no confirmation as to whether hTERT is necessary for the proper functioning of mitochondria or whether it is activated only under conditions of cellular stress.

### 1.6.2. Telomerase as a regulator of gene expression - Wnt/ $\beta$ -catenin complex

The Wnt/ $\beta$ -catenin signalling pathway is a regulator of embryogenesis and is responsible for the self-renewal of adult stem cells in proliferating tissues such as the gut, hair follicle, and the hematopoietic system. Deregulation of the Wnt/ $\beta$ -catenin signalling cascade is one of the key mechanisms responsible for cell proliferation and differentiation and is often associated with the pathogenesis of a variety of diseases, including cancer.<sup>98</sup> The first evidence of direct regulation of the Wnt/ $\beta$ -catenin by telomerase was discovered by J.I. Park and colleagues



in mouse embryonic stem cells and *Xenopus laevis* embryos.<sup>99</sup> The study reported that hTERT acts as a cofactor in the  $\beta$ -catenin transcription complex through interaction with BRG1, an SWI/SNF (SWItch/sucrose non-fermentable) chromatin remodelling factor. hTERT overexpression resulted in the activation of Wnt-dependent reporters *in vitro* and *in vivo*.<sup>99</sup> Other studies also support the formation of an hTERT complex with BRG1 together with nucleostemin, a GTP nuclear binding protein, and/or GNL3L. It was found that such a complex is necessary to maintain a tumour-initiating cell phenotype.<sup>100</sup> However, the research conducted by E.H. Blackburn's group showed no interaction between hTERT and Brg1 or  $\beta$ -catenin.<sup>101</sup> Those discrepancies in the above studies can be explained by differences in the cell lines and mouse models, or that the Wnt/ $\beta$ -catenin pathway is regulated by two mechanisms employed by hTERT and mTERT, respectively.

The correlation between the Wnt pathway and telomerase also confirms the influence of both factors in embryonic development and tissue homeostasis. It has been shown that transient activation of the Wnt/ $\beta$ -catenin pathway induces hTERT mRNA expression and increases telomerase activity in various cell lines. Moreover,  $\beta$ -catenin could also directly regulate the transcription of hTERT, by interacting with KLF4.<sup>102</sup>

The role of telomerase in Wnt signalling should be seen as case-specific and particularly important in cancers with disrupted multiple signalling pathways simultaneously, such as NF- $\kappa$ B and Wnt. Moreover, the discovery of the regulation of telomerase transcription in embryonic stem cells and human cancer cells via the Wnt/ $\beta$ -catenin pathway further emphasizes the importance of regulatory feedback, which ensures telomerase activity and enhances oncogenic signalling.<sup>103</sup>

These observations reveal the non-canonical function of telomerase as a key component of the regulatory Wnt/ $\beta$ -catenin transcription complex. This synergistic role of the enzyme with the transcriptional activity of the complex is independent of its catalytic function in telomeres.

#### 1.6.3. *Telomerase as a regulator of gene expression - NF- $\kappa$ B transcription factor*

Transcription factor NF- $\kappa$ B is a protein complex that is crucial for cell proliferation, differentiation, inflammation, and immunity.<sup>104</sup> The first evidence of direct interaction between the p65 subunit of NF- $\kappa$ B (RelA) and the hTERT protein was found in multiple myeloma cells where p65 was found to be responsible for hTERT nuclear translocation.<sup>105</sup> Ectopic expression of telomerase resulted in increased tumour cell proliferation, protection against cell death, and tumour growth in the xenograft model, which could be mitigated by suppressing NF- $\kappa$ B signalling.<sup>105</sup> On the other hand, silencing the hTERT gene by siRNA significantly inhibited tumour growth, and this process was reversible through overexpression of p65.<sup>106</sup> These findings confirm the functional interdependence between telomerase signalling and the NF- $\kappa$ B pathway. Interestingly, hTERT has been found to bind to p65 and localize to promoters of NF- $\kappa$ B target genes, including interleukins IL-6, TNF- $\alpha$ , and cytokine IL-8, which are responsible for inflammation and carcinogenesis.<sup>107</sup> Such mutual regulation may be one of the mechanisms underlying the accompanying chronic inflammation and prolonged telomerase activity in cancers.

#### 1.6.4. *hTERT in angiogenesis*

The vascular endothelial growth factor (VEGF) is a potent angiogenic factor promoting the growth of new blood vessels.<sup>108</sup> The hTERT induces the expression of VEGF by interacting with the gene promoter and the transcription factor Sp1, leading to stimulation of the angiogenesis.<sup>109</sup> hTERT expression levels are positively correlated with VEGF in human gastric tumours. Deletion of the hTERT gene leads to compromised tumour growth *in vivo* accompanied by decreased VEGF expression.<sup>109</sup> Similarly, inhibition of telomerase in the endothelial cells has been shown to disrupt angiogenesis and tumour growth in glioblastoma xenografts.<sup>110</sup> This study suggests that glioblastoma angiogenesis may be associated with increased telomerase activity. This hypothesis was confirmed in HeLa cells by showing that hTERT is capable of inducing VEGF transcription.<sup>111</sup> Altogether, that study provides strong evidence that hTERT, is involved in the mechanisms of tumour angiogenesis and therefore antitelomerase drugs can be utilized for the treatment of malignant gliomas.

#### 1.6.5. *hTERT in the tumour microenvironment*

The tumour microenvironment (TME) is a key factor in carcinogenesis and metastasis, affecting the stromal cells and the extracellular matrix. Exosomes are a critical component of TME signalling, affecting epithelial-mesenchymal transition (EMT), invasion, and migration.<sup>112,113</sup> Exosomes released by tumour cells promote transformation into fibroblasts which support rapid tumour growth, vascularization, and metastasis.<sup>114</sup> It has been established that hTERT mRNA can be secreted via exosomes to telomerase-negative fibroblasts inducing their phenotypic changes including increased proliferative properties and prolonged viability.<sup>115</sup> In addition, cells become resistant to phleomycin-induced DNA damage and apoptosis.<sup>115</sup> Altogether, the study suggests that telomerase shuttle may potentially alter the cancer microenvironment.

#### 1.6.6. *hTERT in the nervous system*

The catalytic telomerase subunit exerts neuroprotective roles in many neurodegenerative diseases, such as amyotrophic lateral sclerosis (ALS) or mood disorders. Decreased telomerase activity was found in depression-like behaviour in mice and patients with schizophrenia.<sup>116,117</sup> Moreover, Wei et al. showed that genetic variation in hTERT may influence susceptibility to depression.<sup>118</sup> Another study reported an association of hTERT with the reduction of ROS and the protection of DNA in the mitochondria of neurons.<sup>119</sup>

The hTERT plays a crucial role in the modulation of neuronal survival in the developing and postmitotic mature nervous system, by controlling levels of Ca<sup>2+</sup>.<sup>120</sup> The reduction of hTERT leads to ROS formation and oxidative damage in brain cells through the interaction with the tau protein which plays a crucial role in the pathogenesis of many human neurodegenerative diseases.<sup>121</sup> Eitan et al. demonstrated that a controlled and transient increase of telomerase activity in the brain can have a neuroprotective effect in ALS.<sup>122</sup> Interestingly, hTERT has been found in mature



Purkinje neurons, where it may participate in adaptive responses of the neurons to excitotoxic and radiation stress.<sup>123</sup>

Overall, telomerase appears to play an important role in the response of neurons to various types of stress. Further understanding of the neuroprotective mechanisms of telomerase could provide novel therapeutic applications in central nervous system diseases.

### **1.7. Approaches to inhibit telomerase**

The main goal of anti-telomerase drugs is to selectively target cancer cells while minimizing the effect on normal cells. Inhibition of telomerase leads to a decrease in telomere length resulting in cell senescence and apoptosis in telomerase-positive tumours.<sup>124</sup> However, also short-term treatment with telomerase inhibitors could induce cell death because, besides the main, canonical function of this enzyme, many others are not directly related to the extension of telomeric sequences, and their disruption can induce the chemotherapeutic effect. Such a chemotherapeutic response would be desirable as it would lead to the death of cancer cells more quickly.

The comprehensive structure of the telomerase and the multi-level system of its regulation provides the possibility of blocking enzyme activity at various levels. Potential sites of telomerase inhibition include hTERC, hTERT catalytic subunit, assembly of the telomerase complex, and factors involved in telomerase recruitment to the telomeric DNA. There are several approaches to targeting telomerase, including oligonucleotides or small molecules directly interfering with telomerase, immunotherapy against hTERT tumour-associated antigens, or indirect methods such as targeting telomerase function or regulation by the modulation of hTERT gene expression, G-quadruplex stabilization, or incorporation of nucleoside analogues into telomeres to induce genomic instability. Some of the telomerase inhibition approaches are presented in the following sections.

#### **1.7.1. Antisense oligonucleotides**

Antisense oligodeoxynucleotides (ASOs) consist of short, 10-30 nucleotide stretches of DNA, complementary to mRNA molecules. The mechanism of their action is based on the activation of RNase H or blocking translation by inhibiting the recognition of mRNA by the ribosome<sup>125</sup>. Applications of these molecules are currently being explored in many branches of medicine, including oncology, cardiology, and infectiology, one of which is currently used to treat cytomegalovirus retinitis.<sup>126</sup>

Natural oligonucleotides (DNA, RNA) have a limited therapeutic potential due to the susceptibility of the phosphodiester backbone to enzymatic cleavage by cellular nucleases.<sup>127</sup> To overcome the stability problem of these compounds, structural analogues have been developed with improved pharmacological properties.<sup>128</sup> Modifications to traditional antisense oligonucleotides used in inhibiting telomerase include 2'-5'-phosphoramidates (PN) linkages, 2'-O-methyl RNA linkages (2'OMe), 2'-O-(2-methoxyethyl) RNA linkages (2'MOE),



phosphorothioate (PS)-modified oligodeoxynucleotides, peptide nucleic acids (PNA) and locked nucleic acid (LNA) (**Figure 6**).<sup>129–132</sup>

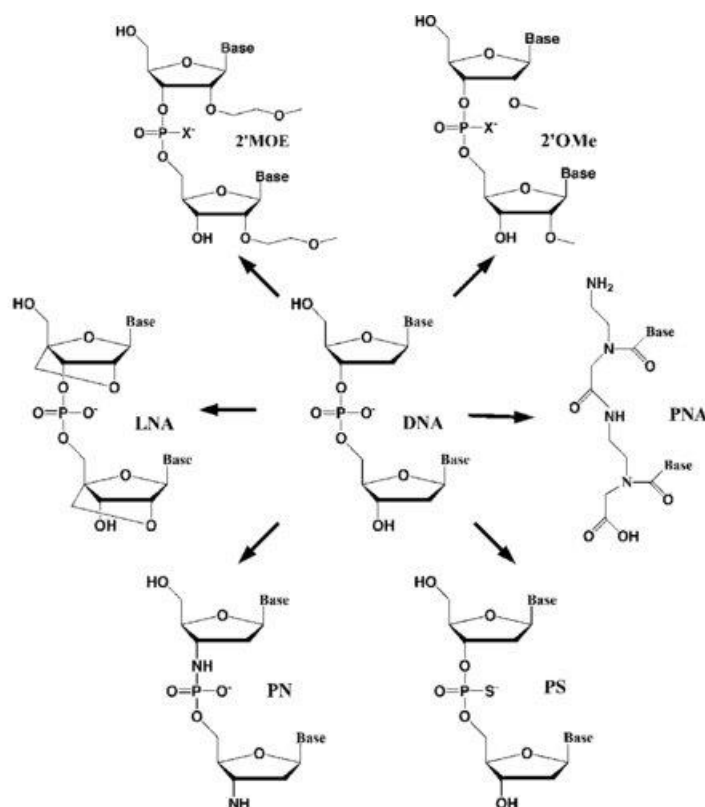


**Figure 6** Modified oligonucleotides as telomerase inhibitors.<sup>133</sup>

In the last few years, the oligonucleotide phosphoramidates have been designed complementary to the hTERC subunit or a sequence of about 100 nucleotides downstream of the template region.<sup>134,135</sup> N3'-P5' phosphoramidates and N3'-P5' thio-phosphoramidates form sequence-specific duplexes with target RNA. One of the derivatives, GRN163 which is N3'-P5' thio-phosphoramidate showed good results in inhibiting telomerase, but the lack of lipid carrier has diminished its potential due to its limited uptake.<sup>136</sup> To solve this problem, a lipid-modified version, the GRN163L (imetelstat), has been developed.<sup>137</sup> Studies have found that although characterized by increased uptake, GRN163L may be less potent than GRN163, possibly due to some interference of the lipid moiety with the telomerase template.<sup>138</sup> Nevertheless, the compound has entered clinical trials and is one of the few that reached the third phase (ClinicalTrials.gov identifier NCT04576156).<sup>139</sup>

### 1.7.2. Stabilization of the G-quadruplex structure

Single-stranded telomere sequences due to the enriched content of guanines can spontaneously form G-quadruplex (G-4) structures, stabilized by Hoogsteen hydrogen bonds. G-4 is known to fold into various spatial variants, like parallel, antiparallel, and hybrid conformation (**Figure 7**), in which a three-dimensional structure protects the telomere end sections from exonucleolytic processing, and thus prevents its degradation.<sup>140–142</sup>

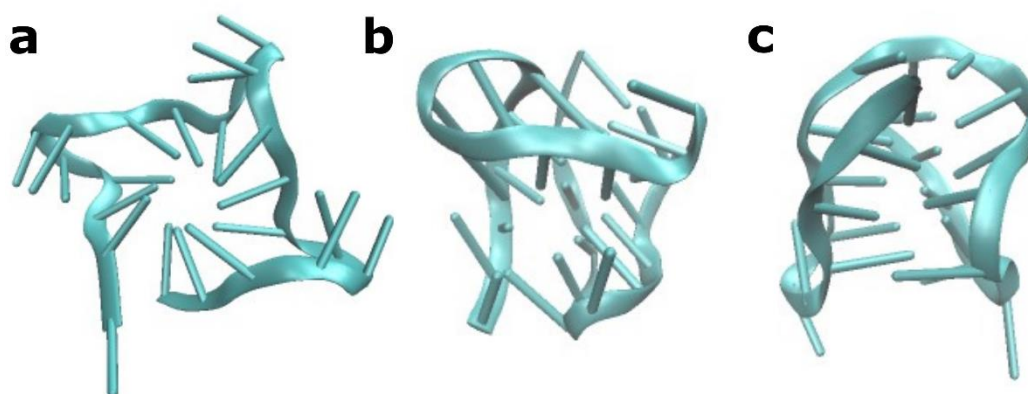


**Figure 7** Sample topologies of G-4. **(a)** parallel (PDB ID: 1KF1); **(b)** antiparallel (PDB ID: 143D); **(c)** hybrid (PDB ID: 2HY9).

One of the approaches to suppress telomerase activity is to inhibit the interaction between telomerase and telomeric DNA, which should be linear for its activity, by stabilizing the G-4 structure. Over the years, several small molecule ligands with high specificity for G-4 have been discovered (**Figure 8**). The stabilization of G-4 structures in telomeres blocks the access of the telomerase to the guanine-rich DNA sequence preventing the enzyme's function and triggering apoptosis in cancer.<sup>143</sup>

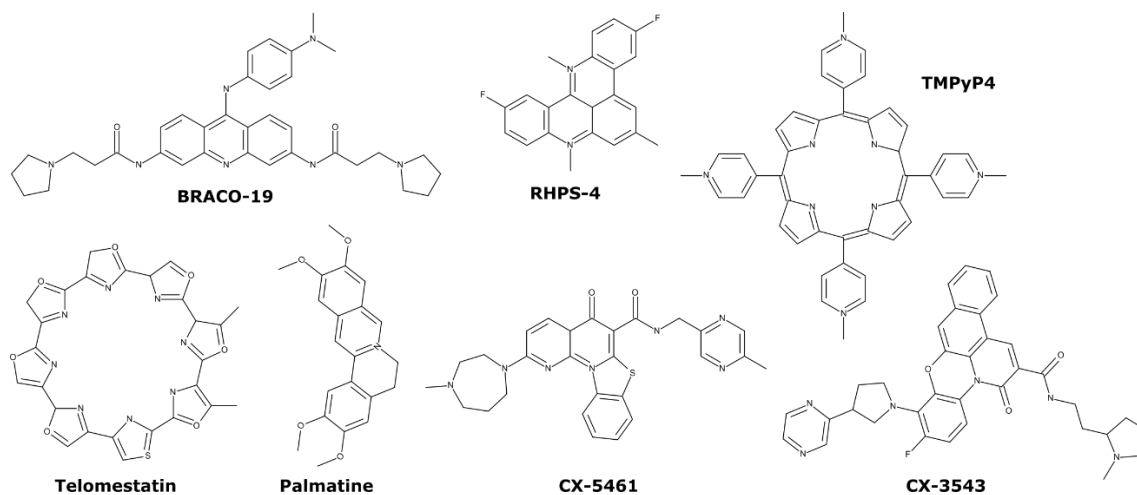


**Figure 8** Examples of G-4 stabilizers.

The first synthetic inhibitors of G-4 were designed based on the dogma assuming the strongest interaction with the guanine-rich DNA strand by intercalation with polycyclic, symmetric compounds with a heteroaromatic structure.<sup>144</sup> Acridine derivatives, such as RHPS4 and BRACO-19 are characterized by a central planar pharmacophore that binds with guanine tetrads of quadruplex DNA through  $\pi$ - $\pi$  interactions.<sup>145,146</sup> Another example is the cationic porphyrin derivative TMPyP4, which inhibits the activity of telomerase, decreases telomere length, and reduces cell growth consequently leading to apoptotic cell death, among others, the osteosarcoma cell line.<sup>145,147</sup> There are also several natural compounds stabilizing the

structure of the G-4, such as telomestatin, isolated from *Streptomyces cancatus*, or palmatine from *Coptidis Rhizoma*.<sup>148,149</sup>

In summary, approximately one thousand different G-4 ligands have been reported.<sup>150,151</sup> Among them, quarfloxin (CX-3543), an anti-neoplastic fluoroquinolone derivative, and CX-5461 have entered clinical trials, but due to the low bioavailability, only studies on CX-5461 are still conducted (phase I; ClinicalTrials.gov identifier NCT02719977).<sup>152–154</sup> However, CX-5461 was also reported as a topoisomerase II inhibitor and an RNA polymerase I inhibitor, thus, its effectiveness may result from a mixed mechanism of the inhibition of various enzymes.<sup>155</sup>

A significant limitation of G-quadruplex stabilizers is their affinity for guanine-rich non-telomeric DNA regions, which may translate into toxicity to healthy cells. Such regions are present in many promoter regions of DNA where G-4 structures are also likely can form. This may indicate that some anticancer activity of already studied molecules can't be related to telomeres but particular oncogene promoter regions. Moreover, some of the compounds, despite their effective antitumour activity *in vitro* and *in vivo*, have not found clinical application due to poor solubility, or the problem of crossing biological barriers.<sup>146,156,157</sup>

### 1.7.3. Direct telomerase inhibitors - synthetic compounds

One of the most extensively studied compounds as a direct telomerase inhibitor is BIBR1532 (**Figure 9**).<sup>158</sup> This compound is a non-nucleosidic, mixed-type non-competitive inhibitor, which effectively inhibits the native and recombinant human telomerase.<sup>159</sup> Treatment of various cancer cell lines (e.g. oral squamous carcinoma, breast cancer, lung cancer) with BIBR1532 inhibited the activity of telomerase and downregulated hTERT expression leading to apoptotic cell death.<sup>160–162</sup> Bryan et al. propose that BIBR1532 binds to a conserved hydrophobic pocket of the CR4/CR5 thumb domain of hTERT, preventing proper telomerase assembly; however, the precise mechanism of its action is still unknown, especially concerning the X-ray structure of the complex between telomerase and BIBR1532.<sup>136</sup> Preclinical studies have demonstrated the synergic effect of combined treatment BIBR1532 with radiation or chemotherapeutics, like paclitaxel or emodin, leading to enhanced telomere dysfunction.<sup>163–165</sup> However, because of its poor pharmacokinetic properties, the clinical applicability of BIBR1532 is restricted.<sup>159</sup>

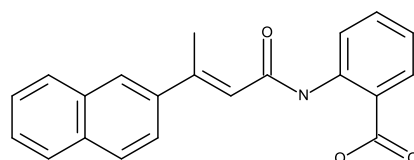


**Figure 9** BIBR1532 structure.<sup>158</sup>

### 1.7.4. Natural compounds and derivatives

Natural products have been primary sources of drugs, and many of them are still widely used in anticancer therapies.<sup>166</sup> Telomerase inhibitors are mostly derived from secondary metabolites such as terpenoids, polyphenols, xanthenes, alkaloids, and sesquiterpene.<sup>167</sup> Khaw et al.

demonstrated that curcumin, a polyphenolic compound, inhibited telomerase activity and induces telomere shortening in brain tumour cells; however, the exact mechanism of telomerase inhibition is still unknown.<sup>168</sup> Another example is chrolactomycin, a tetrahydropyran macrolide antibiotic isolated from *Streptomyces* sp. 569N-3. Studies conducted by Nakai et al. revealed that chrolactomycin inhibited human telomerase in a cell-free assay and a cellular assay<sup>169</sup>. Long-term treatment of human renal carcinoma leads to a decrease in cell proliferation accompanied by telomere shortening.<sup>169</sup> A chemically modified derivative of green tea epigallocatechin gallate, MST-312 directly inhibits telomerase, and it's more effective than the parent compound. Long-term treatment of human monoblastic leukaemia U937 cells with MST-312 triggers progressive telomere shortening and reduction of growth rate.<sup>170</sup>

High biological activity of compounds derived from natural products, prompting many scientists to design their derivatives with improved pharmacological properties. Betori et al. discovered chrolactomycin derivatives as covalent inhibitors of telomerase.<sup>171</sup> The most potent compound, NU-1 inhibited telomerase activity in different telomerase-positive cancer cell lines and had negligible effects on telomerase-negative cancer cells.<sup>171</sup>

Certainly, natural compounds have great therapeutic potential, but nevertheless, none of the molecules targeting telomerase has been tested in animal models so far. One of the problems of most of the discovered molecules is their not fully understood mechanism of action as well as the difficulties related to their synthesis.

#### 1.7.5. Nucleoside analogues

Nucleoside analogues are important drugs, widely used for the treatment of malignancy as well as viral and fungal infections.<sup>172–174</sup> The identification of the hTERT as a functional catalytic reverse transcriptase prompted studies of inhibiting telomerase activity with nucleoside analogues. 3'-Azido-2',3'-dideoxythymidine (AZT) is a thymidine analogue originally used to prevent and treat HIV/AIDS by competitively inhibiting reverse transcriptase.<sup>175</sup> AZT is phosphorylated to active metabolite AZT-TP that competes for incorporation with deoxynucleotides leading to replication inhibition.<sup>175</sup> There is much evidence that AZT inhibits telomerase activity and reduces telomere length in various cell models.<sup>176,177</sup> The mechanism of its action shows that AZT-TP is recognized by telomerase and incorporated into the telomeric end, causing chain termination. A similar observation was reported by Mender et al. with another nucleoside analogue 6-thio-2'-deoxyguanosine (6-thio-dG). Treatment with 6-thio-dG-induced telomere dysfunction in telomerase-positive human cancer cells, but not in telomerase-negative cells.<sup>178</sup>

Nucleoside analogues were also studied in combination therapies. In preclinical studies, simultaneous treatment of human Pharynx FaDu cells with AZT and paclitaxel led to synergistic anticancer activity.<sup>179</sup> Moreover, AZT has entered clinical trials alone or in combination with other drugs, like 5-fluorouracil or methotrexate, but did not reach a composite endpoint.<sup>180</sup>



### 1.7.6. RNA interference-based therapy

RNA interference (RNAi) is a conserved double-stranded RNA (dsRNA) silencing mechanism first observed in *Caenorhabditis elegans*.<sup>181</sup> Long molecules of dsRNA are recognized by the enzyme Dicer (RNase III, helicase) and cleaved into ~21–25 nt discrete small RNA fragments called siRNA. Then, siRNA associates with a multisubunit protein complex, the RNA-induced silencing complex (RISC) with endoribonuclease activity. After recognizing the appropriate siRNA molecule, the complex directs it to the complementary mRNA. The Argonaut protein, which is part of the complex, has RNase H activity and cleaves the siRNA-bound mRNA molecule. Target mRNA is degraded, and therefore its expression is suppressed.<sup>182,183</sup>

The discovery of gene silencing through RNAi provides a new opportunity for drug design and discovery. RNAi products include short interference RNA (siRNA) short hairpin RNA (shRNA), bifunctional short hairpin RNA (bi-shRNA), and microRNA (miRNA).<sup>184</sup> The ability of RNAi to inhibit gene expression has been developed in the treatment of cancers, viral, and genetic disorders.<sup>185</sup> Major targets for siRNA anticancer therapy include oncogenes (like K-ras, c-myc, bcr/abl, or p53) and genes that are involved in angiogenesis (VEGF), survival, apoptosis (survivin), metastasis (MMP), and resistance to chemotherapy (MDR1).<sup>186</sup>

Ge et al. demonstrated that RNAi targeting of hTERT gene expression induces apoptosis and inhibits the proliferation of lung cancer cells.<sup>187</sup> Similarly, in cervical cancers, siRNA targeting hTERT effectively suppresses telomerase activity, cell proliferation, migration, and invasion, and induced apoptotic cell death.<sup>188</sup> Promising results were also obtained by simultaneously inhibiting both hTERT and hTERC expression in oral squamous cell carcinoma and BIU-87 bladder transitional cell cancer.<sup>189,190</sup> This approach effectively suppressed the expression of both hTERC and hTERT mRNA and telomerase activity in BIU-87, and the anticancer effect of combination targeting was more efficient than solely targeting hTERC and hTERT.<sup>189</sup> On the other hand, the anticancer effect of suppressing hTERC in oral squamous cell carcinoma was more direct and efficient, in comparison to combination targeting.<sup>190</sup>

In addition, several studies report the synergic effect of a combination treatment of hTERT siRNA, and commonly used chemotherapeutics, such as doxorubicin, cisplatin, paclitaxel, or radiation.<sup>191,192</sup> In the future, the combination of siRNAs with chemotherapy or radiotherapy may increase their effectiveness and significantly reduce the side effects of treatment.

### 1.7.7. CRISPR Cas9-mediated gene therapy

CRISPR (Clustered Regularly Interspaced Short Palindromic Repeat) technology is a powerful gene manipulation tool containing two components: a guide RNA (gRNA), and a CRISPR-associated endonuclease (Cas protein). The commonly used system involves CRISPR-Cas9, a DNA exonuclease that is directed by a gRNA to generate DNA double-strand breaks (DSBs) at a specific target site in the genome. Upon cleavage by Cas9, the DSBs are repaired by either NHEJ or homology-directed repair cellular (HDR) mechanisms.<sup>193,194</sup>

CRISPR/Cas9 gene editing technology is being widely applied to cancer research, to identify cancer genetic interactions, knockdown oncogenes, or overcome drug resistance.

There are several reports of using the CRISPR/Cas9 gene editing system to target the *hTERT* gene in cancer cells.<sup>195–199</sup> The group of T. Cech demonstrated a two-step CRISPR-Cas9 system allowing modifications to the endogenous *hTERT* locus in human cell lines.<sup>197</sup> Promising results were obtained by Wen et al., who developed a Cas9-based strategy using a double gRNA approach to efficiently edit the *hTERT* gene. They demonstrated that *hTERT* haploinsufficiency is a sufficient dose to suppress tumour growth *in vitro* and *in vivo*.<sup>198</sup>

Undoubtedly CRISPR/Cas9 has become a mainstream tool that offers the simplest, most versatile, and most precise method of genetic manipulation; however, there are several challenges to using this method for cancer therapy. The main limiting factors include the potential toxicity of the currently available delivery systems, off-targeting, and low editing efficiency.<sup>200</sup>

#### 1.7.8. *hTERT* promoter-driven oncolytic adenovirus

Replication-selective tumour-specific viruses present a form of immunotherapy described as genetically modified vectors able to induce the death of cancer cells by lysis. OBP-301 (telomelysin) is a telomerase-specific oncolytic adenovirus, that contains the *hTERT* promoter to regulate the expression of the E1A and E1B genes to facilitate virus replication in cancer cells<sup>201</sup>. *In vivo* studies confirmed the high cytotoxic activity of telomelysin in mouse xenografts toward different types of cancer cells without affecting normal cells.<sup>202,203</sup> The safety of telomelysin has been confirmed in phase I of clinical trials in various solid tumours and its currently being tested in phase II in the treatment of esophagogastric adenocarcinoma in combination with pembrolizumab (ClinicalTrials.gov identifier NCT03921021).<sup>204,205</sup>

Despite, the unique ability of oncolytic viruses to selective target cancers, adenovirus-mediated cancer gene therapy has some limitations and challenges, including manufacturing viruses, limitations to accomplishing a radical cure such as viral delivery, or immunological barriers.<sup>206</sup>

#### 1.7.9. TAGE system

Cancer therapy through the telomerase-activating gene expression (TAGE) system was developed by W. Dai and his group.<sup>207</sup> This method is CRISPR Cas9-based gene therapy enabling inducing selective death in cancer cells expressing telomerase. The TAGE system contains an effectors' gene expression vector containing a 3' single-stranded sequence recognizable and elongated by telomerase. At the same time, the nuclease dead Cas9-VP64 and a telomeric DNA targeting sgRNA (TsgRNA) are released by the adeno-associated vector into a cancer cell, forming the dCas9-VP69-TsgRNA complex. This complex is an artificial transcription factor that interacts with synthesized telomeric DNA at the end of the effector, activating the expression of Cas9 on the effector. Cas9 binds to TsgRNA to form the Cas9-TsgRNA complex, capable of disrupting chromosomes of cancer cells, followed by apoptosis.

This method allowed to effectively kill various cancer cell lines, like HeLa, HT-29, HepG2, PANC-1, MDA-MB-453, RAW264.7, A549, Hepa1-6, and SKOV-3, without affecting normal cells HL7702, MRC-5, and BMSC. Moreover, the TAGE system was also efficient *in vivo* leading to specifically killing cancer cells in mice without side effects or toxicity.

#### 1.7.10. Cancer immunotherapy

Cancer immunotherapy relies on the stimulation of the immune system to recognize and kill cancer cells. Current strategies include T cell infusion, vaccines, oncolytic virus therapy, immune checkpoints, and monoclonal antibodies therapy.<sup>208</sup> Immunotherapies targeting telomerase have demonstrated positive outcomes in cancer treatment.<sup>209–211</sup> hTERT peptides can be recognized by the major histocompatibility complex (MHC) class I or II, to stimulate CD8+ T, and CD4+ T cell response, respectively.<sup>212</sup> There have been two general approaches that have advanced to clinical trials: dendritic cell vaccines and peptide vaccines.<sup>213</sup> Several hTERT-targeting immune-therapeutics are currently being evaluated in clinical trials, and many of them are combined with checkpoint inhibitors, like UCPvax with nivolumab (phase II, ClinicalTrials.gov identifier NCT04263051), or UV1 in combination with ipilimumab and nivolumab (phase II, ClinicalTrials.gov identifier NCT04300244).<sup>214,215</sup>

A primary concern of using cancer vaccines for treatment is their restricted efficacy in patients with a high mutational burden and pre-existing immune responses.<sup>216</sup> Heterogeneity within and between cancer types is another challenge to overcome. Particularly effective will be personalized tumour-specific therapies, targeting several cancer antigens unique to each patient.

#### 1.7.11. Suicide gene therapy

Suicide gene therapy is based on delivering to tumour cells a gene encoding either a toxin or an enzyme making the targeted cell more prone to chemotherapy.<sup>217</sup> One of the approaches involves using the hTERT promoter to induce the expression of pro-apoptotic or suicide genes, such as tumour necrosis factor-related apoptosis-inducing ligand (TRAIL)<sup>218</sup>, FAS-associated death domain protein (FADD)<sup>219</sup>, caspase<sup>220</sup> or chemoattractant protein gene (MCP-1).<sup>221</sup> Then, the suicide gene is expressed in telomerase-positive cells leading to apoptosis. Another approach involves delivering an hTERT-driven prodrug-activating enzyme in conjunction with a prodrug which converts into a toxin via bioactivation in telomerase-positive cells.<sup>222</sup> Plumb et al. developed adenovirus gene therapy vectors that drive the bacterial nitroreductase gene using the transcriptional regulatory regions from the hTERT and hTERC telomerase genes. As a result of the activity of the hTERT promoter, the production of nitroreductase increases, leading to the metabolic transformation of CB1954 pro-drug to an active cytotoxic alkylating agent.<sup>223</sup> This therapy finished the I phase of clinical trials in locally relapsed prostate cancer patients, but the results of those studies are still not published (ClinicalTrials.gov identifier NCT04374240).<sup>224</sup>



Gene-directed enzyme pro-drug therapy greatly enhances the effectiveness of chemotherapeutic agents in tumour cells by high activity of *hTERT* and *hTERC* gene promoters and achieving long-term survival benefits by minimizing its toxicity toward normal cells.

## 2. OBJECT OF RESEARCH

Heterocyclic compounds have clinical applications as anti-bacterial<sup>225</sup>, anti-fungal<sup>226</sup>, anti-inflammatory<sup>227</sup>, anti-viral<sup>228</sup>, and anti-cancer drugs.<sup>229</sup> In addition, heterocycles provide diverse chemical structures and are involved in various biochemical processes playing important functions in living organisms. Their prevalence is partially down to engage in a broad range of intermolecular interactions, such as  $\pi$ -stacking interactions, hydrogen bonding, metal coordination bonds, van der Waals interactions, and hydrophobic forces.<sup>230,231</sup> My PhD work aims to explore different heterocyclic groups of compounds (**Tables 1-3**) as potential telomerase inhibitors. The group of compounds was selected or designed on rational bases and as a preliminary indication that their action can be linked with telomerase inhibition. Several approaches and areas have been studied as mentioned below.

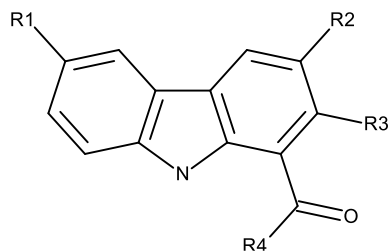
Professor Baginski's group has designed several compounds with a heterocyclic moiety as telomerase inhibitors using *in silico* methods. In their approach, structure-based drug design and scaffold hopping strategy were applied.<sup>232</sup> These compounds, carbazole, and pyrazole derivatives were docked to the *Tribolium castaneum* catalytic subunit of telomerase, which due to the highly conservative amino acid sequence may serve as a good template for human enzyme inhibition.<sup>233</sup> Docking simulations showed that compounds bind well to the active site of telomerase and therefore could be potential new telomerase inhibitors.

Different previously designed carbazoles (**Table 1**) and pyrazoles (**Table 2**) were synthesized by dr Milena Witkowska in dr Slawomir Makowiec's group at the Department of Organic Chemistry, Gdansk University of Technology, and by dr Ewa Wiczerzak's group at the Department of Biomedical Chemistry, University of Gdansk, respectively. Therefore, my first aim during my doctoral studies was to confirm the activity of those compounds as telomerase inhibitors at the cellular and molecular levels. Considering that I am dealing with new chemical entities, I decided that in the case of the false null hypothesis, I attempt to determine the molecular mechanism of their action based on literature studies.

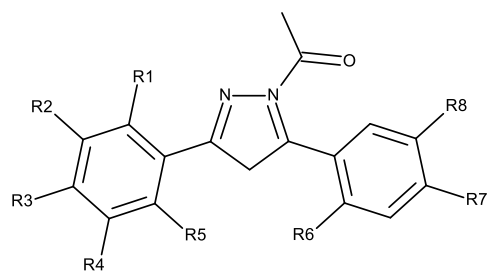
Among existing anti-cancer drugs, anthraquinones have been the key structural motif of many biologically active compounds. Anthraquinones pose anticancer activity mainly through DNA intercalation, which in turn causes single- and double-stranded DNA disruptions leading to apoptotic cell death. Several studies report their anticancer activity as telomerase inhibitors stabilizing G-4 structures. Previous studies showed high cytotoxic activity of dithiocarbamates of 9,10-anthracenedione (anthraquinone) in micromolar and submicromolar concentrations in various cancer cell lines.<sup>234</sup> However, the molecular mechanism of their action was unknown. Anthraquinones (**Table 3**) were synthesized by dr Maryna Stasevych and dr Viktor Zvarych at the Department of Technology of Biologically Active Substances, Pharmacy and Biotechnology, Lviv Polytechnic National University. **The second aim of the study was to explain the cellular and molecular mechanism underlying the cytotoxic activity of these compounds.**

To achieve the goals mentioned above, I have planned several *in vitro* experiments, among others: screening of compounds in terms of action on the cellular target and cytotoxic properties (to select the most active compounds), followed by determination of antiproliferative, antioxidant, DNA-damaging, and anti-migratory properties, and the type of the pathway of compounds-induced cell death.

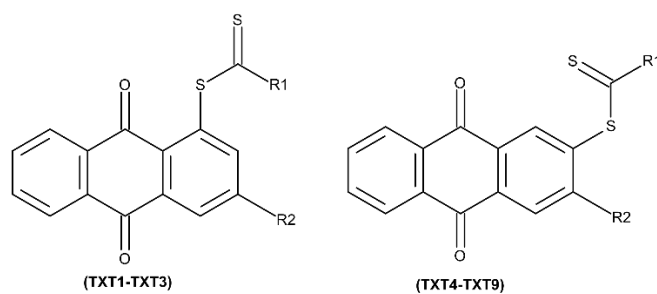
**Table 1** Chemical structure of carbazole derivatives



COMPOUND	R <sub>1</sub>	R <sub>2</sub>	R <sub>3</sub>	R <sub>4</sub>
<b>5AA</b>	H	NH-Boc	OH	O-CH <sub>2</sub> -CH <sub>3</sub>
<b>5AB</b>	H	NH-COO-CH <sub>2</sub> -CH <sub>3</sub>	OH	O-CH <sub>2</sub> -CH <sub>3</sub>
<b>5AC</b>	H	NH-Ac	OH	O-CH <sub>2</sub> -CH <sub>3</sub>
<b>5BA</b>	NH-Boc	NH-Boc	OH	O-CH <sub>2</sub> -CH <sub>3</sub>
<b>5CA</b>	OAc	NH-Boc	OH	O-CH <sub>2</sub> -CH <sub>3</sub>
<b>7AA</b>	H		OH	O-CH <sub>2</sub> -CH <sub>3</sub>
<b>7AB</b>	H		OH	O-CH <sub>2</sub> -CH <sub>3</sub>
<b>7BA</b>				O-CH <sub>2</sub> -CH <sub>3</sub>
<b>8</b>	H	NH-Boc	H	OH

**Table 2** Chemical structure of pyrazole derivatives

COMPOUND	R <sub>1</sub>	R <sub>2</sub>	R <sub>3</sub>	R <sub>4</sub>	R <sub>5</sub>	R <sub>6</sub>	R <sub>7</sub>	R <sub>8</sub>
PCH-1	H		O-CH <sub>2</sub> -O	H	OCH <sub>3</sub>	H	OCH <sub>3</sub>	H
PCH-2	H	OCH <sub>3</sub>	OCH <sub>3</sub>	OCH <sub>3</sub>	H	H		O-CH <sub>2</sub> -O
PCH-3	H	H	CH <sub>3</sub>	H	H	H		O-CH <sub>2</sub> -O
PCH-4	OCH <sub>3</sub>	H	H	H	H	H		O-CH <sub>2</sub> -O
PCH-5	H		O-CH <sub>2</sub> -O	H	H	H		O-CH <sub>2</sub> -O
PCH-6	H	H	OCF <sub>3</sub>	H	H	H		O-CH <sub>2</sub> -O
PCH-7	H	H	OCH <sub>3</sub>	H	H	H		CH <sub>2</sub> -CH <sub>2</sub> -O
PCH-8	H	H	OCH <sub>3</sub>	H	H	OCH <sub>3</sub>		O-CH <sub>2</sub> -O
PCH-9	H		S-CH <sub>2</sub> -O	H	OCH <sub>3</sub>	H	OH	H

**Table 3** Chemical structure of anthraquinone derivatives

COMPOUND	R <sub>1</sub>	R <sub>2</sub>
TXT1	N(CH <sub>2</sub> -CH <sub>3</sub> ) <sub>2</sub>	H
TXT2		H
TXT3		H
TXT4	N(CH <sub>2</sub> -CH <sub>3</sub> ) <sub>2</sub>	H
TXT5	N(CH <sub>2</sub> -CH <sub>3</sub> ) <sub>2</sub>	Cl
TXT6		H
TXT7		Cl
TXT8		H
TXT9		Cl

### 3. RESULTS

#### 3.1. Selection of cancer cell lines

Overexpression of telomerase is observed in the majority of tumours. Many studies reported a high correlation between telomerase activity and hTERT mRNA expression in various cell lines.<sup>235,236</sup> However, the level of its expression differs depending on the cancer cell line. Therefore, the expression of hTERT mRNA was measured in ten cancer cell lines by RT-PCR and is presented in **Figure 10**. Most of the analysed cancer cell lines are characterized by a telomerase-dependent telomere elongation mechanism, besides U2OS, and SKBR3 which have the ALT pathway to maintain the telomere length.<sup>237</sup>

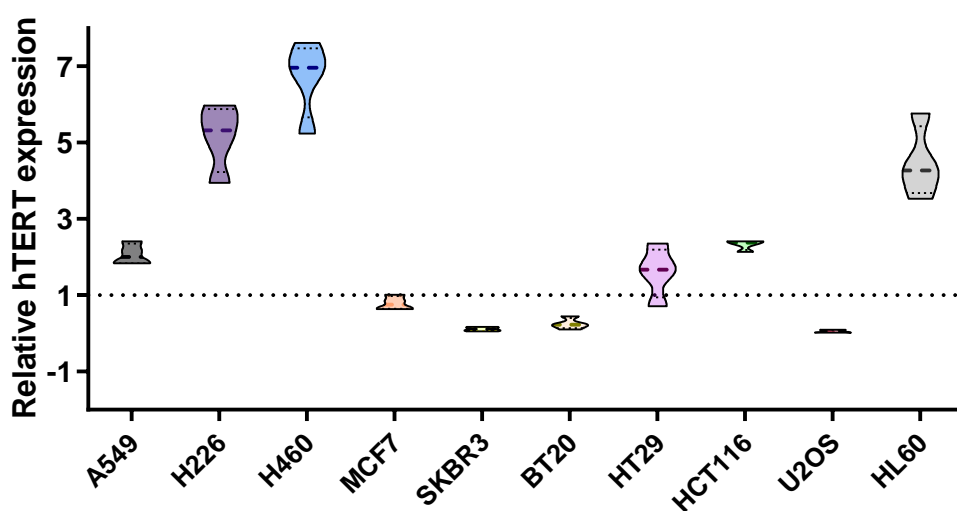


**Figure 10** Relative hTERT mRNA expression in various cancer cell lines quantified using qPCR and normalized to TATA-binding protein. Each bar shows the mean  $\pm$  standard error of the mean (SEM).

Squamous lung cell carcinoma H226, large cell lung carcinoma H460, and promyelocytic leukaemia HL60 exhibited high expression of hTERT. Moderate expression was found in colorectal adenocarcinomas (HT29, HCT116), and lung adenocarcinoma A549, whereas in breast adenocarcinoma (MCF7, SKBR3), invasive ductal carcinoma BT20, and osteosarcoma U2OS cells it was low or undetectable.

A panel of lung cancer cell lines and osteosarcoma U2OS were selected for further study due to the relatively high and low hTERT expression, respectively, and different telomere elongation mechanisms.

#### 3.2. Compounds screening - determination of the inhibitory effect of the compounds against telomerase

The effect of new pyrazole (**Figure 11a**), carbazole (**Figure 11b**), and anthraquinone derivatives (**Figure 12a**) on telomerase activity was examined using the telomerase repeat amplification protocol (TRAP) using the following reference compounds: BIBR1532 (telomerase

inhibitor that noncompetitively blocks the enzymatic activity of hTERT)<sup>159</sup>, mitoxantrone MTX (an anthraquinone derivative showing G-4 stabilizing properties)<sup>238,239</sup>, and TMPyP4 (a cationic porphyrin that may indirectly inhibit telomerase activity by stabilizing telomeric G-4)<sup>240</sup>. The obtained results revealed that none of the tested pyrazole and carbazole derivatives inhibits telomerase activity in a concentration of up to 100  $\mu\text{M}$  (**Figure 11**). On the other hand, most of the anthraquinone derivatives showed inhibitory activity against telomerase (**Figures 12a** and **c**) with calculated  $\text{IC}_{50}$  within the micromolar range (**Figure 12b**). Among tested compounds, TXT2, TXT3, and TXT4 (Teloxantron) showed the potent inhibitory effect on telomerase activity with TXT4 showing the lowest calculated  $\text{IC}_{50}$  value ( $9.61 \pm 0.93 \mu\text{M}$ ), which is 6.7-fold better than positive controls BIBR1532 with  $\text{IC}_{50}$ :  $64.11 \pm 2.53 \mu\text{M}$  (**Figure 12b**). On the other hand, TMPyP4 had a negligible inhibitory effect on telomerase activity in low concentrations (0.01 and 0.1  $\mu\text{M}$ ), whereas higher concentrations lead to inhibition of polymerase, manifested as a lack of internal standard amplification (**Figure 12a**). Moreover, MTX showed limited telomerase inhibitory activity at the highest concentrations, which was also paralleled by a lack of internal standard amplification (**Figure 12a**). Blocking the PCR course enables the proper establishment of  $\text{IC}_{50}$  by these compounds. In comparison, none of the test compounds inhibited Taq polymerase up to 100  $\mu\text{M}$ , as it is indicated by a consistent signal from internal standard amplification (**Figure 12a**). It is necessary to note that compounds that inhibit polymerase may give incorrect results in TRAP assay.

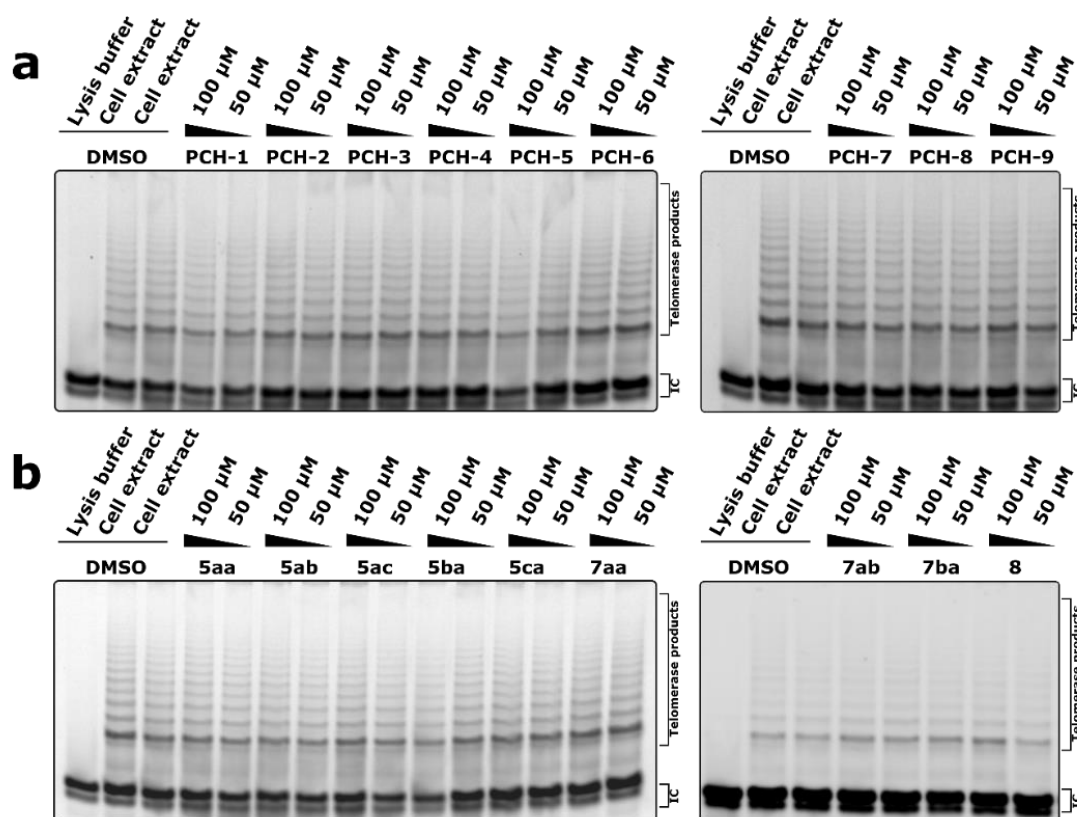


**Figure 11** Detection of telomerase activity by TRAP assay for compounds from Table 1-2. IC: internal standard.

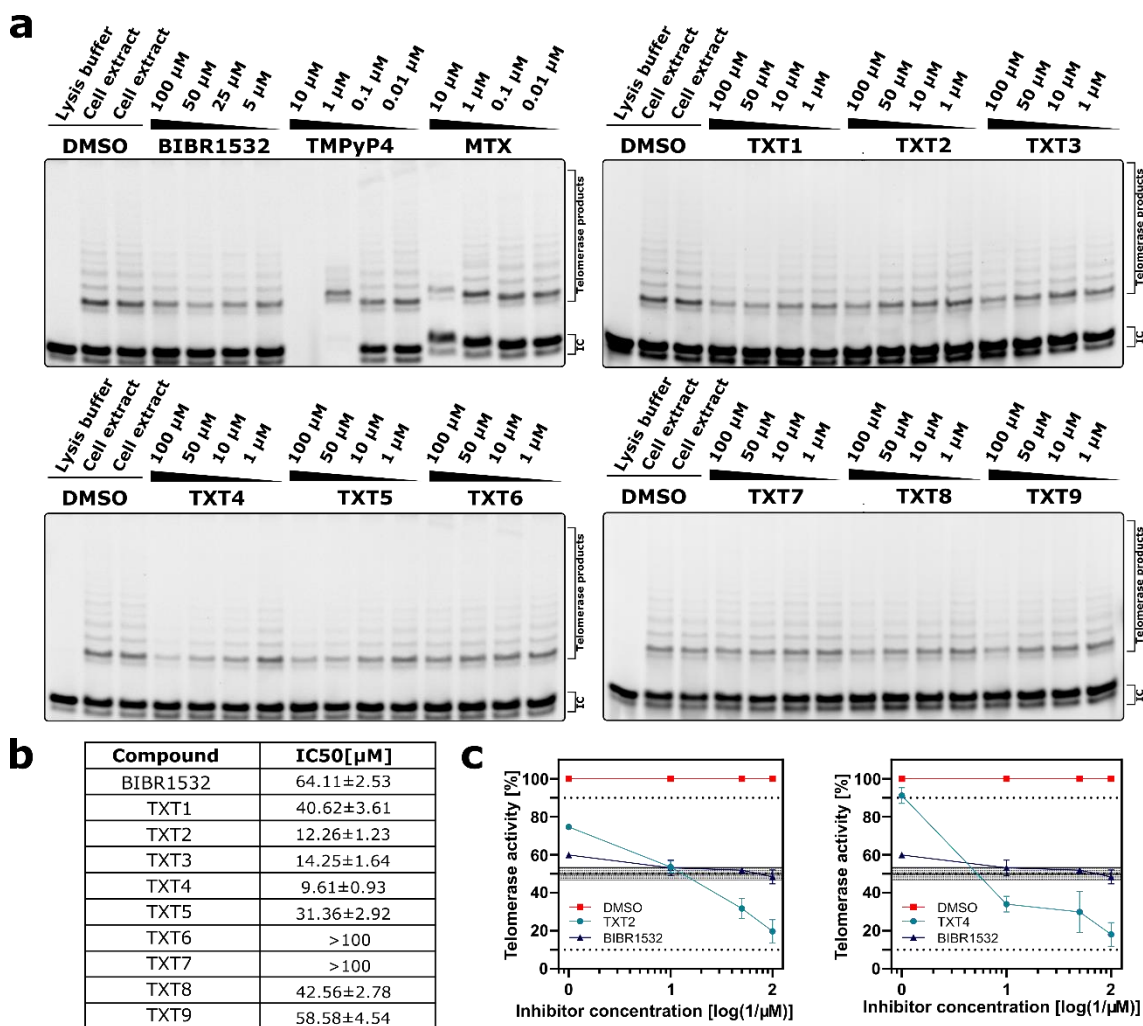


**Figure 12** Detection of telomerase activity by TRAP assay for compounds from Table 3. **(a)** Electrophoresis results from the TRAP assay. IC: internal standard; **(b)** The comparison IC<sub>50</sub> value for inhibition of telomerase; **(c)** Quantification of TRAP assay in the presence of increasing concentrations of TXT2 and TXT4 compounds. Data represent the mean ± standard deviation (s.d.) of three independent experiments.

Despite pyrazole's and carbazole's lack of telomerase-inhibition properties, they can still be identified as new agents that could pose anticancer properties. Therefore, all these compounds were also tested against various cancer and normal cell lines to determine their mechanism of action. For the sake of clarity, each group of compounds is presented in separate sections.

### 3.3. Project I – anthraquinone derivatives as telomerase inhibitors

#### 3.3.1. Determination effect of the anthraquinones on cell viability

Long-term treatment with telomerase inhibitors should lead to replicative senescence, followed by apoptosis; however, also short-term treatment could trigger cancer cell death since telomerase exhibits many non-canonical roles (see subsection 1.6). Therefore, all anthraquinone derivatives were evaluated for their *in vitro* anti-proliferative activity against four cancer cells: A549, H226, H460, U2OS cells, and two normal cell lines: primary human umbilical vein endothelial cells (HUVEC), and human bronchial epithelial (NHBE) cells. The results were expressed as growth inhibitory concentration (IC<sub>50</sub>) values and summarized in **Table 4**. Test compounds showed variable antiproliferative activities against the tested cell lines after 72 h of treatment. In general, compounds were the most cytotoxic against lung cancer cells with the lowest expression of hTERT mRNA, and the shortest telomeres (A549).<sup>241</sup> In most of the cases, there was the same trend of IC<sub>50</sub> value within the cell line: H226>H460>A549, but not with BIBR1532, cisplatin, and etoposide (ETP). The most potent compound against NSCLC cells was TXT1, whereas TXT5 exhibited the lowest activity.

Almost all TXT compounds were less active against U2OS cells, like BIBR1532. On the other hand, TMPyP4 did not exhibit any selectivity against cancer cells, but several papers report that G-4 stabilizers can reduce cell proliferation in ALT cells.<sup>242,243</sup>

The cytotoxic activity of anthraquinone derivatives does not correlate with their ability to inhibit telomerase activity. Moreover, high toxic activity against normal HUVEC, and NHBE cells, as well as moderate activity towards U2OS cells, indicate that compounds are non-selective and could have other additional mechanisms leading to cell death. Therefore, other reference compounds used in common chemotherapy were tested to compare the cytotoxic effect with test compounds. As shown in **Table 4**, anthraquinone derivatives were more active than most standard compounds, besides ETP, and mitoxantrone (MTX). Additionally, all references exhibited similar toxic effects to normal cells, like anthraquinone derivatives.

**Table 4** *In vitro* anticancer activity investigated compounds after 72 h of treatment (IC<sub>50</sub>±SEM [μM]). IC<sub>50</sub> value represents a concentration that inhibits 50% of cell growth.

Compound	A549	H226	H460	U2OS	HUVEC	NHBE
<b>TXT1</b>	1.67±0.03	4.01±0.32	2.19±.012	8.35±0.94	2.92±0.21	1.05±0.05
<b>TXT2</b>	2.64±0.21	4.45±0.21	3.12±0.43	7.74±1.42	3.92±0.11	3.81±0.03
<b>TXT3</b>	2.20±0.09	12.34±2.65	2.47±0.65	18.78±3.21	2.68±0.22	0.31±0.07
<b>TXT4</b>	6.02±1.21	11.87±2.76	8.12±0.21	17.67±1.62	8.51±0.03	7.52±0.17
<b>TXT5</b>	39.79±1.97	71.67±8.68	>100	20.71±3.34	ND	ND
<b>TXT6</b>	2.28±0.93	10.57±2.32	3.69±0.94	7.80±1.63	0.82±0.41	1.45±0.23
<b>TXT7</b>	17.75±2.77	36.45±6.21	43.26±4.66	12.46±2.26	ND	ND
<b>TXT8</b>	2.94±0.38	5.16±2.32	8.29±1.27	4.67±1.65	ND	2.15±0.37



Compound	A549	H226	H460	U2OS	HUVEC	NHBE
TXT9	12.00±2.23	13.29±2.54	12.38±1.44	9.93±1.34	ND	ND
ETP	0.54±0.21	1.03±0.16	0.05±0.01	0.61±0.04	0.37±0.07	4.21±0.23
MTX	0.019±0.002	0.067±0.004	0.043±0.002	0.031±0.003	ND	ND
5-FU	8.12±1.01	4.01±0.76	4.08±0.43	13.02±0.03	3.82±0.04	ND
BIBR1532	65.62±2.13	32.61±2.41	40.57±3.11	107.45±12.54	ND	ND
TMPyP4	12.53±1.12	64.31±3.81	54.13±2.37	45.93±6.19	ND	ND
Cisplatin	30.76±2.83	13.05±1.23	21.49±1.87	31.32±1.16	ND	ND
Imatinib	33.01±2.45	ND	ND	ND	ND	ND

Since compounds TXT1, TXT2, TXT3, and TXT4 were the most active against telomerase, they were selected for more detailed studies at the cellular and molecular levels. First, time course cell viability analysis was performed in NSCLC cells. As depicted in **Table 5**, the metabolic activity of all tested cancer cells decreased gradually with the exposition of all the compounds.

**Table 5** *In vitro* anticancer activity of investigated compounds after 24, 48, and 72 h of treatment ( $IC_{50} \pm SEM$  [ $\mu M$ ]).

A549			
Compound	24h	48h	72h
TXT1	3.67±0.03	2.96±0.08	1.67±0.03
TXT2	5.64±0.21	3.32±0.12	2.64±0.21
TXT3	5.20±0.09	3.95±0.13	2.20±0.09
TXT4	26.02±1.21	17.98±0.21	6.02±1.21
H226			
Compound	24h	48h	72h
TXT1	8.83±0.21	5.74±0.46	4.01±0.32
TXT2	8.32±0.31	5.92±0.33	4.45±0.21
TXT3	28.24±2.26	23.87±4.33	12.34±2.65
TXT4	26.69±2.21	17.84±1.76	11.87±2.76
H460			
Compound	24h	48h	72h
TXT1	8.73±0.99	6.61±0.09	2.19±0.12
TXT2	12.01±0.42	5.67±0.91	3.12±0.43
TXT3	24.52±3.87	13.61±0.33	2.47±0.65
TXT4	15.96±0.76	10.22±1.44	8.12±0.21

### 3.3.2. The antiproliferative potential of anthraquinones

Short-term inhibition of telomerase should lead to cell cycle arrest.<sup>244</sup> Therefore, the effect of compounds on cell cycle progression was evaluated in A549, H226, and H460 cells. Cells were treated for 24, 48, and 72 h, and the percentages of cells in each phase of the cell cycle were determined by flow cytometry. After 24 and 48 h of treatment, the cell cycle profile in A549 cells exhibited a similar pattern as in the DMSO-treated control (**Figure 13**). Longer exposure led to the accumulation of cells in the  $G_0/G_1$  phase with a concomitantly reduced proportion of cells in both the S and  $G_2/M$  phases. The most potent effect was observed for TXT4, which resulted in a significant increase ( $p < 0.0001$ ) in the percentage of cells in  $G_0/G_1$  by 1.5-fold compared to the control. None of the tested compounds modified the cell cycle profiles in H226 cells after either 24 or 48 h of exposure (**Figure 14**). However, 72 hours of treatment with TXT1 and TXT4 caused blocking cells in  $G_0/G_1$  phase, whereas compounds TXT2 and TXT3 resulted in increased cells in S-phase. In H460 cells after 24 h of treatment, compounds TXT1 and TXT4 modified

the distribution of cells in the cycle, resulting in fewer cells in the S-phase with a slight increase in their proportion in the G<sub>0</sub>/G<sub>1</sub> phase (**Figure 15**). However, 48 h of treatment with all test compounds increased the percentage of cells in this phase. Later exposure (72 h) led to an increase in the fraction of cells in the G<sub>0</sub>/G<sub>1</sub> phase, where the most significant rise was observed after treatment with TXT1 ( $p < 0.001$ ). Conversely, ETP in all three cancer cell lines induced G<sub>2</sub>/M cell cycle arrest, as confirmed by the previous reports.<sup>245,246</sup>

Out of all anthraquinones, TXT4 showed the most potent antiproliferative properties on A549 cells; therefore, a more detailed analysis of the cell cycle's course was performed (**Figure 16**). For this purpose, A549 cells were synchronized to a double-thymidine block in the G<sub>1</sub> phase and then exposed to TXT4 for the indicated time. Slight changes in the distribution of cells were observed just after a 2-h exposition compared to the DMSO-treated control. During the next 4-6 hours, a significant proportion of cells accumulated in the S phase. However, this arrest was only temporary, and later treatment gradually increased cell proportion in the G<sub>0</sub>/G<sub>1</sub> phase. On the other hand, ETP inhibited the S-phase cell cycle in the 2-10 h interval, but eventually, after 48 h, it accumulated cells in the G<sub>2</sub>/M phase as it did previously. Since telomerase activity increases in the S-phase, the observed temporary blockade of this phase induced by TXT4 could be related to the anti-telomerase potential of this compound.



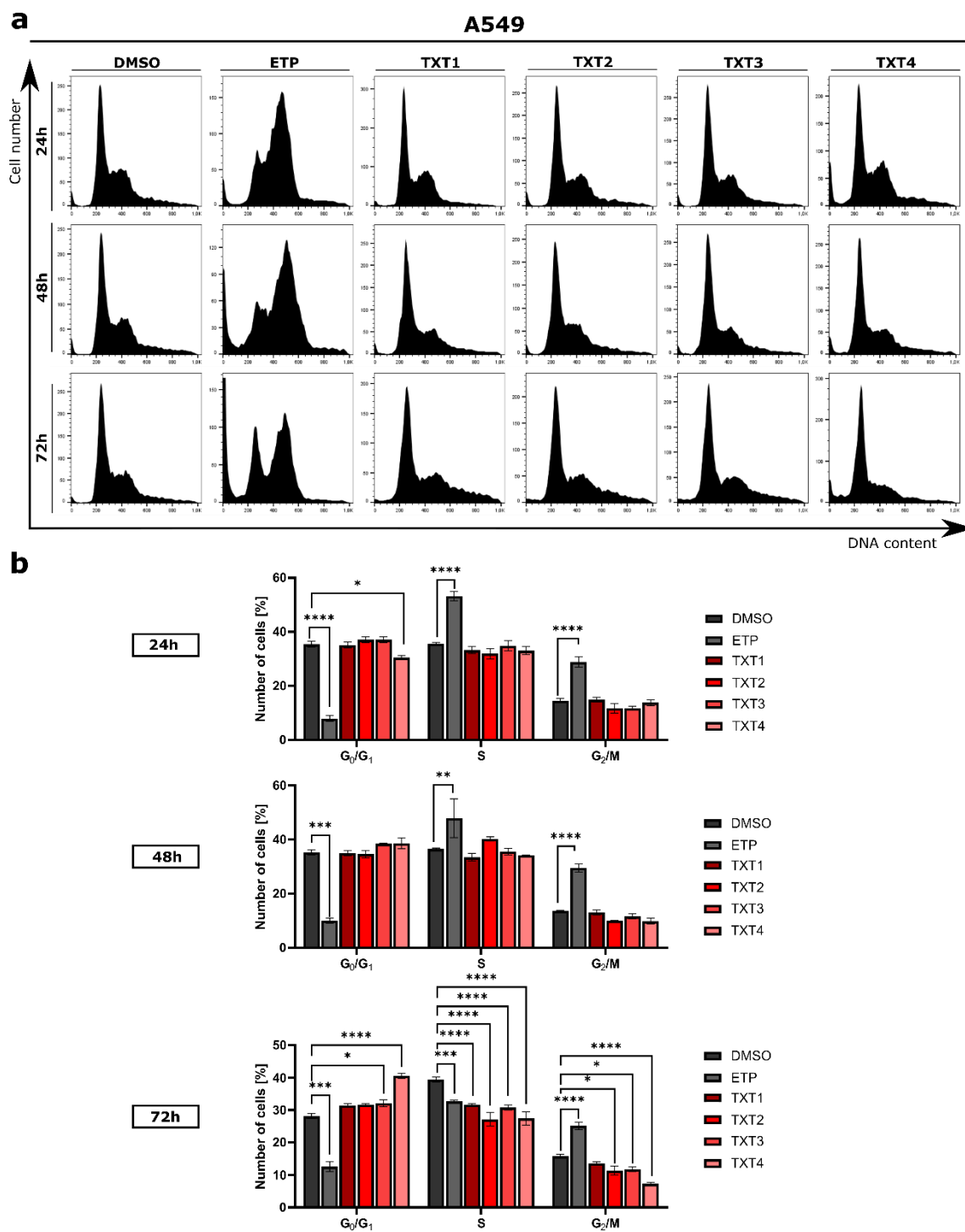


**Figure 13** Cell cycle analysis of A549 cells after treatment with tested compounds for 24, 48, and 72 h. DMSO and ETP were used as negative and positive controls, respectively. **(a)** Representative histograms were obtained after DNA staining; **(b)** The quantification of the analysis is presented on a bar graph. Data represent the mean  $\pm$  SEM of three independent experiments. \*  $p < 0.01$ , \*\*  $p < 0.001$ , \*\*\*  $p < 0.0001$ , \*\*\*\*  $p < 0.00001$  (two-way ANOVA and post hoc Dunnett's test).

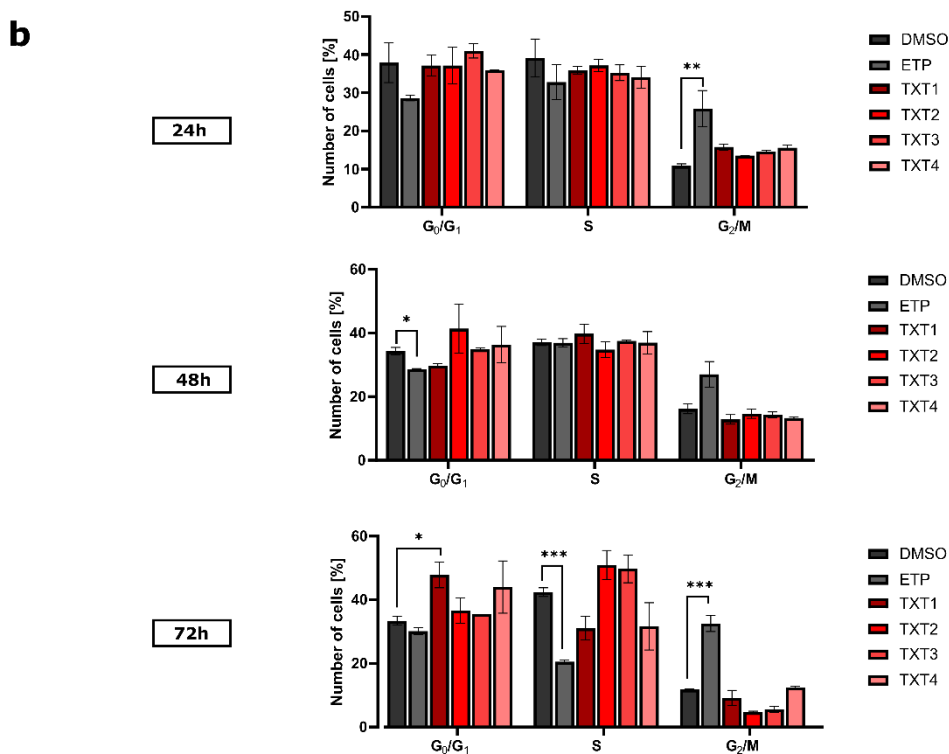
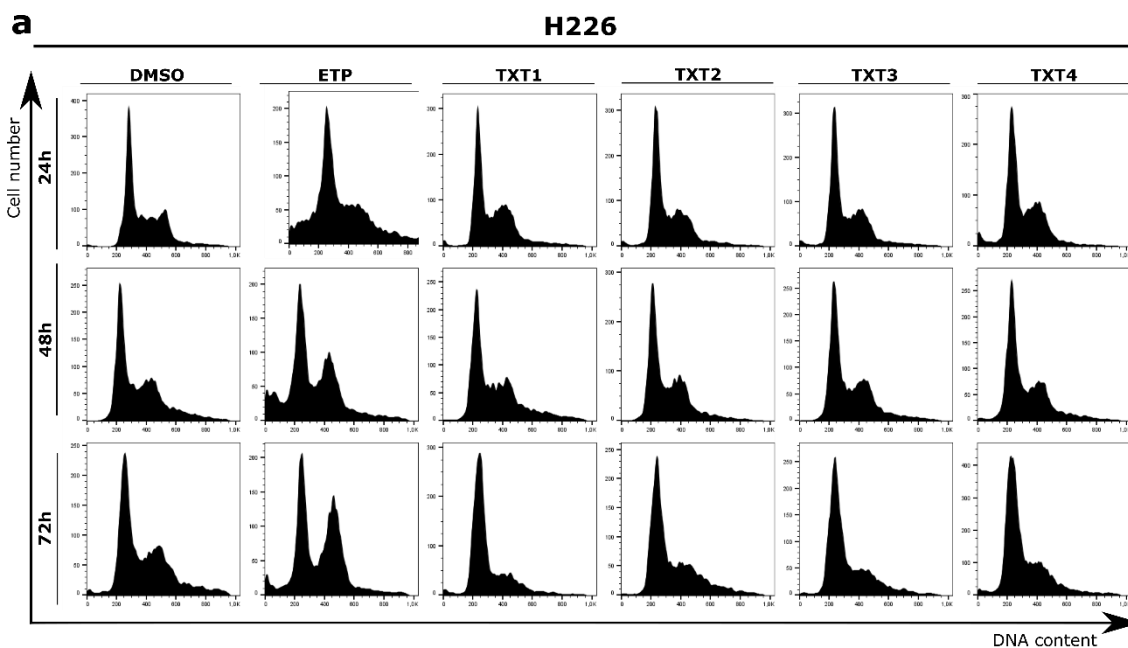


**Figure 14** Cell cycle analysis of H226 cells after treatment with tested compounds for 24, 48, and 72 h. DMSO and ETP were used as negative and positive controls, respectively. **(a)** Representative histograms were obtained after DNA staining; **(b)** The quantification of the analysis is presented on a bar graph. Data represent the mean  $\pm$  SEM of three independent experiments. \*  $p < 0.01$ , \*\*  $p < 0.001$ , \*\*\*  $p < 0.0001$  (two-way ANOVA and post hoc Dunnett's test).

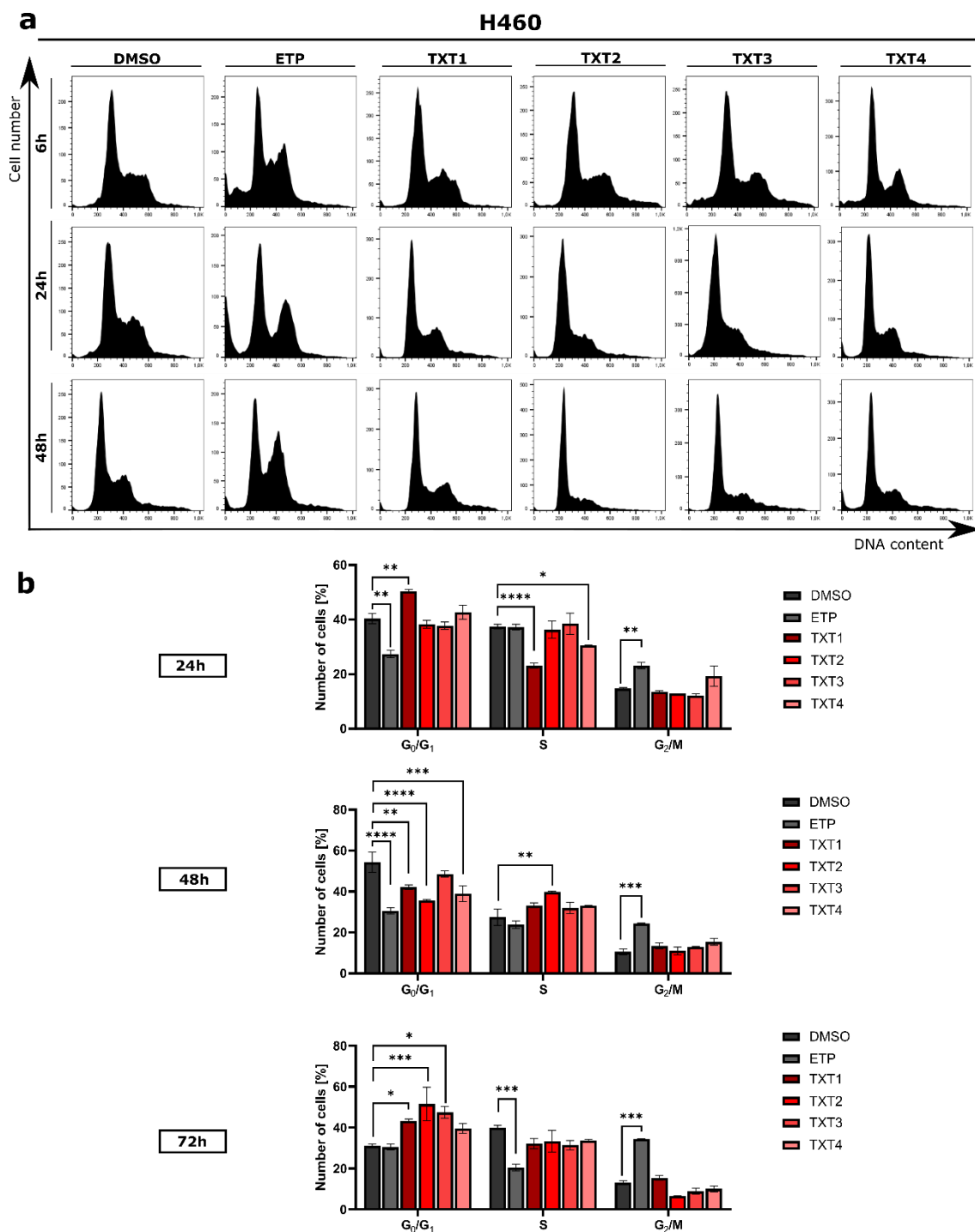


**Figure 15** Cell cycle analysis of H460 cells after treatment with tested compounds for 24, 48, and 72 h. DMSO and ETP were used as negative and positive controls, respectively. **(a)** Representative histograms were obtained after DNA staining; **(b)** The quantification of the analysis is presented on a bar graph. Data represent the mean  $\pm$  SEM of three independent experiments. \*  $p < 0.01$ , \*\*  $p < 0.001$ , \*\*\*  $p < 0.0001$ , \*\*\*\*  $p < 0.00001$  (two-way ANOVA and post hoc Dunnett's test).

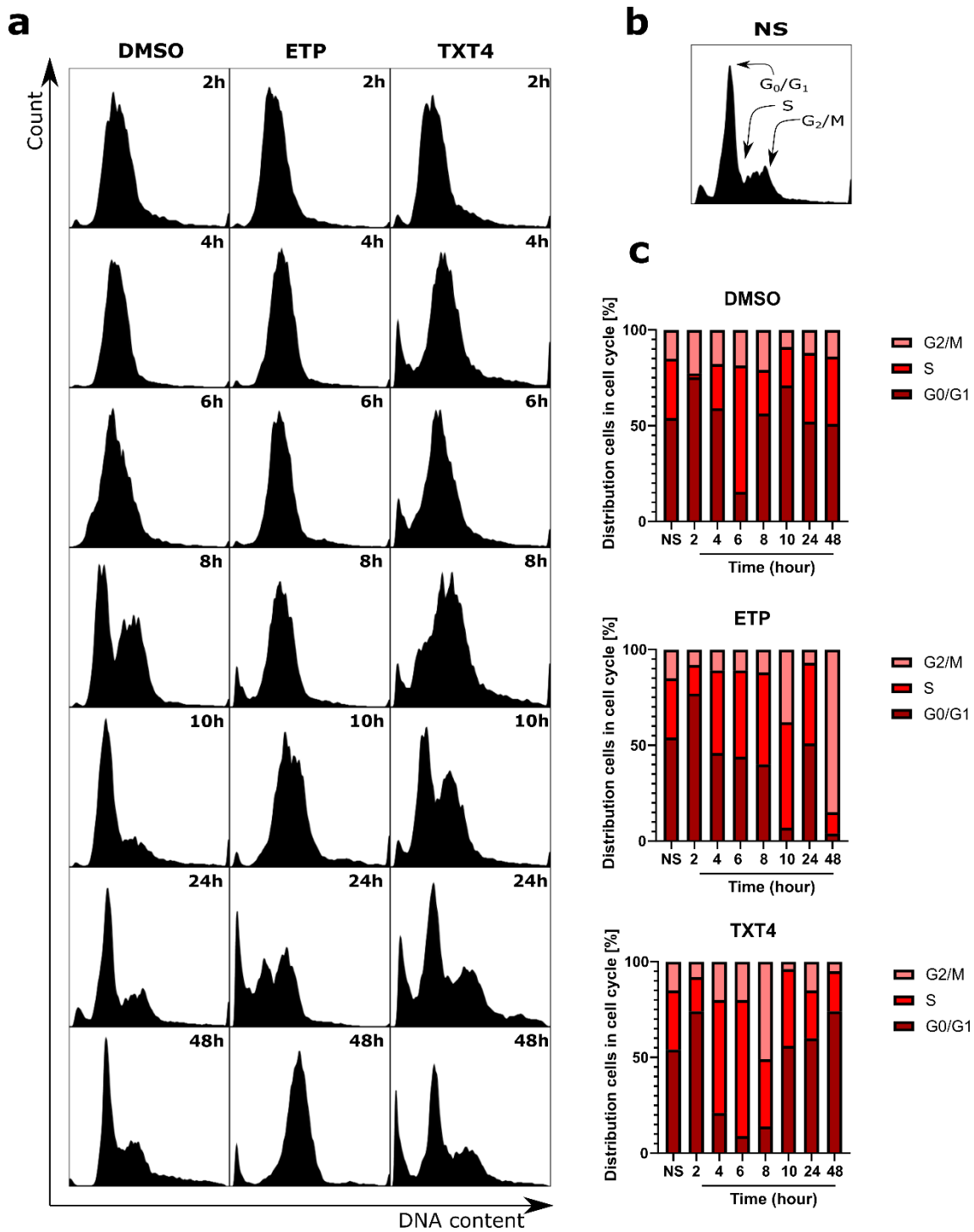


**Figure 16** Cell cycle analysis of A549 cells synchronized in the G<sub>1</sub> phase after DMSO (negative control), ETP (positive control), and TXT4 treatment. **(a)** Representative histograms; **(b)** Cell cycle phases in unsynchronized cells; **(c)** The quantitation of the flow cytometric analysis.

Next, the most potent compounds against telomerase TXT2 and TXT4 were further analysed in a colony formation assay. As depicted in **Figure 17**, compound TXT2 (1, 2, or 6  $\mu\text{M}$ ) significantly inhibited the colony formation capacity in A549, H226, and H460 cells compared to the vehicle (1  $\mu\text{M}$ : \* $p < 0.01$ ; 2  $\mu\text{M}$ , 6  $\mu\text{M}$ : \*\*\*\* $p < 0.00001$ ). The lowest tested concentration of TXT2 (0.5  $\mu\text{M}$ ) affected colony-forming abilities only in A549 cells (\*\*\* $p < 0.0001$ ). TXT4 at the highest concentration of 15  $\mu\text{M}$  remarkably suppressed colony formation in all three tested cell lines. Lower doses of TXT4 reduced colony numbers, but this effect was significant only at 10  $\mu\text{M}$  for A549 (\*\*\*\* $p < 0.00001$ ), H226 (\*\* $p < 0.001$ ), and H460 (\*\*\* $p < 0.0001$ ); and at 4  $\mu\text{M}$  for A549 (\*\*\* $p < 0.0001$ ), and H460 (\*\* $p < 0.001$ ). These results showed that both compounds concentration-dependently inhibit colony formation in NSCLC cell lines. Moreover, the compound's ability to diminish colony formation capacity among NSCLC increases within order H226<H460<A549, similar to the cytotoxic properties of compounds.

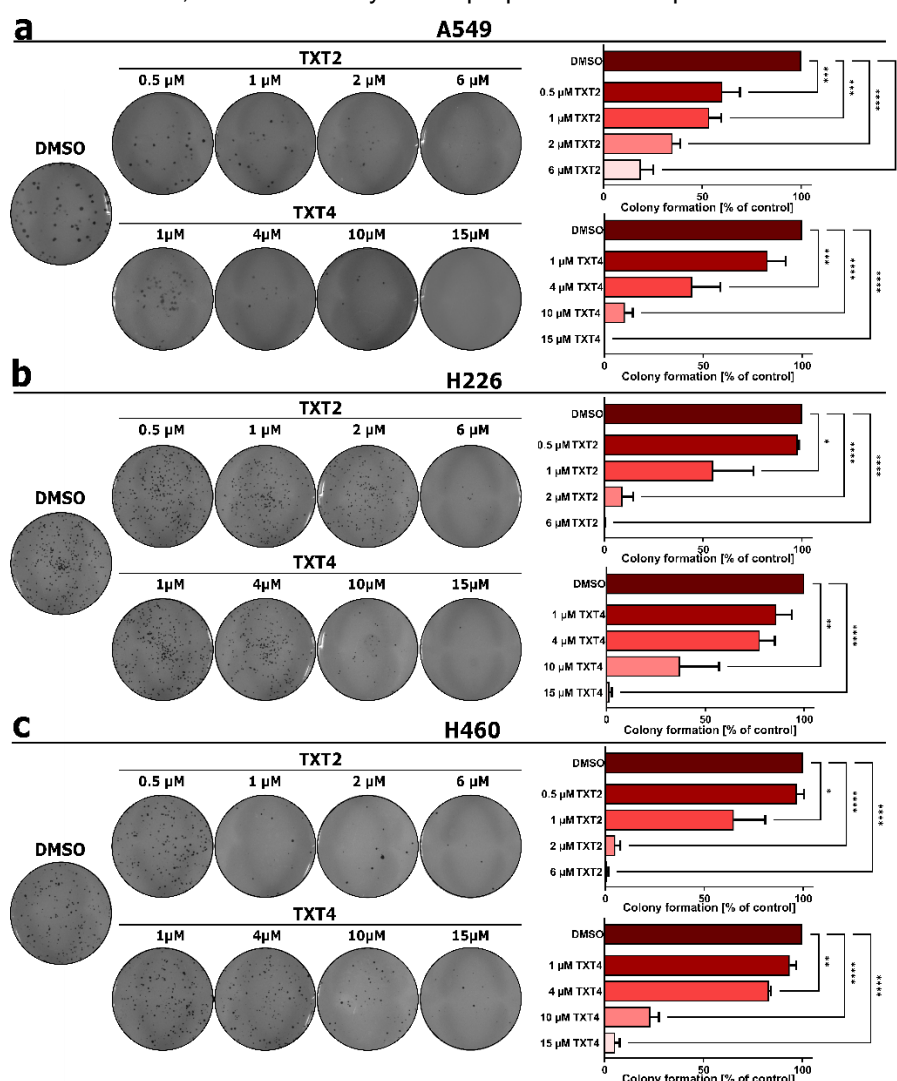


**Figure 17** Colony-forming ability of A549 (a), H226 (b), and H460 (c) cell lines after treatment with negative control (DMSO) and test compounds (TXT2, TXT4). Representative photos of the colony formation assay are presented on the left panel and its quantification is depicted on the right panel. Error bars represent the SEM of data obtained in  $n=3$  independent experiments. \*  $p < 0.01$ , \*\*  $p < 0.001$ , \*\*\*  $p < 0.0001$ , \*\*\*\*  $p < 0.00001$  vs. vehicle (one-way ANOVA and post hoc Dunnett's test).

### 3.3.3. Study of proapoptotic properties - changes in the plasma membrane

During apoptosis, physical changes occur in the plasma membrane such as the exposition of the negatively charged lipid phosphatidylserine in the outer leaflet of the membrane or the budding and formation of apoptotic bodies.<sup>247</sup> Proapoptotic properties of TXT compounds were examined after treatment of NSCLC cells at IC<sub>90</sub> concentration for 6, 24, and 48 h, and stained with 7-AAD, and Annexin V-FITC, which has a high affinity to phosphatidylserine. Dual staining allows the differentiation among live cells (Annexin V-FITC(-)/7-AAD(-)), early-phase apoptotic cells (Annexin V-FITC(+)/7-AAD(-)), late-phase apoptotic cells (Annexin V-FITC(+)/7-AAD(+)), and necrotic cells (Annexin V-FITC(-)/7-AAD(+)). After 6 h of treatment of A549 cells, percentages of surviving cells slightly decreased after exposure to all compounds, but only in the case of cells treated with TXT4, the decrease was significant ( $9.45 \pm 2.77\%$ ;  $p < 0.001$ ) (**Figure 18**). After 24 h of exposure to TXT4, a threefold augmentation in both early and late apoptotic fractions was observed in treated cells in comparison to the vehicle, whereas other compounds induced apoptosis to a small extent. Further incubation (48 h) of A549 cells with most of the compounds led to a significant decrease in the fraction of live cells, and a concomitant increase in Annexin V-positive cells, confirming phosphatidylserine externalization, and the ongoing apoptotic cell death. Only TXT3 did not induce the apoptotic process. Among all anthraquinone derivatives, TXT2 and TXT4 possess the most pronounced pro-apoptotic activity, which was observed accordingly in  $19.11 \pm 2.31\%$ , and  $27.65 \pm 2.89\%$  apoptotic cells. H226 cells undergo time-dependent apoptotic cell death only after treatment with TXT2 and TXT4, leading to an increase of apoptotic fraction up to  $15.33 \pm 1.03\%$ , and  $24.09 \pm 1.26$ , respectively (**Figure 19**). As depicted in **Figure 20**, after 6 h of incubation of H460 cells with all anthraquinones derivatives, the percentage of live cells significantly decreased, and the fraction of apoptotic cells (early+late) was approximately increased 2 times compared to the control. Treatment of H460 cells with TXT2 and TXT4 compounds for 24 and 48 h led to a significant increase in early-, and late apoptotic cells, respectively. Like the treatment of A549 and H226 cells, TXT2, and TXT4 caused the most substantial apoptotic effect in H460 cells among all tested compounds. On the other hand, none of these two compounds evoked apoptosis in ALT-positive cells, similar to BIBR1532 (**Figure 21**). Moreover, under the same conditions, a constant number of necrotic fractions (Annexin V(-)/7-AAD(+)) was observed for all cell lines (**Figures 18-21**). The 7-AAD dye is plasma membrane-impermeable and thus can only enter cells with compromised cell membrane integrity, which enables the detection of late-stage apoptosis or necrosis. These results confirmed that TXT2 and TXT4 could trigger apoptotic rather than necrotic cell death in NSCLC cell lines.





### A549

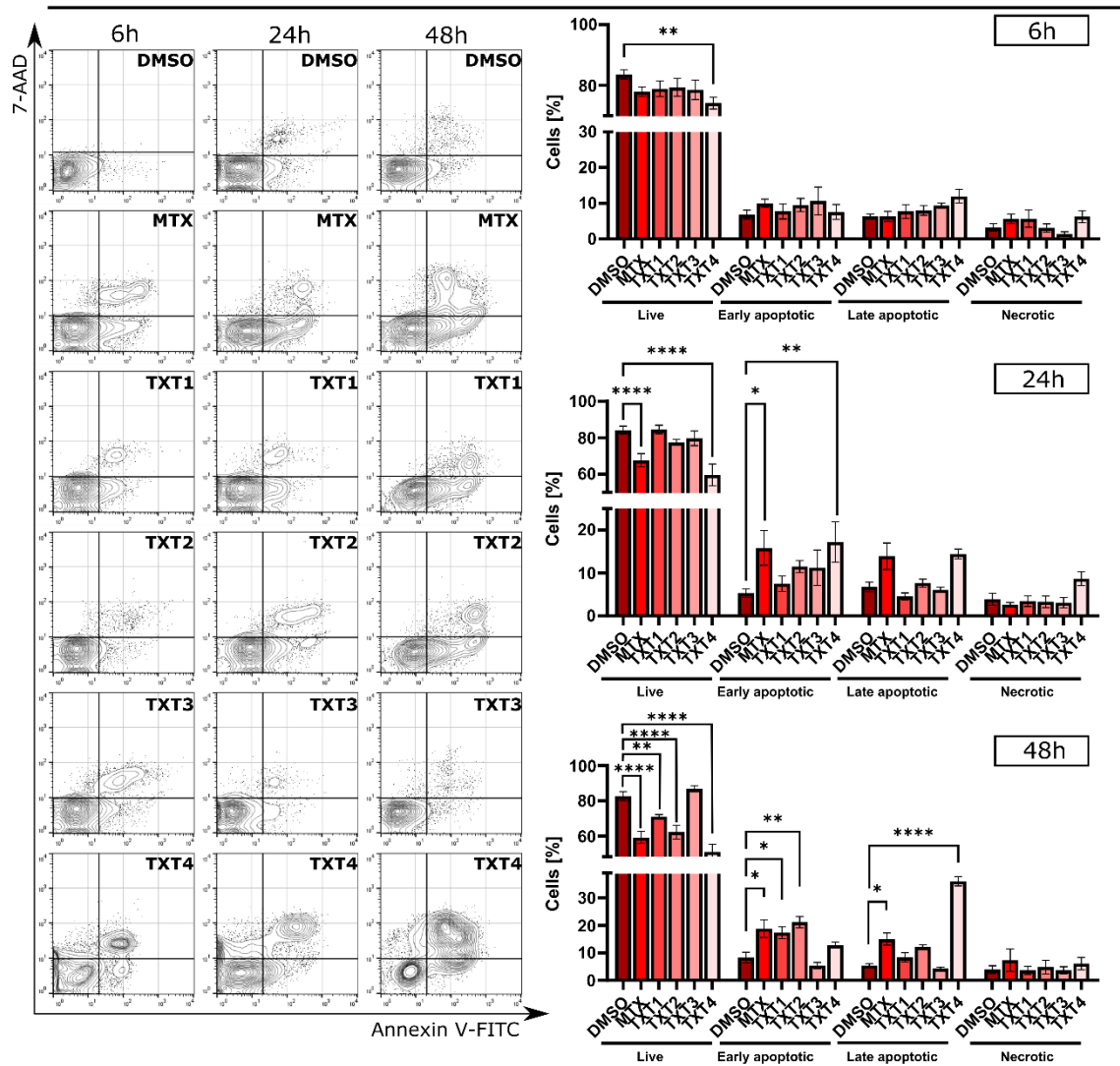


**Figure 18** Flow cytometric analysis of A549 cell line after 6, 24, and 48 h of treatment with compounds, using Annexin V-FITC/7-AAD. DMSO and MTX were used as negative and positive controls, respectively. Representative dot plots are presented on the left panel and the quantitation of data is presented on a bar graph. Data represent the mean  $\pm$  s.d. of three independent experiments. \*  $p < 0.01$ , \*\*  $p < 0.001$ , \*\*\*  $p < 0.0001$ , \*\*\*\*  $p < 0.00001$  (two-way ANOVA and post hoc Dunnett's test).

## H226

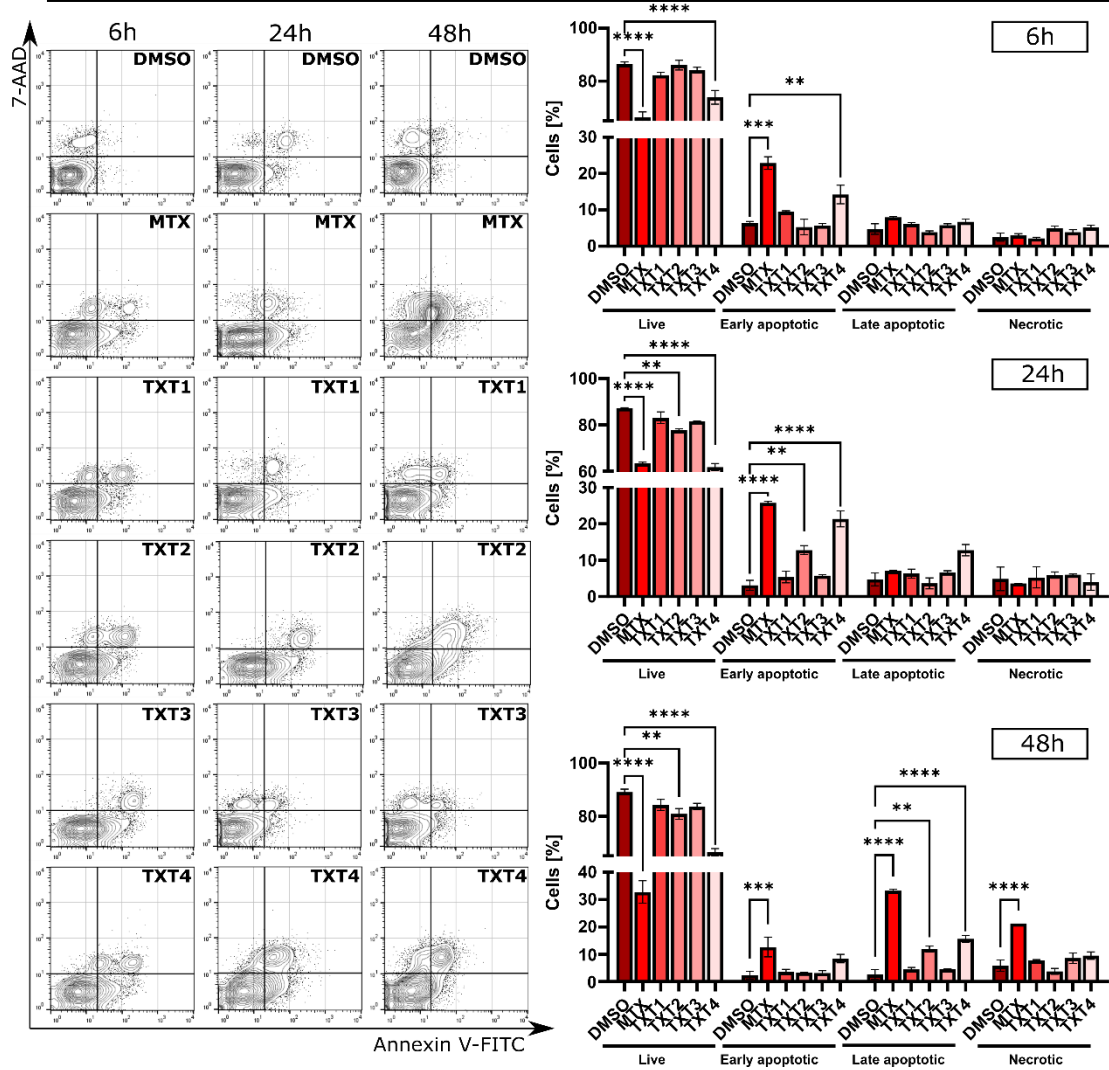


**Figure 19** Flow cytometric analysis of H226 cell line after 6, 24, and 48 h of treatment with compounds, using Annexin V-FITC/7-AAD. DMSO and MTX were used as negative and positive controls, respectively. Representative dot plots are presented on the left panel and the quantitation of data is presented on a bar graph. Data represent the mean  $\pm$  s.d. of three independent experiments. \*  $p < 0.01$ , \*\*  $p < 0.001$ , \*\*\*  $p < 0.0001$ , \*\*\*\*  $p < 0.00001$  (two-way ANOVA and post hoc Dunnett's test).

## H460

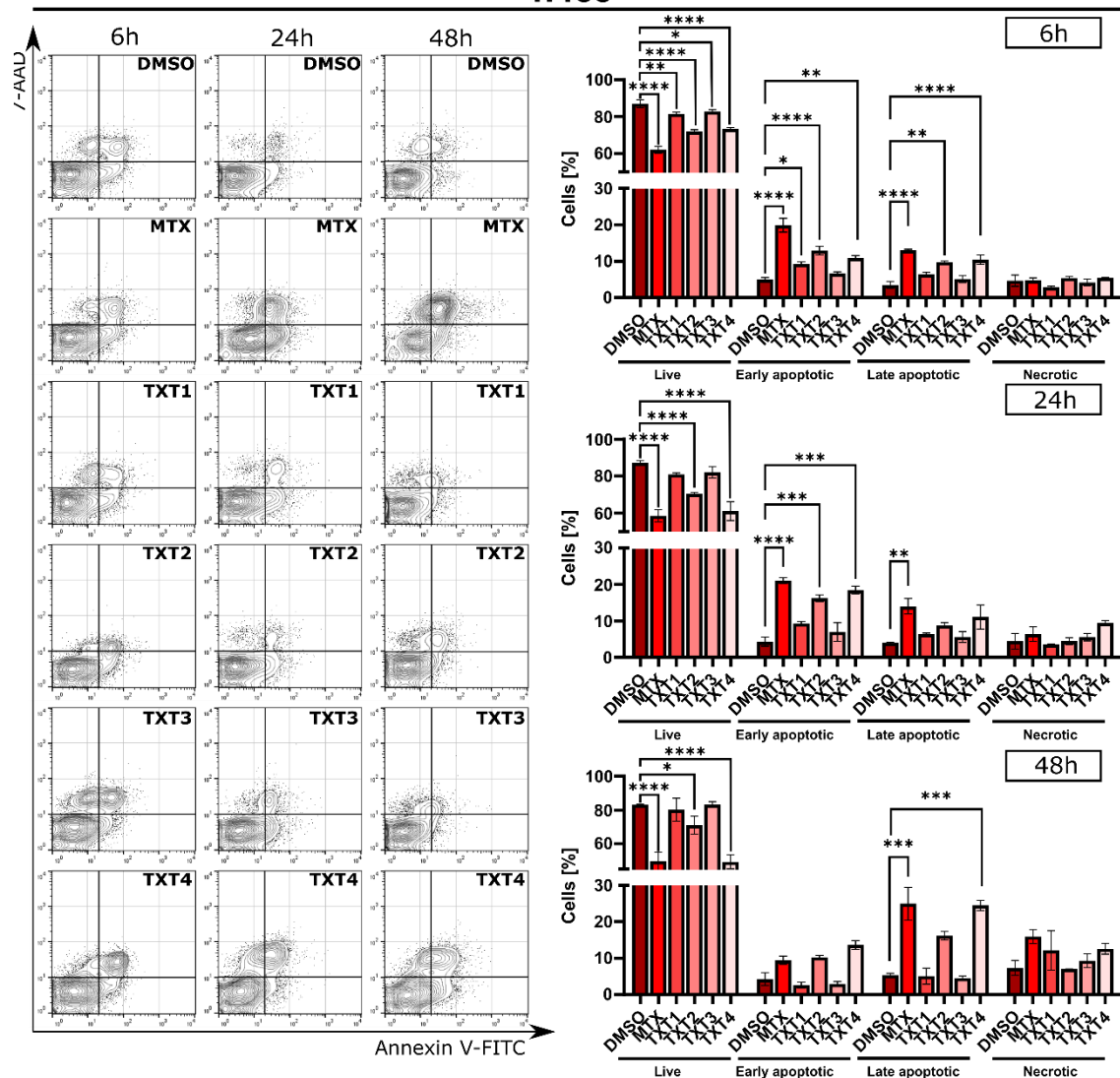


**Figure 20** Flow cytometric analysis of H460 cell line after 6, 24, and 48 h of treatment with compounds, using Annexin V-FITC/7-AAD. DMSO and MTX were used as negative and positive controls, respectively. Representative dot plots are presented on the left panel and the quantitation of data is presented on a bar graph. Data represent the mean  $\pm$  s.d. of three independent experiments. \*  $p < 0.01$ , \*\*  $p < 0.001$ , \*\*\*  $p < 0.0001$ , \*\*\*\*  $p < 0.00001$  (two-way ANOVA and post hoc Dunnett's test).

## U2OS

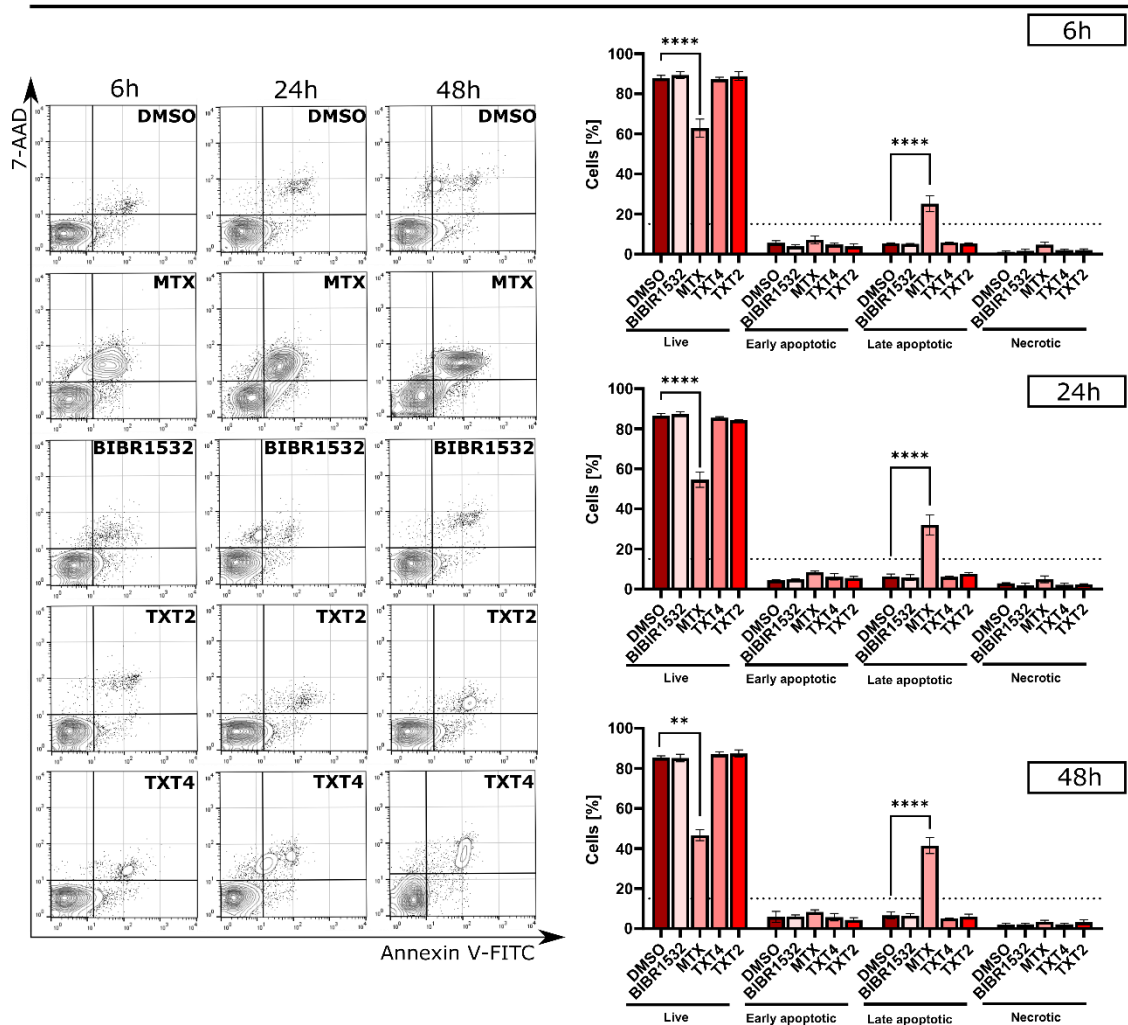


**Figure 21** Flow cytometric analysis of U2OS cell line after 6, 24, and 48 h of treatment with TXT compounds, using Annexin V-FITC/7-AAD. DMSO was used as a negative control, whereas MTX and BIBR1532 were used as positive controls. Representative dot plots are presented on the left panel and the quantitation of data is presented on a bar graph. Data represent mean values  $\pm$  s.d. from at least three independent experiments. \*\* $p < 0.001$ , \*\*\* $p < 0.0001$ , and \*\*\*\* $p < 0.00001$  (two-way ANOVA and post hoc Dunnett's test).

### 3.3.4. Detection of caspase-3 and caspase-7 activity

Caspases are a family of cysteine proteases playing a central role in all stages of apoptosis. Based on their role in apoptosis, they are classified as an upstream initiator (caspase-8 and caspase-9) or downstream executioner (caspase-3, caspase-6, and caspase-7).<sup>248,249</sup> Executioner caspases are considered a point of “no return” in apoptotic cell death. Among them, caspase-3 regulates DNA fragmentation, whereas caspase-7 controls ROS production, and is required for apoptotic cell detachment.<sup>250</sup> To investigate the mechanism of cell death that cancer cells undergo after treatment with anthraquinone derivatives, the ability of compounds to activate caspase-3 and caspase-7 was evaluated by flow cytometry after 24 and 48 h of treatment. The results showed that TXT1, TXT2, and TXT4 significantly activated executioner caspase-3/7

in A549 cells after 48 h of treatment, as revealed by a 4-fold, 5.4-fold, and 4.8-fold increase, respectively (**Figure 22**). Treatment of H226 cells with most of the compounds caused a negligible change in the activation of caspase-3/7 in comparison to the vehicle (**Figure 23**). Among all compounds, only the TXT2 significantly induced caspase-3/7 expression after 48 h of treatment ( $p < 0.01$ ). Moreover, incubation of H460 cells with anthraquinone derivatives (TXT1, TXT2, and TXT4) resulted in time-dependent activation of caspase 3/7 (**Figure 24**). This effect was observed just after 24 h of treatment and was significantly higher after more prolonged exposure (48 h) to compounds. Of note, TXT-mediated activation of effector caspase-3 and -7 was appreciable in two TERT-positive (A549 and H460 cells), but not ALT-positive cell lines (**Figure 25**). Comparing the effect of compounds on activation caspase-3/7 between tested cell lines, there is the same trend as with results obtained in the Annexin V-FITC/7-AAD assay, which is A549>H460>H226.

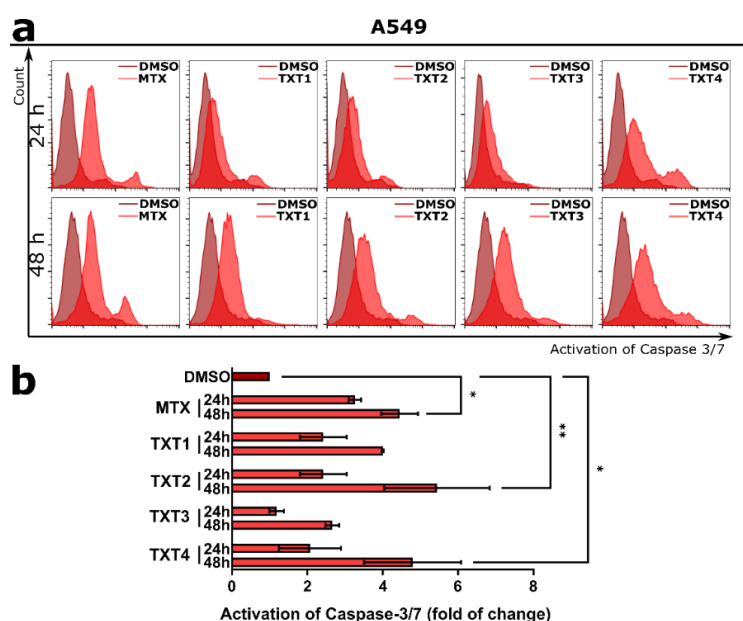


**Figure 22** Modulation of caspase-3/7 in A549 cells after treatment with compounds. DMSO and MTX were used as negative and positive controls, respectively. **(a)** Representative histograms; **(b)** Quantification of analyses. Error bars represent the s.d. of data obtained in  $n=3$  independent experiments.  $*p < 0.01$ ,  $**p < 0.001$  vs. vehicle (one-way ANOVA and post hoc Dunnett's test).

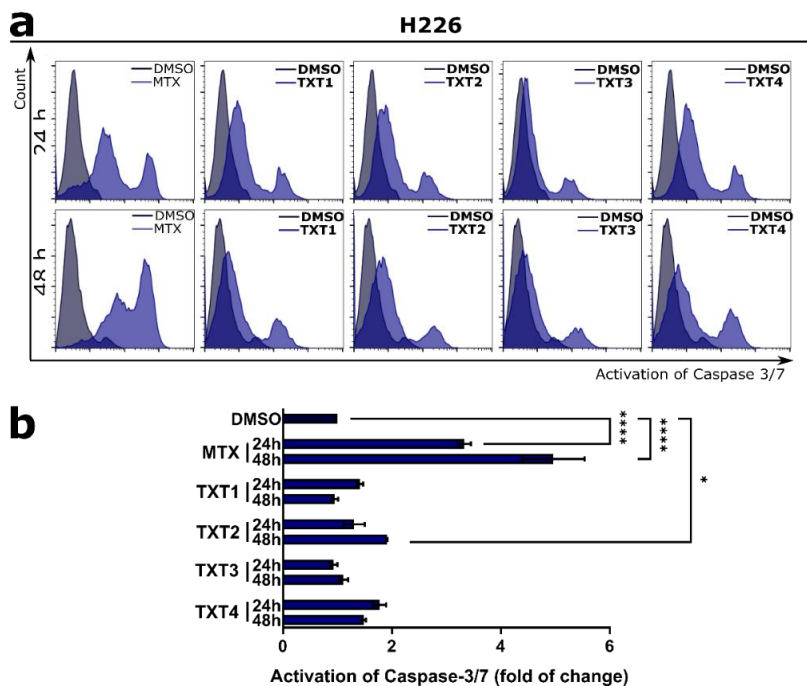


**Figure 23** Modulation of caspase-3/7 in H226 cells after treatment with compounds. DMSO and MTX were used as negative and positive controls, respectively. **(a)** Representative histograms; **(b)** Quantification of analyses. Error bars represent the s.d. of data obtained in n=3 independent experiments. \*p<0.01, \*\*\*\*p<0.00001 vs. vehicle (one-way ANOVA and post hoc Dunnett's test).

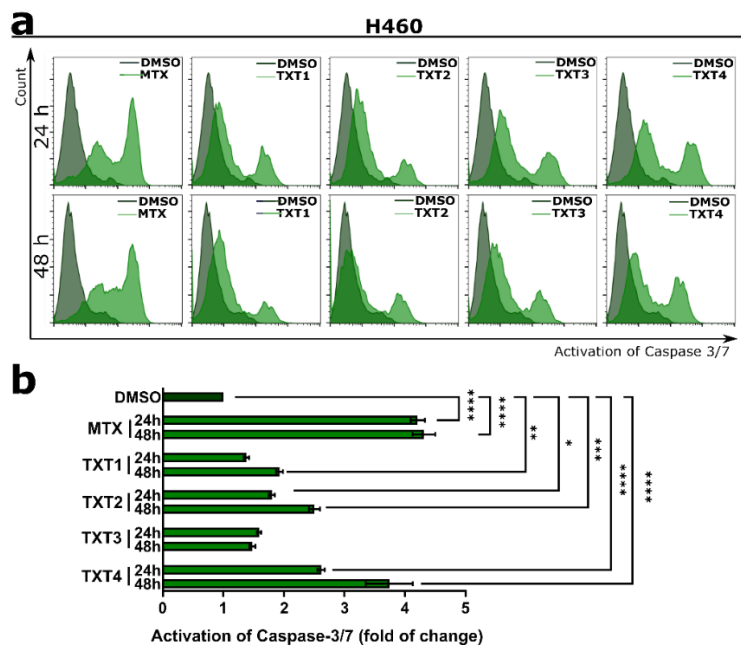


**Figure 24** Modulation of caspase-3/7 in H226 cells after treatment with compounds. DMSO and MTX were used as negative and positive controls, respectively. **(a)** Representative histograms; **(b)** Quantification of analyses. Error bars represent the s.d. of data obtained in n=3 independent experiments. \*p<0.01, \*\*p<0.001, \*\*\*p<0.0991, \*\*\*\*p<0.00001 vs. vehicle (one-way ANOVA and post hoc Dunnett's test).

## U2OS

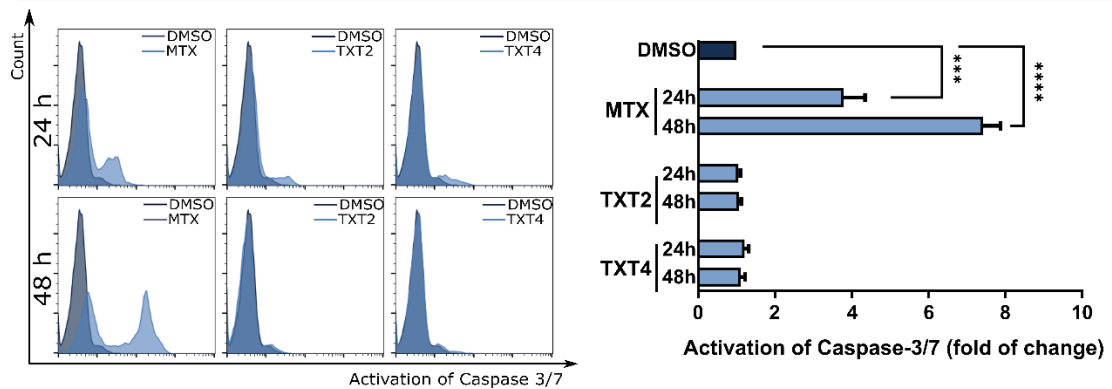


**Figure 25** Modulation of caspase-3/7 in U2OS cells after treatment with compounds. DMSO and MTX were used as negative and positive controls, respectively. Representative histograms are presented on the left panel and the quantification of data is on the bar graph. Error bars represent the s.d. of data obtained in  $n=3$  independent experiments.  $***p<0.0001$ ,  $****p<0.00001$  vs. vehicle (one-way ANOVA and post hoc Dunnett's test).

### 3.3.5. Analyses of expression apoptosis-related proteins

To examine whether TXT-mediated apoptosis occurred through intrinsic or extrinsic pathways, several apoptotic-related factors were monitored by western immunoblotting analyses. As shown in **Figure 26** treatment of both NSCLC cell lines with TXT-compounds triggered a marked increase in the proteolytic cleavage of PARP-1 (poly(ADP-ribose) polymerase-1), a signature event in apoptosis. In addition, a time-dependent decrease in the levels of the inactive (full-length) forms of caspase-8 and caspase-9 and a concomitant appearance of their cleaved forms were also appreciable. In parallel, events downstream of caspase-8 activation, such as processing of Bid to its active form tBid/p15, along with the appearance of cleaved forms of effector caspase-3 were also detected. Moreover, during 72-h culture, TXT compounds did not cause detectable changes in the expression of anti-apoptotic factor Bcl-2 in both NSCLC cells. However, it was noted that the expression of the BH123 protein Bax was significantly reduced in both cell lines, with proteolytic cleavage to p18 Bax in A549 cells, contributing to mitochondrial dysfunction.<sup>251</sup>

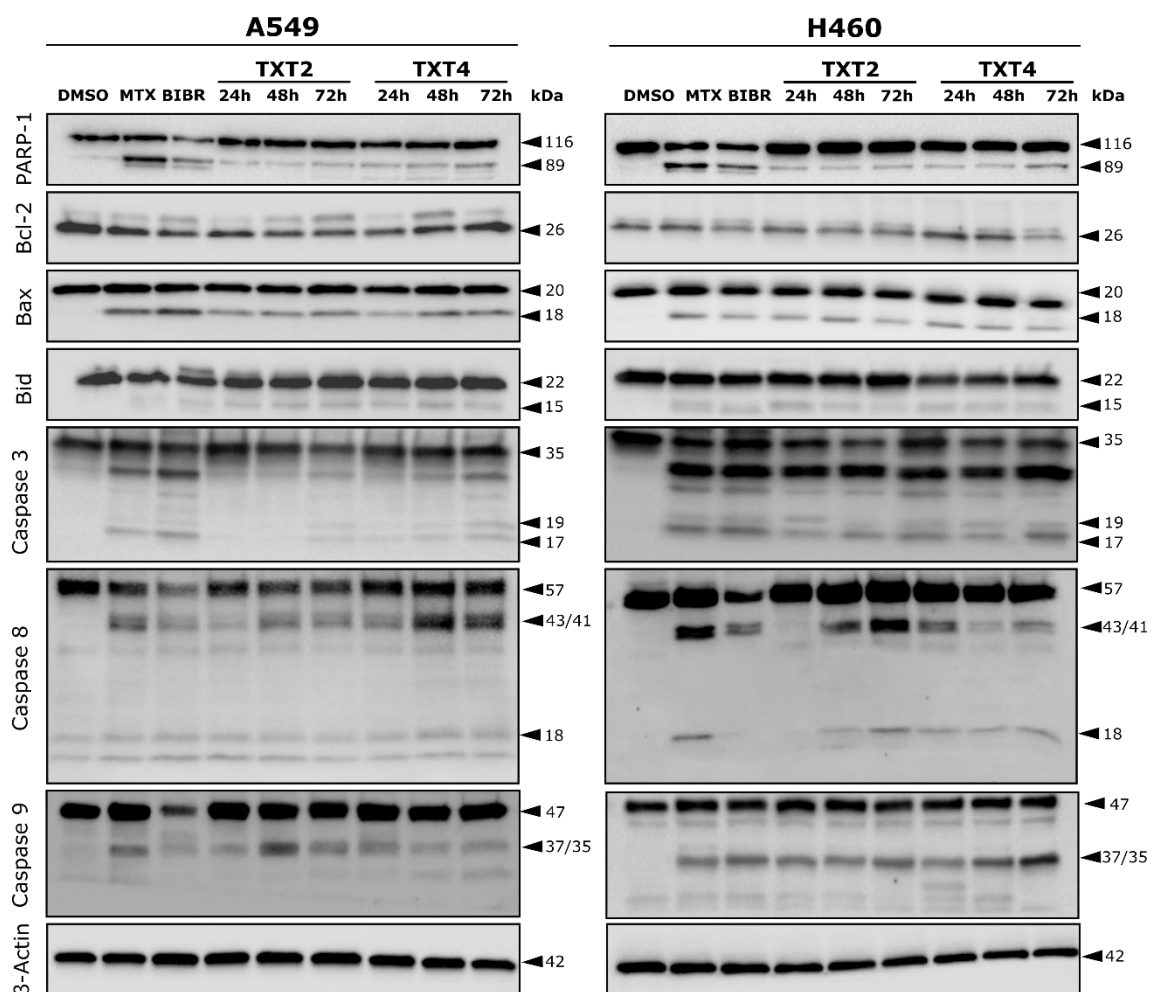


**Figure 26** Representative western immunoblotting showing the amounts of apoptotic-related proteins in A549 and H460 cell lines exposed to TXT compounds. DMSO and MTX were used as negative and positive controls, respectively.  $\beta$ -actin was used to ensure equal protein loading. The numbers on the right indicate the molecular weight (kDa).

### 3.3.6. Impact of anthraquinones on calcium homeostasis

Calcium homeostasis plays a crucial role in mitochondria- and endoplasmic reticulum (ER)-mediated apoptosis.<sup>252</sup> NSCLC cells were treated with TXT2 and TXT4 for 24, and 48 h, and labelled with the  $\text{Ca}^{2+}$ -sensitive fluorescent dye Fluo-4 AM to monitor the intracellular  $\text{Ca}^{2+}$  levels by flow cytometry (**Figure 27**). In A549 cells, both compounds increased  $\text{Ca}^{2+}$  at a similar level, approximately 2-times that compared to the control. When H226 cells were incubated with these compounds, no alteration in calcium homeostasis was observed from the basal level. Treatment of H460 cells led to significant  $\text{Ca}^{2+}$  efflux into the cytosol, revealed as 3.2-fold, and a 2.1-fold increase compared to vehicle, for TXT2, and TXT4, respectively. These results indicate that TXT2 and TXT4 lead to the remodelling of calcium signalling in A549 and H460 cells. The increased intracellular concentration of  $\text{Ca}^{2+}$  can be triggered by ER stress during which the capacity of the ER to fold proteins properly is compromised.<sup>253</sup> Next, released  $\text{Ca}^{2+}$  may accumulate in mitochondria leading to mitochondrial outer membrane permeabilization through



the involvement of the mitochondrial permeability transition pore (mPTP). Opening the mPTP releases pro-apoptotic factors, activating cell death.<sup>254</sup>

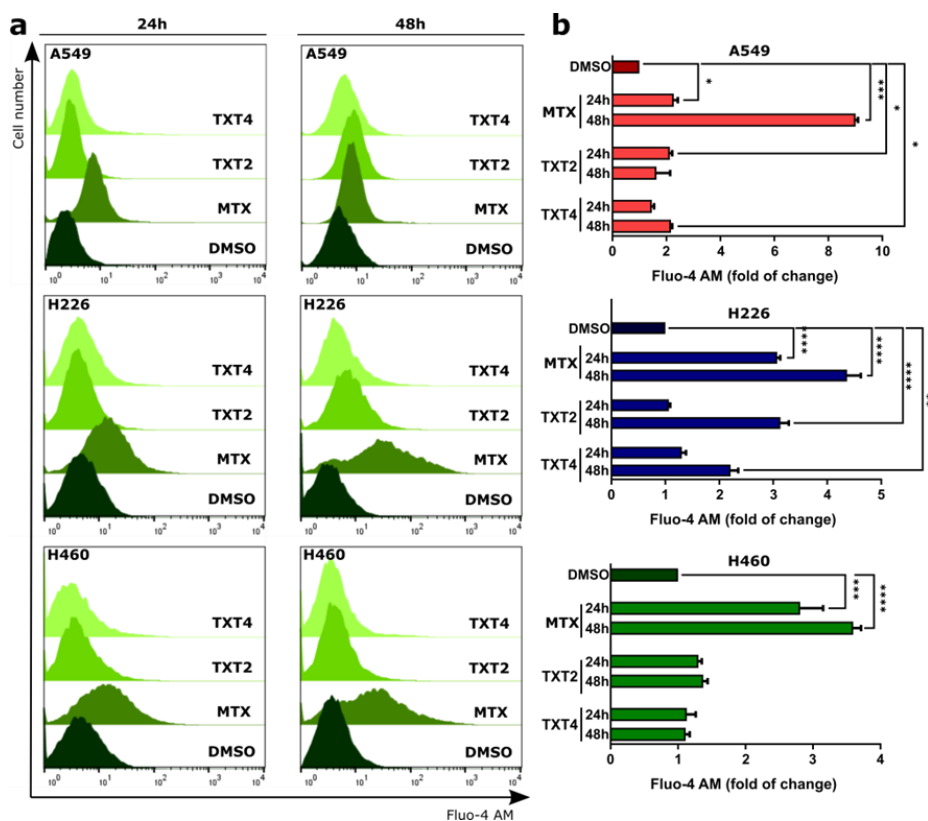


**Figure 27** Flow cytometric analyses of intracellular  $\text{Ca}^{2+}$  levels in A549, H226, and H460 cells after 24 and 48 h of treatment with TXT2 and TXT4. DMSO and MTX were used as reference compounds. **(a)** Representative histograms; **(b)** The quantitation of analysis is presented on a bar graph. Data represent the mean  $\pm$  SEM of three independent experiments. \* $p < 0.01$ , \*\* $p < 0.001$ , \*\*\* $p < 0.0001$ , \*\*\*\* $p < 0.00001$  (one-way ANOVA and post hoc Dunnett's test).

### 3.3.7. Study changes in mitochondria structure

Mitochondria are the main source of energy in cells, regulating important cellular processes, such as metabolism, proliferation, and  $\text{Ca}^{2+}$  homeostasis.<sup>255</sup> Changes in mitochondrial activity may increase ROS levels leading to oxidative stress-inducing telomere damage.<sup>256</sup> The mitochondrial phenotype was investigated in NSCLC cells after treatment with TXT2 and TXT4 compounds and staining with the cationic dye MitoTracker Green. This dye is commonly used to measure mitochondrial mass, whose changes reflect a disrupted balance between mitochondrial biogenesis and rates of mitophagy.<sup>257</sup> As depicted in **Figure 28** none of the tested compounds altered mitochondrial content after 24 h of exposure. Further treatment (48 h) induced a slight increase in mitochondrial mass compared to untreated controls, but only in A549 and H460 cells. There were no changes in the mitochondrial content in the H226 cells at any time point. Additionally, MitoTracker Green labelled A549 and H460 cells were visualized by confocal laser scanning microscopy (**Figures 29** and **30**). After 24 hours of treatment, the mitochondria of both cell lines displayed a common characteristic for increased fission revealed as a circular-

shaped and short structure (**Figure 31**).<sup>258</sup> Concomitantly with the swelling of fragmented mitochondria, a release of the mitochondrial DNA into the cytoplasm was observed, indicating mitochondria outer membrane permeabilization, which may lead to programmed cell death.<sup>259</sup> The lack of change in mitochondrial mass measured by flow cytometry after 24 h of treatment could be caused by enhanced biogenesis of mitochondria coupled with their increased fission.

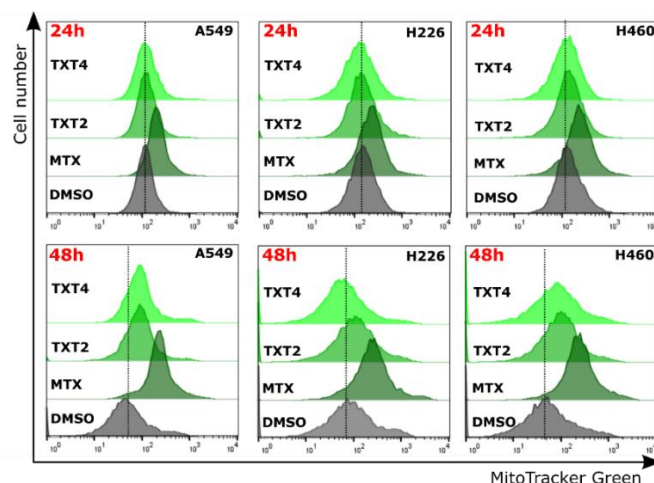


**Figure 28** Analyses of mitochondrial content after 24, and 48 h of treatment A549, H226, and H460 cells with compounds. DMSO and MTX were used as negative and positive controls, respectively.

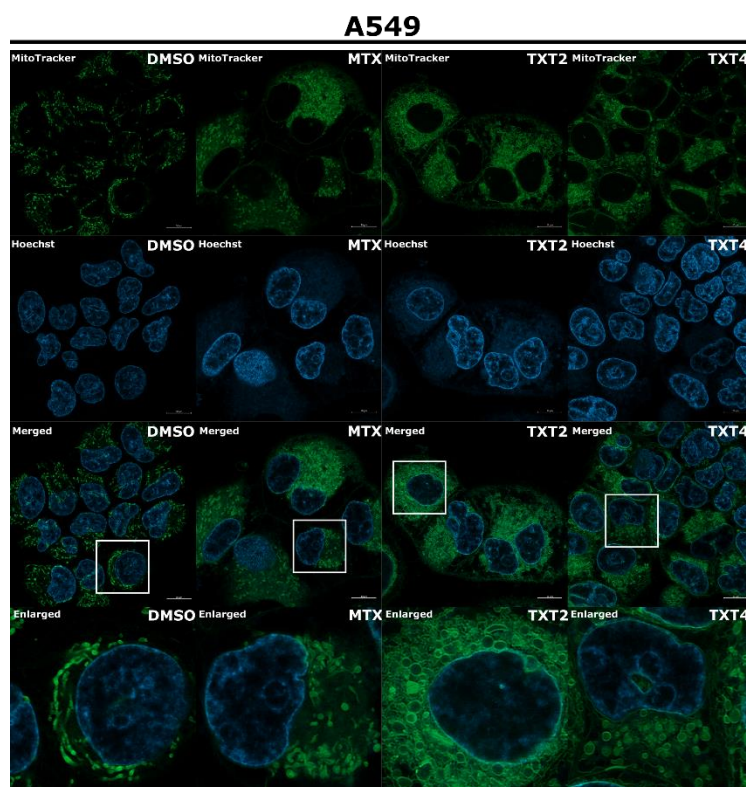


**Figure 29** Representative microscopic images presenting mitochondria structure in A549 cells acquired after 24 h of treatment with TXT2 and TXT4. DMSO and MTX were used as negative and positive controls, respectively; Green—MitoTracker, blue—Hoechst 33342. Scale bars = 10  $\mu$ m.

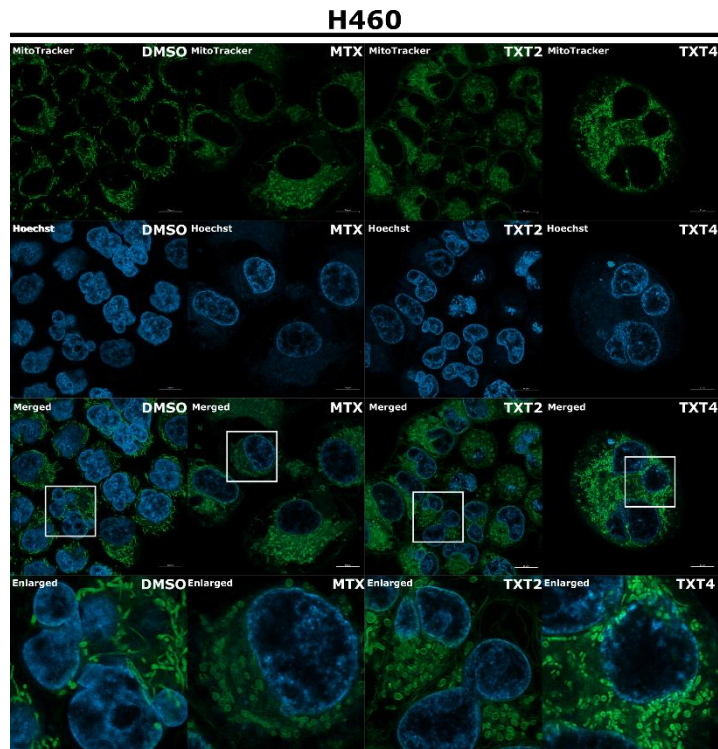


**Figure 30** Representative microscopic images presenting mitochondria structure in H460 cells acquired after 24 h of treatment with TXT2 and TXT4. DMSO and MTX were used as negative and positive controls, respectively; Green—MitoTracker, blue—Hoechst 33342. Scale bars = 10  $\mu$ M.

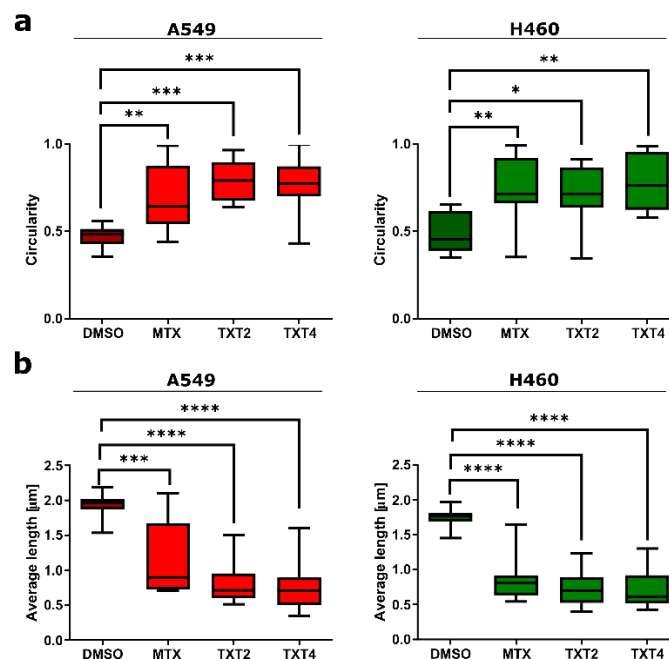


**Figure 31** Quantitative mitochondrial morphometric analyses. **(a)** The circularity of mitochondria (index of elongation); **(b)** Average length ( $\mu$ m) of mitochondria. Error bars represent the s.d. of data obtained in at least  $n=15$  randomly selected locations on the slide. \* $p<0.01$ , \*\* $p<0.001$ , \*\*\* $p<0.0001$ , and \*\*\*\* $p<0.00001$  compared to DMSO (one-way ANOVA and post hoc Dunnett's test).

### 3.3.8. Effect of anthraquinones on stress-induced senescence

A previous study confirmed that anthraquinone derivatives induce apoptotic cell death. However, in all NSCLC cells, a viable fraction of cells was still observed after 72 h of treatment, which suggests that cells were undergoing stress-induced premature senescence (SIPS). Telomerase inhibition leads to the progressive shortening of telomeres leading to replicative senescence.<sup>260</sup> However, some data report that short-term inhibition could also lead to SIPS.<sup>261</sup> Since telomerase protects cells against oxidative stress, its inhibition leads to DNA damage triggering premature senescence. Characterization of cellular senescence upon treatment with anthraquinone derivatives on A549, H226, and H460 cells was performed by detecting senescence-associated  $\beta$ -galactosidase activity (SA- $\beta$ -gal). SA- $\beta$ -gal activity is expressed by the gene coding the lysosomal  $\beta$ -galactosidase (GLB1) and is widely used as a marker of cellular senescence. The GLB1 activity results from the lysosomal compartment expansion due to the accumulation of damaged macromolecules in senescent cells.<sup>262</sup>

As depicted in **Figure 32**, TXT1 and TXT3 did not induce SIPS on A549 and H460 cells, as evidenced by a negligible change in cell morphology and only several cells with SA- $\beta$ -gal activity. In contrast, treatment of A549 and H460 cells with TXT2 and TXT4 led to typical morphological and physiological alterations related to ageing, including an enlarged and flattened appearance, increased granularity, and activity of SA- $\beta$ -gal. Treatment of H226 cells with all test compounds altered their morphology, but to a smaller extent, compared to other cell lines. In addition, increased lysosomal activity was observed only after treatment with TXT1 and TXT2. Moreover, all anthraquinone derivatives induced SIPS only partially, whereas the rest of the cell population did not show typical features of senescence. In comparison, DOX severely affects almost all NSCLC populations, inducing cell senescence accompanied by an increase in SA- $\beta$ -gal activity and size of the cells. In order to further confirm TXT-SIPS, future studies including analyses of typical markers, such as p21 or p16 are warranted

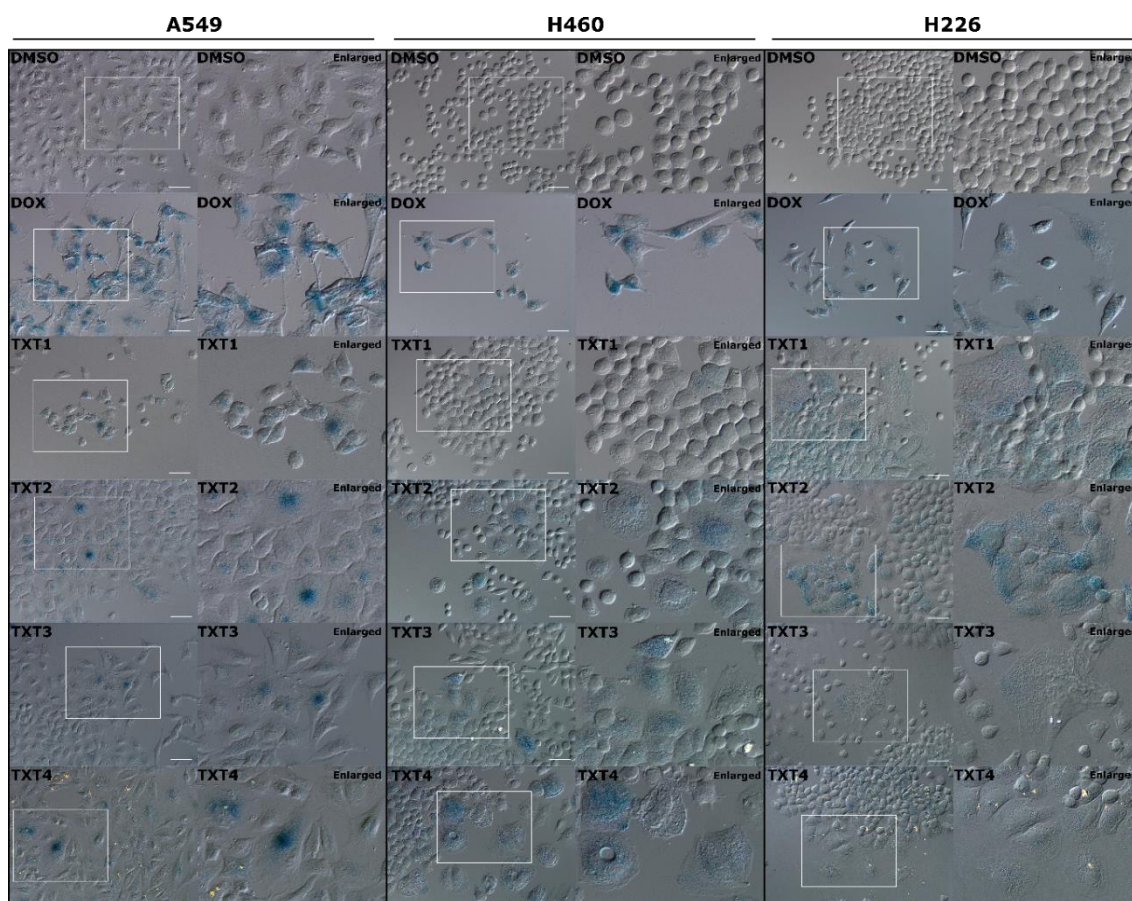


**Figure 32** Representative microscopic images of A549, H460, and H226 cells after staining for senescence-associated  $\beta$ -galactosidase activity. DMSO and DOX were used as negative and positive controls, respectively. Scale bars=50  $\mu$ M.

### 3.3.9. Study of prooxidative properties

Cellular redox homeostasis is essential for the regulation of many signalling pathways.<sup>263</sup> Many anticancer therapies cause disturbances in the redox state in cells by elevating intracellular levels of ROS or inhibiting antioxidant processes.<sup>264</sup> The acceleration of accumulative ROS causes damage to cellular components such as lipids, proteins, and DNA, leading to cancer cell death. In cancer cells, one of the regulators of ROS levels in mitochondria and cytosol is hTERT.<sup>265</sup> Therefore, a time-dependent kinetic analysis of the intracellular ROS levels was performed on NSCLC cells treated with anthraquinone derivatives. As presented in **Figure 33** most of the test compounds did not induce oxidative stress in H226 cells, revealed as a constant signal from the H2DCFDA probe. Only TXT1 significantly increased the ROS level after 24 h of treatment in comparison to the vehicle ( $12.9 \pm 2.49\%$ ;  $p < 0.001$ ); while  $H_2O_2$  increased up to 80% ( $p < 0.00001$ ). Treatment of A549 and H460 cells with TXT1 led to a significant accumulation of ROS under almost all conditions; however, this effect differed between the cell lines, where it increased or decreased with exposure time, for A549 and H460 cells, respectively (**Figures 34** and **35**). Additionally, out of all compounds, TXT1 induced the most ROS in all NSCLC cells after 24 h of exposition, which can translate to its high cytotoxic activity. Compounds TXT2 and TXT3

induced ROS at a similar extent in lines H226 and A549, but less than TXT1 and TXT4 compounds. The TXT4 compound induced a potent accumulation of ROS, just after 1 h of incubation with A549 ( $27.5.2\pm1.47\%$  positive cells; \*\*\*\* $p<0.00001$ ) and H460 ( $37.6\pm3.02\%$  positive cells; \*\*\*\* $p<0.00001$ ) cells, but after 24 h of treatment, the percentage of ROS positive cells decreased almost to basal level.

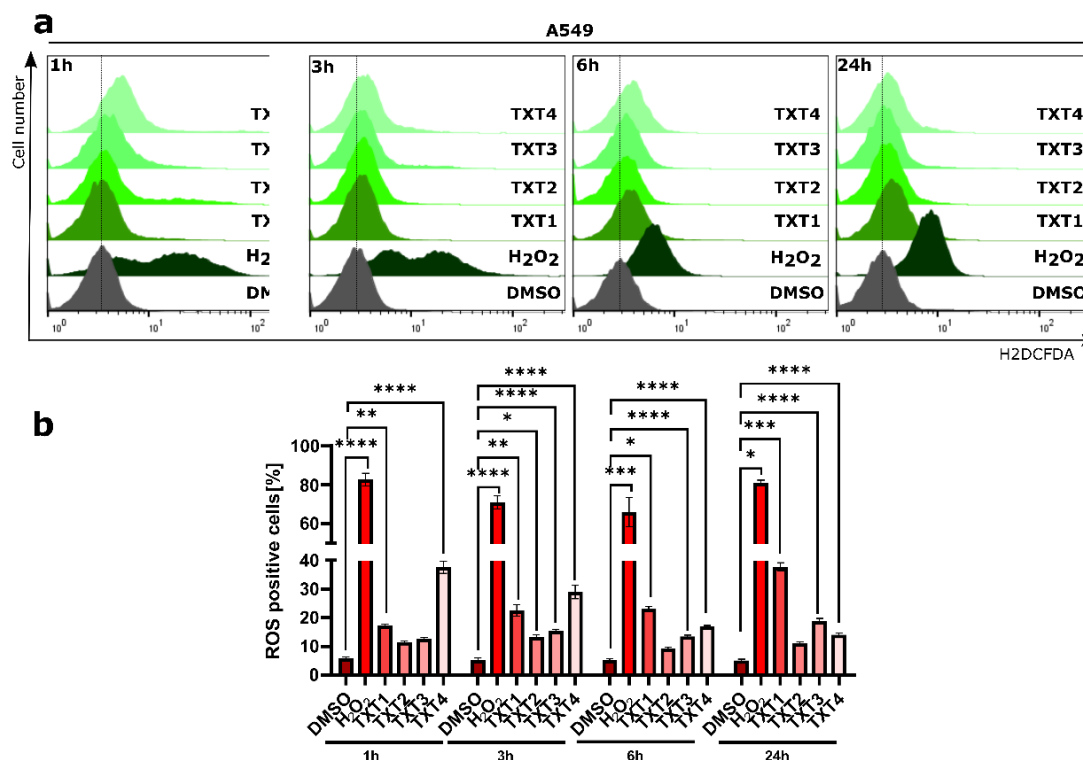


**Figure 33** Flow cytometric analyses of ROS induction in A549 cells after 1, 3, 6, and 24 h of treatment with compounds, using an H<sub>2</sub>DCFDA probe. DMSO and H<sub>2</sub>O<sub>2</sub> were used as negative and positive controls, respectively. **(a)** Representative histograms; **(b)** The quantitation of analysis. Error bars represent the SEM of data obtained in n=3 independent experiments. \*  $p<0.01$ , \*\*  $p<0.001$ , \*\*\*  $p<0.0001$ , \*\*\*\*  $p<0.00001$  vs. vehicle (two-way ANOVA and post hoc Dunnett's test).

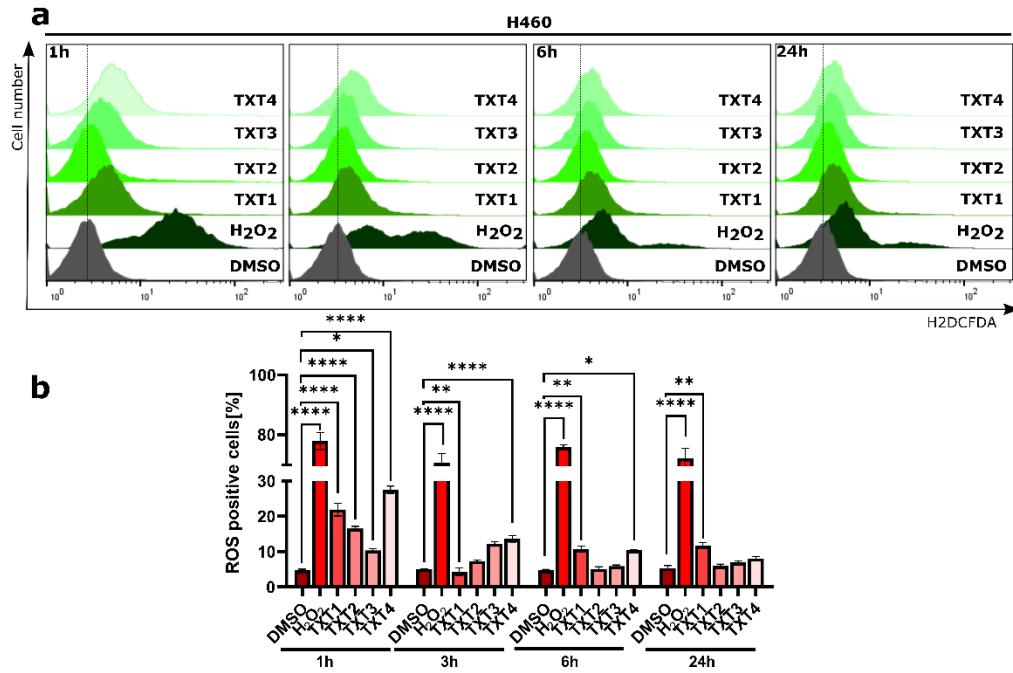


**Figure 34** Flow cytometric analyses of ROS induction in H460 cells after 1, 3, 6, and 24 h of treatment with compounds, using an H<sub>2</sub>DCFDA probe. were used as negative and positive controls, respectively. **(a)** Representative histograms; **(b)** The quantitation of analysis. Error bars represent the SEM of data obtained in n=3 independent experiments. \* p<0.01, \*\* p<0.001, \*\*\* p<0.0001, \*\*\*\* p<0.00001 vs. vehicle (two-way ANOVA and post hoc Dunnett's test).

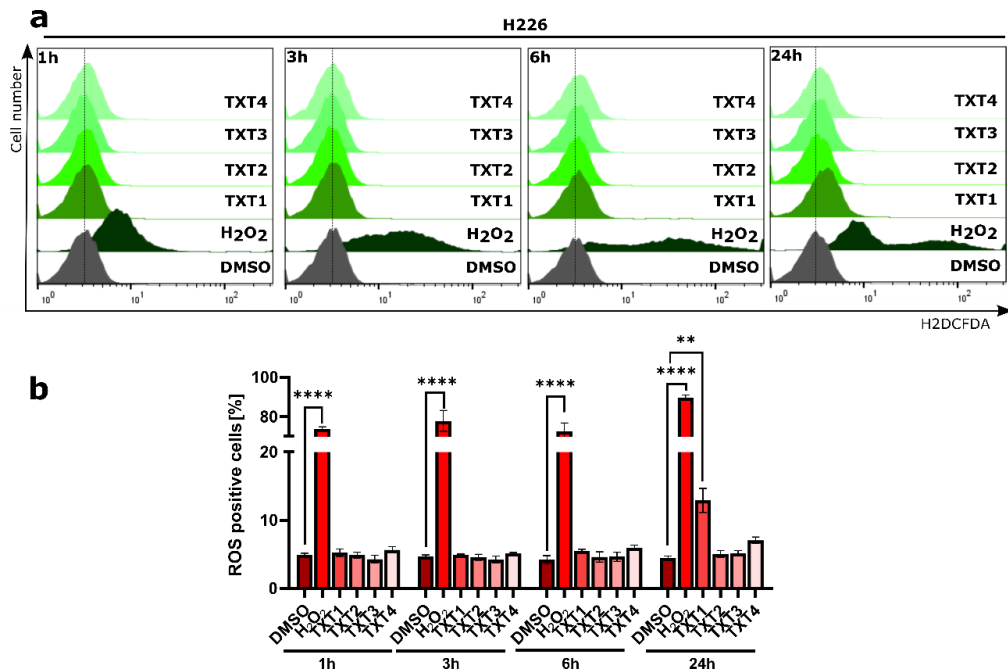


**Figure 35** Flow cytometric analyses of ROS induction in H226 cells after 1, 3, 6, and 24 h of treatment with compounds, using an H<sub>2</sub>DCFDA probe. were used as negative and positive controls, respectively. **(a)** Representative histograms; **(b)** The quantitation of analysis. Error bars represent the SEM of data obtained in n=3 independent experiments. \* p<0.01, \*\* p<0.001, \*\*\* p<0.0001, \*\*\*\* p<0.00001 vs. vehicle (two-way ANOVA and post hoc Dunnett's test).

### 3.3.10. Impact of anthraquinones on DNA damage

Several studies reported a link between telomerase inhibition and DNA damage correlated with uncapped or dysfunctional telomeres.<sup>266,267</sup> One of the DNA double-strand break' markers is the phosphorylation of histone variant H2AX on Serine 139, forming nuclear foci.<sup>268</sup> The level of DNA damage was studied on TERT-positive A549 and H460 cells, TERT-negative: normal NHBE and HUVEC cells, and ALT-positive U2OS cells exposed to equitoxic concentrations of the compounds. As presented in **Figure 36**, TXT2 and TXT4 induced a potent rise of DNA DSBs in NSCLC cells, as evidenced by the accumulation of  $\gamma$ -H2AX fraction in the two TERT-positive cell lines. More extended exposition to these compounds resulted in a decrease in DSBs and as a consequence of DNA repair pathways' activation. Treatment with TXT1 and TXT3 led to a negligible increase in  $\gamma$ -H2AX positive cells. Conversely, NHBE/TERT(-), HUVEC/TERT(-), and U2OS cells exposed to TXT2/TXT4 showed no evidence of increased DNA damage, in comparison to MTX which evokes a massive rise of  $\gamma$ -H2AX in TERT(-) ALT(+) cells, and 8.7% in TERT(-) cells (**Figures 37** and **38**). TXT1 and TXT3 induced a time-dependent increase of DSBs in HUVEC/TERT(-) and NHBE/TERT(-) cells, respectively, but not in TERT(-) ALT(+) cells. Accumulation of  $\gamma$ -H2AX after treatment in normal TERT(-) cells with TXT1 and TXT3 was significantly higher than in cancer cells, which may reflect their high toxicity. Interestingly, compounds induced more DSBs in A549 than in H460 cells, which correlates with their cytotoxic and pro-apoptotic properties. Moreover, the compounds' ability to induce DSBs rises with their potential to inhibit telomerase.

To investigate the possible influence of TXT-mediated inhibition of telomerase activity on the induction of telomere dysfunction-induced foci (TIFs), which are markers for telomeric localized DNA damage, the co-localization of  $\gamma$ -H2AX and TRF2 (one of the shelterin-associated proteins that can directly bind to telomeric DNA) was investigated by immunofluorescence microscopy (**Figure 39a**). The incidence of telomere dysfunctions as judged by TIFs has remarkably increased in Teloxantron-treated A549/TERT(+) cells, with the respect to MTX- and DMSO-treated control, as indicated by the extent of the overlapping between  $\gamma$ -H2AX and TRF2 fluorescent signal (**Figures 39b**, **Figures 40a** and **d**) as well as by the calculated Mander's (MCC:  $0.922\pm 0.055$ ) and Pearson's (PCC:  $0.723\pm 0.046$ ) correlation coefficients (**Figures 40b** and **c**). This evidence was confirmed by combined immunofluorescence and fluorescence in situ hybridization (FISH), which showed that the majority of telomeric signals colocalized with  $\gamma$ -H2AX after 72 h of treatment with TXT4 (**Figure 40e**). Conversely, no differences in TIFs formation were observed in NHBE or U2OS cells treated with TXT4 with respect to DMSO (**Figure 41**).





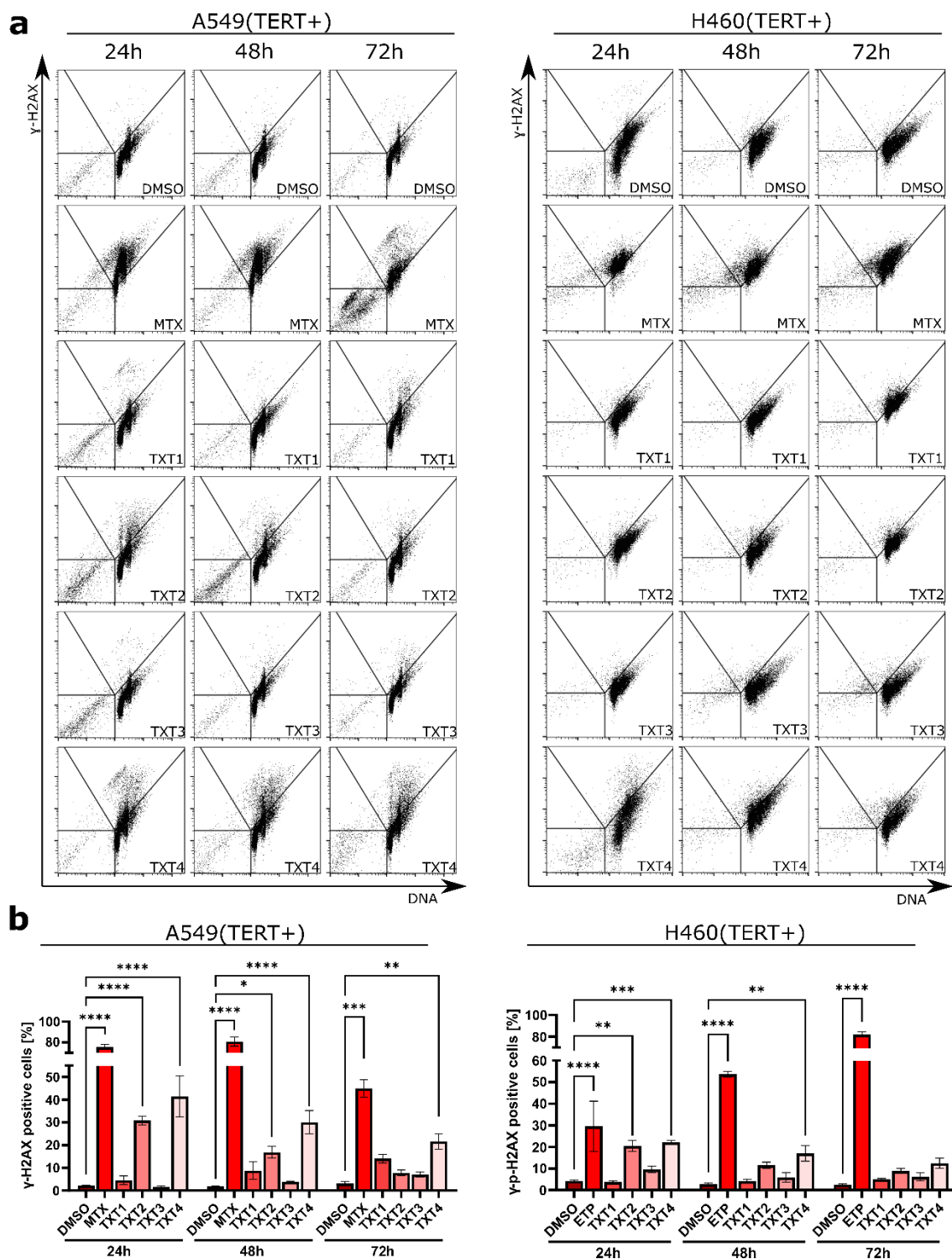


**Figure 36** Flow cytometric analyses of induction  $\gamma$ -H2AX in A549, and H460 cell lines at 24, 48, and 72 h of treatment. DMSO and MTX were used as negative and positive controls, respectively. **(a)** Representative histograms; **(b)** The quantification of the analysis is presented on a bar graph. Data represent the mean  $\pm$  s.d. of three independent experiments. \*  $p < 0.01$ , \*\*  $p < 0.001$ , \*\*\*  $p < 0.0001$ , \*\*\*\*  $p < 0.00001$  (two-way ANOVA and post hoc Dunnett's test).

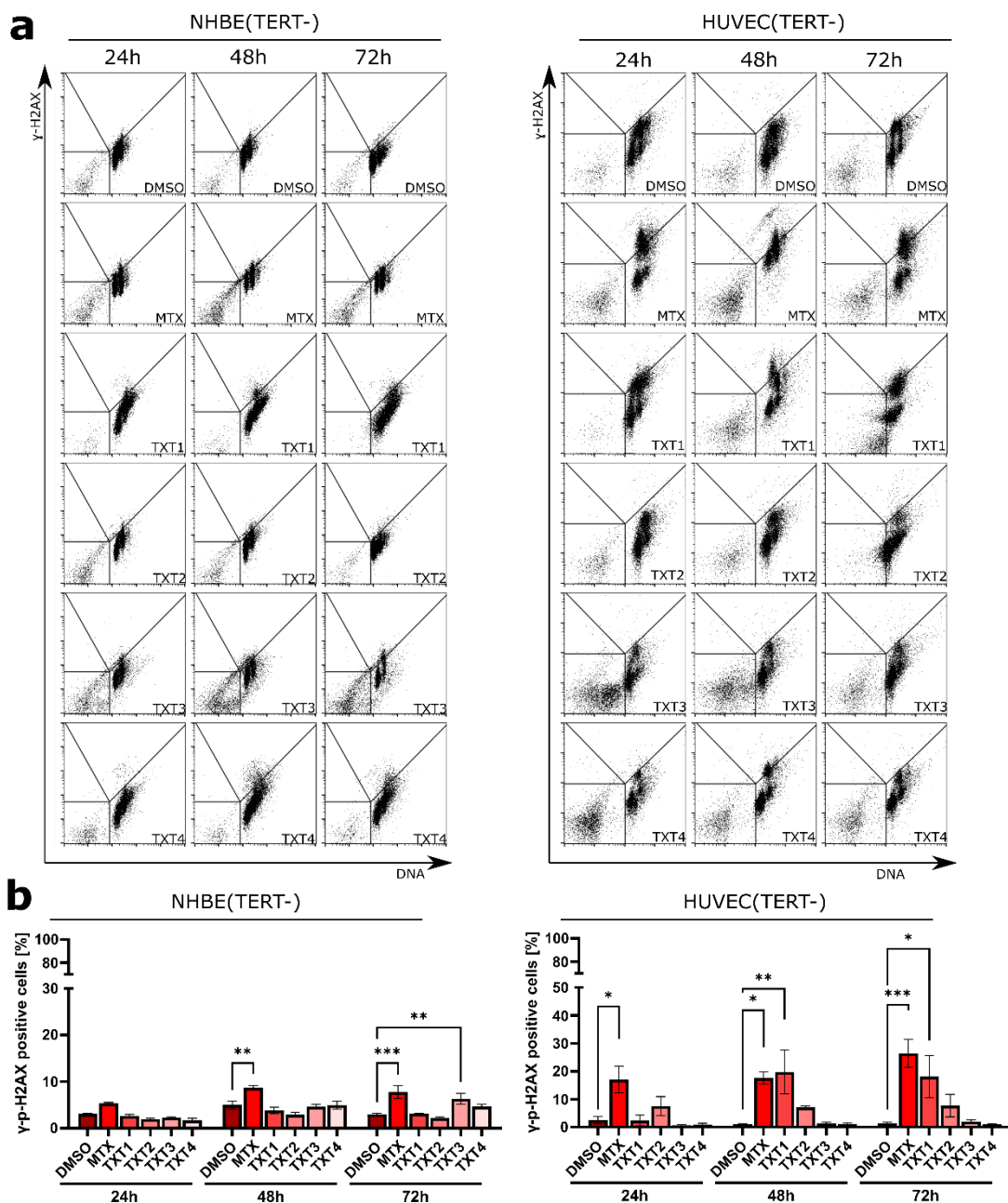


**Figure 37** Flow cytometric analyses of induction  $\gamma$ -H2AX in NHBE, and HUVEC cell lines at 24, 48, and 72 h of treatment. DMSO and MTX were used as negative and positive controls, respectively. **(a)** Representative histograms; **(b)** The quantification of analysis is presented on a bar graph. Data represent the mean  $\pm$  s.d. of three independent experiments. \*  $p < 0.01$ , \*\*  $p < 0.001$ , \*\*\*  $p < 0.0001$  (two-way ANOVA and post hoc Dunnett's test).

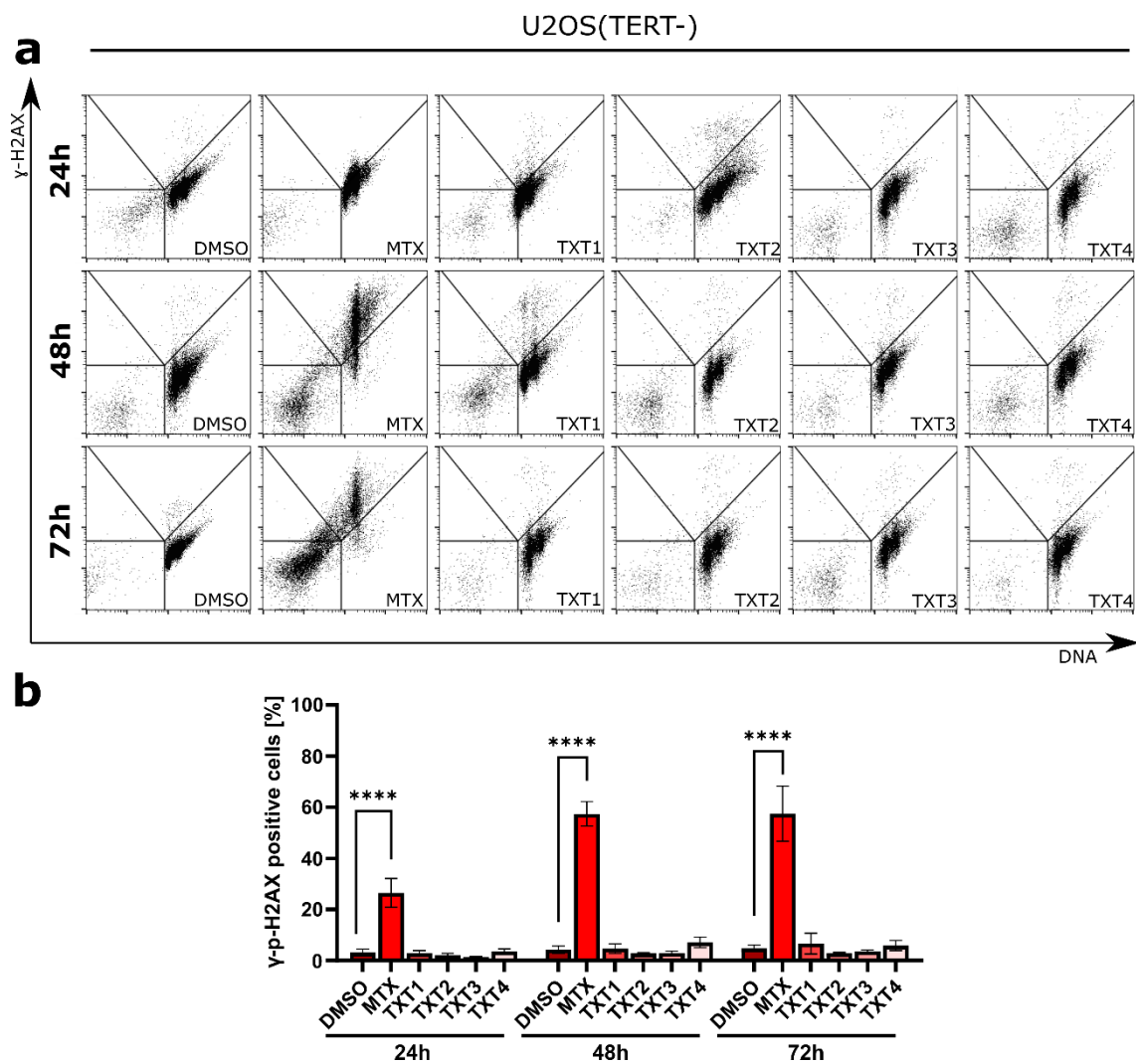


**Figure 38** Flow cytometric analyses of induction  $\gamma$ -H2AX in U2OS cell line at 24, 48, and 72 h of treatment. DMSO and MTX were used as negative and positive controls, respectively. **(a)** Representative histograms; **(b)** The quantification of analysis is presented on a bar graph. Data represent the mean  $\pm$  s.d. of three independent experiments. \*\*\*\*  $p < 0.00001$  (two-way ANOVA and post hoc Dunnett's test).

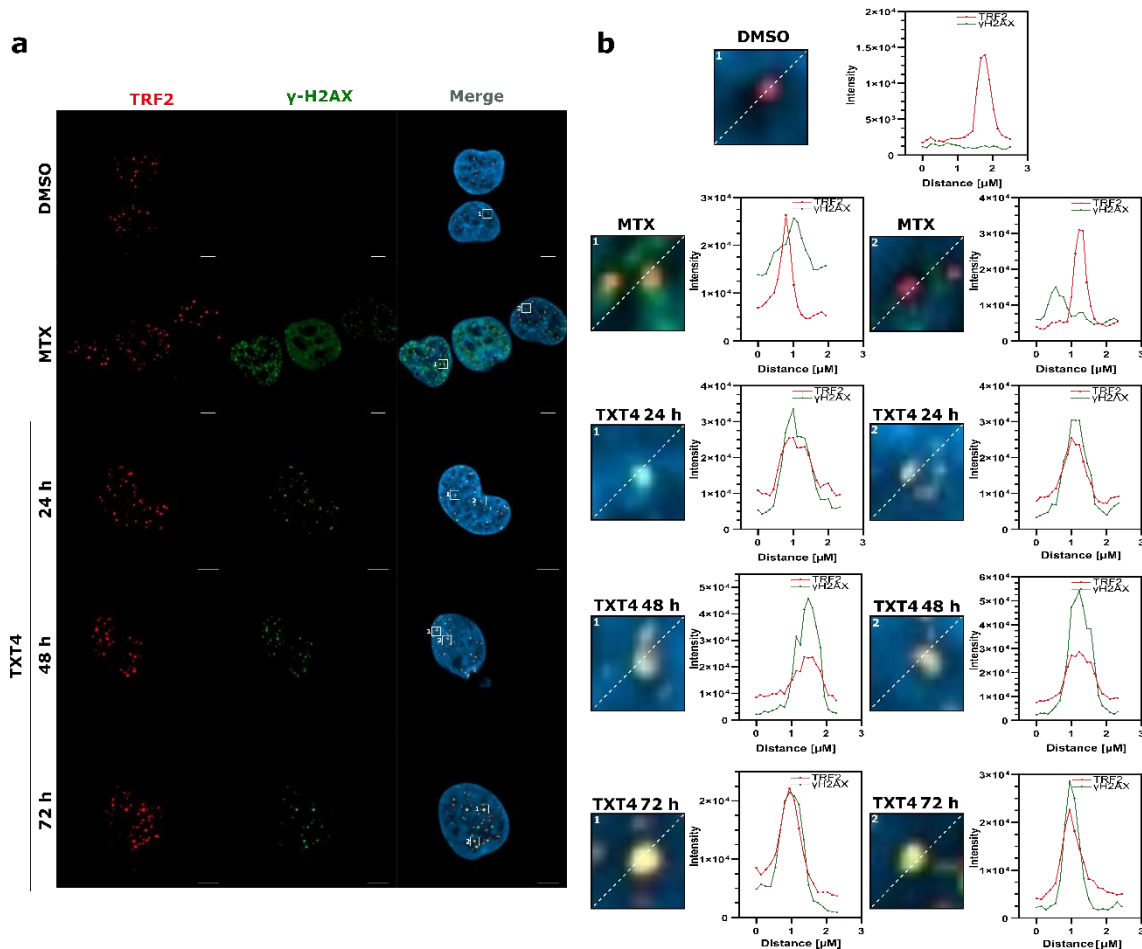


**Figure 39** TXT4 induces telomere dysfunctions in TERT-positive cells. **(a)** Representative high-resolution images obtained by laser scanning confocal microscopy showing the colocalization of  $\gamma$ -H2AX and TRF2 as a function of time in A549 cells after treatment with TXT4. DMSO and MTX were used as negative and positive controls, respectively. Scale bars=10  $\mu$ m. Nuclei were counterstained with DAPI (4',6-diamidino-2-phenylindole); **(b)** Representative line scans showing the overlapping between  $\gamma$ -H2AX (green) and TRF2 (red) fluorescent signal corresponding to the marked area reported in panel a.

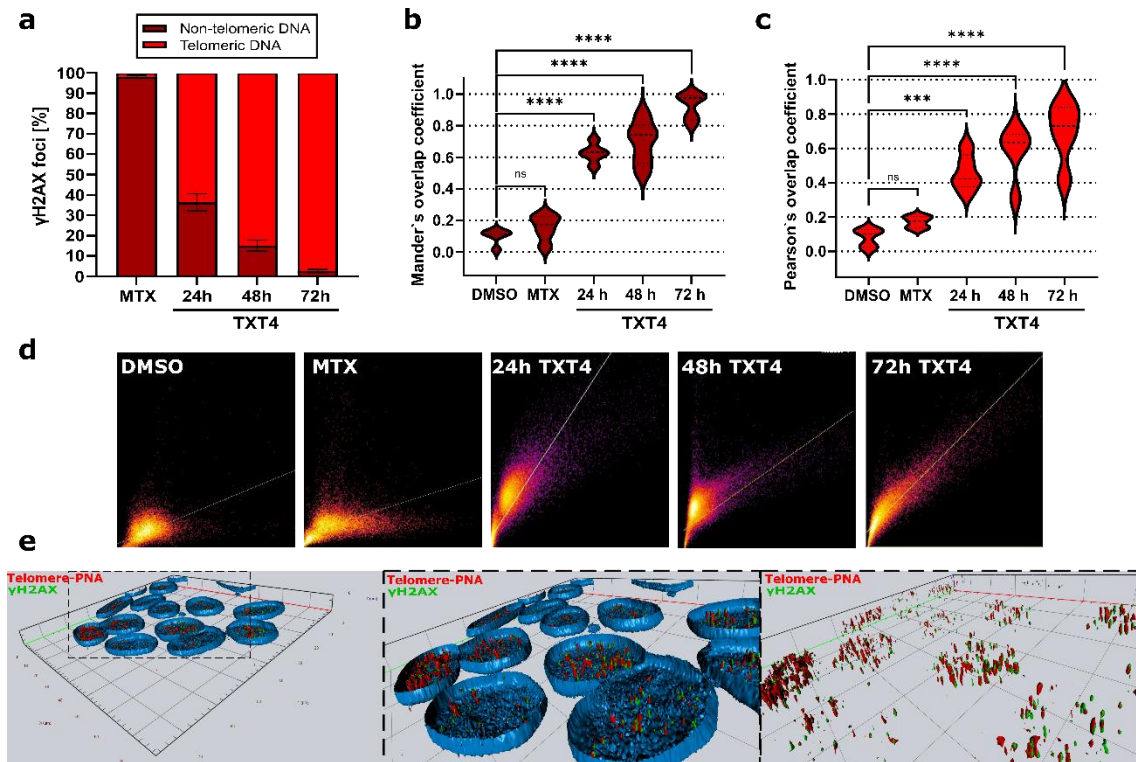


**Figure 40** TXT4 induces telomere dysfunctions in TERT-positive cells. **(a)** Quantification of  $\gamma$ -H2AX nuclear foci. Bright red bars indicate the fraction (%) of  $\gamma$ -H2AX nuclear foci that localize at the telomeric level within the overall amount of DNA damage nuclear foci; **(b and c)** Graphical representation of the calculated Mander's and Pearson's overlapping coefficients. Error bars represent the s.d. of data obtained in at least  $n=15$  randomly selected locations on the slide. ns>0.05, \*\* $p<0.001$ , \*\*\* $p<0.0001$ , and \*\*\*\* $p<0.00001$  compared to DMSO (two-way ANOVA and post hoc Dunnett's test); **(d)** Scatter plots showing the overlapping between  $\gamma$ -H2AX (green) and TRF2 (red) fluorescent signal corresponding to the colocalization of pixels in the Figure 36a; **(e)** Combined immunofluorescence and telomeric FISH (fluorescence in situ hybridization) showing the co-localization between  $\gamma$ -H2AX (green) and telomeric DNA (red) in A549 cells exposed for 72 h to TXT4. A 3-D reconstruction of microscopy images captured in a Z-stack has been reported.

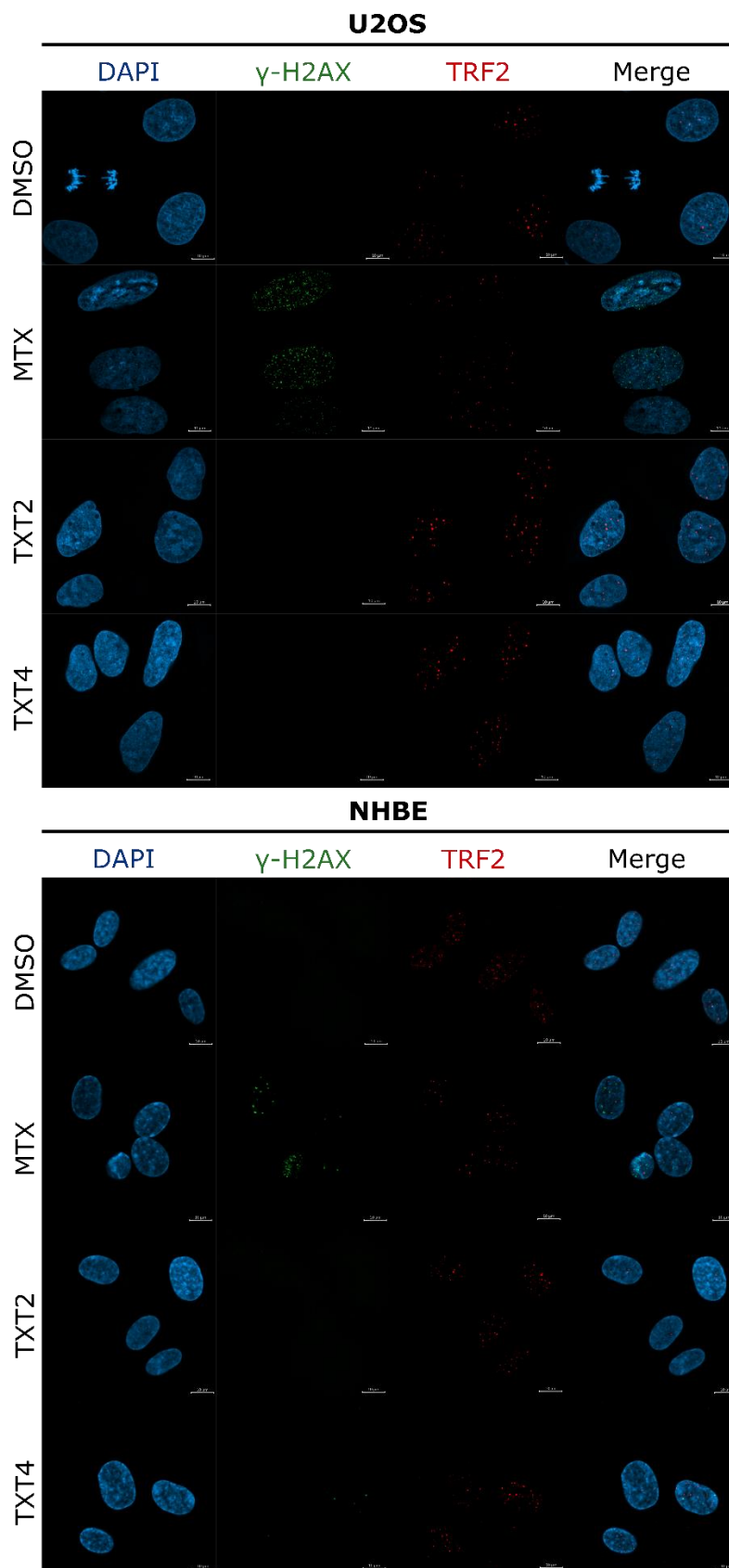


**Figure 41** Representative high-resolution laser scanning confocal images showing the  $\gamma$ -H2AX with TRF2 after treatment NHBE and U2OS cell lines. DMSO and MTX were used as negative and positive controls, respectively. Scale bars=10  $\mu$ m. Nuclei were counterstained with DAPI.

### 3.3.11. Assessment of the DDR protein network

Induction of DNA damage is known to trigger a DDR, which eventually leads to cell cycle arrest, DNA repair, or cell death. The two main DDR signalling pathways involve the ATM/Chk2 (ataxia telangiectasia mutated kinase/checkpoint kinase 2) cascade and the ATR/Chk1 (ataxia telangiectasia mutated and Rad3-related kinase/checkpoint kinase 1) cascade.<sup>269</sup> Therefore, the effect of TXT2 and TXT4 on the expression of the DDR protein network was analysed by Western blot analysis (**Figure 42**). Treatment with TXT2 and TXT4 caused an increase in the phosphorylation of ATM and ATR in both A549 and H460 NSCLC cells, with a greater effect in A549 compared to H460 cells. Additionally, phosphorylation of Chk2 at threonine 68 and of Chk1 at serine 345, which are downstream targets of ATM and ATR, respectively, was induced by both compounds in A549 and H460 cells. Conversely, the exposure of ALT-positive cancer cells to TXT compounds failed to evoke the activation of both ATM- and ATR-dependent signalling cascade (**Figure 42**).

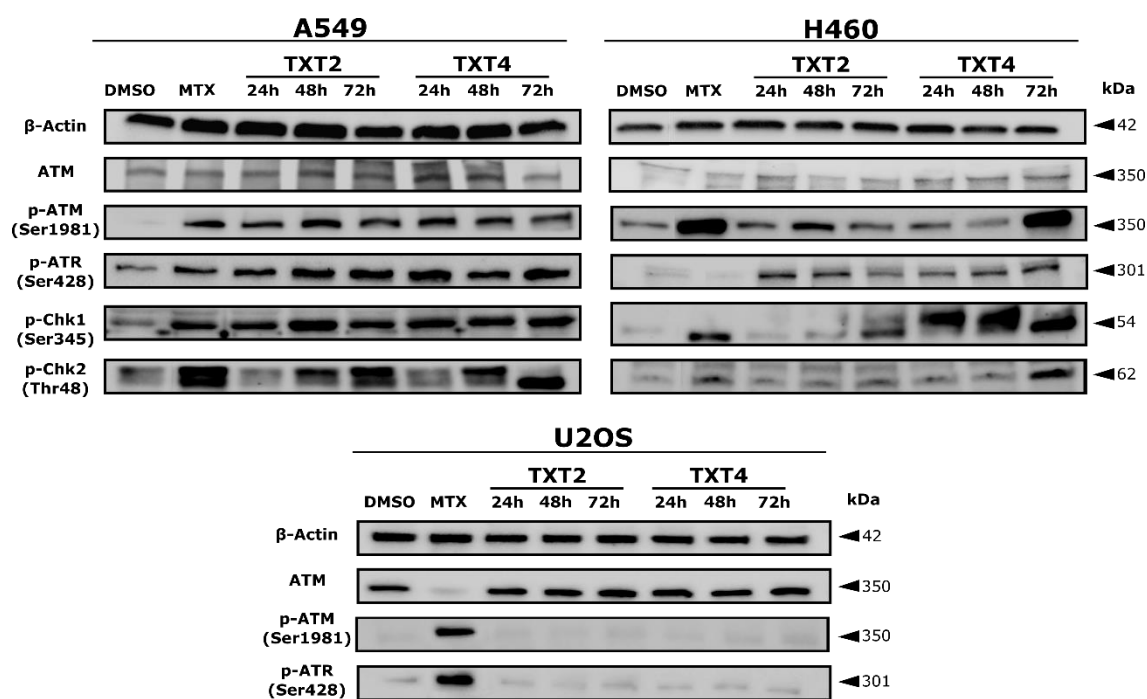


**Figure 42** Representative Western immunoblot showing the levels of DNA damage-related proteins in TXT2- and TXT4- treated A549, H460, and U2OS cells. DMSO and MTX were included as negative and positive controls, respectively.  $\beta$ -actin was used to ensure equal protein loading. The numbers on the right indicate the molecular weight (kDa).

### 3.3.12. Genotoxicity evaluation using comet assay

The genotoxic properties of the compounds were evaluated in A549 cells after 24 h of treatment, using the alkaline comet assay. This method is commonly used to detect SSBs and DSBs in the cells and reflects the physical status of genomic DNA. Unexpectedly, none of the tested compounds induced DNA damage in tested conditions, unlike  $H_2O_2$  which increased

the average tail length by 40% compared to the control (**Figure 43**). Interestingly, similar limitations of comet assay were observed also by others, e.g., Nikolova et al. show that mitomycin C is ineffective in the comet assay, whereas it was identified as a genotoxicant in the  $\gamma$ -H2AX assay in the same concentration.<sup>270</sup>

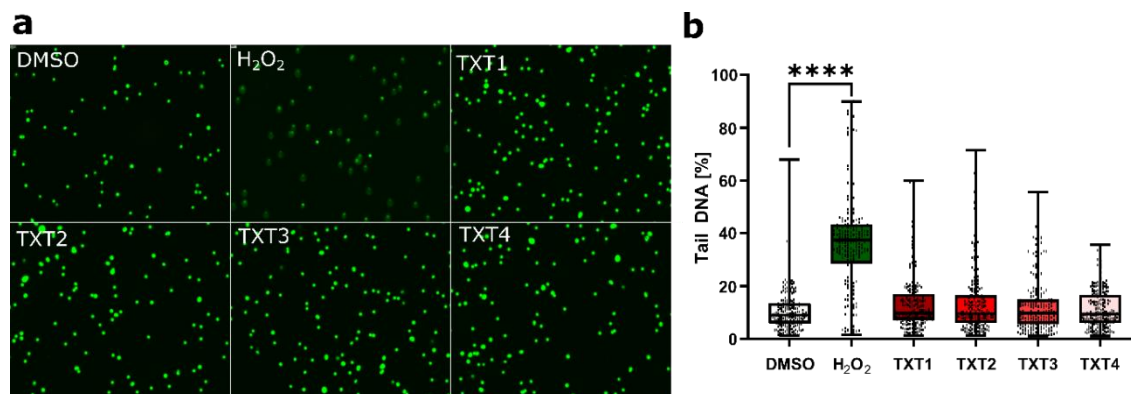


**Figure 43** Genotoxicity evaluation. **(a)** Representative microscopic images of the comet in A549 cells after treatment with compounds for 24 h. DMSO and H<sub>2</sub>O<sub>2</sub> were used as positive and negative controls, respectively. **(b)** The quantification of analyses expressed in % of tail DNA. Error bars represent the SEM of data obtained in n=3 independent experiments. \*\*\*\* p<0.00001 vs. vehicle (one-way ANOVA and post hoc Dunnett's test).

### 3.3.13. Analysing G-4 stabilizing properties of anthraquinones

Several anthraquinone derivatives have been shown to interact with telomeric DNA via G-4 stabilization.<sup>271,272</sup> Therefore, the ability of our compounds to promote telomeric G-4 DNA thermal stabilization was evaluated using FRET melting assay in comparison to the reference compound TMPyP4 and MTX known for having G-4 stabilizing properties. In particular, FRET melting profiles indicated that both reference compounds showed good telomeric G-4 stabilizing properties, with  $\Delta T_m$  values of +15.8 and +19.7°C for MTX and TMPyP4, respectively (**Figure 44**). Conversely, none of the TXT compounds showed marked telomeric G-4 stabilizing properties, as revealed by the lack of a significant shift of the  $T_m$  and the melting profiles that were superimposable to that observed for DMSO (**Figure 44**). This evidence would indicate that the 9,10-anthraquinone derivative-mediated inhibition of telomerase activity observed in the TRAP assay occurred with a mechanism that does not involve telomeric G-4 stabilization.



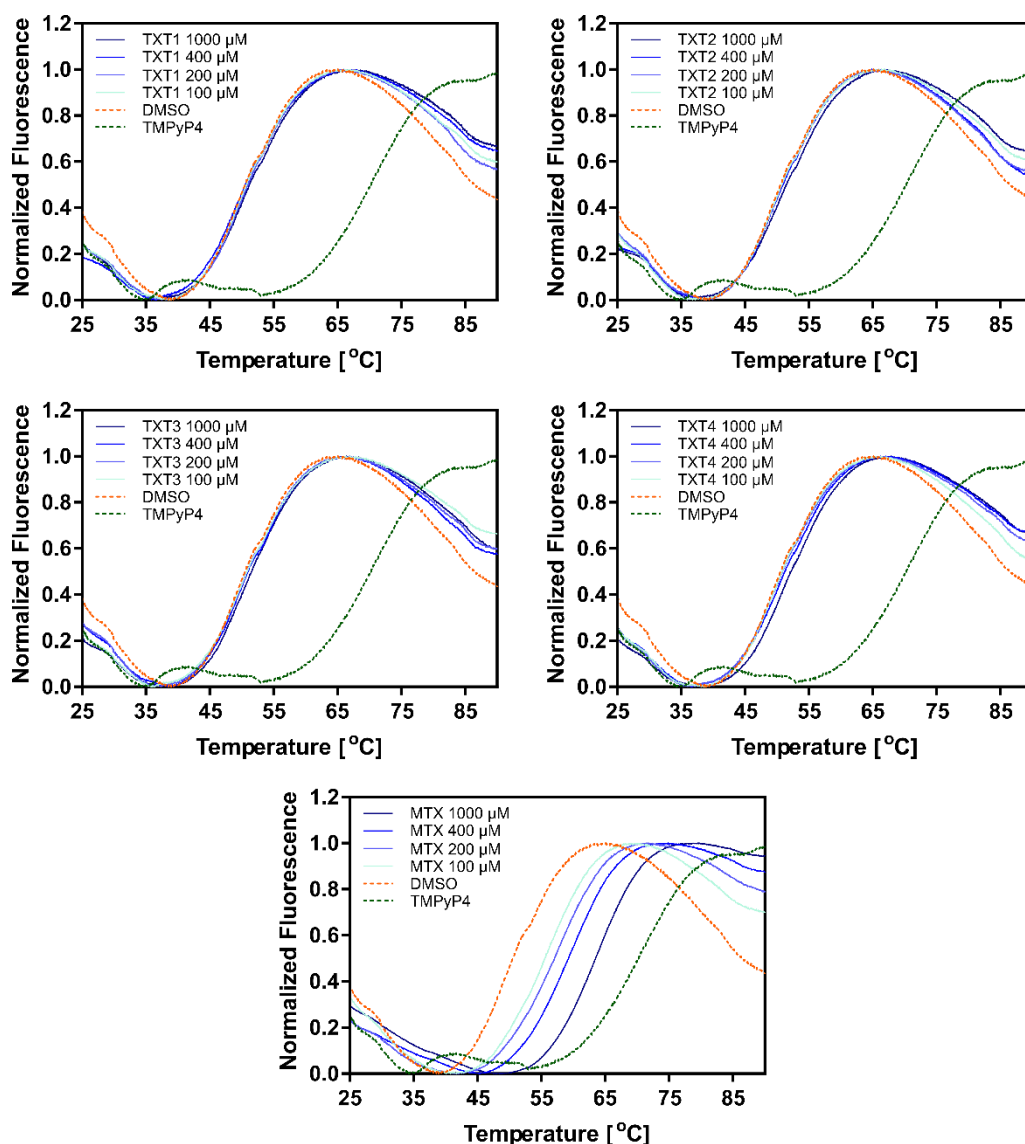


**Figure 44** FRET melting profiles of a human telomeric DNA sequence in the presence of increasing concentrations of MTX, TXT2, or TXT4 compounds. DMSO and TMPyP4 were used as negative and positive controls for telomeric G-4 stabilization, respectively.

### 3.3.14. Analysis of TXT4 to interact with hTERT

The ability of TXT4 to interact with and likely stabilize telomerase in intact cells was analysed by the cellular thermal shift assay (CETSA) (**Figure 45**). CETSA allows rapid assessment of the target engagement of drugs under a physiologically relevant condition based on the ligand-induced thermal stabilization of the target protein. In particular, our data showed that a prominent shift in the melting curve of hTERT and a concomitant increase in the denaturation temperature ( $\Delta T_m = 10.23^\circ\text{C}$ ) occurred in the presence of TXT4 compared to DMSO. This evidence suggests that the binding of TXT4 to native hTERT protein would induce its aggregation in living systems.

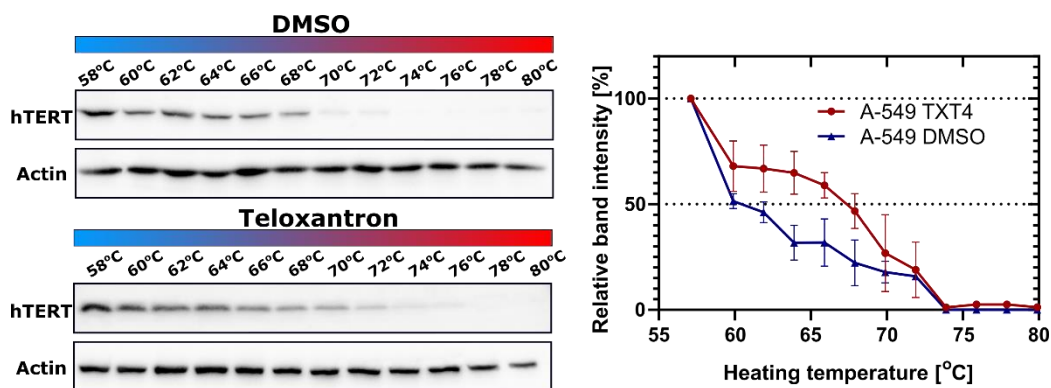


**Figure 45** Representative western blots showing the thermal stabilization of TERT protein upon treatment with Teloxantron (TXT4) with respect to DMSO (left panel) and the band intensity of hTERT in DMSO- and TXT4-treated A549 cells has been reported as a function of heating temperatures (right panel). The data have been reported as the percentage of the band intensity with respect to the samples exposed to the lowest temperature (58 °C) upon densitometric analyses of western immunoblots and represent mean values  $\pm$  s.d. from at least three independent experiments. The arrow indicates the shift towards the right of the melting curve, and the consequent increase in  $\Delta T_m$  indicates the capability of a compound to interfere with the folding of the target protein.

### 3.3.15. Analyses of hTERT mRNA expression

Telomerase enzymatic activity regulates hTERT and its RNA template component. Therefore, to verify the inhibitory effects of hit compound TXT4 on telomerase activity, levels of expression of hTERT mRNA were examined by RT-PCR analyses (**Figure 46**). Treatment A549 and H460 cells led to a time-dependent decrease of hTERT mRNA expression compared to the vehicle; however, this effect was less pronounced in cells with a higher basal level of hTERT mRNA (H226). In comparison, BIBR1532 exhibited similar activity in both A549 and H460 cells. At the same time of treatment, TXT4 led to 2-fold more and 2-fold less decrease of telomerase mRNA expression than BIBR1532 in A549, and H460 cells, respectively. It is worth emphasizing that either TXT4 or BIBR1532 did not modulate the expression of hTERT mRNA in H226 cells.

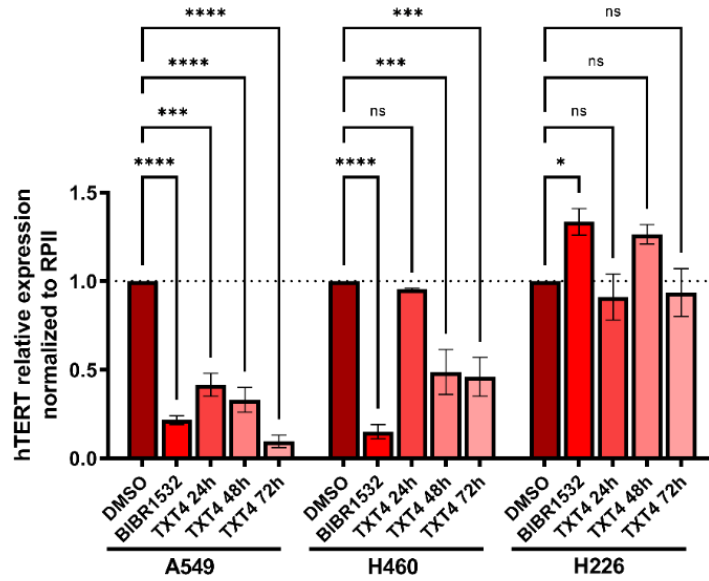


**Figure 46** RT-PCR analyses of hTERT mRNA expression in A549, H460, and H226 cells after treatment with TXT4 for 24, 48, and 72 h. DMSO and BIBR1532 were used as negative and positive controls, respectively. Expression of hTERT was normalized to RNA polymerase subunit (RPII). Error bars represent the SEM of data obtained in n=3 independent experiments. ns  $p > 0.05$ , \*  $p < 0.01$ , \*\*\*  $p < 0.0001$ , \*\*\*\*  $p < 0.00001$  vs. vehicle (two-way ANOVA and post hoc Dunnett's test).

### 3.3.16. Effect of TXT2 and TXT4 on cytoskeleton structure

Cortactin (CCTN) is an actin-binding protein playing a crucial role in the formation of a branched cytoskeleton network.<sup>273</sup> Aberrant activation of CCTN enhances the EMT and therefore is associated with relevant disease processes, like proliferation, adhesion, migration, and invasion.<sup>274</sup> Upregulation of CCTN has been found in several cancers, including brain, colorectal, and lung cancer. Li et al. show that CCTN is overexpressed in lung cancer tissues and contributes to the progression and poor prognosis of NSCLC.<sup>275</sup>

CCTN and actin assembly was investigated after treatment of A549, H460, and H226 cells with TXT2 and TXT4 for 48 h. Representative microscopic images and their quantification are present in **Figure 47**. None of the tested compounds changed the structure of the cytoskeleton in all NSCLC cell lines. However, a significant decrease in CCTN fluorescence was noted after treatment of A549 (TXT2/TXT4:  $p < 0.001$ ) and H460 cells (TXT2:  $p < 0.01$ ), and this effect was congruous for both TXT2 and TXT4. Treatment with ETP led to a higher deactivation of CCTN in A549 and H460 cells but was less effective towards H226 cells, similar to TXT2 and TXT4. Reduced cortactin expression may reflect a disturbance in lamellipodia formation and therefore decreased cell motility.

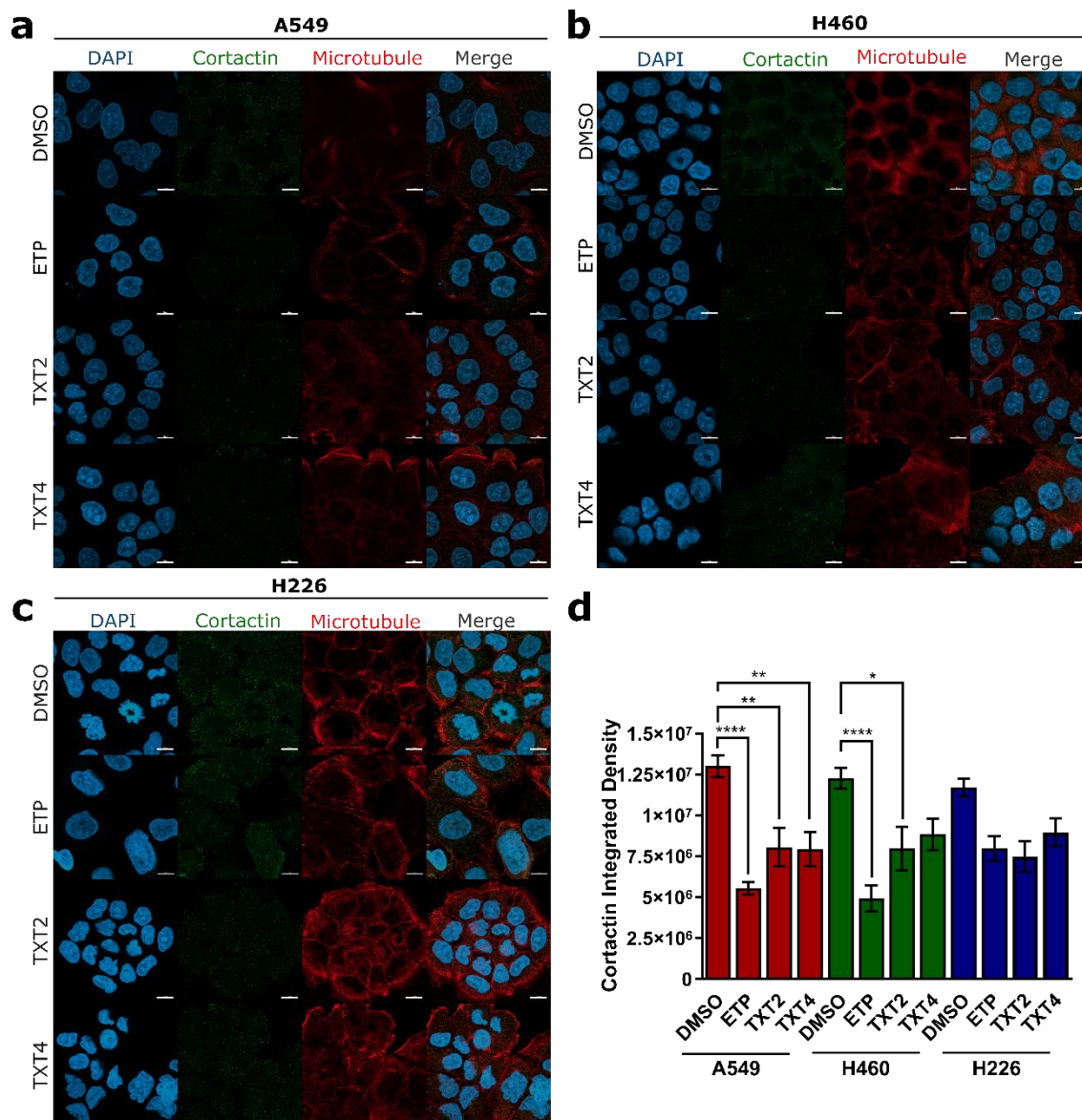


**Figure 47** Representative microscopy images after treatment A549 (a), H460 (b), and H226 (c) cells with TXT2 and TXT4 for 48 h. DMSO and ETP were used as negative and positive controls, respectively. The microtubule is depicted in red, cortactin in green, and the nucleus is stained with DAPI (blue). Scale bars=10  $\mu$ m; (d) The quantification of the mean cortactin fluorescence intensity in control and compounds-treated NSCLC cells. Data represent the mean  $\pm$  SEM of 15 randomly selected locations on the slide. \*  $p < 0.01$ , \*\*  $p < 0.001$ , \*\*\*\*  $p < 0.00001$  vs. vehicle (two-way ANOVA and post hoc Dunnett's test).

### 3.3.17. Analyses of anti-migratory properties of TXT2 and TXT4

A monolayer wound healing assay was performed to explore the anti-migratory properties of TXT2 and TXT4 (Figures 48 and 49). Both anthraquinones significantly reduced the motility of A549 cells in each tested condition; however, the anti-migratory property of TXT2 was more pronounced than TXT4. After 48 h of incubation with DMSO (1%), the wound area was repopulated completely. In comparison, the gap area in the cells TXT2 (10  $\mu\text{M}$ ) and TXT4 (15  $\mu\text{M}$ ) treated was filled only at 20% ( $p < 0.0001$ ) and 52% ( $p < 0.01$ ).

Interestingly, control H226 and H460 cells exhibited lower motility than A549. The kinetic curve course of filling the wound area was similar in control and anthraquinones-treated H226 cells (Figure 48). Migration of H460 cells was moderately but not significantly inhibited compared to A549-treated cells. At the end of exposition to TXT2 (2  $\mu\text{M}$ ) and TXT3 (15  $\mu\text{M}$ ), the wound area was repopulated accordingly at 51% and 53%, whereas DMSO-treated control was at 25%. TXT2 at 10  $\mu\text{M}$  induced cancer cell death therefore, it is not considered in this assay with such a concentration. Of note, there was a positive correlation between reducing *hTERT* mRNA expression and the anti-migratory properties of TXT4. In more detail, a more pronounced inhibition of cell motility was observed in A549, in which TXT4-modulated expression of *hTERT* mRNA was the most reduced. In comparison, TXT4 did not alter either migration or expression of *hTERT* mRNA in H226 cells.

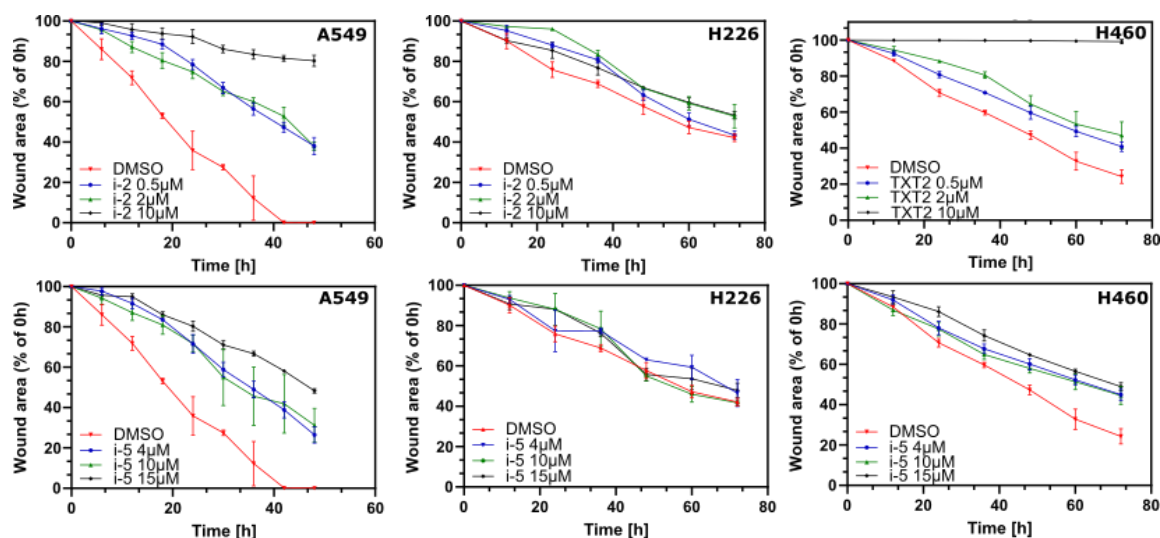


**Figure 48** Analysis of cell migration using *in vitro* wound healing assay. Quantification of the wound areas after culture insert removal. DMSO was used as a negative control. Data represent the mean  $\pm$  SEM of three independent experiments.

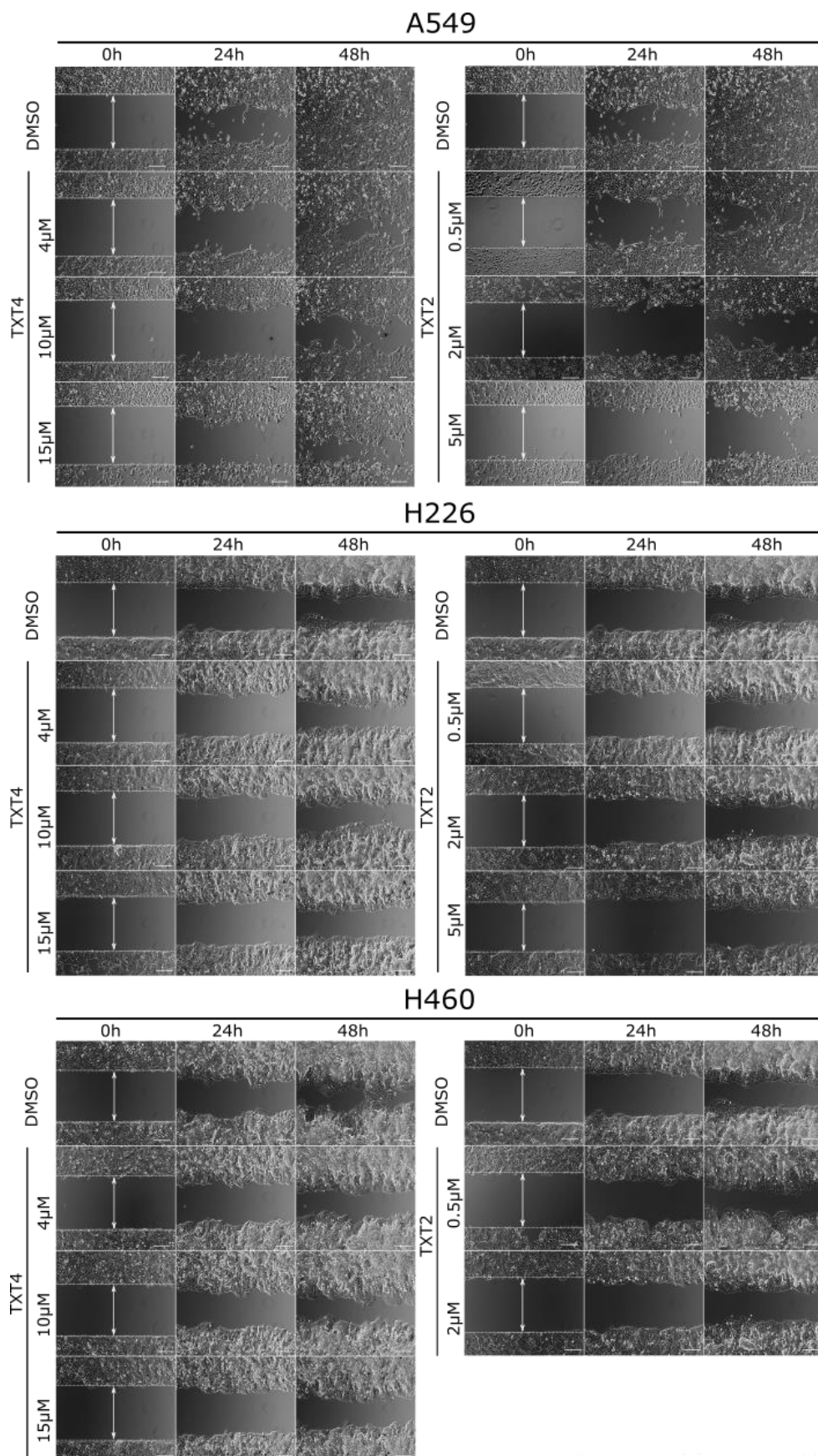


**Figure 49** Representative time-lapse microscopy images of A549, H226, and H460 cells after culture insert removal. DMSO was used as a negative control. Scale bars=100  $\mu\text{m}$ .

### 3.3.18. Impact of TXT4 on the expression of autophagy-related proteins

Autophagy (macroautophagy) is a catabolic process characterized by the formation of double-membrane vesicles (autophagosomes) that engulf cellular macromolecules and organelles and target them to the lysosomes.<sup>276</sup> Autophagy could have a diverse role in carcinogenesis: a protective role by suppressing malignant transformation at an early stage of cancer and promoting cell survival to overcome stressful stimuli such as hypoxia and nutrient deprivation.<sup>277</sup>

Many studies report crosstalk between autophagy and apoptosis. Several scenarios are possible: autophagy induction may prevent apoptosis, apoptosis activation may suppress autophagy to complete cell death, or autophagy may precede and trigger apoptosis.<sup>278</sup> In previous studies, I confirmed that TXT4 induces apoptotic cell death in NSCLCs. To verify how TXT4 modulates the autophagic pathway, the expression of typical autophagy markers was examined by Western blot. Chloroquine (CQ) and bafilomycin A1 (BafA1) were used as autophagy inhibitors, whereas induction autophagy was achieved by the cultivation of cells in a low-serum medium (LS).<sup>279,280</sup>

During autophagy, the cytosolic form of a microtubule-associated protein light chain 3 (LC3-I) binds to phosphatidylethanolamine (PE) to form LC3-PE conjugate (LC3-II) on the surface of nascent autophagosomes.<sup>281</sup> However, increased expression of LC3-II can be observed in both activated autophagy and inhibited the last stage of this pathway. (autophagosome fusion with lysosomes and, or lysosomal degradation).<sup>281</sup> During autophagy flux, p62 binds to LC3 and mediates the assembly and removal of ubiquitinated protein aggregates. Therefore, inhibition of p62 is related to autophagy activation.<sup>281</sup>

As shown in **Figure 50**, 48 h treatment with TXT4 alone did not significantly affect the expression of the LC3-II, similar to serum-starved cells. CQ and BafA1 resulted in the conversion of LC3I to LC3II, which was inhibited when co-treated with TXT4 or in a low serum medium. A similar effect was for p62 and lysosomal associated membrane protein 1 (LAMP1), where TXT4 itself did not modulate their expression, but a combination treatment with autophagy inhibitors significantly weakened their activity, reducing the expression of both proteins. Additionally, the colocalization of punctate LC3 and LAMP 1 in A549 cells was assayed using confocal microscopy (**Figure 51**). As expected, BafA1 delocalized the foci of LC3 and LAMP-1, thereby inhibiting autophagic flux by decreasing autophagosome-lysosome fusion in TXT4-treated A549 cells.

Overall, these results indicate that TXT4 induces autophagy without a survival role, as evidenced by the prolonged exposure of NSCLC cells to TXT4, leading to apoptosis.

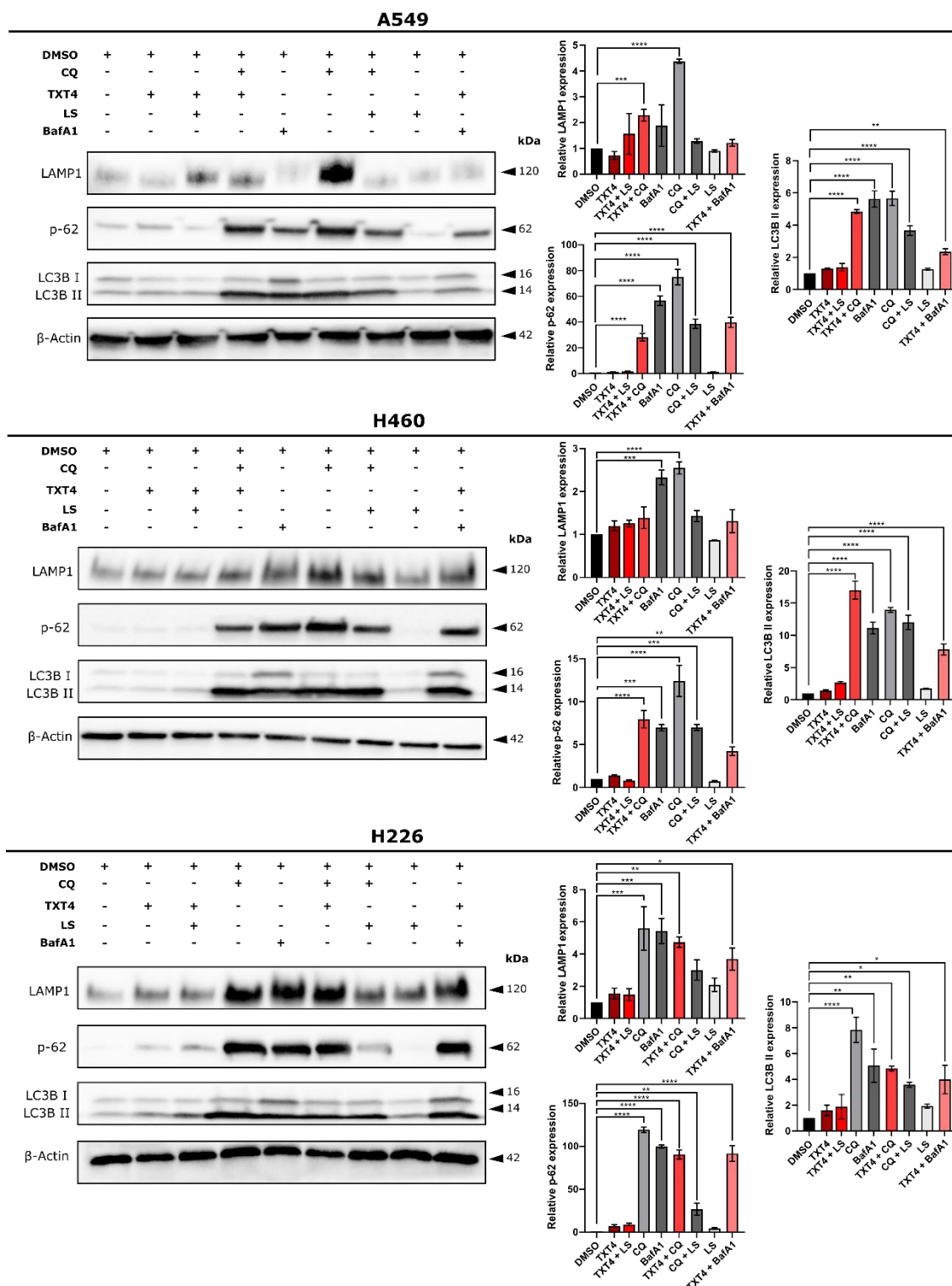


**Figure 50** Western blot analysis showing the effect of TXT4 on the expression of autophagy-related proteins in A549, H460, and H226 cells after 48 h of treatment. (CQ – Chloroquine, LS – low serum, BafA1 – Bafilomycin A1). Error bars represent the SEM of data obtained in n=3 independent experiments.  $\beta$ -actin was used to ensure equal protein loading. The numbers on the right indicate the molecular weight (kDa). \*  $p < 0.01$ , \*\*  $p < 0.001$ , \*\*\*  $p < 0.0001$ , \*\*\*\*  $p < 0.00001$  vs. vehicle (two-way ANOVA and post hoc Dunnett's test).



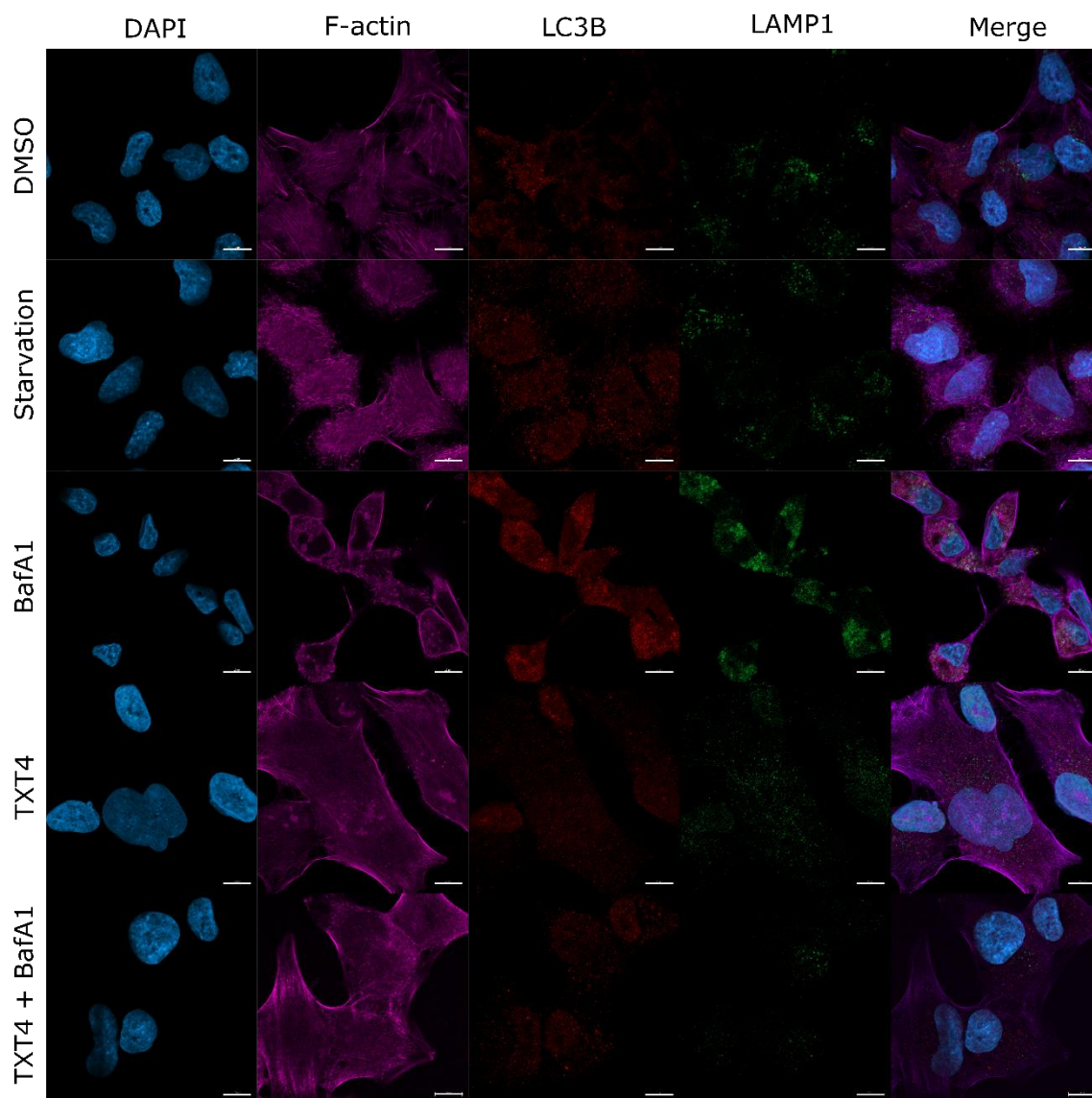


**Figure 51** Representative microscopy images presenting immunofluorescence of A549 cells at 48 h of treatment. DMSO and BafA1 were used as references. The actin filaments are depicted in pink, LC3B in red, LAMP1 in green, and the nucleus is stained with DAPI (blue). Scale bars=10  $\mu$ m.

### 3.3.19. Effect of TXT4 on cancers with overexpression ABC transporters.

Multidrug resistance (MDR) of cancer cells is associated with several biochemical changes, principally occurring due to the overexpression of ATP-binding cassette (ABC) transporters, which can increase the efflux of many chemotherapeutic drugs.<sup>282</sup> The most crucial transporters ABC, responsible for the majority of MDR are ABCB1, ABCC1, and ABCG2.<sup>283</sup> To study the TXT4's ability to induce MDR in cancer cells, the effect of TXT4 on cell growth was determined on two pairs of leukaemia cells expressing ABCB1 (HL-60/MX2), ABCG2 (HL-60/VINC) or not (HL-60/Al, HL-60) by MTT assay after 72 h of treatment. As depicted in **Figure 52**, TXT4 exerted slightly weaker cytotoxic effects on cells overexpressed ABCB1 (HL-60/MX2:  $IC_{50}$   $1.23 \pm 0.15$   $\mu$ M) compared to parental cell line (HL-60/AL:  $IC_{50}$   $1.13 \pm 0.09$   $\mu$ M). However, TXT4 was more effective against cells with overexpressed ABCB1 (HL-60/VINC:  $IC_{50}$   $3.02 \pm 0.24$   $\mu$ M) than the parental cells (HL-60:  $IC_{50}$   $3.48 \pm 0.81$   $\mu$ M). On the other hand, vincristine (ABCB1 substrate) and MTX (ABCG2 substrate) exhibited significantly decreased inhibition of cell viability in the resistance cell lines ( $p < 0.00001$ ). Despite  $IC_{50}$  values of MDR and parental cells being similar, the contents of TXT4 in HL-60 and HL-60/VINC were analysed using HPLC-MS to confirm those results. During the 0-60 min incubation time, TXT4 reached 30  $\mu$ M per cell, corresponding to the total concentration used for the treatment (**Figure 53**). No changes in compound accumulation were observed in resistant and sensitive cells. The release kinetics show that after wash-up, the intracellular concentration of TXT4 decreased almost 5-fold, but further washing did not significantly change the concentration. HL-60/VINC cells released more TXT4 than HL-60 cells, but the difference wasn't significant ( $p > 0.05$  student's T-test). Overall, my findings suggest that increased expression of either ABCB1 or ABCB2 is ineffective in abolishing the cytotoxic effect of TXT4. However, although TXT4 is not a substrate for the investigated transporters, cancer cells can still become resistant to TXT4 either by ejection of the compound by other transporters or by activating the ALT mechanism.

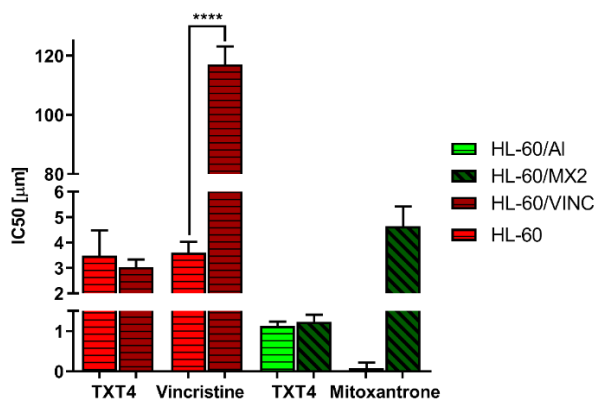


**Figure 52** Comparison of IC<sub>50</sub> for HL-60 with overexpressed ABCG2 (HL-60/MX2) and ABCB1 (HL-60/VINC). Error bars represent the SEM of data obtained in n=3 independent experiments. \*\*\*\* p<0.00001 vs. vehicle (two-way ANOVA and post hoc Dunnett's test).

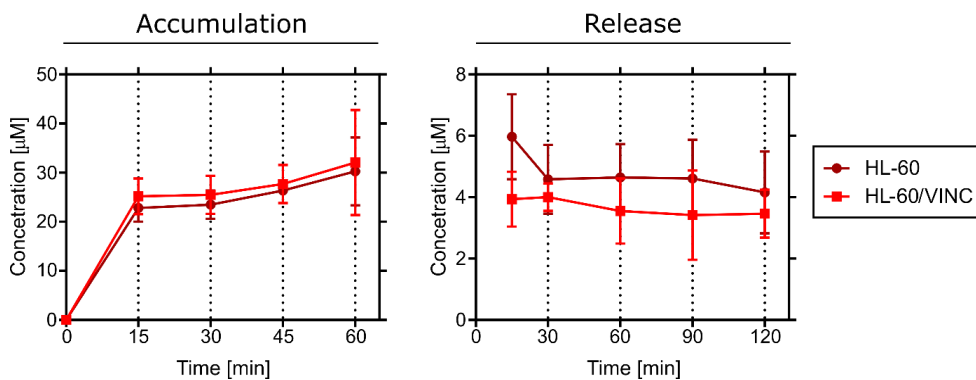


**Figure 53** Uptake and efflux of TXT4 in HL-60 and HL-60/VINC cells *in vitro* measured by HPLC.

### 3.3.20. Impact of long-term treatment of TXT4

To investigate the long-term cellular consequences of TXT4 treatment, A549 cells were cultivated in the presence of TXT4 at a non-cytotoxic concentration (4  $\mu$ M) or an equivalent volume of DMSO (1%) using the same culture conditions. According to the literature, A549 cells compared to other NSCLCs displayed the shortest telomeres and therefore were chosen for this analysis.<sup>241</sup> Periodically, cells were photographed, counted, and examined by flow cytometry (cell cycle assay), Western blot (hTERT expression), qPCR (mRNA hTERT expression; telomere length), and TRAP assay. Additionally, at the same time intervals, colony-forming and cytotoxic properties of TXT4 were analysed.

During the first four weeks of treatment, telomere length was almost not affected. However, the ability of cells to form colonies decreases around 1.5-fold compared to the vehicle. In the 12th week of treatment, telomerase activity decreased by 80% and hTERT expression by 65% compared to the control (**Figures 54e, f, and g**). From that point on, cells began to divide more slowly, and colony formation capacity decreased markedly (**Figures 54a, b, and d**). At week 16 of treatment, a significant shortening of telomeres was observed, with enzyme activity and expression remaining at a similar level (**Figures 54c, e, and f**). After 24 weeks of exposure to TXT4, A549 cells almost lost their ability to form colonies and divide, the telomeres shortened 4-times compared to the control, and the enzyme nearly lost its enzymatic capacity. Moreover, hTERT mRNA and protein expression were almost abrogated (**Figures 54g and h**).

During treatment, cells were as sensitive to the effects of TXT4 and chemotherapeutic agents such as cisplatin, MTX, ETP, and 5-FU as they were before the initiation of treatment, evidenced by the same IC<sub>50</sub> values which were obtained earlier (see chapter 3.3.1). Moreover, with time, cells began accumulating in the G<sub>2</sub>/M phase, and a fraction of polyploid cells also appeared (**Figure 55a**). Microscopic analysis showed that some cells fused, forming giant polyploid cancer cells (**Figure 55b**). Such cells could exhibit cancer stem cell properties and are highly related to tumour recurrence and metastasis.<sup>284</sup>



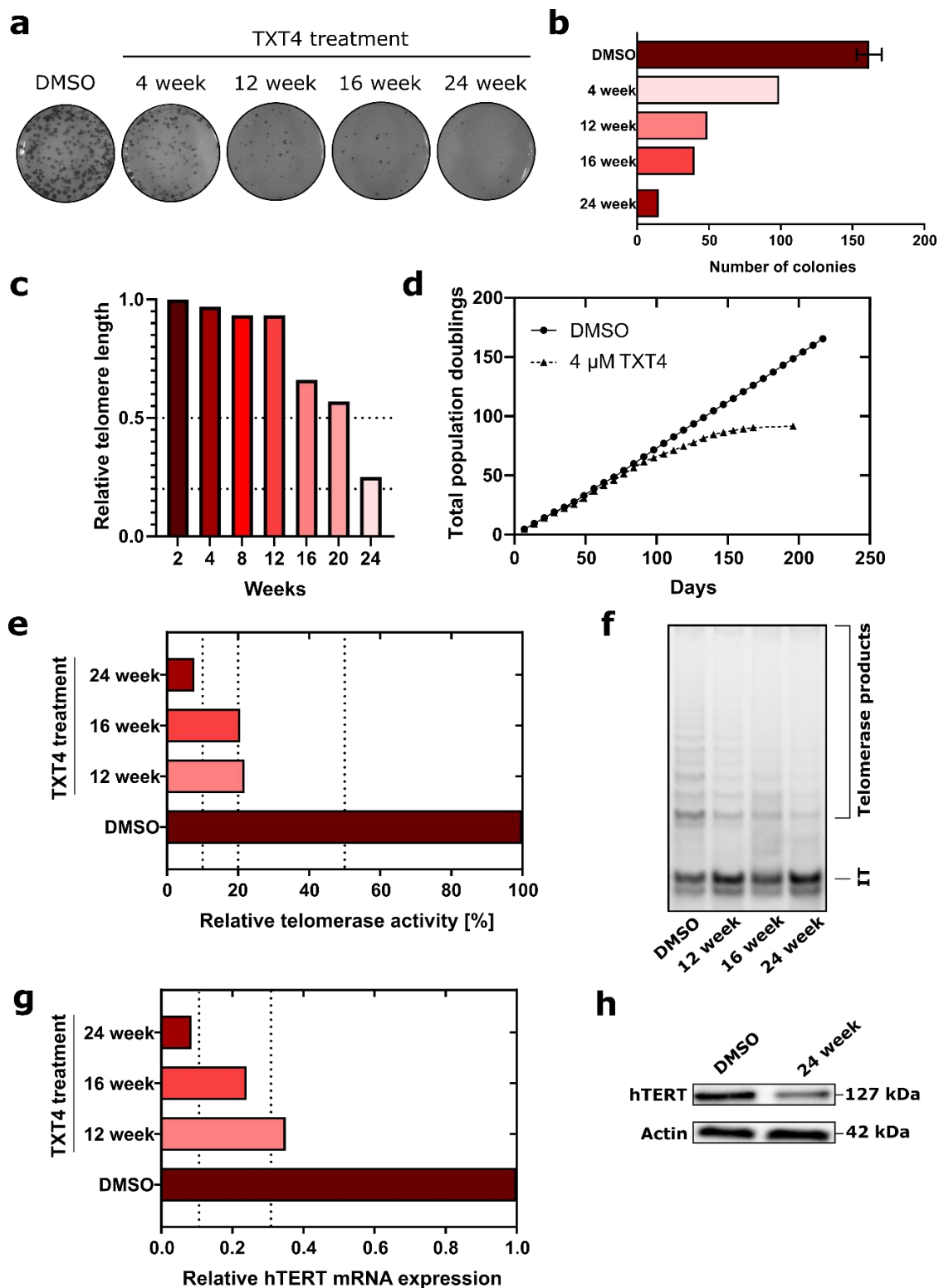


**Figure 54** Effect of long-term treatment A549 cells with 4  $\mu$ M of TXT4. DMSO was used as a negative control. **(a)** Colony-forming assay in A549 cells treated with TXT4 for 4, 12, 16, and 24 weeks; **(b)** Quantification of a; **(c)** Analyses of relative telomere length; **(d)** Cell proliferation capacity; **(e, f)** TRAP gel and its quantification. IT: internal control; **(g)** Relative hTERT mRNA expression; **(h)** Western blot analyses of hTERT protein.



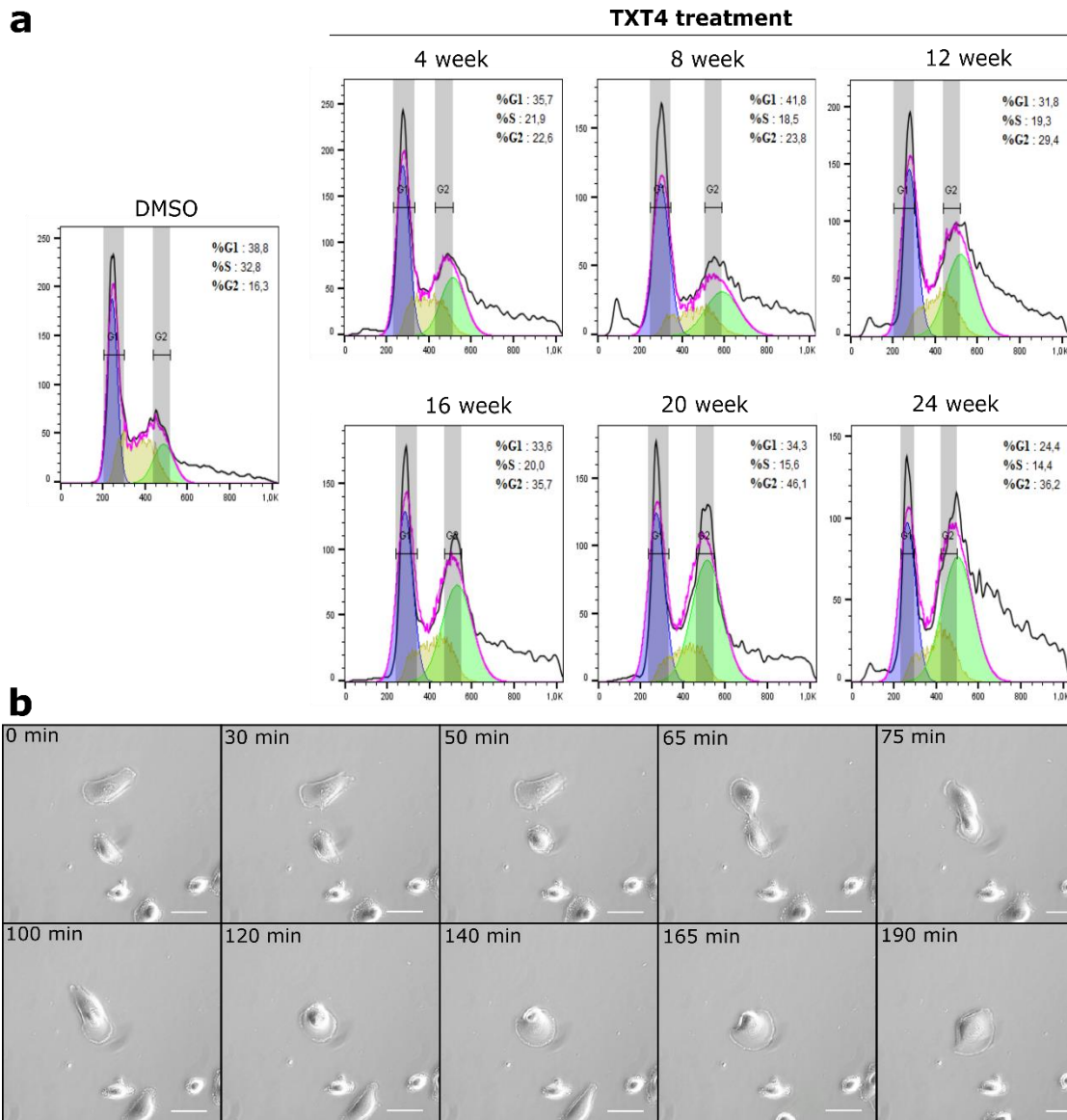


**Figure 55** Effect of long-term treatment A549 cells with 4  $\mu\text{M}$  of TXT4. **(a)** Representative histograms after DNA staining long-term treatment A549 cells with TXT4; **(b)** Time-lapse microscopy images of A549 cells in the 20<sup>th</sup> week of treatment. Scale bars=200  $\mu\text{m}$ .

### 3.3.21. Analysis of changes in phosphorylation of protein tyrosine kinases

Previous studies suggest that examined compounds may also have off-target activity, which triggers cell death. Anthraquinone derivatives could exert antitumour activity via different targets, including topoisomerase, kinases, and DNA.<sup>285</sup> The ability of compounds to intercalate with DNA or inhibit topoisomerase I or II $\alpha$  was excluded using the DNA unwinding assay (see chapter **3.3.22**). Many data report that anthraquinones could inhibit the phosphorylation of various protein tyrosine kinases (PTKs), e.g. emodin (1,3,8-trihydroxy-6-methyl-anthraquinone) or chrysophanol (1,8-dihydroxy-3-methylanthrone).<sup>286,287</sup> PTK regulates many critical signalling pathways involved in cell proliferation, differentiation, metabolism, and motility, and its aberrant expression has been implicated in various types of cancer<sup>288</sup>. Considering the role of PTK and anthraquinones' structural formulas, compounds were investigated by an enzyme-linked immunosorbent assay (ELISA) to study their possible inhibitory activity towards PTK. Imatinib, a selective PTK inhibitor currently used in medical treatment, was used as a reference.<sup>289</sup> As depicted in **Figure 56a** all tested compounds decreased PTK activity in a concentration-dependent manner. Compounds TXT2 and TXT4 displayed the most potent inhibitory activity against PTK and were more effective at 1  $\mu$ M concentration than imatinib. To further test the ability of tested compounds to suppress phosphorylation of PTK, high serum-supported A549 cells were treated with increasing concentrations of compounds and analysed by flow cytometry. Representative histograms and their quantification are presented in **Figures 56b** and **c**. All of the compounds, besides TXT3, decreased the phosphorylation of p-Tyr in a concentration-dependent manner. TXT2 and TXT4 in a 20  $\mu$ M concentration markedly reduced protein tyrosine phosphorylation (TXT2:  $p < 0.01$ ; TXT4:  $p < 0.001$ ), leading to an almost 2-fold decrease in the p-Tyr expression in comparison to the vehicle. Moreover, both compounds exhibit higher activity than imatinib.



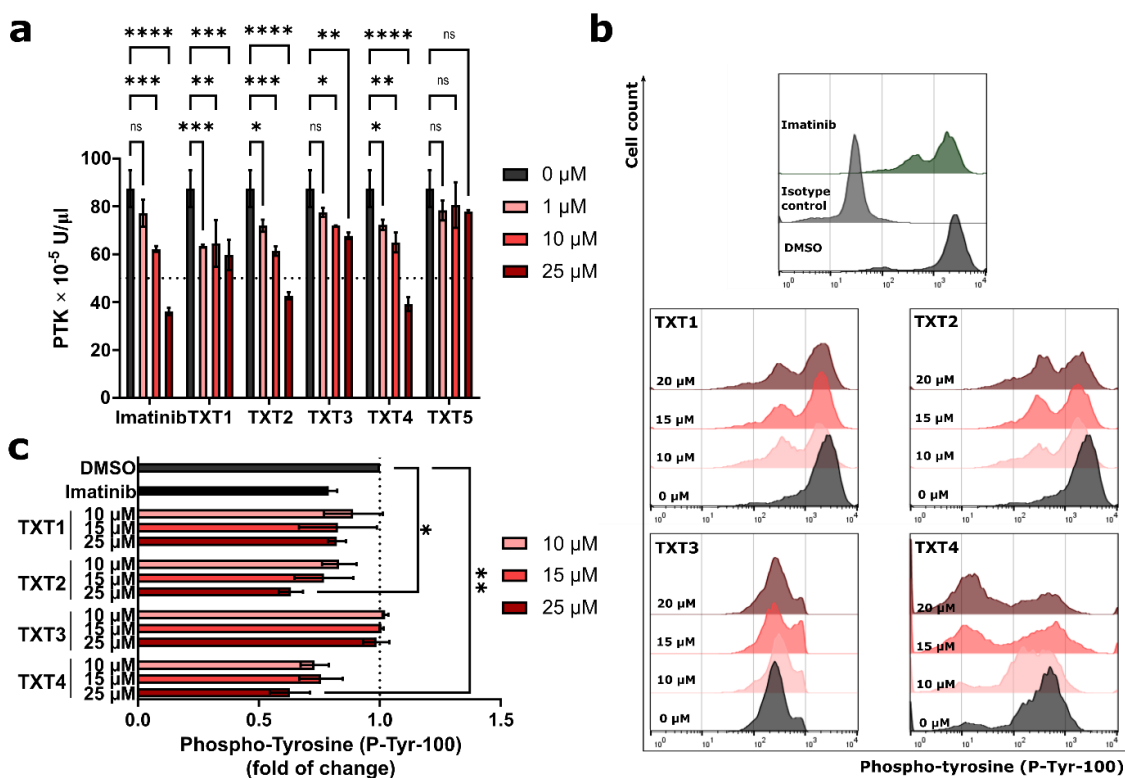


**Figure 56** Analysis of changes in phosphorylation of tyrosine kinases after TXT treatment. DMSO and imatinib were used as negative and positive controls, respectively. **(a)** *In vitro* determination of PTK activity using A549 extracts determined by ELISA; **(b)** Representative histograms of compounds-treated A549 cells after intracellular phospho-flow cytometry; **(c)** Quantification of intracellular phospho-flow cytometry. Error bars represent the SEM of data obtained in n=3 independent experiments. \* p<0.01, \*\* p<0.001, \*\*\* p<0.0001, \*\*\*\* p<0.00001 vs. vehicle (one-way ANOVA and post hoc Dunnett's test).

Additionally, A549 cells treated with compounds at 20 μM were analysed using confocal microscopy (**Figure 57**). Within a 4-h treatment with TXT2 or TXT4, a dramatic decrease in p-Tyr staining was observed. TXT1 displayed similar activity to imatinib, where no apparent changes were observed to TXT3. Those results are consistent with those obtained in ELISA and flow cytometry tests.



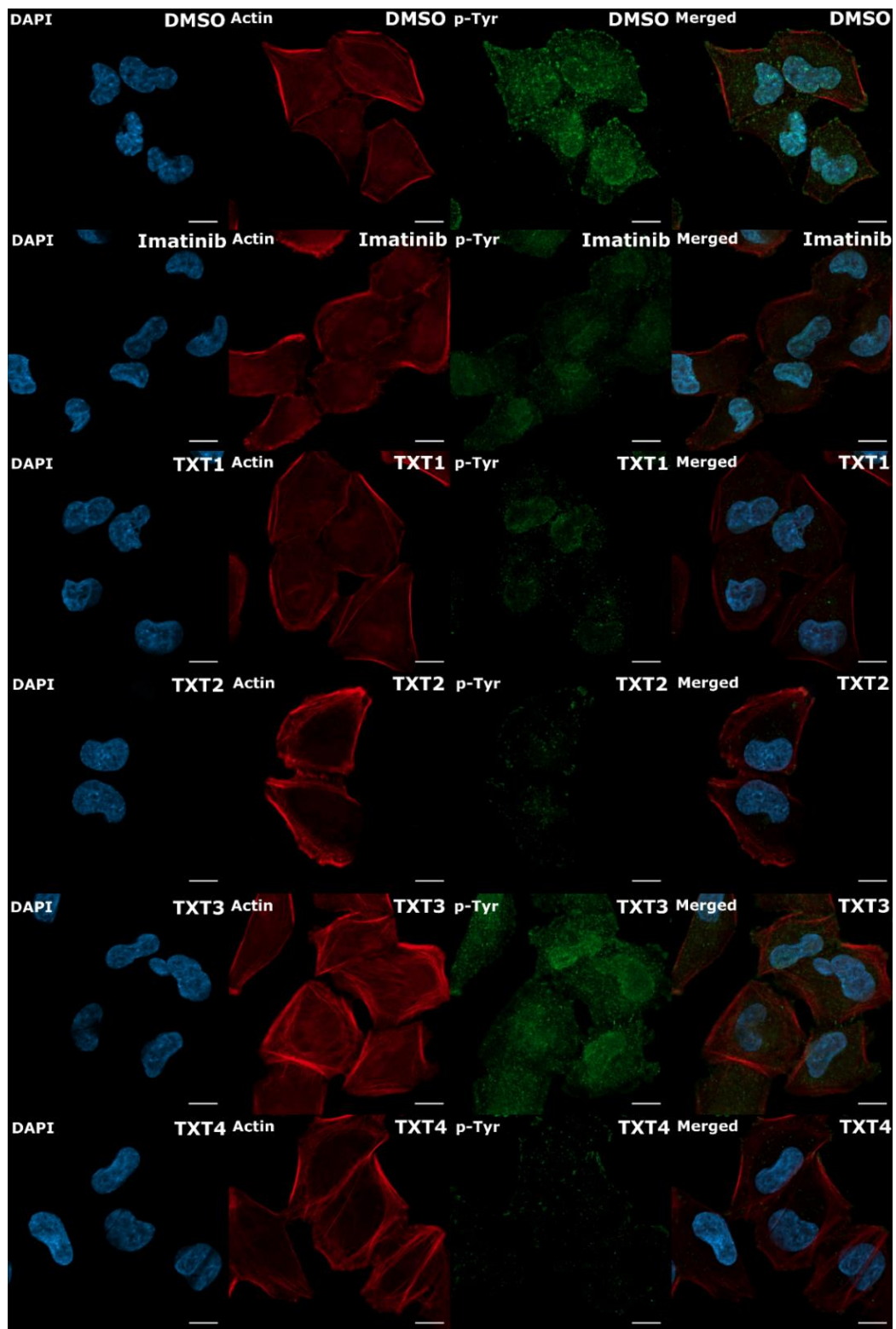


**Figure 57** Representative microscopy images presenting immunofluorescence of microtubule and p-Tyr foci in A549 cells at 4 h of treatment. DMSO and imatinib were used as negative and positive controls, respectively. The microtubules are depicted in red, p-Tyr in green, and the nucleus is stained with DAPI (blue). Scale bars=10  $\mu$ m.



To identify tyrosine kinase targets for TXT2 and TXT4, A549 cells were treated with compounds for 6 hours and analysed using a human RTK phosphorylation Ab array. This method enables screening simultaneously an expression of 71 different RTKs (**Figure 58**). The relative phosphorylation levels of all investigated target molecules after treatment with compounds are presented in **Figures 59-61**. Compound TXT2 at 10  $\mu$ M fully inhibited phosphorylation of 45 tested PTKs, whereas 20 of the PTKs were significantly activated. Compound TXT4 downregulates all investigated p-PTKs, besides Fyn, which was slightly activated. Interestingly, imatinib also activates this kinase at a similar level. Since TXT4 inhibited most of the PTKs, it's hard to highlight those that are worth further investigation. The experiment should be repeated with smaller concentrations, which may exclude cascade inhibition. However, some of the PTKs have a distinctly higher basal expression, which may indicate that they exhibit more functions in cancer progression than other analysed proteins. To clarify correlations between tested RTKs, they were classified into appropriate families or types, accordingly to the literature (**Figure 62**). The investigated cell line has higher basal expression of non-receptor kinases from ACK (ACK1), FAK (FAK), SRC (FRK, HCK, Lyn, SRMS), and TEC (Bmx, BTK, ITK) families, and receptor kinases from type II (IGF-IR, Insulin-R), type X (AXL), and type XV (ROS). TXT4 significantly downregulated the expression of all those kinases, which may translate to its cytotoxic activity on telomerase-negative cells. Human RTK phosphorylation Ab array is only a semi-quantitative method, so further research is needed for more accurate analysis such as ELISA.

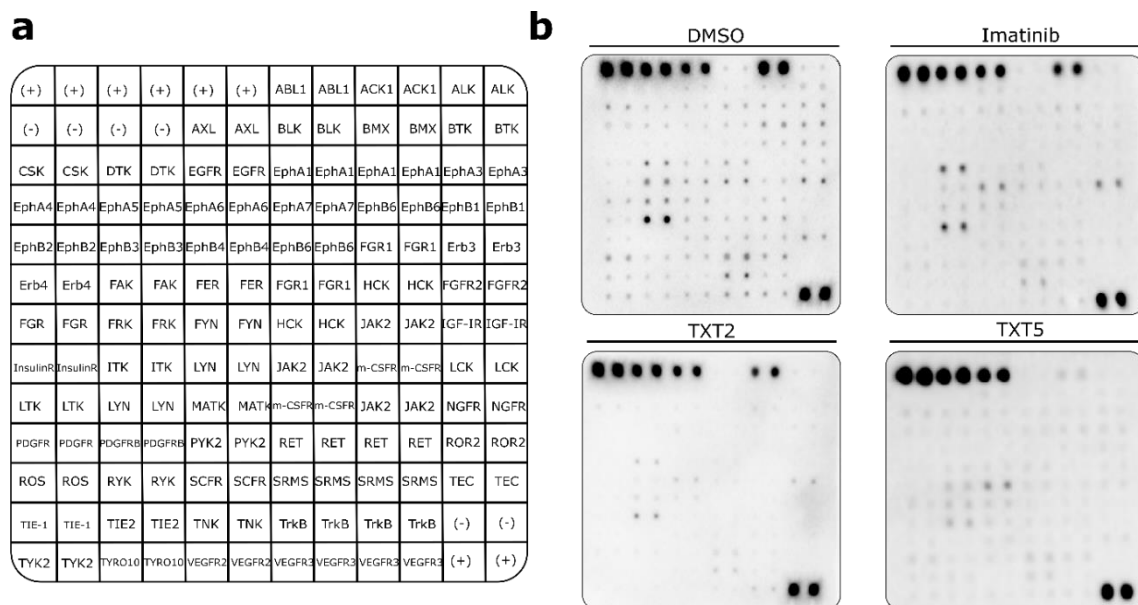


**Figure 58** Analysis of changes in phosphorylation of tyrosine kinases after TXT treatment. **(a)** Template presenting the location of tyrosine kinase antibody; **(b)** Proteom profiler analysis of A549 cells after treatment with compounds. DMSO and imatinib were used as negative and positive controls, respectively.

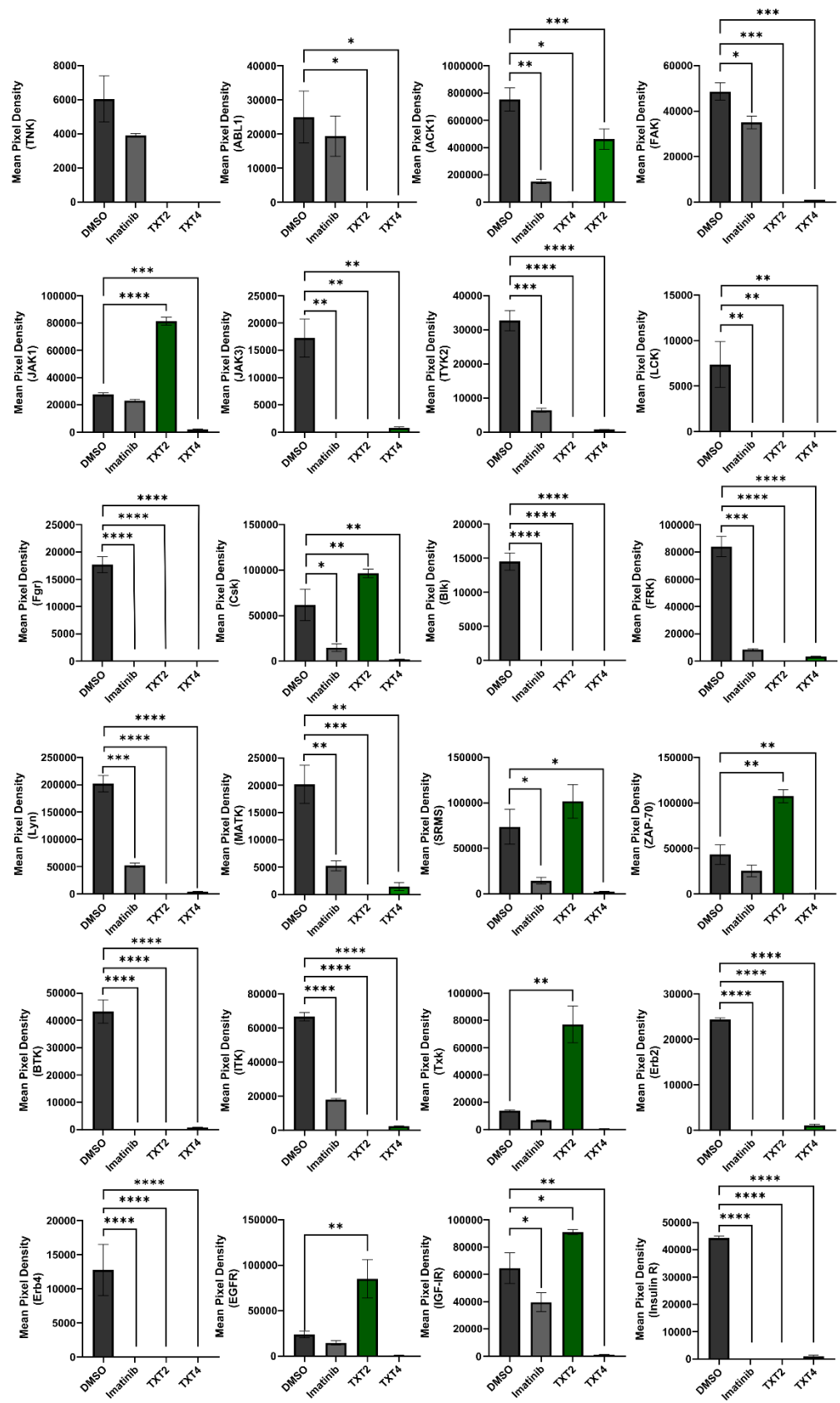


**Figure 59** The relative phosphorylation levels of p-PTKs after treatment of A549 cells with compounds. \*  $p < 0.01$ , \*\*  $p < 0.001$ , \*\*\*  $p < 0.0001$ , \*\*\*\*  $p < 0.00001$  vs. vehicle (one-way ANOVA and post hoc Dunnett's test).

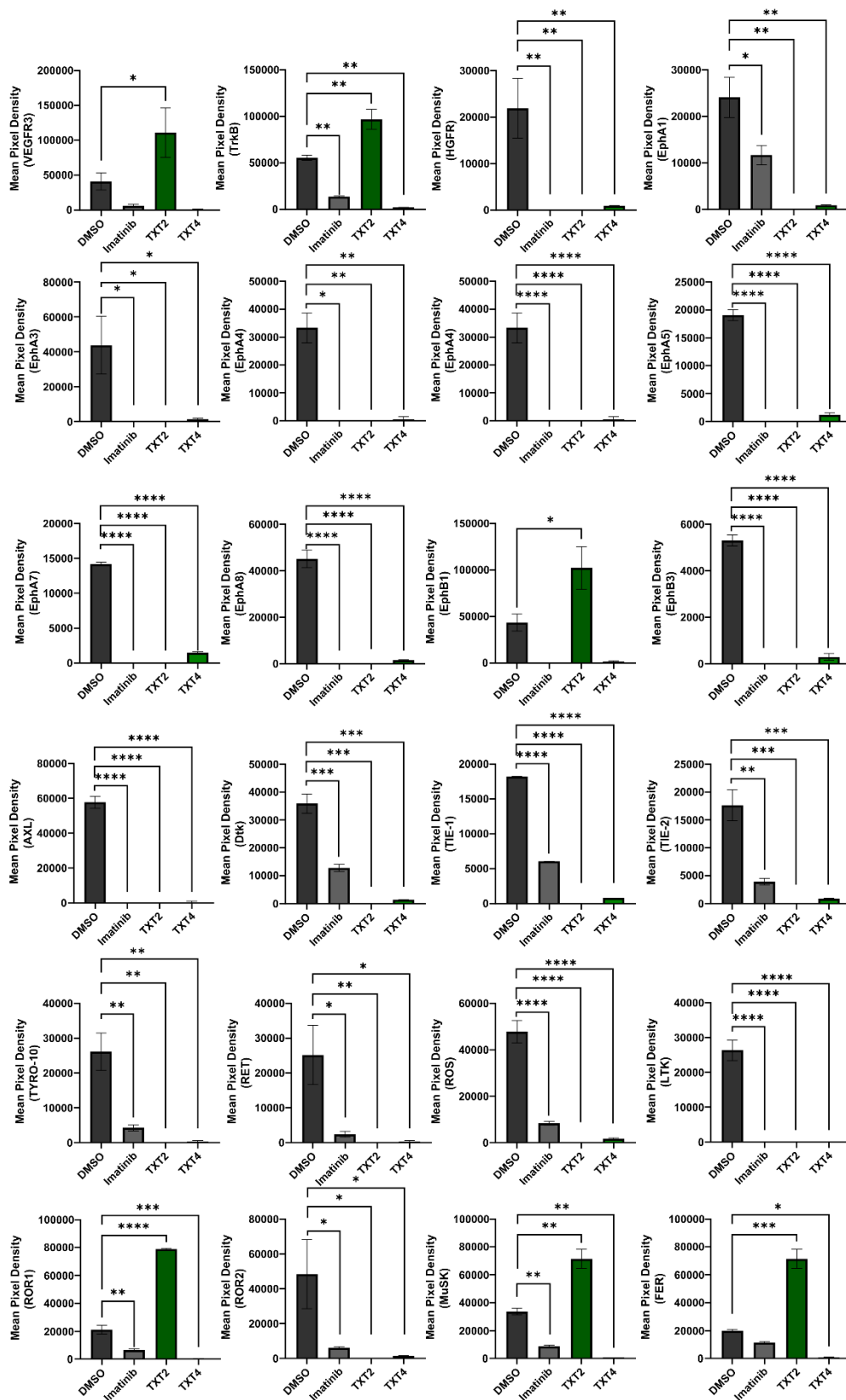


**Figure 60** The relative phosphorylation levels of p-PTKs after treatment of A549 cells with compounds.  
 \*  $p < 0.01$ , \*\*  $p < 0.001$ , \*\*\*  $p < 0.0001$ , \*\*\*\*  $p < 0.00001$  vs. vehicle (one-way ANOVA and post hoc Dunnett's test).

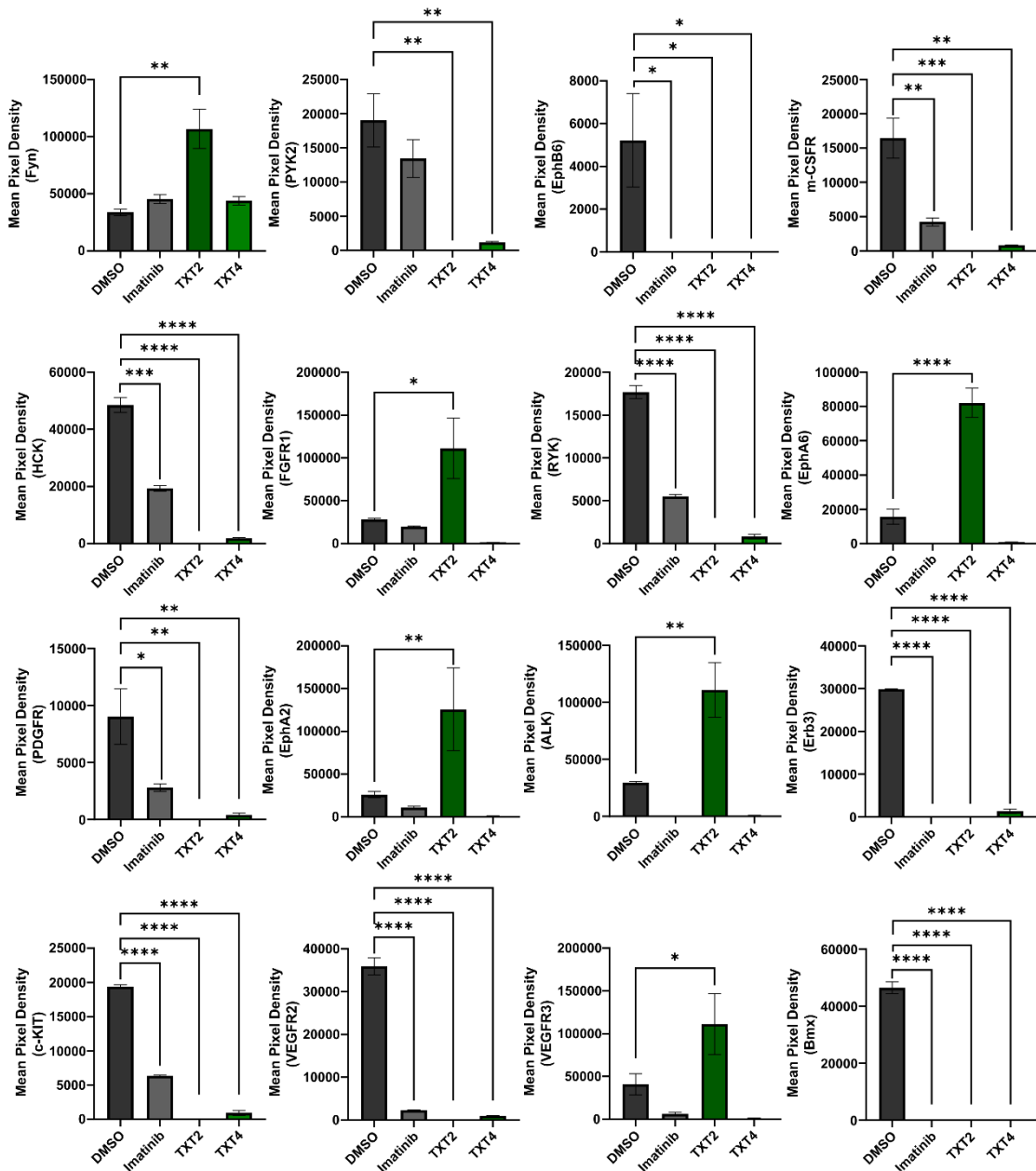


**Figure 61** The relative phosphorylation levels of p-PTKs after treatment of A549 cells with compounds.  
 \*  $p < 0.01$ , \*\*  $p < 0.001$ , \*\*\*  $p < 0.0001$ , \*\*\*\*  $p < 0.00001$  vs. vehicle (one-way ANOVA and post hoc Dunnett's test).

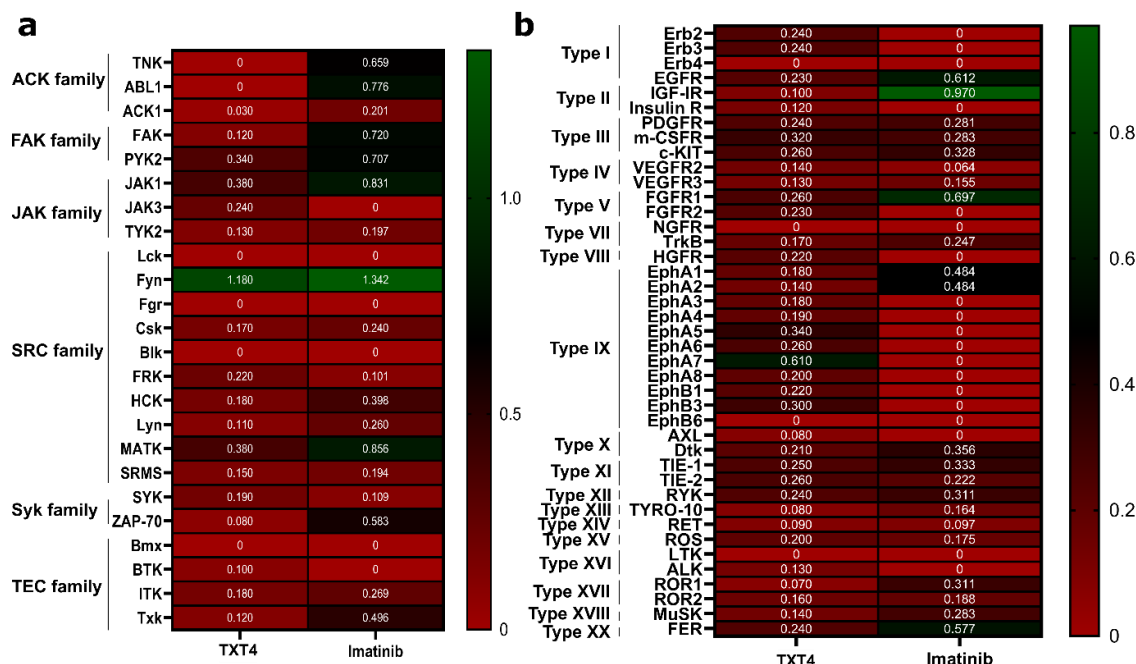


**Figure 62** Profiling changes in PTKs after treatment with TXT4 or Imatinib with the respect to the vehicle. Nonreceptor and receptor PTKs are presented on the left, and right panels, respectively.

### 3.3.22. Study of anthraquinones and carbazoles as DNA intercalators and topoisomerase inhibitors

Carbazole and anthraquinone derivatives form a class of DNA-binding agents currently used in cancer chemotherapy.<sup>290,291</sup> These molecules contain a planar chromophore characteristic of DNA intercalating agents.<sup>292</sup> Compounds substituted with nitrogen-containing side chains are prone to bind the negatively charged phosphate groups of DNA.<sup>293–295</sup> Some intercalators interact not only with DNA but also with DNA-modifying enzymes, such as topoisomerases. These enzymes modulate DNA topology and act by generating single- (type I) or double-strand (type II) DNA breaks and are involved in DNA repair, replication, transcription, and reorganization of the chromatin.<sup>296</sup>

Possible mechanisms of intercalation of carbazole and anthraquinone into the DNA were investigated by studying their interaction by a topological method using unwinding and relaxation assays. During DNA intercalation, the circular duplex DNA plasmid unwinds, leading to a change in torsional tension.<sup>297</sup> Topoisomerases release torsional stress of both positive and negatively supercoiled DNA leading to the relaxation of DNA. **Figure 63a** presents the results of relaxed plasmid pBR322 with various concentrations of the selected carbazole and anthraquinone derivatives. None of the tested compounds modified DNA besides DOX, which is a well-characterized intercalating agent. Further analyses with supercoiled DNA plasmid show that neither carbazole nor anthraquinone inhibited topoisomerase I activity, evidenced by similar end-products as in DMSO-treated control. (**Figure 63b**). In comparison, camptothecin (CPT) prevents plasmid relaxation and inhibits DNA topoisomerase I activity. In addition, M.A. Mateusz Olszewski

investigated compounds in human topoisomerase II  $\alpha$  relaxation assay, however, none of the tested compounds inhibited enzyme activity (data not shown).

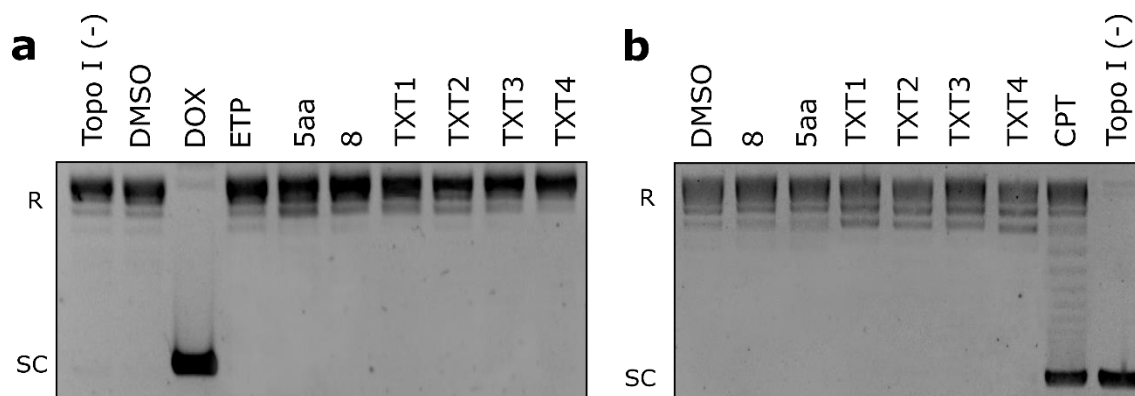


**Figure 63** Effect of carbazole and anthraquinone derivatives on DNA unwinding and topoisomerase I activity **(a)** Agarose gel electrophoresis of relaxed (R) pBR322 DNA; **(b)** Agarose gel electrophoresis of supercoiled (SC) pBR322 DNA.

### 3.3.23. Structure-activity relationship analysis

Determining a compound's structure/function relationships is essential to design and synthesise new molecules with improved pharmacological properties. Anthraquinones under study differ in biological activity, and some of their properties can be related to a particular structure fragment. In all analysed compounds, the chlorine atom in the 3rd position significantly decreased the cytotoxic activity and the anti-telomerase potential. Compounds with dithiocarbamate moiety in the 2nd position were mostly less cytotoxic than the 1st substituted analogue. In analogues of dithiocarbamate moiety in the 2nd position, replacing N-morpholino with N-pyrrolidine substituents resulted in a complete loss of their activity against telomerase but did not affect cytotoxic potential; On the other hand, both N-pyrrolidine and N-morpholino analogues in compounds bearing dithiocarbamate moiety in the 1st position possess similar cytotoxic and anti-telomerase activity *in vitro*; nevertheless, it's worth emphasizing that the N-morpholino compound did not exert typical features of anti-telomerase drugs. The tertiary amide N-(CH<sub>2</sub>CH<sub>3</sub>)<sub>2</sub> group increases the anti-telomerase potential, but only in the dithiocarbamate moiety analogue in the 2nd position. Moreover, among all the tested compounds, (9,10-dioxo-1-anthryl) pyrrolidine-1-carbodithioate (TXT4) was the most active against telomerase.



### 3.4. Project II - carbazole derivatives

Most of the results regarding the anticancer activity of carbazole derivatives are included in the manuscript *From tryptophan to novel mitochondria-disruptive agent, synthesis and biological evaluation of 1,2,3,6-tetrasubstituted carbazoles* (Witkowska, M. §, Maciejewska, N. §, Ryczkowska, M., Olszewski, M., Baginski, M., Makowiec, E. *J. Med. Chem.* **238**, 114453, 2022) attached as ANNEX 1. The remaining results are placed in chapters **3.3.22**, **3.4.2**, and **3.4.3**.

#### 3.4.1. Scientific problem addressed

Anticancer activity of carbazole may arise from multiple diverse mechanisms.<sup>290</sup> **Therefore, the aim was to explain the mechanism underlying the cytotoxicity of the two most active 3,6-substituted carbazole derivatives by testing numerous hypotheses.** To this end, several potential targets were investigated, such as the cell cycle, cytoskeleton, topoisomerase I, topoisomerase II  $\alpha$ , protein tyrosine kinases, DNA intercalation, and ROS generation. Because of the negative results, most of those studies are not published and are in chapters **3.3.22** and **3.4.3**.

Anticancer activity of compounds was evaluated against a broad panel of human cell lines, including non-small cell lung adenocarcinoma (A549), colon cancer (HCT116), bone osteosarcoma (U2OS), breast carcinoma (MCF7), liver cancer cells (HepG2), and noncarcinogenic embryonic kidney cells (HEK29). Among the 11 tested compounds, **5aa** and **8** exhibited the highest antiproliferative activity against HCT116 and U2OS cells, whereas none of the compounds displayed toxicity against the HEK293 cell line up to 50  $\mu$ M. Compared to **5aa**, compound **8** showed a significantly higher cytotoxic potency. However, due to the high similarity in the structure formula, both compounds were further examined against HCT116 and U2OS cells to define their impact on cell cycle distribution, ability to form colonies, migration, and cell death.

I established that both tested compounds altered cell cycle progression, but the observed effect differs depending on the cell line and the compound. Moreover, the arrest of the cell cycle in tested cancer cells was somewhat temporary, which suggests that the examined compounds are not inhibitors of the cell cycle. Next, I showed that **5aa** and **8** inhibit the ability to form colonies in HCT116 and exert anti-migratory properties.

Due to the high triplet energy core structure, carbazole has been commonly utilized in the design of blue light-emitting diodes.<sup>298</sup> This unique property allows for determining the compartmentalization of both compounds in adiposomes by high-resolution laser scanning confocal microscopy. Lipid droplets regulate cancer cell proliferation, migration, and survival, and their increased content is associated with tumour aggressiveness and resistance to chemotherapy.<sup>299,300</sup> Dubey et al. show that the accumulation of hydrophobic drugs into the oil phase of adiposomes can influence their activation and toxicity to cells.<sup>301</sup> However, in the case of **5aa** and **8**, additional studies are warranted in the future to define the exact influence of their accumulation.





Further analyses revealed that compounds induced massive oxidative stress in colon cancer HCT116, and U2OS cells. ROS formation can lead to DNA oxidation followed by mutagenic alterations in DNA bases or double-helix breaks, resulting in cell death.<sup>302</sup> Using flow cytometry and confocal microscopy, I have shown that both compounds induced DSBs in HCT116 and U2OS cells leading to apoptosis, but only in HCT-116 cells. Interestingly, compounds triggered mitochondrial damage and loss of transmembrane potential but do not release apoptotic factors. Moreover, long-term treatment induced cell senescence in both analysed cell lines.

#### 3.4.2. *Role of reactive oxygen species in carbazole-induced cancer cell death*

The publication in ANNEX 1 proved that carbazoles induce apoptosis in HCT116 cells. Since oxidative stress caused by compounds was reversible upon treatment with the antioxidant, after publishing results, I continued studies on them to determine if ROS is the primary mechanism leading to the death of cancer cells. For this purpose, HCT116 cells were co-treated with lead compounds and NAC, followed by an analysis of apoptosis and levels of  $\gamma$ -H2AX. As shown in **Figure 64**, co-culture of NAC with compound **8** or **5aa** prevented apoptosis, as evidenced by the comparable level of live cell fraction at each treatment time point as with the control. Moreover, in the same treatment conditions, DNA DSB-inducing properties of compounds were significantly diminished by NAC, but this effect was more pronounced after treatment with **8** (**Figure 65**). These results demonstrated that the primary mechanism of **8** and **5aa** causing HCT116 cell death is the induction of oxidative stress.

As enclosed in ANNEX 1, the pathway of cell death induced by compounds **5aa** and **8** in the U2OS cell line has not been determined. The absence of apoptosis after treatment of U2OS cells with carbazoles could indicate that the compounds inhibit this process by activating autophagy. To assess the molecular mechanism of carbazole-mediated autophagy, the expression of p-62 and LC3B after treatment with compounds and, or chloroquine was analysed by Western blot (**Figure 66**). Compounds **8** and **5aa** caused slight degradation of p-62 and significantly increased LC3B-II expression, leading to 5.8 ( $p=0.0149$ ) and 6.8 ( $p=0.0067$ ) augmentations, respectively, compared to the controls. In addition, compound **8** lowered the effect of chloroquine, reducing the expression of both p-62 and LC3B-II, which implies that **8** induces autophagy in U2OS cells.

Compounds **5aa** and **8** disrupted mitochondrial structures in HCT116 cells (see ANNEX 1). Further microscopic analysis showed that both compounds also altered mitochondria in U2OS cells, which can be related to mitophagy (**Figure 67**). This process refers to the sequestration of mitochondria by autophagosomes and delivery of them to lysosomes for degradation.<sup>303</sup> However, further studies are warranted, such as determining levels of LC3B-II and ubiquitin in mitochondrial fraction or colocalization between mitochondrial and autophagosomes.

Since lysosomes are the endpoint of autophagic cell death, their structure after treatment with carbazoles was determined using confocal microscopy. As shown in **Figure 67**, **5aa** and **8** increased the number and size of lysosomes compared to the DMSO-treated control. Those

results are consistent with others, e.g., Florey et al. reported that inducers of lysosomal LC3 lipidation are increasing lysosome size because of swelling induced by the fusion of lysosome and osmotic stress.<sup>304</sup>

It is well-established that autophagy can protect cancer cells from apoptosis in response to oxidative stress. Therefore, U2OS cells were co-treated with CQ and **5aa** or **8** to investigate whether autophagy inhibition renders an increased proapoptotic effect of the carbazole (**Figure 68**). Shortly after 24 hours of co-treatment of CQ with **5aa** or **8**, the fraction of apoptotic cells significantly increased to about 30% (early + late apoptosis). Further treatment with CQ and **5aa** resulted in a similar percentage of apoptotic cells, while with compound **8**, the fraction of apoptotic cells increased to 52%. In addition, NAC partially blocked the apoptotic effect induced by combined treatment with carbazoles and CQ, suggesting that ROS plays a crucial role in U2OS cell death.



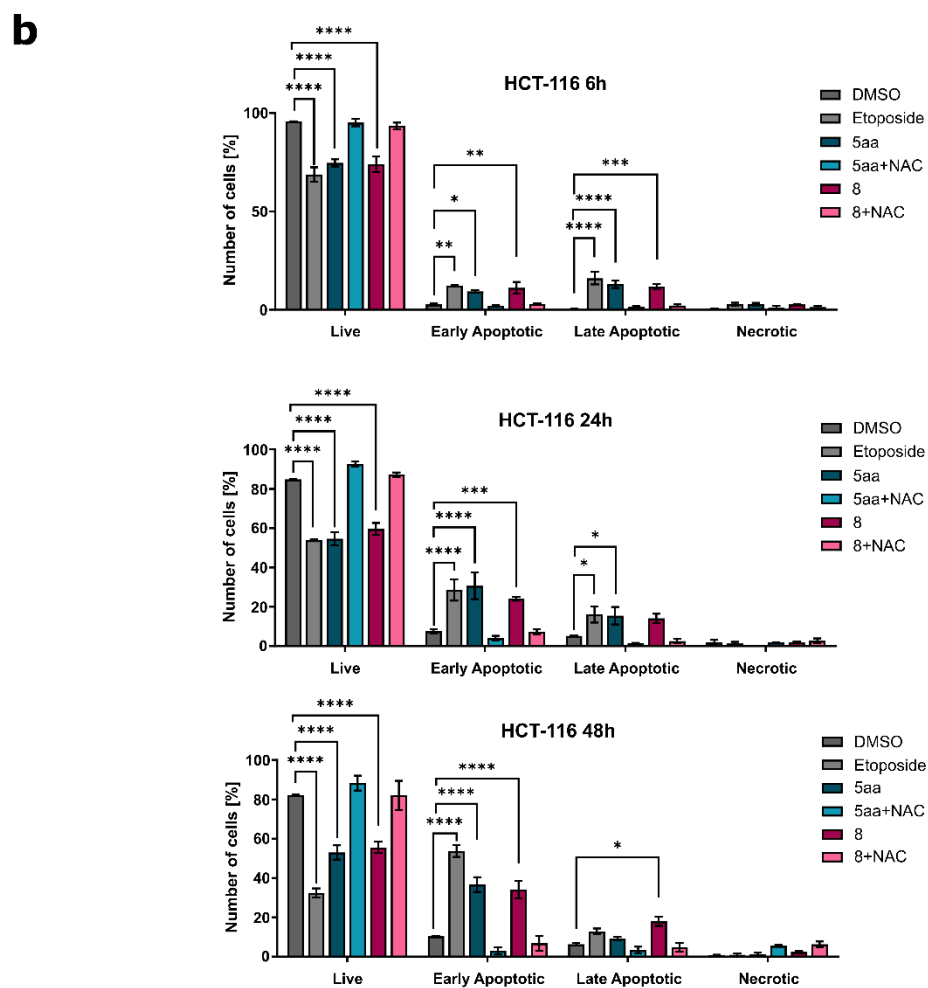
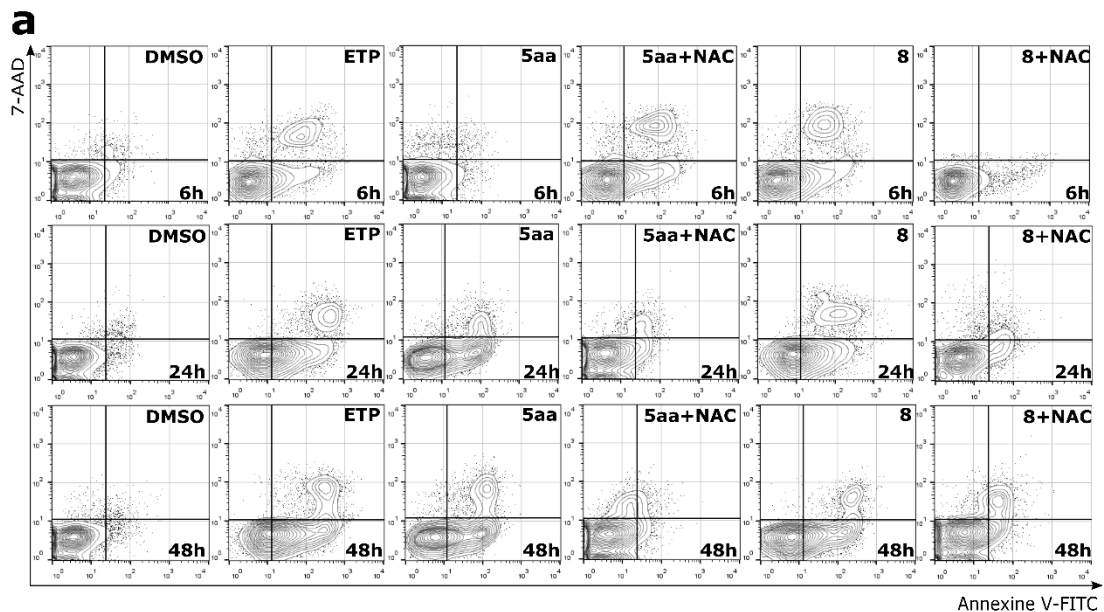


**Figure 64** Flow cytometric analysis of HCT116 cells after 6, 24, and 48 h of treatment with compounds, using Annexin V/7-AAD. DMSO and ETP were used as negative and positive controls, respectively. **(a)** Representative dot-plot; **(b)** The quantification of analysis is presented on a bar graph. Data represent the mean  $\pm$  SEM of three independent experiments. \*  $p < 0.01$ , \*\*  $p < 0.001$ , \*\*\*  $p < 0.0001$ , \*\*\*\*  $p < 0.00001$  (two-way ANOVA and post hoc Dunnett's test).



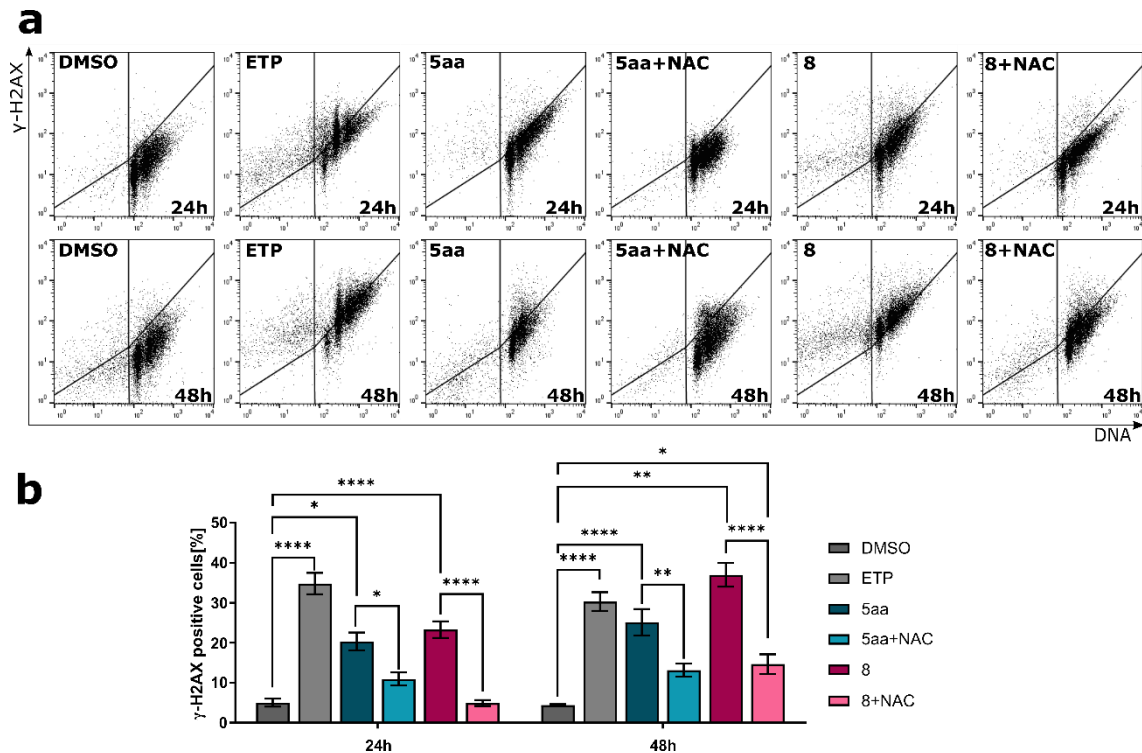


**Figure 65** Flow cytometric analyses of induction  $\gamma$ -H2AX in HCT116 cell lines after 24 and 48 h of treatment. DMSO and ETP were used as negative and positive controls, respectively **(a)** Representative histograms; **(b)** The quantification of the analysis is presented on a bar graph. Data represent the mean  $\pm$  SEM of three independent experiments. \*  $p < 0.01$ , \*\*  $p < 0.001$ , \*\*\*  $p < 0.0001$ , \*\*\*\*  $p < 0.00001$  (two-way ANOVA and post hoc Dunnett's test).

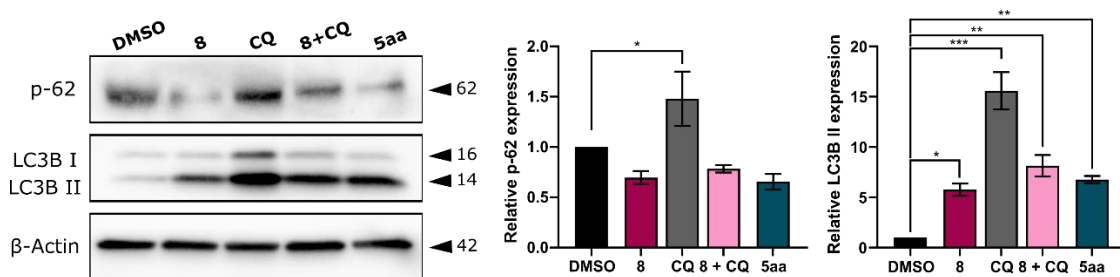


**Figure 66** Western blot analysis showing the effect of **8** and **5aa** on the expression of autophagy-related proteins in U2OS cells after 48 h of treatment. DMSO and CQ were used as negative and positive controls, respectively. The quantification of the analysis is presented on a bar graph. Data represent the mean  $\pm$  SEM of two independent experiments. \*  $p < 0.01$ , \*\*  $p < 0.001$ , \*\*\*  $p < 0.0001$  (one-way ANOVA and post hoc Dunnett's test).

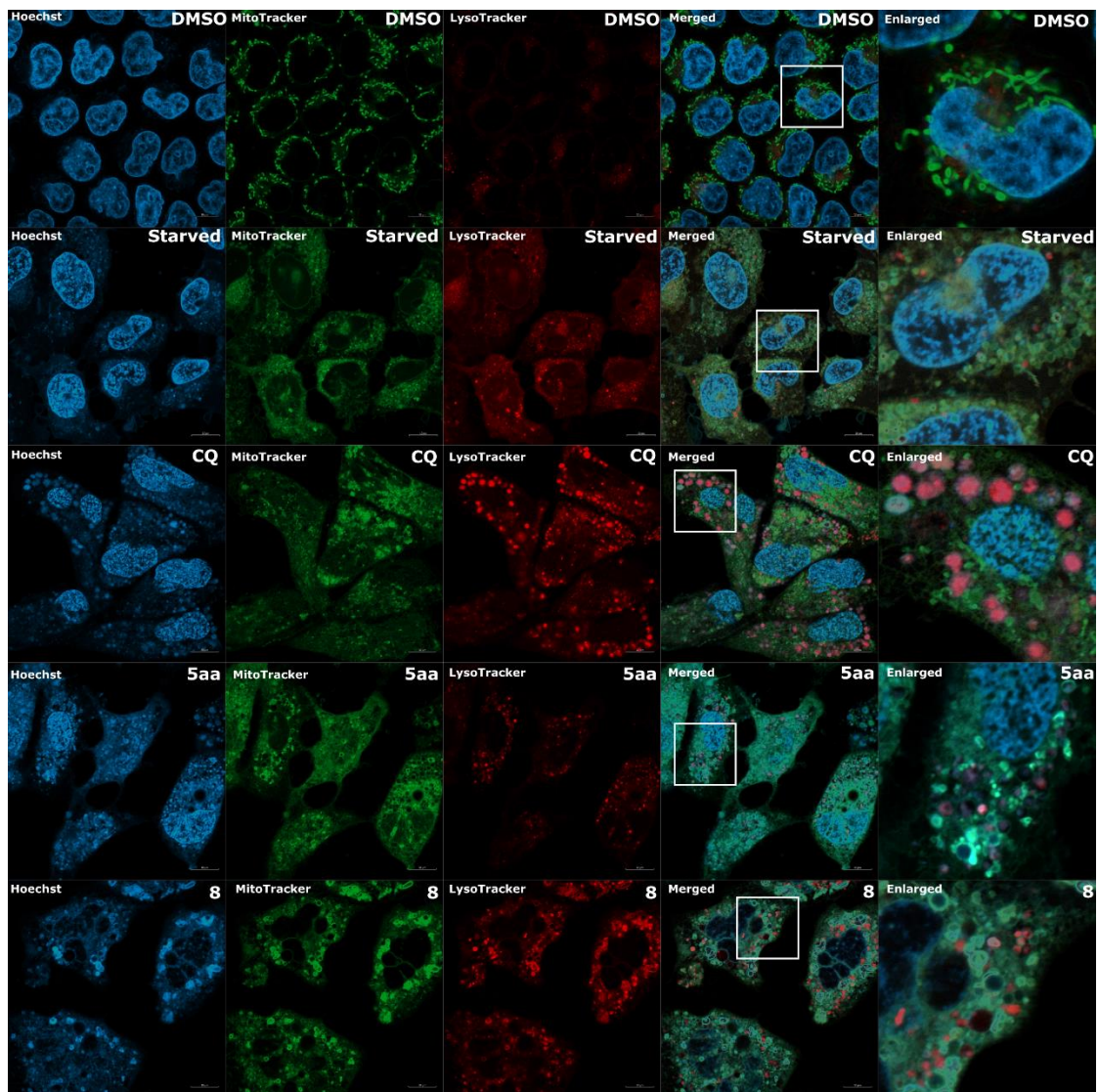


**Figure 67** Representative microscopic images presenting mitochondria and lysosome structures in U2OS cells acquired after 24 h of treatment with 5aa and 8. CQ and DMSO were used as positive and negative controls, respectively; Green—MitoTracker, red—LysoTracker, and blue—Hoechst 33342. Scale bars=10  $\mu$ M.

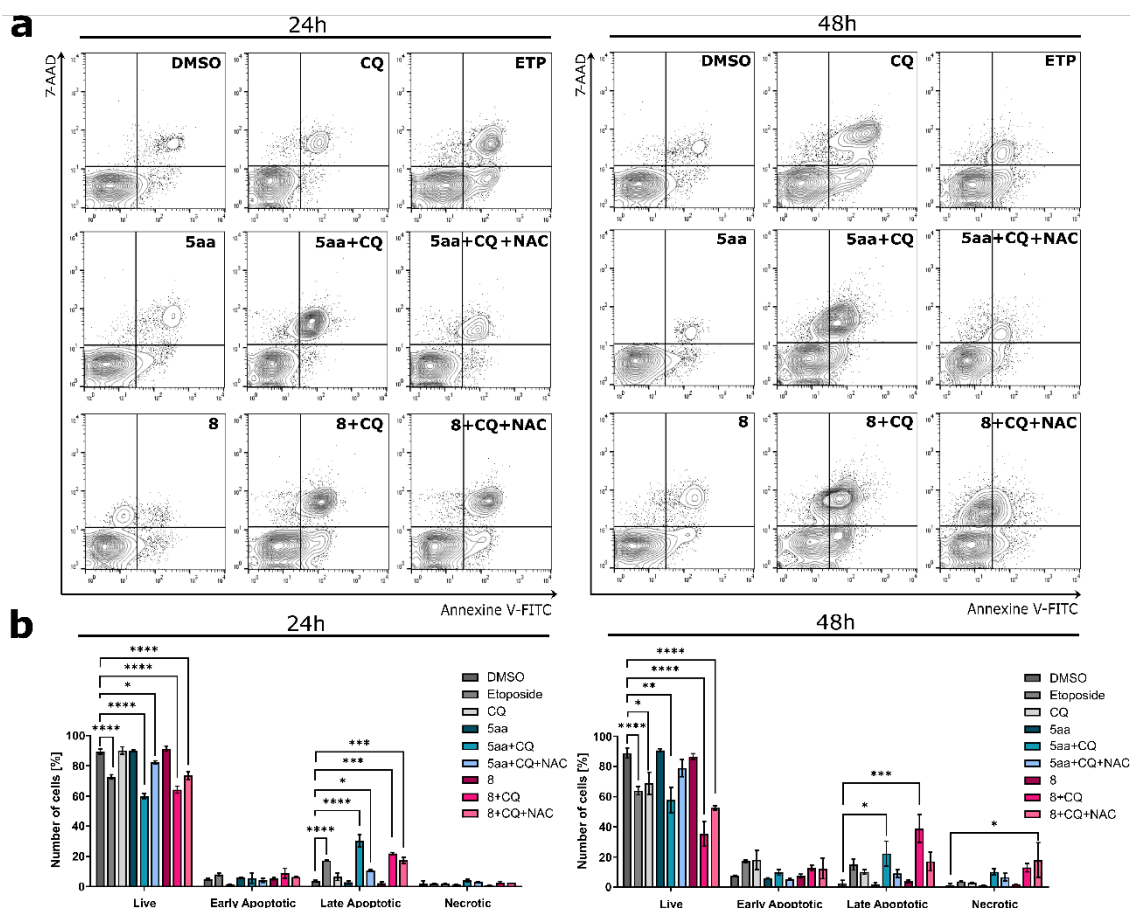


**Figure 68** Flow cytometric analysis of U2OS cell line after 24, and 48 h of treatment with compounds, using Annexin V/7-AAD. DMSO and ETP were used as negative and positive controls, respectively **(a)** Representative dot-plot; **(b)** The quantification of analysis is presented on a bar graph. Data represent the mean  $\pm$  SEM of three independent experiments. \*  $p < 0.01$ , \*\*  $p < 0.001$ , \*\*\*  $p < 0.0001$ , \*\*\*\*  $p < 0.00001$  (two-way ANOVA and post hoc Dunnett's test).

### 3.4.3. Determination impact 5aa and 8 on PTK activity

As mentioned before, carbazole derivatives are known to target tyrosine kinases. Thus, **5aa** and **8** were considered possible inhibitors of PTKs using ELISA. However, as depicted in **Figure 69**, none of the compounds altered PTKs activity, besides the reference, imatinib.

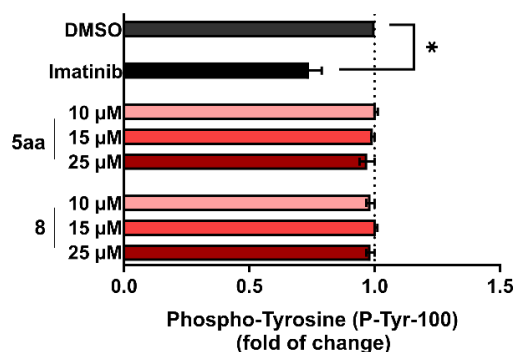


**Figure 69** *In vitro* determination of PTKs activity using A549 extracts determined by ELISA. DMSO and imatinib were used as negative and positive controls, respectively. Error bars represent the SEM of data obtained in n=3 replicates. \* p<0.01, vs. vehicle (one-way ANOVA and post hoc Dunnett's test).

### 3.5. Project III – pyrazole derivatives

Results regarding the activity of pyrazole derivatives are included in the manuscript *Novel chalcone-derived pyrazoles as potential therapeutic agents for the treatment of non-small cell lung cancer* (Maciejewska, N., Olszewski, M., Jurasz, J., Serocki, M., Dzierzynska, M., Cekala, K., Wieczerek, E., Baginski, M., *Sci. Rep.* **12**, 3703, 2022), attached as ANNEX 2.

#### 3.5.1. Scientific problem addressed

The work aimed to explain the mechanism of pyrazole activity, with a focus on compound **PCH-1**, which was selected as the most potent during initial screening. Several cell lines, including A549, H226, and H460 were used as models of non-small cell lung cancer (NSCLC), whereas a human embryonic kidney HEK293 was used as a model of the non-cancerogenic cell line. I established that **PCH-1** inhibited the cell viability of all NSCLC cells without significantly affecting kidney cells. Moreover, **PCH-1** showed superior activity to the reference compound cisplatin, which is commonly used in chemotherapy for NSCLC.<sup>305</sup>

Prolonged exposure to **PCH-1** resulted in the accumulation of cells at the G<sub>2</sub>/M phase, which is a typical feature of antimetabolic drugs.<sup>306</sup> Furthermore, the structural formula of investigated pyrazoles partially overlaps with combretastatin A-4, which is a known microtubule-destabilizing agent.<sup>307</sup> *In vitro* microtubule polymerization assay and confocal microscopy analysis confirmed that **PCH-1** interferes with microtubule polymerization by blocking microtubule assembly. In addition, a series of docking simulations were performed by M. Eng. Jakub Jurasz (Gdansk University of Technology), which results suggest the interaction of **PCH-1** with the vinblastine binding site on tubulin. Further analysis showed that **PCH-1** induces caspase-dependent apoptotic cell death in all NSCLC cells.

The remaining experiments I performed on A549 cells because they were the most sensitive to **PCH-1** treatment. Using this cell line, I investigated the molecular mechanisms responsible for **PCH-1**-induced apoptosis. I have found that **PCH-1** altered the expression of several apoptosis-related proteins, suggesting the activation of both cell surface death receptors and

mitochondrial apoptosis pathways. Finally, I have shown that **PCH-1** inhibits the EMT, decreases cell motility, and induces oxidative stress in A549 cells.

In this work, I have found that **PCH-1** induces G<sub>2</sub>/M phase arrest by stabilization of tubulin polymerization and cellular apoptosis through extrinsic and intrinsic pathways. Moreover, I have found that **PCH-1** has potent antimetastatic and prooxidant properties.



## 4. DISCUSSION

Over the years, substantial progress in understanding the molecular mechanisms driven by telomerase in living organisms has been achieved. Telomerase in tumours provides replicative immortality, and its overexpression has been considered a hallmark of cancer. Many approaches to inhibit telomerase have been discovered and studied extensively.<sup>308–310</sup> Among them, immunotherapy and gene therapy have gained much attention recently. Despite their rapid development in the field of oncology, many issues hamper their applicability in cancer treatment. The primary limitations include high variability in response to treatment, including nonspecific toxicity, low bioavailability, instability, and problems with delivery. Antisense oligonucleotides such as imetelstat show promising results in clinical trials; however, other large-molecule agents likewise have some disadvantages, e.g., the intravenous route's administration and high costs making them often unaffordable for most patients. On the other hand, small-molecule drugs are inexpensive and have good oral bioavailability, but neither telomerase-targeting compounds have been approved as a drug, and the exact mechanism of action has not been demonstrated in any of the molecules discovered.

Compounds that were rationally designed, including carbazoles and pyrazoles, that were the subject of my doctoral dissertation proved unsuccessful. The ineffectiveness of *in silico* methods in developing new telomerase inhibitors may result from limited information on the enzyme structure.<sup>310</sup> Although the usually analysed molecular docking studies structure of hTERT from the flour beetle *Tribolium castaneum* has high amino acid homology similar to the human sequence, it lacks the TEN domain of the enzyme. Only in 2018 did Collins's group established the Cryo-EM structure of substrate-bound human telomerase holoenzyme, and this discovery was much later than the design of the compounds under study.<sup>311</sup>

Anthraquinones have been recognized as cancer growth inhibitors targeting topoisomerases, telomerase, matrix metalloproteinases, and protein kinase.<sup>312</sup> Several drugs containing an anthraquinone scaffold, such as doxorubicin, epirubicin, pixantrone, valrubicin, and MTX, are clinically used to treat various types of cancers.<sup>313</sup> As part of this work, I defined the cellular and molecular mechanism of anthraquinone action using classical methods, including a literature review. I determined that compounds inhibit telomerase activity *in vitro* and exhibit cytotoxic activity toward NSCLC cells. Among all anthraquinones, I have selected the four most active compounds toward telomerase for more detailed studies. I have excluded some of the typical targets for compounds in this group, such as intercalation to DNA or disrupting the structure of tubulin. However, I have found that two compounds, TXT2 and TXT4, have additional off-target activities - protein tyrosine kinases. The same compounds were most active against telomerase, exhibiting typical features for telomerase-targeting drugs, such as inducing apoptosis, DNA damage, cellular senescence, and reducing the abilities of cells to form colonies. Interestingly, despite TXT3 having a similar potential to inhibit telomerase activity as TXT2, no typical signs

of enzyme inhibition were observed. Likewise, to TXT3, TXT1 did not induce apoptosis, DSBs, or senescence. Moreover, both compounds exhibit higher toxicity to normal than cancer cells, so I did not continue studies regarding the type of cell death induced by them.

I observed the same trend of anticancer activity of TXT-compounds among NSCLC cells, which was A549>H460>H226, ranging from cytotoxic activity, prooxidative, and proapoptotic potential to anti-migratory properties. Moreover, the TXT-mediated cell cycle arrest was also dependent on the cell line. Bashash et al. have reported that telomerase inhibition by BIBR1532 lead to G<sub>0</sub>/G<sub>1</sub> cell cycle arrest in acute lymphoblastic leukaemia cells,<sup>314</sup> whereas De Rossi's group showed that the same compound induced cell cycle arrest in the S-phase in Epstein–Barr virus (EBV)-driven B-cell malignancies.<sup>244</sup> Interestingly, Thompson et al. demonstrated that inhibition of telomerase by imetelstat triggered the G<sub>2</sub>/M cell cycle arrest in breast and colon cancers<sup>315</sup>. All those studies provide evidence that telomerase inhibition is not cell-cycle specific.

On the note, despite A549, H226, and H460 cells being both non-small cell lung cancers, they differ in terms of cancer subtypes and growth capacity, with A549 being an adenocarcinoma, H226 a squamous carcinoma, and H460 a large carcinoma. Hence, there may be differences in the cellular and molecular response to TXT compounds. Moreover, there are known clinical differences between NSCLC subtypes, such as higher metastatic rates of adenocarcinoma than squamous carcinoma. Among others, large carcinoma is the most aggressive subtype, characterized by increased vascularity and the ability to metastasize. The high anticancer potency of test compounds toward A549 cells is especially noteworthy since adenocarcinoma is the most common NSCLC.<sup>316</sup>

All known telomerase-targeting anthraquinones act as stabilizers of telomeric G-4 DNA, altering the binding of telomerase enzyme to DNA and blocking telomerase activity *in vitro* and *in vivo*.<sup>317–319</sup> Most of the telomerase-targeting compounds are nonselective because G-4 structures also occur in additional G-rich DNA sequences other than telomeres, which may cause high toxicity to normal cells.<sup>320</sup> A major finding of this study is that the tested compounds unexpectedly failed to stabilize telomeric G-4, but rather blocked the activity of the hTERT protein component. In fact, even a more advanced study showed that TXT4 is able to bind to the hTERT, as assessed by CETSA analyses. Moreover, I have found that TXT4 also downregulated the expression of hTERT mRNA in A549 and H460 cells. Similar to TXT compounds, the two most known telomerase inhibitors, BIBR1532 and imetelstat, likewise inhibited telomerase activity and hTERT mRNA expression simultaneously;<sup>321,322</sup> however, the low selectivity of TXT compounds may suggest that the observed effect is only indirect, and hence no-resulting from enzyme inhibition per se, but being a part of the molecular cascade leading to cell death.

Telomerase inhibition affects the normal kinetics of telomere capping, resulting in the accumulation of DNA damage signals. Uncapped telomeres are perceived as DNA damage in the absence of proper capping.<sup>323</sup> However, DNA damage is a double-edged sword guarding

the genome. If left unrepaired, DNA damage in a normal cell contributes to mutations, and subsequently genomic instability, which is the major hallmark of cancer development and progression. Nonetheless, agents that are commonly used in cancer treatment, such as platinum drugs, anthracyclines, topoisomerase poisons, and radiation, activate DNA damage in tumour cells causing altered expression of DNA repair genes.<sup>324</sup> In some types of cancers, multiple molecular mechanisms mending DNA lesions at nontelomeric chromosomal sequences are observed, which effectively increase intrinsic resistance to radiotherapy and chemotherapy.<sup>325</sup> DNA on telomeres has a different DNA repair capacity than the rest of the genome, due to the inhibition of the NHEJ repair pathway to prevent end-to-end chromosome fusions. NHEJ is the predominant DSB repair pathway, which is inhibited by shelterin proteins, which block the access to telomeric overhang by promoting the formation of the t-loop. For this reason, telomeric DNA damage is irreparable and leads to persistent DDR which triggers signalling cascades that drive cells to either apoptosis or senescence.<sup>323,326</sup>

The study revealed a functional link between DNA damage and inhibition of telomerase in cancer cells. Compounds TXT2 and TXT4 activated DSBs in TERT-positive A-549 and H460 cell lines, which was manifested by increased levels of  $\gamma$ -H2AX. On the other hand, none of these compounds induced DSBs in TERT-negative normal bronchial epithelial cells, umbilical vein endothelial cells, or ALT-positive osteosarcoma cells, suggesting that the induction of DSBs is dependent on telomerase inhibition. Further analyses of A549-treated cells showed that TXT4 induced DSBs on telomeres which may affect telomere-maintenance kinetics and homeostasis. In addition, even after 24 h of treatment, a high amount of DNA damage was found in these cells, with a significant proportion in extratelomeric regions. Longer exposure resulted in a marked decrease in DSBs within a chromosome, but without repairing telomeric DNA. It could be hypothesized that the superior distance between broken DNA ends in telomeric regions compared to that of broken ends forming on internal chromosome regions would impede joining, and thus slow down DNA repair in telomeric regions.<sup>327</sup> Moreover, at a high dose, TXT4 could not only suppress the catalytic activity of telomerase but also severely compromise the functions of other proteins involved in the enzyme assembly resulting in telomere damage rather than replicative stress. Short-term exposure to TXT2/TXT4 induced both ATM- and ATR-mediated DDR related to telomere dysfunctions.<sup>328</sup> Activation of ATM, as well as ATR, was followed by the induction of signalling cascade via phosphorylation of its downstream checkpoint effector kinases, Chk1 and Chk2, which are needed for cells to enter mitosis. In addition, telomerase inhibition could cause perturbation of individual subunits from the shelterin protein by compacting telomeric chromatin leading to direct damage to the telomere structure.<sup>329</sup> Indeed, Karlseder et al. described that DNA damage and cell cycle arrest occur as a result of changes in telomerase composition rather than telomere shortening.<sup>330</sup> However, although Nakamura et al. reported that  $\gamma$ -H2AX can be a biomarker to evaluate the efficacy of telomerase inhibition, I cannot exclude that the DSBs observed on telomeres are not only associated with telomerase but may also be related to an additional mechanism leading to cell death.<sup>331</sup>



Cells with DNA damage that fail to undergo repair evoke secondary responses, leading to apoptotic cell death through either mitochondrial (intrinsic) or death receptor (extrinsic) pathway. During the intrinsic-mediated pathway, mitochondrial outer membrane permeabilization (MOMP), which is considered a “point of no return,” directly induces the release of death-promoting proteins.<sup>332</sup> MOMP requires transient exposure of the Bak or Bax BH3 domain and facilitates the efflux of cytochrome c into the cytoplasm, which together with apoptotic protease activating factor 1 activates the initiator caspase 9.<sup>332</sup> Activated caspase-9 cleaves and activates the downstream effector caspase-3 and caspase-7. Extrusion of the mitochondrial inner membrane into the cytosol and its permeabilization cause widening of Bax/Bak pores and trigger the release of mitochondrial DNA.<sup>333</sup> My study demonstrated that TXT2 and TXT4 triggered apoptotic cell death in A549 and H460 cancer cell lines in a time-dependent manner. Apoptosis was induced by direct activation of caspase-3 or by cleavage of Bid, resulting in mitochondrial dysfunction and subsequent activation of caspase-9 and caspase-3. Additionally, I observed the cleavage of caspase-8, which is an executing protein in the extrinsic apoptotic pathway. In the death receptor pathway, activation of caspase-8 mediates the generation of truncated Bid, forming a signalling link between the extrinsic tumour necrosis factor family and mitochondrial-based apoptotic pathway.<sup>334</sup> The “BH3 domain only” of tBid binds the Bax canonical groove, leading to its oligomerization, as well as MOMP.<sup>335</sup> Treatment with TXT2 and TXT4 led to the activation of both Bid and Bax, which indicates the activation of extrinsic apoptosis involving transmembrane receptor-mediated interactions. My observations are supported by an earlier study showing that inhibition of telomerase induced both intrinsic and extrinsic apoptosis in acute myeloid leukaemia stem cells.<sup>336</sup> Shamas and co-workers reported that siRNA-mediated inhibition of telomerase activated both mitochondrial- and death-receptor-mediated pathways in Barrett’s adenocarcinoma SEG-1 cells.<sup>337</sup> In addition, Giunco et al. observed that short-term inhibition of TERT by BIBR1532 in human malignant B cells xenografted in zebrafish led to apoptosis with the induction of DDR.<sup>338</sup> Nevertheless, it should be noted that profound apoptosis in A549 cells could be not only due to telomerase inhibition but may also result from TXT-induced ROS cellular levels. Of note, there is no evidence in the literature for a direct correlation between telomerase inhibition and the induction of oxidative stress.

Besides the proapoptotic properties of TXT4, I have shown that it also triggers autophagy in all NSCLC cells, which is not exactly related to telomerase inhibition. Ali et al. showed that hTERT inhibits the mTOR complex 1 in several cell lines, leading to the activation of autophagy, whereas TERT-deficient cells could not execute autophagy flux properly.<sup>339</sup> Moreover, Stohr’s group suggests that autophagy did not play a significant role in telomere dysfunction cell death.<sup>340</sup> Observed increased autophagy flux after treatment with TXT4 can be related to inhibition of the Src kinases family. Indeed, Zhao et al. found that the Src/FAK signalling pathway inhibition promotes AMP-activated protein kinase (AMPK) dependent autophagy.<sup>341</sup> Moreover, Wu et al. reported that treatment of prostate cancer cells with a well-known inhibitor of the Src kinases family, saracatinib, induced autophagy by inhibiting the Akt/mTOR/p70S6K signalling pathway.<sup>342</sup>



The metastasis cascade is a multistep process driven by remodelling a cytoskeleton, enabling cell migration and invasion.<sup>343</sup> In my studies, I have demonstrated that TXT2 and TXT4 decreased A549 and H460 cell motility, which was manifested in a reduced signal of cortactin, and slower repopulation of the wound area with the respect to control. Despite finding a positive correlation between the reduction of *hTERT* mRNA expression and the ability to inhibit migration of cancer cells, the anti-migratory properties of TXT compounds are rather linked to the inhibition of some of the PTKs e.g., Src family kinases, FAK kinase, AXL, or others. In fact, Li et al. reported that *hTERT* regulates cell adhesion and migration, but independently of telomerase activity.<sup>344</sup> Conversely, there is much evidence that PTKs-targeted compounds inhibit migration as well as invasion of cancers, e.g., Pichot et al. showed that inhibition of Src family kinases by dasatinib inhibits migration and invasiveness of breast cancer cells,<sup>345</sup> whereas Yo et al. reported that inhibition of FAK in hepatoblastoma cells promoted cells detachment and inhibited cell motility through deregulation Rho GTPases.<sup>346</sup> Moreover, Ullrich's group demonstrated that inhibition of AXL interfered with migration and invasion of human malignant glioma.<sup>347</sup>

Current chemotherapy treatment involves the use of multiple drugs at the same time. Combination therapy increases the chances of successful treatment but raises the risk of side effects.<sup>348</sup> On the other hand, multi-target drugs gain several advantages, such as more predictable pharmacokinetics, fewer drug interactions, and better patient compliance.<sup>349</sup> Many studies have confirmed the synergistic effect of telomerase targeting compounds with PTK or topoisomerase inhibitors<sup>350,351</sup>. A recent study by Hu and co-workers showed that treatment of myelofibrosis hematopoietic stem cells and progenitor cells with ruxolitinib, a Janus kinase inhibitor, in combination with imetelstat was more effective than treatment with the kinase inhibitor used as single agent.<sup>352</sup> Similarly, Gupta et al. showed that combined inhibition of telomerase and p21<sup>(waf1)</sup> synergistically suppressed tumour growth in different cell lines.<sup>353</sup> Moreover, Goldblatt, et al. demonstrated that the use of imetelstat combined with paclitaxel, an inhibitor of microtubule depolymerization, caused a significant reduction in the invasive potential of MDA-MB-231 breast cancer cells, allowing for effective growth inhibition at lower doses of both drugs, compared to treatment with single agents.<sup>354</sup> Of note, such a combination regimen has been evaluated in phase II clinical trials in patients with locally recurrent or metastatic breast cancer (ClinicalTrials.gov identifier NCT01256762).<sup>355</sup>

The TXT4 is a multi-targeting compound, which may positively affect its therapeutic effectiveness, but it also translates into the compound's toxicity. The TXT4 toxicity can be reduced by improving its delivery e.g., by using nano-based systems for encapsulation of the compound inside a nontoxic molecule, such as liposomes, biocompatible polymers, inorganic formulations, and many others.<sup>356–361</sup> Konda et al showed that encapsulation of mitoxantrone in macrocyclic cage-like compounds increased its uptake in mouse breast cancer cells and reduced the toxicity in mice.<sup>359</sup> Whereas another group reported that encapsulation of doxorubicin with PLGA or poly(lactic-co-glycolic acid) overcomes its toxicity to normal cells.<sup>361</sup>

It is worth emphasizing that despite the lead compound TXT4 exhibiting similar cytotoxic potency to normal cells as to cancers, it was also efficacious in non-cytotoxic concentrations towards A549 cells, decreasing their motility and inducing replicative senescence by telomere shortening. Moreover, the long-term treatment led to a decrease in the capability to form colonies and cancer growth capacity as well. Importantly, cells did not acquire the typical resistance to compounds; however, I observed cancer cell fusion, which may increase cell heterogeneity, leading to enhanced drug resistance or metastatic capacity.<sup>302</sup>

As shown in this work, the TXT compounds exhibit many interesting anti-cancer properties that certainly require further research, among others: mechanistic and kinetic studies of telomerase inhibition, assessment of TXT4 applicability in combination therapy, or its modification to improve its selectivity.

Although telomerase has many functions in carcinogenesis, the development of telomerase inhibitors raises several questions: *(i)* clinical relevance of telomerase inhibition in cancer patients is still controversial due to the expected delayed therapeutic effect (i.e., the lag time needed for telomeres to shorten to a critical size before a cancer cell undergoes senescence and/or cell death; *(ii)* the ALT mechanism may be activated as an adaptive response to telomerase inhibition leading to chemoresistance;<sup>362,363</sup> *(iii)* can cancer cells gain drug resistance through another mechanism (such as cell fusion)? However, despite this, there is still a hope to introduce telomerase inhibitors as drugs in anti-cancer therapy that will harm non-canonical enzyme functions or to employ them in combination therapy.



## 5. CONCLUSION

### ANTHRAQUINONES

- Anticancer activity of anthraquinones increases within NSCLC cells in order H226<H460<A549, ranging from cytotoxic activity, prooxidative, and proapoptotic potential to anti-migratory properties.
- The most promising compounds, TXT2 and TXT4 exhibit at least two distinct mechanisms by inhibition of telomerase activity and protein tyrosine kinases.
- Anthraquinones exhibit minor selectivity against cancer cells and relatively high toxicity towards healthy cells, which may be due to at least more than one molecular mechanism of their action.
- TXT2 and TXT4 at cytotoxic concentrations trigger DNA damage and apoptotic cell death through intrinsic and extrinsic apoptotic pathways on hTERT-positive A549 and H460 cells.
- Long-term treatment with TXT4 led to progressive telomere shortening along with reducing colony forming and growth capacity.
- The study will bring novel results important for extending our knowledge on the new small-molecule telomerase inhibitors, which could be a starting point for further development of new anticancer agents targeting telomerase based on the 9,10-anthracenedione scaffold.

### CARBAZOLES

- Carbazoles were inactive towards telomerase *in vitro* assay.
- Carbazole derivatives exhibit the most potent cytotoxic properties towards colon carcinoma and osteosarcoma and no toxicity towards non-cancerogenic kidney cells.
- The most active compounds, 5aa and 8 display anticancer activity by blocking cell cycle progression, decreasing colony formation capacity and cell motility.
- Compounds 5aa and 8 trigger caspase-independent apoptotic or autophagy cell death in colon and osteosarcoma cells, respectively.
- Carbazole-induced cancer cell death is driven by excessive ROS production - the primary mechanism of their action.

### PYRAZOLES

- Pyrazoles were inactive towards telomerase *in vitro* assay.



- The majority of the investigated pyrazoles inhibited the growth of non-small lung cancer cells, whereas dimethoxy analogue PCH-1 was found to be the most potent cytotoxic without significantly affecting non-cancerogenic kidney cells.
- PCH-1 induces G<sub>2</sub>/M phase arrest by the stabilization of tubulin polymerization and cellular apoptosis through extrinsic and intrinsic pathways.
- PCH-1 has potent antimetastatic and prooxidant properties.



## 6. MATERIALS AND METHODS

### 6.1. Materials

All reagents and materials were purchased from Sigma-Aldrich (Saint Louis, United States) unless otherwise stated.

#### 6.1.1. Antibodies

**Table 6** List of antibodies used in Western blot

Antibody name	Company	Dilution
anti-TERT (Y182), ab32020	Abcam	1:1000
anti-ATR (ab10312)	Abcam	1:1000
anti-ATM (2C1 [1A1]) (ab78)	Abcam	1:1000
anti-Phospho-ATR (Ser428) (#2853)	Cell Signalling	1:1000
anti-Phospho-Chk2 (Thr68) (C13C1) (#2197)	Cell Signalling	1:500
anti-Phospho-Chk1 (Ser345) (133D3) (#2348)	Cell Signalling	1:500
anti-Phospho-Histone H2A.X (Ser139) (20E3) (#9718)	Cell Signalling	1:1000
anti-Phospho-ATM (Ser1981) (D6H9) (#5883)	Cell Signalling	1:1000
anti-Caspase-3 (#9662)	Cell Signalling	1:1000
anti-Caspase-9 (#9502)	Cell Signalling	1:1000
anti-Caspase-8 (1C12) (#9746)	Cell Signalling	1:500
anti-PARP (#9542)	Cell Signalling	1:1000
anti-Bcl-2 (#4223)	Cell Signalling	1:1000
anti-BID (#2002)	Cell Signalling	1:1000
anti-Bax (#2772)	Cell Signalling	1:1000
anti-LAMP1 (D4O1S), #15665	Cell Signalling	1:1000
anti-LC3B, #2775	Cell Signalling	1:1000
anti-actin, sc-1616	Santa Cruz Biotechnology	1:1000
anti-mouse- horseradish peroxidase HRP, 715-035-150	Jackson ImmunoResearch Labs	1:10000
anti-rabbit-HRP, 711-035-152	Jackson ImmunoResearch Labs	1:10000
anti-goat-HRP, 705-036-147	Jackson ImmunoResearch Labs	1:10000

**Table 7** List of antibodies used in immunofluorescence

Antibody name	Company	Dilution
Alexa Fluor 488-conjugated anti-H2AX (pS139), #560445	BD Pharmingen	1:200
Anti-TRF2, ab108997	Abcam	1:500
anti-LAMP1 (D4O1S), #15665	Cell Signalling	1:300
anti-LC3B, #2775	Cell Signalling	1:250
anti-cortactin, #3503	Cell Signalling	1:250
anti-phospho-tyrosine (P-Tyr-100), #9411	Cell Signalling	1:500
anti- $\beta$ -tubulin, #T8328	Sigma-Aldrich	1:250
anti-mouse Alexa Fluor 488, #SA5-10166	Invitrogen	1:500
anti-rabbit Alexa Fluor 594, sc-516250	Santa Cruz Biotechnology	1:500
Alexa Fluor 647 phalloidin, A22287	Thermo Fisher Scientific	1:500

### 6.1.2. Oligonucleotides

All oligonucleotides were purchased from Genomed (Warsaw, Poland).

**Table 8** Primer sequences used for RT-PCR (5'-3')

Gene	Forward Primer	Reverse Primer
telomere	CGGTTTGTGGTTGGGTTGGGTTGGGTT TTGGGTTTGGGTT	GGCTTGCCTTACCCTTACCCTTACCCTTACC CTTACCCT
IFNB1	GGTTACCTCCGAAACTGAAGA	CCTTTCATATGCAGTACATTAGCC
RPII	CTTCACGGTGCTGGGCATT	GTGCGGCTGCTTCCATAA
hTERT	CATCAGGGGCAAGTCCTACG	AAGTTCACCACGCAGCCATA

**Table 9** Primer sequences used for TRAP (5'-3')

Primers	Sequence
Cy5-TS	AATCCGTCGAGCAGAGTT
TSNT	AATCCGTCGAGCAGAGTTAAAAGGCCGAGAAGCGAT
NT	ATCGTTCTCGGCCTTTT
ACX	CGCGGCTTACCCTTACCCTTACCCTAACC

## 6.2. Methods

### 6.2.1. Cell lines cultivation

The NSCLC: A-549, H226, H460, human osteosarcoma U2OS, human promyelocytic leukaemia HL-60, human colorectal cells HCT116, normal human bronchial epithelial cells NHBE2594, and human umbilical vein endothelial cells HUVEC were obtained from the American Type Culture Collection. Subclones HL-60/MTX and HL-60/VINC were selected from accordingly HL-60 and HL-60/AL cell lines by exposure to stepwise increasing concentrations of the mitoxantrone (MTX) and vincristine (VINC), respectively. HL-60/AL is a late-passage HL-60 cells. All cell lines were maintained at 37°C in a humidified atmosphere containing 5% CO<sub>2</sub> and were routinely screened for Mycoplasma contamination. The NSCLC and leukaemias were cultured in RPMI-1640 medium (Corning, New York, USA), U2OS, and HCT116 in McCoy's 5A medium (Corning), HUVEC in EGM-2 (Endothelial Cell Growth Medium-2, Lonza, Walkersville, USA), and NHBE in BEGM (Bronchial Epithelial Cell Growth Medium, Lonza). Medium for adherent cancer cell lines was supplemented with 10% fetal bovine serum (Corning), 2 mM L-glutamine (Corning), and antibiotics (penicillin 62.6 µg/ml and streptomycin 40 µg/ml). Mediums for cancer cell lines in suspension culture were supplemented with 20% fetal bovine serum, 2 mM L-glutamine, and antibiotics. The culture mediums used for normal cell lines contained supplements and growth factors according to the manufacturer's instructions.

### 6.2.2. TRAP assay

A549 cells ( $1.6 \times 10^5$ ) were cultured for overnight attachment. Day after, cells were collected and lysed with NP-40 buffer (10 mM pH 8 Tris-base, 1 mM EGTA, 1 mM EDTA, 1% (v/v) Nonidet-P40, 0.25 mM Sodium deoxycholate, 10% v/v Glycerol, 150 mM NaCl [POCH S.A., Gliwice, Poland], 5 mM 2-mercaptoethanol, 0.1 M 4-(2-Aminoethyl) benzenesulfonyl fluoride hydrochloride [AEBSF]). Protein concentration was determined using the DC Protein Assay Kit (Bio-Rad, Hercules, USA), and the samples were stored at  $-80^\circ\text{C}$  until analysed. The PCR reaction was performed in a TRAP buffer (200 mM pH 8.3 Tris-base, 15 mM  $\text{MgCl}_2$  [POCH S.A.], 630 mM KCl [POCH S.A.], 0.5% (v/v) Tween 20 [Thermo Fisher Scientific, Waltham, USA]), 0.1 mg/ml BSA, 50  $\mu\text{M}$  dNTPs (Thermo Fisher Scientific), oligonucleotides Cy5-TS (100 ng/ $\mu\text{l}$ ), TSNT (0.01 attomol/ $\mu\text{l}$ ), NT (100 ng/ $\mu\text{l}$ ), ACX (100 ng/ $\mu\text{l}$ ), 2 U of Taq polymerase (Thermo Fisher Scientific), 0.1  $\mu\text{g}$  of protein, and 0.4% (v/v) DMSO or compounds. After telomerase elongation, and denaturation for 40 min at  $25^\circ\text{C}$ , and 5 min at  $95^\circ\text{C}$ , respectively, PCR was conducted in 30 cycles ( $95^\circ\text{C}$ , 30 s;  $52^\circ\text{C}$ , 30 s; and  $72^\circ\text{C}$  for 45 s). The PCR products were separated by electrophoresis on 8% nondenaturing polyacrylamide gel at 110 V for 4.5 h. Next gel was fixated in 0.5 M NaCl, 50% ethanol (POCH S.A), and 40 mM sodium acetate pH 4.2 for 15 min at room temperature (RT), and subsequently visualized using ChemiDoc XRS+ Imaging System (Bio-Rad Laboratories). Band intensities of PCR products were measured by Image Lab Software 6.0.1 (Bio-Rad) and quantitatively analysed by densitometry. Relative telomerase activity (RTA) was calculated using the following formula:  $\text{RTA} = (\text{XTP}/\text{XIT})/(\text{CTP}/\text{CIT}) * 100\%$  where X and C indicate band intensities of the samples and telomerase positive controls, respectively.

### 6.2.3. Cell viability assay

The cell viability assay was performed for A-549, H226, H460, U2OS, NHBE, HUVEC, HL-60, HL-60/MTX, HL-60/AL, and HL-60/VINC after treatment with the test and reference compounds by using the 3-(4,5-dimethylthiazol-2-yl)-2,5-diphenyltetrazolium bromide (MTT) assay. Briefly, adherent cells were seeded onto 96-well culture plates for attachment overnight. Suspension cells were plated onto 24-well plates on the same day as treatment. Then, all cells were treated with DMSO (1%) and the agents in triplicates. After incubation, the MTT solution (0.4 mg/ml) was added to each well for 2-4 h. Formazan crystals were dissolved in 100  $\mu\text{M}$  DMSO, or 10% SDS in 10 mM HCl, for adherent, and suspension cells, respectively. The absorbance of each well was measured at 450 nm for adherent and 560/660 nm for suspension cells with an ASYS UVM340 microplate reader (Biochrom Ltd., Cambridge, UK). The 50% inhibitory concentration ( $\text{IC}_{50}$ ) was defined as the concentration that decreased the absorbance of the DMSO-treated cells by 50% of the vehicle. The  $\text{IC}_{50}$  values were calculated in GraphPad Prism software (GraphPad Prism version 9.0.0 for Windows, GraphPad Software, San Diego, USA) by plotting the survival curve as a function of dose from a minimum of 3 independent experiments.

#### 6.2.4. Analysis of cell cycle distribution

Cells were plated onto tissue culture plates and allowed to attach overnight. Unsynchronized cells were treated with compounds at IC<sub>90</sub> concentration or 1% (v/v) DMSO for 24, 48, and 72 h, while synchronized cells were treated for 2, 4, 6, 8, and 10 h. Synchronization of the cells was performed by double thymidine block according to the protocol reported by Chen et al.<sup>364</sup> After incubation, the cells were collected by trypsinization, fixed in ice-cold 75% ethanol, and stored at -20°C until analysis. Prior to the measure, the cells were rinsed with PBS and stained with 20 µg/µl PI and 50 µg/µl RNase A (Thermo Fisher Scientific) in phosphate-buffered saline (PBS) for 30 min at RT. The distribution of a population of cells to the different stages of the cell cycle was analysed by flow cytometry (Guava EasyCyte 8 cell sorter, Merck Millipore, Burlington, USA) and FlowJo software v10 (BD Biosciences, Haryana, India). Each experiment was repeated three times independently.

#### 6.2.5. Colony formation assay

Cells were plated onto 6-well plates (500 cells/well) and allowed to attach overnight in a fresh medium. Next, the cells were pretreated with a 1% (v/v) DMSO solution of the examined compound for 24 h. Then, they were washed and cultured for an additional 9 days. After incubation, the cells were washed twice with PBS, fixed with 100% methanol for 30 min, and stained with 0.5% crystal violet for 15 min. The colonies were photographed and analysed by ImageJ 1.53n software (National Institutes of Health, Bethesda, USA) as previously described.<sup>365</sup>

#### 6.2.6. Apoptosis and caspase 3/7 assay

Cells were plated onto tissue culture plates and allowed to attach overnight. Next, cells were treated with compounds at IC<sub>90</sub> concentration or 1% (v/v) DMSO for 24, 48, and 72 h. After the indicated time, cells were collected by trypsinization, washed twice with PBS, followed by incubation with Annexin V FITC conjugate (#A13199; Thermo Fisher Scientific) for apoptosis assay and with CellEvent™ Caspase-3/7 Green Flow Cytometry Assay Kit (#C10427; Thermo Fisher Scientific) for caspase-3/7 activation according to the manufacturer's protocols. The analysis was performed by flow cytometry (Guava EasyCyte 8 cell sorter, Merck Millipore) and FlowJo software v10. Each experiment was repeated three times independently.

#### 6.2.7. Calcium efflux assay

Cells were plated onto tissue culture plates and allowed to attach overnight. Day after, cells were treated with 1% (v/v) DMSO, test compounds, or MTX at IC<sub>90</sub> concentration for 24 and 48 h. Next, cells were stained with 1 µM Fluo-4 AM (#F14201; Thermo Fisher Scientific) for 60 min at 37°C and washed in Hank's Balanced Salt Solution (Thermo Fisher Scientific) for 30 min. After, cells were collected by trypsinization and analysed using flow cytometry (Guava EasyCyte 8 cell

sorter, Merck Millipore) and FlowJo software v10. Each experiment was repeated three times independently.

#### 6.2.8. Quantification of lysosomal and mitochondrial cellular content

Lysosomal and mitochondrial labelling was performed according to the manufacturer's instructions. Briefly, after overnight attachment, cells were treated with compounds at IC<sub>90</sub> concentration or 1% (v/v) DMSO for 6, 24, and 48 h at 37°C. Thereafter, cells were stained with 75 nM LysoTracker Red DND-99 (#L7528; Thermo Fisher Scientific) and 100 nM Mitotracker Green FM probe (#M7514; Thermo Fisher Scientific) 30 min before the end of incubation, followed by collection by trypsinization. The analysis was performed by flow cytometry (Guava EasyCyte 8 cell sorter, Merck Millipore) and FlowJo software v10. Each experiment was repeated three times independently.

#### 6.2.9. Live cell imaging

For the analysis of mitochondrial morphology, cells were grown on a covered glass-bottomed 12-well plate and allowed to attach overnight. On the next day, cells were exposed for 6 h to the tested compounds at their IC<sub>90</sub> concentration or to 1% (v/v) DMSO. Then, mitochondrial labelling was performed by incubating the cells with 100 nM MitoTracker Green FM probe (#M7514; Thermo Fisher Scientific) and 1 µg/ml Hoechst 33342 (Thermo Fisher Scientific) for 15 min, according to the manufacturer's instructions. After staining, the cells were suspended in a fresh growth medium. Images were acquired with an LSM 800 inverted laser scanning confocal microscope (Carl Zeiss, Jena, German), equipped with an Airyscan detector for high-resolution confocal scanning using a ×63 1.4 NA Plan Apochromat objective (Carl Zeiss). Cells were incubated in an incubation chamber at 37°C with 5% CO<sub>2</sub>. During imaging, the parameters of laser intensity, exposure times, gain settings, and so on were kept constant for both compound-treated and DMSO-treated cells.

#### 6.2.10. Mitochondrial morphometric analyses

Analysis of mitochondrial circularity was performed using the mitochondrial morphology plugin of ImageJ (NIH) developed by Dagda et al.<sup>366</sup> The mitochondrial length was analysed with a macro developed by Merrill et al.<sup>367</sup> Data were obtained in at least n=15 randomly selected locations on the slide.

#### 6.2.11. β-Galactosidase in situ assay for cellular senescence

The β-Galactosidase assay was performed according to the protocol established by Dimri et al. with slight modification.<sup>368</sup> Briefly, cells were treated with 1% (v/v) DMSO or test compounds for 72 h at 37°C and 5% CO<sub>2</sub>. The medium was changed to fresh, and cells were cultivated for an additional 48 h. Next, cells were washed twice with PBS and fixed with 2% formaldehyde and 0.2% glutaraldehyde for 5 min in RT. Then, cells were washed twice with PBS and incubated with β-Gal staining buffer (5 mM Potassium Ferricyanide [Thermo Fisher Scientific], 5 mM Potassium

Ferrocyanide [Thermo Fisher Scientific], 2 mM MgCl<sub>2</sub>, 6 M NaCl, 1 mg/ml X-Gal in citrate/sodium phosphate buffer 40 mM pH 6) for 16 h in 37°C without CO<sub>2</sub>. After staining, cells were washed with citric acid and phosphate buffer (40 mM, pH 4). The slides were washed twice in PBS and mounted in a mounting medium (90% glycerol, 2.5 mg 1,4-diazabicyclo[2.2.2]octane [DABCO]). Images were acquired with a fluorescence microscope (Olympus BX60; Tokyo, Japan) with an appropriate filter.

#### 6.2.12. Intracellular ROS measurement

Cells were plated onto tissue culture plates and allowed to attach overnight. Day after, cells were treated with compounds at IC<sub>90</sub> concentration, 1% (v/v) DMSO, or 250 μM H<sub>2</sub>O<sub>2</sub> for the indicated time. In the case of carbazole derivatives, the effect of combination treatment with 2 mM NAC was also studied. Before 30 min the end of treatment, cells were stained with 1 μM CM-H2DCFDA (#C6827; Thermo Fisher Scientific). Next, cells were detached by trypsinization and stained with 10 μg/ml 7-Aminoactinomycin D (7-AAD; Thermo Fisher Scientific). The analysis was performed by flow cytometry (Guava EasyCyte 8 cell sorter, Merck Millipore) and FlowJo software v10. Each experiment was repeated three times independently.

#### 6.2.13. H2AX phosphorylation assay

Cells were plated onto tissue culture plates and allowed to attach overnight. Day after, all cells were treated with 10 μM of compounds or 1% (v/v) DMSO for 24, 48, and 72 h. After incubation, the cells were collected by trypsinization, fixed in ice-cold 75% ethanol, and stored at -20°C until analysis. Next, cells were rehydrated with PBS in ice for 10 min, followed by permeabilization in 0.2% Triton X-100 in PBS for 5 min at room temperature. After centrifugation, cells were washed with 1% BSA in PBS and incubated with Alexa Fluor™ 488-conjugated mouse anti-γH2AX (Ser139) antibody (1:100 dilution; #613406; BioLegend, San Diego, USA) for 1.5 h in 37°C. Samples were washed with 1% BSA in PBS and stained with 20 μg/μl propidium iodide and 50 μg/μl RNaseA in PBS for 30 min at room temperature. The analysis was performed by flow cytometry (Guava EasyCyte 8 cell sorter, Merck Millipore) and FlowJo software v10. Each experiment was repeated three times independently.

#### 6.2.14. Immunofluorescence

Cells (2x10<sup>5</sup>) were seeded onto tissue culture plates with a glass slide to attach overnight. Day after, cells were exposed to tested compounds at their IC<sub>90</sub> concentration or 1% (v/v) DMSO for the indicated time. The cells were washed in PBS and fixed for 15 min at RT with 4% (w/v) paraformaldehyde (PFA) in PBS, and permeabilized for 15 min in 0.25% Triton X-100 in PBS. Next, cells were blocked with 3% BSA in PBS-T (PBS with 0.1% Tween-20) for 1 h at RT and incubated with primary antibodies for 1.5 h at 37°C in a humidified chamber. The cells were washed three times with PBS-T followed by incubation with appropriate peroxidase-conjugated secondary antibodies for 1 h in a humidified chamber at 37°C. The cells were washed three times

for 10 min with PBS-T, stained with 0.25 µg/ml DAPI for 15 min, and mounted onto slides with PBS-glycerol (90%) containing 2.5% (w/v) DABCO. Images were acquired with an LSM 800 inverted laser scanning confocal microscope (Carl Zeiss) with an airyscan detector using a ×63 1.4 NA Plan Apochromat objective (Carl Zeiss). Confocal images were acquired with the parameters (laser intensity, exposure times, gain settings, etc.) kept constant for both cells treated with compounds and cells treated with DMSO. All used antibodies are presented in **Table 7**. Correlations of overlapping pixel intensities were calculated using thresholded MCC and PCC from Z-stack images. Data were obtained in at least n=15 randomly selected locations on the slide. The scatter plots and coefficients were analysed using the JACoP plugin under ImageJ as previously described.<sup>369</sup>

#### 6.2.15. Combined immunofluorescence and telomere FISH

After immunofluorescence, cells were fixed with 4% PFA in PBS for 15 min and washed twice with PBS. FISH was performed as described by Cesare et al.<sup>370</sup> Briefly, coverslips were dehydrated with a series of ethanol solutions, denatured for 5 min at 80°C, and hybridized with 0.3 µg/ml Alexa Fluor 647-labelled CCCTAA PNA probe (Panagene Inc, Daejeon, South Korea) overnight at RT. Then, coverslips were washed, dehydrated, mounted onto slides with PBS-glycerol (90%) containing 2.5% (w/v) DABCO, and stained with 0.25 µg/ml DAPI. Cells were visualized and analysed as described for immunofluorescence.

#### 6.2.16. Western blot

Cells ( $1.5 \times 10^6$ ) were seeded onto tissue culture plates to attach overnight. Day after, cells were treated with compounds at their  $IC_{90}$  concentration for 24, 48, and 72 h. The cells treated with 1% (v/v) DMSO served as the negative control. The total protein content was extracted from the cells using the NP-40 cell lysis buffer (10 mM Tris-HCl pH 7.4, 10 mM NaCl, 3 mM  $MgCl_2$ , 0.5% Nonidet P-40, cOmplete Mini EDTA-free Protease Inhibitor Cocktail). Protein concentration was determined using the DC Protein Assay Kit (Bio-Rad), and the samples were stored at -80°C until analyses. Then, 30 µg of protein extract was separated by 4-15% sodium dodecyl sulfate-polyacrylamide gel electrophoresis, followed by separated by transfer onto microporous polyvinylidene difluoride membranes (Bio-Rad). The membranes were blocked with 5% (w/v) non-fat dry milk or bovine serum albumin in TBST buffer (0.2 M Tris-base, 0.137 M NaCl, 0.1% Tween 20) for 1 h at RT, and incubated overnight with primary antibodies at 4°C. The membranes were washed three times with TBST, incubated with appropriate peroxidase-conjugated secondary antibodies for 1 h at RT, and again washed. Proteins were detected by an enhanced chemiluminescence detection reagent kit (Thermo Fisher Scientific) and a ChemiDoc XRS+ Imaging System (Bio-Rad). The band intensity was measured using Image Lab 5.2 software (Bio-Rad). All used antibodies are presented in **Table 6**.



#### 6.2.17. Genotoxic activity (comet assay)

The genotoxic properties of anthraquinone derivatives were studied using the comet assay. Briefly,  $2 \times 10^5$  A549 cells were seeded in 24-well plates and incubated to attach overnight. The next day, cells were treated with test compounds at  $IC_{90}$  concentration for 24 h. For reference,  $450 \mu\text{M}$   $\text{H}_2\text{O}_2$  and 1% (v/v) DMSO were used. After exposure, cells were collected by trypsinization and centrifugation (1000 rpm, 5 min,  $4^\circ\text{C}$ ). Then, cells were washed in ice-cold PBS and centrifuged again. Cells were mixed in equal volumes with 1% (w/v) LMP agarose and placed on microscope slides pre-coated with NMP agarose 1% (w/v) in distilled water, followed by closing with a coverslip and allowed to solidify on ice for 10 min. The coverslips were carefully removed, and the slides were placed in lysis buffer (3 mM NaCl, 0.127 mM EDTA, 3 mM NaCl, 10 mM Trizma-Base, 1% Triton X-100, pH 10) for 24 h at  $4^\circ\text{C}$ . Then, slides were transferred to the electrophoresis apparatus (Bio-Rad) filled with ice-cold electrophoretic buffer (300 mM NaOH, 1 mM  $\text{Na}_2\text{EDTA}$ , pH>13). The slides were allowed to stay in the alkaline buffer for 20 min in the dark, followed by electrophoresis (300 mA, 26 V, 30 min,  $4^\circ\text{C}$ ). After separation, slides were washed twice with neutralizing buffer for 5 min at  $4^\circ\text{C}$ . Then, slides were air-dried and stained with Sybr Green (Thermo Fisher Scientific) for 30 min at  $4^\circ\text{C}$ . Comets were analysed using a fluorescence microscope (Carl Zeiss, Dresden, Germany) equipped with Metafer4® software (Carl Zeiss). The results are presented as the mean $\pm$ SEM of the percentage of DNA in the tail calculated in 200 comets per gel.

#### 6.2.18. FRET

The initial DNA melting screen was performed using a dual-labelled G4-forming sequence from the human telomere (5'-FAM-[GGG-TTA-GGG-TTA-GGG-TTA-GGG]-TAMRA-3') (Genomed), which forms a well-characterized parallel stranded G-4 structure. The oligonucleotide was prepared as a 400 nM solution in 10 mM sodium cacodylate buffer (pH 7.2) with 90 mM NaCl and 10 mM KCl, and the solution was thermally annealed by heating at  $95^\circ\text{C}$  for 5 min and allowed to cool overnight to RT. On the next day, equal volumes of the probe were added to the compound solutions in DMSO, to achieve the following relative compound:probe ratios: 10:1, 5:1, 2:1, 1:1, and 0.5:1. The solutions were distributed in 96-well plates (Roche Life Science, Penzberg, Germany) to obtain a total reaction volume of 20  $\mu\text{l}$ . A probe solution containing 0.5% DMSO was used as a negative control. Measurements were carried out in triplicate using a LightCycler 480 thermocycler (Roche Life Science) with a filter setting of 465 nm/510 nm at a range of 30– $95^\circ\text{C}$  with a rate of  $0.01^\circ\text{C}/\text{s}$ . Melting points were determined using GraphPad Prism software and the Hill model with a variable coefficient.

#### 6.2.19. CETSA

CETSA was performed as described by Jafari et al.<sup>371</sup> Briefly, cells were cultured in 100 $\times$ 20 mm tissue culture dishes until they reached 80% confluence, and treated with 1% (v/v) DMSO or 15  $\mu\text{M}$  TXT4 for 6 h. After exposure to the compounds, cells were harvested by scraping,





collected by centrifugation at 20,000 g for 10 min at 4°C, and then resuspended in PBS. The cell suspension was aliquoted in PCR tubes and heated in a thermal cycler for 3 min at 57–80°C. Subsequently, cells were lysed by repeated freeze-thaw cycles using liquid nitrogen and a heating block set at 25°C. The soluble protein fraction was separated by centrifugation at 20,000 g for 20 min at 4°C and subjected to Western blot analysis.

#### 6.2.20. DNA extraction

Genomic DNA was isolated using a Genomic Mini kit (116-250; A&A Biotechnology, Gdansk, Poland) according to manufacturer instructions. DNA concentration was measured by absorbance at 260 nm using a NanoDrop ND-1000 spectrophotometer (Thermo Fisher Scientific). The ratio of absorbance at 260 and 280 nm (A<sub>260</sub>/A<sub>280</sub>) was used to assess the purity of DNA. A ratio of ~1.8 was considered pure.

#### 6.2.21. RNA extraction

Cells (1.5x10<sup>6</sup>) were seeded onto tissue culture plates to attach overnight. After 24 h cells were exposed to test, reference compounds, or 1% (v/v) DMSO for the indicated time. After treatment, cells were washed twice with PBS, lysed with TRIzol Reagent (Thermo Fisher Scientific), and stored until analyses at -80°C. Total RNA was isolated using the Total RNA ZolOut kit (043-100; A&A Biotechnology) according to manufacturer instructions. RNA concentration was measured by absorbance at 260 nm using a NanoDrop ND-1000 spectrophotometer (Thermo Fisher Scientific). The ratio of absorbance at 260 and 280 nm (A<sub>260</sub>/A<sub>280</sub>) was used to assess the purity of RNA. A ratio of ~2.0 was considered pure.

#### 6.2.22. Analysis expression of hTERT by RT-PCR

First-strand cDNA was synthesized using a PrimeScript RT reagent kit with a gDNA eraser (#RR047B, TaKaRa), obtaining a concentration of 50 µg/µl. Reaction parameters were as follows: genomic DNA elimination at 42°C for 2 min, cDNA synthesis at 37°C for 15 min, and 85°C for 5 s. qPCR reaction was prepared by TB Green Premix Ex Taq (#RR82WR; TaKaRa) and detected using Light Cycler 480 (Roche Life Science). The following thermal profile was applied: 1 cycle at 95°C for 30 sec, 45 cycles at 95°C for 5 s, 60°C for 60 s, and 96°C for 5 s. Melting curve analysis was performed ramping from 60°C to 95°C and rising by 0.5°C every 2 s. The primer sequences for RT-PCR analysis are listed in **Table 8**. Analysis of relative gene expression was calculated in terms of fold induction concerning the DMSO-treated cells using the comparative method<sup>308</sup>. All experiments were conducted in triplicate.

#### 6.2.23. Wound healing migration assay

Antimigratory properties of TXT2 and TXT4 were investigated by wound healing assay. A549, H226, and H460 cell lines were plated into an Ibidi-silicone insert on a glass-bottom 24-well plate for live-cell imaging and incubated overnight. The next day, inserts were dislodged, and the cells were washed twice with a fresh medium. To prevent cell proliferation, cells were preincubated



with 10 µg/ml mitomycin C for 1 h<sup>308</sup>. Then, cells were washed twice with a fresh medium, exposed to various concentrations of compounds, and placed into an imaging chamber (cellVivo incubation system; Olympus, Japan) maintained at 37°C with 5 % CO<sub>2</sub> for incubation. Concentrations of compounds were chosen according to experimental data, which showed that these concentrations have no cytotoxic effect on cells in this particular cell density. Monitoring the migration of the cells was performed using live-cell microscopy with time-lapse photography. Images were taken every 15 min for 48 h under ×10 magnification acquired using a phase-contrast fluorescence microscope (IX83 Inverted Microscope; Olympus) connected to an XC50 digital colour camera (Olympus). Using cellSens software (Olympus), the images were combined to generate a video. The gap area was measured using ImageJ software.

#### 6.2.24. HPLC-MS analysis

TXT4 concentration was quantified using an LC-DAD-MS system equipped with a degasser, a binary pump, an auto-sampler, a thermostatic column compartment combined with a diode array detector (1200 Series), and an MS detector with an electrospray source and quadrupole analyzer (1260 Infinity II and 6470 Triple Quad LC/MS, Agilent Technologies, Waldbronn, Germany). Analyses were performed on a Zorbax Eclipse XDB-C18 column with a standard dimension of 250 mm × 4.6 mm containing 5 µm particles (Agilent Technologies). The mobile phase comprised 0.05 M HCOONH<sub>4</sub> (**a**) and acetonitrile (**b**). All samples were analysed using a gradient presented in **Table 10**. The rate of flow of the mobile phase was 1.0 mL min<sup>-1</sup>. TXT4 was detected at 254 nm with the column temperature set at 25°C. The injection volume of samples was 10 µL.

The electrospray source was set up on a positive mode with followed interface conditions: gas temperature 300°C with a flow of 5 l/min, sheath gas temperature 250°C with a flow of 11 l/min, the capillary voltage of 3500 V, and nebulizer 45 psi. The MS spectra were collected in a scanning mode (MS2 SCAN) in the range of 150–1500 (m/z). Quantitative analysis was performed using MassHunter Qualitative Analysis B.07.00 (Agilent Technologies).

**Table 10** Mobile phase composition

t [min]	0	15	17	17.5	23
%B	50	100	100	50	50

#### 6.2.25. TXT4 accumulation studies

Cellular accumulation of TXT4 was determined by incubation of 1 × 10<sup>6</sup> cells in a 100 mm<sup>2</sup> Petri dish in a complete growth medium at 37°C. HL-60 and HL-60/VINC cell lines were incubated at their IC<sub>50</sub> values of TXT4. Cells were treated for 15, 30, 45, and 60 min, and collected by centrifugation (200 × g, 5 min, 4°C). Then, HL-60 and HL-60/VINC cells were washed in ice-cold PBS or PBS with 1 µM valsopodar (PSC 833) respectively. Valsopodar is a selective P-glycoprotein inhibitor and was used to prevent the efflux of TXT4 from cells<sup>307</sup>. Next, cells were resuspended in acetonitrile and filtered through a PTFE membrane, and the cell-associated drug

concentrations were determined by high-performance liquid chromatography coupled with mass spectrometry (HPLC-MS). The solvent used as a mobile phase in HPLC-MS analysis and extraction of the compound from cells was selected experimentally.

#### 6.2.26. *TXT4* efflux studies

Cells were incubated with *TXT4* for 1 h as described in the drug accumulation section. After treatment cells were washed in PBS, the medium containing compound was changed, and the cells were cultured for an additional 15, 30, 60, 90, and 120 min at 37°C. At the end of each period, cells were washed as previously described. The efflux of *TXT4* at each time point was determined in the section on *TXT4* accumulation.

#### 6.2.27. *Impact of long-term treatment of TXT4*

A549 cells were cultivated with *TXT4* (4 µM) or an equivalent volume of DMSO (1% v/v) for 164 days. Cells were counted and passages every week, followed by adding compounds after cell attachment (the day after). Periodically, the cell pellet was collected by trypsinization, snap frozen, and stored at -80°C until analysis. At the indicated time, cells were analysed in colony formation assay, flow cytometry, and live cell imaging (wound healing assay), as described above.

#### 6.2.28. *Quantification of relative telomere length by real-time PCR*

Cells were cultivated with 4 µM of compound *TXT4* for 72 h for 164 days. The compound was added twice per week, and cells were passaged once per week. Every week, cells were counted and collected by trypsinization. The cell pellet was washed twice with PBS and stored until analysis at -80°C. Then genomic DNA (gDNA) was isolated using the Genomic Midi AX kit (895-20; A&A Biotechnology) according to manufacturer instructions. DNA concentration was measured using a NanoDrop ND-1000 spectrophotometer (Thermo Fisher Scientific). The ratio of absorbance at 260 and 280 nm ( $A_{260}/A_{280}$ ) was used to assess the purity of DNA. A ratio of ~1.8 was considered pure. Next, qPCR was performed according to Vasilishina et al.<sup>372</sup> Briefly, each 10 µl qPCR consisted of 2× Maxima SYBR Green qPCR Master Mix (Thermo Fisher Scientific), 10 ng gDNA, and primer sets (1 µM TEL/1 µM IFNB1). The IFNB1 9 (gene coding interferon beta 1) gene is located on chromosome 9 and is represented by a single copy in the haploid genome. The primer sequences for RT-PCR analysis are listed in **Table 8**. qPCR reaction was prepared with Light Cycler 480 (Roche Life Science) using the following cycling conditions: 10 min at 95°C, 35 cycles at 95°C for 15 s, and 60°C for 1 min. Analysis of relative telomere length was calculated in terms of fold induction concerning the DMSO-treated cells using the comparative method.<sup>373</sup>

#### 6.2.29. *Universal tyrosine kinase assay*

The activity of PTK was measured in A549 cell extract using Universal Tyrosine Kinase Assay Kit (#MK410; TaKaRa, Shiga, Japan), according to the manufacturer's instructions. Briefly, A549 cells were collected with extraction buffer and centrifuged (10000 g, 10 min, 4°C). Then, each



sample was mixed with 40 mM ATP-2Na solution and incubated for 30 min at 37°C. Then the sample solution was removed, washed four times with washing solution, and blocked with blocking solution for 30 min at 37°C. Next, an anti-phosphotyrosine (PY20)-HRP solution was added to each well and incubated for 30 min at 37°C. Wells were washed four times and incubated with HRP substrate solution for 20 min at 37°C, followed by stopping the reaction with a stop solution. Then the absorbance at 450 nm was measured with an ASYS UVM340 microplate reader (Biochrom Ltd.). The activity of PTK was calculated using the PTK standard curve supplied by the kit.

#### 6.2.30. *Phospho-flow cytometry*

Cells were plated onto tissue culture plates and allowed to attach overnight. The complete medium was then changed to medium with 1% FBS for 12 h prior to stimulation. Next, cells were pretreated with compounds for 45 min, washed, and treated with compounds in 20% FBS for an additional 75 min. Cells were then scrapped in 1 mM EDTA in PBS, washed 2-3 times with PBS, and collected by centrifugation (1100 rpm, 5 min, 4°C). Cells were fixed with 4% PFA in PBS for 15 min at 4°C and centrifuged (1100 rpm, 5 min, 4°C). After fixation, cells were permeabilized by slowly adding 4.5 ml ice-cold 100% methanol to pre-chilled cells in 0.5 ml PBS, with gentle vortexing, to a final concentration of 90% methanol. Samples were incubated for 45 min on ice. Cells were then washed with incubation buffer (0.5 % BSA in PBS), centrifuged (1100 rpm, 5 min, 4°C), and blocked-in blocking buffer at RT for 30 min. Next, cells were incubated with anti-p-Tyr-100 (1:1500 dilution; #9411; Cell Signalling, Danvers, USA) or IgG Isotype control (1 ug/ml dilution; ab37355; Abcam, Cambridge, UK) antibodies at RT for 1 h, followed by incubation with anti-mouse IgG cross-adsorbed secondary antibody conjugated to DyLight 488 (1:200 dilution; #SA5-10166; Thermo Fisher Scientific) for 30 min at RT. Subsequently, cells were washed twice with PBS-T and stained with 7-AAD and RNase A (50 µg/ml) in the dark at RT for 15 min. The analysis was performed by flow cytometry (Guava EasyCyte 8 cell sorter, Merck Millipore) and FlowJo software v10. Each experiment was repeated independently three times.

#### 6.2.31. *RTK phosphorylation array*

A549 cells were serum-starved for 12 h, followed by treatment with 20 µM of compounds for 45 min, washing, and additional treatment in 20% FBS for 75 min. Then cells were harvested using lysis buffer and analysed using RayBio Human Phospho Array Kit (#AAH-PRTK-1-4; RayBiotech, Inc, Seoul, Korea) according to the manufacturer's instructions. Briefly, RTK array membranes were blocked with a blocking Cocktail buffer for 1 h, followed by incubation with 300 µg of protein from experimental samples for 5 h. After extensive washes, membranes were incubated with biotinylated antibodies overnight at 4°C. Then, membranes were washed and incubated with HRP-conjugated streptavidin for 2 h in RT. The unbound HRP antibody was washed out, and each membrane array was detected by chemiluminescence using ChemiDoc Imaging System (Bio-Rad). Signal intensities were measured using densitometric analysis with ImageLab and normalized using positive control spotted on the membrane.

#### 6.2.32. DNA unwinding assay

DNA unwinding assay was performed according to the manufacturer's instructions (#DUKSR002; Inspiralis, Norwich, UK). Briefly, the reaction was initiated by the addition of 1 U wheat germ topoisomerase I to a mixture containing buffer, test compounds, and relaxed plasmid pBR322. After 30 min of incubation at 37°C, the reaction was terminated by adding 50 µl of butanol and 20 µl of water. The aqueous layer was mixed with chloroform/isoamyl alcohol (24:1) and loading buffer (#B7024S; New England BioLabs, Ipswich, USA). Mixtures were loaded onto 1% (w/v) agarose gel and subjected to electrophoresis in 1xTBE at 30 V for 12 h. Gels were stained with ethidium bromide (1 µg/ml) for 15 min, followed by destained in 1 mM MgSO<sub>4</sub> for 15 min, and visualized by ChemiDoc Imaging System (Bio-Rad).

#### 6.2.33. Human topoisomerase I relaxation assay

The human topoisomerase I relaxation assay was performed according to the manufacturer's instructions (#HTRS1; Inspiralis). Briefly, the reaction was initiated by the addition of 1 U human topoisomerase I to a mixture containing buffer, test compounds, and supercoiled plasmid pBR322. After 30 min of incubation at 37°C, the reaction was stopped by adding 50 µl of butanol and 20 µl of water, and the procedure was continued as in **6.2.32**.

#### 6.2.34. Determination of the role of ROS in carbazole derivatives-related cell death

HCT116 and U2OS cells were plated onto tissue culture plates and allowed to attach overnight. Next, cells were treated in various combinations of compounds at IC<sub>90</sub> concentration, 70 µM CQ, and 2 mM NAC for 6, 24, and 48 h. After the indicated time, cells were maintained as described in chapters **6.2.6** and **6.2.13**.

#### 6.2.35. Statistical analyses

Statistical analyses were performed using GraphPad Prism 9 software. Data were obtained from at least three independent experiments and are presented as mean±SEM or mean±s.d. Statistical significance was calculated in comparison to the DMSO-treated control (1% v/v) using one-way or two-way ANOVA (post hoc Dunnet's test).



## 7. REFERENCES

1. Cancer. <https://www.who.int/news-room/fact-sheets/detail/cancer>, access: 02.07.22.
2. Global Cancer Observatory. <https://gco.iarc.fr/>, access: 05.07.22.
3. Wu, S., Zhu, W., Thompson, P., & Hannun, Y. A. Evaluating intrinsic and non-intrinsic cancer risk factors. *Nat. Commun.* **9**, 3490 (2018).
4. Debela, D. T., Muzazu, S. G., Heraro, K. D., Ndalama, M. T., Mesele, B. W., Haile, D. C., Kitui, S. K., & Manyazewal, T. New approaches and procedures for cancer treatment: Current perspectives. *SAGE Open Med.* **9**, 205031212110343 (2021).
5. Singh, R. K., Kumar, S., Prasad, D. N. & Bhardwaj, T. R. Therapeutic journey of nitrogen mustard as alkylating anticancer agents: Historic to future perspectives. *Eur. J. Med. Chem.* **151**, 401–433 (2018).
6. Pantziarka, P., Capistrano I, R., De Potter, A., Vandeborne, L. & Bouche, G. An open access database of licensed cancer drugs. *Front. Pharmacol.* **12**, 627574 (2021).
7. Mohs, R. C. & Greig, N. H. Drug discovery and development: Role of basic biological research. *Alzheimer's Dement. Transl. Res. Clin. Interv.* **3**, 651-657 (2017).
8. Kumar, B., Singh, S., Skvortsova, I. & Kumar, V. Promising targets in anti-cancer drug development: recent updates. *Curr. Med. Chem.* **24**, 4729-4752 (2017).
9. Sun, D., Gao, W., Hu, H. & Zhou, S. Why 90% of clinical drug development fails and how to improve it? *Acta Pharm. Sin. B* **12**, 3049–3062 (2022).
10. Thomas, S. E., Mendes, V., Kim, S. Y., Malhotra, S., Ochoa-Montaño, B., Blaszczyk, M., & Blundell, T. L. Structural biology and the design of new therapeutics: from hiv and cancer to mycobacterial infections: A paper dedicated to John Kendrew. *J. Mol. Biol.* **429**, 2677–2693 (2017).
11. Wang, C., Xu, P., Zhang, L., Huang, J., Zhu, K., & Luo, C. Current strategies and applications for precision drug design. *Front. Pharmacol.* **9**, 787 (2018).
12. Zoete, V., Grosdidier, A. & Michielin, O. Docking, virtual high throughput screening and in silico fragment-based drug design. *J. Cell. Mol. Med.* **13**, 238 (2009).
13. Kuntz, I. D., Blaney, J. M., Oatley, S. J., Langridge, R. & Ferrin, T. E. A geometric approach to macromolecule-ligand interactions. *J. Mol. Biol.* **161**, 269–288 (1982).
14. Ferreira, L. G., Dos Santos, R. N., Oliva, G. & Andricopulo, A. D. Molecular docking and structure-based drug design strategies. *Molecules* **20**, 13384 (2015).
15. Adelusi, T. I., Oyedele, A. Q. K., Boyenle, I. D., Ogunlana, A. T., Adeyemi, R. O., Ukachi, C. D., Idris, M. O., Olaoba, O. T., Adedotun, I. O., Kolawole, O. E., Xiaoxing, Y., & Abdul-Hammed, M. Molecular modeling in drug discovery. *Inform. Med. Unlocked* **29**, 100880

- (2022).
16. Hartenfeller, M. & Schneider, G. De novo drug design. *Methods Mol. Biol.* **672**, 299–323 (2011).
  17. Aminpour, M., Montemagno, C. & Tuszynski, J. A. an overview of molecular modeling for drug discovery with specific illustrative examples of applications. *Molecules* **24**, 1693 (2019).
  18. Shay, J. W., Zou, Y., Hiyama, E. & Wright, W. E. Telomerase and cancer. *Hum. Mol. Genet.* **10**, 677–685 (2001).
  19. Mizukoshi, E. & Kaneko, S. Telomerase-targeted cancer immunotherapy. *Int. J. Mol. Sci.* **20**, 1823 (2019).
  20. Jäger, K. & Walter, M. Therapeutic targeting of telomerase. *Genes* **7**, 39 (2016).
  21. Harley, C. B. Telomerase and cancer therapeutics. *Nat. Rev. Cancer* **8**, 167–179 (2008).
  22. Tian, X., Chen, B. & Liu, X. Telomere and telomerase as targets for cancer therapy. *Proc. Natl. Acad. Sci. U. S. A.* **85**, 6622–6 (1988).
  23. Moyzis, R. K., Buckingham, J. M., Cram, L. S., Dani, M., Deaven, L. L., Jones, M. D., Meyne, J., Ratliff, R. L., & Wu, J. R. A highly conserved repetitive DNA sequence, (TTAGGG)<sub>n</sub>, present at the telomeres of human chromosomes. *Proc. Natl. Acad. Sci. U. S. A.* **85**, 6622–6 (1988).
  24. Lim, C. J. & Cech, T. R. Shaping human telomeres: from shelterin and CST complexes to telomeric chromatin organization. *Nat. Rev. Mol. Cell Biol* **22**, 283–298 (2021).
  25. Schmutz, I. & De Lange, Shelterin *T. Curr. Biol.* **26**, R397–R399 (2016).
  26. Akincilar, S. C., Chan, C. H. T., Ng, Q. F., Fidan, K. & Tergaonkar, V. Non-canonical roles of canonical telomere binding proteins in cancers. *Cell. Mol. Life Sci.* **78**, 4235–4257 (2021).
  27. Porreca, R. M., Herrera-Moyano, E., Skourti, E., Law, P. P., Gonzalez Franco, R., Montoya, A., Faull, P., Kramer, H., & Vannier, J. B. TRF1 averts chromatin remodelling, recombination and replication dependent-break induced replication at mouse telomeres. *Elife* **9**, e49817 (2020).
  28. Arnoult, N. & Karlseder, J. Complex interactions between the DNA-damage response and mammalian telomeres. *Nat. Struct. Mol. Biol.* **22**, 859-866 (2015).
  29. De Lange, T. T-loops and the origin of telomeres. *Nat. Rev. Mol. Cell Biol.* **5**, 323–329 (2004).
  30. Luke-Glaser, S., Poschke, H. & Luke, B. Getting in (and out of) the loop: regulating higher order telomere structures. *Front. Oncol.* **2**, 180 (2012).



31. Gu, P., Jia, S., Takasugi, T., Tesmer, V. M., Nandakumar, J., Chen, Y., & Chang, S. Distinct functions of POT1 proteins contribute to the regulation of telomerase recruitment to telomeres. *Nat. Commun.* **12**, 5514 (2021).
32. Denchi, E. L. & de Lange, T. Protection of telomeres through independent control of ATM and ATR by TRF2 and POT1. *Nature* **448**, 1068–1071 (2007).
33. Pike, A. M., Strong, M. A., Ouyang, J. P. T. & Greider, C. W. TIN2 functions with TPP1/POT1 to stimulate telomerase processivity. *Mol. Cell. Biol.* **39**, e00593-18 (2019).
34. Kaur, P., Barnes, R., Pan, H., Detwiler, A. C., Liu, M., Mahn, C., Hall, J., Messenger, Z., You, C., Piehler, J., Smart, R. C., Riehn, R., Opresko, P. L., & Wang, H. TIN2 is an architectural protein that facilitates TRF2-mediated trans- and cis-interactions on telomeric DNA. *Nucleic Acids Res.* **49**, 13000–13018 (2021).
35. Lototska, L., Yue, J. X., Li, J., Giraud-Panis, M. J., Songyang, Z., Royle, N. J., Liti, G., Ye, J., Gilson, E., & Mendez-Bermudez, A. Human RAP1 specifically protects telomeres of senescent cells from DNA damage. *EMBO Rep.* **21**, e49076 (2020).
36. Samassekou, O., Gadjji, M., Drouin, R. & Yan, J. Sizing the ends: Normal length of human telomeres. *Ann. Anat. - Anat. Anzeiger* **192**, 284–291 (2010).
37. Wynford-Thomas, D. & Kipling, D. The end-replication problem. *Nature* **389**, 551–551 (1997).
38. Shay, J. W. & Wright, W. E. Hayflick, his limit and cellular ageing. *Nat. Rev. Mol. Cell Biol.* **1**, 72–76 (2000).
39. Aviv, A., Anderson, J. J. & Shay, J. W. Mutations, cancer and the telomere length paradox. *Trends Cancer* **3**, 253–258 (2017).
40. Hayashi, M. T., Cesare, A. J., Rivera, T. & Karlseder, J. Cell death during crisis is mediated by mitotic telomere deprotection. *Nature* **522**, 492–496 (2015).
41. Shay, J. W. & Wright, W. E. Senescence and immortalization: role of telomeres and telomerase. *Carcinogenesis* **26**, 867–874 (2005).
42. Castro-Vega, L. J., Jouravleva, K., Ortiz-Montero, P., Liu, W. Y., Galeano, J. L., Romero, M., Popova, T., Bacchetti, S., Vernet, J. P., & Londoño-Vallejo, A. The senescent microenvironment promotes the emergence of heterogeneous cancer stem-like cells. *Carcinogenesis* **36**, 1180–1192 (2015).
43. Shay, J. W. & Wright, W. E. Role of telomeres and telomerase in cancer. *Semin. Cancer Biol.* **21**, 349–353 (2011).
44. Dilley, R. L. & Greenberg, R. A. ALTERNative telomere maintenance and cancer. *Trends in Cancer* **1**, 145–156 (2015).



45. Bryan, T. M., Englezou, A., Dalla-Pozza, L., Dunham, M. A. & Reddel, R. R. Evidence for an alternative mechanism for maintaining telomere length in human tumors and tumor-derived cell lines. *Nat. Med.* **3**, 1271–1274 (1997).
46. Bryan, T. M. & Reddel, R. R. Telomere dynamics and telomerase activity in in vitro immortalised human cells. *Eur. J. Cancer Part A* **33**, 767–773 (1997).
47. Napier, C. E., Huschtscha, L. I., Harvey, A., Bower, K., Noble, J. R., Hendrickson, E. A., & Reddel, R. R. ATRX represses alternative lengthening of telomeres. *Oncotarget* **6**, 16543–58 (2015).
48. O’Sullivan, R. J. & Almouzni, G. Assembly of telomeric chromatin to create ALternative endings. *Trends Cell Biol.* **24**, 675–685 (2014).
49. Flynn, R. L., Cox, K. E., Jeitany, M., Wakimoto, H., Bryll, A. R., Ganem, N. J., Bersani, F., Pineda, J. R., Suvà, M. L., Benes, C. H., Haber, D. A., Boussin, F. D., & Zou, L. Alternative lengthening of telomeres renders cancer cells hypersensitive to ATR inhibitors. *Science (80- )* **347**, 273–277 (2015).
50. Jafri, M. A., Ansari, S. A., Alqahtani, M. H. & Shay, J. W. Roles of telomeres and telomerase in cancer, and advances in telomerase-targeted therapies. *Genome Med.* **8**, 69 (2016).
51. Schmidt, J. C., Dalby, A. B. & Cech, T. R. Identification of human TERT elements necessary for telomerase recruitment to telomeres. *Elife* **3**, 1–20 (2014).
52. Macneil, D. E., Bensoussan, H. J. & Autexier, C. Telomerase regulation from beginning to the end. *Genes (Basel)* **7**(9), 64 (2016).
53. Garus, A. & Autexier, C. Dyskerin: an essential pseudouridine synthase with multifaceted roles in ribosome biogenesis, splicing, and telomere maintenance. *RNA* **27**, 1441-1458 (2021).
54. Schmidt, J. C. & Cech, T. R. Human telomerase: biogenesis, trafficking, recruitment, and activation. *Genes Dev.* **29**, 1095 (2015).
55. Sobinoff, A. P. & Pickett, H. A. Alternative lengthening of telomeres: DNA repair pathways converge. *Trends Genet.* **33**, 921–932 (2017).
56. Forsythe, H. L., Jarvis, J. L., Turner, J. W., Elmore, L. W. & Holt, S. E. Stable association of hsp90 and p23, but not hsp70, with active human telomerase. *J. Biol. Chem.* **276**, 15571–15574 (2001).



57. Venteicher, A. S., Meng, Z., Mason, P. J., Veenstra, T. D. & Artandi, S. E. Identification of ATPases pontin and reptin as telomerase components essential for holoenzyme assembly. *Cell* **132**, 945-957 (2008).
58. Hockemeyer, D. & Collins, K. Control of telomerase action at human telomeres. *Nat. Struct. Mol. Biol.* **22**, 848–852 (2015).
59. Lee, J. H., Jeong, S. A., Khadka, P., Hong, J. & Chung, I. K. Involvement of SRSF11 in cell cycle-specific recruitment of telomerase to telomeres at nuclear speckles. *Nucleic Acids Res.* **43**, 8435–8451 (2015).
60. A549 ATCC® CCL-185™. [https://www.lgcstandards-atcc.org/Products/All/CCL-185?geo\\_country=cz#characteristics](https://www.lgcstandards-atcc.org/Products/All/CCL-185?geo_country=cz#characteristics), access: 16.09.21.
61. Eitan, E., Braverman, C., Tichon, A., Gitler, D., Hutchison, E. R., Mattson, M. P., & Priel, E. Excitotoxic and radiation stress increase TERT levels in the mitochondria and cytosol of cerebellar purkinje neurons. *Cerebellum* **15**, 509–517 (2016).
62. Horikawa, I., Cable, P. L., Mazur, S. J., Appella, E., Afshari, C. A., & Barrett, J. C. Downstream E-box-mediated regulation of the human telomerase reverse transcriptase (hTERT) gene transcription: evidence for an endogenous mechanism of transcriptional repression. *Mol. Biol. Cell* **13**, 2585–2597 (2002).
63. Yuan, X., Larsson, C. & Xu, D. Mechanisms underlying the activation of TERT transcription and telomerase activity in human cancer: old actors and new players. *Oncogene* **38**, 6172–6183 (2019).
64. Lee, D. D., Leão, R., Komosa, M., Gallo, M., Zhang, C. H., Lipman, T., Remke, M., Heidari, A., Nunes, N. M., Apolónio, J. D., Price, A. J., De Mello, R. A., Dias, J. S., Huntsman, D., Hermanns, T., Wild, P. J., Vanner, R., Zadeh, G., Karamchandani, J., Das, S., ... Tabori, U. DNA hypermethylation within TERT promoter upregulates TERT expression in cancer. *J. Clin. Invest.* **129**, 223 (2018).
65. Yuan, X., Larsson, C. & Xu, D. Mechanisms underlying the activation of TERT transcription and telomerase activity in human cancer: old actors and new players. *Oncogene* **38**, 6172 (2019).
66. Ramlee, M. K., Wang, J., Toh, W. X. & Li, S. Transcription regulation of the human telomerase reverse transcriptase (hTERT) gene. *Genes (Basel)*. **7**, 6172 (2016).
67. Jafri, M. A., Ansari, S. A., Alqahtani, M. H. & Shay, J. W. Roles of telomeres and telomerase in cancer, and advances in telomerase-targeted therapies. *Genome Med.* **8**, 69 (2016).
68. You, H., Wu, Y., Chang, K., Shi, X., Chen, X. D., Yan, W., & Li, R. Paradoxical prognostic impact of TERT promoter mutations in gliomas depends on different histological and genetic backgrounds. *CNS Neurosci. Ther.* **23**, 790-797 (2017).

69. Bell, R. J., Rube, H. T., Kreig, A., Mancini, A., Fouse, S. D., Nagarajan, R. P., Choi, S., Hong, C., He, D., Pekmezci, M., Wiencke, J. K., Wensch, M. R., Chang, S. M., Walsh, K. M., Myong, S., Song, J. S., & Costello, J. F. Cancer. The transcription factor GABP selectively binds and activates the mutant TERT promoter in cancer. *Science* **348**, 1036–1039 (2015).
70. Hsu, C. P., Lee, L. W., Tang, S. C., Hsin, I. L., Lin, Y. W., & Ko, J. L. Epidermal growth factor activates telomerase activity by direct binding of Ets-2 to hTERT promoter in lung cancer cells. *Tumour Biol.* **36**, 5389–5398 (2015).
71. Chan, A. K., Yao, Y., Zhang, Z., Chung, N. Y., Liu, J. S., Li, K. K., Shi, Z., Chan, D. T., Poon, W. S., Zhou, L., & Ng, H. K. TERT promoter mutations contribute to subset prognostication of lower-grade gliomas. *Mod. Pathol.* **28**, 177–186 (2015).
72. Huang, F. W., Bielski, C. M., Rinne, M. L., Hahn, W. C., Sellers, W. R., Stegmeier, F., Garraway, L. A., & Kryukov, G. V. TERT promoter mutations and monoallelic activation of TERT in cancer. *Oncogenesis* **4**, e176 (2015).
73. Killela, P. J., Reitman, Z. J., Jiao, Y., Bettegowda, C., Agrawal, N., Diaz, L. A., Jr, Friedman, A. H., Friedman, H., Gallia, G. L., Giovanella, B. C., Grollman, A. P., He, T. C., He, Y., Hruban, R. H., Jallo, G. I., Mandahl, N., Meeker, A. K., Mertens, F., Netto, G. J., Rasheed, B. A., ... Yan, H. TERT promoter mutations occur frequently in gliomas and a subset of tumors derived from cells with low rates of self-renewal. *Proc. Natl. Acad. Sci.* **110**, 6021–6026 (2013).
74. Huang, D. S., Wang, Z., He, X. J., Diplas, B. H., Yang, R., Killela, P. J., Meng, Q., Ye, Z. Y., Wang, W., Jiang, X. T., Xu, L., He, X. L., Zhao, Z. S., Xu, W. J., Wang, H. J., Ma, Y. Y., Xia, Y. J., Li, L., Zhang, R. X., Jin, T., ... Tao, H. Q. Recurrent TERT promoter mutations identified in a large-scale study of multiple tumour types are associated with increased TERT expression and telomerase activation. *Eur. J. Cancer* **51**, 969–976 (2015).
75. Vinagre, J., Almeida, A., Pópulo, H., Batista, R., Lyra, J., Pinto, V., Coelho, R., Celestino, R., Prazeres, H., Lima, L., Melo, M., da Rocha, A. G., Preto, A., Castro, P., Castro, L., Pardal, F., Lopes, J. M., Santos, L. L., Reis, R. M., Cameselle-Teijeiro, J., ... Soares, P. Frequency of TERT promoter mutations in human cancers. *Nat. Commun.* **4**, 2185 (2013).
76. Stoehr, R., Taubert, H., Zinnall, U., Giedl, J., Gaisa, N. T., Burger, M., Ruemmele, P., Hurst, C. D., Knowles, M. A., Wullich, B., & Hartmann, A. Frequency of TERT promoter mutations in prostate cancer. *Pathobiology* **82**, 53–57 (2015).
77. Jafri, M. A., Ansari, S. A., Alqahtani, M. H. & Shay, J. W. Roles of telomeres and telomerase in cancer, and advances in telomerase-targeted therapies. *Genome Medicine* **8**, 69 (2016).
78. Cong, Y.-S., Wright, W. E. & Shay, J. W. Human telomerase and its regulation. *Microbiol. Mol. Biol. Rev.* **66**, 407–425 (2002).



79. Lai, S. R., Phipps, S. M. O., Liu, L., Andrews, L. G. & Tollefsbol, T. O. Epigenetic control of telomerase and modes of telomere maintenance in aging and abnormal systems. *Front. Biosci.* **10**, 1779–1796 (2005).
80. Renaud, S., Loukinov, D., Abdullaev, Z., Guilleret, I., Bosman, F. T., Lobanenkov, V., & Benhattar, J. *Nucleic Acids Res.* **35**, 1245–1256 (2007).
81. Wong, M. S., Wright, W. E. & Shay, J. W. Alternative splicing regulation of telomerase: a new paradigm? *Trends Genet.* **30**, 430–438 (2014).
82. Rosen, J., Jakobs, P., Ale-Agha, N., Altschmied, J. & Haendeler, J. Non-canonical functions of telomerase reverse transcriptase – impact on redox homeostasis. *Redox Biol.* **34**, 101543 (2020).
83. Thompson, C. A. H. & Wong, J. M. Y. Non-canonical functions of telomerase reverse transcriptase: emerging roles and biological relevance. *Curr. Top. Med. Chem.* **20**, 498–507 (2020).
84. Zheng, Q., Huang, J. & Wang, G. Mitochondria, telomeres and telomerase subunits. *Front. Cell Dev. Biol.* **7**, 274 (2019).
85. Romaniuk, A., Paszal-Jaworska, A., Totoń, E., Lisiak, N., Hołysz, H., Królak, A., Grodecka-Gazdecka, S., & Rubiś, B. The non-canonical functions of telomerase: to turn off or not to turn off. *Mol. Biol. Rep.* **46**, 1401–1411 (2019).
86. Ling, X., Wen, L. & Zhou, Y. Role of mitochondrial translocation of telomerase in hepatocellular carcinoma cells with multidrug resistance. *Int. J. Med. Sci.* **9**, 545 (2012).
87. Barnes, R. P., Fouquerel, E. & Opresko, P. L. The impact of oxidative DNA damage and stress on telomere homeostasis. *Mech. Ageing Dev.* **177**, 37-45 (2019).
88. Pestana, A., Vinagre, J., Sobrinho-Simões, M. & Soares, P. TERT biology and function in cancer: beyond immortalisation. *J. Mol. Endocrinol.* **58**, R129–R146 (2017).
89. Saldanha, S. N., Andrews, L. G. & Tollefsbol, T. O. Analysis of telomerase activity and detection of its catalytic subunit, hTERT. *Anal. Biochem.* **315**, 1–21 (2003).
90. Miao, G. Y., Zhou, X., Zhang, X., Xie, Y., Sun, C., Liu, Y., Gan, L., & Zhang, H. Telomere-mitochondrion links contribute to induction of senescence in MCF-7 cells after carbon-ion irradiation. *Asian Pac. J. Cancer Prev.* **17**, 1993–1998 (2016).
91. Muzza, M., Colombo, C., Cirello, V., Perrino, M., Vicentini, L., & Fugazzola, L. Oxidative stress and the subcellular localization of the telomerase reverse transcriptase (TERT) in papillary thyroid cancer. *Mol. Cell. Endocrinol.* **431**, 54–61 (2016).
92. Singhapol, C., Pal, D., Czapiewski, R., Porika, M., Nelson, G., & Saretzki, G. C. Mitochondrial telomerase protects cancer cells from nuclear DNA damage and apoptosis. *PLoS One* **8**, e52989 (2013).

93. Kovalenko, O. A., Caron, M. J., Ulema, P., Medrano, C., Thomas, A. P., Kimura, M., Bonini, M. G., Herbig, U., & Santos, J. H. A mutant telomerase defective in nuclear-cytoplasmic shuttling fails to immortalize cells and is associated with mitochondrial dysfunction. *Aging Cell* **9**, 203–219 (2010).
94. Lipinska, N., Romaniuk, A., Paszel-Jaworska, A., Toton, E., Kopczynski, P., & Rubis, B. Telomerase and drug resistance in cancer. *Cell. Mol. Life Sci.* **74**, 4121–4132 (2017).
95. Ling, X., Wen, L. & Zhou, Y. Role of mitochondrial translocation of telomerase in hepatocellular carcinoma cells with multidrug resistance. *Int. J. Med. Sci.* **9**, 545–554 (2012).
96. Park, H. H., Lee, K. Y., Kim, S., Lee, J. W., Choi, N. Y., Lee, E. H., Lee, Y. J., Lee, S. H., & Koh, S. H. Novel vaccine peptide GV1001 effectively blocks  $\beta$ -amyloid toxicity by mimicking the extra-telomeric functions of human telomerase reverse transcriptase. *Neurobiol. Aging* **35**, 1255–1274 (2014).
97. Li, P., Tong, Y., Yang, H., Zhou, S., Xiong, F., Huo, T., & Mao, M. Mitochondrial translocation of human telomerase reverse transcriptase in cord blood mononuclear cells of newborns with gestational diabetes mellitus mothers. *Diabetes Res. Clin. Pract.* **103**, 310–318 (2014).
98. Clevers, H. Wnt/ $\beta$ -Catenin Signalling in development and disease. *Cell* **127**, 469–480 (2006).
99. Park, J. I., Venteicher, A. S., Hong, J. Y., Choi, J., Jun, S., Shkreli, M., Chang, W., Meng, Z., Cheung, P., Ji, H., McLaughlin, M., Veenstra, T. D., Nusse, R., McCrea, P. D., & Artandi, S. E. Telomerase modulates Wnt signalling by association with target gene chromatin. *Nature* **460**, 66-72 (2009).
100. Okamoto, N., Yasukawa, M., Nguyen, C., Kasim, V., Maida, Y., Possemato, R., Shibata, T., Ligon, K. L., Fukami, K., Hahn, W. C., & Masutomi, K. Maintenance of tumour initiating cells of defined genetic composition by nucleostemin. *Proc. Natl. Acad. Sci. U. S. A.* **108**, 20388–20393 (2011).
101. Listerman, I., Gazzaniga, F. S. & Blackburn, E. H. An investigation of the effects of the core protein telomerase reverse transcriptase on wnt signalling in breast cancer cells. *Mol. Cell. Biol.* **34**, 280-289 (2014).
102. Hoffmeyer, K., Raggioli, A., Rudloff, S., Anton, R., Hierholzer, A., Del Valle, I., Hein, K., Vogt, R., & Kemler, R. Wnt/ $\beta$ -catenin signalling regulates telomerase in stem cells and cancer cells. *Science* **336**, 1549–1554 (2012).
103. Ghosh, A., Saginc, G., Leow, S. C., Khattar, E., Shin, E. M., Yan, T. D., Wong, M., Zhang,



- Z., Li, G., Sung, W. K., Zhou, J., Chng, W. J., Li, S., Liu, E., & Tergaonkar, V. Telomerase directly regulates NF- $\kappa$ B-dependent transcription. *Nat. Cell Biol.* **14**, 1270–1281 (2012).
104. Oeckinghaus, A. & Ghosh, S. The NF- $\kappa$ B family of transcription factors and its regulation. *Cold Spring Harb. Perspect. Biol.* **1**, a000034 (2009).
105. Akiyama, M., Hideshima, T., Hayashi, T., Tai, Y. T., Mitsiades, C. S., Mitsiades, N., Chauhan, D., Richardson, P., Munshi, N. C., & Anderson, K. C. Nuclear factor- $\kappa$ B p65 mediates tumour necrosis factor  $\alpha$ -induced nuclear translocation of telomerase reverse transcriptase protein. *Cancer Res.* **63**, 18-21 (2003).
106. Prasad, R. R., Mishra, D. K., Kumar, M. & Yadava, P. K. Human telomerase reverse transcriptase promotes the epithelial to mesenchymal transition in lung cancer cells by enhancing c-MET upregulation. *Heliyon* **8**, e08673 (2022).
107. Chung, S. S., Wu, Y., Okobi, Q., Adekoya, D., Atefi, M., Clarke, O., Dutta, P., & Vadgama, J. V. Proinflammatory cytokines IL-6 and TNF- $\alpha$  increased telomerase activity through NF- $\kappa$ B/STAT1/STAT3 activation, and withaferin A inhibited the signalling in colorectal cancer cells. *Mediators Inflamm.* **2017**, 5958429 (2017).
108. Niu, G. & Chen, X. Vascular endothelial growth factor as an anti-angiogenic target for cancer therapy. *Curr. Drug Targets* **11**, 1000-1017 (2010).
109. Liu, N., Ding, D., Hao, W., Yang, F., Wu, X., Wang, M., Xu, X., Ju, Z., Liu, J. P., Song, Z., Shay, J. W., Guo, Y., & Cong, Y. S. hTERT promotes tumour angiogenesis by activating VEGF via interactions with the Sp1 transcription factor. *Nucleic Acids Res.* **44**, 8693-8703 (2016).
110. Falchetti, M. L., Mongiardi, M. P., Fiorenzo, P., Petrucci, G., Pierconti, F., D'Agnano, I., D'Alessandris, G., Alessandri, G., Gelati, M., Ricci-Vitiani, L., Maira, G., Larocca, L. M., Levi, A., & Pallini, R. Inhibition of telomerase in the endothelial cells disrupts tumour angiogenesis in glioblastoma xenografts. *Int. J. cancer* **122**, 1236–1242 (2008).
111. Zhou, L., Zheng, D., Wang, M., Cong, Y.-S. Telomerase reverse transcriptase activates the expression of vascular endothelial growth factor independent of telomerase activity. *Biochem. Biophys. Res. Commun.* **386**, 739–743 (2009).
112. Webber, J., Steadman, R., Mason, M. D., Tabi, Z. & Clayton, A. Cancer exosomes trigger fibroblast to myofibroblast differentiation. *Cancer Res.* **70**, 9621–9630 (2010).
113. Skog, J., Würdinger, T., van Rijn, S., Meijer, D. H., Gainche, L., Sena-Esteves, M., Curry, W. T., Jr, Carter, B. S., Krichevsky, A. M., & Breakefield, X. O. Glioblastoma microvesicles transport RNA and proteins that promote tumour growth and provide diagnostic biomarkers. *Nat. Cell Biol.* **10**, 1470–1476 (2008).

114. Li, C., Teixeira, A. F., Zhu, H. J. & ten Dijke, P. Cancer associated-fibroblast-derived exosomes in cancer progression. *Mol. Cancer* **20**, 154 (2021).
115. Gutkin, A., Uziel, O., Beery, E., Nordenberg, J., Pinchasi, M., Goldvaser, H., Henick, S., Goldberg, M., & Lahav, M. Tumour cells derived exosomes contain hTERT mRNA and transform nonmalignant fibroblasts into telomerase positive cells. *Oncotarget* **7**, 59173–59188 (2016).
116. Zhou, Q. G., Hu, Y., Wu, D. L., Zhu, L. J., Chen, C., Jin, X., Luo, C. X., Wu, H. Y., Zhang, J., & Zhu, D. Y. Hippocampal telomerase is involved in the modulation of depressive behaviors. *J. Neurosci.* **31**, 12258-1269 (2011).
117. Porton, B., Delisi, L. E., Bertisch, H. C., Ji, F., Gordon, D., Li, P., Benedict, M. M., Greenberg, W. M., & Kao, H. T. Telomerase levels in schizophrenia: a preliminary study. *Schizophr. Res.* **106**, 242-247 (2008).
118. Wei, Y. B., Martinsson, L., Liu, J. J., Forsell, Y., Schalling, M., Backlund, L., & Lavebratt, C. hTERT genetic variation in depression. *J. Affect. Disord.* **189**, 62–69 (2016).
119. Li, J., Qu, Y., Chen, D., Zhang, L., Zhao, F., Luo, L., Pan, L., Hua, J., & Mu, D. The neuroprotective role and mechanisms of TERT in neurons with oxygen-glucose deprivation. *Neuroscience* **252**, 346–358 (2013).
120. Kang, H. J., Choi, Y. S., Hong, S. B., Kim, K. W., Woo, R. S., Won, S. J., Kim, E. J., Jeon, H. K., Jo, S. Y., Kim, T. K., Bachoo, R., Reynolds, I. J., Gwag, B. J., & Lee, H. W. Ectopic expression of the catalytic subunit of telomerase protects against brain injury resulting from ischemia and NMDA-induced neurotoxicity. *J. Neurosci.* **24**, 1280-1287 (2004).
121. Spilisbury, A., Miwa, S., Attems, J. & Saretzki, G. The role of telomerase protein TERT in Alzheimer's disease and in tau-related pathology in vitro. *J. Neurosci.* **35**, 1659-1674 (2015).
122. Eitan, E., Tichon, A., Gazit, A., Gitler, D., Slavin, S., & Priel, E. Novel telomerase-increasing compound in mouse brain delays the onset of amyotrophic lateral sclerosis. *EMBO Mol. Med.* **4**, 313-329 (2012).
123. Eitan, E., Braverman, C., Tichon, A., Gitler, D., Hutchison, E. R., Mattson, M. P., & Priel, E. Excitotoxic and radiation stress increase TERT levels in the mitochondria and cytosol of cerebellar purkinje neurons. *Cerebellum* **15**, 509–517 (2016).
124. Shay, J. W. & Keith, W. N. Targeting telomerase for cancer therapeutics. *Br. J. Cancer* **98**, 677–683 (2008).

125. Roberts, T. C., Langer, R. & Wood, M. J. A. Advances in oligonucleotide drug delivery. *Nat. Rev. Drug Discov.* **19**, 673–694 (2020).
126. Dhuri, K., Bechtold, C., Quijano, E., Pham, H., Gupta, A., Vikram, A., & Bahal, R. Antisense oligonucleotides: an emerging area in drug discovery and development. *J. Clin. Med.* **9**, 2004 (2020).
127. Galderisi, U., Cascino, A. & Giordano, A. Antisense oligonucleotides as therapeutic agents. *J. Cell. Physiol.* **181**, 251–257 (1999).
128. Kondo, Y. & Kondo, S. Telomerase RNA inhibition using antisense oligonucleotide against human telomerase RNA linked to a 2',5'-Oligoadenylate. *Methods Mol Biol.* **405**, 97–112 (2007).
129. Kondo, S., Kondo, Y., Li, G., Silverman, R. H. & Cowell, J. K. Targeted therapy of human malignant glioma in a mouse model by 2-5A antisense directed against telomerase RNA. *Oncogene* **16**, 3323–3330 (1998).
130. Ye, J., Wu, Y. L., Zhang, S., Chen, Z., Guo, L. X., Zhou, R. Y., & Xie, H. Inhibitory effect of human telomerase antisense oligodeoxyribonucleotides on the growth of gastric cancer cell lines in variant tumour pathological subtype. *World J. Gastroenterol.* **11**, 2230–2237 (2005).
131. Shammass, M. A., Liu, X., Gavory, G., Raney, K. D., Balasubramanian, S., & Shmookler Reis, R. J. Targeting the single-strand G-rich overhang of telomeres with PNA inhibits cell growth and induces apoptosis of human immortal cells. *Exp. Cell Res.* **295**, 204–214 (2004).
132. Elayadi, A. N., Braasch, D. A. & Corey, D. R. Implications of high-affinity hybridization by locked nucleic acid oligomers for inhibition of human telomerase. *Biochemistry* **41**, 9973–81 (2002).
133. Guittat, L., Alberti, P., Gomez, D., De Cian, A., Pennarun, G., Lemarteleur, T., Belmokhtar, C., Paterski, R., Morjani, H., Trentesaux, C., Mandine, E., Boussin, F., Mailliet, P., Lacroix, L., Riou, J. F., & Mergny, J. L. Targeting human telomerase for cancer therapeutics. *Cytotechnology* **45**, 75–90 (2004).
134. Pruzan, R., Pongracz, K., Gietzen, K., Wallweber, G. & Gryaznov, S. Allosteric inhibitors of telomerase: oligonucleotide n3'-->p5' phosphoramidates. *Nucleic Acids Res.* **30**, 559–68 (2002).
135. Gryaznov, S., Pongracz, K., Matray, T., Schultz, R., Pruzan, R., Aimi, J., Chin, A., Harley, C., Shea-Herbert, B., Shay, J., Oshima, Y., Asai, A., & Yamashita, Y. Telomerase inhibitors – oligonucleotide phosphoramidates as potential therapeutic agents. *Nucleos., Nucleot. Nucl.* **20**, 401–410 (2001).





136. Bryan, C., Rice, C., Hoffman, H., Harkisheimer, M., Sweeney, M., & Skordalakes, E. Structural basis of telomerase inhibition by the highly specific BIBR1532. *Structure* **23**, 1934 (2015).
137. Röth, A., Harley, C. B. & Baerlocher, G. M. Imetelstat (GRN163L) - Telomerase-based cancer therapy. *Recent Results Cancer Res.* **184**, 221–234 (2010).
138. Ruden, M. & Puri, N. Novel anticancer therapeutics targeting telomerase. *Cancer Treat. Rev.* **39**, 444–456 (2013).
139. A study comparing imetelstat versus best available therapy for the treatment of intermediate-2 or high-risk myelofibrosis (MF) who have not responded to janus kinase (JAK)-inhibitor treatment - <https://clinicaltrials.gov/ct2/show/NCT04576156>, access: 12.06.2022.
140. Zhang, J., Zheng, K., Xiao, S., Hao, Y. & Tan, Z. Mechanism and manipulation of DNA:RNA hybrid G-quadruplex formation in transcription of G-rich DNA. *J. Am. Chem. Soc.* **136**, 1381–1390 (2014).
141. Lipps, H. J. & Rhodes, D. G-quadruplex structures: in vivo evidence and function. *Trends Cell Biol.* **19**, 414–422 (2009).
142. Xue, Y., Kan, Z. Y., Wang, Q., Yao, Y., Liu, J., Hao, Y. H., & Tan, Z. Human telomeric DNA forms parallel-stranded intramolecular G-quadruplex in K<sup>+</sup> solution under molecular crowding condition. *J. Am. Chem. Soc.* **129**, 11185–11191 (2007).
143. Neidle, S. Quadruplex Nucleic Acids as Novel Therapeutic Targets. *J. Med. Chem.* **59**, 5987–6011 (2016).
144. Hänsel-Hertsch, R., Di Antonio, M. & Balasubramanian, S. DNA G-quadruplexes in the human genome: detection, functions and therapeutic potential. *Nat. Rev. Mol. Cell Biol.* **18**, 279–284 (2017).
145. Han, F., X., Wheelhouse R. T. & Hurley, L. H. Interactions of TMPyP4 and TMPyP2 with quadruplex DNA. structural basis for the differential effects on telomerase inhibition. *J. Am. Chem. Soc.* **121**, 3561–3570 (1999).
146. Taetz, S., Baldes, C., Mürdter, T. E., Kleideiter, E., Piotrowska, K., Bock, U., Haltner-Ukomadu, E., Mueller, J., Huwer, H., Schaefer, U. F., Klotz, U., & Lehr, C. M. Biopharmaceutical characterization of the telomerase inhibitor BRACO19. *Pharm. Res.* **23**, 1031–1037 (2006).
147. Gowan, S. M., Heald, R., Stevens, M. F. & Kelland, L. R. Potent inhibition of telomerase by small-molecule pentacyclic acridines capable of interacting with G-quadruplexes. *Mol. Pharmacol.* **60**, 981–8 (2001).



148. Kim, M. Y., Vankayalapati, H., Shin-Ya, K., Wierzba, K. & Hurley, L. H. Telomestatin, a potent telomerase inhibitor that interacts quite specifically with the human telomeric intramolecular G-quadruplex. *J. Am. Chem. Soc.* **124**, 2098–2099 (2002).
149. Ji, X., Sun, H., Zhou, H., Xiang, J., Tang, Y., & Zhao, C. The interaction of telomeric DNA and C-myc22 G-quadruplex with 11 natural alkaloids. *Nucleic Acid Ther.* **22**, 127–136 (2012).
150. Li, Q., Xiang, J. F., Yang, Q. F., Sun, H. X., Guan, A. J., & Tang, Y. L. G4LDB: a database for discovering and studying G-quadruplex ligands. *Nucleic Acids Res.* **41**, D1115-23 (2013).
151. Kosiol, N., Juranek, S., Brossart, P., Heine, A. & Paeschke, K. G-quadruplexes: a promising target for cancer therapy. *Mol. Cancer* **20**, 1–18 (2021).
152. A phase I study of CX5461 - <https://clinicaltrials.gov/ct2/show/NCT02719977>. access: 12.05.22
153. Zimmer, J., Tacconi, E., Folio, C., Badie, S., Porru, M., Klare, K., Tumiaty, M., Markkanen, E., Halder, S., Ryan, A., Jackson, S. P., Ramadan, K., Kuznetsov, S. G., Biroccio, A., Sale, J. E., & Tarsounas, M. Targeting BRCA1 and BRCA2 deficiencies with G-quadruplex-interacting compounds. *Mol. Cell* **61**, 449–460 (2016).
154. Xu, H., Di Antonio, M., McKinney, S., Mathew, V., Ho, B., O'Neil, N. J., Santos, N. D., Silvester, J., Wei, V., Garcia, J., Kabeer, F., Lai, D., Soriano, P., Banáth, J., Chiu, D. S., Yap, D., Le, D. D., Ye, F. B., Zhang, A., Thu, K., ... Aparicio, S. CX-5461 is a DNA G-quadruplex stabilizer with selective lethality in BRCA1/2 deficient tumour s. *Nat. Commun.* **8**, 14432 (2017).
155. Khot, A., Brajanovski, N., Cameron, D. P., Hein, N., MacLachlan, K. H., Sanij, E., Lim, J., Soong, J., Link, E., Blombery, P., Thompson, E. R., Fellowes, A., Sheppard, K. E., McArthur, G. A., Pearson, R. B., Hannan, R. D., Poortinga, G., & Harrison, S. J. First-in-human RNA polymerase I transcription inhibitor CX-5461 in patients with advanced hematologic cancers: Results of a phase I dose-escalation study. *Cancer Discov.* **9**, 1036–1049 (2019).
156. Ruggiero, E. & Richter, S. N. G-quadruplexes and G-quadruplex ligands: targets and tools in antiviral therapy. *Nucleic Acids Res.* **46**, 3270–3283 (2018).
157. Zhang, W., Chen, M., Ling Wu, Y., Tanaka, Y., Juan Ji, Y., Lin Zhang, S., He Wei, C., & Xu, Y. Formation and stabilization of the telomeric antiparallel G-quadruplex and inhibition of telomerase by novel benzothioxanthene derivatives with anti-tumour activity. *Sci. Rep.* **5**, 13693 (2015).
158. Damm, K., Hemmann, U., Garin-Chesa, P., Huel, N., Kauffmann, I., Priepke, H., Niestroj, C., Daiber, C., Enenkel, B., Guilliard, B., Lauritsch, I., Müller, E., Pascolo, E., Sauter, G.,

- Pantic, M., Martens, U. M., Wenz, C., Lingner, J., Kraut, N., Rettig, W. J., ... Schnapp, A. A highly selective telomerase inhibitor limiting human cancer cell proliferation. *EMBO J.* **20**, 6958–6968 (2001).
159. Pascolo, E., Wenz, C., Lingner, J., Huel, N., Priepeke, H., Kauffmann, I., Garin-Chesa, P., Rettig, W. J., Damm, K., & Schnapp, A. Mechanism of human telomerase inhibition by BIBR1532, a synthetic, non-nucleosidic drug candidate. *J. Biol. Chem.* **277**, 15566–15572 (2002).
160. Cesmeli, S., Goker Bagca, B., Caglar, H. O., Ozates, N. P., Gunduz, C., & Biray Avci, C. Combination of resveratrol and BIBR1532 inhibits proliferation of colon cancer cells by repressing expression of LncRNAs. *Med. Oncol.* **39**, 12 (2021).
161. Doğan, F., Özateş, N. P., Bağca, B. G., Abbaszadeh, Z., Söğütlü, F., Gasımlı, R., Gündüz, C., & Biray Avcı, Ç. Investigation of the effect of telomerase inhibitor BIBR1532 on breast cancer and breast cancer stem cells. *J. Cell. Biochem.* **120**, 1282–1293 (2018).
162. Altamura, G., Degli Uberti, B., Galiero, G., De Luca, G., Power, K., Licenziato, L., Maiolino, P., & Borzacchiello, G. The small molecule BIBR1532 exerts potential anti-cancer activities in preclinical models of feline oral squamous cell carcinoma through inhibition of telomerase activity and down-regulation of TERT. *Front. Vet. Sci.* **7**, 620776 (2021).
163. Shi, Y., Sun, L., Chen, G., Zheng, D., Li, L., & Wei, W. A combination of the telomerase inhibitor, BIBR1532, and paclitaxel synergistically inhibit cell proliferation in breast cancer cell lines. *Target. Oncol.* **10**, 565–573 (2015).
164. Ding, X., Cheng, J., Pang, Q., Wei, X., Zhang, X., Wang, P., Yuan, Z., & Qian, D. BIBR1532, a selective telomerase inhibitor, enhances radiosensitivity of non-small cell lung cancer through increasing telomere dysfunction and ATM/CHK1 inhibition. *Int. J. Radiat. Oncol. Biol. Phys.* **105**, 861–874 (2019).
165. Liu, R., Liu, J., Wang, S., Wang, Y., Zhang, T., Liu, Y., Geng, X., & Wang, F. Combined treatment with emodin and a telomerase inhibitor induces significant telomere damage/dysfunction and cell death. *Cell Death Dis.* **10**, 527 (2019).
166. Huang, M., Lu, J. J. & Ding, J. Natural products in cancer therapy: past, present and future. *Nat. Products Bioprospect.* **11**, 5–13 (2021).
167. Ganesan, K. & Xu, B. Molecular sciences telomerase inhibitors from natural products and their anticancer potential. *Int. J. Mol. Sci.* **19**, 13 (2017).
168. Hande, M. P., Khaw, A. K., Hande, M. P. & Kalthur, G. Curcumin inhibits telomerase and induces telomere shortening and apoptosis in brain tumour cells. *J. Cell. Biochem.* **114**, 1257–1270 (2013).
169. Nakai, R., Ishida, H., Asai, A., Ogawa, H., Yamamoto, Y., Kawasaki, H., Akinaga, S., Mizukami, T., & Yamashita, Y. Telomerase inhibitors identified by a forward chemical

- genetics approach using a yeast strain with shortened telomere length. *Chem. Biol.* **13**, 183–190 (2006).
170. Seimiya, H., Oh-hara, T., Suzuki, T., Naasani, I., Shimazaki, T., Tsuchiya, K., & Tsuruo, T. Telomere shortening and growth inhibition of human cancer cells by novel synthetic telomerase inhibitors MST-312, MST-295, and MST-1991. *Mol Cancer Ther.* **1**, 657–665 (2002).
171. Nakai, R., Ishida, H., Asai, A., Ogawa, H., Yamamoto, Y., Kawasaki, H., Akinaga, S., Mizukami, T., & Yamashita, Y. Telomerase inhibitors identified by a forward chemical genetics approach using a yeast strain with shortened telomere length. *Chem. Biol.* **13**, 183–190 (2006).
172. Chien, M., Anderson, T. K., Jockusch, S., Tao, C., Li, X., Kumar, S., Russo, J. J., Kirchdoerfer, R. N., & Ju, J. Nucleotide analogues as inhibitors of SARS-CoV-2 polymerase, a key drug target for COVID-19. *J. Proteome Res.* **19**, 4690–4697 (2020).
173. Thomson, J. M. & Lamont, I. L. Nucleoside analogues as antibacterial agents. *Front. Microbiol.* **10**, 952 (2019).
174. Galmarini, C. M., Mackey, J. R. & Dumontet, C. Nucleoside analogues: mechanisms of drug resistance and reversal strategies. *Leuk.* **15**, 875–890 (2001).
175. Fischl, M. A., Richman, D. D., Hansen, N., Collier, A. C., Carey, J. T., Para, M. F., Hardy, W. D., Dolin, R., Powderly, W. G., & Allan, J. D. The safety and efficacy of zidovudine (AZT) in the treatment of subjects with mildly symptomatic human immunodeficiency virus type 1 (HIV) infection. A double-blind, placebo-controlled trial. The AIDS Clinical Trials Group. *Ann. Intern. Med.* **112**, 727–737 (1990).
176. Strahl, C. & Blackburn, E. H. Effects of reverse transcriptase inhibitors on telomere length and telomerase activity in two immortalized human cell lines. *Mol. Cell. Biol.* **16**, 53–65 (1996).
177. Hsieh, Y. & Tseng, J. J. Azidothymidine (AZT) inhibits proliferation of human ovarian cancer cells by regulating cell cycle progression. *Anticancer Res.* **40**, 5517–5527 (2020).
178. Mender, I., Gryaznov, S., Dikmen, Z. G., Wright, W. E. & Shay, J. W. Induction of telomere dysfunction mediated by the telomerase substrate precursor 6-thio-2'-deoxyguanosine. *Cancer Discov.* **5**, 82 (2015).
179. Johnston, J. S., Johnson, A., Gan, Y., Wientjes, M. G. & Au, J. L. S. Synergy between 3'-azido-3'-deoxythymidine and paclitaxel in human pharynx FaDu cells. *Pharm. Res.* **20**, 957–961 (2003).
180. Gomez, D. E., Armando, R. G. & Alonso, D. F. AZT as a telomerase inhibitor. *Front. Oncol.* **2**, 113 (2012).

181. Grishok, A. RNAi mechanisms in *Caenorhabditis elegans*. *FEBS Lett.* **579**, 5932–5939 (2005).
182. Fjose, A., Ellingsen, S., Wargelius, A. & Seo, H. C. RNA interference: mechanisms and applications. *Biotechnol. Annu. Rev.* **7**, 31–57 (2001).
183. Wilson, R. C. & Doudna, J. A. Molecular mechanisms of RNA interference. *Annu. Rev. Biophys.* **42**, 217–239 (2013).
184. Kubowicz, P., Zelazarczyk, D. & Pekala, E. RNAi in clinical studies. *Curr. Med. Chem.* **20**, 1801–1816 (2013).
185. Bumcrot, D., Manoharan, M., Koteliensky, V. & Sah, D. W. Y. RNAi therapeutics: a potential new class of pharmaceutical drugs. *Nat. Chem. Biol.* **2**, 711–719 (2006).
186. Devi, G. R. siRNA-based approaches in cancer therapy. *Cancer Gene Ther.* **13**, 819–829 (2006).
187. Ge, L., Shao, W., Zhang, Y., Qiu, Y., Cui, D., Huang, D., & Deng, Z. RNAi targeting of hTERT gene expression induces apoptosis and inhibits the proliferation of lung cancer cells. *Oncol. Lett.* **2**, 1121–1129 (2011).
188. Shi, Y. A., Zhao, Q., Zhang, L. H., Du, W., Wang, X. Y., He, X., Wu, S., & Li, Y. L. Knockdown of hTERT by siRNA inhibits cervical cancer cell growth in vitro and in vivo. *Int. J. Oncol.* **45**, 1216–1224 (2014).
189. Cheng, W., Wei, Z., Gao, J., Zhang, Z., Ge, J., Jing, K., Xu, F., & Xie, P. Effects of combined siRNA-TR and-TERT on telomerase activity and growth of bladder transitional cell cancer BIU-87 cells. *J. Huazhong Univ. Sci. Technol. - Med. Sci.* **30**, 391–396 (2010).
190. Cheng, W., Wei, Z., Gao, J., Zhang, Z., Ge, J., Jing, K., Xu, F., & Xie, P. Telomerase inhibition strategies by siRNAs against either hTR or hTERT in oral squamous cell carcinoma. *Cancer Gene Ther.* **18**, 318–325 (2011).
191. Dong, X., Liu, A., Zer, C., Feng, J., Zhen, Z., Yang, M., & Zhong, L. siRNA inhibition of telomerase enhances the anti-cancer effect of doxorubicin in breast cancer cells. *BMC Cancer* **9**, 133 (2009).
192. Barczak, W., Sobecka, A., Golusinski, P., Masternak, M. M., Rubis, B., Suchorska, W. M., & Golusinski, W. hTERT gene knockdown enhances response to radio- and chemotherapy in head and neck cancer cell lines through a DNA damage pathway modification. *Sci. Reports* **8**, 5949 (2018).
193. Ran, F. A., Hsu, P. D., Wright, J., Agarwala, V., Scott, D. A., & Zhang, F. Genome engineering using the CRISPR-Cas9 system. *Nat. Protoc* **8**, 2281–2308 (2013).
194. Katti, A., Diaz, B. J., Caragine, C. M., Sanjana, N. E. & Dow, L. E. CRISPR in cancer biology and therapy. *Nat. Rev. Cancer* **22**, 259–279 (2022).



195. Xi, L., Schmidt, J. C., Zaug, A. J., Ascarrunz, D. R. & Cech, T. R. A novel two-step genome editing strategy with CRISPR-Cas9 provides new insights into telomerase action and TERT gene expression. *Genome Biol.* **16**, 231 (2015).
196. Quazi, S. An overview of CAR T cell mediated B cell maturation antigen therapy. *Clin. Lymphoma. Myeloma Leuk.* **22**, e392-e404 (2022).
197. Zhou, Z., Li, Y., Xu, H., Xie, X., He, Z., Lin, S., Li, R., Jin, S., Cui, J., Hu, H., Liu, F., Wu, S., Ma, W., & Songyang, Z. An inducible CRISPR/Cas9 screen identifies DTX2 as a transcriptional regulator of human telomerase. *iScience* **25**, 103813 (2022).
198. Wen, L., Zhao, C., Song, J., Ma, L., Ruan, J., Xia, X., Chen, Y. E., Zhang, J., Ma, P. X., & Xu, J. CRISPR/Cas9-mediated TERT disruption in cancer cells. *Int. J. Mol. Sci.* **21**, 653 (2020).
199. Quazi, S. Telomerase gene therapy: a remission toward cancer. *Med. Oncol.* **39**, 105 (2022).
200. Uddin, F., Rudin, C. M. & Sen, T. CRISPR gene therapy: applications, limitations, and implications for the future. *Front. Oncol.* **10**, 1387 (2020).
201. Kawashima, T., Kagawa, S., Kobayashi, N., Shirakiya, Y., Umeoka, T., Teraishi, F., Taki, M., Kyo, S., Tanaka, N., & Fujiwara, T. Telomerase-specific replication-selective virotherapy for human cancer. *Clin. Cancer Res.* **10**, 285–292 (2004).
202. Nakajima, O., Ichimaru, D., Urata, Y., Fujiwara, T., Horibe, T., Kohno, M., & Kawakami, K. Use of telomelysin (OBP-301) in mouse xenografts of human head and neck cancer. *Oncol. Rep.* **22**, 1039–1043 (2009).
203. Huang, P., Watanabe, M., Kaku, H., Kashiwakura, Y., Chen, J., Saika, T., Nasu, Y., Fujiwara, T., Urata, Y., & Kumon, H. Direct and distant antitumour effects of a telomerase-selective oncolytic adenoviral agent, OBP-301, in a mouse prostate cancer model. *Cancer Gene Ther.* **15**, 315–322 (2008).
204. Nemunaitis, J., Tong, A. W., Nemunaitis, M., Senzer, N., Phadke, A. P., Bedell, C., Adams, N., Zhang, Y. A., Maples, P. B., Chen, S., Pappen, B., Burke, J., Ichimaru, D., Urata, Y., & Fujiwara, T. A phase I study of telomerase-specific replication competent oncolytic adenovirus (telomelysin) for various solid tumors. *Mol. Ther.* **18**, 429–434 (2010).
205. Phase 2 study of telomelysin (OBP-301) in combination with pembrolizumab in esophagogastric adenocarcinoma - <https://clinicaltrials.gov/ct2/show/NCT03921021?term=Telomelysin&draw=2&rank=2>, access: 12.05.22
206. Zheng, M., Huang, J., Tong, A. & Yang, H. Oncolytic Viruses for Cancer Therapy: Barriers and Recent Advances. *Mol. Ther. Oncolytics* **15**, 234-247 (2019).

207. Dai, W., Xu, X., Wang, D., Wu, J. & Wang, J. Cancer therapy with a CRISPR-assisted telomerase-activating gene expression system. *Oncogene* **38**, 4110–4124 (2019).
208. Taefehshokr, N., Baradaran, B., Baghbanzadeh, A. & Taefehshokr, S. Promising approaches in cancer immunotherapy. *Immunobiology* **225**, 151875 (2020).
209. Zanetti, M. A second chance for telomerase reverse transcriptase in anticancer immunotherapy. *Nat. Rev. Clin. Oncol.* **14**, 115–128 (2016).
210. Ellingsen, E. B., Mangsbo, S. M., Hovig, E. & Gaudernack, G. Telomerase as a target for therapeutic cancer vaccines and considerations for optimizing their clinical potential. *Front. Immunol.* **12**, 682492 (2021).
211. Liu, J. P., Chen, W., Schwarer, A. P., & Li, H. Telomerase in cancer immunotherapy. *Biochim. Biophys. Acta* **1805**, 35–42 (2010).
212. Mizukoshi, E. & Kaneko, S. Telomerase-targeted cancer immunotherapy. *Int. J. Mol. Sci.* **20**, 1823 (2019).
213. Negrini, S., De Palma, R. & Filaci, G. Anti-cancer immunotherapies targeting telomerase. *Cancers (Basel)* **12**, 2260 (2020).
214. Evaluation of UCPVax plus nivolumab as second line therapy in advanced non small cell lung cancer - <https://www.clinicaltrials.gov/ct2/show/NCT04263051>, access: 15.05.22
215. Nivolumab and ipilimumab +/- UV1 vaccination as second line treatment in patients with malignant mesothelioma - <https://clinicaltrials.gov/ct2/show/NCT04300244>, access: 15.05.22
216. Ellingsen, E. B., Mangsbo, S. M., Hovig, E. & Gaudernack, G. Telomerase as a target for therapeutic cancer vaccines and considerations for optimizing their clinical potential. *Front. Immunol.* **12**, 682492 (2021).
217. Zarogoulidis, P., Darwiche, K., Sakkas, A., Yarmus, L., Huang, H., Li, Q., Freitag, L., Zarogoulidis, K., & Malecki, M. Suicide gene therapy for cancer – current strategies. *J. Genet. Syndr. Gene Ther.* **4**, 16849 (2013).
218. Lin, T., Huang, X., Gu, J., Zhang, L., Roth, J. A., Xiong, M., Curley, S. A., Yu, Y., Hunt, K. K., & Fang, B. Long-term tumor-free survival from treatment with the GFP-TRAIL fusion gene expressed from the hTERT promoter in breast cancer cells. *Oncogene* **21**, 8020–8028 (2002).
219. Komata, T., Koga, S., Hirohata, S., Takakura, M., Germano, I. M., Inoue, M., Kyo, S., Kondo, S., & Kondo, Y. A novel treatment of human malignant gliomas in vitro and in vivo: FADD gene transfer under the control of the human telomerase reverse transcriptase gene promoter. *Int. J. Oncol.* **19**, 1015–1020 (2001).

220. Kyo, S., Takakura, M., Fujiwara, T. & Inoue, M. Understanding and exploiting hTERT promoter regulation for diagnosis and treatment of human cancers. *Cancer Sci.* **99**, 1528–1538 (2008).
221. Nakamura, M., Kyo, S., Kanaya, T., Yatabe, N., Maida, Y., Tanaka, M., Ishida, Y., Fujii, C., Kondo, T., Inoue, M., & Mukaida, N. hTERT-promoter-based tumor-specific expression of MCP-1 effectively sensitizes cervical cancer cells to a low dose of cisplatin. *Cancer Gene Ther.* **11**, 1–7 (2004).
222. Doloff, J. C. & Waxman, D. J. Adenoviral vectors for prodrug activation-based gene therapy for cancer. *Anticancer. Agents Med. Chem.* **14**, 115-126 (2014).
223. Plumb, J. A., Bilsland, A., Kakani, R., Zhao, J., Glasspool, R. M., Knox, R. J., Evans, T. R., & Keith, W. N. Telomerase-specific suicide gene therapy vectors expressing bacterial nitroreductase sensitize human cancer cells to the pro-drug CB1954. *Oncogene* **20**, 7797–803 (2001).
224. Patel, P., Young, J. G., Mautner, V., Ashdown, D., Bonney, S., Pineda, R. G., Collins, S. I., Searle, P. F., Hull, D., Peers, E., Chester, J., Wallace, D. M., Doherty, A., Leung, H., Young, L. S., & James, N. D. A phase I/II clinical trial in localized prostate cancer of an adenovirus expressing nitroreductase with CB1984. *Mol. Ther.* **17**, 1292–1299 (2009).
225. Heravi, M. M. & Zadsirjan, V. Prescribed drugs containing nitrogen heterocycles: an overview. *RSC Adv.* **10**, 44247–44311 (2020).
226. Sheng, C. & Zhang, W. New lead structures in antifungal drug discovery. *Curr. Med. Chem.* **18**, 733–766 (2011).
227. Sharma, S., Kumar, D., Singh, G., Monga, V. & Kumar, B. Recent advancements in the development of heterocyclic anti-inflammatory agents. *Eur. J. Med. Chem.* **200**, 112438 (2020).
228. De, A., Sarkar, S. & Majee, A. Recent advances on heterocyclic compounds with antiviral properties. *Chem. Heterocycl. Compd.* **57**, 410-416 (2021).
229. Ali, I., Lone, M., Al-Othman, Z., Al-Warthan, A. & Sanagi, M. Heterocyclic scaffolds: centrality in anticancer drug development. *Curr. Drug Targets* **16**, 711–734 (2015).
230. Panggabean, J. A., Adiguna, S. P., Murniasih, T., Rahmawati, S. I., Bayu, A., & Putra, M. Y. Structure–activity relationship of cytotoxic natural products from Indonesian marine sponges. *Rev. Bras. Farmacogn.* **32**, 12–38 (2022).
231. Tandon, R., Singh, I., Luxami, V., Tandon, N. & Paul, K. Recent advances and developments of in vitro evaluation of heterocyclic moieties on cancer cell lines. *Chem. Rec.* **19**, 362–393 (2019).





232. Kalathiya, U., Padariya, M. & Baginski, M. Molecular modeling and evaluation of novel dibenzopyrrole derivatives as telomerase inhibitors and potential drug for cancer therapy. *IEEE/ACM Trans. Comput. Biol. Bioinforma.* **11**, 1196–1207 (2014).
233. Gillis, A. J., Schuller, A. P. & Skordalakes, E. Structure of the *Tribolium castaneum* telomerase catalytic subunit TERT. *Nat.* **455**, 633–637 (2008).
234. Stasevych, M., Zvorych, V., Lunin, V., Deniz, N. G., Gokmen, Z., Akgun, O., Ulukaya, E., Poroikov, V., Glorizova, T., & Novikov, V. Computer-aided prediction and cytotoxicity evaluation of dithiocarbamates of 9,10-anthracenedione as new anticancer agents. *SAR QSAR Environ. Res.* **28**, 355–366 (2017).
235. Toshikuni, N., Nouse, K., Higashi, T., Nakatsukasa, H., Onishi, T., Kaneyoshi, T., Kobayashi, Y., Kariyama, K., Yamamoto, K., & Tsuji, T. Expression of telomerase-associated protein 1 and telomerase reverse transcriptase in hepatocellular carcinoma. *Br. J. Cancer* **82**, 833–837 (2000).
236. Kirkpatrick, K. L., Clark, G., Ghilchick, M., Newbold, R. F. & Mokbel, K. hTERT mRNA expression correlates with telomerase activity in human breast cancer. *Eur. J. Surg. Oncol.* **29**, 321–326 (2003).
237. Pompili, L., Leonetti, C., Biroccio, A. & Salvati, E. Diagnosis and treatment of ALT tumors: Is Trabectedin a new therapeutic option? *J. Exp. Clin. Cancer Res.* **36**, 189 (2017).
238. Pradeep, T. P. & Barthwal, R. A 4:1 stoichiometric binding and stabilization of mitoxantrone-parallel stranded G-quadruplex complex established by spectroscopy techniques. *J. Photochem. Photobiol. B Biol.* **162**, 106–114 (2016).
239. Zheng, X. H., Nie, X., Liu, H. Y., Fang, Y. M., Zhao, Y., & Xia, L. X. TMPyP4 promotes cancer cell migration at low doses, but induces cell death at high doses. *Sci. Reports* **6**, 26592 (2016).
240. Konieczna, N., Romaniuk-Drapała, A., Lisiak, N., Totoń, E., Paszal-Jaworska, A., Kaczmarek, M., & Rubiś, B. Telomerase inhibitor TMPyP4 alters adhesion and migration of breast-cancer cells MCF7 and MDA-MB-231. *Int. J. Mol. Sci.* **20**, 2670 (2019).
241. Frink, R. E., Peyton, M., Schiller, J. H., Gazdar, A. F., Shay, J. W., & Minna, J. D. Telomerase inhibitor imetelstat has preclinical activity across the spectrum of non-small cell lung cancer oncogenotypes in a telomere length dependent manner. *Oncotarget* **7**, 31639–31651 (2016).
242. Yang, S. Y., Chang, E., Lim, J., Kwan, H. H., Monchaud, D., Yip, S., Stirling, P. C., & Wong, J. G-quadruplexes mark alternative lengthening of telomeres. *NAR Cancer* **3**, zcab031 (2021).

243. Amato, R., Valenzuela, M., Berardinelli, F., Salvati, E., Maresca, C., Leone, S., Antoccia, A., & Sgura, A. G-quadruplex Stabilization fuels the ALT pathway in ALT-positive osteosarcoma cells. *Genes (Basel)* **11**, 304 (2020).
244. Celeghin, A., Giunco, S., Freguja, R., Zangrossi, M., Nalio, S., Dolcetti, R., & De Rossi, A. Short-term inhibition of TERT induces telomere length-independent cell cycle arrest and apoptotic response in EBV-immortalized and transformed B cells. *Cell Death Dis.* **7**, e2562 (2016).
245. Higginbottom, K., Cummings, M., Newland, A. C. & Allen, P. D. Etoposide-mediated deregulation of the G2M checkpoint in myeloid leukaemic cell lines results in loss of cell survival. *Br. J. Haematol.* **119**, 956–964 (2002).
246. Nam, C., Doi, K. & Nakayama, H. Etoposide induces G2/M arrest and apoptosis in neural progenitor cells via DNA damage and an ATM/p53-related pathway. *Histol. Histopathol.* **25**, 485–493 (2010).
247. Saraste, A. & Pulkki, K. Morphologic and biochemical hallmarks of apoptosis. *Cardiovasc. Res.* **45**, 528–537 (2000).
248. Aral, K., Aral, C. A. & Kapila, Y. The role of caspase-8, caspase-9, and apoptosis inducing factor in periodontal disease. *J. Periodontol.* **90**, 288–294 (2019).
249. Slee, E. A., Adrain, C. & Martin, S. J. Executioner caspase-3, -6, and -7 perform distinct, non-redundant roles during the demolition phase of apoptosis. *J. Biol. Chem.* **276**, 7320–7326 (2001).
250. Brentnall, M., Rodriguez-Menocal, L., De Guevara, R. L., Cepero, E. & Boise, L. H. Caspase-9, caspase-3 and caspase-7 have distinct roles during intrinsic apoptosis. *BMC Cell Biol.* **14**, 32 (2013).
251. Cao, X., Deng, X. & May, W. S. Cleavage of Bax to p18 Bax accelerates stress-induced apoptosis, and a cathepsin-like protease may rapidly degrade p18 Bax. *Blood* **102**, 2605–2614 (2003).
252. Marchi, S., Patergnani, S., Missiroli, S., Morciano, G., Rimessi, A., Wieckowski, M. R., Giorgi, C., & Pinton, P. Mitochondrial and endoplasmic reticulum calcium homeostasis and cell death. *Cell Calcium* **69**, 62–72 (2018).
253. Rao, R. V., Ellerby, H. M. & Bredesen, D. E. Coupling endoplasmic reticulum stress to the cell death program. *Cell Death Differ.* **11**, 372–380 (2004).
254. Prevarskaya, N., Ouadid-Ahidouch, H., Skryma, R. & Shuba, Y. Remodelling of Ca<sup>2+</sup> transport in cancer: how it contributes to cancer hallmarks? *Philos. Trans. R. Soc. B Biol. Sci.* **369**, 20130097 (2014).
255. Zhang, D., Wang, F., Li, P. & Gao, Y. Mitochondrial Ca<sup>2+</sup> homeostasis: emerging roles and clinical significance in cardiac remodeling. *Int. J. Mol. Sci.* **23**, 3025 (2022).



256. Wang, L., Lu, Z., Zhao, J., Schank, M., Cao, D., Dang, X., Nguyen, L. N., Nguyen, L., Khanal, S., Zhang, J., Wu, X. Y., El Gazzar, M., Ning, S., Moorman, J. P., & Yao, Z. Q. Selective oxidative stress induces dual damage to telomeres and mitochondria in human T cells. *Aging Cell* **20**, e13513 (2021).
257. Vyas, S., Zaganjor, E. & Haigis, M. C. Mitochondria and Cancer. *Cell* **166**, 555–566 (2016).
258. Scott, I. & Youle, R. J. Mitochondrial fission and fusion. *Essays Biochem.* **47**, 85-98 (2010).
259. Gottlieb, E., Armour, S. M., Harris, M. H. & Thompson, C. B. Mitochondrial membrane potential regulates matrix configuration and cytochrome c release during apoptosis. *Cell Death Differ.* **10**, 709–717 (2003).
260. Deng, Y. & Chang, S. Role of telomeres and telomerase in genomic instability, senescence and cancer. *Lab. Investig.* **8**, 1071-1076 (2007).
261. Hallows, S. E., Regnault, T. R. H. & Betts, D. H. Telomerase inhibition causes premature senescence of fetal guinea pig muscle cells. *bioRxiv* 2020.02.21.959320 (2020)
262. Lee, B. Y., Han, J. A., Im, J. S., Morrone, A., Johung, K., Goodwin, E. C., Kleijer, W. J., DiMaio, D., & Hwang, E. S. Senescence-associated beta-galactosidase is lysosomal beta-galactosidase. *Aging Cell* **5**, 187–195 (2006).
263. Le Gal, K., Schmidt, E. E. & Sayin, V. I. Cellular redox homeostasis. *Antioxidants* **10**, 1377 (2021).
264. Kim, S. J., Kim, H. S. & Seo, Y. R. Understanding of ROS-inducing strategy in anticancer therapy. *Oxid. Med. Cell. Longev.* **2019**, 5381692 (2019).
265. Shin, W. H. & Chung, K. C. Human telomerase reverse transcriptase positively regulates mitophagy by inhibiting the processing and cytoplasmic release of mitochondrial PINK1. *Cell Death Dis.* **11**, 425 (2020).
266. Liu, R., Liu, J., Wang, S., Wang, Y., Zhang, T., Liu, Y., Geng, X., & Wang, F. Combined treatment with emodin and a telomerase inhibitor induces significant telomere damage/dysfunction and cell death. *Cell Death Dis.* **10**, 527 (2019).
267. Masutomi, K., Possemato, R., Wong, J. M., Currier, J. L., Tothova, Z., Manola, J. B., Ganesan, S., Lansdorp, P. M., Collins, K., & Hahn, W. C. The telomerase reverse transcriptase regulates chromatin state and DNA damage responses. *Proc. Natl. Acad. Sci. U. S. A.* **102**, 8222–8227 (2005).
268. Rogakou, E. P., Pilch, D. R., Orr, A. H., Ivanova, V. S. & Bonner, W. M. DNA double-stranded breaks induce histone H2AX phosphorylation on serine 139. *J. Biol. Chem.* **273**, 5858–5868 (1998).
269. Huang, R. X. & Zhou, P. K. DNA damage response signalling pathways and targets for radiotherapy sensitization in cancer. *Signal Transduct. Target. Ther.* **5**, 60 (2020).

270. Nikolova, T., Marini, F. & Kaina, B. Genotoxicity testing: Comparison of the  $\gamma$ H2AX focus assay with the alkaline and neutral comet assays. *Mutat. Res. - Genet. Toxicol. Environ. Mutagen.* **822**, 10–18 (2017).
271. Lin, Y. H., Chuang, S. M., Wu, P. C., Chen, C. L., Jeyachandran, S., Lo, S. C., Huang, H. S., & Hou, M. H. Selective recognition and stabilization of new ligands targeting the potassium form of the human telomeric G-quadruplex DNA. *Sci. Rep.* **6**, 31019 (2016).
272. Roy, S., Ali, A., Kamra, M., Muniyappa, K. & Bhattacharya, S. Specific stabilization of promoter G-Quadruplex DNA by 2,6-disubstituted amidoanthracene-9,10-dione based dimeric distamycin analogues and their selective cancer cell cytotoxicity. *Eur. J. Med. Chem.* **195**, 112202 (2020).
273. Jeannot, P. & Besson, A. Cortactin function in invadopodia. *Small GTPases* **11**, 256-270 (2020).
274. Ji, R., Zhu, X. J., Wang, Z. R. & Huang, L. Q. Cortactin in epithelial–mesenchymal transition. *front. cell dev. biol.* **8**, 585619 (2020).
275. Li, Y., Zhang, H., Gong, H., Yuan, Y., Li, Y., Wang, C., Li, W., Zhang, Z., Liu, M., Liu, H., & Chen, J. miR-182 suppresses invadopodia formation and metastasis in non-small cell lung cancer by targeting cortactin gene. *J. Exp. Clin. Cancer Res.* **37**, 141 (2018).
276. Glick, D., Barth, S. & Macleod, K. F. Autophagy: cellular and molecular mechanisms. *J. Pathol.* **221**, 3–12 (2010).
277. Lim, S. M., Mohamad Hanif, E. A. & Chin, S. F. Is targeting autophagy mechanism in cancer a good approach? The possible double-edge sword effect. *Cell Biosci.* **11**, 56 (2021)
278. Jung, S., Jeong, H. & Yu, S. W. Autophagy as a decisive process for cell death. *Exp. Mol. Med.* **52**, 921–930 (2020).
279. Li, T., Tong, H., Yin, H., Luo, Y., Zhu, J., Qin, Z., Yin, S., & He, W. Starvation induced autophagy promotes the progression of bladder cancer by LDHA mediated metabolic reprogramming. *Cancer Cell Int.* **21**, 597 (2021).
280. Mauthe, M., Orhon, I., Rocchi, C., Zhou, X., Luhr, M., Hijlkema, K. J., Coppes, R. P., Engedal, N., Mari, M., & Reggiori, F. Chloroquine inhibits autophagic flux by decreasing autophagosome-lysosome fusion. *Autophagy* **14**, 1435-1455 (2018).
281. Klionsky, D. J., Abdelmohsen, K., Abe, A., Abedin, M. J., Abeliovich, H., Acevedo Arozena, A., Adachi, H., Adams, C. M., Adams, P. D., Adeli, K., Adihetty, P. J., Adler, S. G., Agam, G., Agarwal, R., Aghi, M. K., Agnello, M., Agostinis, P., Aguilar, P. V., Aguirre-Ghiso, J., Airoidi, E. M., ... Zughaier, S. M. Guidelines for the use and interpretation of assays for monitoring autophagy (3rd edition). *Autophagy* **12**, 1-222 (2016).
282. Choi, C. H. ABC transporters as multidrug resistance mechanisms and the development of chemosensitizers for their reversal. *Cancer Cell Int.* **5**, 30 (2005).



283. Xiao, H., Zheng, Y., Ma, L., Tian, L. & Sun, Q. Clinically-relevant ABC transporter for anti-cancer drug resistance. *Front. Pharmacol.* **12**, 648407 (2021).
284. Song, Y., Zhao, Y., Deng, Z., Zhao, R. & Huang, Q. Stress-induced polyploid giant cancer cells: unique way of formation and non-negligible characteristics. *Front. Oncol.* **11**, 724781 (2021).
285. Tikhomirov, A., Shtil, A. & Shchekotikhin, A. Advances in the discovery of anthraquinone-based anticancer agents. *Recent Pat. Anticancer. Drug Discov.* **13**, 159-183 (2017).
286. Baier, A. & Szyszka, R. Compounds from natural sources as protein kinase inhibitors. *Biomolecules* **10**, 1–30 (2020).
287. Jayasuriya, H., Koonchanok, N. M., Geahlen, R. L., Mclaughlin, J. L. & Chang, C. J. Emodin, a protein tyrosine kinase inhibitor from *Polygonum cuspidatum*. *J. Nat. Prod.* **55**, 696–698 (1992).
288. Yang, Y., Li, S., Wang, Y., Zhao, Y. & Li, Q. Protein tyrosine kinase inhibitor resistance in malignant tumors: molecular mechanisms and future perspective. *Signal Transduct. Target. Ther.* **7**, 1–36 (2022).
289. Druker, B. J. Imatinib as a paradigm of targeted therapies. *Adv. Cancer Res.* **91**, 1–30 (2004).
290. Issa, S., Prandina, A., Bedel, N., Rongved, P., Yous, S., Le Borgne, M., & Bouaziz, Z. Carbazole scaffolds in cancer therapy: a review from 2012 to 2018. *J. Enzyme Inhib. Med. Chem.* **34**, 1321-1346 (2019).
291. Weber, G. F. DNA damaging drugs. *Mol. Ther. Cancer*, 9–112 (2015).
292. Trieb, M., Rauch, C., Wibowo, F. R., Wellenzohn, B. & Liedl, K. R. Cooperative effects on the formation of intercalation sites. *Nucleic Acids Res.* **32**, 4696 (2004).
293. Lown, J. W., Morgan, A. R., Yen, S. F., Wang, Y. H. & Wilson, W. D. Characteristics of the binding of the anticancer agents mitoxantrone and ametantrone and related structures to deoxyribonucleic acids. *Biochemistry* **24**, 4028–4035 (1985).
294. Krishnamoorthy, C. R., Yen, S. F., Smith, J. C., Lown, J. W. & Wilson, W. D. Stopped-flow kinetic analysis of the interaction of anthraquinone anticancer drugs with calf thymus DNA, Poly[d(G-C)]•Poly[d(G-C)], and Poly[d(A-T)]•Poly[d(A-T)]. *Biochemistry* **25**, 5933–5940 (1986).
295. Tanious, F. A., Wilson, W. D., Patrick, D. A., Tidwell, R. R., Colson, P., Houssier, C., Tardy, C., & Bailly, C. Sequence-dependent binding of bis-amidine carbazole dications to DNA. *Eur. J. Biochem.* **268**, 3455–3464 (2001).
296. Delgado, J. L., Hsieh, C. M., Chan, N. L. & Hiasa, H. Topoisomerases as Anticancer Targets. *Biochem. J.* **475**, 373-398 (2018).

297. Pommier, Y., Covey, J. M., Kerrigan, D., Markovits, J. & Pham, R. DNA unwinding and inhibition of mouse leukemia L1210 DNA topoisomerase I by intercalators. *Nucleic Acids Res.* **15**, 6713-6731 (1987).
298. Byeon, S. Y., Han, S. H. & Lee, J. Y. Carbazole-dibenzothiophene core as a building block of host materials for blue phosphorescent organic light-emitting diodes. *Dye. Pigment.* **155**, 114–120 (2018).
299. Li, Z., Liu, H. & Luo, X. Lipid droplet and its implication in cancer progression. *Am. J. Cancer Res.* **10**, 4112-4122 (2020).
300. Petan, T. Lipid droplets in cancer. *Rev. Physiol. Biochem. Pharmacol.* **10**, 4112-4122 (2020).
301. Dubey, R., Stivala, C. E., Nguyen, H. Q., Goo, Y. H., Paul, A., Carette, J. E., Trost, B. M., & Rohatgi, R. Lipid droplets can promote drug accumulation and activation. *Nat. Chem. Biol.* **16**, 206-213 (2020).
302. Witkowska, M., Maciejewska, N., Ryczkowska, M., Olszewski, M., Bagiński, M., & Makowiec, S. From tryptophan to novel mitochondria-disruptive agent, synthesis and biological evaluation of 1,2,3,6-tetrasubstituted carbazoles. *Eur. J. Med. Chem.* **238**, 114453 (2022).
303. Ashrafi, G. & Schwarz, T. L. The pathways of mitophagy for quality control and clearance of mitochondria. *Cell Death Differ.* **20**, 31–42 (2012).
304. Thomas, R. L. & Gustafsson, Å. B. Mitochondrial autophagy: an essential quality control mechanism for myocardial homeostasis. *Circ. J.* **77**, 2449-2254 (2013).
305. Fennell, D. A., Summers, Y., Cadranel, J., Benepal, T., Christoph, D. C., Lal, R., Das, M., Maxwell, F., Visseren-Grul, C., & Ferry, D. Cisplatin in the modern era: The backbone of first-line chemotherapy for non-small cell lung cancer. *Cancer Treat. Rev.* **44**, 42–50 (2016).
306. Van Vuuren, R. J., Visagie, M. H., Theron, A. E. & Joubert, A. M. Antimitotic drugs in the treatment of cancer. *Cancer Chemother. Pharmacol.* **76**, 1101-1112 (2015).
307. Barnes, N. G., Parker, A. W., Ahmed Mal Ullah, A. A., Ragazzon, P. A. & Hadfield, J. A. A 2-step synthesis of Combretastatin A-4 and derivatives as potent tubulin assembly inhibitors. *Bioorg. Med. Chem.* **28**, 115684 (2020).
308. Guterres, A. N. & Villanueva, J. Targeting telomerase for cancer therapy. *Oncogene* **39**, 5811–5824 (2020).
309. Andrews, L. G. & Tollefsbol, T. O. Methods of telomerase inhibition. *Methods Mol. Biol.* **405**, 1-7 (2008).
310. Baginski, M. & Serbakowska, K. In silico design of telomerase inhibitors. *Drug Discovery*



*Today* **25**, 1213–1222 (2020).

311. Nguyen, T., Tam, J., Wu, R. A., Greber, B. J., Toso, D., Nogales, E., & Collins, K. Cryo-EM structure of substrate-bound human telomerase holoenzyme. *Nature* **557**, 190–195 (2018).
312. Siddamurthi, S., Gutti, G., Jana, S., Kumar, A. & Singh, S. K. Anthraquinone: a promising scaffold for the discovery and development of therapeutic agents in cancer therapy. *Future Med. Chem.* **12**, 1037–1069 (2020).
313. Malik, M. S., Alsantali, R. I., Jassas, R. S., Alsimaree, A. A., Syed, R., Alsharif, M. A., Kalpana, K., Morad, M., Althagafi, I. I., & Ahmed, S. A. Journey of anthraquinones as anticancer agents – a systematic review of recent literature. *RSC Adv.* **11**, 35806–35827 (2021).
314. Bashash, D., Ghaffari, S. H., Mirzaee, R., Alimoghaddam, K. & Ghavamzadeh, A. Telomerase inhibition by non-nucleosidic compound BIBR1532 causes rapid cell death in pre-B acute lymphoblastic leukemia cells. *Leuk. Lymphoma* **54**, 561–568 (2013).
315. Thompson, C., Gu, A., Yang, S. Y., Mathew, V., Fleisig, H. B., & Wong, J. Transient telomerase inhibition with imetelstat impacts DNA damage signals and cell-cycle kinetics. *Mol. Cancer Res.* **16**, 1215–1225 (2018).
316. Nicholson, A. G., Tsao, M. S., Beasley, M. B., Borczuk, A. C., Brambilla, E., Cooper, W. A., Dacic, S., Jain, D., Kerr, K. M., Lantuejoul, S., Noguchi, M., Papotti, M., Rekhtman, N., Scagliotti, G., van Schil, P., Sholl, L., Yatabe, Y., Yoshida, A., & Travis, W. D. The 2021 WHO classification of lung tumors: impact of advances since 2015. *J. Thorac. Oncol.* **17**, 362–387 (2022).
317. Roy, S., Ali, A., Kamra, M., Muniyappa, K. & Bhattacharya, S. Specific stabilization of promoter G-Quadruplex DNA by 2,6-disubstituted amidoanthracene-9,10-dione based dimeric distamycin analogues and their selective cancer cell cytotoxicity. *Eur. J. Med. Chem.* **195**, 112202 (2020).
318. Tikhomirov, A. S., Tsvetkov, V. B., Kaluzhny, D. N., Volodina, Y. L., Zatonsky, G. V., Schols, D., & Shchekotikhin, A. E. Tri-armed ligands of G-quadruplex on heteroarene-fused anthraquinone scaffolds: Design, synthesis and pre-screening of biological properties. *Eur. J. Med. Chem.* **159**, 59–73 (2018).
319. Ranjan, N., Davis, E., Xue, L. & Arya, D. P. Dual recognition of the human telomeric G-quadruplex by a neomycin–anthraquinone conjugate. *Chem. Commun.* **49**, 5796–5798 (2013).
320. Spiegel, J., Adhikari, S. & Balasubramanian, S. The structure and function of DNA G-quadruplexes. *Trends Chem.* **2**, 123–136 (2020).
321. Mosoyan, G., Kraus, T., Ye, F., Eng, K., Crispino, J. D., Hoffman, R., & Iancu-Rubin, C.

- Imetelstat, a telomerase inhibitor, differentially affects normal and malignant megakaryopoiesis. *Leukemia* **31**, 2458-2467 (2017).
322. Lavanya, C., Venkataswamy, M. M., Sibin, M. K., Srinivas Bharath, M. M. & Chetan, G. K. Down regulation of human telomerase reverse transcriptase (hTERT) expression by BIBR1532 in human glioblastoma LN18 cells. *Cytotechnology* **70**, 1143-1154 (2018).
323. Hewitt, G., Jurk, D., Marques, F. D., Correia-Melo, C., Hardy, T., Gackowska, A., Anderson, R., Taschuk, M., Mann, J., & Passos, J. F. Telomeres are favoured targets of a persistent DNA damage response in ageing and stress-induced senescence. *Nat. Commun.* **3**, 708 (2012).
324. Cheung-Ong, K., Giaever, G. & Nislow, C. DNA-damaging agents in cancer chemotherapy: serendipity and chemical biology. *Chem. Biol.* **20**, 648–659 (2013).
325. Zeng-Rong, N., Paterson, J., Alpert, L., Tsao, M. S., Viallet, J., & Alaoui-Jamali, M. A. Elevated DNA repair capacity is associated with intrinsic resistance of lung cancer to chemotherapy. *Cancer Res.* **55**, 4760–4764 (1995).
326. Fumagalli, M., Rossiello, F., Clerici, M., Barozzi, S., Cittaro, D., Kaplunov, J. M., Bucci, G., Dobрева, M., Matti, V., Beausejour, C. M., Herbig, U., Longhese, M. P., & d'Adda di Fagagna, F. Telomeric DNA damage is irreparable and causes persistent DNA damage response activation. *Nat. Cell Biol.* **14**, 355-365 (2012).
327. Soutoglou, E., Dorn, J. F., Sengupta, K., Jasin, M., Nussenzweig, A., Ried, T., Danuser, G., & Misteli, T. Positional stability of single double-strand breaks in mammalian cells. *Nat. Cell Biol.* **9**, 675–682 (2007).
328. Guo, X., Deng, Y., Lin, Y., Cosme-Blanco, W., Chan, S., He, H., Yuan, G., Brown, E. J., & Chang, S. Dysfunctional telomeres activate an ATM-ATR-dependent DNA damage response to suppress tumorigenesis. *EMBO J.* **26**, 4709–4719 (2007).
329. Bandaria, J. N., Qin, P., Berk, V., Chu, S. & Yildiz, A. Shelterin protects chromosome ends by compacting telomeric chromatin. *Cell* **164**, 735-746 (2016).
330. Karlseder, J., Smogorzewska, A. & De Lange, T. Senescence induced by altered telomere state, not telomere loss. *Science* **295**, 2446–2449 (2002).
331. Nakamura, A. J., Chiang, Y. J., Hathcock, K. S., Horikawa, I., Sedelnikova, O. A., Hodes, R. J., & Bonner, W. M. Both telomeric and non-telomeric DNA damage are determinants of mammalian cellular senescence. *Epigenetics Chromatin* **1**, 6 (2008).
332. Chipuk, J. E., Bouchier-Hayes, L. & Green, D. R. Mitochondrial outer membrane permeabilization during apoptosis: the innocent bystander scenario. *Cell Death Differ.* **13**, 1396–1402 (2006).
333. Cosentino, K. & García-Sáez, A. J. MIM through MOM: the awakening of Bax and Bak pores. *EMBO J.* **37**, e100340 (2018).



334. Yang, P., Peairs, J. J., Tano, R., Zhang, N., Tyrell, J., & Jaffe, G. J. Caspase-8–Mediated apoptosis in human RPE cells. *Invest. Ophthalmol. Vis. Sci.* **48**, 3341–3349 (2007).
335. Korsmeyer, S. J., Wei, M. C., Saito, M., Weiler, S., Oh, K. J., & Schlesinger, P. H. Pro-apoptotic cascade activates BID, which oligomerizes BAK or BAX into pores that result in the release of cytochrome c. *Cell Death Differ.* **7**, 1166–1173 (2000).
336. Rafat, A., Dizaji Asl, K., Mazloumi, Z., Movassaghpour, A. A., Talebi, M., Shanehbandi, D., Farahzadi, R., Nejati, B., & Nozad Charoudeh, H. Telomerase inhibition on acute myeloid leukemia stem cell induced apoptosis with both intrinsic and extrinsic pathways. *Life Sci.* **295**, 120402 (2022).
337. Shamma, M. A., Koley, H., Batchu, R. B., Bertheau, R. C., Protopopov, A., Munshi, N. C., & Goyal, R. K. Telomerase inhibition by siRNA causes senescence and apoptosis in Barrett's adenocarcinoma cells: Mechanism and therapeutic potential. *Mol. Cancer* **4**, 24 (2005).
338. Giunco, S., Zangrossi, M., Dal Pozzolo, F., Celegghin, A., Ballin, G., Petrara, M. R., Amin, A., Argenton, F., Godinho Ferreira, M., & De Rossi, A. Anti-proliferative and pro-apoptotic effects of short-term inhibition of telomerase in vivo and in human malignant b cells xenografted in zebrafish. *Cancers (Basel)*. **12**, 2052 (2020).
339. Ali, M., Devkota, S., Roh, J. II, Lee, J. & Lee, H. W. Telomerase reverse transcriptase induces basal and amino acid starvation-induced autophagy through mTORC1. *Biochem. Biophys. Res. Commun.* **478**, 1198–1204 (2016).
340. Mar, F. A., Debnath, J. & Stohr, B. A. Autophagy-independent senescence and genome instability driven by targeted telomere dysfunction. *Autophagy* **11**, 527–537 (2015).
341. Zhao, M., Finlay, D., Kwong, E., Liddington, R., Viollet, B., Sasaoka, N., & Vuori, K. Cell adhesion suppresses autophagy via Src/FAK-mediated phosphorylation and inhibition of AMPK. *Cell. Signal.* **89**, 110170 (2022).
342. Wu, Z., Chang, P. C., Yang, J. C., Chu, C. Y., Wang, L. Y., Chen, N. T., Ma, A. H., Desai, S. J., Lo, S. H., Evans, C. P., Lam, K. S., & Kung, H. J. Autophagy blockade sensitizes prostate cancer cells towards Src family kinase inhibitors. *Genes Cancer* **1**, 40-49 (2010).
343. Novikov, N. M., Zolotaryova, S. Y., Gautreau, A. M. & Denisov, E. V. Mutational drivers of cancer cell migration and invasion. *Br. J. Cancer* **124**, 102–114 (2020).
344. Liu, H., Liu, Q., Ge, Y., Zhao, Q., Zheng, X., & Zhao, Y. hTERT promotes cell adhesion and migration independent of telomerase activity. *Sci. Rep.* **6**, 22886 (2016).
345. Pichot, C. S., Hartig, S. M., Xia, L., Arvanitis, C., Monisvais, D., Lee, F. Y., Frost, J. A., & Corey, S. J. Dasatinib synergizes with doxorubicin to block growth, migration, and invasion of breast cancer cells. *Br. J. Cancer* **101**, 38–47 (2009).
346. Yu, H., Gao, M., Ma, Y., Wang, L., Shen, Y., & Liu, X. Inhibition of cell migration by focal

- adhesion kinase: Time-dependent difference in integrin-induced signalling between endothelial and hepatoblastoma cells. *Int. J. Mol. Med.* **41**, 2573-2588 (2018).
347. Vajkoczy, P., Knyazev, P., Kunkel, A., Capelle, H. H., Behrndt, S., von Tengg-Kobligk, H., Kiessling, F., Eichelsbacher, U., Essig, M., Read, T. A., Erber, R., & Ullrich, A. Dominant-negative inhibition of the Axl receptor tyrosine kinase suppresses brain tumour cell growth and invasion and prolongs survival. *Proc. Natl. Acad. Sci. U. S. A.* **103**, 5799–5804 (2006).
  348. Bayat Mokhtari, R., Homayouni, T. S., Baluch, N., Morgatskaya, E., Kumar, S., Das, B., & Yeger, H. Combination therapy in combating cancer. *Oncotarget* **8**, 38022-38043 (2017).
  349. Talevi, A. Multi-target pharmacology: Possibilities and limitations of the 'skeleton key approach' from a medicinal chemist perspective. *Front. Pharmacol.* **6**, 205 (2015).
  350. Thompson, C. A., Gu, A., Yang, S., Venna, M., Fleising, H. B., Wong, J. M. Y. Transient telomerase inhibition alters cell cycle kinetics. *bioRxiv* 158287 (2017).
  351. Liu, R., Liu, J., Wang, S., Wang, Y., Zhang, T., Liu, Y., Geng, X., & Wang, F. Combined treatment with emodin and a telomerase inhibitor induces significant telomere damage/dysfunction and cell death. *Cell Death Dis.* **10**, 527 (2019).
  352. Hu, C. S., Huang, F., Hoffman, R. & Wang, X. Combination treatment with imetelstat, a telomerase inhibitor, and ruxolitinib depletes myelofibrosis hematopoietic stem cells and progenitor cells. *Blood* **134**, 2963–2963 (2019).
  353. Gupta, R., Dong, Y., Solomon, P. D., Wettersten, H. I., Cheng, C. J., Min, J. N., Henson, J., Dogra, S. K., Hwang, S. H., Hammock, B. D., Zhu, L. J., Reddel, R. R., Saltzman, W. M., Weiss, R. H., Chang, S., Green, M. R., & Wajapeyee, N. Synergistic tumour suppression by combined inhibition of telomerase and CDKN1A. *Proc. Natl. Acad. Sci. U. S. A.* **111**, E3062-71 (2014).
  354. Goldblatt, E. M., Gentry, E. R., Fox, M. J., Gryaznov, S. M., Shen, C., & Herbert, B. S. The telomerase template antagonist GRN163L alters MDA-MB-231 breast cancer cell morphology, inhibits growth, and augments the effects of paclitaxel. *Mol. Cancer Ther.* **8**, 2027–2035 (2009).
  355. Imetelstat in Combination with paclitaxel (with or without bevacizumab) in patients with locally recurrent or metastatic breast cancer - <https://clinicaltrials.gov/ct2/show/NCT01256762>, access: 05.06.22
  356. Thambiraj, S., Vijayalakshmi, R. & Ravi Shankaran, D. An effective strategy for development of docetaxel encapsulated gold nanoformulations for treatment of prostate cancer. *Sci. Reports* **11**, 2808 (2021).
  357. Fens, M. H., Hill, K. J., Issa, J., Ashton, S. E., Westwood, F. R., Blakey, D. C., Storm, G., Ryan, A. J., & Schiffelers, R. M. Liposomal encapsulation enhances the antitumour efficacy of the vascular disrupting agent ZD6126 in murine B16.F10 melanoma. *Br. J.*

- Cancer* **99**, 1256–1264 (2008).
358. Gonzalez-Fajardo, L., Mahajan, L. H., Ndaya, D., Hargrove, D., Manautou, J. E., Liang, B. T., Chen, M. H., Kasi, R. M., & Lu, X. Reduced in vivo toxicity of doxorubicin by encapsulation in cholesterol-containing self-assembled nanoparticles. *Pharmacol. Res.* **107**, 93–101 (2016).
359. Konda, S. K., Maliki, R., McGrath, S., Parker, B. S., Robinson, T., Spurling, A., Cheong, A., Lock, P., Pigram, P. J., Phillips, D. R., Wallace, L., Day, A. I., Collins, J. G., & Cutts, S. M. Encapsulation of mitoxantrone within cucurbit[8]uril decreases toxicity and enhances survival in a mouse model of cancer. *ACS Med. Chem. Lett.* **8**, 538–542 (2017).
360. Naim, M. J., Alam, O., Nawaz, F., Alam, M. J. & Alam, P. Current status of pyrazole and its biological activities. *J. Pharm. Bioallied Sci.* **8**, 2-17 (2016).
361. Kucuksayan, E., Bozkurt, F., Yilmaz, M. T., Sircan-Kucuksayan, A., Hanikoglu, A., & Ozben, T. A new combination strategy to enhance apoptosis in cancer cells by using nanoparticles as biocompatible drug delivery carriers. *Sci. Reports* **11**, 13027 (2021).
362. Hu, Y., Shi, G., Zhang, L., Li, F., Jiang, Y., Jiang, S., Ma, W., Zhao, Y., Songyang, Z., & Huang, J. Switch telomerase to ALT mechanism by inducing telomeric DNA damages and dysfunction of ATRX and DAXX. *Sci. Reports* **6**, 32280 (2016).
363. Hu, J., Hwang, S. S., Liesa, M., Gan, B., Sahin, E., Jaskelioff, M., Ding, Z., Ying, H., Boutin, A. T., Zhang, H., Johnson, S., Ivanova, E., Kost-Alimova, M., Protopopov, A., Wang, Y. A., Shirihai, O. S., Chin, L., & DePinho, R. A. Antitelomerase therapy provokes ALT and mitochondrial adaptive mechanisms in cancer. *Cell* **148**, 651–663 (2012).
364. Chen, G. & Deng, X. Cell synchronization by double thymidine block. *Bio-protocol* **8**, e3994 (2018).
365. Guzmán, C., Bagga, M., Kaur, A., Westermarck, J. & Abankwa, D. ColonyArea: an ImageJ plugin to automatically quantify colony formation in clonogenic assays. *PLoS One* **9**, e92444 (2014).
366. Dagda, R. K., Cherra, S. J., 3rd, Kulich, S. M., Tandon, A., Park, D., & Chu, C. T. Loss of PINK1 function promotes mitophagy through effects on oxidative stress and mitochondrial fission. *J. Biol. Chem.* **284**, 13843-13855 (2009).
367. Merrill, R. A., Flippo, K. H. & Strack, S. Measuring mitochondrial shape with imageJ. *NeuroMethods* **123**, 31–48 (2017).
368. Dimri, G. P., Lee, X., Basile, G., Acosta, M., Scott, G., Roskelley, C., Medrano, E. E., Linskens, M., Rubelj, I., & Pereira-Smith, O. A biomarker that identifies senescent human cells in culture and in aging skin in vivo. *Proc. Natl. Acad. Sci. U. S. A.* **92**, 9363–9367 (1995).
369. Bolte, S. & Cordelières, F. P. A guided tour into subcellular colocalization analysis in light



- microscopy. *J. Microsc.* **224**, 213–232 (2006).
370. Cesare, A. J., Heaphy, C. M. & O'Sullivan, R. J. Visualization of telomere integrity and function in vitro and in vivo using immunofluorescence techniques. *Curr. Protoc. Cytom.* **73**, 12.40.1-12.40.31 (2015).
371. Jafari, R., Almqvist, H., Axelsson, H., Ignatushchenko, M., Lundbäck, T., Nordlund, P., & Martinez Molina, D. The cellular thermal shift assay for evaluating drug target interactions in cells. *Nat. Protoc.* **9**, 2100–2122 (2014).
372. Vasilishina, A., Kropotov, A., Spivak, I. & Bernadotte, A. Relative human telomere length quantification by real-time PCR. *Methods Mol. Biol.* **1896**, 39–44 (2019).
373. Schmittgen, T. D. & Livak, K. J. Analyzing real-time PCR data by the comparative CT method. *Nat. Protoc.* **3**, 1101–1108 (2008).

## 8. AUTHORS CONTRIBUTION

### **8.1. Project II - From tryptophan to novel mitochondria-disruptive agent, synthesis and biological evaluation of 1,2,3,6-tetrasubstituted carbazoles**

Conceptualization: Natalia Maciejewska

Methodology: Milena Witkowska & Małgorzata Ryczkowska (compounds synthesis); Natalia Maciejewska & Mateusz Olszewski (biological evaluation)

Validation: Milena Witkowska (chemistry); Natalia Maciejewska & Mateusz Olszewski (biological evaluation)

Formal analysis: Milena Witkowska (chemistry); Natalia Maciejewska & Mateusz Olszewski (biological evaluation)

Writing—original draft preparation: Natalia Maciejewska (abstract, biological evaluation, conclusion); Mateusz Olszewski (editing); Milena Witkowska (chemistry); Sławomir Makowski (introduction), Maciej Baginski (editing)

Graphical conceptualization: Natalia Maciejewska

Writing—review and editing: Natalia Maciejewska; Sławomir Makowski

#### **The extended list of authors' contribution**

<b>Part</b>	<b>Contribution</b>
Publication Design	I have designed the outline of the manuscript regarding the biological evaluation
Experimental and Planning	Conception I have planned the following experiments: <ul style="list-style-type: none"><li>- Antimicrobial susceptibility test (together with Olszewski M.)</li><li>- Cell viability assay using MTT assay (together with Olszewski M.)</li><li>- Flow cytometry analyses of the cell cycle with propidium iodide (PI) staining (together with Olszewski M.)</li><li>- Flow cytometry analyses of <math>\gamma</math>H2AX as DNA damage marker (together with Olszewski M.)</li><li>- Flow cytometry analyses of reactive oxygen species generation (together with Olszewski M.)</li><li>- Apoptosis and caspase 3/7 assay using flow cytometry and fluorescence microscopy (together with Olszewski M.)</li><li>- Analyse of cell senescence by flow cytometry</li><li>- Colony formation assay (together with Olszewski M.)</li><li>- Analyse of antimigratory properties by wound healing assay</li><li>- Immunofluorescence microscopy for actin, and <math>\gamma</math>H2AX</li><li>- Analysis of mitochondrial morphology by confocal live cell-imaging</li></ul>

- Detection of SA- $\beta$ -Gal, as a marker of cell senescence (together with Olszewski M.)

#### Experiment Execution

I have executed the following experiments:

- Antimicrobial susceptibility test (together with Olszewski M.)
- Cell viability assay for A549, U2OS, and HEK293 cells using MTT assay
- Flow cytometry analyses of the cell cycle with propidium iodide (PI) staining (together with Olszewski M.)
- Flow cytometry analyses of  $\gamma$ H2AX as DNA damage marker (together with Olszewski M.)
- Flow cytometry analyses of reactive oxygen species generation (together with Olszewski M.)
- Apoptosis and caspase 3/7 assay using flow cytometry and fluorescence microscopy (together with Olszewski M.)
- Detection of cell senescence by flow cytometry
- Colony formation assay
- Wound healing assay
- Immunofluorescence microscopy for actin, and  $\gamma$ H2AX
- Analysis of mitochondrial morphology by confocal live cell-imaging
- Intracellular compartmentalization of compounds in lipid droplets by confocal live cell-imaging
- Analysis of mitochondrial membrane potential by confocal live cell-imaging
- Detection of SA- $\beta$ -Gal as a marker of cell senescence (together with Olszewski M.)

#### Experiment Interpretation

I have interpreted the following experiments:

- Antimicrobial susceptibility test (together with Olszewski M.)
- Cell viability assay using MTT assay (together with Olszewski M.)
- Flow cytometry analyses of  $\gamma$ H2AX as DNA damage marker (together with Olszewski M.)
- Flow cytometry analyses of reactive oxygen species generation
- Apoptosis and caspase 3/7 assay using flow cytometry and fluorescence microscopy
- Analyse cell senescence by flow cytometry
- Colony formation assay
- Analyse of antimigratory properties by wound healing assay
- Immunofluorescence microscopy for actin, and  $\gamma$ H2AX
- Analysis of mitochondrial morphology by confocal live cell-imaging
- Analysis of intracellular compartmentalization in lipid droplets by confocal live cell-imaging



## Writing

- Analysis of mitochondrial membrane potential by confocal live cell-imaging
- Detection of SA- $\beta$ -Gal, as a marker of cell senescence

I have written the following chapters (with English corrections and contributions from Bagiński M., Olszewski, M.):

- Abstract (together with Makowiec M.)
- Effects of carbazole derivatives on the viability of the panel of human cell lines
- Effects of new carbazole derivatives on cell cycle distribution
- Selective accumulation of 5aa and 8 in cancer cell LDs revealed by intrinsic fluorescence
- Antimigratory properties
- Apoptosis
- Effect of carbazole analogs on mitochondrial ROS generation
- Changes in mitochondrial morphology in HCT-116 cell line after treatment with 5aa and 8
- Oxidative DNA damage
- Induction of cell senescence
- Conclusion (together with Makowiec M.)
- Methods

## Figures Prepared

I have prepared the following figures:

- **Figure 2.** Effects of the carbazole derivatives on the viability of A-549, U-2 OS, HCT-116, Hep-G2, MCF-7, and HEK-293 cells after treatment for 72 h.
- **Figure 5** Colocalization analyses.
- **Figure 6** Analysis of cell migration by in vitro wound healing assay.
- **Figure 7** Apoptosis assay.
- **Figure 8** Flow cytometric analyses of ROS induction in HCT-116 (A) and U-2 OS (B) cells after 1, 3, 6, and 24 h of treatment with compounds 8 and 5aa, using H2DCFDA probe.
- **Figure 9** Analysis of  $\Delta\Psi_m$ . JC-1 staining images of HCT-116 (A) and U-2 OS (D) cells acquired after 6 and 24 h of treatment with 5aa and 8 (together with Olszewski, M.)
- **Figure 10** Quantitative mitochondrial morphometric analyses.
- **Figure 11** Representative microscopy images presenting immuno-fluorescence in HCT-116 (A) and U-2 OS (B) cells indicating the formation of  $\gamma$ -H2AX foci and changes in microtubule structure upon treatment with 5aa and 8 (24, 48, and 72 h. (together with Olszewski M.)
- **Figure 12** SA- $\beta$ -Gal staining
- **Figure S1** Colocalization analyses
- **Figure S2** Apoptosis assay

	<ul style="list-style-type: none"> <li>- <b>Figure S3</b> Flow cytometric analyses of ROS induction in HCT-116 cells after pre-treated with N-acetyl-L-cysteine (NAC).</li> <li>- <b>Figure S4</b> Quantitation of flow cytometric analysis of ROS induction in HCT-116 cells</li> <li>- <b>Figure S5</b> Flow cytometric analyses of ROS induction in U-2 OS cells after pre-treated with N-acetyl-L-cysteine (NAC).</li> <li>- <b>Figure S6</b> Quantitation of flow cytometric analysis of ROS induction in U-2 OS cells.</li> <li>- <b>Figure S7</b> SA-<math>\beta</math>-Gal staining</li> </ul>
Tables Prepared	- <b>Table S1</b> Antifungal and antibacterial activities of compounds defined as MIC [ $\mu$ M].
Literature Studies and References	I have prepared and compiled literature and references for this manuscript, besides the introduction part.

### **8.2. Project III - Novel chalcone-derived pyrazoles as potential therapeutic agents for the treatment of non-small cell lung cancer**

Conceptualization: Natalia Maciejewska

Methodology: Natalia Maciejewska; Mateusz Olszewski; Jakub Jurasz (molecular modeling); Marcin Serocki; Maria Dzierzynska & Katarzyna Cekala (compound synthesis)

Validation: Natalia Maciejewska

Formal analysis: Natalia Maciejewska; Mateusz Olszewski; Jakub Jurasz (molecular modeling)

Writing—original draft preparation: Natalia Maciejewska; Mateusz Olszewski (editing); Jakub Jurasz (molecular modeling); Maria Dzierzynska (results: Design of compounds, methods: Synthesis of the designed compounds, General procedure for the synthesis of chalcones, General procedure for the synthesis of chalcone-derived pyrazoles)

Graphical conceptualization: Natalia Maciejewska

Writing—review and editing: Natalia Maciejewska; Ewa Wieczerzak; Maciej Baginski

#### **The extended list of authors' contribution**

Part	Contribution
Publication Design	I have designed the outline of the manuscript.
Experimental and Planning	I have planned the following experiments: <ul style="list-style-type: none"> <li>- Cell viability assay using MTT assay (together with Olszewski M.)</li> <li>- Colony formation assay</li> <li>- Morphology assessment</li> <li>- Flow cytometry analyses of the cell cycle with propidium iodide (PI) staining</li> </ul>



- Immunofluorescence microscopy for tubulin, and aurora B
- Apoptosis and caspase 3/7 assay using flow cytometry and fluorescence microscopy
- Analysis apoptotic and EMT-related proteins by Western blot
- Analyse anti-migratory properties by wound healing assay
- Flow cytometry analyses of reactive oxygen species generation

#### Experiment Execution

I have executed the following experiments:

- Cell viability assay using MTT assay
- Colony formation assay
- Morphology assessment
- Flow cytometry analyses of the cell cycle with propidium iodide (PI) staining (together with Olszewski M.)
- Immunofluorescence microscopy for tubulin, and aurora B
- Apoptosis and caspase 3/7 assay using flow cytometry and fluorescence microscopy (together with Olszewski M.)
- Analysis apoptotic and EMT-related proteins by Western blot
- Analyse anti-migratory properties by wound healing assay
- Flow cytometry analyses of reactive oxygen species generation

#### Experiment Interpretation

I have interpreted the following experiments:

- Cell viability assay using MTT assay
- Colony formation assay
- Morphology assessment
- Flow cytometry analyses of the cell cycle with propidium iodide (PI) staining
- Immunofluorescence microscopy for tubulin, and aurora B
- Apoptosis and caspase 3/7 assay using flow cytometry and fluorescence microscopy (together with Olszewski M.)
- HTS-tubulin polymerization assay
- Analysis apoptotic and EMT-related proteins by Western blot
- Analyse anti-migratory properties by wound healing assay
- Flow cytometry analysis of reactive oxygen species generation

#### Writing

I have written the following chapters:

- Abstract
- Introduction
- **PCH-1** compound shows the potent cytotoxic effect towards NSCLC and non-toxic to normal cells
- **PCH-1** arrest cells in G2/M checkpoint
- **PCH-1** disrupt microtubule assembly
- **PCH-1** induce caspase-dependent apoptotic cell death
- **PCH-1** deregulates several apoptotic and EMT-related proteins
- **PCH-1** induce intracellular oxidative stress
- Discussion
- Methods

Figures Prepared

I have prepared the following figures:

- **Figure 2** (a) Effect of compound **PCH-1** on cell viability after 72 h incubation with compound (b) Representative photos of the colony formation assay are presented on the left panel and its quantification is depicted on the right panel.
- **Figure 3** cell cycle analyses of A-549, H226, and H460 cells after **PCH-1** treatment. (together with Olszewski M.)
- **Figure 4** (a) Kinetic curves of a 120-min kinetic reaction of tubulin polymerization. Representative microscopy images (b–j) presenting immunofluorescence of microtubule assembly and Aurora B in A-549 cells after 6 h of treatment.
- **Figure 5** Representative microscopy images presenting immunofluorescence of microtubule assembly and Aurora B in A-549 cells at 6, and 24 h of treatment with **PCH-1**.
- **Figure 6** western blotting analyses showing the effects of **PCH-1** on the expression of apoptotic, and EMT-related proteins in the A-549 cell line.
- **Figure 7** Analysis of cell migration by in vitro wound healing assay.
- **Figure 9** Molecular mechanism of action **PCH-1** compound against lung cancer cells.
- **Figure S1** Flow cytometric analysis of A-549, H226, and H460 cells after Alexa Fluor 488 Annexin V /PI staining.
- **Figure S2** Fluorescence images of A-549, H226, and H460 cells at 6, 24, and 48 h of treatment with **PCH-1** or DMSO.
- **Figure S3** Flow cytometric analyses of caspase-3/7 activation in A-549, H226, and H460 cell lines at 6, 24, and 48 h of treatment.
- **Figure S4 (a-c)** Full length western blot presented in Figure 6 of the main article. Red boxes denote the cropped regions of the blots.
- **Figure S4 d** Representative images of a nitrocellulose membranes stained with Ponceau S dye for protein detection during western blot.
- **Figure S5** Analysis of TGF- $\beta$ 1 stimulated and unstimulated A-549 cell migration after treatment with **PCH-1** by in vitro wound healing assay presented as time-lapse microscopy images after culture insert removal.
- **Figure S6** Flow cytometry analyses of ROS level at 3, 6, and 24 h of treatment A-549 cells with **PCH-1**.
- **Table 1** Chemical structures of approved and clinically tested chalcones.

Tables Prepared

Literature Studies  
and References

- **Table 3** In vitro growth inhibitory activity of pyrazoles and reference compounds presented as an  $IC_{50} \pm SD$  ( $\mu M$ ) value representing a concentration that inhibits 50% of cell growth.

I have prepared and compiled literature and references for this manuscript.

## PROFESSIONAL EXPERIENCE

- January 2022 – Present      Department of Pharmaceutical Technology and Biochemistry  
Faculty of Chemistry  
Gdansk University of Technology  
**Project leader**  
**Project:** NCN grant PRELUDIUM 21: UMO-2021/41/N/NZ7/03707  
*Anticancer activity of novel derivatives of 9,10-anthraquinone dithiocarbamates*
- February 2022 – September 2022      Molecular Pharmacology Unit  
Department of Experimental Oncology and Molecular Medicine  
Fondazione IRCCS Istituto Nazionale dei Tumori di Milano  
**Research intern**  
**Project:** InterPhD2 Program: *Development of interdisciplinary doctoral program with international dimension* funded by European Union under the European Social Fund (Project No. POWR.03.02.00-IP.08-00-DOK/16)  
**Academic fellowship:** *G-quadruplex-ligands as novel therapeutics for dedifferentiated liposarcoma*
- September 2017 – January 2022      Department of Pharmaceutical Technology and Biochemistry,  
Faculty of Chemistry  
Gdansk University of Technology  
**Research investigator**  
**Project:** NCBiR grant: STRATEGMED3/306853/9/NCBR/2017  
*New anticancer compounds interfering function of telomeres (Targetello)*
- January 2021 – March 2021      Department of Pharmaceutical Technology and Biochemistry  
Faculty of Chemistry  
Gdansk University of Technology  
**Research investigator**  
**Project:** NCBiR grant: POIR.01.01.01-00-0353/17-00  
*Technology of extraction of polyphenolic compounds in the production of raw materials for the production of dietary supplements and anticancer medical components*



## SCIENTIFIC ACHIEVEMENTS

### Publication in Journals indexed by Journal Citation Report (list A)

1. Chylewska, A., Dąbrowska, A., Ramotowska, S., **Maciejewska, N.**, Olszewski, M., Bagiński, M., Makowski, M. *The photosensitive and pH-dependent activity of pyrazine-functionalized carbazole derivative as promising antifungal and imaging agent*. Scientific Reports **10** (2020) <https://doi.org/10.1038/s41598-020-68758-w> (IF<sup>1</sup>: 4.379; MEiN<sup>2</sup>: 140; Q1)
2. Lica J., Wieczór, M., Grabe G.J., Heldt M., Jancz, M., Misiak M., Gucwa, K., Brankiewicz, W., **Maciejewska, N.**, Stupak, A., Bagiński M., Rolka, K., Hellmann A., Składanowski A., *Effective Drug Concentration and Selectivity Depends on Fraction of Primitive Cells*. International Journal of Molecular Sciences **22** (2021) <https://doi.org/10.3390/ijms22094931> (IF<sup>1</sup>: 6.208; MEiN<sup>2</sup>: 140; Q1)
3. Marković, S.M, **Maciejewska, N.**, Olszewski, M., Višnjevac, A., Puertad, A., Padrón, J. M., Novaković, I., Kojić, S., Fernandes, H. S., Sousag, S. F., Ramotowska, S., Chylewska, A., Makowski, M., Todorović, T. R., Filipović, N. R. *Study of the anticancer potential of Cd complexes of selenazoyl-hydrazones and their sulphur isosters*. European Journal of Medicinal Chemistry **238** (2022) <https://doi.org/10.1016/j.ejmech.2022.114449> (IF<sup>1</sup>: 7.008; MEiN<sup>2</sup>: 140; Q1)
4. Witkowska, M. §, **Maciejewska, N. §**, Ryczkowska, M., Olszewski, M., Baginski, M., Makowiec, M., *From tryptophan to novel mitochondria-disruptive agent, synthesis and biological evaluation of 1,2,3,6-tetra-substituted carbazoles*. European Journal of Medicinal Chemistry **238** (2022) <https://doi.org/10.1016/j.ejmech.2022.114453> (IF<sup>1</sup>: 7.008; MEiN<sup>2</sup>: 140; Q1)
5. Mech-Warda, P., Gieldoń, A., Kawiak, A., **Maciejewska, N.**, Olszewski, M., Makowski, M., Chylewska, A. *Low-Molecular Pyrazine-Based DNA Binders: Physicochemical and Antimicrobial Properties*. Molecules **27** (2022) <https://doi.org/10.3390/molecules27123704> (IF<sup>1</sup>: 4.148; MEiN<sup>2</sup>: 140; Q2)
6. Ryczkowska, M. §, **Maciejewska, N. §**, Olszewski, M., Witkowska, M., Makowiec, M., *Design, synthesis, and biological evaluation of tetrahydroquinolinones and tetrahydroquinolines with anticancer activity*. Scientific Reports **12** (2022) <https://doi.org/10.1038/s41598-022-13867-x> (IF<sup>1</sup>: 4.996; MEiN<sup>2</sup>: 140; Q1)
7. **Maciejewska, N.**, Olszewski, M., Jurasz, J., Serocki, M., Dzierzynska, M., Cekala, K., Wieczerek, E., Baginski, M., *Novel chalcone-derived pyrazoles as potential therapeutic agents for the treatment of non-small cell lung cancer*. Scientific Reports **12** (2022) <https://doi.org/10.1038/s41598-022-07691-6> (IF<sup>1</sup>: 4.996; MEiN<sup>2</sup>: 140 Q1)

Cumulative Impact Factor: 37.943

§ Contributed equally

✉ Corresponding author

<sup>1</sup> 2-year Impact Factor (IF) according to Journal Citation Report for the 2021 year. All numbers are based on Scimago Journal & Country Rank (<https://www.scimagojr.com/>, accessed July 2022).

<sup>2</sup> Journal ratings according to the Ministry of National Education (MEiN) for the 2022 year. All numbers are based on the publicly available search engine (<https://punktacjczasopism.pl/>, accessed July 2022).

### Chapters in scientific monographs in Polish:

1. **Maciejewska, N.**, Baginski, M., *Telomeraza jako cel terapii przeciwnowotworowej*, Na pograniczu chemii i biologii, tom XXXVIII, Wydawnictwo naukowe UAM 79-90, ISBN: 978-83-232-3432-6 (2018)

## Post-conference publications:

1. **Maciejewska, N.**, Baginski, M., *Future of medicine: personalized oncology*, The Book of Articles National Scientific Conference „Zrozumieć Naukę” II edition, 127-133, ISBN: 978-83-950109-4-1 (2018)

## Conference presentations in English

1. **Maciejewska, N.**, Olszewski, M., Jurasz, J., Stasevych, M., Zvarych, V., Baginski, M., *Telomerase inhibition with preferential persistent damage of telomeres*, Cancer cell signalling: Linking molecular knowledge to cancer therapy, Cavtat, Croatia, 16.09.22–20.09.22
2. **Maciejewska, N.**, Olszewski, M., Baginski, M., *Discovery of new pyrazole derivatives disrupting microtubule assembly*, Congress - Innovative Cancer Science: Translating Biology to Medicine, Sevilla, Spain, 20.06.22-23.06.22
3. **Maciejewska, N.**, Serocki, M., Baginski, M., Stasevych, M., Zvarych, V., Novikov, V., *Dithiocarbamates of 9,10-anthracenedione disrupt telomere function by telomerase inhibition*. EFMC-ISMIC & EFMC-YMCS Virtual Poster Session, 9.09.2020
4. **Maciejewska, N.**, Serocki, M., Lapiejko M., Baginski, M., Stasevych, M., Zvarych, V., Novikov, V., *Biological evaluation of new small-molecule anthraquinone-based derivatives*. VII EFMC International Symposium on Advances in Synthetic and Medicinal Chemistry, Athens, Greece, 1.08–5.08.2019
5. **Maciejewska, N.**, Serocki, M., Jurasz, J., Baginski, M., Stasevych, M., Zvarych, V., Novikov, V., *New anticancer compounds with dual mechanisms of action as inhibitors of tyrosine kinase protein and telomerase: in silico studies and biological evaluation*. EFMC-YMCS 6<sup>th</sup> EFMC Young Medicinal Chemist Symposium, Athens, Greece, 5.08-6.08.2019
6. **Maciejewska, N.**, Serocki, M., Lapiejko M., Baginski, M., Stasevych, M., Zvarych, V., Novikov, V., *Novel dithiocarbamates derivatives of 9,10-anthracenedione as potential anticancer agents*. Structural and Molecular Biology of the DNA Damage Response, Madrid, Spain, 20.05-22.05.2019
7. **Maciejewska, N.**, Baginski, M., *Effect of selected methylxanthines derivatives on telomerase activity in lung carcinoma cells*. 5th EFMC Young Medicinal Chemist Symposium, Lubljana, Slovenia, 6.09–7.09.2018
8. **Maciejewska, N.**, Baginski, M., *Caffeine – new insight of known antioxidant*, Congress Bio2018, Gdansk, Poland, 17.09–21.09.2018

## Patent application

1. Brankiewicz, W., Baginski, M., Padariyam, M., Kalathiya, U., Prusinowski, M., Wegrzyn, K., Drab, M., Makowiec, S., Zyllich-Stachula, A., Zebrowska, J., Skowron, P., **Maciejewska, N.**, Szajewski, M., Krzemieniecki, R., PCT/PL2022/050017 – *New anticancer compounds interfering function of telomeres* (2020).

## ANNEXES

**A1 PUBLICATION:** Witkowska, M.§, **Maciejewska, N.§**, Ryczkowska, M., Olszewski, M., Baginski, M., Makowiec, From tryptophan to novel mitochondria-disruptive agent, synthesis and biological evaluation of 1,2,3,6-tetrasubstituted carbazoles, *European Journal of Medicinal Chemistry* **238**, 114453 (2022). <https://doi.org/10.1016/j.ejmech.2022.114453> IF 7.008 (2022), MEiN 140 (2022)

**A2 PUBLICATION:** **Maciejewska, N.**, Olszewski, M., Jurasz, J., Serocki, M., Dzierzynska, M., Cekala, K., Wieczerzak, E., Baginski, M., Novel chalcone-derived pyrazoles as potential therapeutic agents for the treatment of non-small cell lung cancer, *Scientific Reports* **12**, 3703 (2022). <https://doi.org/10.1038/s41598-022-07691-6> IF 4.996 (2022), MEiN 140 (2022)

**§ Contributed equally**



## From tryptophan to novel mitochondria-disruptive agent, synthesis and biological evaluation of 1,2,3,6-tetrasubstituted carbazoles

Milena Witkowska<sup>a,1</sup>, Natalia Maciejewska<sup>b,1</sup>, Małgorzata Ryczkowska<sup>a</sup>, Mateusz Olszewski<sup>b</sup>, Maciej Bagiński<sup>b</sup>, Sławomir Makowiec<sup>a,\*</sup>

<sup>a</sup> Department of Organic Chemistry, Faculty of Chemistry, Gdansk University of Technology, Narutowicza 11/12, 80-233, Gdansk, Poland

<sup>b</sup> Department of Pharmaceutical Technology and Biochemistry, Faculty of Chemistry, Gdansk University of Technology, Narutowicza 11/12, 80-233, Gdansk, Poland

### ARTICLE INFO

#### Keywords:

Carbazole  
Oxidative cyclization  
Manganese  
Indole  
Apoptosis  
ROS  
DNA damage  
Colon cancer  
Osteosarcoma

### ABSTRACT

Mitochondrial targeting plays an important role in anticancer therapy. The Mn(III)-promoted cyclization of 5-(1H-indol-3-yl)-3-oxopentanoic acid allow to obtain novel substituted carbazole derivatives that can act as mitochondria-disruptive agents. The starting materials used for the synthesis of these new aminocarbazoles are oxopentanoate derivatives of tryptophan. The scope and limitation of this method of synthesis are determined by a series of experiments. The prepared carbazole derivatives are screened for their *in vitro* anticancer activity against a broad panel of human cancer cells and normal cell lines. Among the tested compounds, the most active ones are examined further against human colon cancer cells (HCT-116) and human bone osteosarcoma (U-2 OS), in complex *in vitro* cellular assays, including studies on cell cycle distribution, intracellular compartmentalization, antimigratory properties, mitochondrial generation of reactive oxygen species, DNA damage, and type of cellular death. The results reveal that the synthesized compounds display potent oxidative activity inducing massive accumulation of DNA double-strand breaks, which lead to a parallel change in the assembly of mitochondria causing their dysfunction. These findings provide new leads for the treatment of colon cancer and osteosarcoma.

### 1. Introduction

For over half a century, the carbazole scaffolds have been a predominant structural motif of many biologically active compounds used in medicine, including both natural and synthetic molecules. The carbazole motif can be found in drugs including alkaloids [1,2], HIV-integrase inhibitors [3], antipapillomavirus agent [4],  $\alpha$ - and  $\beta$ -adrenoreceptor antagonists [5,6], antinausea drug ondasteron [7], antitumor agents [8,9], and antimicrobial agents [10]. However, to ensure a wide application of carbazole derivatives, there is a need to develop efficient methods of synthesis. A significant number of synthesis methods have been proposed for these derivatives so far. Among them, we can specify the synthetic routes based on the reaction of biaryls. These routes include the use of a biphenyl moiety bearing a nitrogen atom in ortho position which reacts mostly by oxidative cyclization pathway to produce a carbazole structure with  $\text{PhI}(\text{OAc})_2$  as an oxidizer [11,12], cyclization of biphenyl ortho-substituted triazene moiety [13],

reductive cyclization of *o*-nitrobiaryls [14], and double *N*-arylation of 2,2'-biphenylene ditriflate (Scheme 1) [15]. Another group of the proposed approaches makes use of an indole fragment and results in the formation of a third aromatic ring. These include gold-catalyzed cyclization of 3-acylindole/yne [16], reaction of indole-ynes with nitromethanes [17], Pd/Cu-cocatalyzed cross-coupling of 2-allyl-3-iodoindoles with terminal alkynes [18], and synthesis of carbazoles from indoles, ketones, or alkenes using oxygen as an oxidant [19].

The third group of approaches for the synthesis of carbazole derivatives involves the use of two separate phenyl systems as starting materials. These include oxidative ring fusion using hypervalent iodine compounds [20] and palladium-catalyzed *N*-arylation followed by oxidative biaryl coupling [21].

Recently, we developed a method for the formation of functionalized carbazoles using indole derivatives as starting materials. In this method, 5-(1H-indol-yl)-3-oxo-pentanoate undergoes oxidative cyclization and

\* Corresponding author.

E-mail address: [mak@pg.edu.pl](mailto:mak@pg.edu.pl) (S. Makowiec).

<sup>1</sup> These authors contributed equally.

<https://doi.org/10.1016/j.ejmech.2022.114453>

Received 7 October 2021; Received in revised form 27 April 2022; Accepted 7 May 2022

Available online 13 May 2022

0223-5234/© 2022 Elsevier Masson SAS. All rights reserved.





aromatization with a manganese triacetate or  $\text{NEt}_3/\text{I}_2/\text{Ln}(\text{OTf})_3$  system [22]. However, we focused on designing and synthesizing a carbazole core with improved anticancer properties. According to previous *in silico* studies, a carbazole scaffold functionalized with one or two amino groups at positions 3 and 6 can show enhanced anticancer potency if it is acylated or alkylated [23,24].

A combination of these two ideas—developing a new method for the preparation of functionalized carbazole scaffold and improving its pharmacological properties—prompted us to investigate if it is possible to obtain a carbazole scaffold with amino groups at positions 3 and 6 through oxidative cyclization of 5-(1H-indol-yl)-3-oxo-pentanoates and subsequently subject the prepared carbazoles to acylation or alkylation (Fig. 1). Although a number of carbazole derivatives with anticancer potential have been discovered in the past two decades, the phenomenon of chemoresistance of tumors urges us to search for novel molecules with anticancer properties. Therefore, in this work, we synthesized a series of new 3,6-substituted carbazole derivatives and examined their antiproliferative activity, in order to develop potent antitumor agents.

## 2. Results and discussion

### 2.1. Chemistry

As described in our previous work, for undergoing oxidative cyclization with an  $\text{Mn}(\text{OAc})_3$  or  $\text{NEt}_3/\text{I}_2/\text{Ln}(\text{OTf})_3$  system, the substrate must contain indole and 3-oxopentane fragments. Thus, tryptophan was used as a substrate as it contains an amine group at position 3. The availability of substrates plays an important role in the selection of such an approach. A wide range of tryptophan derivatives, which are the substrate at the first stage of synthesis, are available. However, in the light of oxidizing conditions during the cyclization reaction, the presence of an amino group can lead to undesirable side reactions. In addition, for introducing two amino/amido/hydroxy groups, the tryptophan derivative used for cyclization must be functionalized with an

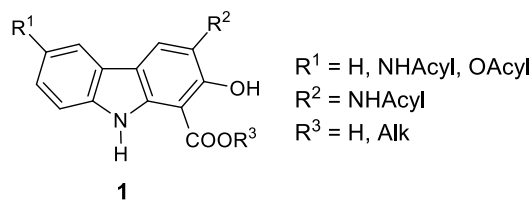
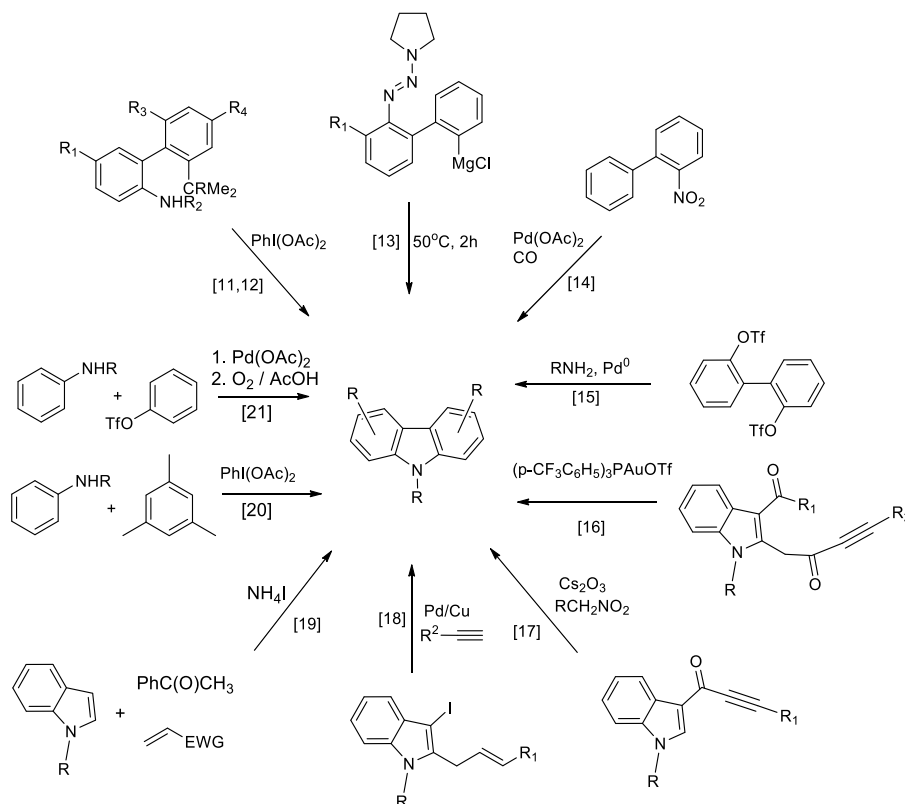


Fig. 1. Structures of the newly designed carbazoles.

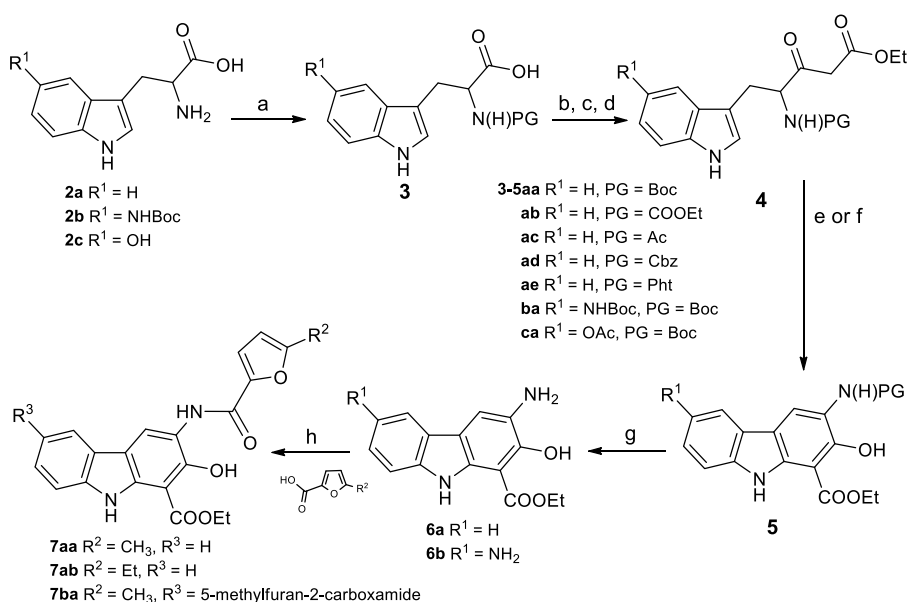
amino, amido, or hydroxyl group at position 6. The synthetic strategy used for the preparation of compounds based on 1,2,3,6-tetrasubstituted carbazole scaffold is depicted in Scheme 2.

Tryptophans **2** were protected in a typical manner with five different protective groups: permanent Pht [25], Ac [26], etoxycarbonyl [27], and two easily removable Z [28] and Boc [29]. In the next step, a tryptophan derivative was activated with carbonyldiimidazole followed by the carbon acylation of potassium enolate, resulting in the formation of ketoesters **4** [30,31]. Based on our previous experience with oxidative cyclization of 3-oxoesters and 3-oxoamides [22] at the key stage of synthesis, we decided to investigate two available methods. The first one involved the generation of 1,3-dicarbonyl radicals using manganese triacetate followed by cyclization and subsequent oxidation and aromatization [32–35]. The second method was applied for ring closure using a combination of transition metal triflates together with iodine in the presence of a tertiary amine. The results obtained for the cyclization of ketoesters **4** are presented in Table 1.

The experiments clearly demonstrated that application of manganese triacetate is advantageous for the cyclization of ketoesters. Yttrium triflate showed low effectiveness, whereas scandium triflate did not show any benefits in the cyclization of ethyl 3-((*tert*-butoxycarbonyl)amino)-2-hydroxy-9H-carbazole-1-carboxylate. These results are in line with our previous observations which also proved that  $\text{Mn}(\text{OAc})_3$  was



Scheme 1. Selected examples of the synthesis routes of carbazole scaffold.



**Scheme 2.** Reagents and conditions used for the preparation of compounds based on 1,2,3,6-tetrasubstituted carbazoles scaffold: (a) PA, 190 °C, 15' or Ac<sub>2</sub>O, MeOH, 12 h or Boc<sub>2</sub>O, NaHCO<sub>3</sub>, dioxane, 24 h or Cbz-Cl, K<sub>2</sub>CO<sub>3</sub>, Acetone; H<sub>2</sub>O; (b) CDI, THF, 2 h, 20 °C (c) MgCl<sub>2</sub>, KOOCCH<sub>2</sub>COOEt, 1 h, 20 °C, (d) 50 °C, 12 h; (e) Mn(OAc)<sub>3</sub>·2H<sub>2</sub>O 2.5 eq, AcOH, 2.5 h, 70 °C (f) M(OTf)<sub>3</sub> 2 eq, NEt<sub>3</sub> 2.5 eq, I<sub>2</sub> 1.5 eq, DCM, 12h, 20 °C; (g) Only in the case of PG or R<sup>1</sup> = NHBoc, TFA, DCM, 2h, 20 °C; (h) TBTU, NEt<sub>3</sub>, DMF.

**Table 1**  
Results of oxidative cyclization of ketoesters **4**.

Entry	4, 5	MX <sub>3</sub>	R <sup>1</sup>	PG	Yield of 5 [%]
1	aa	Y(OTf) <sub>3</sub>	H	Boc	12
2	aa	Sc(OTf) <sub>3</sub>	H	Boc	–
3	aa	Mn(OAc) <sub>3</sub>	H	Boc	67
4	ab	Mn(OAc) <sub>3</sub>	H	COOEt	28
5	ac	Mn(OAc) <sub>3</sub>	H	Ac	29
6	ad	Mn(OAc) <sub>3</sub>	H	Cbz	–
7	ae	Y(OTf) <sub>3</sub>	H	Pht	–
8	ae	Sc(OTf) <sub>3</sub>	H	Pht	–
9	ae	Mn(OAc) <sub>3</sub>	H	Pht	–
10	ba	Mn(OAc) <sub>3</sub>	NHBoc	Boc	36
11	ca	Mn(OAc) <sub>3</sub>	OAc	Boc	25

effective for the cyclization of ketoesters while transition metal triflates with iodine should be used for the cyclization of ketoamides [22].

It was observed that the phthaloyl-protected derivative did not undergo oxidative cyclization regardless of the applied oxidation system. This finding is surprising considering that this derivative was believed to be the least susceptible to side reactions when in contact with an oxidizing reagent. We also did not obtain the desired product with Cbz-protected derivative; however, in this case, we expected a negative result due to the possible oxidation and radical reactions of benzyl protons.

Molecular docking performed in studies on anticancer agents [23] indicated that an effective structure should contain a second acyloamino or acyloxy group at position 6 of the carbazole system. Therefore, we attempted to prepare compounds **5ba** and **5ca**. In addition, molecular docking studies indicated the need for a five-member aromatic ring with one or two amino groups as a substituent. Thus, in the next step, we removed the acid-labile amino protective group and performed acylation with 2-furoic acid or 5-methyl-2-furoic acid under typical conditions. The results of the synthesis of furanoyl derivatives are summarized in Table 2.

**Table 2**  
Synthesis of ethyl 3-(5-alkylfuran-2-carboxamido)-2-hydroxy-9H-carbazole-1-carboxylate derivatives **7aa-ba**.

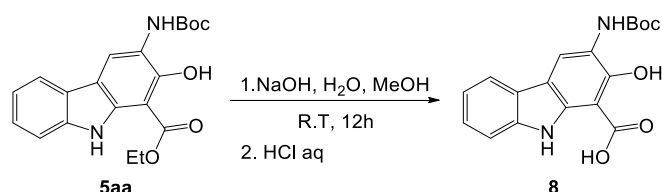
Run	5	R <sup>1</sup>	R <sup>2</sup>	R <sup>3</sup>	R <sup>4</sup>	7	Yield of 7 [%]
1	aa	H	CH <sub>3</sub>	H	H	aa	15
2	aa	H	Et	H	H	ab	31
3	ba	NHBoc	CH <sub>3</sub>			ba	54

To increase water solubility and bioavailability, the most promising compound **5aa** was saponified to obtain 3-((*tert*-butoxycarbonyl)amino)-2-hydroxy-9H-carbazole-1-carboxylic acid **8** (Scheme 3).

## 2.2. Biological activity

### 2.2.1. Effects of carbazole derivatives on the viability of the panel of human cell lines

The newly synthesized carbazole derivatives were screened for their *in vitro* anticancer activity against a broad panel of human cancer cell lines, including human non-small cell lung adenocarcinoma (A-549), human colon cancer (HCT-116), human bone osteosarcoma (U-2 OS), human breast carcinoma (MCF-7), human liver cancer cells (Hep-G2), and normal human embryonic kidney cells (HEK293) using the colorimetric MTT (3-(4,5-dimethylthiazol-2-yl)-2,5-diphenyltetrazolium bromide) assay. We found that most of the compounds were inactive at IC<sub>50</sub>



**Scheme 3.** Saponification of ester **5aa**.

> 50  $\mu\text{M}$  (half maximal inhibitory concentration or  $\text{IC}_{50}$  refers to the concentration of a compound required to inhibit cell growth by 50% compared to the untreated control), while others exhibited a moderate (**9**, **5ca**) or remarkable (**5aa**, **8**) activity toward the tested cell lines (Table 3). Among the cancer cell lines used for the analysis, **5aa** and **8** showed potent antiproliferation activity at submicromolar concentrations against HCT-116 and U-2 OS cells after 72 h of treatment (Fig. 2 and Table 3).

Compared to **5aa**, compound **8** showed a significant 3–6 times higher cytotoxic potency (Fig. 2). The  $\text{IC}_{50}$  of compound **8** determined for HCT-116 and U-2 OS cells was  $3.75 \pm 0.49$  and  $2.35 \pm 0.24$   $\mu\text{M}$ , respectively (Table 3). Although, none of the tested compounds displayed toxicity against the human noncarcinogenic HEK-293 cell line. Further studies were carried out only on the most cytotoxic compounds **5aa** and **8** to compare the changes in their biological activity depending on their structure. In addition, the compounds were tested for antimicrobial activity. The obtained results indicated that the compounds did not show any activity against the tested strains of bacteria and fungi, which proves their selectivity toward cancer cells (Table S1, Supporting Information).

### 2.2.2. Effects of new carbazole derivatives on cell cycle distribution

To investigate whether the high cytotoxic activity of the newly synthesized compounds (**5aa**, **8**) was caused by the cell cycle arrest, we analyzed the DNA content of cells by flow cytometry. The stained DNA histograms of A-549, HCT-116, and U-2 OS cells treated with each of the derivatives at the  $\text{IC}_{50}$  values for 24, 48, and 72 h are shown in Fig. 3. For HCT-116 cell line, the highest number of cells were observed in the G2/M phase, a moderate number in the S phase, and the least number in the G0/G1 phase after 24 h of treatment with compound **8**. Similar results were observed for all cell lines after 24 h of treatment with this compound. In HCT-116 cell line, continuous treatment with **8** induced the S phase arrest which lasted for 72 h. However, in A-549 cell line, cell cycle progression through the G2/M phase peaked between 24 and 48 h, and the cells were finally arrested in the S phase after 72 h of incubation.

Colony formation assays were performed to measure the clonogenic survival of HCT-116 and U-2 OS cell lines which were the most susceptible to the tested compounds. The results showed that both compounds **5aa** and **8** significantly decreased the colony-forming ability of cell lines compared to the control group (1% dimethyl sulfoxide (DMSO) alone), and the effect was more pronounced with increasing doses (Fig. 4A and Fig. 4B). Compound **8** caused a greater decrease in

**Table 3**

*In vitro* anticancer activity of carbazole derivatives ( $\text{IC}_{50} \pm \text{SD}$  ( $\mu\text{M}$ )) on A-549, HCT-116, U-2 OS, MCF-7, Hep-G2, and HEK-293 cell lines.

Compound	Cell Lines					
	HCT-116	A-549	MCF-7	U-2 OS	Hep-G2	HEK-293
	$\text{IC}_{50}$ [ $\mu\text{M}$ ]					
<b>9<sup>22</sup></b>	$28.82 \pm 1.432$	>50	>50	$43.17 \pm 2.07$	>50	>50
<b>4aa</b>	>50	>50	>50	>50	>50	>50
<b>5aa</b>	$10.73 \pm 0.61$	$16.94 \pm 0.75$	>50	$15.65 \pm 1.50$	>50	>50
<b>5ab</b>	>50	>50	>50	>50	>50	>50
<b>5ac</b>	>50	>50	>50	>50	>50	>50
<b>5ba</b>	>50	>50	>50	>50	>50	>50
<b>5ca</b>	$46.43 \pm 3.25$	>50	>50	$37.50 \pm 2.13$	>50	>50
<b>7aa</b>	>50	>50	>50	>50	>50	>50
<b>7 ab</b>	>50	>50	>50	>50	>50	>50
<b>7ba</b>	>50	>50	>50	>50	>50	>50
<b>8</b>	$3.75 \pm 0.49$	$11.50 \pm 1.23$	>50	$2.35 \pm 0.24$	>50	>50
<b>5-FU</b>	$5.78 \pm 0.38$	$8.12 \pm 1.01$	$8.41 \pm 0.98$	$13.02 \pm 0.03$	$18.98 \pm 1.98$	$41.01 \pm 0.87$

clonogenicity in U-2 OS (Fig. 4C) and HCT-116 (Fig. 4D) cell lines (75.5% (1  $\mu\text{M}$ ) and 84.5% (10  $\mu\text{M}$ ), respectively), compared to **5aa**.

### 2.2.3. Selective accumulation of **5aa** and **8** in cancer cell LDs revealed by intrinsic fluorescence

The inherent fluorescence of compounds allowed determining their fate in living cells by high-resolution laser scanning confocal microscopy. The local fluorescence of both compounds suggested their compartmentalization to a specific intracellular organelle, and thus their accumulation in adiposomes. The cell distribution of the tested compounds was evaluated after short-term exposure and after co-labeling with the neutral lipid dye BODIPY. In the HCT-116 cell line, after 2 h of treatment, localization of **8** and **5aa** was clearly visible, with considerable accumulation in lipid droplets (LDs) (Fig. 5A–C and Figs. S1A–C). To evaluate whether the signal of the compounds spatially overlapped with that of BODIPY, correlations of overlapping pixel intensities were calculated using thresholded Mander's (MCC) and Pearson's colocalization coefficient (PCC) (Fig. 5F and Fig. S1F, Supporting Information). The results showed high correlation coefficients for both **5aa** (MCC:  $0.922 \pm 0.055$ ; PCC:  $0.723 \pm 0.046$ ) and **8** (MCC:  $0.935 \pm 0.067$ ; PCC:  $0.811 \pm 0.056$ ), indicating the substantial colocalization between compounds- and BODIPY-derived signals. This proves that **5aa** and **8** selectively accumulated in the LDs of the treated cells. Representative line scan (corresponding to the top panel in Fig. 5A) showing the colocalization of LDs with compounds is presented in Fig. 5D and Fig. S1D. Scatter plots showing the correlations of compound/BODIPY pixel intensities are depicted in Fig. 5E and Fig. S1E. The mechanism of accumulation of compounds in adiposomes is unknown, but it can be assumed that the high hydrophobic character of those molecules favored their selective partitioning into an oil-like hydrophobic environment inside LDs. Recent reports suggest that the efficacy of drugs can be modulated by LDs, which constitute their store and supplement the enzymes necessary for the metabolism of hydrophobic small molecules, influencing their activation [36].

### 2.2.4. Antimigratory properties

One of the first steps of cancer metastasis is cell migration, which is a hallmark of malignancy. Therefore, we studied the antimigratory effect of carbazole derivatives on HCT-116 and U-2 OS cell lines using a wound healing assay. In comparison to solvent-treated cells, treatment with compounds **8** and **5aa** caused dose-dependent inhibition of migration in both cells, which was tracked by time-lapse microscopy (Fig. 6A and Fig. 6B). After 24 h of exposure to the tested compounds, the inhibition of migration in HCT-116 cell line was not found to be significant. However, treatment with 10  $\mu\text{M}$  of each compound caused significant inhibition of migration after 60 h ( $56.97 \pm 9.64\%$  and  $64.37 \pm 6.181\%$  by **5aa** and **8**, respectively) (Fig. 6C). The antimigratory property of **5aa** was less pronounced in U-2 OS cells, but compound **8** showed a greater antimigratory activity in these cells in comparison to HCT-116 cells (Fig. 6C and D). Interestingly, the migration-inhibitory effect of **8** was higher in both cell lines and at any point in time of treatment in comparison to **5aa**.

### 2.2.5. Apoptosis

To further assure the proapoptotic activity of compounds **5aa** and **8**, a flow cytometric analysis was performed, after dual-staining the cells with 7-aminoactinomycin D (7-AAD) and Annexin V-fluorescein isothiocyanate (FITC) which allows differentiating the viable, early apoptotic, late apoptotic, and necrotic cells. After 6 h of treatment with compound **5aa** and **8** at their  $\text{IC}_{50}$  concentration, a significant decrease in the percentage of surviving cells was observed for HCT-116 cell line (Fig. 7A and Fig. 7B). An increase in the percentage of early apoptotic cells was observed with both compounds, but only in the case of cells treated with **8** the increase was significant ( $11.23 \pm 2.97\%$ ;  $p < 0.01$ ). As shown in Fig. 7A and B, after 24 h of exposure to both compounds, a threefold augmentation in apoptosis (early and late) was observed in

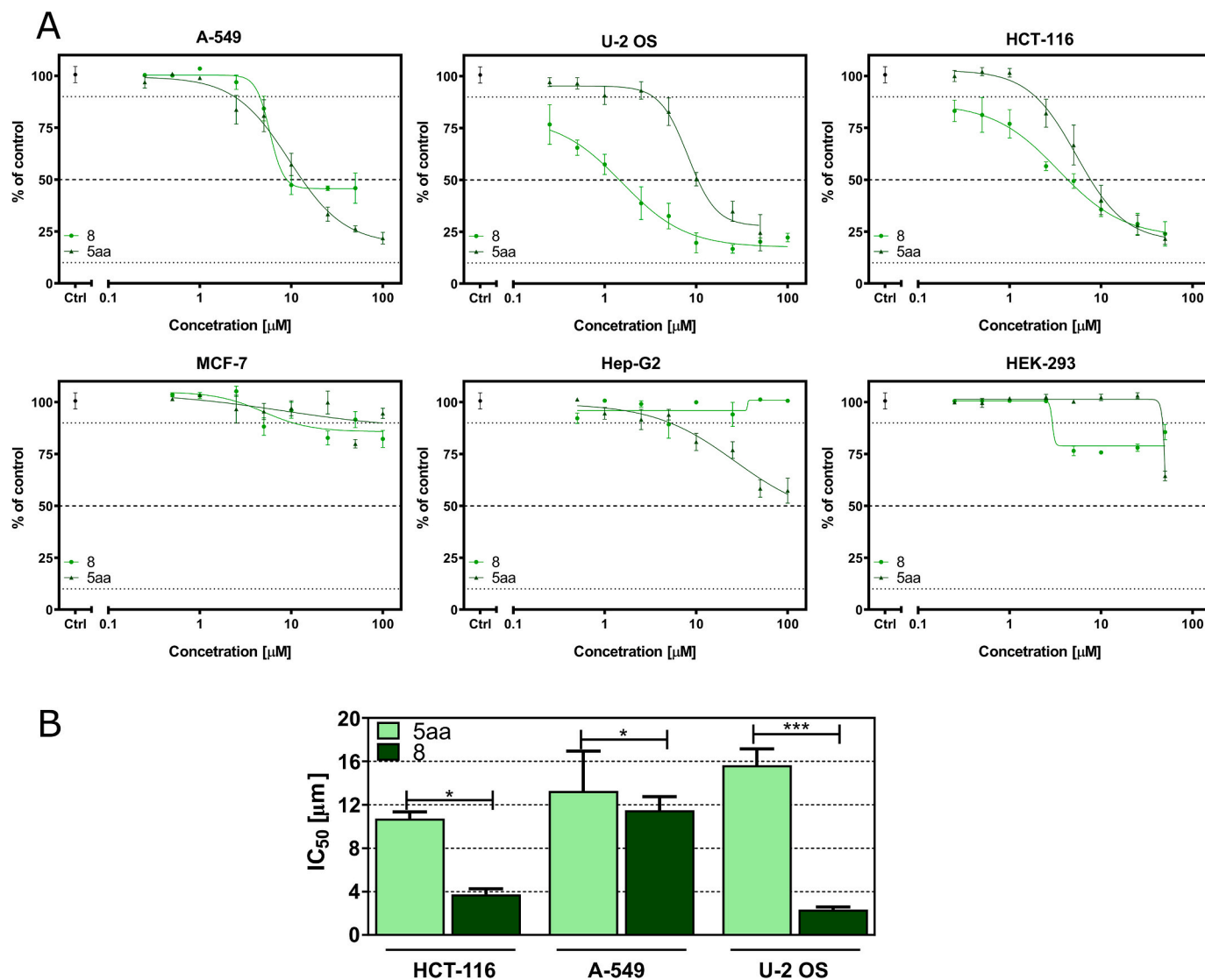


**Fig. 2.** Effects of the carbazole derivatives on the viability of A-549, U-2 OS, HCT-116, Hep-G2, MCF-7, and HEK-293 cells after treatment for 72 h. (A) Dose-response curves of **5aa** and **8** were determined by the MTT assay. (B) IC<sub>50</sub> values estimated for compounds **5aa** and **8**. All data are presented as mean  $\pm$  SD of  $n = 3$  independent experiments performed in triplicates. Statistical differences were analyzed with a one-way ANOVA post hoc Bonferroni test. \* $p < 0.01$ , \*\*\* $p < 0.0001$  vs. vehicle.

treated cells in comparison to vehicle. Further incubation (48 h) caused a significant increase in the percentages of apoptotic cells, while necrotic fraction was determined at  $1.16 \pm 0.83\%$  and  $2.38 \pm 0.41\%$  after treatment with **5aa** and **8** compounds, respectively (Fig. 7A–C). These results confirmed that **5aa** and **8** can trigger apoptotic rather than necrotic cell death in HCT-116 cell line. Interestingly, in the U-2 OS cell line, no apoptosis was observed at any of the studied time points (Fig. S2, Supplementary Information).

Caspases are crucial cell mediators of programmed cell death related to the stages of apoptosis [37]. Therefore, we investigated the effect of compounds **5aa** and **8** on the activation of two effector caspases: caspase-3 and caspase-7. Both these caspases play an important role in cell apoptosis. In the HCT-116 cell line, both compounds caused a negligible change in the activation of caspase-3/7 in comparison to DMSO (Fig. 7D and E). This suggests that apoptosis of cells proceeded through a caspase-independent death effector pathway.

#### 2.2.6. Effect of carbazole analogs on mitochondrial ROS generation

ROS (reactive oxygen species) play a pivotal role in activating cell death pathways [38]. To study the impact of **5aa** and **8** on oxidative

stress, intracellular ROS production in HCT-116 cells treated with these compounds was analyzed using an H2DCFDA probe. The results showed that compound **5aa** caused persistent, but mostly insignificant ROS generation in HCT-116 cells, whereas exposure to **8** induced a rapid and persistent increase of ROS (Fig. 8A and Fig. 8C). A 15- $\mu$ M concentration of **8** induced tremendous accumulation of ROS ( $64.2 \pm 7.7\%$  positive cells, 24 h; \*\*\* $p < 0.001$ ) relative to **5aa** ( $19.6 \pm 7.3\%$  positive cells, 24 h; \* $p < 0.05$ ) in HCT-116 cell line. Dysregulation of redox homeostasis could lead to cell death, including apoptosis and autophagy. To study whether the elevated ROS level was the primary cause of death in cells exposed to compound **8**, they were pretreated with *N*-acetyl-L-cysteine (NAC), a known antioxidant and ROS scavenger. It was observed that NAC diminished ROS generation induced by compound **8** in HCT-116 cell line (Fig. S3 and Fig. S4, Supplementary Information). This implied that NAC restored the cellular redox balance which was primarily altered by **8**. To study the general applicability of ROS generation caused by tested compounds in other cancers, changes of ROS were also investigated in the U-2 OS cell line (Fig. 8B and D). The results revealed that both compounds caused similar time-dependent accumulation of ROS, but this effect was reduced after treatment with **8** in comparison to

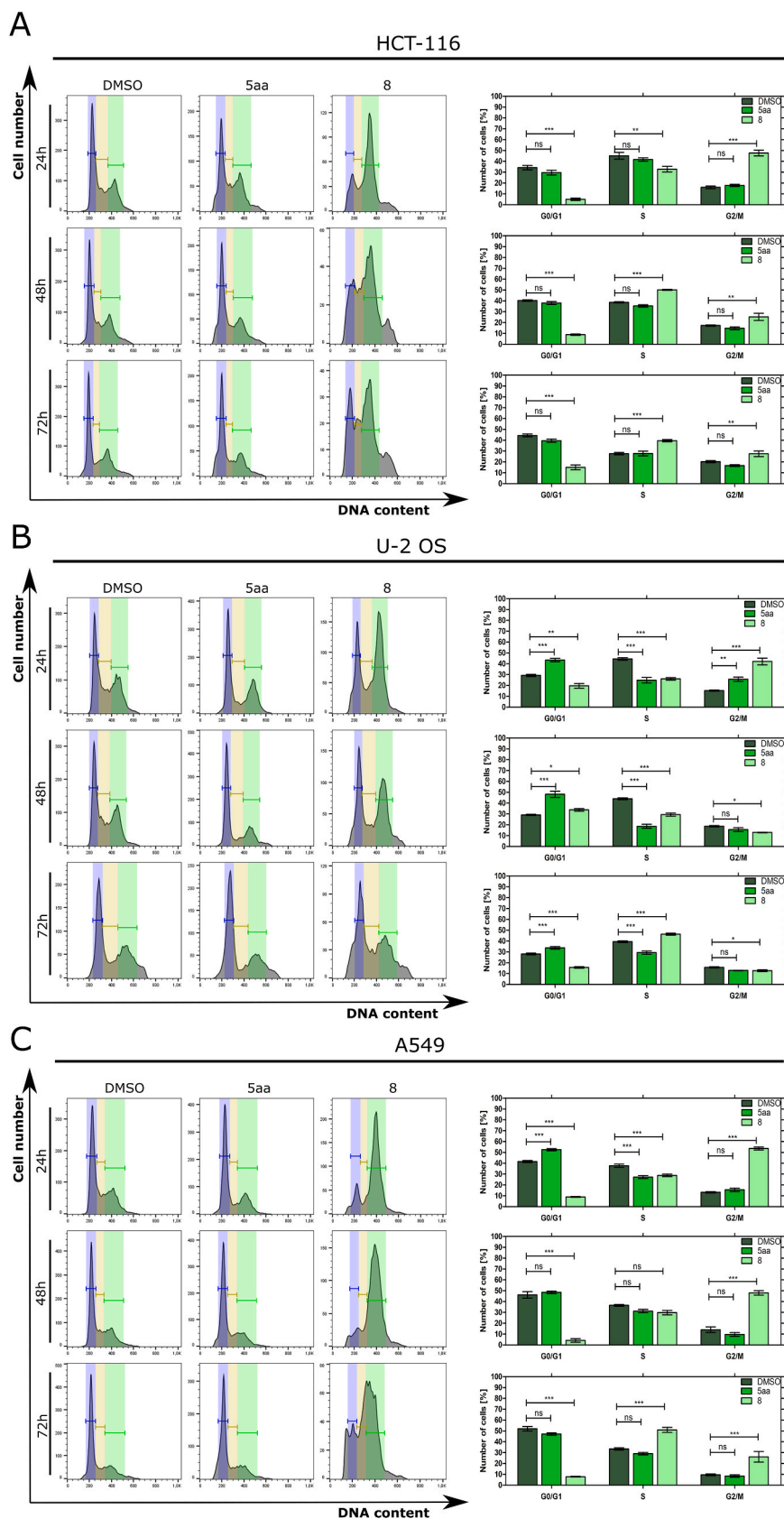


**Fig. 3.** Cell cycle analysis of HCT-116 (A), U-2 OS (B), and A-549 (C) cells after treatment with compounds 5aa and 8. The left panel shows representative histograms obtained after DNA staining. The right panel represents the results of statistical analyses of histograms. Error bars represent the SEM of data obtained in  $n = 3$  independent experiments. Statistical differences were analyzed with a one-way ANOVA post hoc Bonferroni test. \* $p < 0.01$ , \*\* $p < 0.001$ , \*\*\* $p < 0.0001$  vs. vehicle.

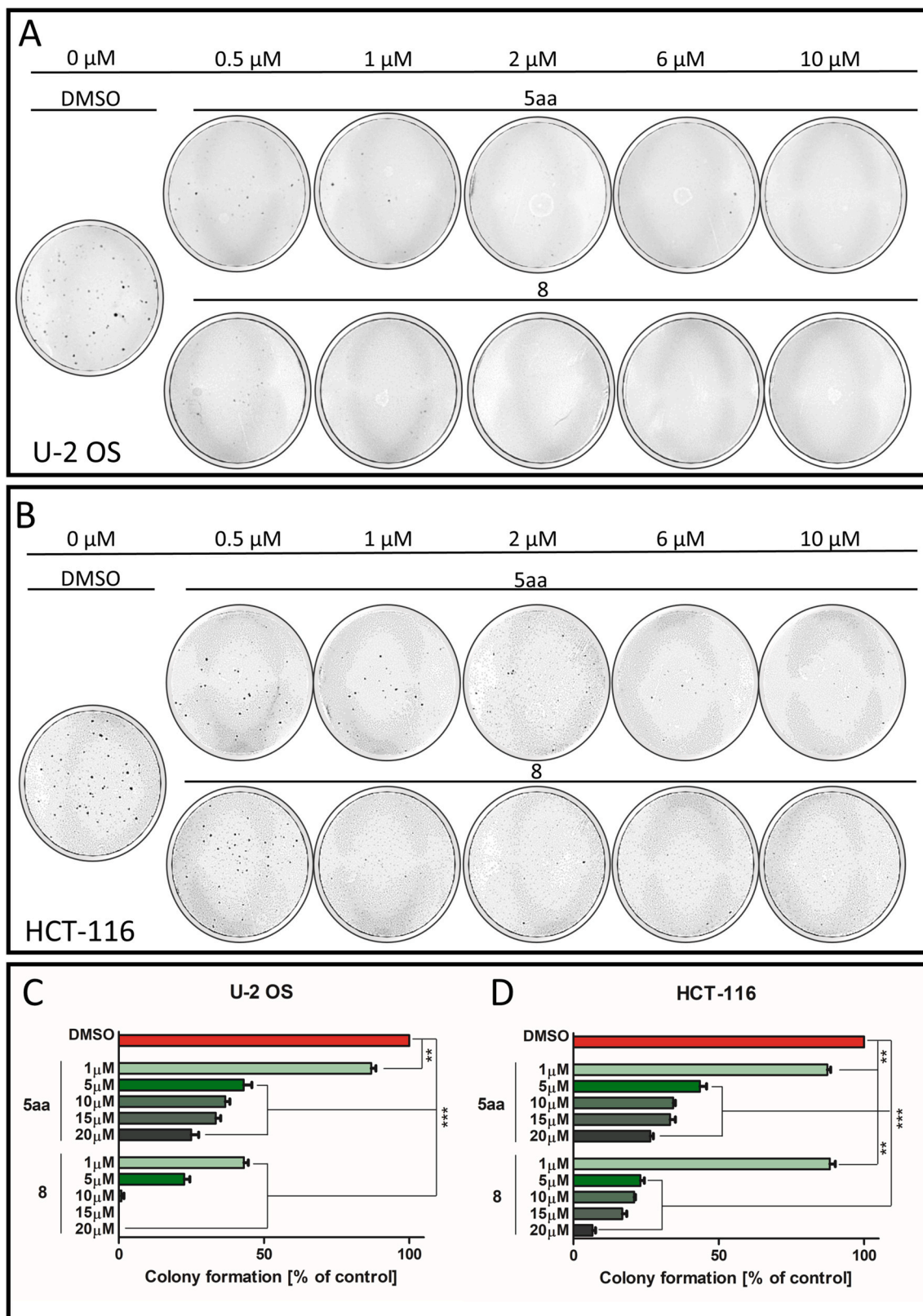
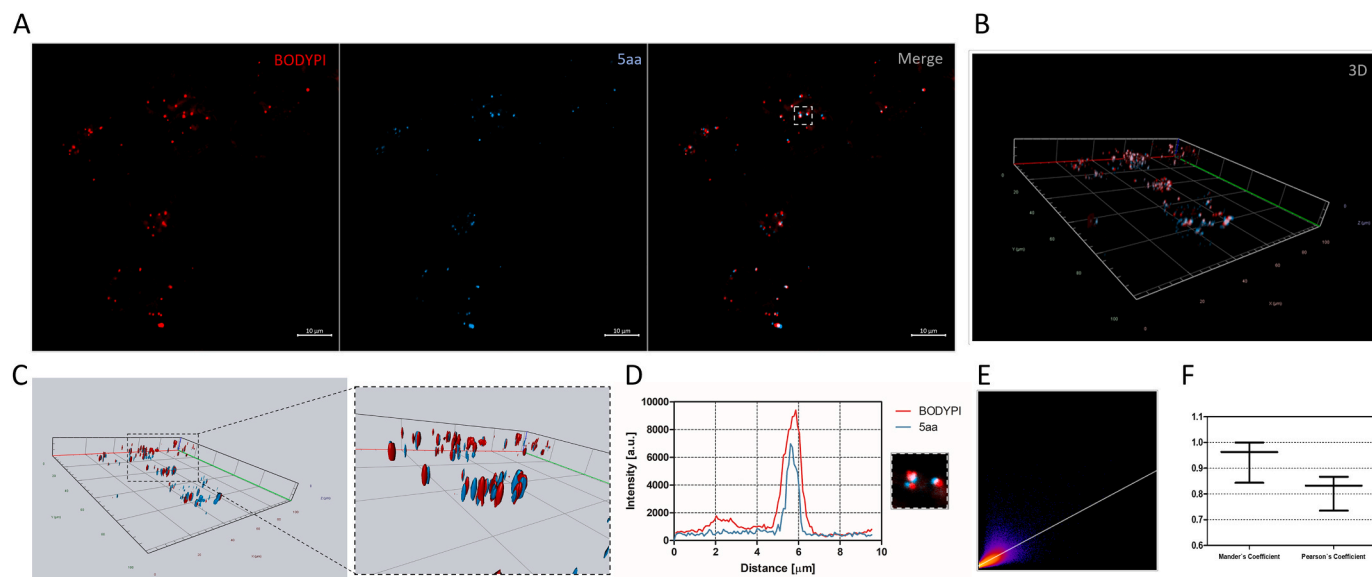


Fig. 4. Colony-forming ability of U-2 OS (A) and HCT-116 (B) cell lines after treatment with control (DMSO) and tested compounds (5aa, 8). Quantitative clonogenicity assays are illustrated in (C) and (D). Error bars represent the SEM of data obtained in  $n = 3$  independent experiments.  $**p < 0.001$ ,  $***p < 0.0001$  vs. vehicle.



**Fig. 5.** Colocalization analyses. (A–C) Representative confocal images showing the intracellular colocalization of LDs (BODYPI) with compound **5aa** in HCT-116 cell line captured in Z-stack (B) and rendered with three-dimensional reconstruction (C). (D) Representative line scan (corresponding to top panel in (A)) showing the colocalization of LDs with compounds. (E) Scatter plot corresponding to the colocalization of pixels. (F) Correlations of overlapping pixel intensities are described as thresholded MCC and PCC from Z-stack images.

HCT-116 cells. The level of induced ROS was found to be abolished after NAC pretreatment, as also observed in HCT-116 cells (Fig. 5 and Fig. S6, Supplementary Information). Taken together, it seems that cellular stress is of importance in the anticancer activity of these novel carbazole analogs.

### 2.2.7. Changes in mitochondrial morphology in HCT-116 and U-2 OS cell lines after treatment with **5aa** and **8**

Overproduction of ROS can influence mitochondrial functions and initiate mitochondrial-mediated cell death via loss of mitochondrial transmembrane potential ( $\Delta\Psi_m$ ) in cancer cells [39]. Therefore, we monitored  $\Delta\Psi_m$  using a 5,5,6,6'-tetrachloro-1,1',3,3'-tetraethylbenzimidazolcarbocyanine iodide (JC-1) fluorescent probe. In apoptotic or necrotic cells, mitochondria sequester the red-fluorescent JC-1 aggregate and diffuse it out in monomeric form to the cytosol, emitting green fluorescence [40]. Fig. 9 shows the representative histograms of JC-1-stained HCT-116 and U-2 OS cells, and the aggregate/monomer ratio determined by flow cytometry in different treated groups. The results obtained from stained cells showed a significant time-dependent reduction of  $\Delta\Psi_m$  in both **5aa**- and **8**-treated HCT-116 and U-2 OS cells. Furthermore, the observed loss of  $\Delta\Psi_m$  induced by **8** was higher compared to **5aa** after treatment for a short time (6 h) indicating a decrease in the aggregate/monomer ratio ( $1.83 \pm 0.24$  and  $3.18 \pm 0.44$ , respectively) as compared to control. However, after exposure to **5aa** and **8** for 24 h, the polarization of mitochondrial membrane was restored in HCT-116 cells, but only partially. The collapse of  $\Delta\Psi_m$  has often been viewed as a point of no return in cell death [41]. Moreover,  $\Delta\Psi_m$  maintains a driving force for energy production, and a gradual loss of this potential can disrupt the coupling efficiency between phosphorylation and oxidation, resulting in considerable bioenergetic deficits. Besides the loss of ATP production through aerobic respiration, maintenance of  $\Delta\Psi_m$  is required for the import of several mitochondrial proteins that affect different mitochondrial functions [42].

Previous studies have shown that mitochondrial morphology is a sensitive indicator of the action of some chemotherapeutics and changes occur in morphology before cell death [43,44]. In addition to mitochondrial outer membrane permeabilization, the mitochondrial network succumbs to substantial fragmentation caused by decreased fusion and elevated mitochondrial fission [45]. Therefore, we

investigated the influence of the studied compounds on mitochondrial phenotype. After treatment, the mitochondria of cells were visualized by confocal microscopy after labeling with mitochondria-targeted cationic dye MitoTracker Green and staining with DNA minor groove-binding ligand Hoechst 33342 (Fig. 10A). The results indicated that mitochondrial morphology was altered in cells exposed to both tested compounds **8** and **5aa** after 6 h of treatment and the cells showed a tendency to form short (Fig. 10C), circular-shaped (Fig. 10E) mitochondria, all of which are consistent with increased fission [46]. Compound **8** caused a stronger reduction in mitochondrial length than **5aa** ( $50.34 \pm 8.47\%$  and  $36.71 \pm 7.61\%$ , respectively;  $**p < 0.001$ ), in comparison to the control. Quantification of mitochondrial morphology also revealed an increased number of mitochondria (Fig. 10B) and a reduction in the average size of mitochondria (Fig. 10D), which suggests massive swelling of fragmented mitochondria. Both tested compounds induced the release of mitochondrial DNA into the cytosol by increasing the permeabilization of the mitochondrial inner membrane, which could potentially lead to cell death-associated inflammation [47]. The observed alterations in mitochondrial phenotype were probably reflected by oxidative stress caused by treatment with the studied compounds.

### 2.2.8. Oxidative DNA damage

Elevated intracellular levels of ROS lead to the oxidation of nucleotides, thereby inducing DNA double-strand breaks (DSBs) in a replication-dependent manner [39]. Therefore, we investigated the phosphorylation of H2AX at Ser 139, a marker of DSB, in treated HCT-116 and U-2 OS cell lines. As shown in Fig. 11, **5aa** and **8** caused a comparable increase in H2AX phosphorylation at the early stage of exposure (24 h) in HCT-116 and U-2 OS cells. In HCT-116 cell line, the level of p-H2AX remained similar after longer exposure (48 and 72 h). However, a significant increase in the level of p-H2AX was observed at 48 h ( $51.0 \pm 2.8\%$  positive cells;  $***p < 0.001$ ) and 72 h ( $68.2 \pm 3.4\%$  positive cells;  $***p < 0.001$ ) in compound **8**-treated U-2 OS cells, but not in the cells treated with **5aa**. Massive accumulation of DNA DSBs in cells treated with **8** could be one of the mechanisms of the observed G2/M arrest in these cells.

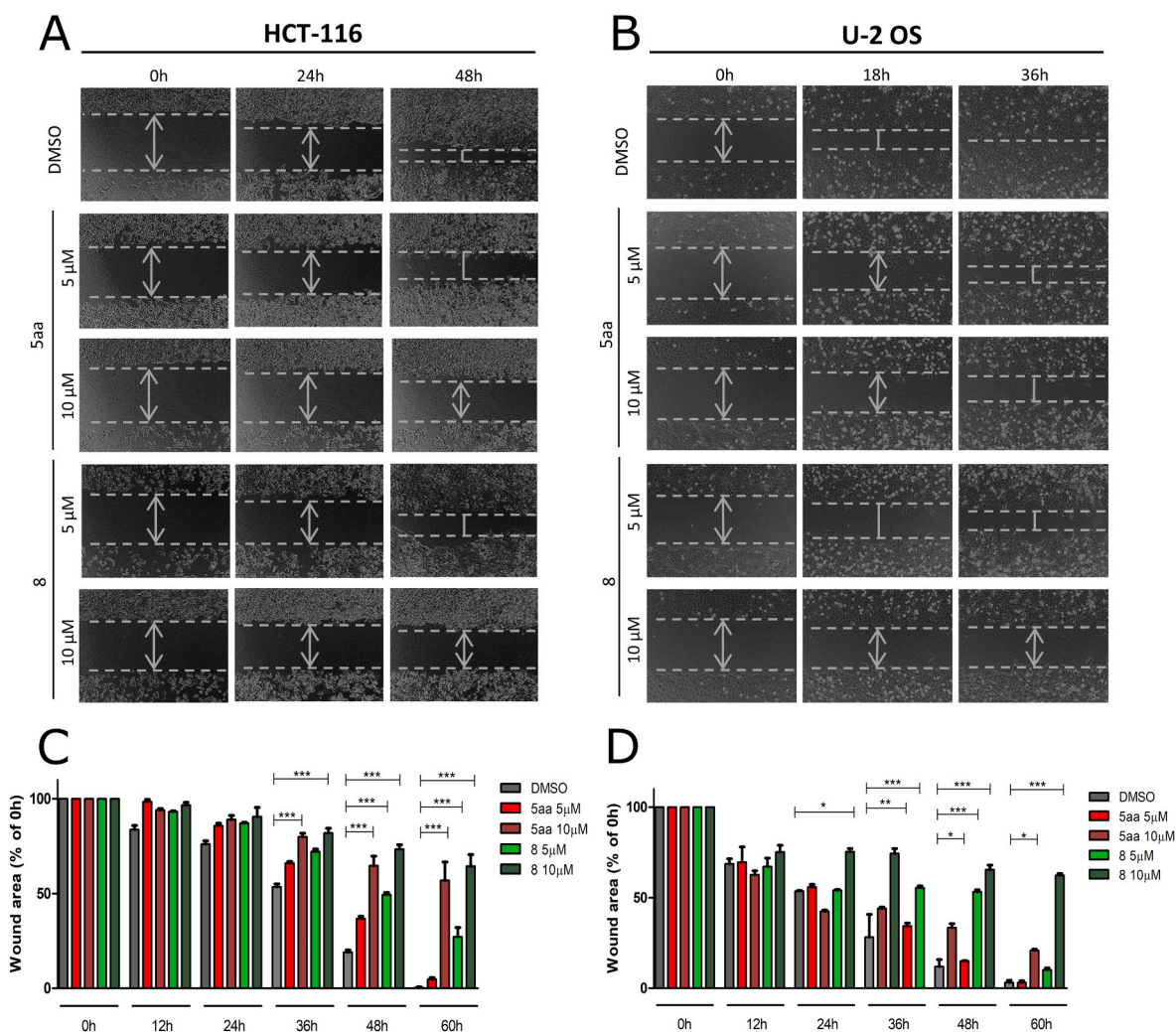


**Fig. 6.** Analysis of cell migration by *in vitro* wound healing assay. Time-lapse microscopy images of wound closure of untreated and compound **5aa** and compound **8**-treated HCT-116 (A) and U-2 OS (B) cell lines at 0, 24, and 48 h after the removal of culture insert. Scale bars = 100  $\mu$ m. Quantification of wound area is shown in (C) and (D). Data represent the mean  $\pm$  SEM of  $n = 3$  independent experiments. Statistical differences were analyzed with a one-way ANOVA post hoc Bonferroni test. <sup>ns</sup> $p > 0.05$ , <sup>\*\*\*</sup> $p < 0.0001$  vs. vehicle.

### 2.2.9. Induction of cell senescence

Treatment with different doses of drugs may promote the suppression of carcinoma through different mechanisms. However, a low concentration of drugs may result in the induction of premature senescence rather than cell death [48]. Therefore, we examined the accumulation of the molecular markers of stress-induced premature senescence in cells treated with **5aa** and **8** for 24 and 48 h. For this purpose, the cells were washed, cultured for an additional 96 or 72 h, and stained with x-gal. It was observed that compound **8** induced cellular senescence in HCT-116 cells in all treatment time points, similar to the positive control (Doxorubicin), which indicates the high activity of senescence-associated  $\beta$ -galactosidase (SA- $\beta$ -Gal) (Fig. 12A and Fig. 12B), as well as flattening and enlargement of cells (Fig. 12C). On the other hand, the morphology of **5aa**-treated cells did not change during cultivation in comparison to vehicle. Similar results were obtained in the case of U-2 OS cells, except that the activity of SA- $\beta$ -Gal did not increase after treatment (Fig. S7, Supplementary Information).

### 3. Conclusion

In summary, a novel series of anticancer compounds based on a substituted carbazole scaffold were synthesized. The application of a recently developed method of synthesis allowed convenient formation

of three or four substituted aminocarbazoles from oxopentanoate tryptophan derivatives in a three-step process. Among the synthesized carbazole derivatives, compounds **5aa** and **8** were found to be the most active, which effectively inhibited the growth of HCT-116 and U-2 OS cells compared with 5-fluorouracil used as reference compound. Compound **8** showed a 3–6 times higher anticancer activity against these cell lines than compound **5aa**, which indicates that the structural modification of compound **5aa** led to the discovery of a compound with better anticancer properties. Annexin-V staining revealed that treatment with both compounds for 6–48 h induced 10–40% ( $p < 0.05$ ) apoptotic cell death in HCT-116 cell line, while negligible change occurred in apoptosis in U-2 OS cell line. Compound **8** induced intense senescence in both HCT-116 and U-2 OS cell lines. This reveals that both compounds exhibited a different mechanism of action depending on the cell line. Furthermore, they displayed a potent oxidative effect in HCT-116 and U-2 OS cells, inducing massive accumulation of DNA DSBs, which led to a parallel change in the assembly of mitochondria causing their dysfunction. These findings are expected to provide new leads for the treatment of colon cancer and osteosarcoma.

### 4. Experimental section

*General:* Commercially available reagents were purchased from



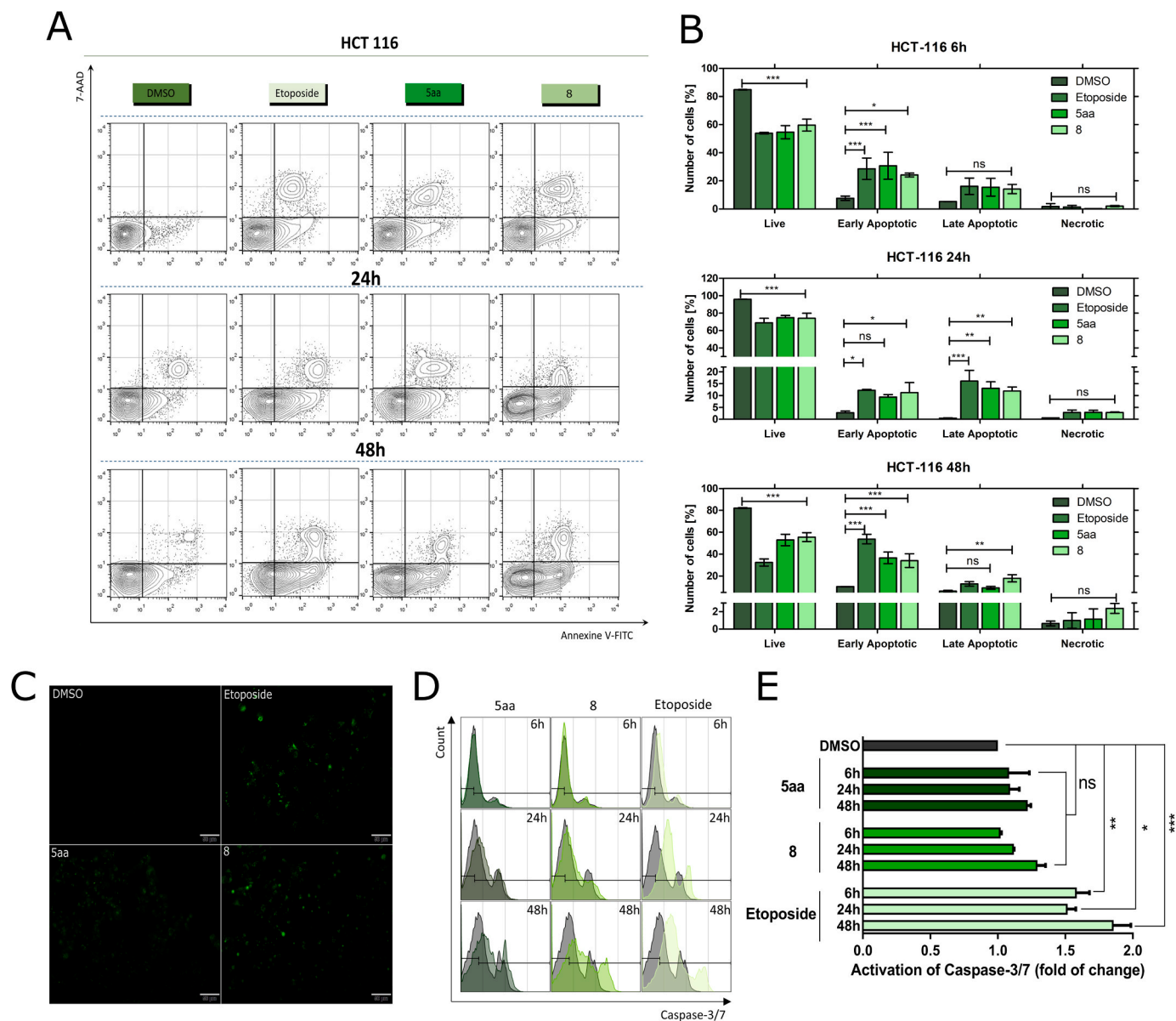


**Fig. 7.** Apoptosis assay. (A, B) Flow cytometric analysis of HCT-116 cell line after 6, 24, and 48 h of treatment with compounds **8** and **5aa**, using Annexin V/7-AAD. DMSO and Etoposide were used as reference compounds. Representative dot-plot analyses are shown in the left panels (A), and quantitation of analysis is presented in the right panels (B). (C) Microscopic images obtained after 48 h of treatment with the indicated compounds and staining with Annexin V. Modulation of caspase-3/7 in HCT-116 cells after treatment with compounds are presented on representative histograms (D) and bar charts (E). Error bars represent the SEM of data obtained in  $n = 3$  independent experiments. Statistical differences were analyzed with a two-way ANOVA.  $^{ns}p > 0.05$ ,  $^*p < 0.01$ ,  $^{**}p < 0.001$ ,  $^{***}p < 0.0001$  vs. vehicle.

Sigma-Aldrich or Acros and used without further purification. THF was distilled in the presence of potassium under argon shortly before use. DCM was distilled over  $P_4O_{10}$  and stored over molecular sieves. The reagents 2-((*tert*-butoxycarbonyl)amino)-3-(1H-indol-3-yl)propanoic acid (**3aa**) [29], 2-((ethoxycarbonyl)amino)-3-(1H-indol-3-yl)propanoic acid (**3ab**) [27], 2-acetamido-3-(1H-indol-3-yl)propanoic acid (**3ac**) [26], 2-(((benzyloxy)carbonyl)amino)-3-(1H-indol-3-yl)propanoic acid (**3ad**) [28], and 2-(1,3-dioxoisindolin-2-yl)-3-(1H-indol-3-yl)propanoic acid (**3ae**) [25] were prepared as described in the literature. Analytical thin-layer chromatography was performed on aluminum sheets of UV-254 Merck silica gel, and flash chromatography using SilicaFlash P60 silica gel (40–63  $\mu$ m).  $^1H$  and  $^{13}C$  NMR spectra were recorded with Bruker Avance III HD 400 MHz, and NMR chemical shifts were reported in  $\delta$  (ppm) using residual solvent peaks as standards with the coupling constant  $J$  measured in Hz. High-resolution mass spectra were recorded with an Agilent 6540 Q-TOF system. Melting points were

determined with a Warsztat Elektromechaniczny W-wa apparatus and were used uncorrected.

#### 4.1. Boc-protected tryptophans. General procedure [29]

To a solution of **2b-c** (10 mmol) and  $NaHCO_3$  (1.64 g, 19 mmol) in a dioxane:water 1:1 mixture (20 ml) at 0 °C di-*tert*-butyl dicarbonate (3.37 ml, 15 mmol) was added in one portion. The reaction mixture was stirred 13 h at R.T concentrated in a vacuum. The residue was washed with AcOEt (2  $\times$  15 ml) and discarded. The water layer was acidified to pH = 3 with 5% aqueous HCl and extracted with AcOEt (2  $\times$  15 ml), organic extract was dried with  $MgSO_4$  filtered and evaporated to dryness under reduced pressure. The crude products were used without additional purification.

In the case of 5-hydroksytryptophane **2c**, the crude product was subject to additional O-acetylation with the following procedure.

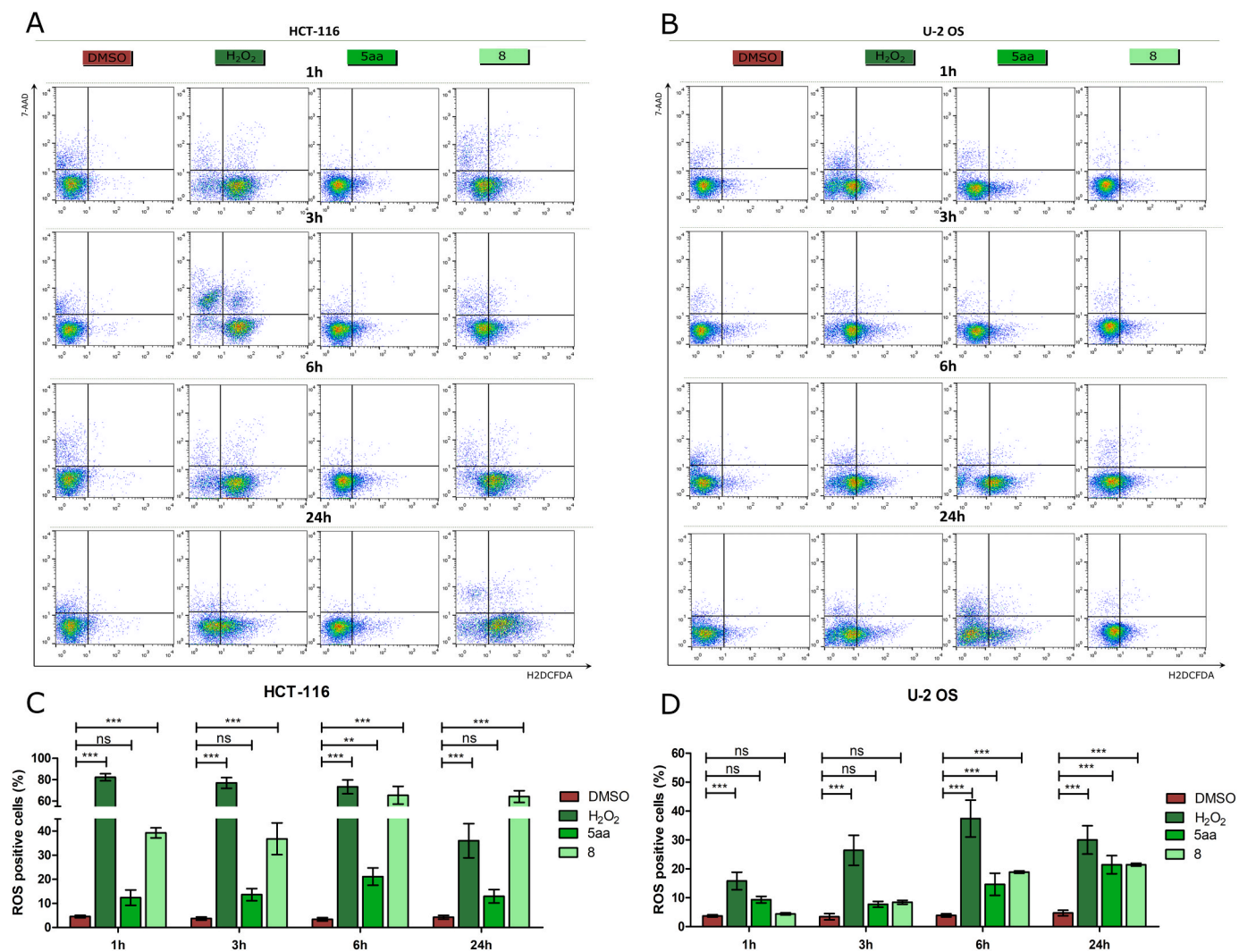


**Fig. 8.** Flow cytometric analyses of ROS induction in HCT-116 (A) and U-2 OS (B) cells after 1, 3, 6, and 24 h of treatment with compounds **8** and **5aa**, using H<sub>2</sub>DCFDA probe. DMSO and H<sub>2</sub>O<sub>2</sub> were used as reference compounds. The quantitation of analysis is presented in (C) and (D). Error bars represent the SEM of data obtained in n = 4 independent experiments. Statistical differences were analyzed with a two-way ANOVA. <sup>ns</sup>p > 0.05, <sup>\*\*</sup>p < 0.001, <sup>\*\*\*</sup>p < 0.0001 vs. vehicle.

Crude *N*-Boc-5-hydroxytryptophane (100 mg, 0.31 mmol) was dissolved in 1 N NaOH (0.7 ml) and acetic anhydride was added (63  $\mu$ l, 0.67 mmol). The reaction mixture was stirred for 3 h at R. T. under argon. The solution was acidified with 5% citric acid and extracted with AcOEt (3  $\times$  5 ml), organic extract was washed with brine (5 ml), dried with MgSO<sub>4</sub> filtered, and evaporated to dryness under reduced pressure. The crude products were used without additional purification.

#### 4.2. 2-((*tert*-butoxycarbonyl)amino)-3-(5-((*tert*-butoxycarbonyl)amino)-1*H*-indol-3-yl)propanoic acid (**3ba**)

Colorless oil; yield 98%; <sup>1</sup>H NMR (400 MHz, CDCl<sub>3</sub>,  $\delta$ ): 8.54 (bs, 1H), 7.54 (bs, 1H), 7.13–7.05 (m, 2H), 6.88 (s, 1H), 6.76–6.69 (m, 1H), 5.23–5.11 (m, 1H), 4.62–4.60 (m, 1H), 3.20–3.04 (m, 2H), 1.55 (s, 9H), 1.43 (s, 9H); <sup>13</sup>C NMR (100 MHz, CDCl<sub>3</sub>,  $\delta$ ): 175.6, 171.3, 155.6, 133.3, 130.1, 127.8, 124.2, 116.5, 111.4, 110.6, 109.6, 80.0, 53.9, 28.5, 28.4; HRMS (ESI+): *m/z* [M + H]<sup>+</sup> calcd for C<sub>21</sub>H<sub>30</sub>N<sub>3</sub>O<sub>6</sub>, 420.2135; found, 420.2157.

#### 4.3. 3-(5-acetoxy-1*H*-indol-3-yl)-2-((*tert*-butoxycarbonyl)amino)propanoic acid (**3ca**)

Colorless oil; yield 39%; <sup>1</sup>H NMR (400 MHz, CDCl<sub>3</sub>,  $\delta$ ): 8.46 (s, 1H),

7.29–7.25 (m, 2H), 6.92–6.87 (m, 2H), 5.17–5.15 (m, 1H), 4.64–4.63 (m, 1H), 3.31–3.18 (m, 2H), 2.33 (s, 3H), 1.46 (s, 9H); <sup>13</sup>C NMR (100 MHz, CDCl<sub>3</sub>,  $\delta$ ): 172.1, 171.4, 166.2, 150.8, 139.4, 129.3, 123.4, 119.9, 111.4, 107.0, 106.1, 75.5, 55.7, 23.6, 23.3, 16.4; HRMS (ESI+): *m/z* [M + Na]<sup>+</sup> calcd for C<sub>18</sub>H<sub>22</sub>N<sub>2</sub>O<sub>6</sub>Na, 385.1375; found, 385.1397.

#### 4.4. General procedure for preparation of ethyl 5-(1*H*-indol-3-yl)-3-oxopentanoate derivatives (**4aa-ca**)

To a solution of *N*-protected Trp **3aa-ca** (0.59 mmol) in dry THF (12 ml) carbonyldiimidazole (106 mg, 0.65 mmol) was added. The resulting mixture was stirred for 2 h at R.T under argon. Then MgCl<sub>2</sub> (56 mg, 0.59 mmol) was added following by ethyl potassium malonate (100 mg, 0.59 mmol). The resulting reaction mixture was stirred for 1 h at R.T under argon and then was heated to 40–45 °C stirred for an additional 12 h. After completion of the reaction, the mixture was filtered and concentrated in vacuum. The residue was purified with flash chromatography as specified below.

#### 4.5. Ethyl 4-((*tert*-butoxycarbonyl)amino)-5-(1*H*-indol-3-yl)-3-oxopentanoate (**4aa**)

Purification by flash column chromatography (EtOAc/Hex, 1:3).

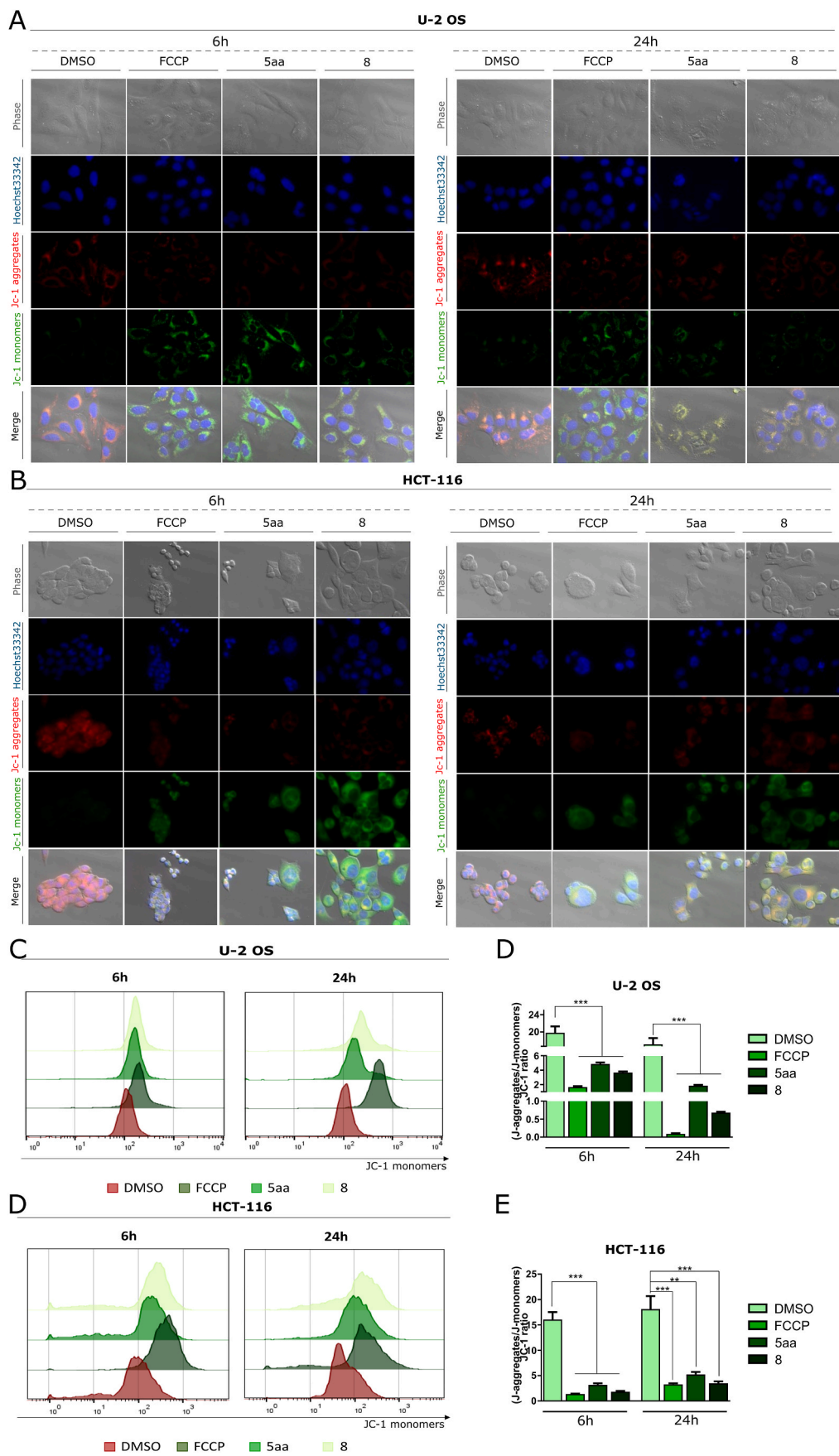


**Fig. 9.** Analysis of  $\Delta\Psi_m$ . JC-1 staining images of HCT-116 (A) and U-2 OS (D) cells acquired after 6 and 24 h of treatment with 5aa and 8. FCCP was used as a reference. Flow cytometric analyses of JC-1 staining are presented on representative histograms (B, E) and bar charts with statistical quantifications of JC-1 ratio (J-aggregates/J-monomers) (C, F). Data represent the mean  $\pm$  SEM of at least  $n = 4$  independent experiments. Statistical differences were analyzed with a Bonferroni post hoc test.  $**p < 0.0001$ ,  $***p < 0.0001$  compared with control (DMSO).

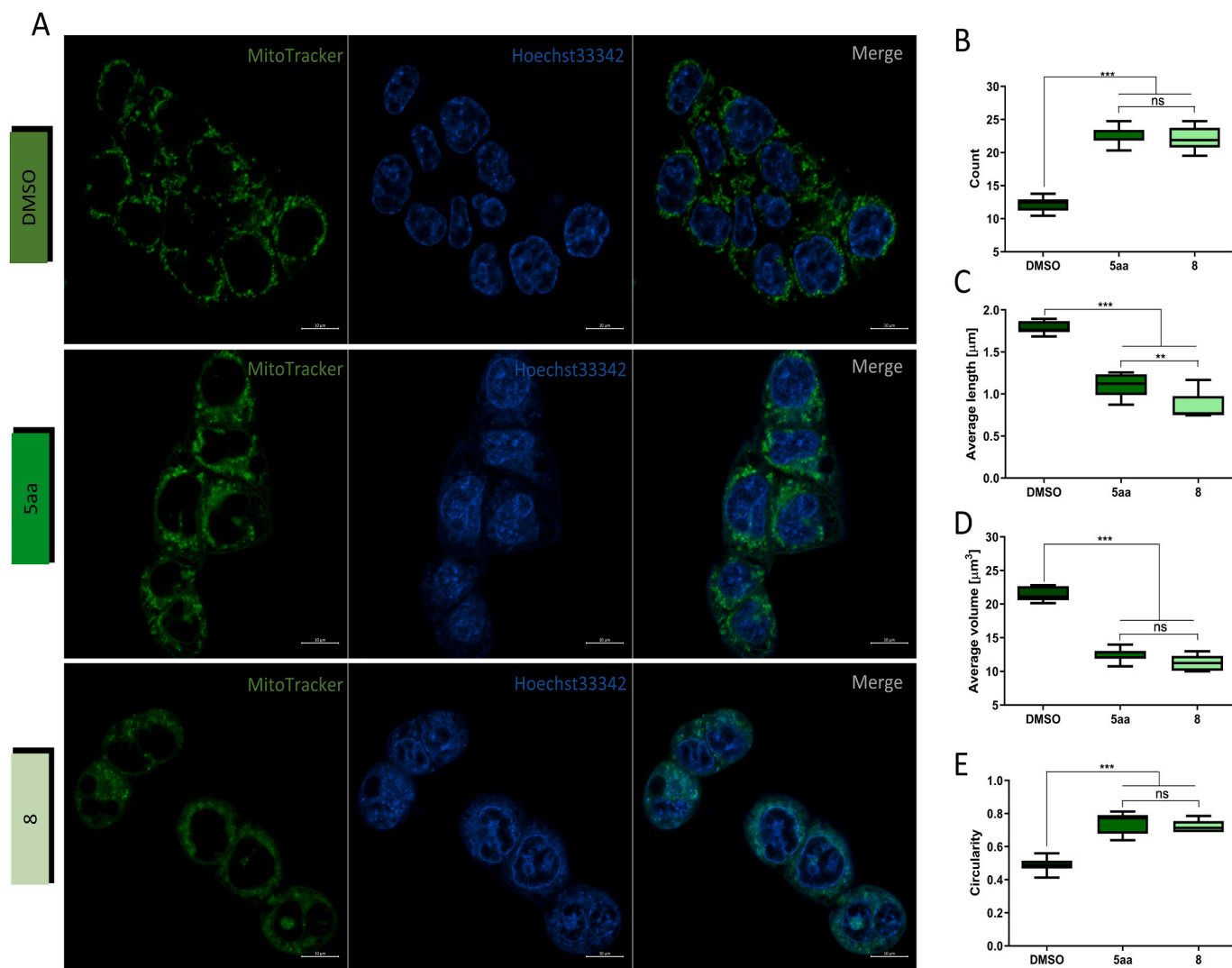


**Fig. 10.** Quantitative mitochondrial morphometric analyses. (A) Representative confocal images of the mitochondrial morphology of HCT-116 cells acquired after 6 h of treatment with compounds **5aa** and **8**, and with DMSO (scale bar = 10 μm); Green—MitoTracker, blue—Hoechst 33342. (B) Number of counted mitochondrial particles. (C) Average length (μm) and (D) volume (μm<sup>3</sup>) of mitochondria. (E) Circularity of mitochondria (index of elongation). Statistical quantification of mitochondrial morphology was performed based on Z-axis confocal stacks. Data represent mean ± SEM of at least n = 4 independent experiments. Statistical differences were analyzed with a Bonferroni post hoc test. \*\*\**p* < 0.0001, \*\**p* < 0.001 compared with control (DMSO).

White amorphous solid; yield 44%; <sup>1</sup>H NMR (400 MHz, CDCl<sub>3</sub>, δ): 8.23 (s, 1H), 7.65–7.63 (m, 1H), 7.40–7.37 (m, 1H), 7.25–7.22 (m, 1H), 7.20–7.12 (m, 1H), 7.04–7.03 (m, 1H), 5.18–5.16 (m, 1H), 4.74–4.69 (m, 1H), 4.18–4.13 (m, 2H), 3.51 (d, *J* = 16.0 Hz, 1H), 3.44 (d, *J* = 16.0 Hz, 1H), 3.34–3.22 (m, 2H), 1.44 (s, 9H), 1.26 (t, *J* = 8.0 Hz, 3H); <sup>13</sup>C NMR (100 MHz, CDCl<sub>3</sub>, δ): δ = 202.7, 167.0, 155.4, 136.2, 127.5, 123.0, 122.3, 119.8, 118.8, 111.2, 110.0, 80.1, 61.4, 59.9, 47.0, 28.3, 26.9, 14.0; HRMS (ESI<sup>+</sup>): *m/z* [M + Na]<sup>+</sup> calcd for C<sub>18</sub>H<sub>22</sub>N<sub>2</sub>O<sub>6</sub>Na, 397.1738; found, 397.1692.

#### 4.6. Ethyl 4-((ethoxycarbonyl)amino)-5-(1H-indol-3-yl)-3-oxopentanoate (**4ab**)

Purification by flash column chromatography (EtOAc/Hex, 1:2). Colorless oil; yield 16%; <sup>1</sup>H NMR (400 MHz, CDCl<sub>3</sub>, δ): 8.27 (s, 1H), 7.66–7.64 (m, 1H), 7.39–7.36 (m, 1H), 7.25–7.20 (m, 1H), 7.20–7.13 (m, 1H), 7.03 (s, 1H), 5.36 (d, *J* = 7.2 Hz, 1H), 4.81–4.76 (m, 1H), 4.18–4.10 (m, 4H), 3.50 (d, *J* = 16.0 Hz, 1H), 3.44 (d, *J* = 16.0 Hz, 1H), 3.34–3.25 (m, 2H), 1.27–1.22 (m, 6H); <sup>13</sup>C NMR (100 MHz, CDCl<sub>3</sub>, δ): 202.4, 166.9, 156.2, 136.2, 127.4, 123.1, 122.4, 119.9, 118.7, 111.3, 109.8, 61.5, 60.1, 47.2, 27.1, 14.0; HRMS (ESI<sup>+</sup>): *m/z* [M + H]<sup>+</sup> calcd

for C<sub>18</sub>H<sub>23</sub>N<sub>2</sub>O<sub>5</sub>, 347.1607; found, 347.1614.

#### 4.7. Ethyl 4-acetamido-5-(1H-indol-3-yl)-3-oxopentanoate (**4ac**)

Purification by flash column chromatography (EtOAc/Hex, 1:3). Yellow amorphous solid; yield 46%; <sup>1</sup>H NMR (400 MHz, CDCl<sub>3</sub>, δ): 8.53 (s, 1H), 7.62–7.60 (m, 1H), 7.38–7.36 (m, 1H), 7.23–7.19 (m, 1H), 7.16–7.13 (m, 1H), 7.01 (s, 1H), 6.38 (d, *J* = 7.2 Hz, 1H), 5.06–5.00 (m, 1H), 4.15 (q, *J* = 7.2 Hz, 2H), 3.50 (d, *J* = 16.0 Hz, 1H), 3.45 (d, *J* = 16.0 Hz, 1H), 3.34–3.22 (m, 2H), 1.94 (s, 3H), 1.24 (t, *J* = 7.2 Hz, 3H); <sup>13</sup>C NMR (100 MHz, CDCl<sub>3</sub>, δ): 201.9, 170.5, 166.9, 136.2, 127.5, 123.1, 122.3, 119.8, 118.5, 111.5, 109.5, 61.6, 58.9, 47.2, 26.6, 22.9, 14.0; HRMS (ESI<sup>+</sup>): *m/z* [M + H]<sup>+</sup> calcd for C<sub>17</sub>H<sub>21</sub>N<sub>2</sub>O<sub>4</sub>, 317.1501; found, 317.1495.

#### 4.8. Ethyl 4-((benzyloxy)carbonyl)amino)-5-(1H-indol-3-yl)-3-oxopentanoate (**4ad**)

Purification by flash column chromatography (EtOAc/Hex, 1:3). Yellow amorphous solid; yield 28%; <sup>1</sup>H NMR (400 MHz, CDCl<sub>3</sub>, δ): 8.19 (s, 1H), 7.63 (d, *J* = 7.6 Hz, 1H), 7.42–7.30 (m, 6H), 7.26–7.20 (m,

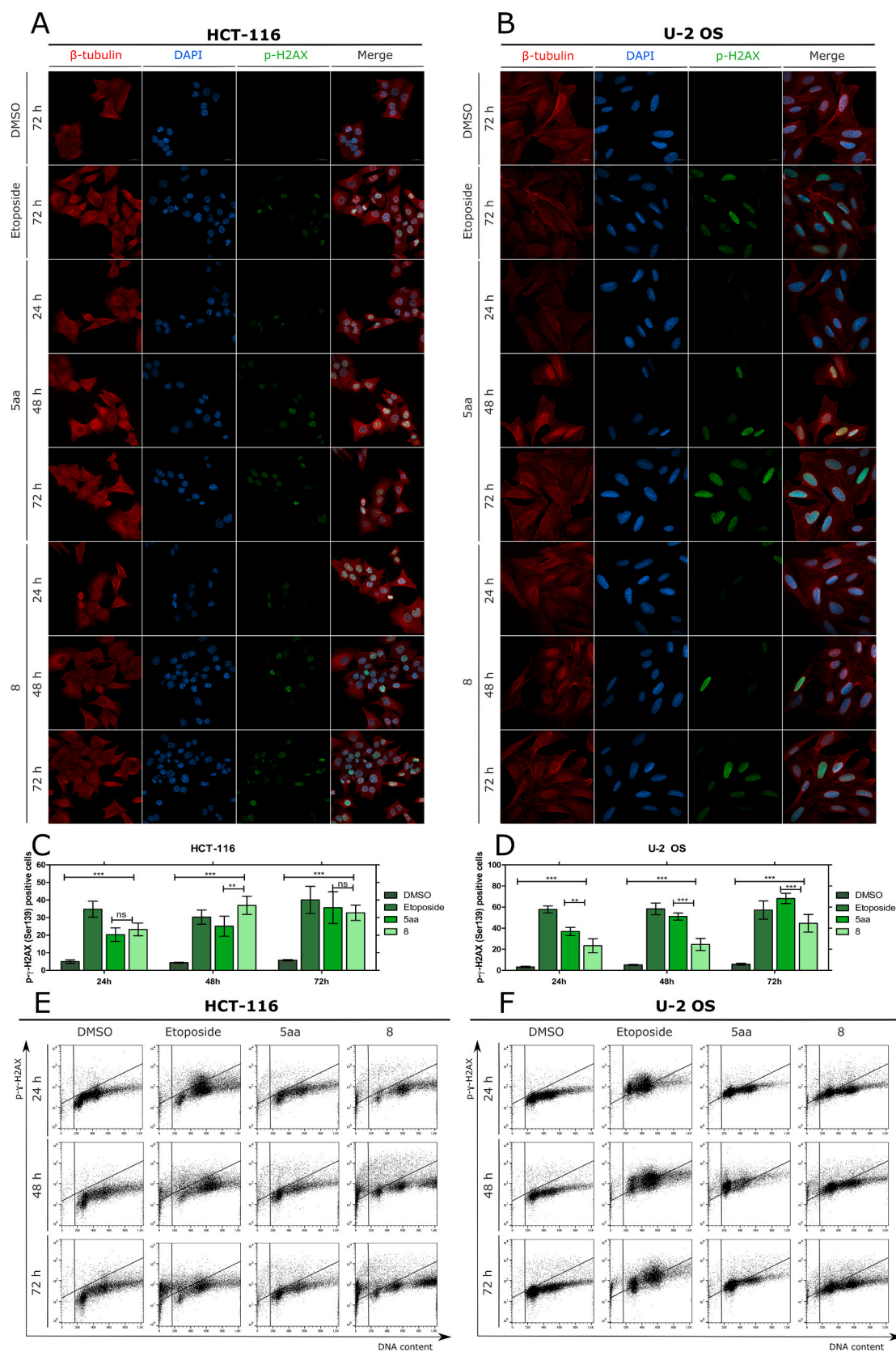


**Fig. 11.** Representative microscopy images presenting immunofluorescence in U-2 OS (A) and HCT-116 (B) cells indicating the formation of  $\gamma$ -H2AX foci and changes in microtubule structure upon treatment with **5aa** and **8** (24, 48, and 72 h). Etoposide and DMSO were used as reference compounds. The microtubule is depicted in red,  $\gamma$ -H2AX in green, and nucleus in blue (DAPI). Scale bars = 100  $\mu$ m. (C, D) Representative dot-plot diagrams after flow cytometric analyses of p- $\gamma$ -H2AX staining. (E) Quantification showing the average percent of p- $\gamma$ -H2AX-positive cells plotted as a bar graph depicting mean  $\pm$  SEM. Error bars represent the SEM of data obtained in  $n = 3$  independent experiments. Statistical differences were analyzed with a two-way ANOVA.

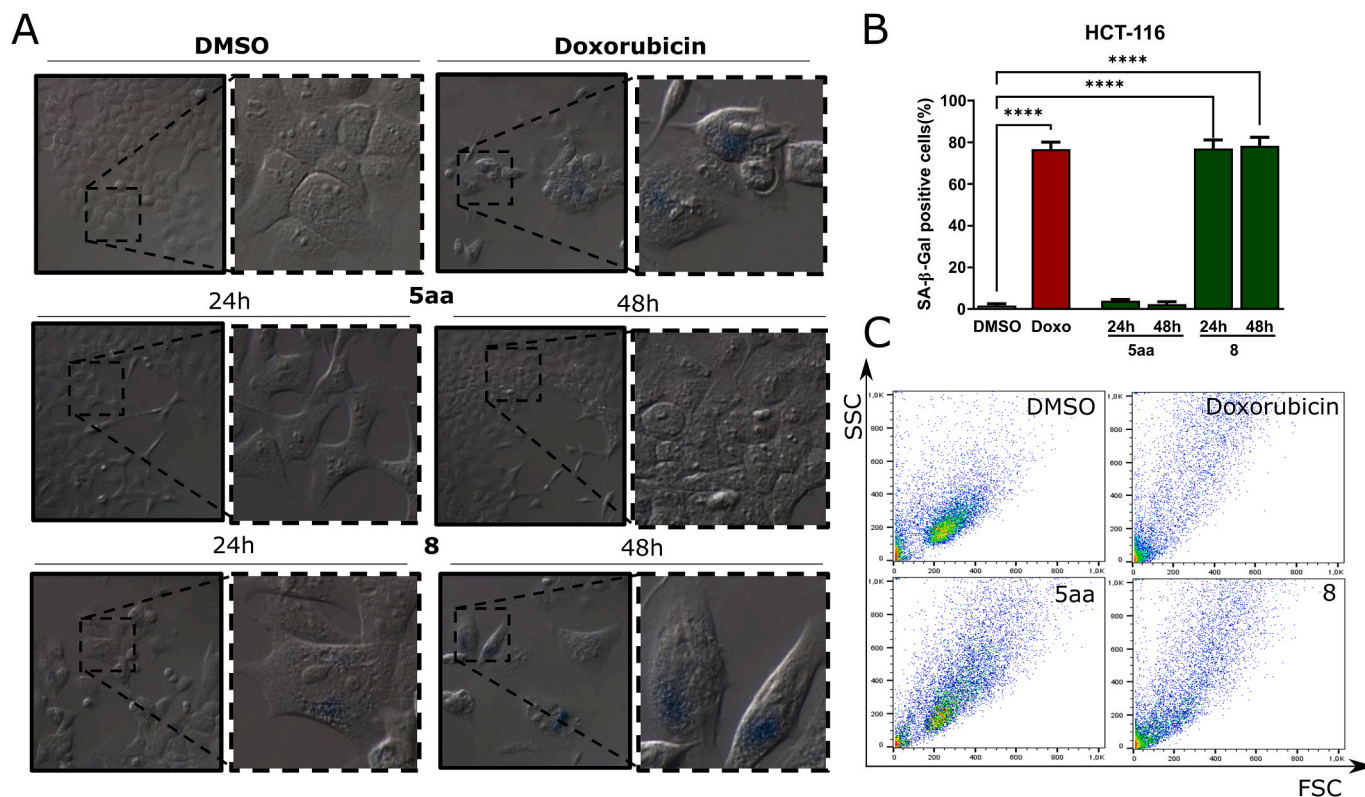


**Fig. 12.** (A) Representative microscopy images showing SA-β-Gal staining and morphology of HCT-116 cells acquired after 24 or 48 h of treatment with the investigated compounds (10 μM **5aa**, 10 μM **8**) and prolonged culturing for 96 or 72 h. Doxorubicin was used as a reference compound. (B) Quantification showing the average percent of SA-β-Gal-positive cells plotted as a bar graph depicting mean ± SEM. (C) Representative dot-plot analyses after 48 h of treatment with the investigated compounds (10 μM **5aa**, 10 μM **8**) and prolonged culturing for 96 h. Error bars represent the SEM of data obtained in n = 10 random fields of view. Statistical differences were analyzed with a two-way ANOVA. \*\*\*p < 0.0001 vs. vehicle.

1 H), 7.17–7.12 (m, 1 H), 7.01–6.95 (m, 1 H), 5.48 (d,  $J = 7.6$  Hz, 1 H), 5.12 (s, 2 H), 4.82 (dd,  $J = 13.6$  Hz,  $J = 6.4$  Hz, 1 H), 4.15 (q,  $J = 7.2$  Hz, 2 H), 3.50 (d,  $J = 16.0$  Hz, 1 H), 3.44 (d,  $J = 16.0$  Hz, 1 H), 3.56–3.40 (m, 2 H), 3.35–3.25 (m, 2H), 1.24 (t,  $J = 6.8$  Hz, 3 H).

#### 4.9. Ethyl 4-(1,3-dioxoisindolin-2-yl)-5-(1H-indol-3-yl)-3-oxopentanoate (**4ae**)

Purification by flash column chromatography (EtOAc/Hex, 1:3). Yellow amorphous solid; yield 25%;  $^1\text{H NMR}$  (400 MHz,  $\text{CDCl}_3$ ):  $\delta = 7.98$  (bs, 1 H), 7.79–7.75 (m, 2 H), 7.69–7.65 (m, 2 H), 7.64–7.62 (m, 1 H), 7.29–7.27 (m, 1 H), 7.17–7.12 (m, 1 H), 7.10–7.05 (m, 1 H), 7.03 (d,  $J = 2$  Hz, 1 H), 5.30 (dd,  $J = 10.0$  Hz,  $J = 6.0$  Hz, 1 H), 4.22–4.16 (m, 2 H), 3.84–3.73 (m, 2 H), 1.72–1.64 (m, 2 H), 0.92 (t,  $J = 7.6$  Hz, 3 H).

#### 4.10. Ethyl 4-((tert-butoxycarbonyl)amino)-5-(5-((tert-butoxycarbonyl)amino)-1H-indol-3-yl)-3-oxopentanoate (**4ba**)

Purification by flash column chromatography (EtOAc/Hex, 1:2). Colorless oil; yield 43%;  $^1\text{H NMR}$  (400 MHz,  $\text{CDCl}_3$ ):  $\delta = 8.36$  (s, 1 H), 7.53 (s, 1 H), 7.27–7.23 (m, 1 H), 7.23–7.19 (m, 1 H), 6.97 (s, 1 H), 6.59 (s, 1 H), 5.17 (d,  $J = 7.6$  Hz, 1 H), 4.67–4.62 (m, 1 H), 4.18–4.13 (m, 2 H), 3.50 (d,  $J = 16.0$  Hz, 1 H), 3.43 (d,  $J = 16.0$  Hz, 1 H), 3.25–3.14 (m, 2 H), 1.55 (s, 9 H), 1.42 (s, 9 H), 1.30–1.23 (m, 3 H).  $^{13}\text{C NMR}$  (100 MHz,  $\text{CDCl}_3$ ):  $\delta = 202.8$ , 167.0, 155.4, 153.7, 133.2, 130.9, 127.6, 124.0, 116.4, 111.5, 109.8, 109.5, 80.1, 61.4, 59.8, 47.0, 28.4, 26.9, 14.1. HRMS (ESI+):  $m/z$  [M + H] $^+$  calcd for  $\text{C}_{25}\text{H}_{36}\text{N}_3\text{O}_7$ : 490.2552; found: 490.2574.

#### 4.11. Ethyl 5-(5-acetoxy-1H-indol-3-yl)-4-((tert-butoxycarbonyl)amino)-3-oxopentanoate (**4ca**)

Purification by flash column chromatography (EtOAc/Hex, 1:2). Colorless oil; yield 49%;  $^1\text{H NMR}$  (400 MHz,  $\text{CDCl}_3$ ):  $\delta = 8.38$  (s, 1 H), 7.53–7.31 (m, 2H), 7.01 (s, 1 H), 6.94–6.91 (m, 1 H), 5.16 (d,  $J = 7.2$  Hz, 1 H), 4.68–4.63 (m, 1 H), 4.19–4.12 (m, 2 H), 3.52 (d,  $J = 16.0$  Hz, 1 H), 3.45 (d,  $J = 16.0$  Hz, 1 H), 3.28–3.15 (m, 2 H), 2.34 (s, 3 H), 1.44 (s, 9 H), 1.30–1.24 (m, 3 H);  $^{13}\text{C NMR}$  (100 MHz,  $\text{CDCl}_3$ ):  $\delta = 202.4$ , 170.5, 167.0, 155.3, 144.4, 134.0, 127.9, 124.5, 116.5, 111.8, 110.8, 110.3, 80.0, 61.5, 59.9, 46.9, 28.3, 26.7, 21.2, 14.1; HRMS (ESI+):  $m/z$  [M + H] $^+$  calcd for  $\text{C}_{22}\text{H}_{29}\text{N}_2\text{O}_7$ , 433.1975; found, 433.1981.

#### 4.12. General procedure for oxidative cyclization of 3-oxoesters **4aa-ca** with $\text{Mn}(\text{OAc})_3 \cdot 2\text{H}_2\text{O}$

Ester **4aa-ca** (0.1 mmol) was dissolved in AcOH (2 ml). To a resulted solution  $\text{Mn}(\text{OAc})_3 \cdot 2\text{H}_2\text{O}$  (67 mg, 0.25 mmol) was added. The resulting mixture was heated for 2.5 h at 70 °C. After completion of the reaction, the solvent was removed under vacuum, and the residue was purified with flash chromatography as specified below.

#### 4.13. General procedure for oxidative cyclization of 3-oxoesters **4aa-ae** with transition metal triflates

Ester **4aa-ae** (0.2 mmol) was dissolved in anhydrous DCM (4 ml). A resulting solution (0.4 mmol) of metal triflate specified in Table 1 was added, followed by  $\text{I}_2$  (0.3 mmol) and  $\text{NEt}_3$  (0.5 mmol, 69 μL). The resulting mixture was stirred for 12 h at R.T. After completion of the reaction, the residue was dissolved in DCM (30 mL) and washed with aqueous sat.  $\text{Na}_2\text{SO}_3$ . The organic layer was dried with  $\text{MgSO}_4$ , the

solvent was removed under vacuum, and the residue was purified with flash chromatography as specified below.

#### 4.14. Ethyl 3-((tert-butoxycarbonyl)amino)-2-hydroxy-9H-carbazole-1-carboxylate (5aa)

Purification by flash column chromatography (EtOAc/Hex, 1:5). Yellow amorphous solid; yield 67%;  $^1\text{H NMR}$  (400 MHz,  $\text{CDCl}_3$ ,  $\delta$ ): 11.60 (s, 1H), 9.01 (s, 1H), 8.97 (s, 1H), 8.02 (d,  $J = 7.6$  Hz, 1H), 7.46–7.44 (m, 1H), 7.40–7.36 (m, 1H), 7.27–7.23 (m, 1H), 7.14 (s, 1H), 4.66 (q,  $J = 7.2$  Hz, 2H), 1.61 (t,  $J = 7.2$  Hz, 3H), 1.60 (s, 9H);  $^{13}\text{C NMR}$  (100 MHz,  $\text{CDCl}_3$ ,  $\delta$ ): 170.5, 153.3, 150.8, 138.6, 133.9, 124.7, 123.3, 120.7, 120.0, 119.7, 116.9, 115.4, 110.6, 96.2, 80.3, 62.2, 28.5, 14.6; HRMS (ESI+):  $m/z$  [ $\text{M}$ ] $^+$  calcd for  $\text{C}_{20}\text{H}_{22}\text{N}_2\text{O}_5$ , 370.1528; found, 370.1481.

#### 4.15. Ethyl 3-((ethoxycarbonyl)amino)-2-hydroxy-9H-carbazole-1-carboxylate (5ab)

Purification by flash column chromatography (EtOAc/Hex, 1:5). Yellow amorphous solid; yield 28%;  $^1\text{H NMR}$  (400 MHz,  $\text{CDCl}_3$ ,  $\delta$ ):  $\delta = 11.56$  (s, 1H), 8.96 (s, 1H), 8.92 (s, 1H), 7.98 (d,  $J = 8.0$  Hz, 1H), 7.44–7.42 (m, 1H), 7.40–7.36 (m, 1H), 7.26–7.20 (m, 2H), 4.63 (q,  $J = 7.2$  Hz, 2H), 4.32 (q,  $J = 7.2$  Hz, 2H), 1.59 (t,  $J = 7.2$  Hz, 3H), 1.40 (t,  $J = 7.2$  Hz, 3H);  $^{13}\text{C NMR}$  (100 MHz,  $\text{CDCl}_3$ ,  $\delta$ ): 170.4, 154.1, 150.9, 138.7, 134.1, 124.8, 123.2, 120.2, 120.1, 119.6, 117.0, 115.4, 110.6, 96.2, 62.2, 61.2, 14.7, 14.6; HRMS (ESI+):  $m/z$  [ $\text{M} + \text{H}$ ] $^+$  calcd for  $\text{C}_{18}\text{H}_{19}\text{N}_2\text{O}_5$ , 343.1294; found, 343.1277.

#### 4.16. Ethyl 3-acetamido-2-hydroxy-9H-carbazole-1-carboxylate (5ac)

Purification by flash column chromatography (EtOAc/Hex, 1:2). Yellow amorphous solid; yield 29%;  $^1\text{H NMR}$  (400 MHz,  $\text{CDCl}_3$ ,  $\delta$ ): 11.65 (s, 1H), 9.19 (s, 1H), 9.01 (s, 1H), 8.00 (d,  $J = 7.6$  Hz, 1H), 7.80 (s, 1H), 7.45–7.43 (m, 1H), 7.40–7.36 (m, 1H), 7.27–7.24 (m, 1H), 4.64 (q,  $J = 7.2$  Hz, 2H), 2.29 (s, 3H), 1.60 (t,  $J = 7.2$  Hz, 3H);  $^{13}\text{C NMR}$  (100 MHz,  $\text{CDCl}_3$ ,  $\delta$ ): 170.5, 168.3, 151.0, 138.7, 134.5, 124.9, 123.2, 120.2, 119.8, 118.6, 115.4, 110.6, 96.1, 62.3, 24.8, 14.6; HRMS (ESI+):  $m/z$  [ $\text{M} + \text{H}$ ] $^+$  calcd for  $\text{C}_{17}\text{H}_{17}\text{N}_2\text{O}_4$ , 313.1187; found, 313.1165.

#### 4.17. Ethyl 3,6-bis((tert-butoxycarbonyl)amino)-2-hydroxy-9H-carbazole-1-carboxylate (5ba)

Purification by flash column chromatography (EtOAc/Hex, 1:4). Colorless oil; yield 36%;  $^1\text{H NMR}$  (400 MHz,  $\text{CDCl}_3$ ,  $\delta$ ): 11.61 (s, 1H), 8.91 (s, 1H), 8.87 (s, 1H), 7.97 (s, 1H), 7.35 (s, 2H), 7.09 (s, 1H), 6.56 (s, 1H), 4.65 (q,  $J = 7.2$  Hz, 2H), 1.60 (t,  $J = 7.2$  Hz, 3H), 1.60 (s, 9H), 1.58 (s, 9H);  $^{13}\text{C NMR}$  (100 MHz,  $\text{CDCl}_3$ ,  $\delta$ ): 170.5, 166.7, 153.2, 151.1, 135.3, 134.5, 131.2, 123.6, 120.5, 117.3, 115.3, 110.6, 96.1, 80.3, 80.2, 62.2, 28.5, 14.6; HRMS (ESI+):  $m/z$   $\text{M}^+$  calcd for  $\text{C}_{25}\text{H}_{31}\text{N}_3\text{O}_7$ , 485.2162; found, 485.2173.

#### 4.18. Ethyl 6-acetoxy-3-((tert-butoxycarbonyl)amino)-2-hydroxy-9H-carbazole-1-carboxylate (5ca)

Purification by flash column chromatography (EtOAc/Hex, 1:4). White amorphous solid; yield 25%;  $^1\text{H NMR}$  (400 MHz,  $\text{CDCl}_3$ ,  $\delta$ ): 11.63 (s, 1H), 9.00 (s, 1H), 8.91 (s, 1H), 7.72–7.71 (m, 1H), 7.41–7.39 (m, 1H), 7.13–7.07 (m, 2H), 4.67 (q,  $J = 7.2$  Hz, 2H), 2.37 (s, 3H), 1.61 (t,  $J = 7.2$  Hz, 3H), 1.59 (s, 9H);  $^{13}\text{C NMR}$  (100 MHz,  $\text{CDCl}_3$ ,  $\delta$ ): 170.4, 170.3, 153.2, 151.2, 144.4, 136.4, 134.6, 123.8, 120.9, 118.4, 116.9, 115.2, 112.4, 110.9, 96.3, 80.4, 62.3, 28.4, 21.2, 14.6; HRMS (ESI+):  $m/z$  [ $\text{M} + \text{Na}$ ] $^+$  calcd for  $\text{C}_{22}\text{H}_{24}\text{N}_2\text{O}_7\text{Na}$ , 451.1480; found, 451.1455.

#### 4.19. General procedure for preparation of ethyl 3-(5-alkylfuran-2-carboxamido)-2-hydroxy-9H-carbazole-1-carboxylate derivatives (7aa-ba)

Compound **5aa** or **5ba** (0.135 mmol) was dissolved in dry DCM (1 ml) and TFA 0.5 ml was added. The reaction mixture was stirred and monitored with TLC until the substrate disappears. Then solvents were removed under reduced pressure, and the residue was evaporated three times with 3 ml of toluene. Crude trifluoroacetic acid salts of **6aa** or **6ba** were used for the next step without purification.

Residue was dissolved in DMF (2 ml), and 5-methylfuran-2-carboxylic acid or 5-ethylfuran-carboxylic acid (0.135 mmol) was added followed by  $\text{NEt}_3$  (225  $\mu\text{L}$ , 1.63 mmol) and TBTU (53 mg, 0.163 mmol). The reaction mixture was stirred for 18h at R. T. Solvent was removed under reduced pressure, the residue was purified with flash chromatography as specified below.

#### 4.20. Ethyl 2-hydroxy-3-(5-methylfuran-2-carboxamido)-9H-carbazole-1-carboxylate (7aa)

Purification by flash column chromatography (EtOAc/Hex, 1:3). Yellow oil; yield 15%;  $^1\text{H NMR}$  (400 MHz,  $\text{CDCl}_3$ ,  $\delta$ ): 10.04 (s, 1H), 9.28 (s, 1H), 8.38 (s, 1H), 8.12 (d,  $J = 7.6$  Hz, 1H), 7.52–7.46 (m, 3H), 7.31–7.27 (m, 1H), 7.15–7.14 (d,  $J = 3.6$  Hz, 1H), 6.16–6.15 (m, 1H), 4.37 (q,  $J = 7.2$  Hz, 2H), 2.51 (s, 3H), 1.17 (t,  $J = 7.2$  Hz, 3H);  $^{13}\text{C NMR}$  (100 MHz,  $\text{CDCl}_3$ ,  $\delta$ ): 165.8, 158.9, 156.3, 154.7, 146.2, 142.1, 140.3, 127.0, 123.4, 122.4, 121.7, 120.8, 120.2, 118.8, 116.4, 111.1, 109.4, 105.9, 61.5, 14.2, 13.7; HRMS (ESI+):  $m/z$  [ $\text{M} + \text{H}$ ] $^+$  calcd for  $\text{C}_{21}\text{H}_{19}\text{N}_2\text{O}_5$ , 379.1294; found, 379.1277.

#### 4.21. Ethyl 3-(5-ethylfuran-2-carboxamido)-2-hydroxy-9H-carbazole-1-carboxylate (7ab)

Purification by flash column chromatography (EtOAc/Hex, 1:3). Yellow oil; yield 31%;  $^1\text{H NMR}$  (400 MHz,  $\text{CDCl}_3$ ,  $\delta$ ): 10.05 (s, 1H), 9.34 (s, 1H), 8.40 (s, 1H), 8.13 (d,  $J = 7.6$  Hz, 1H), 7.53–7.52 (m, 1H), 7.50–7.46 (m, 1H), 7.32–7.28 (m, 2H), 7.17–7.16 (m, 1H), 6.16–6.15 (m, 1H), 4.37 (q,  $J = 7.2$  Hz, 2H), 2.85 (q,  $J = 7.2$  Hz, 2H), 1.14 (t,  $J = 7.2$  Hz, 6H);  $^{13}\text{C NMR}$  (100 MHz,  $\text{CDCl}_3$ ,  $\delta$ ):  $\delta = 165.8$ , 164.5, 160.1, 156.4, 146.1, 141.9, 140.3, 126.7, 123.5, 122.5, 121.6, 120.8, 120.2, 118.5, 116.2, 111.1, 107.6, 105.8, 61.5, 21.5, 13.7, 11.7. HRMS (ESI+):  $m/z$  [ $\text{M} + \text{H}$ ] $^+$  calcd for  $\text{C}_{22}\text{H}_{21}\text{N}_2\text{O}_5$ , 393.1449; found, 393.1426.

#### 4.22. Ethyl 2-((5-methylfuran-2-carbonyloxy)-3,6-bis(5-methylfuran-2-carboxamido)-9H-carbazole-1-carboxylate (7ba)

Purification by flash column chromatography (EtOAc/Hex, 1:3). Colorless oil; yield 54%;  $^1\text{H NMR}$  (400 MHz,  $\text{CDCl}_3$ ,  $\delta$ ): 9.96 (s, 1H), 9.09 (s, 1H), 8.33 (s, 1H), 8.23 (s, 1H), 8.21 (d,  $J = 1.7$  Hz, 1H), 7.81 (dd,  $J = 8.7$  Hz,  $J = 2.0$  Hz, 1H), 7.50 (d,  $J = 3.4$  Hz, 1H), 7.44 (d,  $J = 8.7$  Hz, 1H), 7.18 (d,  $J = 3.3$  Hz, 1H), 7.13 (d,  $J = 3.3$  Hz, 1H), 6.30 (dd,  $J = 3.4$  Hz,  $J = 0.8$  Hz, 1H), 6.18 (dd,  $J = 3.3$  Hz,  $J = 0.9$  Hz, 1H), 6.14 (dd,  $J = 3.3$  Hz,  $J = 0.8$  Hz, 1H), 4.33 (q,  $J = 7.2$  Hz, 2H), 2.50 (s, 3H), 2.43 (s, 3H), 2.26 (s, 3H), 1.16 (t,  $J = 7.2$  Hz, 3H);  $^{13}\text{C NMR}$  (100 MHz,  $\text{CDCl}_3$ ,  $\delta$ ): 165.6, 158.9, 156.4, 156.3, 156.2, 157.8, 154.7, 146.5, 146.2, 142.1, 139.2, 138.2, 137.4, 130.6, 123.2, 122.3, 122.1, 121.7, 120.5, 119.3, 116.3, 116.2, 112.5, 111.5, 109.0, 108.9, 108.8, 106.0, 61.4, 14.2, 13.9, 13.8, 13.7; HRMS (ESI+):  $m/z$  [ $\text{M} + \text{H}$ ] $^+$  calcd for  $\text{C}_{33}\text{H}_{28}\text{N}_3\text{O}_9$ , 610.1825; found, 610.1838.

#### 4.23. 3-((tert-butoxycarbonyl)amino)-2-hydroxy-9H-carbazole-1-carboxylic acid (8)

Compound **5aa** (20 mg, 0.054 mmol) was dissolved in 0.5 M solution of NaOH ( $\text{H}_2\text{O}:\text{MeOH}$  1:1) (2 ml) and stirred for 12 h at R. T. Solution was acidified with 2 M HCl to pH = 3, and extracted with DCM (3  $\times$  5

ml). Organic layers was washed with water (5 ml) brine (5 ml) and dried with MgSO<sub>4</sub>. Solvent was removed under reduced pressure and the residue was purified with flash chromatography. (EtOAc/Hex, 1:3). White amorphous solid; yield 99%;

<sup>1</sup>H NMR (400 MHz, CDCl<sub>3</sub>, δ): 11.52 (s, 1H), 9.00 (s, 1H), 8.96 (s, 1H), 8.01 (d, *J* = 8.0 Hz, 1H), 7.46–7.44 (m, 1H), 7.40–7.36 (m, 1H), 7.26–7.22 (m, 1H), 7.13 (s, 1H), 1.61 (s, 9H); <sup>13</sup>C NMR (100 MHz, CDCl<sub>3</sub>, δ): 170.9, 153.3, 150.8, 138.7, 133.8, 124.8, 123.3, 120.6, 120.0, 119.7, 117.1, 115.5, 110.6, 96.0, 80.4, 28.5;

#### 4.24. Cell cultivation

HCT-116 cell line, which was kindly provided by Prof. Bert Vogelstein (Johns Hopkins University, Howard Hughes Medical Institute, USA), was cultured in McCoy's 5A medium. A-549 (CCL-185), Hep-G2 (HB-8065), U-2 OS (HTB-96), MCF-7 (HB-8065), and HEK-293 (CRL-1573) were obtained from ATCC. A-549 and MCF-7 were cultured in RPMI-1640 medium, U-2 OS in McCoy's 5A medium, and HEK-293 and Hep-G2 in Dulbecco's Modified Eagle medium. The culture medium used for cancer cell lines was supplemented with 10% fetal bovine serum, 2 mM L-glutamine, and antibiotics (penicillin 62.6 µg/ml and streptomycin 40 µg/ml). Cancer cells were cultured under humidified atmosphere containing 5% CO<sub>2</sub> at 37 °C and routinely screened for *Mycoplasma* contamination.

#### 4.25. Cell viability assay

The cell viability was determined after treatment with the synthesized compounds using the MTT (Sigma-Aldrich) assay. Briefly, cells were seeded into 96-well culture plates and allowed to adhere overnight. Then, they were exposed to various concentrations of compounds for 72 h. For vehicle control, DMSO (Merck) and Etoposide (Sigma-Aldrich) were used. After incubation, the MTT solution (0.4 mg/ml, final concentration) was added to the cells in each well, and the plates were incubated for an additional 2–3 h at 37 °C. After incubation, the cells were stained, and the medium was replaced with 100 µl DMSO.

The absorbance of formazan was measured at 450 nm using an ASYS UVM340 microplate reader (Biochrom Ltd.). The IC<sub>50</sub> value was estimated for each compound in GraphPad Prism 8 software based on the curves plotted using survival as a function of dose, averaged from three independent experiments.

#### 4.26. Flow cytometry

For flow cytometric experiments, HCT-116, A-549, and U-2 OS cells were seeded into Petri dishes and allowed to attach overnight. Then, they were incubated with each of the investigated compounds for the appropriate time. Analysis was performed using a Guava easyCyte 8 cell sorter (Merck Millipore) and FlowJo v10 software. Each experiment was repeated independently three times.

#### 4.27. Cell cycle analysis

For analyzing the cell cycle, the harvested cells were fixed in ice-cold 75% ethanol and stored overnight at –20 °C. Then, they were rehydrated with phosphate-buffered saline (PBS) for 10 min. Subsequently, the cells were stained with 20 µg/µl propidium iodide (Sigma-Aldrich) and 50 µg/µl RNaseA (Thermo-Fisher) in PBS for 30 min at room temperature and measured.

#### 4.28. H2AX phosphorylation

After treatment with the studied compounds, the cells were harvested and fixed in 75% ethanol overnight or longer at –20 °C. To detect H2AX phosphorylation, the cells were rehydrated with PBS in ice for 10 min and permeabilized in 0.2% Triton X-100 in PBS for 5 min at room

temperature. Then, they were washed with 1% bovine serum albumin (BSA) in PBS and incubated with Alexa Fluor™ 488-conjugated mouse anti-γH2AX (Ser139) antibody (#613406, 1:100 dilution; BioLegend). DNA was stained with 20 µg/µl propidium iodide and 50 µg/µl RNaseA in PBS for 30 min at room temperature and measured.

#### 4.29. Mitochondrial membrane potential

For determining the mitochondrial membrane potential, 10 µM Carbonyl cyanide-*p*-trifluoromethoxyphenylhydrazone FCCP (Sigma-Aldrich) was added 30 min before the end of incubation of cells with the investigated drug. The positive control consisted of 10 µM FCCP. After treatment, the culture medium of the HCT-116 and U-2 OS cells was replaced by a fresh medium supplemented with 5 µg/ml JC-1 dye (Sigma-Aldrich) and the cells were incubated in dark for 20 min at 37 °C. Subsequently, the cells were washed twice with PBS and measured.

#### 4.30. Reactive oxygen species generation

For analyzing the ROS generation, 1 µM CM-H<sub>2</sub>DCFDA (#C6827; Thermo-Fisher) probe was added to the cells in each plate 30 min before the end of the drug treatment. As a reference, 250 µM H<sub>2</sub>O<sub>2</sub> was used. After treatment, the cells were detached with 0.05% trypsin solution in PBS and Hank's Balanced Salt Solution, treated with 7-AAD (Sigma-Aldrich), and measured.

#### 4.31. Apoptosis and caspase 3/7 assay

As a positive control Cells were harvested and stained with Annexin V-FITC or Alexa Fluor 488 conjugate (#A13201; Thermo-Fisher) for performing apoptosis assay or with the reagents in the CellEvent™ Caspase-3/7 Green Flow Cytometry Assay Kit (Thermo-Fisher, #C10427) for investigating the activation of caspase-3/7, according to the manufacturer's protocol. Finally, they were stained with 7-AAD (Sigma-Aldrich) and measured. For positive control, 10 µM Etoposide was used.

#### 4.32. Senescence

After harvesting, the size and granularity of unstained cells were evaluated by analyzing the side scattering and forward scattering. Doxorubicin (Sigma-Aldrich) was used as a reference compound for the analysis.

#### 4.33. Colony formation assay

HCT-116 and U-2 OS cell lines were seeded into six-well plates at a density of 500 cells well<sup>-1</sup>. After attachment, the cells were pretreated with DMSO or different concentrations of **8** and **5aa** for 24 h. Then, they were washed and cultured for an additional 9 days. Finally, the cell colonies were fixed in methanol and stained with 0.5% crystal violet. The visible colonies were counted by ImageJ software, and percentage viability was calculated in comparison to the control.

#### 4.34. Wound healing migration assay

The possible antimigratory effects of the tested compounds were investigated by wound healing assay. HCT-116 and U-2 OS cell lines were seeded into an Ibidi-silicone insert on a cover glass-bottom 24-well plate for live-cell imaging and incubated for 24 h to allow the attachment of cells. After incubation, the inserts were dislodged and the cells were washed twice with a fresh medium to remove any unattached cells. Then, the cells were exposed to various concentrations of compounds, and the plates containing cells were placed inside an imaging chamber (cellVivo incubation system; Olympus) maintained at 37 °C with 5% CO<sub>2</sub> for incubation. Live-cell microscopy with time-lapse photography



was performed to monitor the migration of cells. Images were captured every 15 min for 48 h under  $\times 10$  magnification using a phase-contrast fluorescence microscope (IX83 Inverted Microscope; Olympus) which was connected to an XC50 digital color camera (Olympus). Using cellSens software (Olympus), the images were combined to generate a video. The distance between gaps was measured using ImageJ software.

#### 4.35. Immunofluorescence

Cells were treated with **5aa** and **8** at their respective  $IC_{50}$  concentrations or with DMSO (1%) or Etoposide for 24, 48, and 72 h. After treatment, they were fixed with 4% Paraformaldehyde (Sigma-Aldrich) for 15 min, permeabilized with 0.2% Triton X-100 for 15 min, and blocked with 3% BSA in PBS with 0.1% Triton X-100 (PBS-T) for 1 h at room temperature. Then, the cells were incubated with Alexa Fluor 488 mouse anti-H2AX (pS139) (#560445, 1:200 dilution; BD Pharmingen) and anti- $\beta$ -Tubulin (#T8328; Sigma-Aldrich) antibodies diluted in PBS-T with 3% BSA in a humidified chamber at 37 °C for 1.5 h. Next, they were incubated with Alexa Fluor 594-conjugated anti-rabbit IgG (#sc-516250, 1:1000 dilution; Santa Cruz Biotechnology) for 1 h in a humidified chamber at 37 °C. Thereafter, the cells were stained with 1  $\mu$ g/ml DAPI for 10 min. Images were acquired with an LSM 800 inverted laser-scanning confocal microscope (Carl Zeiss), equipped with an airyscan detector for high-resolution confocal scanning using a  $\times 63$  1.4 NA Plan Apochromat objective (Carl Zeiss).

#### 4.36. Confocal live-cell imaging

For the analysis of mitochondrial morphology, HCT-116 cells were grown on a cover glass-bottom confocal 12-well plate. After 6 h of treatment with the tested compounds at their  $IC_{50}$  concentration and with DMSO, mitochondria were labeled by incubating the cells with MitoTracker Green FM probe (Thermo-Fisher) and Hoechst 33342 (Thermo-Fisher) for 15 min, according to the manufacturer's protocol. After incubation, the medium was replaced with a fresh growth medium. Confocal Z-stack images were acquired at 0.5- $\mu$ m intervals for 10 stacks, with the parameters (laser intensity, exposure times, gain settings, etc.) kept constant for both cells treated with compounds and cells treated with DMSO. The excitation wavelengths for MitoTracker Green FM and Hoechst 33342 were 488 and 350 nm, respectively.

Colocalization study was carried out the same way as the analysis of mitochondrial morphology with some modifications: (1) the cells were treated for 2 h with 10  $\mu$ M of tested compounds, and (2) labeled with BODYPI (Thermo-Fisher) according to the manufacturer's protocol. The excitation wavelengths for BODYPI and tested compounds were 580 and 345 nm, respectively. Correlations of overlapping pixel intensities were calculated using thresholded MCC and PCC from Z-stack images. The scatter plot and coefficients were analyzed using the JACop plugin for ImageJ as previously described [49].

Images were acquired with an LSM 800 inverted laser-scanning confocal microscope (Carl Zeiss), equipped with an airyscan detector for high-resolution confocal scanning using a  $\times 63$  1.4 NA Plan Apochromat objective (Carl Zeiss). Cells were incubated in an incubation chamber maintained at 37 °C with 5%  $CO_2$  during the experiments.

#### 4.37. Quantitative mitochondrial morphometric analyses

Morphometric analyses, counting of mitochondrial particles, and analysis of circularity were performed using the mitochondrial morphology plugin of ImageJ (NIH) developed by Dagda et al. [50] The average mitochondrial volume was measured using the Particle Analyzer plugin of ImageJ (NIH). All measurements were obtained from the Z-axis confocal stacks. The mitochondrial length was determined with a macro developed by Merrill et al. [51] All data were compiled and analyzed in GraphPad Prism 8.

#### 4.38. Detection of SA- $\beta$ -Gal

SA- $\beta$ -Gal was detected using the protocol described by Dimri et al. [52] Briefly, after incubation, the cells were washed with PBS and fixed for 5 min at room temperature in 3% formaldehyde (Sigma-Aldrich). Then, they were washed three times with PBS and incubated for 12–16 h at 37 °C (without  $CO_2$ ) with staining solution (1 mg/ml X-gal; A&A Biotechnology) in 40 mM citric acid/sodium phosphate (pH 6.0; Sigma-Aldrich), 5 mM potassium ferrocyanide (Fisher Scientific), 5 mM potassium ferricyanide (Fisher Scientific), 150 mM NaCl (POCH S.A), and 2 mM  $MgCl_2$  (POCH S.A). After incubation, the cells were washed again with 40 mM citric acid/sodium phosphate (pH 4.0) and observed under a BX60 inverted microscope (Olympus). SA- $\beta$ -Gal-positive cells were quantified by counting the cells in 20 random fields of view using ImageJ software. Doxorubicin (Sigma-Aldrich) was used as a reference compound for the analysis.

#### 4.39. Statistical analyses

Statistical analyses were performed using GraphPad Prism 8 software. Data were obtained from  $n = 3$  independent experiments and are presented as mean  $\pm$  SEM. Statistical significance was calculated in comparison to the vehicle using one-way analysis of variance (ANOVA) post hoc Tukey's test unless stated otherwise. A probability level of  $p < 0.05$  was considered to be statistically significant.

#### Declaration of competing interest

The authors declare that they have no known competing financial interests or personal relationships that could have appeared to influence the work reported in this paper.

#### Acknowledgements

This work was supported by grant no. 2014/13/B/NZ7/02207 "New inhibitors of catalytic subunit of telomerase" from the National Science Centre (Krakow, Poland). The abstract graphic was created with [Bio-Render.com](https://BioRender.com).

#### Appendix A. Supplementary data

Supplementary data to this article can be found online at <https://doi.org/10.1016/j.ejmech.2022.114453>.

#### References

- [1] H.J. Knolker, K.R. Reddy, *Chem. Rev.* 102 (2002) 4303.
- [2] A.W. Schmidt, K.R. Reddy, H.J. Knolker, *Chem. Rev.* 112 (2012) 3193.
- [3] H. Yan, T.C. Mizutani, N. Nomura, T. Takakura, Y. Kitamura, H. Miura, M. Nishizawa, M. Tatsumi, N. Yamamoto, W. Sugiura, *Antivir. Chem. Chemother.* 16 (2005) 363.
- [4] S.D. Boggs, J.D. Cobb, K.S. Gudmundsson, L.A. Jones, R.T. Matsuoka, A. Millar, D. E. Patterson, V. Samano, M.D. Trone, S. Xie, X. Zhou, *Org. Process Res. Dev.* 11 (2007) 539.
- [5] J.D. Ha, S.K. Kang, H.G. Cheon, J.K. Choi, *Bull. Kor. Chem. Soc.* 25 (2004) 1784.
- [6] G. Romeo, L. Materia, V. Pittala, M. Modica, L. Salerno, M. Siracusa, F. Russoa, K. P. Minneman, *Bioorg. Med. Chem.* 14 (2006) 5211.
- [7] P. Bod, K. Harsányi, F. Trischler, E. Feckes, A. Csehi, E. Hegedis, M. Donát, G. S. Komlósi, E.H. Sziki, U. S. Jpn. Outlook 5 (478) (1995), 949 26 Dec.
- [8] E. Ravina, *The Evolution of Drug Discovery: from Traditional Medicines to Modern Drugs* Weinheim, Wiley-VCH, 2011.
- [9] J.E. Saxton, *Nat. Prod. Rep.* 11 (1994) 493.
- [10] Y. Zhang, V.K.R. Tangadanchu, Y. Cheng, R.-G. Yang, J.-M. Lin, Ch. Zhou, *ACS Med. Chem. Lett.* 9 (2018) 244–249.
- [11] S. Maiti, A. Bose, P. Mal, J. Org. Chem. 83 (2018) 8127–8138.
- [12] P. A. Bal, S. Maiti, P. Mal, J. Org. Chem. 83 (2018) 11278–11287.
- [13] C. Liu, P. Knochel, *Org. Lett.* 7 (2005) 2543–2546.
- [14] J.H. Smitrovich, J.W. Davies, *Org. Lett.* 6 (2004) 533–535.
- [15] A. Kuwahara, K. Nakano, K. Nozaki, *J. Org. Chem.* 70 (2005) 413–419.
- [16] L. Wang, G. Li, Y. Liu, *Org. Lett.* 13 (2011) 3786–3789.
- [17] S. Singh, R. Samineneni, S. Pabbaraja, G. Mehta, *Org. Lett.* 21 (2019) 3372–3376.
- [18] C. Zhu, S. Ma, *Org. Lett.* 16 (2014) 1542–1545.

- [19] S.S. Chen, Y. Li, P. Ni, B. Yang, H. Huang, G. Deng, *J. Org. Chem.* 82 (2017) 2935–2942.
- [20] S. Maiti, P. Mal, *Org. Lett.* 19 (2017) 2454–2457.
- [21] T. Watanabe, S. Oishi, N. Fujii, H. Ohno, *J. Org. Chem.* 74 (2009) 4720–4726.
- [22] M. Szweczyk, M. Ryczkowska, S. Makowicz, *Synthesis* 51 (2019) 4625–4634.
- [23] U. Kalathiya, M. Padariya, M. Baginski, *IEEE ACM Trans. Comput. Biol. Bioinf* 11 (2014) 1196–1207.
- [24] U. Kalathiya, M. Padariya, M. Baginski, *Sci. Rep.* 9 (2019) 8707.
- [25] A. Coste, G. Karthikeyan, F. Couty, G. Evano, *Synthesis* 17 (2009) 2927–2934.
- [26] L. Wang, Y. Murai, T. Yoshida, M. Okamoto, K. Masuda, Y. Sakihama, Y. Hashidoko, Y. Hatanaka, M. Hashimoto, *Biosci. Biotechnol. Biochem.* 78 (2014) 1129–1134.
- [27] X. Liu, Y. Liu, G. Chai, B. Qiao, X. Zhao, Z. Jiang, *Org. Lett.* 20 (2018) 6298–6301.
- [28] I. Wauters, H. Goossens, E. Delbeke, K. Muylaert, B.I. Roman, K. Van Hecke, V. Van Speybroeck, C.V. Stevens, *Org. Chem.* 80 (2015) 8046–8054.
- [29] N. Naganna, N. Madhavan, *J. Org. Chem.* 79 (2014) 11549–11557.
- [30] K. Satoh, A. Imura, A. Miyadera, K. Kanai, Y. Yukimto, *Chem. Pharm. Bull.* 46 (1998) 587–590.
- [31] C. Mordant, S. Reymond, H. Tone, D. Lavergne, R. Touati, B.B. Hassine, V. Ratovelomanana-Vidal, J.-P. Genet, *Tetrahedron* 63 (2007) 6115–6123.
- [32] A. D'Annibale, A. Pesce, S. Resta, C. Trogolo, *Tetrahedron* 53 (1997) 13129–13138.
- [33] B. Atteni, A. Cerreti, A. D'Annibale, S. Resta, C. Trogolo, *Tetrahedron* 53 (1998) 12029–12038.
- [34] P. Punda, S. Makowicz, *New J. Chem.* 37 (2013) 2254.
- [35] P. Punda, M. Schielmann, S. Makowicz, *Lett. Org. Chem.* 14 (2017) 337–346.
- [36] R. Dubey, C.E. Stivala, H.Q. Nguyen, Y.-H. Goo, A. Paul, J.E. Carette, B.M. Trost, R. Rohatgi, *Nat. Chem. Biol.* 16 (2) (2020) 206–213.
- [37] M. Olsson, B. Zhivotovsky, *Cell Death Differ.* 18 (9) (2011) 1441–1449.
- [38] G.Y. Liou, P. Storz, *Free Radic. Res.* 44 (5) (2010) 479–496.
- [39] D.B. Zorov, M. Juhaszova, S.J. Sollott, *Physiol. Rev. Suppl.* 94 (3) (2014) 909–950.
- [40] L.F. Sivandzade, A. Bhalerao, L. Cucullo, *BIO-PROTOCOL* 9 (1) (2019) e3128.
- [41] S.W.G. Tait, D.G. Green, *Oncogene* 27 (50) (2008) 6452–6461.
- [42] S.M. Gasser, G. Daumt, G. Schatzfj, *J. Biol. Chem.* 257 (21) (1982) 12034–12041.
- [43] E. Alirol, J.C. Martinou, *Oncogene* 25 (2006) 4706–4716.
- [44] A.P. Trotta, J.E. Chipuk, *Cell. Mol. Life Sci.* 74 (11) (2017) 1999–2017.
- [45] D. Arnoult, *Trends Cell Biol.* 17 (1) (2007) 6–12.
- [46] M. Bonora, A. Bononi, E. De Marchi, C. Giorgi, M. Lebedzinska, S. Marchi, S. Patergnani, A. Rimessi, J.M. Suski, A. Wojtala, M.R. Wieckowski, G. Kroemer, L. Galluzzi, P. Pinton, *Cell Cycle* 12 (4) (2013) 674–683.
- [47] J.S. Riley, G. Quarato, C. Cloix, J. Lopez, J. O'Prey, M. Pearson, J. Chapman, H. Sesaki, L.M. Carlin, J.F. Passos, A. Wheeler, A. Oberst, M.K. Ryan, S.W.G. Tait, *EMBO J.* 37 (17) (2018), e99238.
- [48] A. Chandrasekaran, M. del P.S. Idelchik, J.A. Melendez, *Redox Biol.* 11 (2017) 91–102.
- [49] S. Bolte, F.P. Cordelières, *J. Microsc.* 224 (2006) 213–232.
- [50] R.K. Dagda, S.J. Cherra, S.M. Kulich, A. Tandon, D. Park, C.T.J. Chu, *Biol. Chem.* 284 (2009) 13843–13855.
- [51] R.A. Merrill, K.H. Flippo, S. Strack, *Neuromethods* 123 (2017) 31–48.
- [52] G.P. Dimri, X. Lee, G. Basile, M. Acosta, G. Scott, C. Roskelley, E.E. Medrano, M. Linskens, I. Rubelj, O. Pereira-Smith, M. Peacocke, J. Campisi, *Natl. Acad. Sci. U. S. A.* 92 (20) (1995) 9363–9367.

## Supplemental File

### **From tryptophan to novel mitochondria-disruptive agent, synthesis and biological evaluation of 1,2,3,6-tetrasubstituted carbazoles**

Milena Witkowska<sup>a‡</sup>, Natalia Maciejewska<sup>b‡</sup>, Małgorzata Ryczkowska<sup>a</sup>, Mateusz Olszewski<sup>b</sup>, Maciej Bagiński<sup>b</sup>, Sławomir Makowiec<sup>a\*</sup>

<sup>a</sup>Department of Organic Chemistry, Faculty of Chemistry, Gdansk University of Technology, Narutowicza 11/12, 80-233, Gdansk, Poland.

<sup>b</sup>Department of Pharmaceutical Technology and Biochemistry, Faculty of Chemistry, Gdansk University of Technology, Narutowicza 11/12, 80-233, Gdansk, Poland.

‡These authors contributed equally.

#### **Figures**

Figure S1 Colocalization analyses

Figure S2 Apoptosis assay

Figure S3 Flow cytometric analyses of ROS induction in HCT-116 cells.

Figure S4 Quantitation of flow cytometric analysis of ROS induction in HCT-116 cells

Figure S5 Flow cytometric analyses of ROS induction in U-2 OS cells

Figure S6 Quantitation of flow cytometric analysis of ROS induction in U-2 OS cells

Figure S7 Microscopy images and flow cytometry quantifications of SA- $\beta$ -Gal staining of U-2 OS cells

#### **Table**

Table S1 Antifungal and antibacterial activities of compounds defined as MIC

#### **Methods**

Antimicrobial Susceptibility Test

#### **Spectra**

<sup>1</sup>H and <sup>13</sup>C NMR spectra of compounds: **3ba, 3ca, 4aa, 4ab, 4ac, 4ad, 4ae, 4ba, 4ca, 5aa, 5ab, 5ac, 5ba, 5ca, 7aa, 7ab, 7ba, 8**

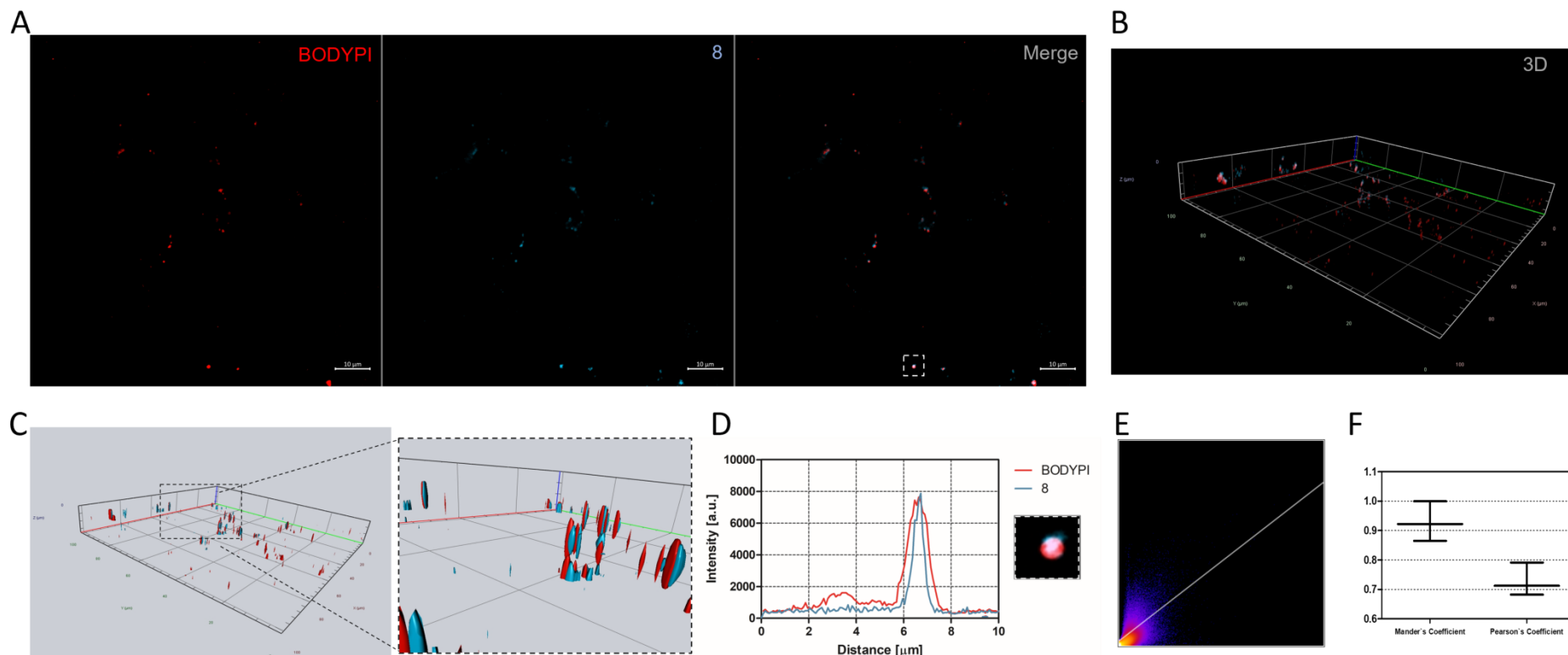


**Figure S1 Colocalization analyses.** (A-C) Representative confocal images of intracellular colocalization of lipid droplets (BODYPI) and compound **8** in HCT-116 cell line captured in Z-stack (B) and rendered with 3D-reconstruction (C). (D) Representative linescan (corresponding to top panel in A) showing colocalization LD with compounds. (E) Scatter plot correspond to the colocalization of pixels. (F) Correlations of overlapping pixel intensities described as thresholded Mander's (MCC) and Pearson's (PCC) colocalization coefficients from z-stack images.

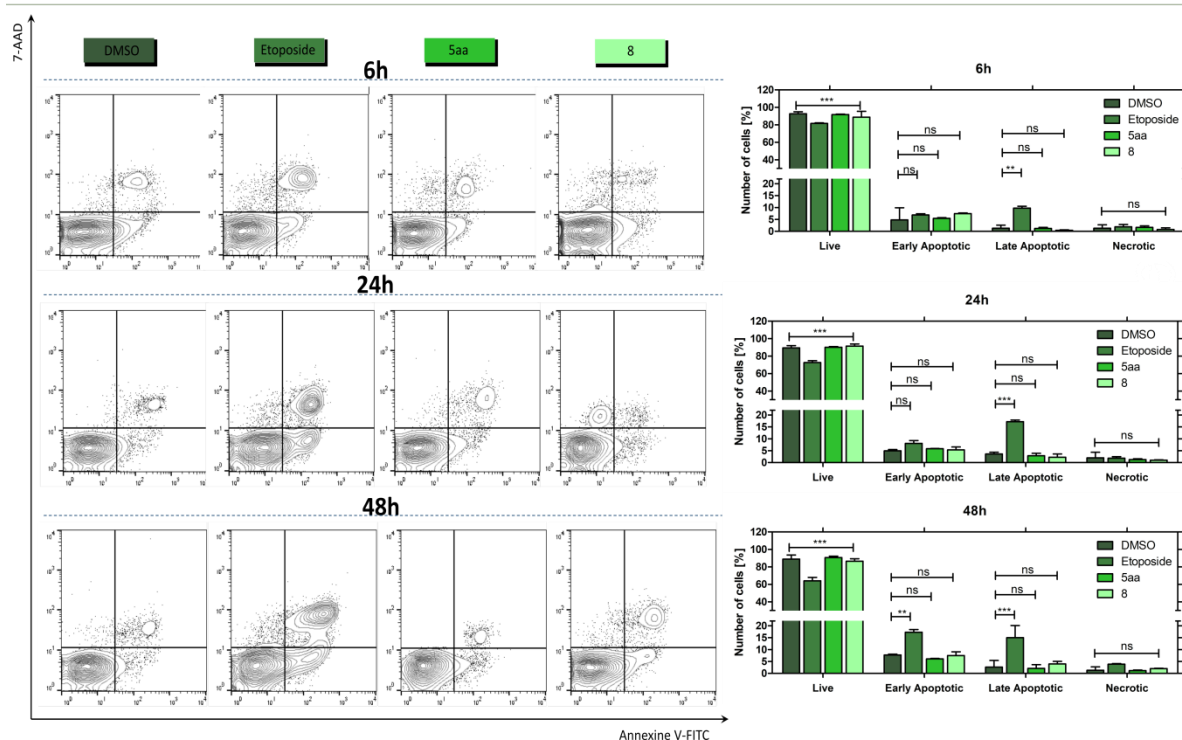


**Figure S2** Apoptosis assay. (A-B) Flow cytometric analysis of U-2 OS cell line after 6h, 24h, and 48h of treatment with tested compounds: **8** and **5aa**, using Annexin V/7-AAD. DMSO and Etoposide were used as reference compounds. In the left panels (A) representative dot-plot analyses. The quantitation of analysis was presented in right panels (B). Error bars represent the SEM of data obtained in  $n=3$  independent experiments. Statistical differences were analyzed with two-way ANOVA test. ns  $> 0.05$ , \*  $p < 0.01$ , \*\*  $p < 0.001$ , \*\*\*  $p < 0.0001$  vs. vehicle.

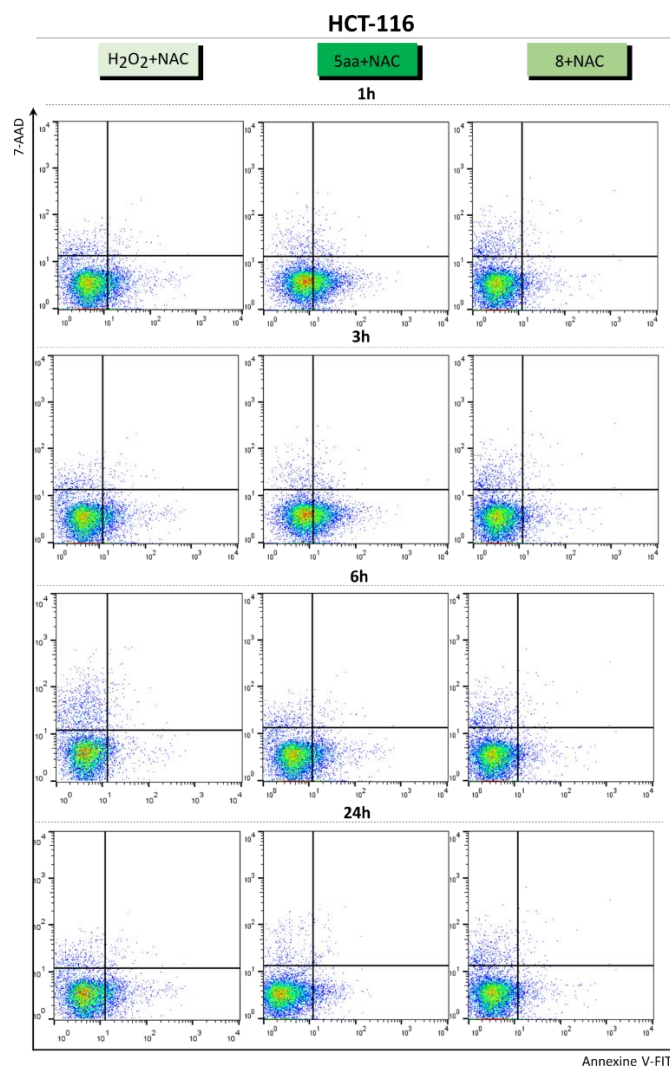


**Figure S3** Flow cytometric analyses of ROS induction in HCT-116 cells after pre-treated with N-acetyl-L-cysteine (NAC), and 1 h, 3 h, 6 h and 24 h of treatment with compounds: **8** and **5aa**, using H<sub>2</sub>DCFDA probe. DMSO and H<sub>2</sub>O<sub>2</sub> were used as reference compounds.

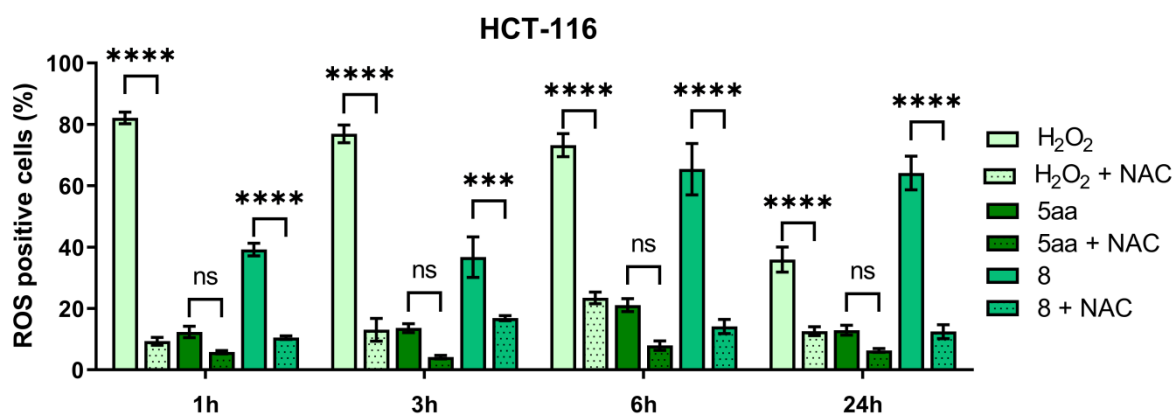


**Figure S4** Quantitation of flow cytometric analysis of ROS induction in HCT-116 cells. Error bars represent the SEM of data obtained in n=4 independent experiments. Statistical differences were analyzed with two-way ANOVA test. ns > 0.05, \*\* p < 0.001, \*\*\* p < 0.0001 vs. vehicle.



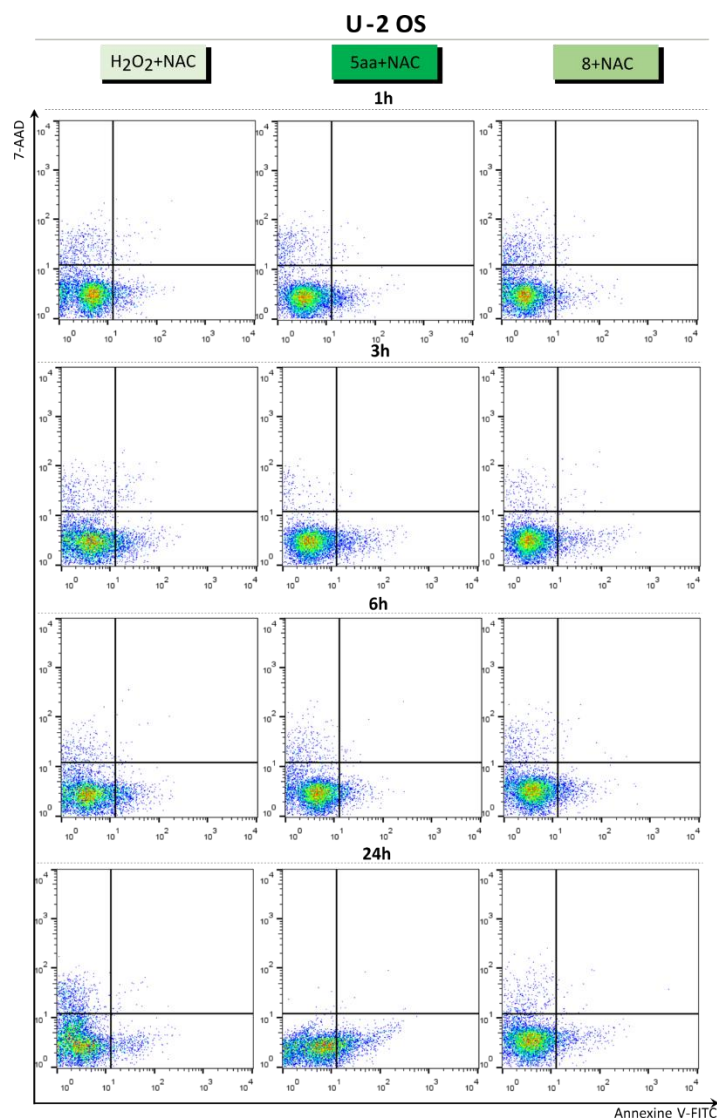


**Figure S5** Flow cytometric analyses of ROS induction in U-2 OS cells after pre-treated with N-acetyl-L-cysteine (NAC), and 1 h, 3 h, 6 h and 24 h of treatment with compounds: **8** and **5aa**, using H<sub>2</sub>DCFDA probe. DMSO and H<sub>2</sub>O<sub>2</sub> were used as reference compounds.

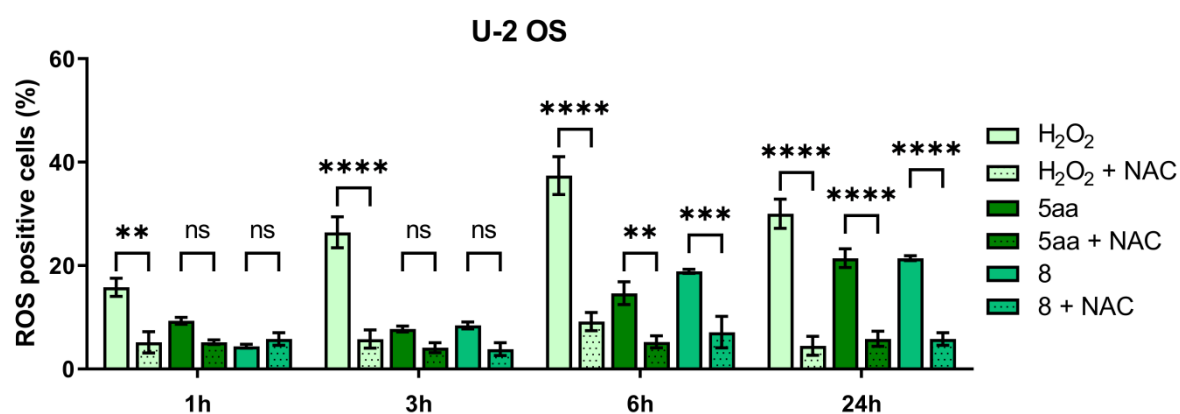


**Figure S6** Quantitation of flow cytometric analysis of ROS induction in U-2 OS cells. Error bars represent the SEM of data obtained in n=4 independent experiments. Statistical differences were analyzed with two-way ANOVA test. ns > 0.05, \*\* p < 0.001, \*\*\* p < 0.0001 vs. vehicle.

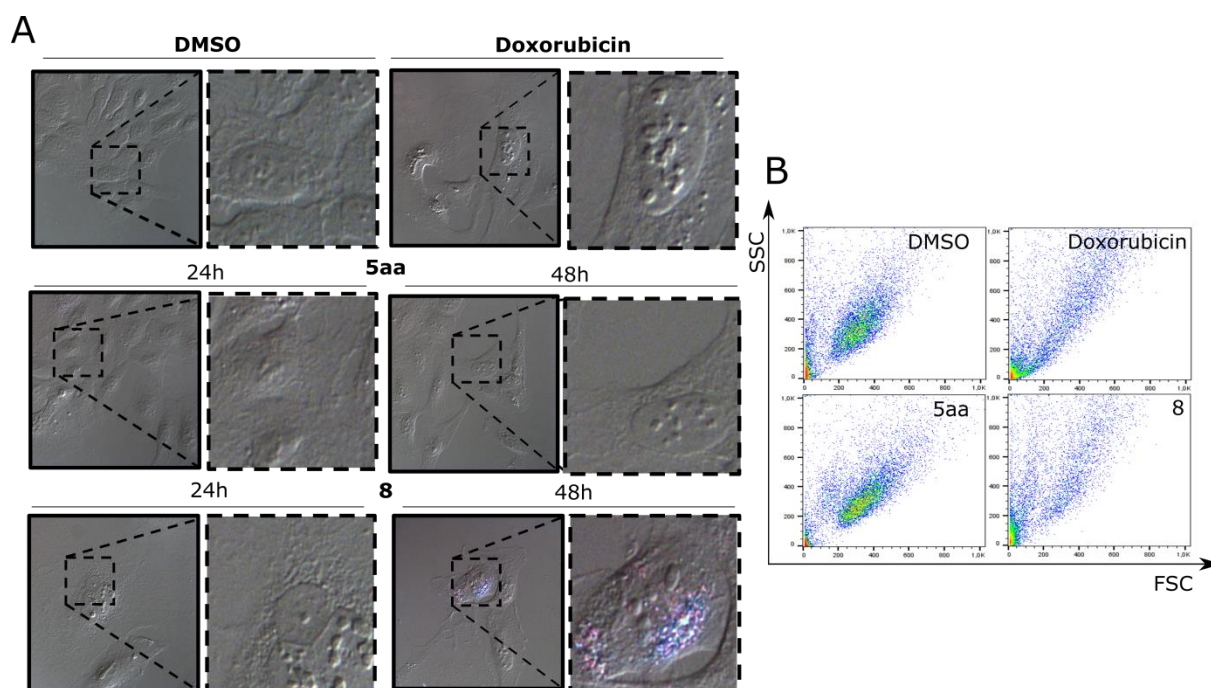


**Figure S7 (A)** Representative microscopy images of SA- $\beta$ -Gal staining and cell morphology of U-2 OS cell line after 24h or 48h of treatment with investigated compounds (10 $\mu$ M 5aa, 10 $\mu$ M 8) and additional post-culturing for 96h or 72h. Doxorubicin was used as reference compounds. **(B)** Representative dot-plot analyses after 48h of treatment with investigated compounds (10 $\mu$ M 5aa, 10 $\mu$ M 8) and additional post-culturing for 96h. Error bars represent the SEM of data obtained in n=10 random fields of view. Statistical differences were analyzed with two-way ANOVA test. \*\*\* p<0.0001 vs. vehicle

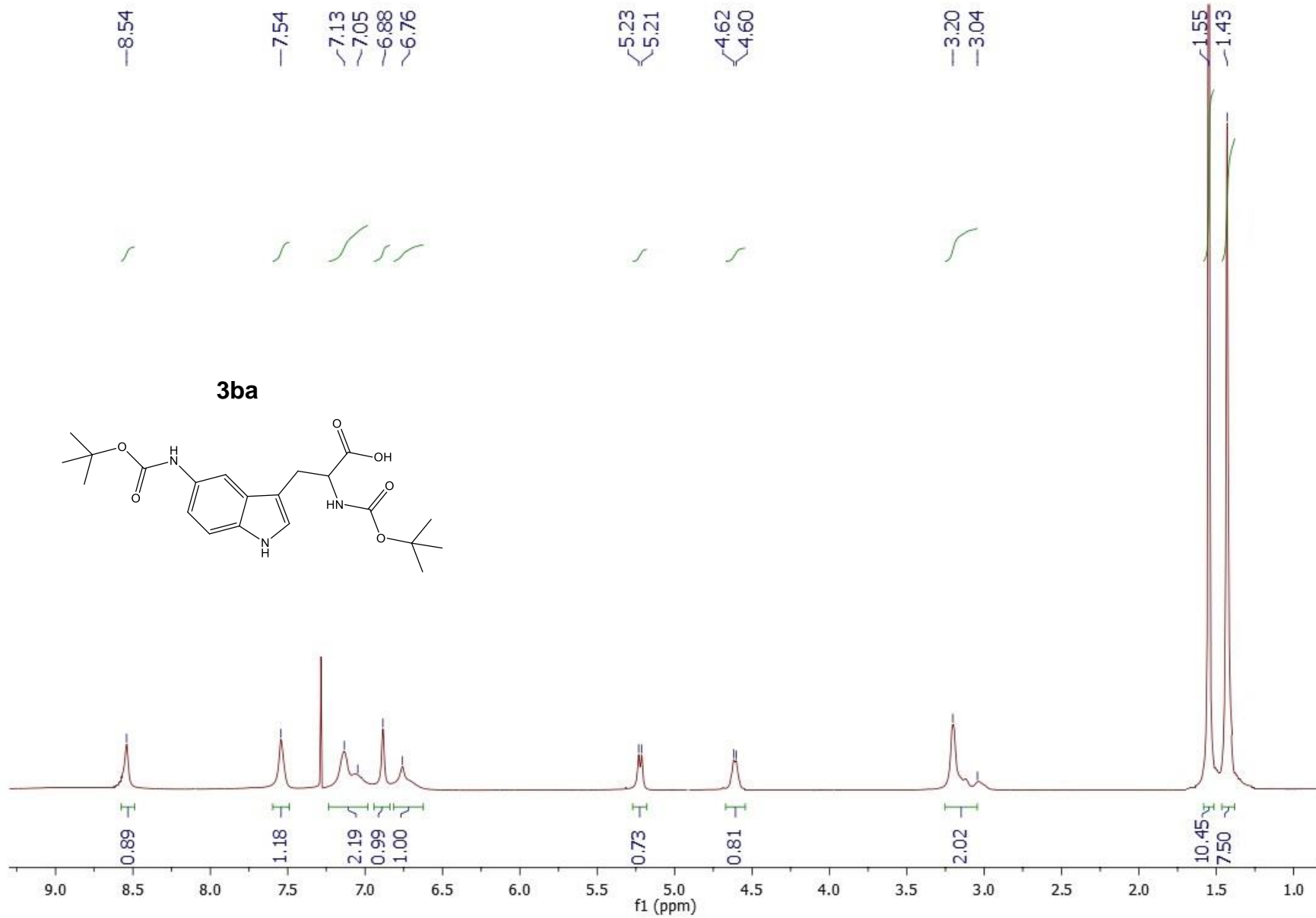


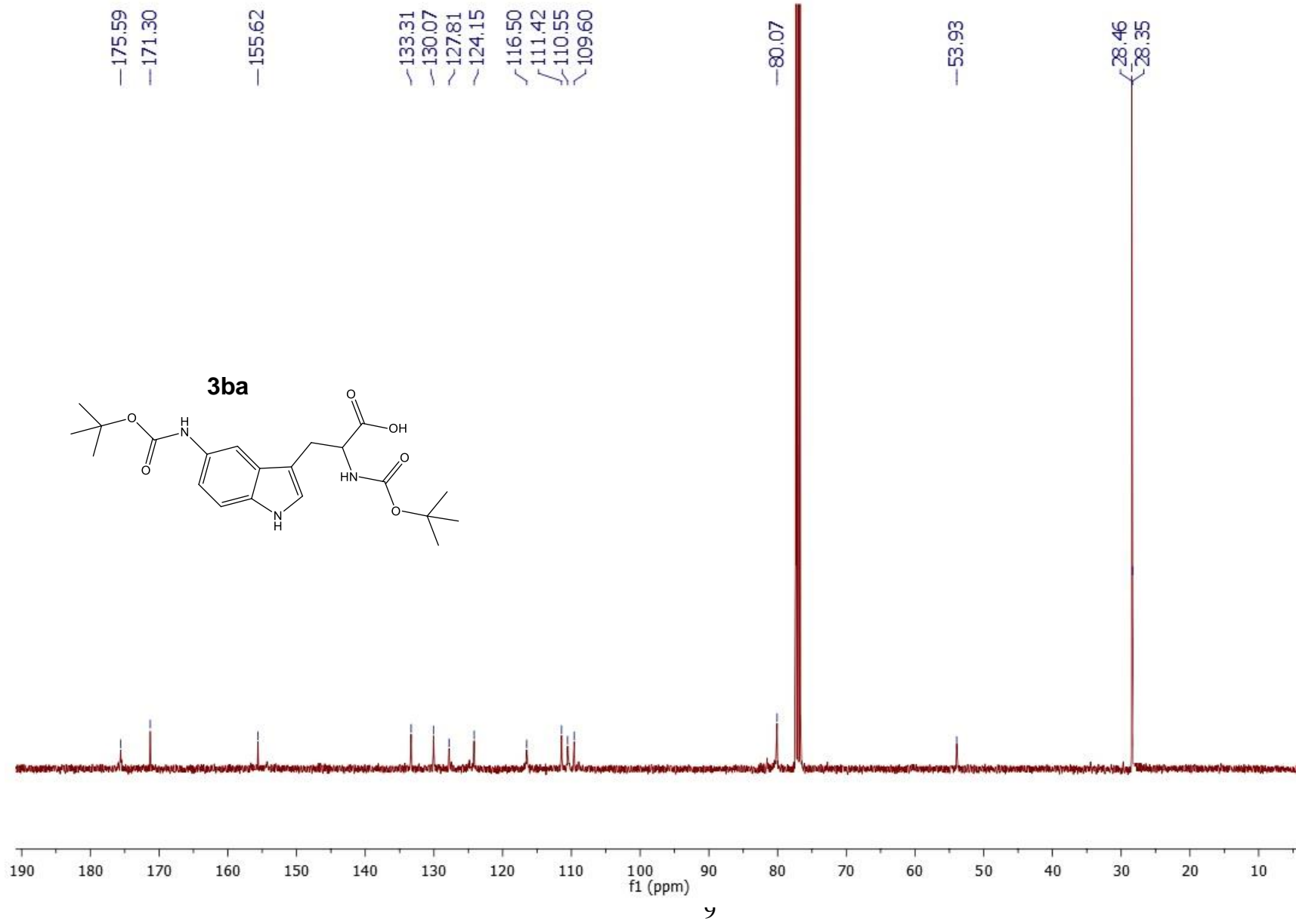
**Table S2** Antifungal and antibacterial activities of compounds defined as MIC [ $\mu\text{M}$ ].

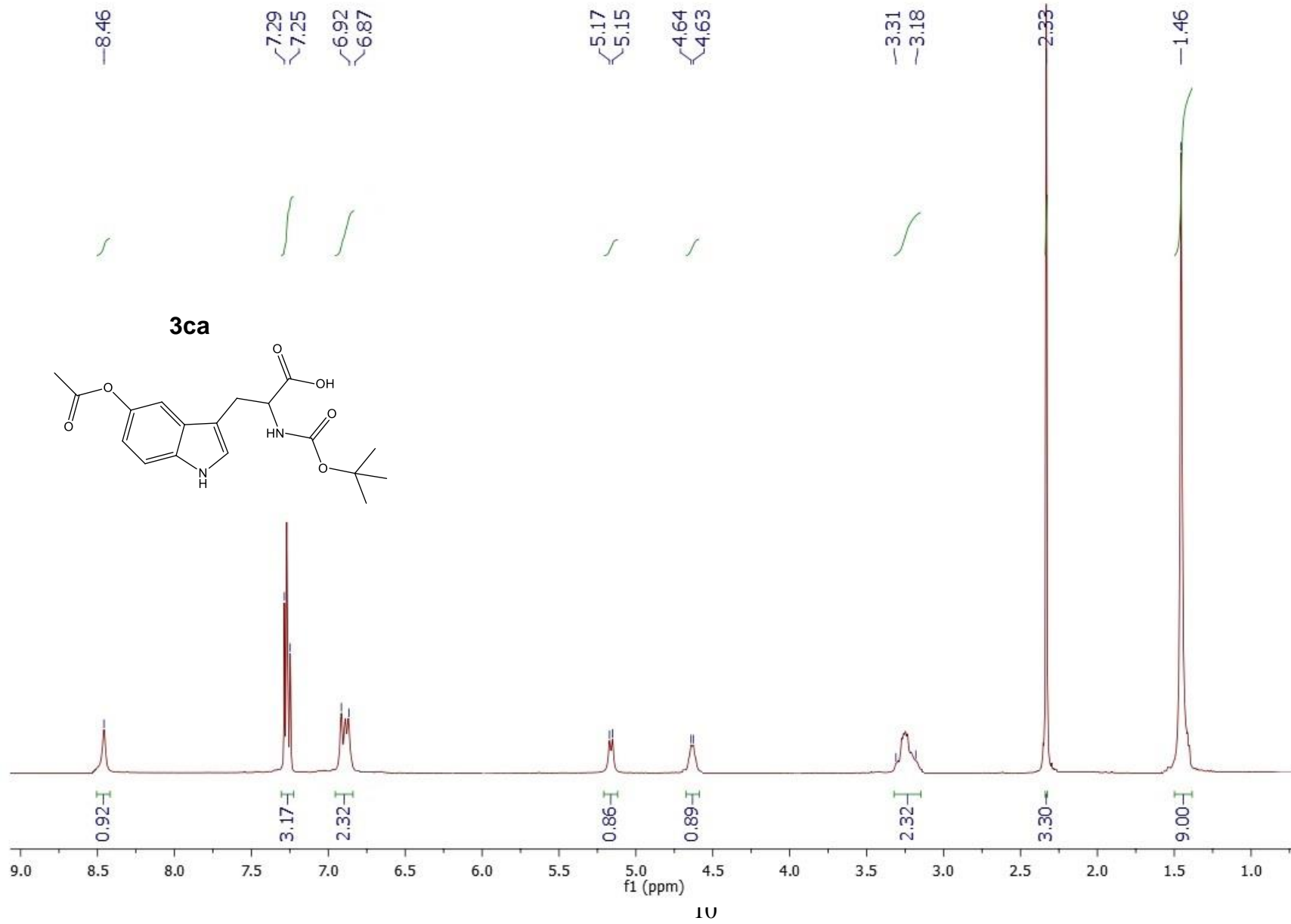
Compound	Bacterial strain			Fungal strain		
	<i>Escherichia coli</i>	<i>Bacillus cereus</i>	<i>Candida albicans</i>	<i>Candida albicans</i> Sc	<i>Candida krusei</i>	<i>Candida glabrata</i>
	MIC [ $\mu\text{M}$ ]					
<b>AS262</b>	>500	>500	>250	>250	>250	>250
<b>4aa</b>	>500	>500	>250	>250	>250	>250
<b>5aa</b>	>500	>500	>250	>250	>250	>250
<b>5ab</b>	>500	>500	>250	>250	>250	>250
<b>5ac</b>	>500	>500	>250	>250	>250	>250
<b>5ba</b>	>500	>500	>250	>250	250	>250
<b>5ca</b>	>500	>500	>250	>250	>250	>250
<b>7aa</b>	>500	>500	>250	>250	>250	>250
<b>7ab</b>	>500	>500	>250	>250	>250	>250
<b>7ba</b>	>500	>500	>250	>250	>250	>250
<b>8</b>	>500	>500	>250	>250	>250	>250
<b>Ciprofloxacin</b>	0.005	0.25	-	-	-	-
<b>Fluconazole</b>	-	-	125	125	62.5	62.5

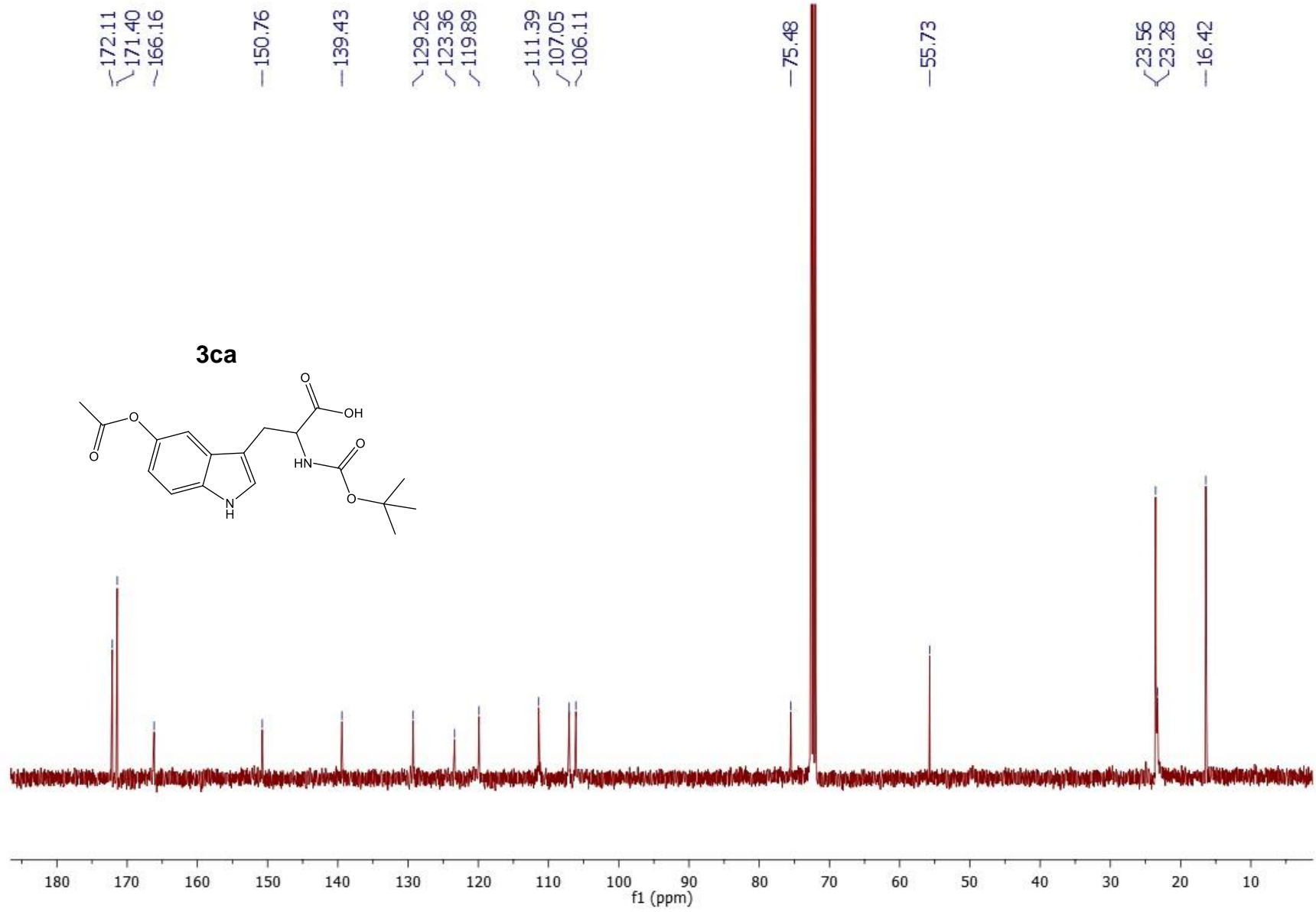
## Methods

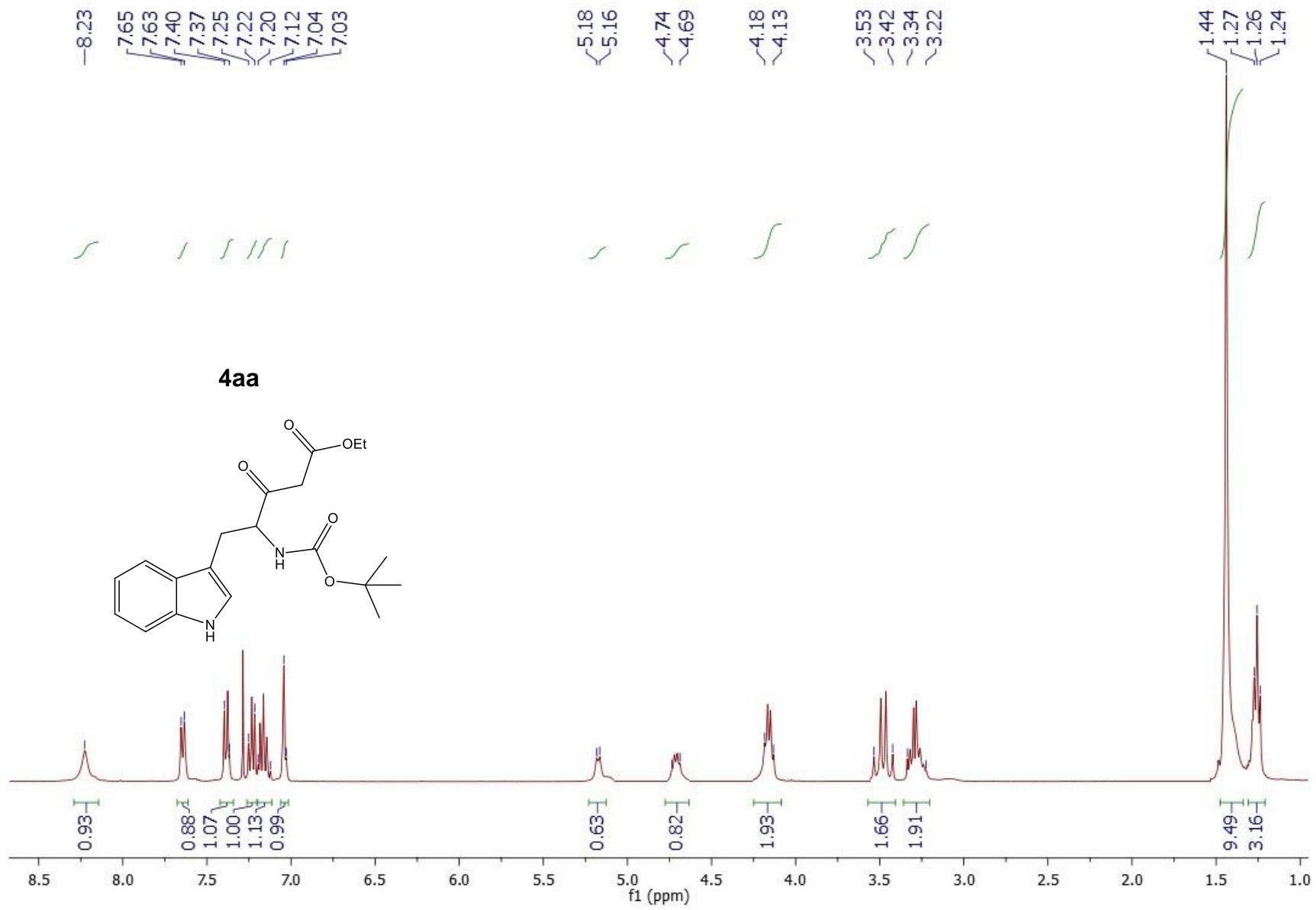
*Antimicrobial Susceptibility Test:* The synthesized carbazole derivatives were assessed for their antimicrobial activity against a panel of bacterial and fungal strains by broth microdilution method according to guidelines of the Clinical and Laboratory Standards Institute (M07-A10 and M27-A3 documents). The antimicrobial activity was determined using commercial strains of bacteria: *Bacillus cereus* (PCM 2003) as an example of Gram-positive bacteria and *Escherichia coli* (ATCC 25922) as an example of Gram-negative bacteria, and the fungi: *Candida albicans* (ATCC 10231), *Candida glabrata* (DSM 11226), and *Candida krusei* (DSM 6128). Briefly, DMSO was used to dissolve the tested compounds. Mueller-Hinton broth (MHS) (Sigma-Aldrich) and RPMI 1640 medium (Corning) were used for preparing serial dilutions of investigated and reference compounds using the 96-well microtiter plates. To each dilution in a ratio 1:1 was added the inoculum amounting  $10^5$  CFU/ml of all studied microorganisms prepared from 24 h cultures of bacteria and fungi grow at 37 °C. The results were obtained after 24h incubation at 37 °C under agitation at 180 rpm. Minimum Inhibitory Concentration (MIC) was established visually as the lowest concentration where no growth was observed after incubation with compounds. Ciprofloxacin and Fluconazole were used as control antimicrobial agents.

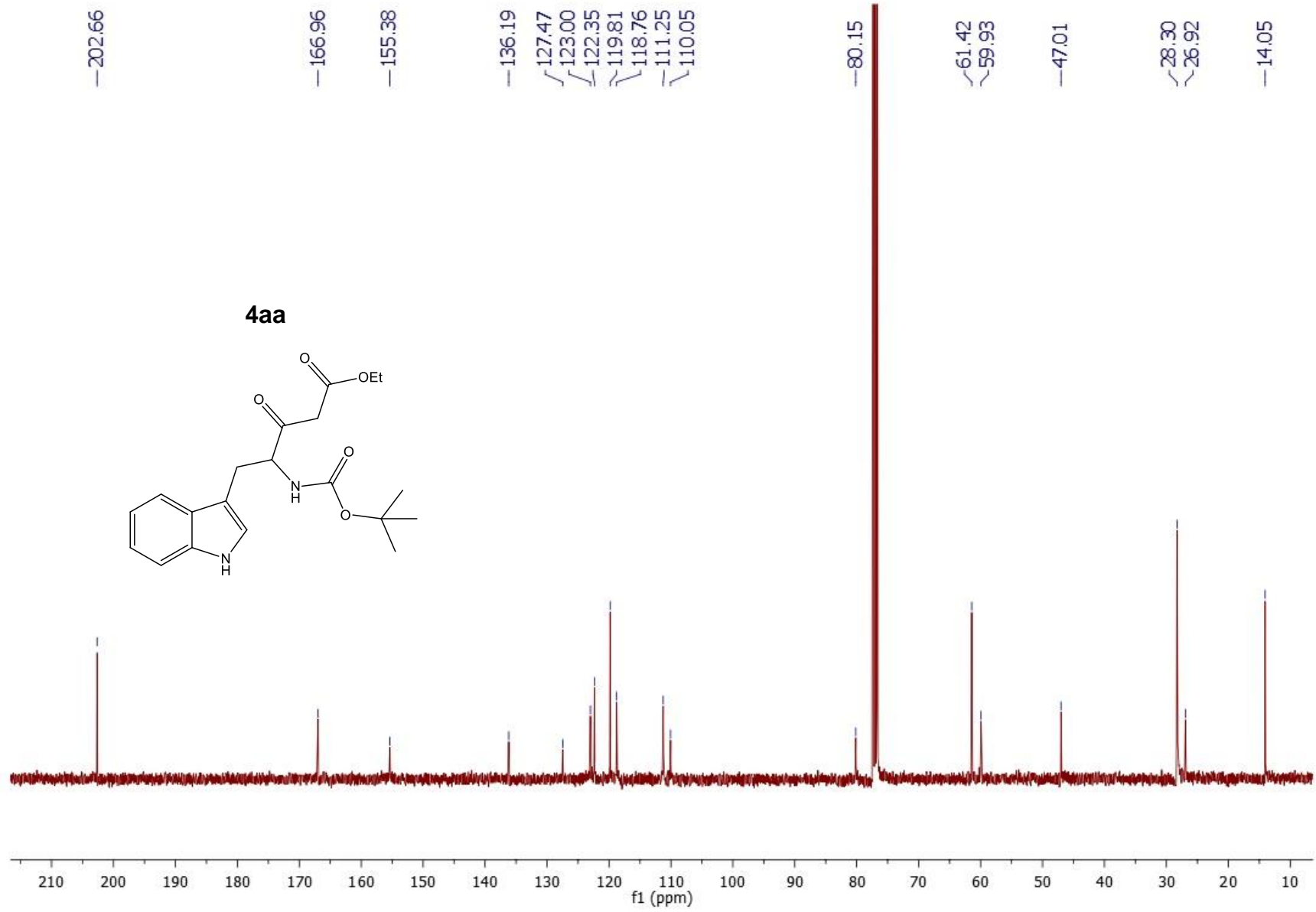


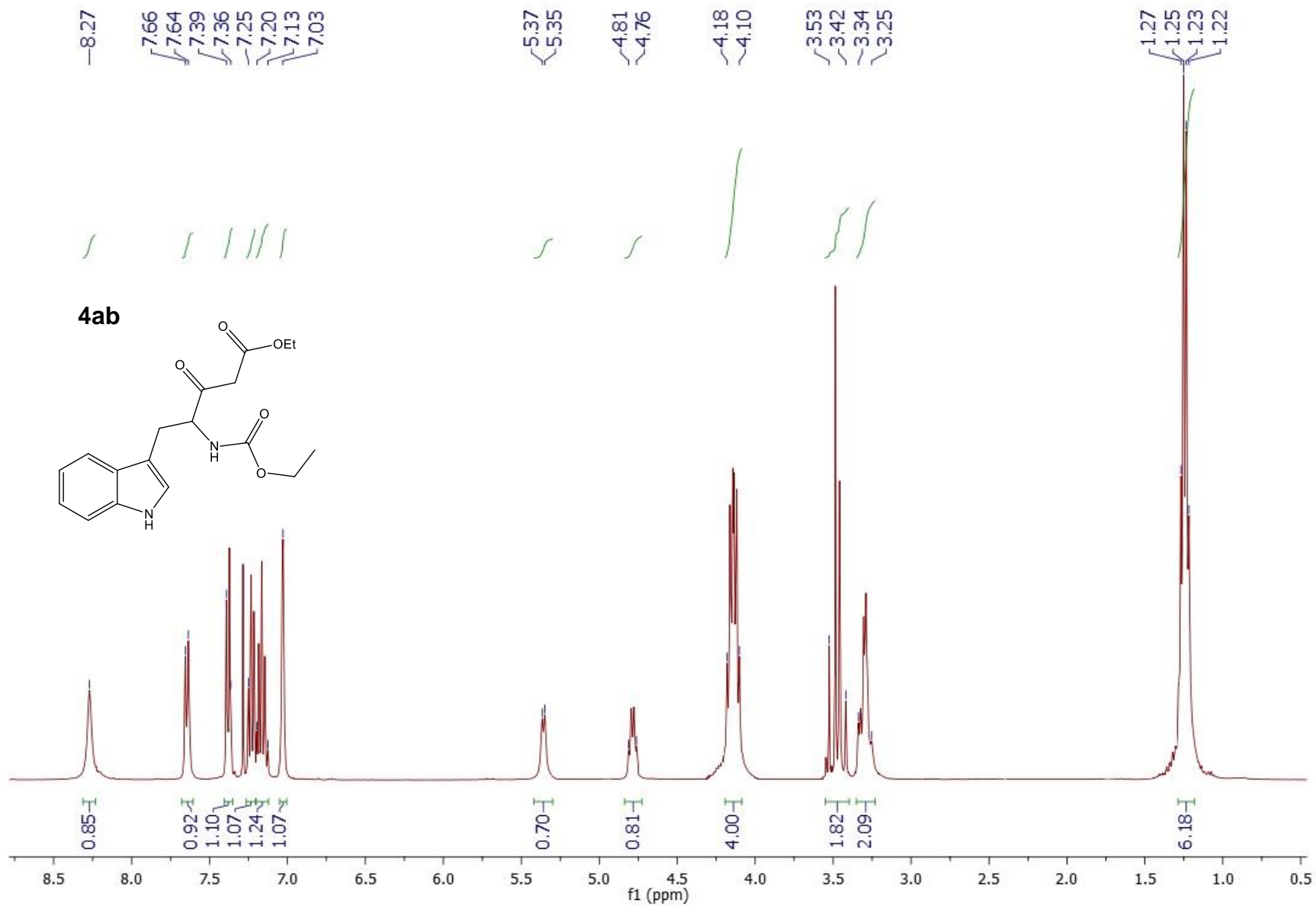




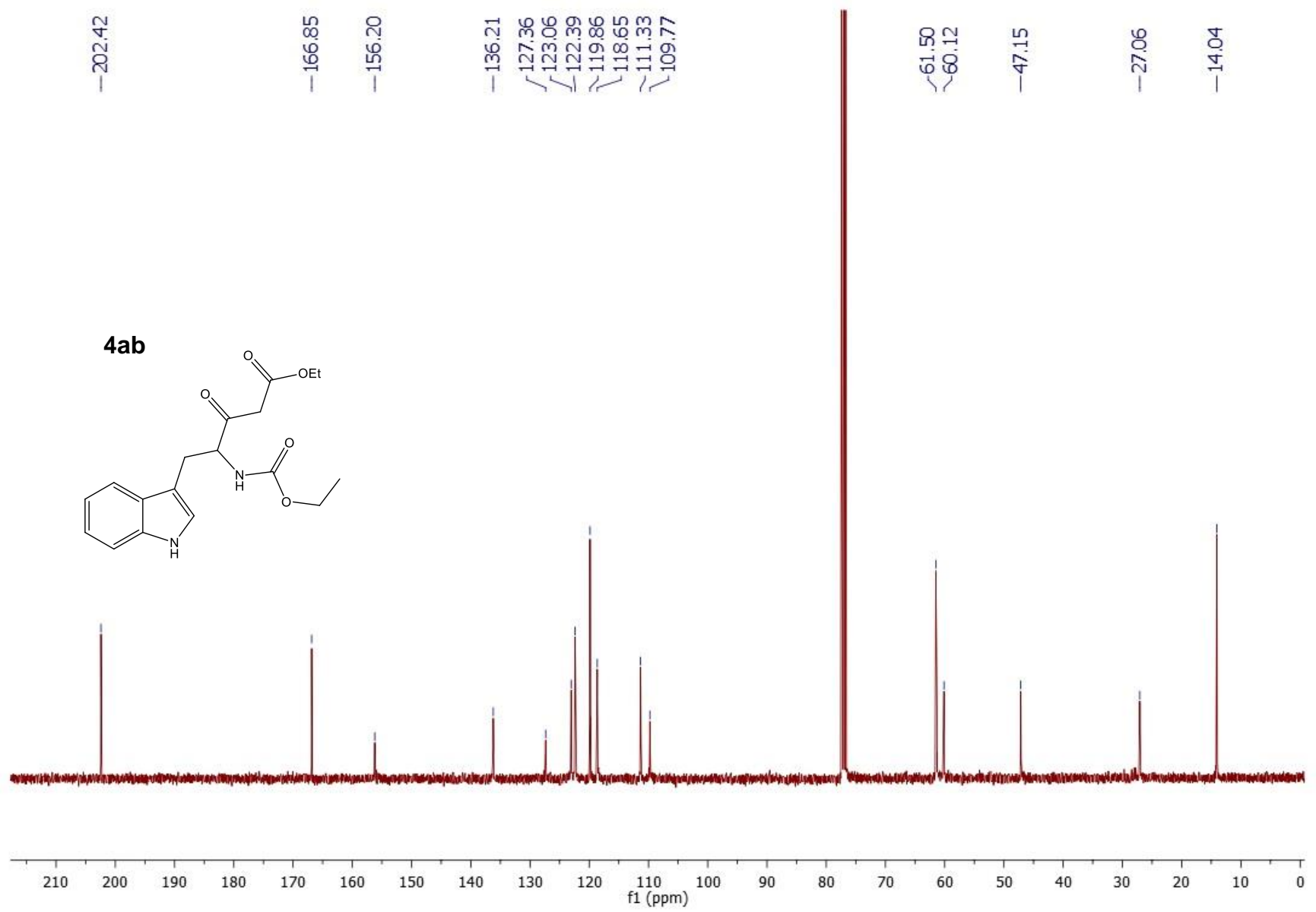
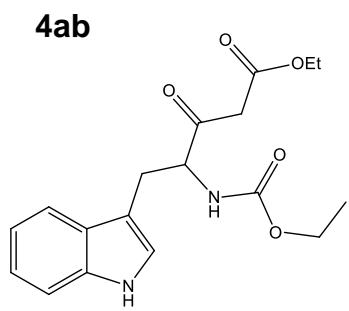


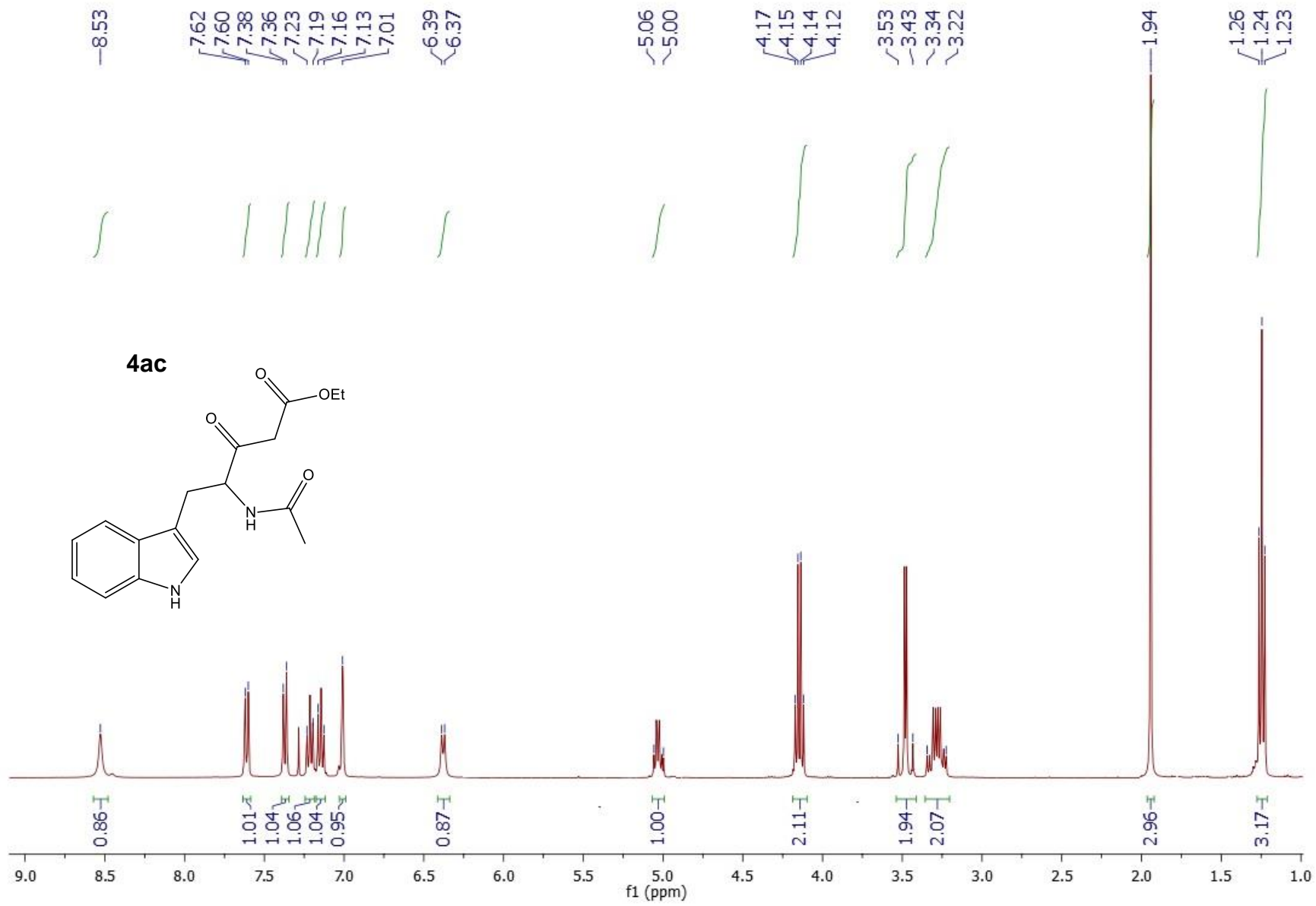


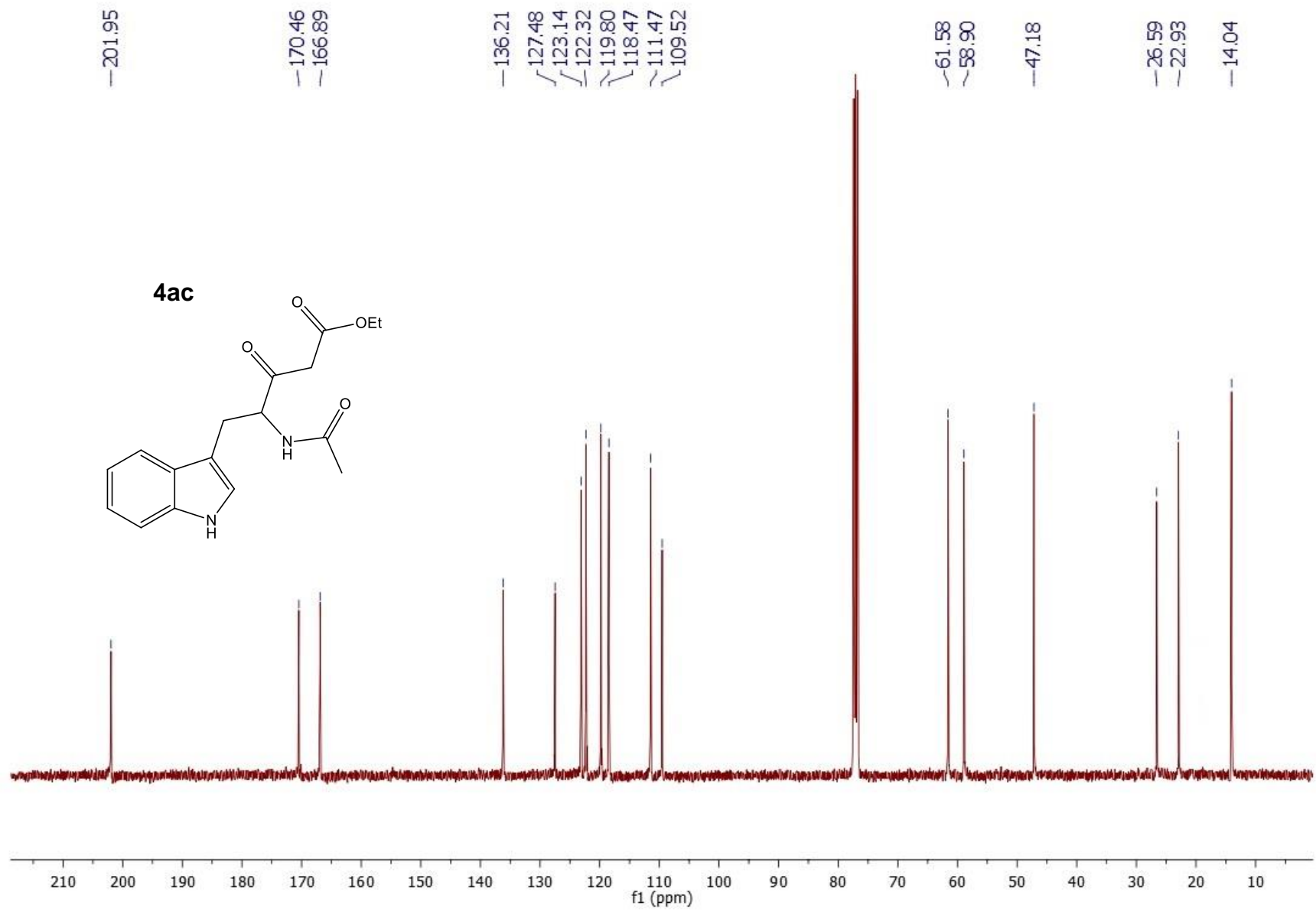


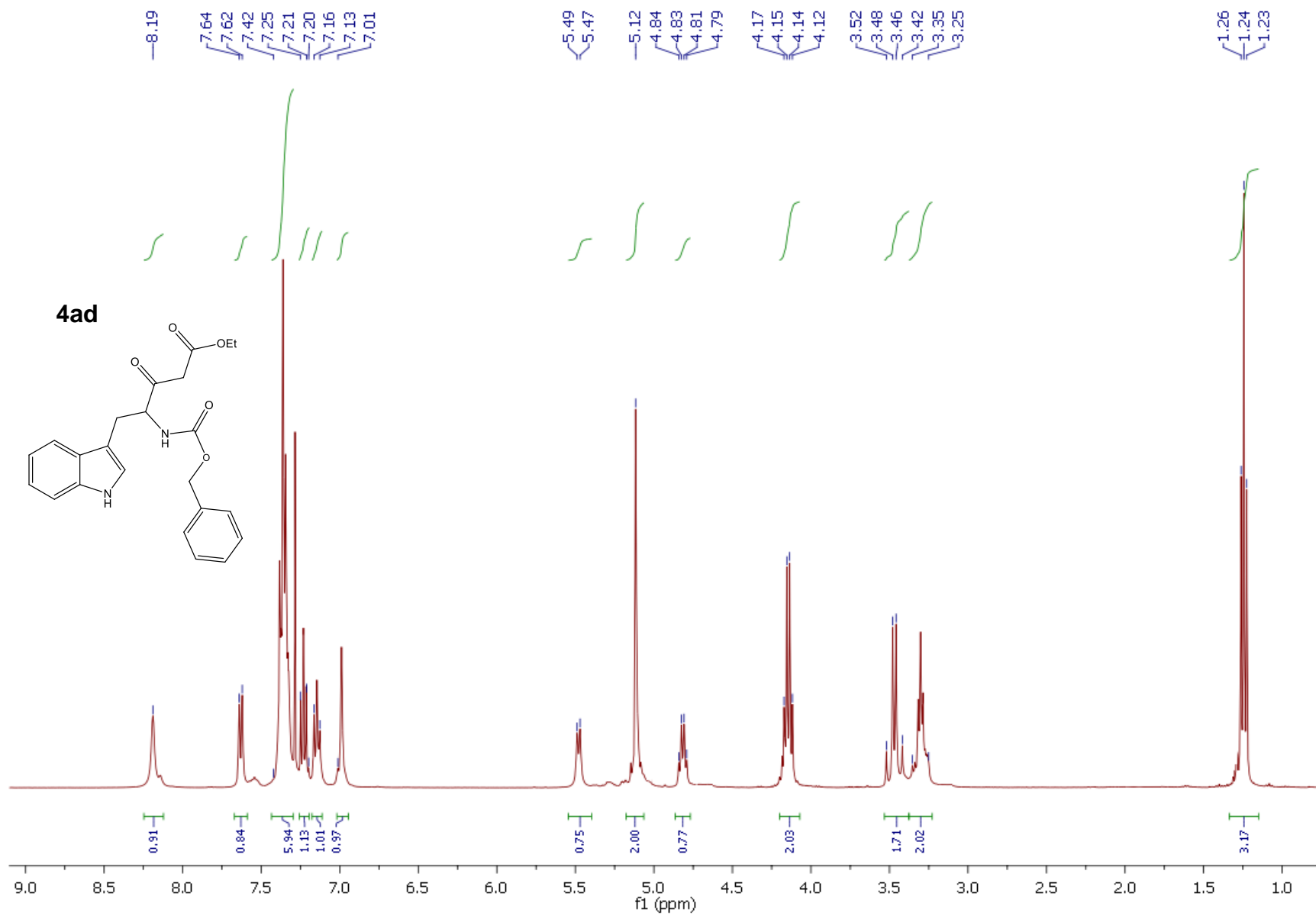


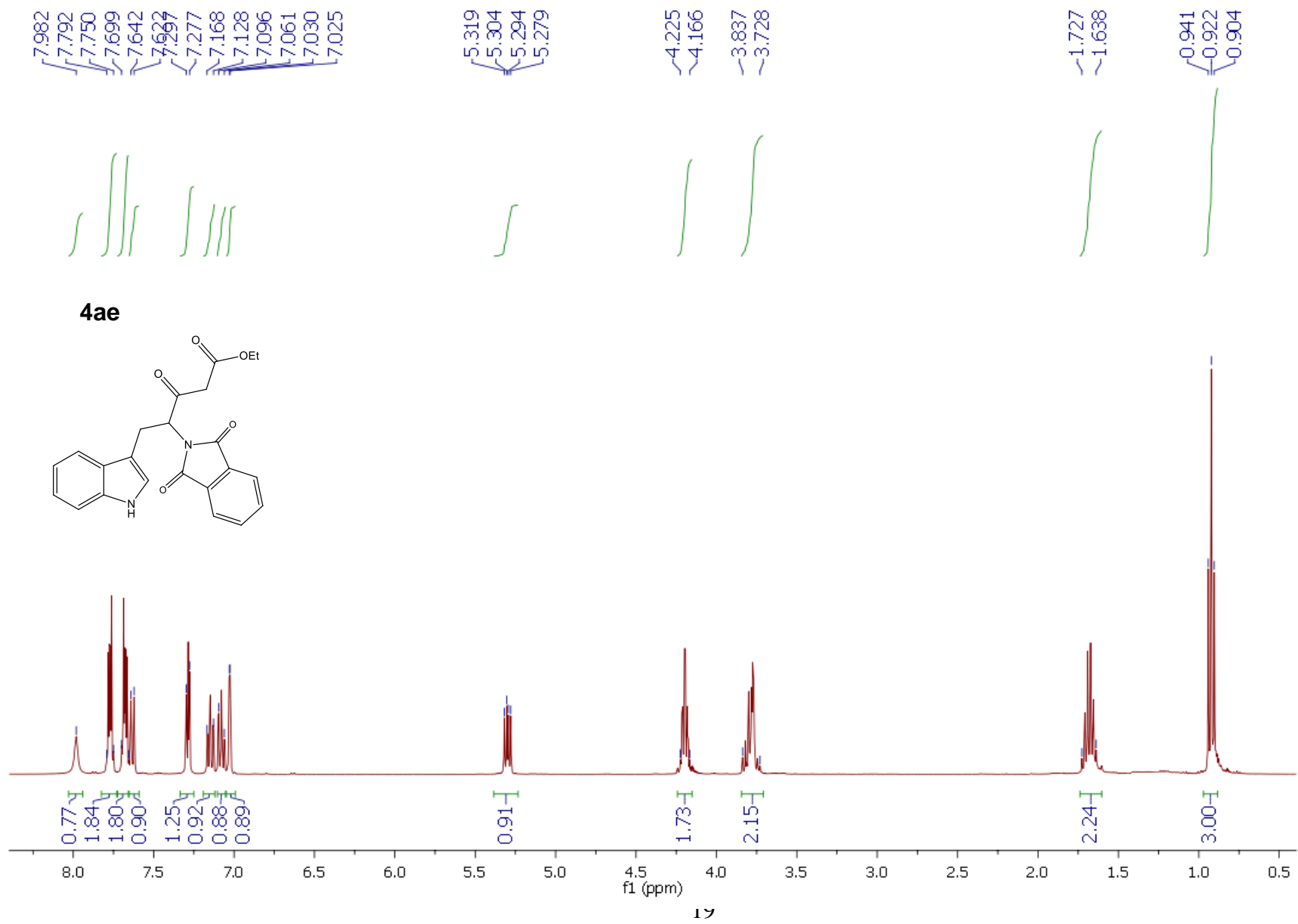


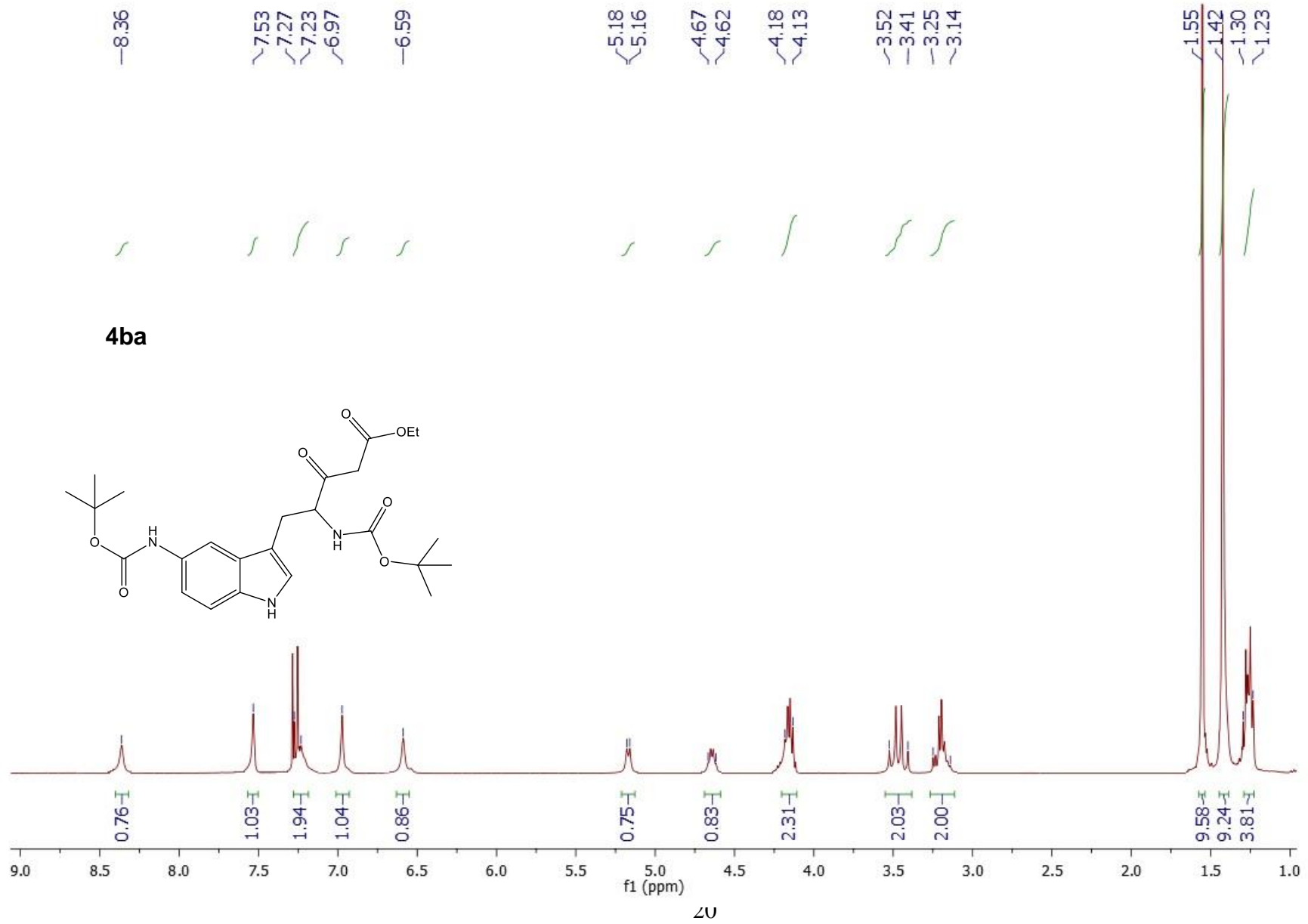


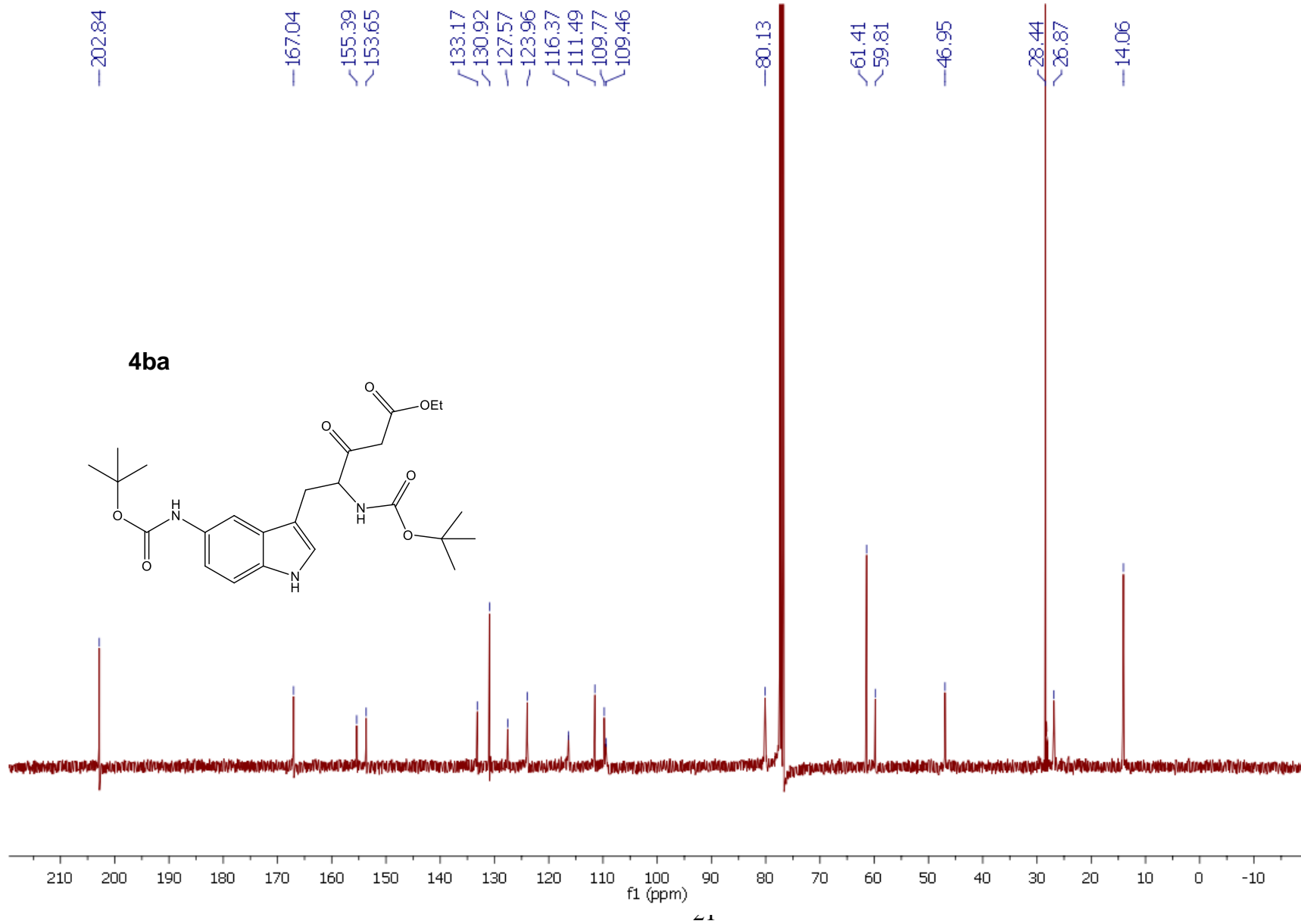


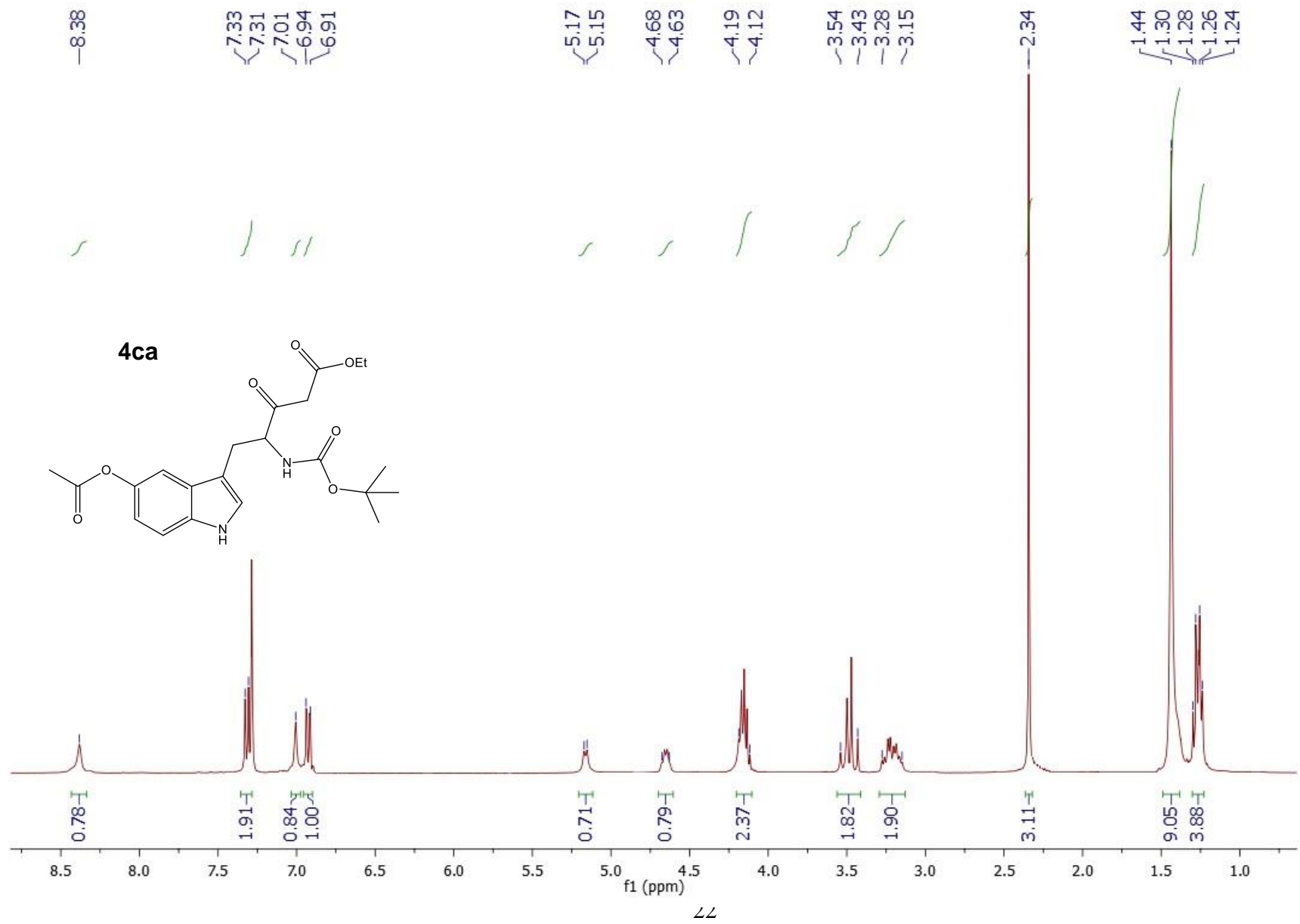




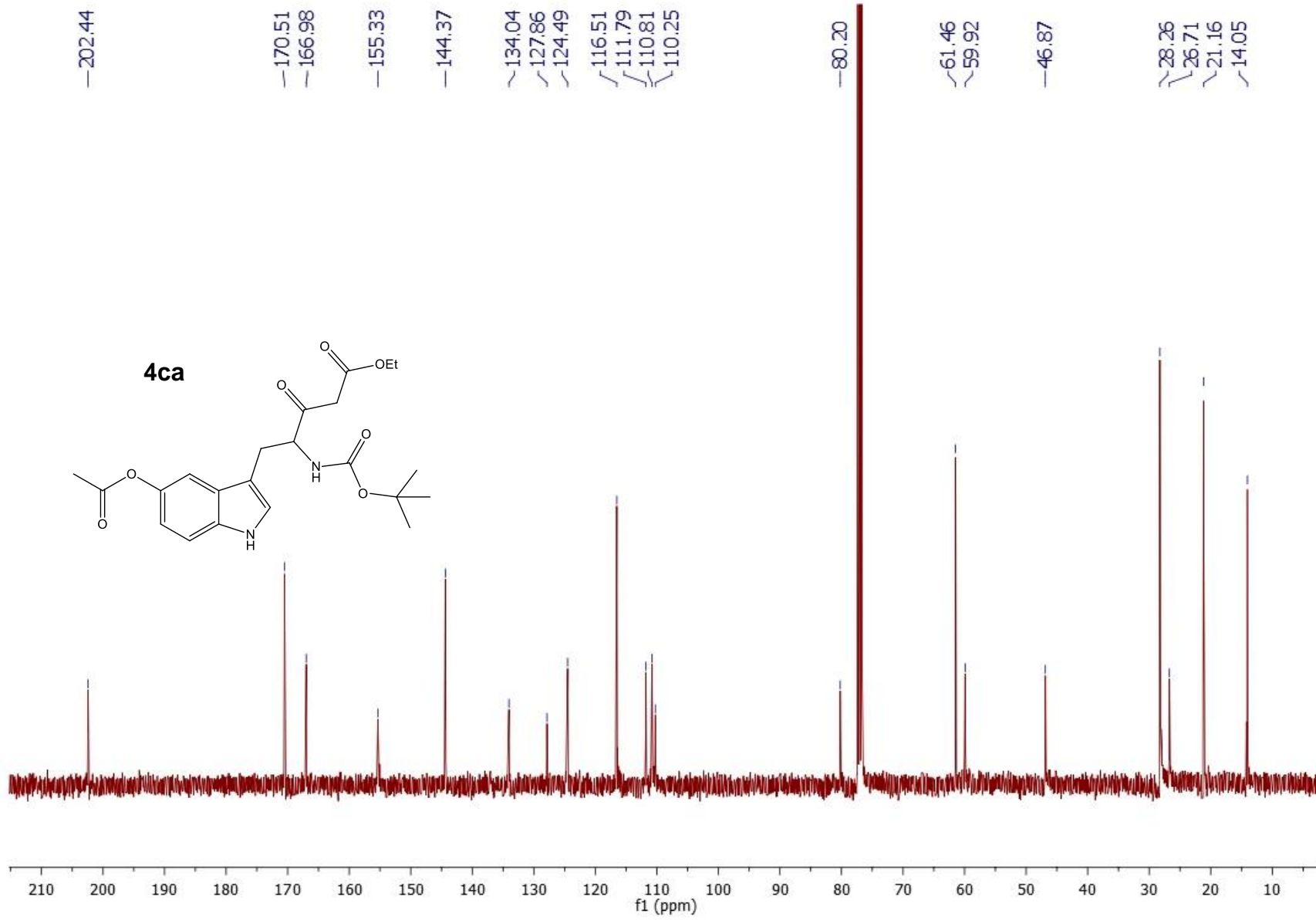


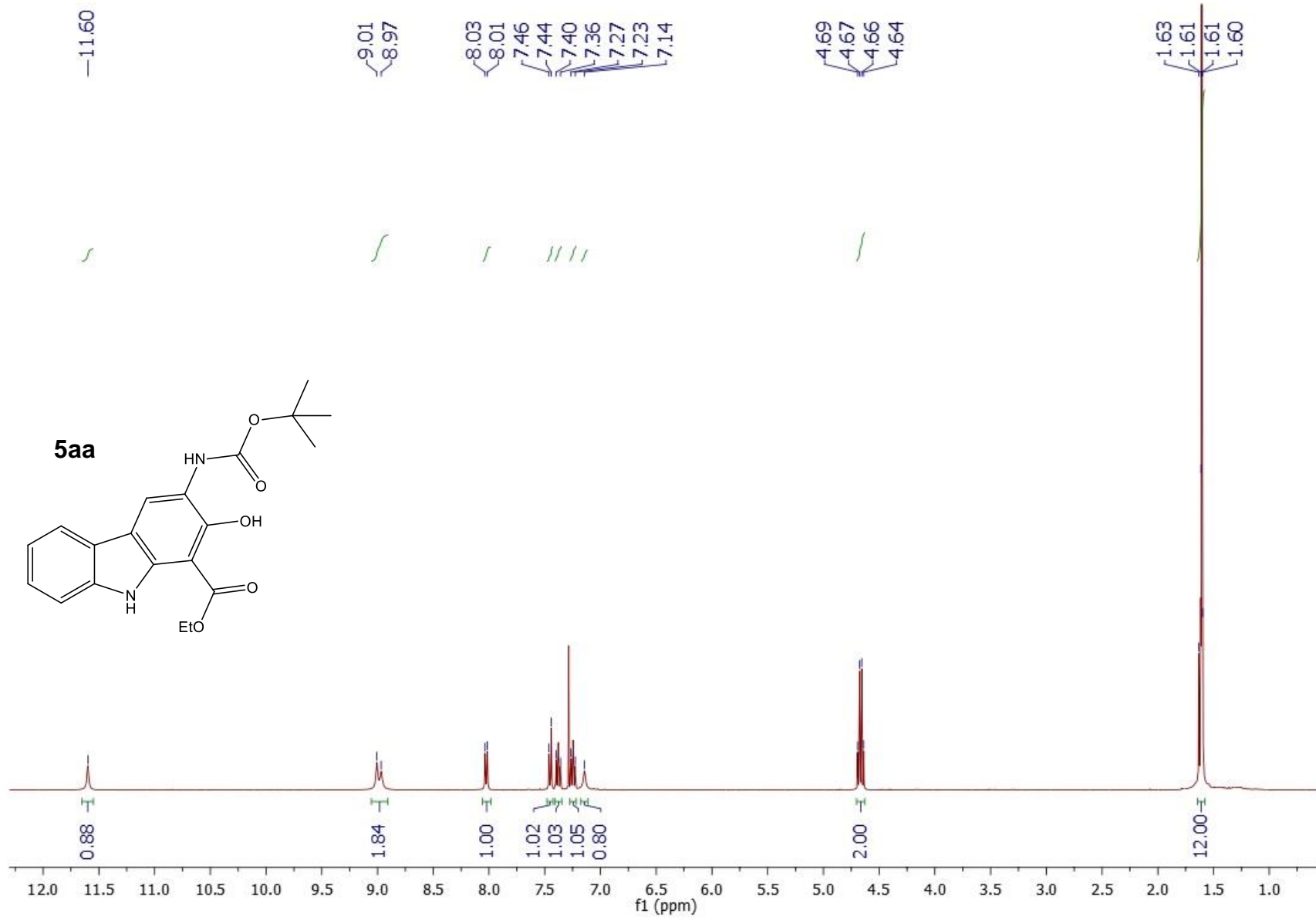


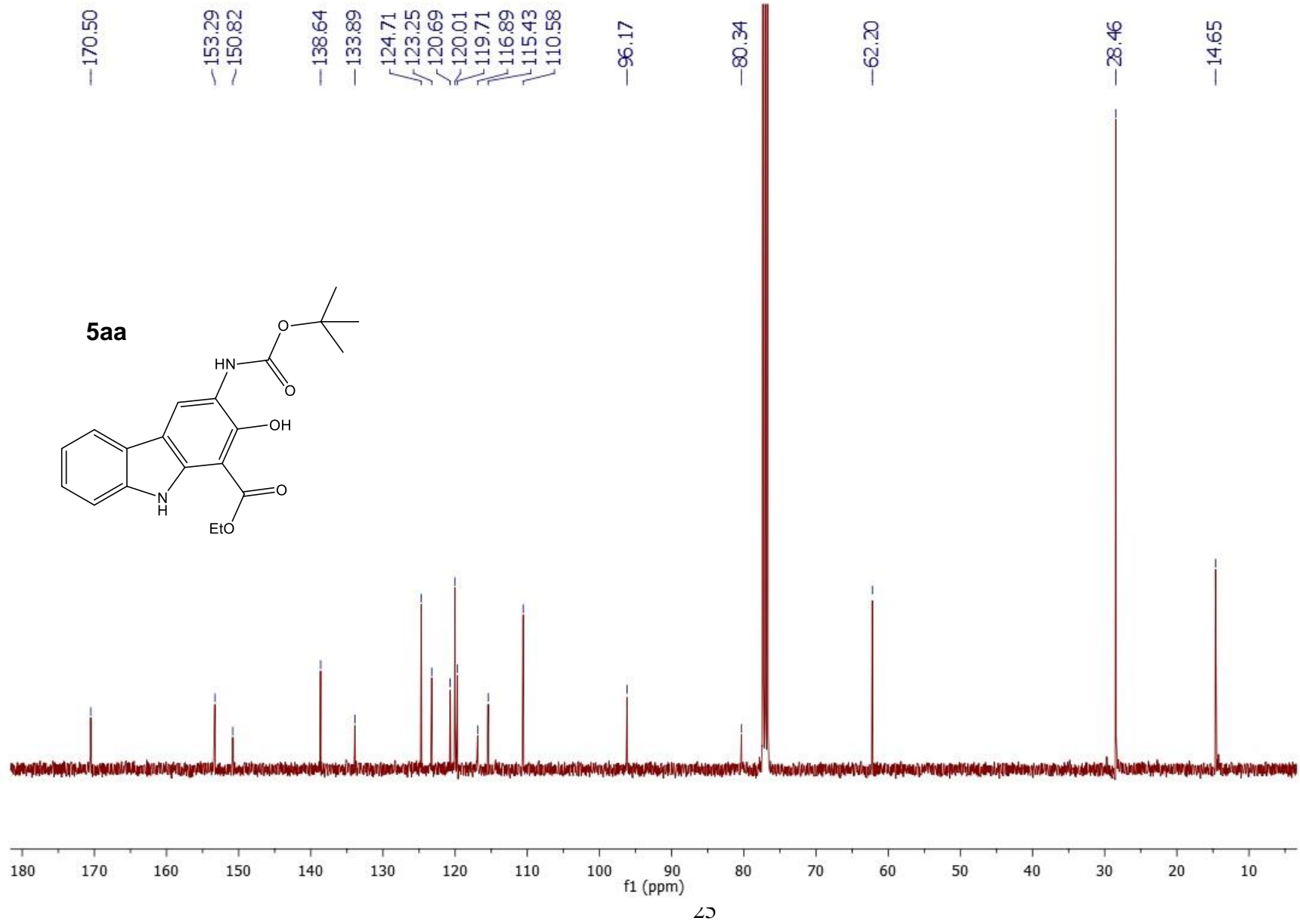
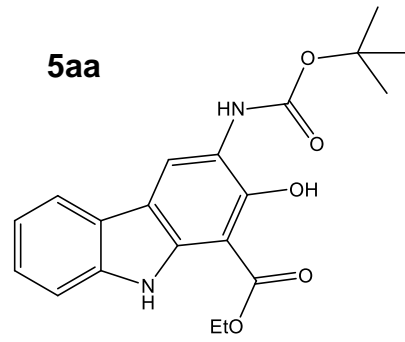


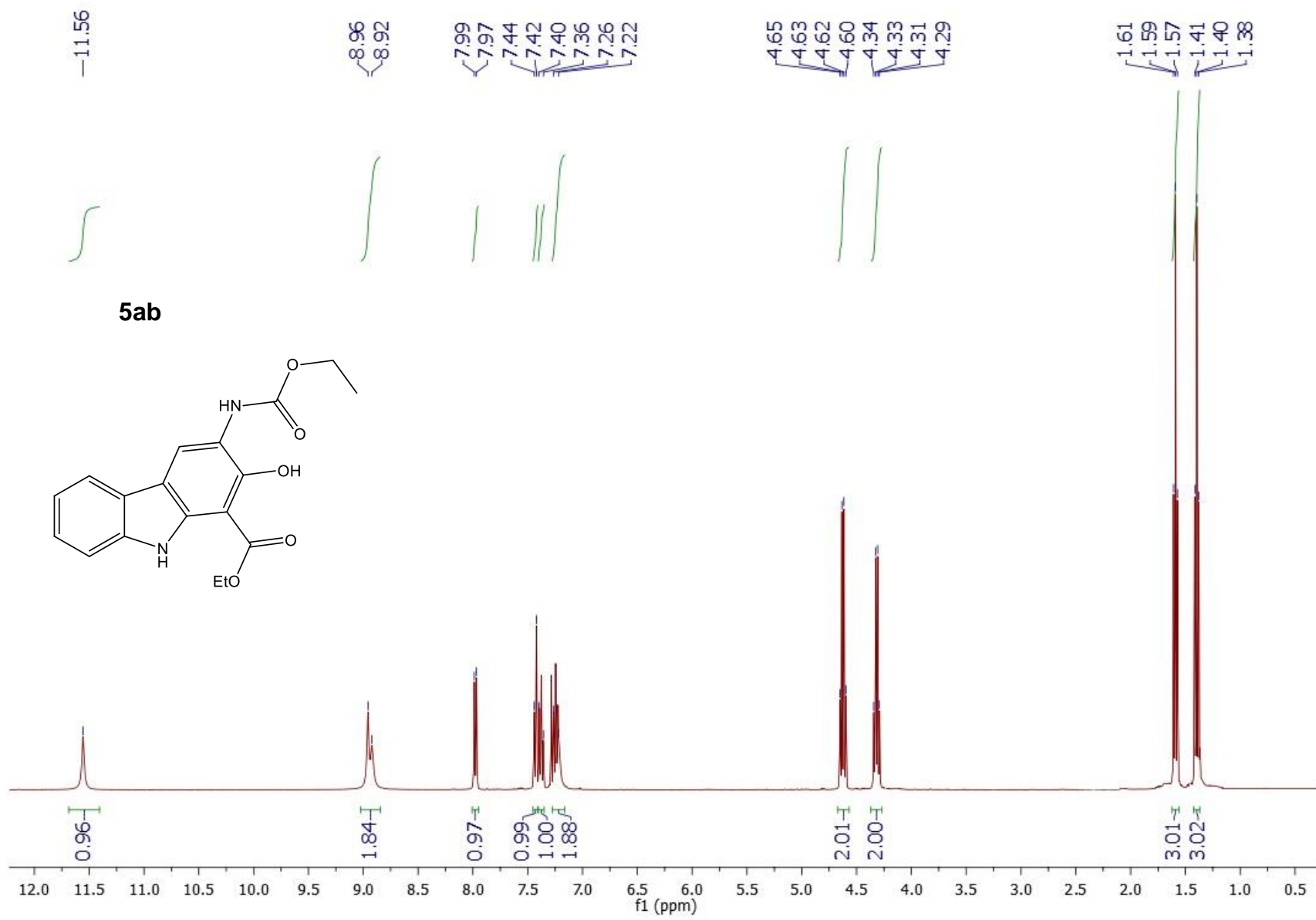


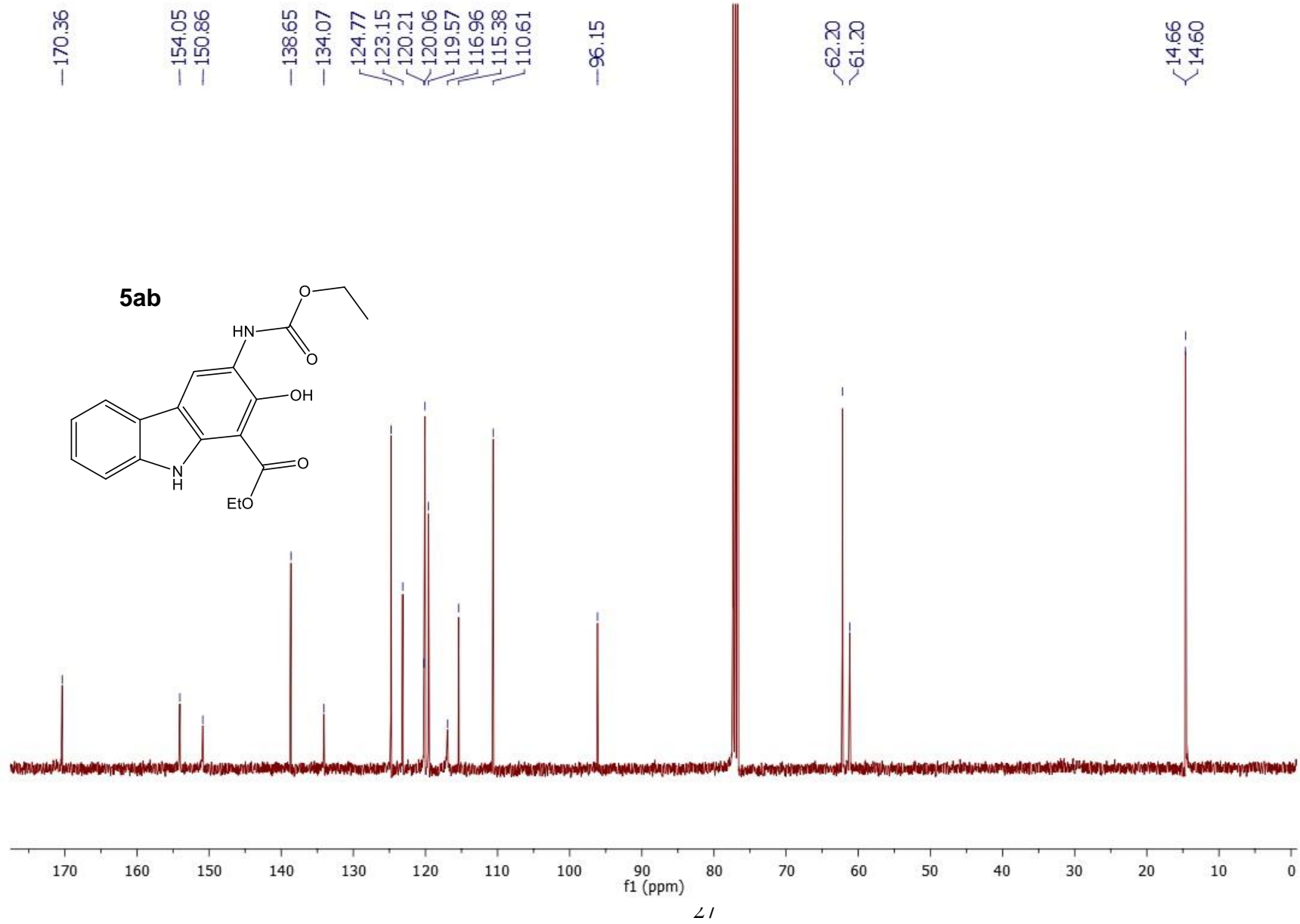


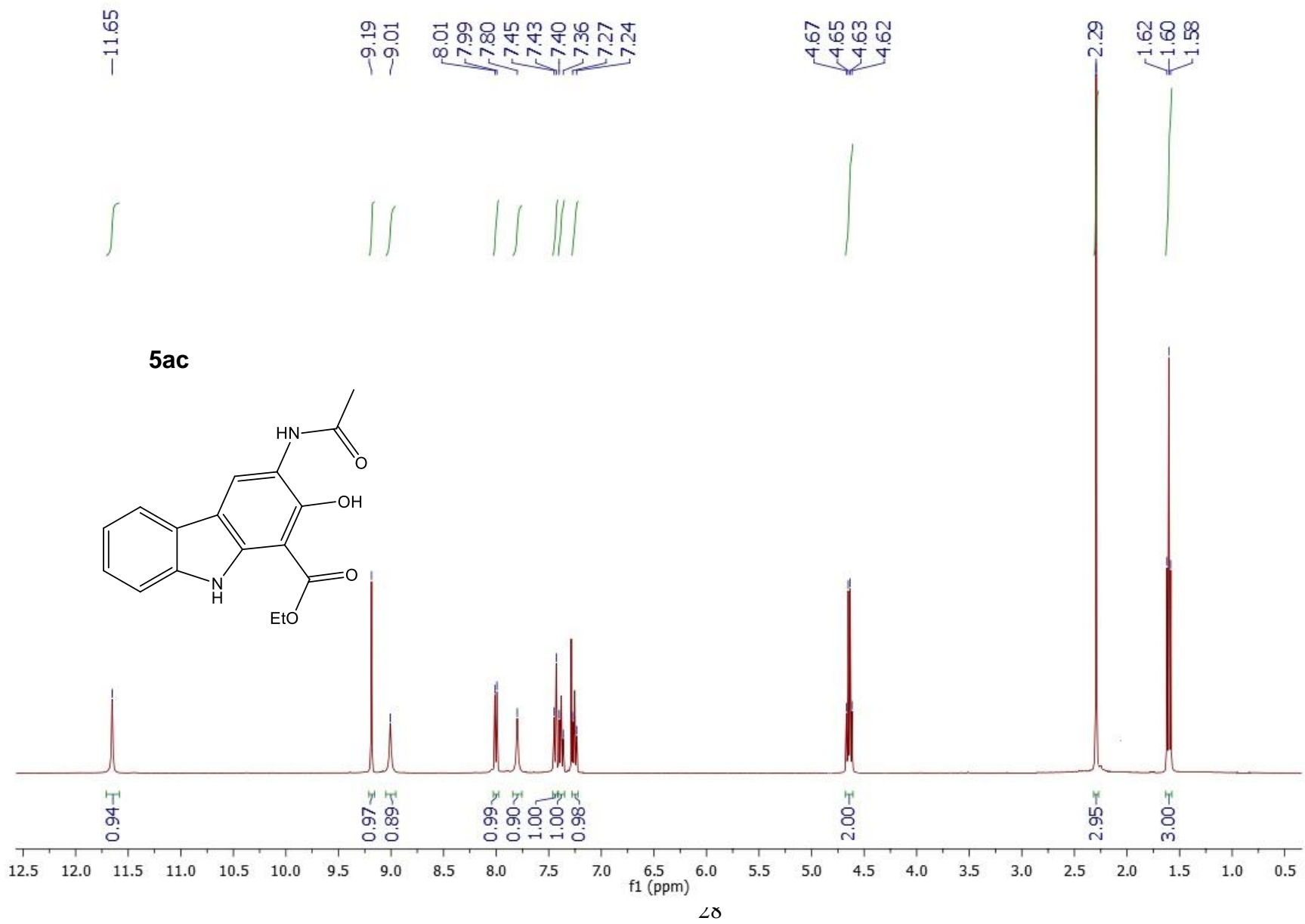




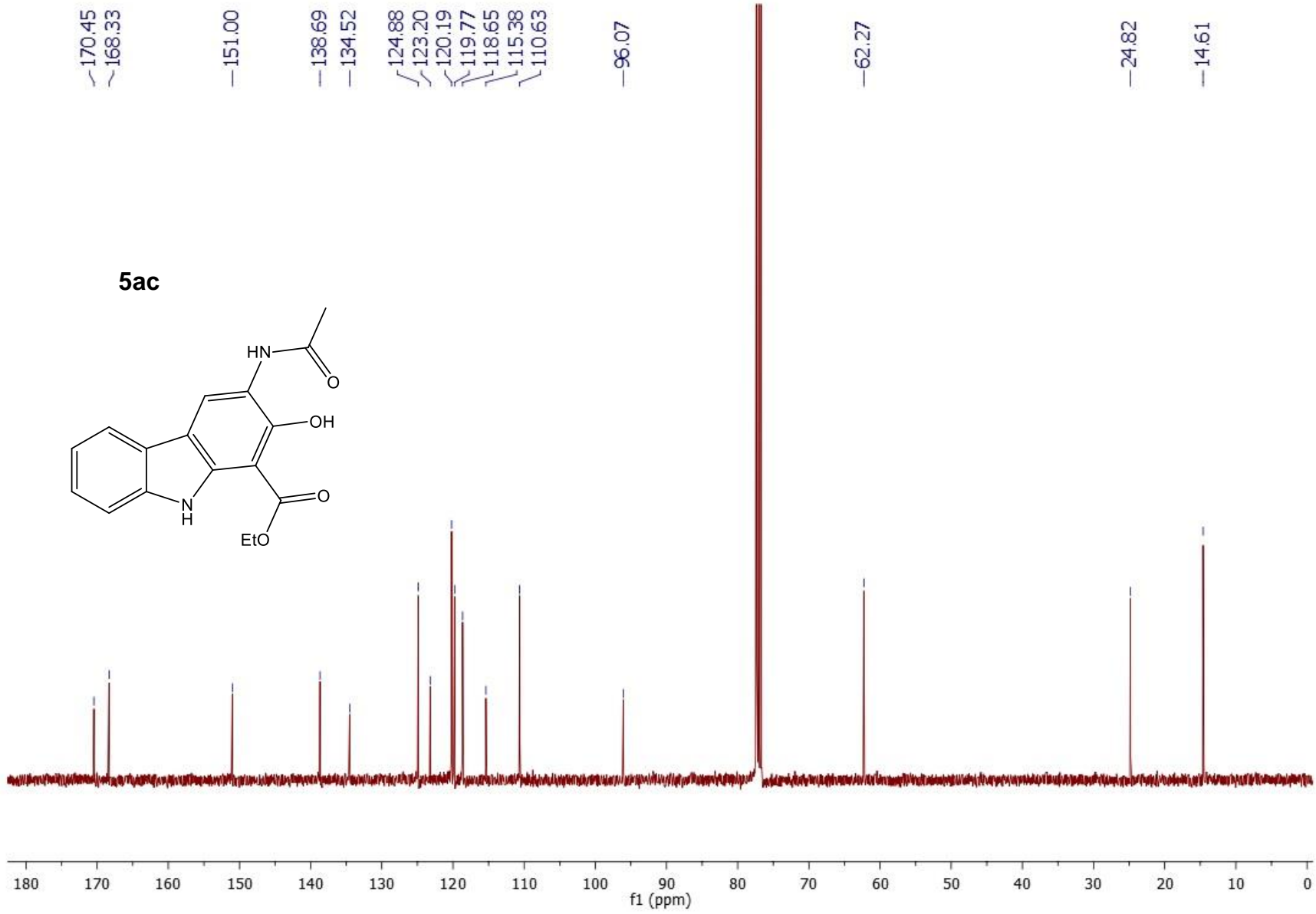
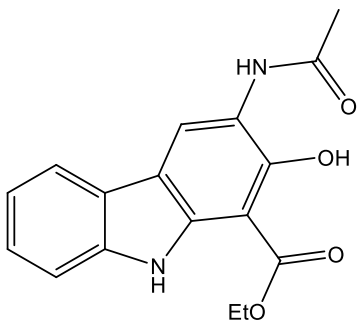


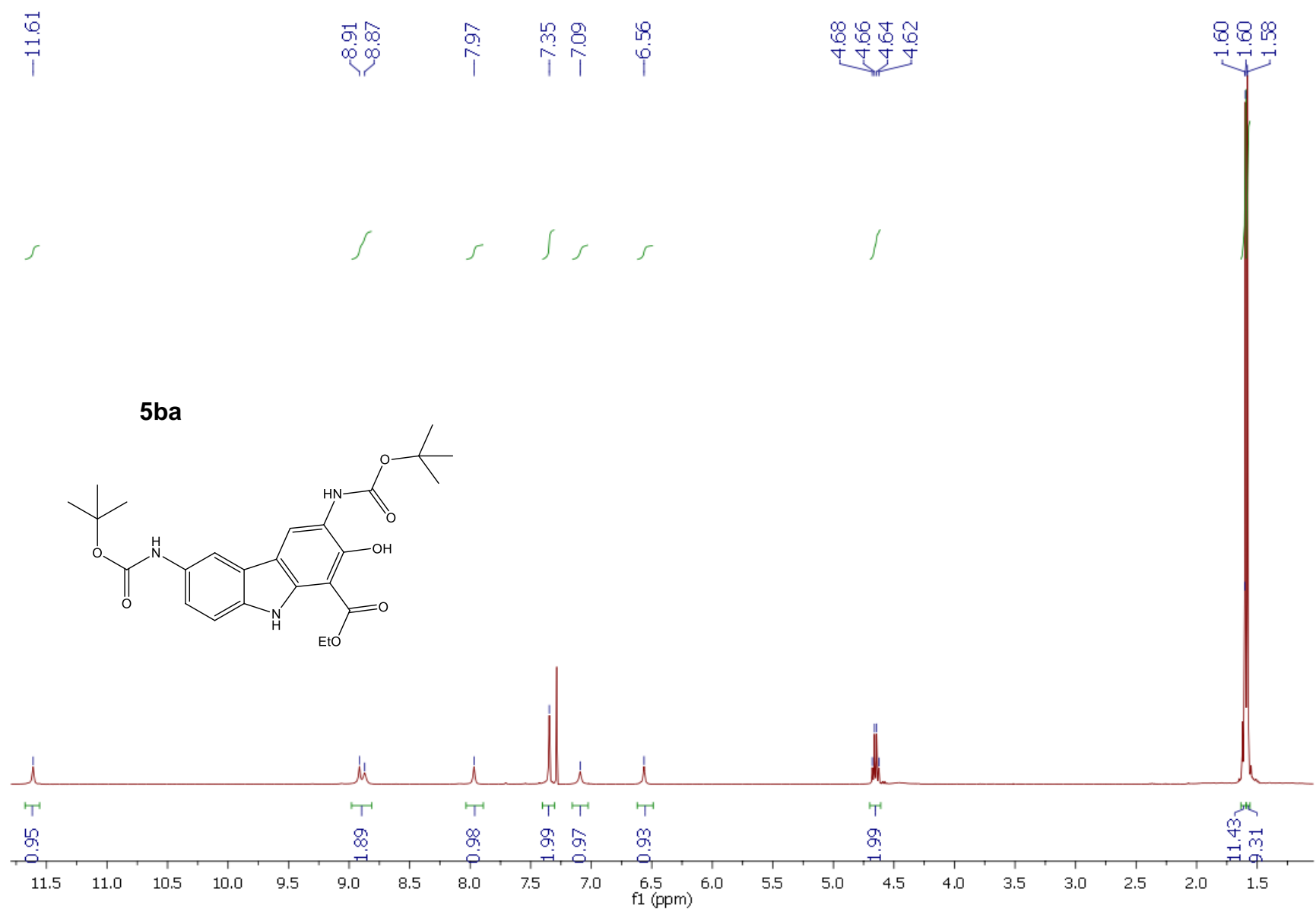




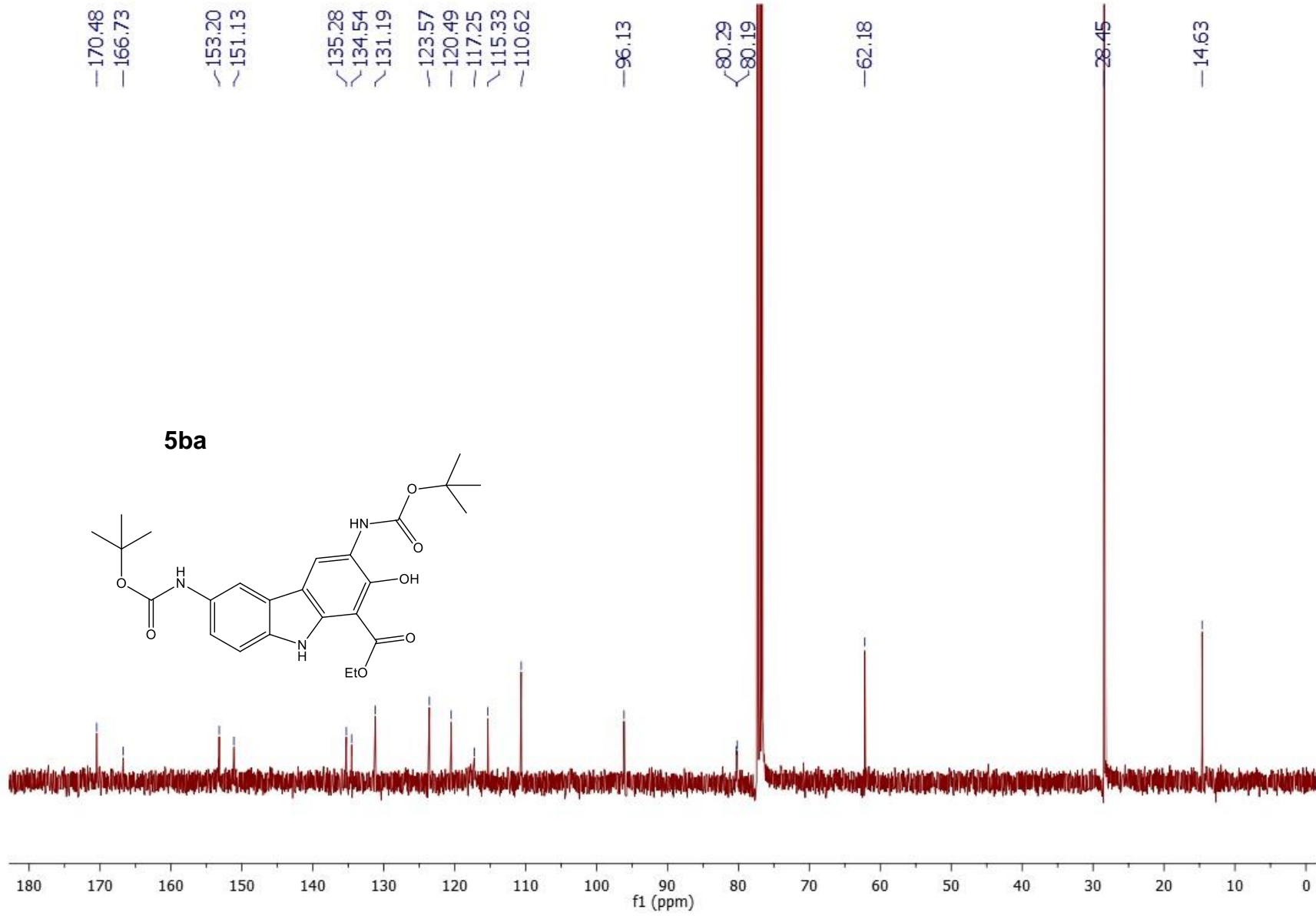


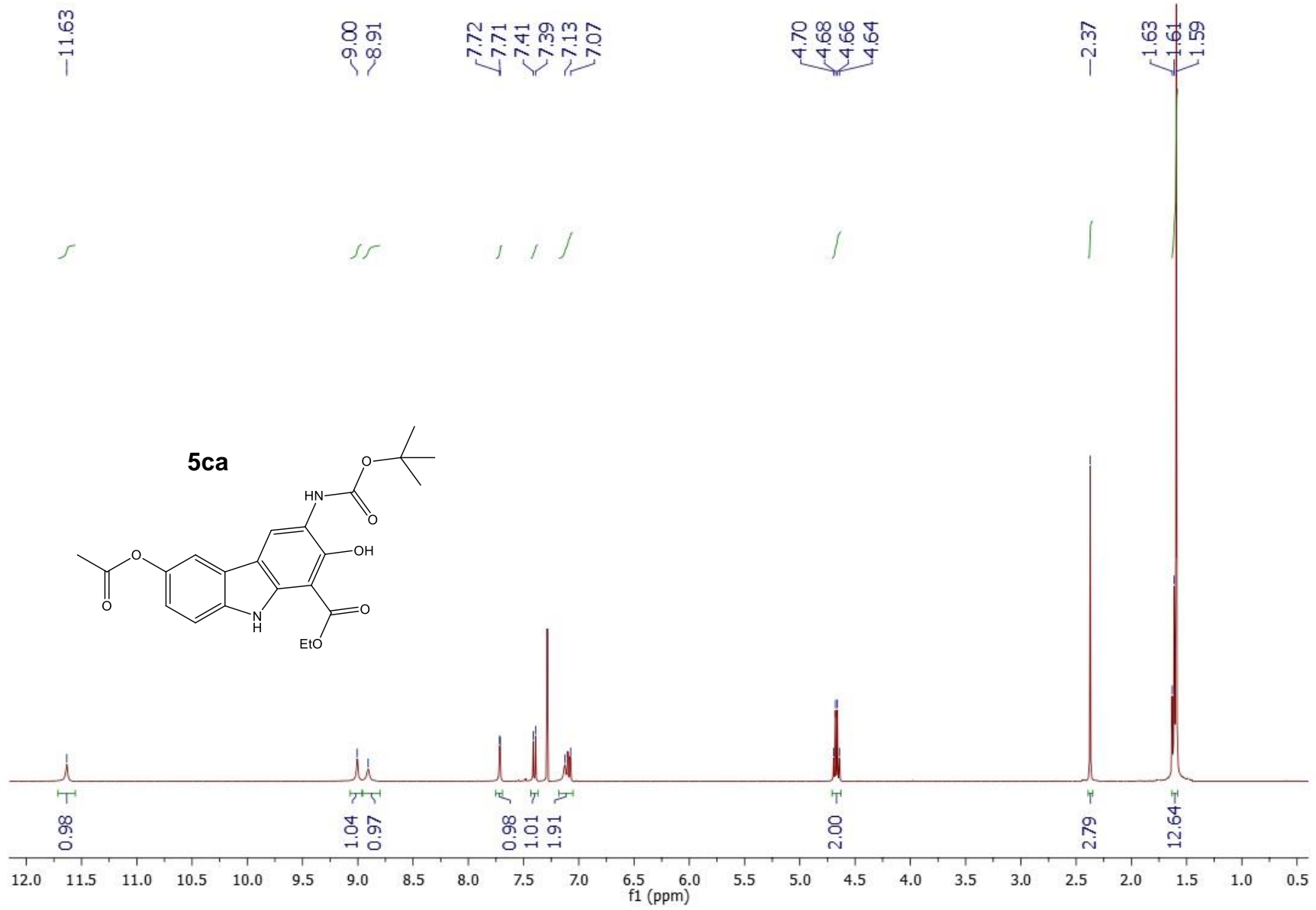
**5ac**

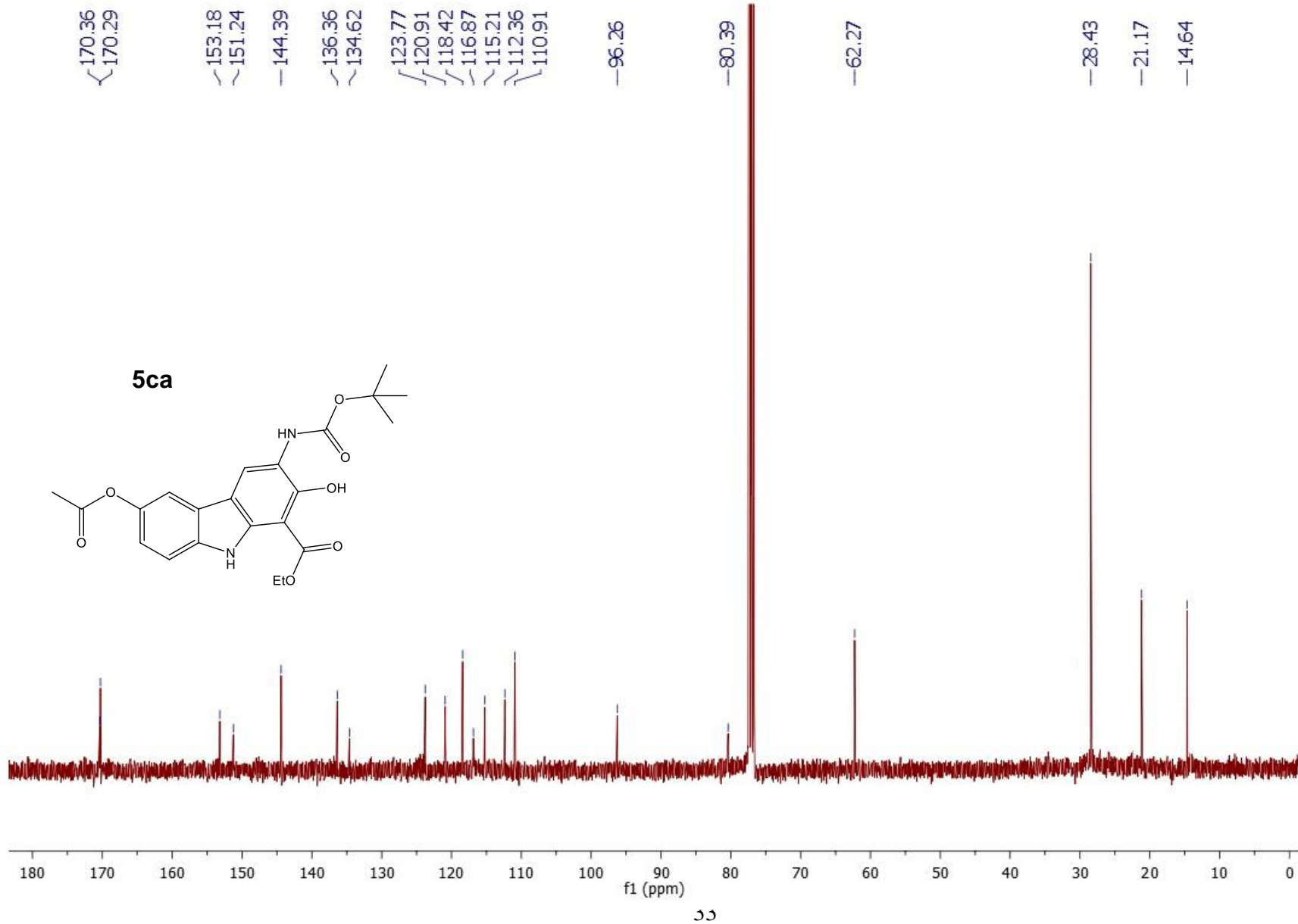
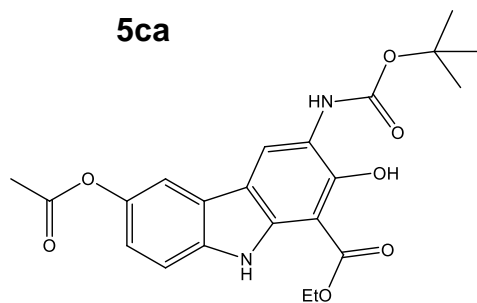


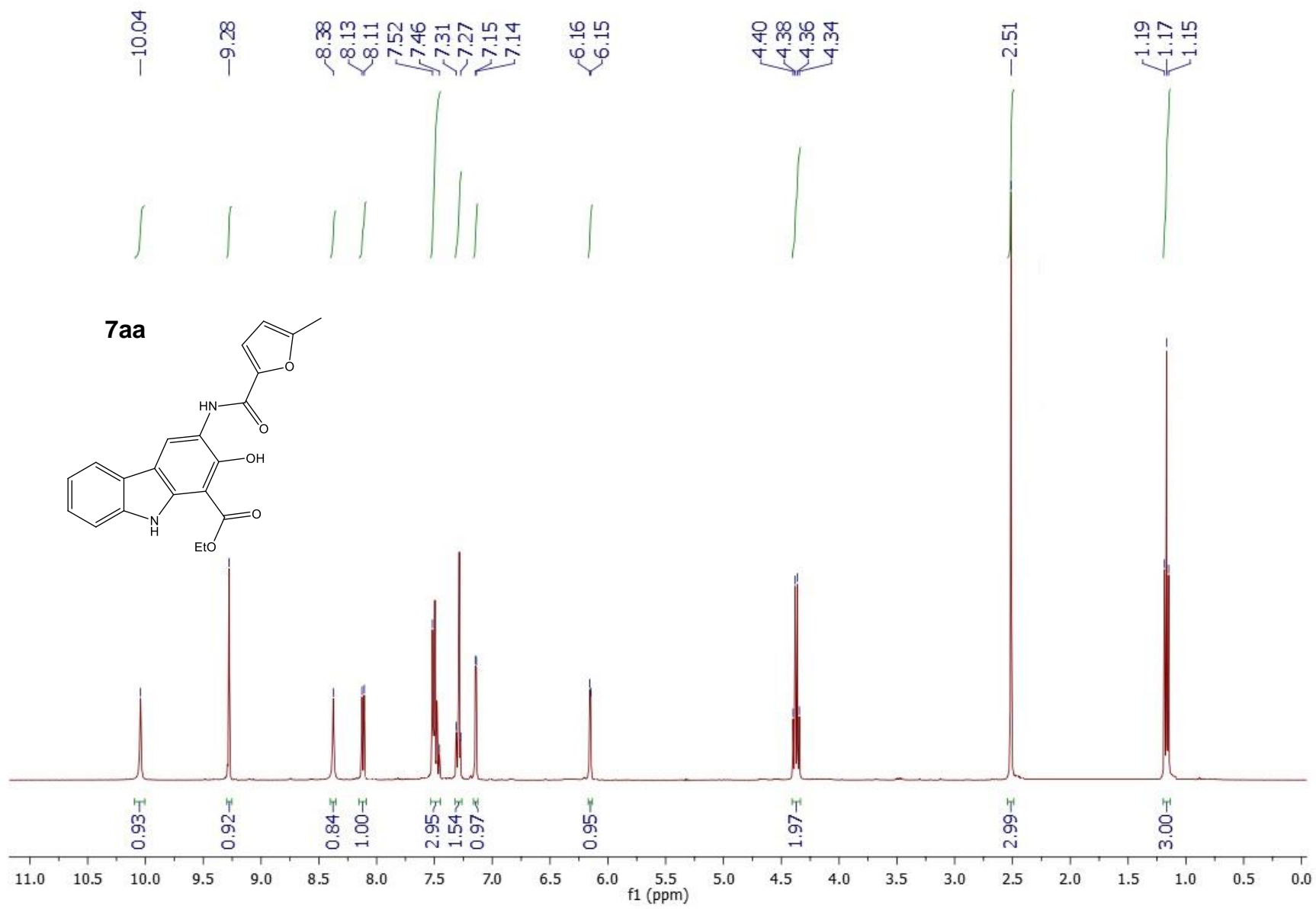


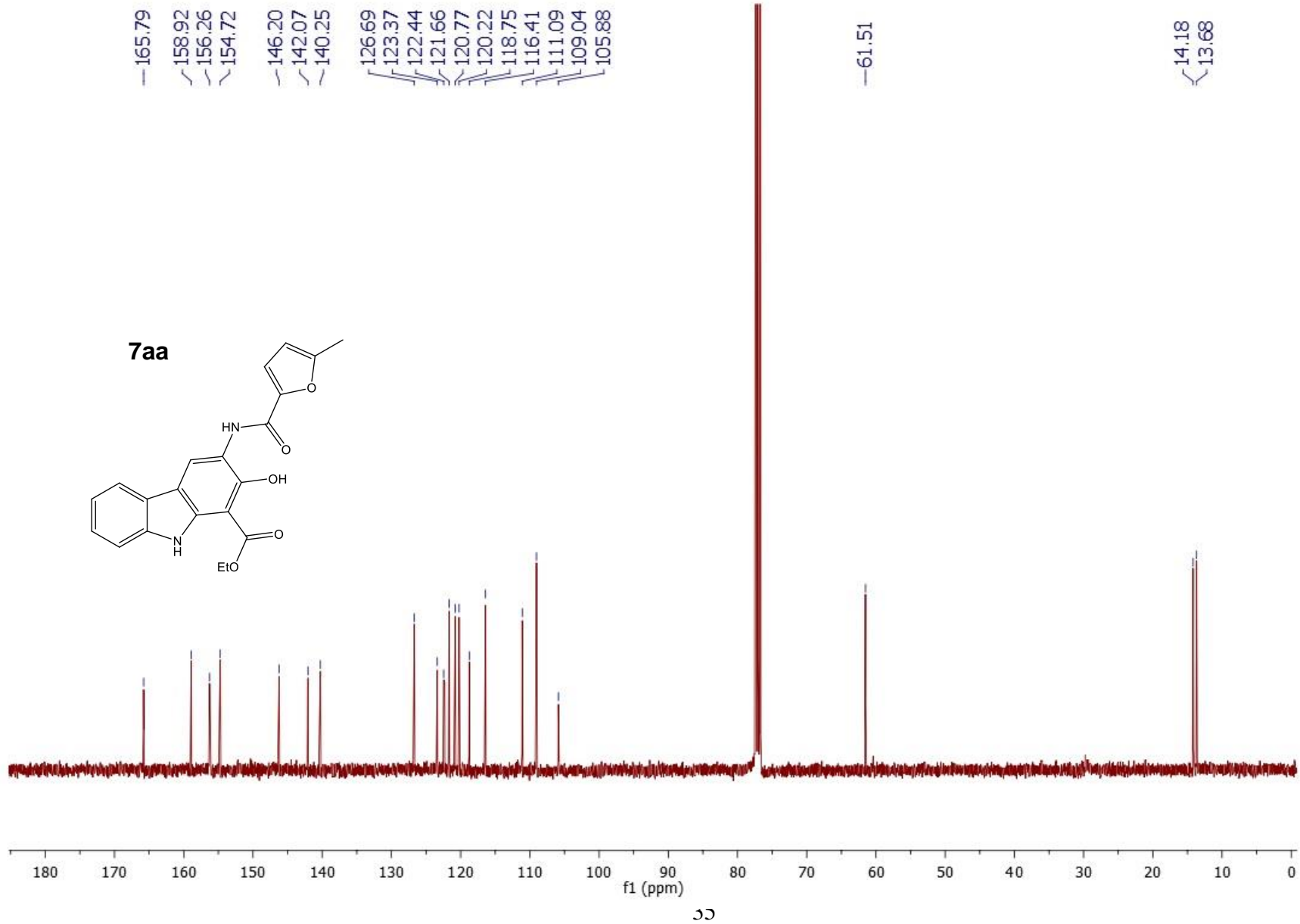
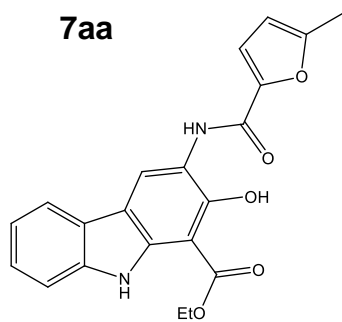


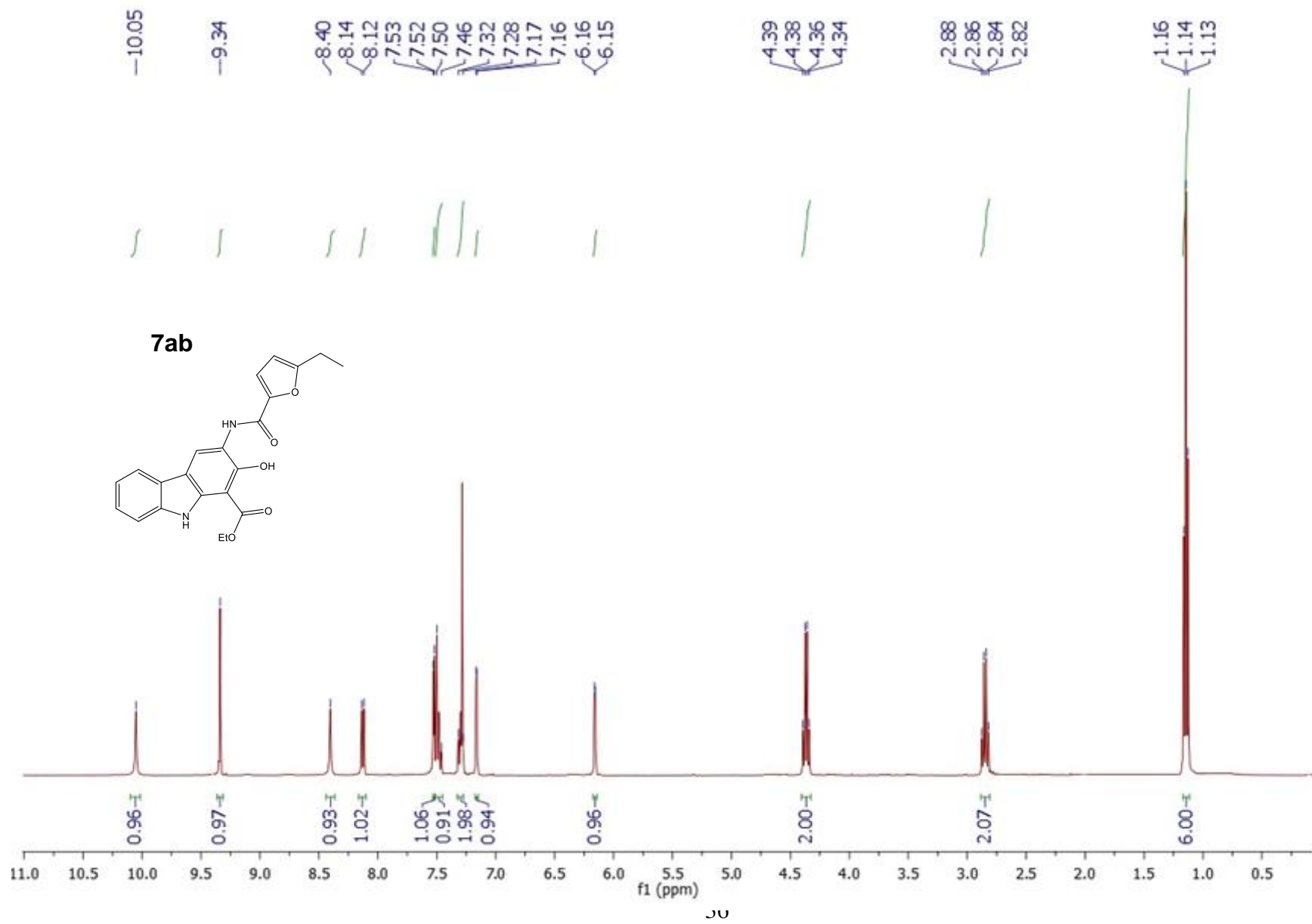


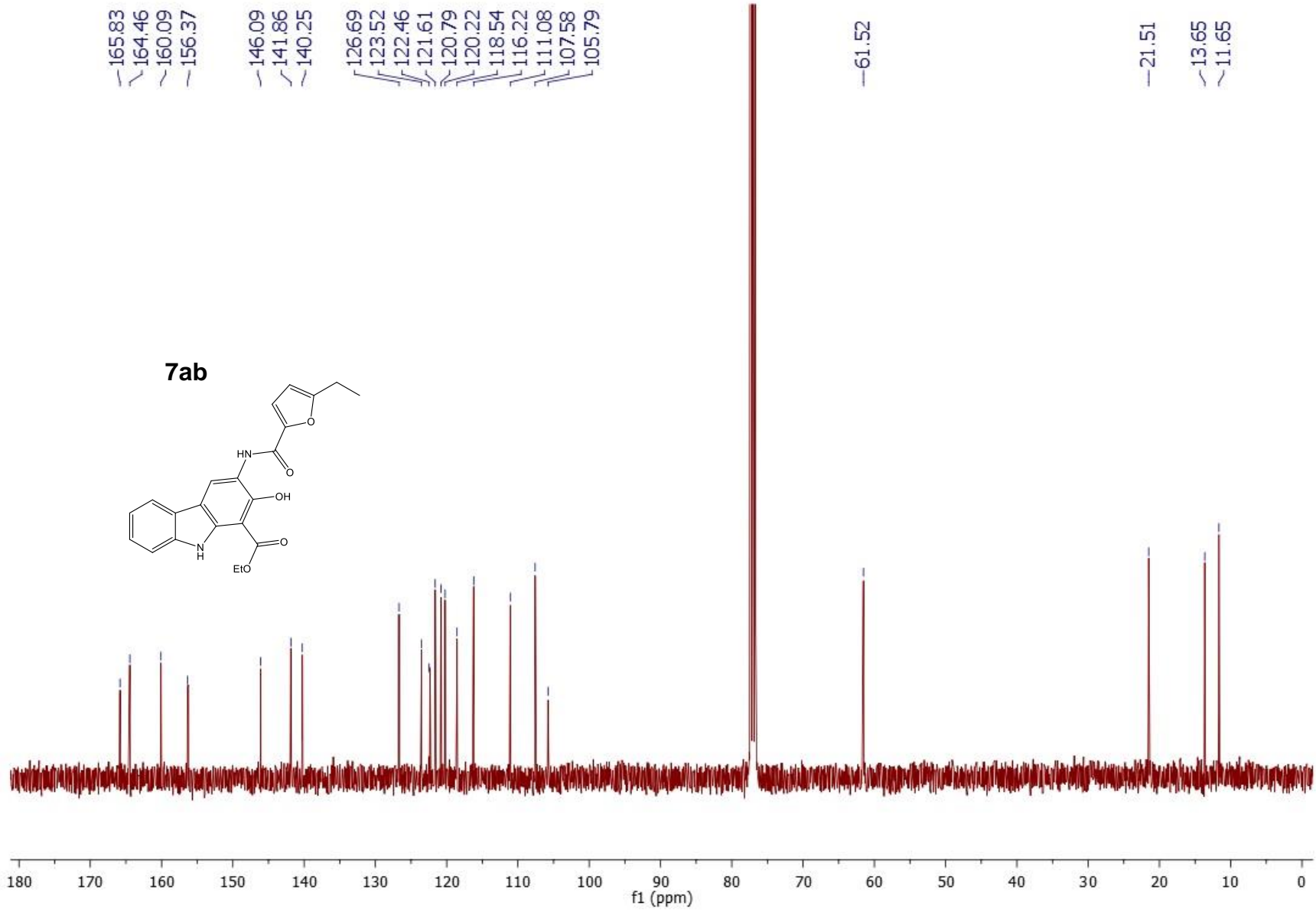


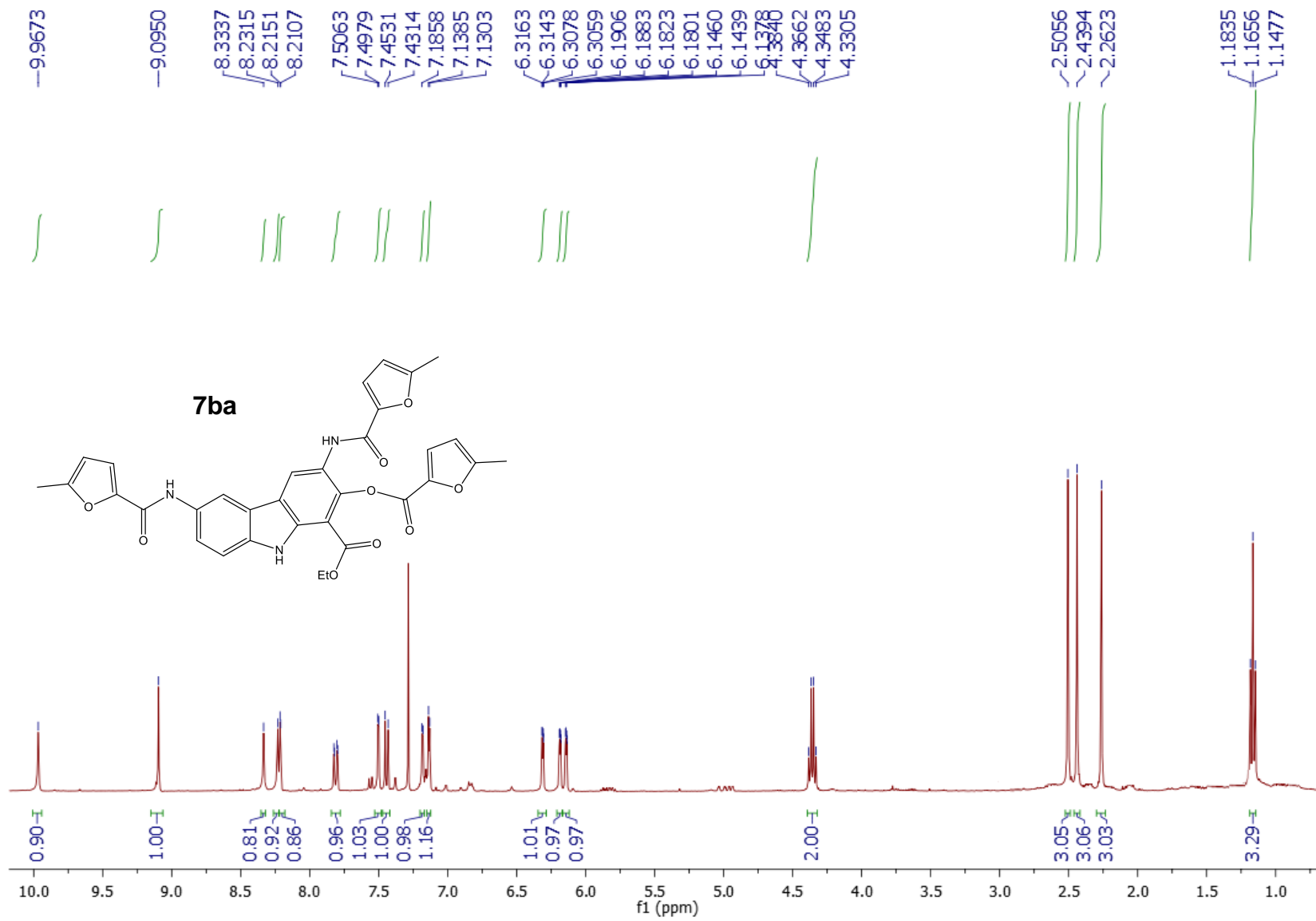




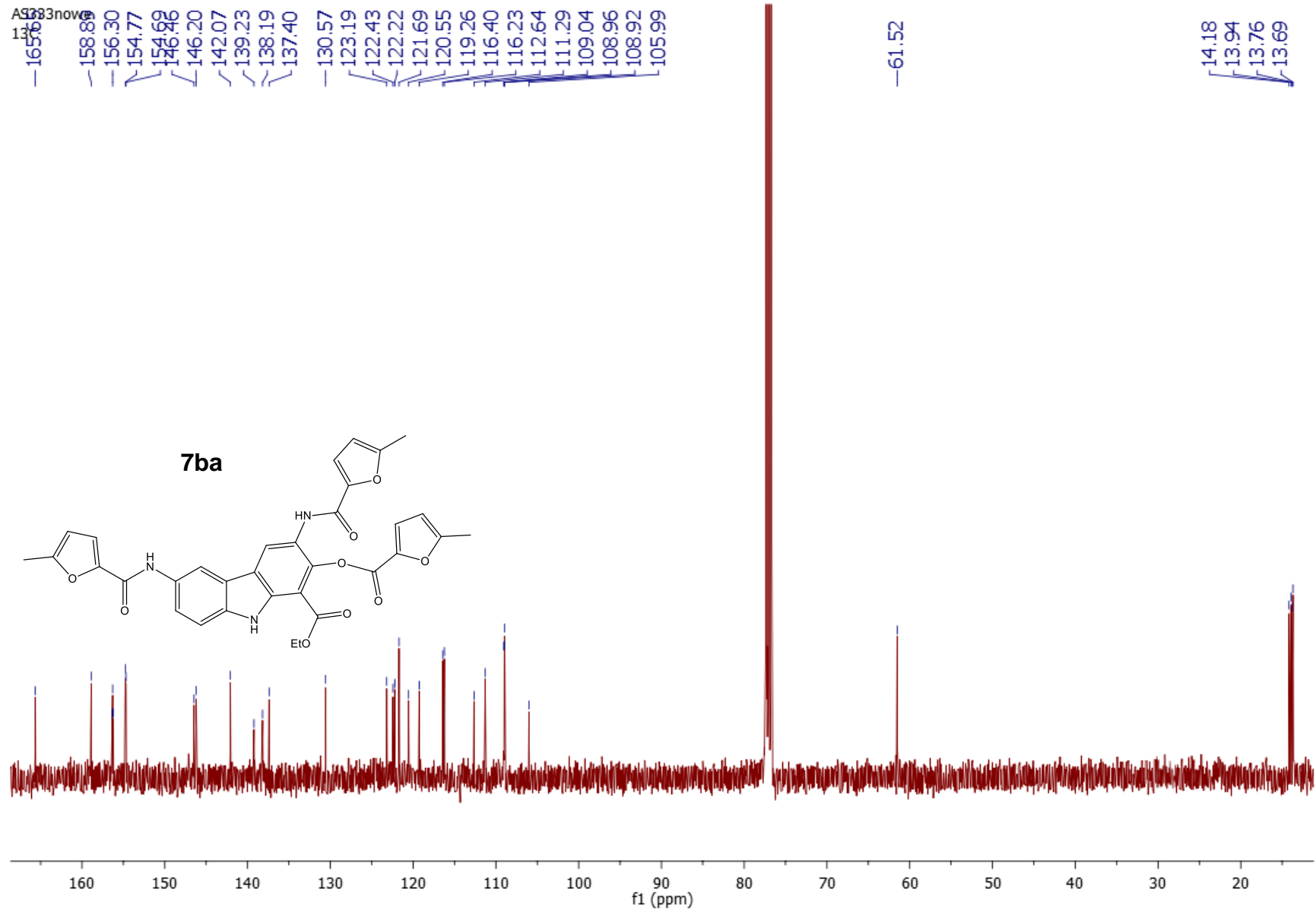


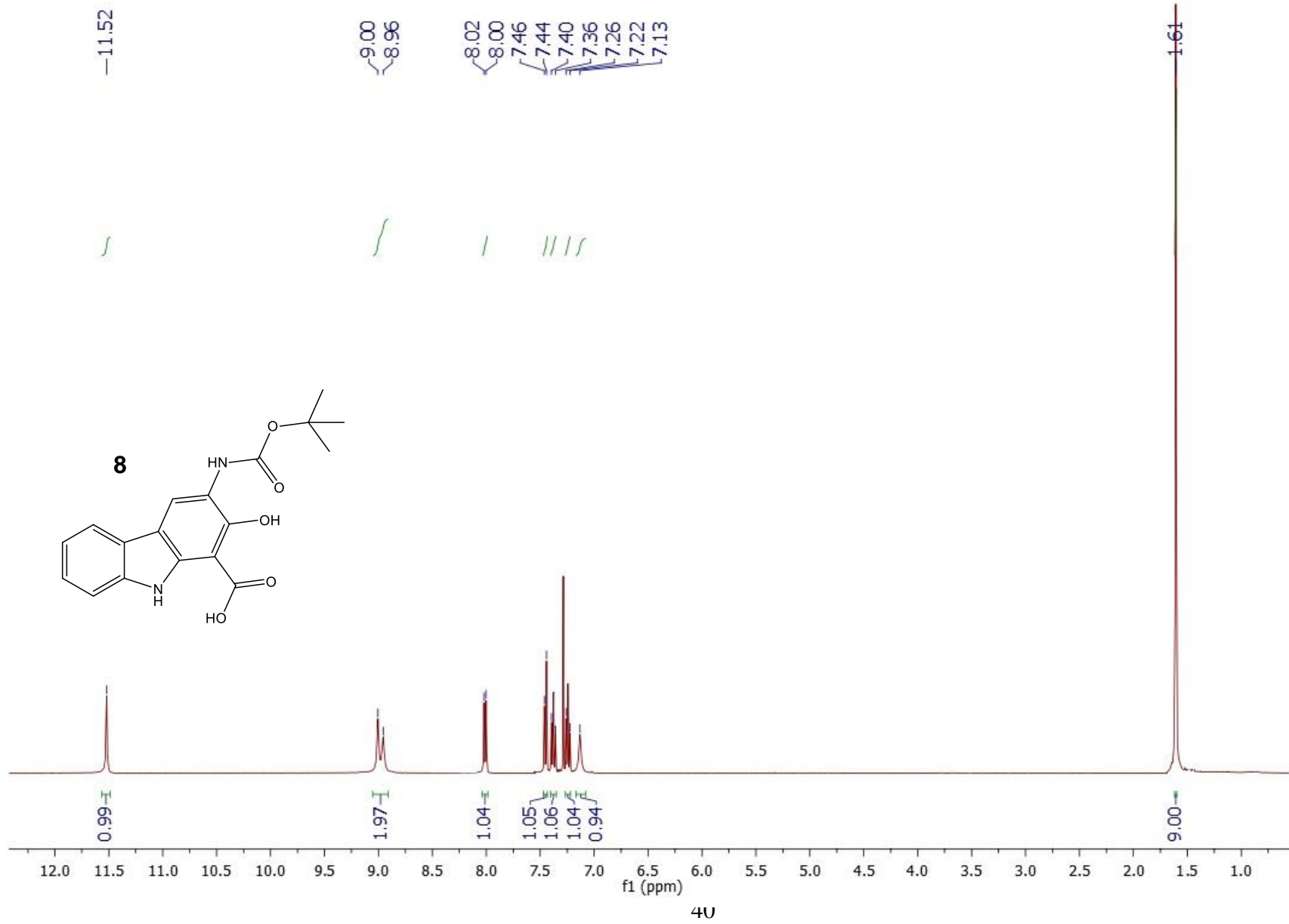


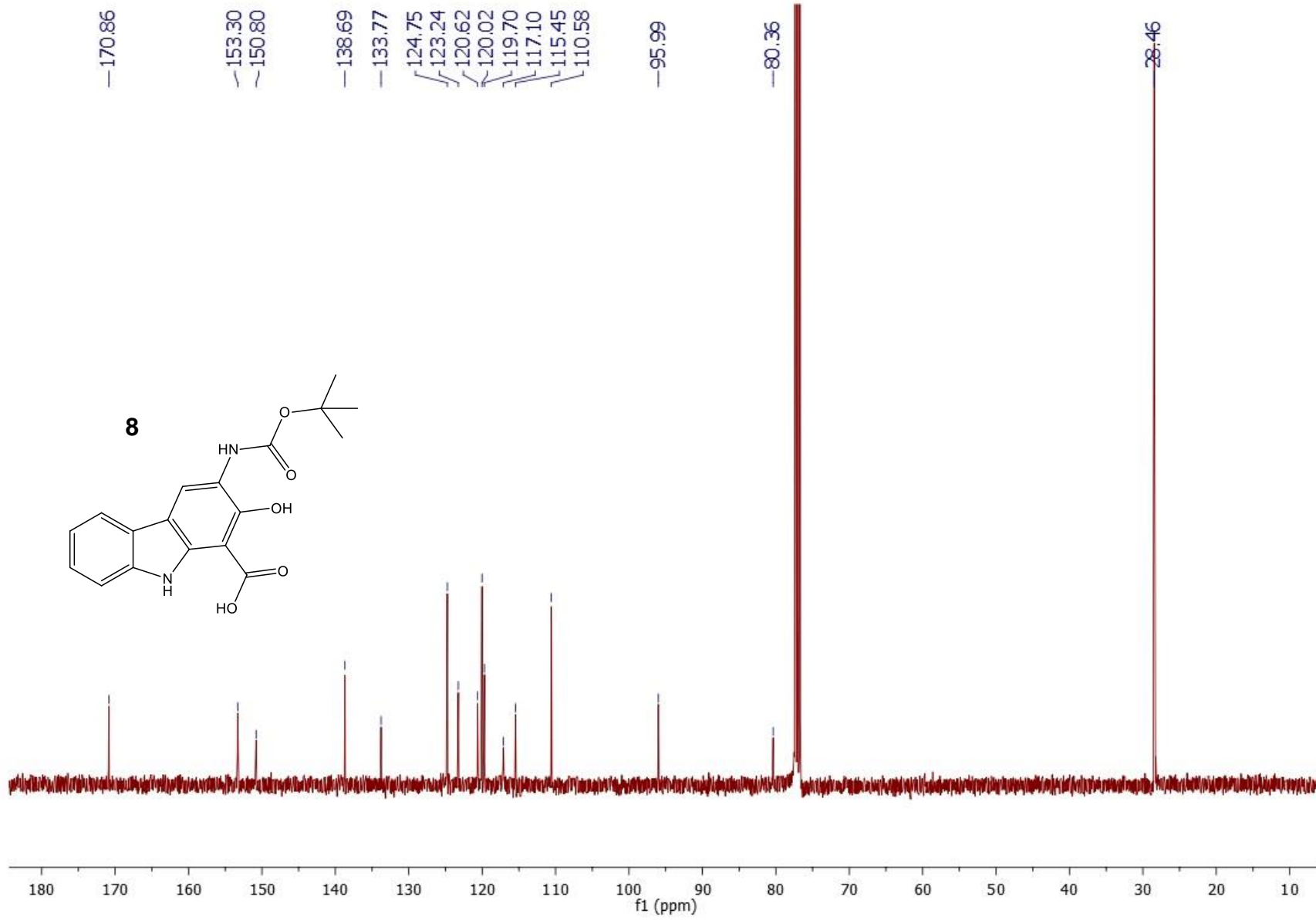
















OPEN

## Novel chalcone-derived pyrazoles as potential therapeutic agents for the treatment of non-small cell lung cancer

Natalia Maciejewska<sup>1✉</sup>, Mateusz Olszewski<sup>1</sup>, Jakub Jurasz<sup>1</sup>, Marcin Serocki<sup>3</sup>, Maria Dzierzynska<sup>2</sup>, Katarzyna Cekala<sup>2</sup>, Ewa Wieczerzak<sup>2</sup> & Maciej Baginski<sup>1</sup>

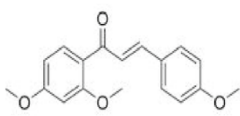
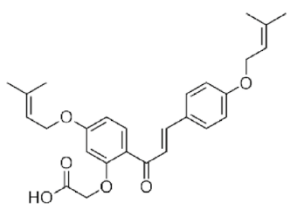
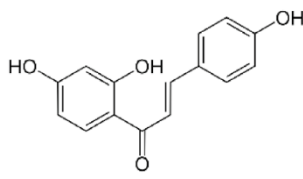
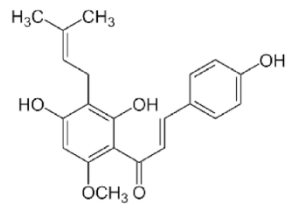
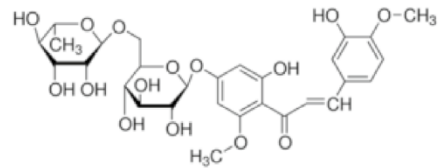
Lung cancer is considered to account for approximately one-fifth of all malignant tumor-related deaths worldwide and is therefore one of the most lethal malignancies. Pyrazole scaffold possesses a wide range of biological and pharmacological activities, which play important roles in medicinal chemistry. The present study reports the synthesis and in vitro biological characterization of nine pyrazoles derived from chalcones as potential anticancer agents for non-small cell lung cancer A-549, H226, and H460 cell lines. Most of the compounds efficiently inhibited the growth of all the tested cancer cell lines at micromolar concentrations. One of the most active compounds (PCH-1) was further evaluated for its effect on cell cycle distribution, apoptosis, migration, epithelial–mesenchymal transition, and oxidative stress. Furthermore, studies on the mechanism of action revealed that PCH-1 disrupts microtubule assembly, leading to cancer cell death. Molecular modeling studies confirmed the potent interaction of PCH-1 with the vinblastine binding site on tubulin. Overall, this study provides novel opportunities to identify anticancer agents in the pyrazole series.

Chalcones are an important class of natural compounds from the flavonoids family and are present in many edible plants such as fruits (tomatoes and citrus), nuts, vegetables, and tea<sup>1</sup>. Chalcone family members have often been used in traditional medicine and possess a large number of biological properties, including anticancer, antibacterial, antifungal, antimalarial, antidiabetic, anti-inflammatory, and antioxidant activities<sup>2</sup>. Several chalcones are currently being used in clinical practice or are undergoing clinical trials, exemplified by the selected analogs shown in Table 1. Chalcones have received considerable attention not only because of their broad spectrum of activities but also because of ease of synthesis and modification of the main core and good safety profile pertinent for oral administration<sup>3</sup>.

Chemically, chalcones have a scaffold of 1,3-diphenylprop-2-en-1-one either in *trans* or *cis* isomerism with two aromatic rings linked by a three-carbon  $\alpha,\beta$ -unsaturated carbonyl system<sup>12</sup>. The predominant configuration is *trans*-isomer that is more stable thermodynamically<sup>4</sup>. Structural modification mainly focuses on both phenyl rings. Similar to naturally occurring chalcones, methoxy and hydroxy groups in positions on the phenyl rings are important for anticancer activities of chalcone derivatives<sup>13</sup>. Marquina et al. reported that 2'-hydroxy-4'-alkoxy chalcone derivatives exhibit strong cytotoxic activity against PC-3 cells by inducing a G2/M phase arrest and mitochondrial apoptotic pathway<sup>14</sup>. Wang et al. found that chalcones bearing the 3-hydroxyl-4-methoxy phenyl moiety demonstrated high cytotoxic activity against the MCF-7 breast cancer cell line and displayed potent tubulin polymerization inhibitory activity<sup>15</sup>. Moreover, Pawlak et al. established that 2'-hydroxy-2'',5''-dimethoxychalcone exerted a potent antitumor activity on canine lymphoma and leukemia cells and that the addition of two methoxy groups increased the proapoptotic activities of chalcones<sup>16</sup>.

Structurally, methoxylated chalcones are related to natural combretastatin A-4 and colchicine because of congruous spatial orientation between two aromatic rings<sup>17</sup>. Similar to combretastatin and colchicine, methoxylated chalcones bind to tubulin and prevent its polymerization, leading to cell cycle arrest by interruption of mitotic spindle assembly and resulting in cell death<sup>18</sup>. The methoxy substituent in A ring of chalcones appeared to be the crucial pharmacophoric group for the inhibition of tubulin polymerization<sup>19,20</sup>. Moreover, structural manipulations that vary in the basic structural framework or substitutions pattern have also been reported for

<sup>1</sup>Faculty of Chemistry, Gdansk University of Technology, Gabriela Narutowicza 11/12, 80-233 Gdańsk, Poland. <sup>2</sup>Faculty of Chemistry, University of Gdansk, Wita Stwosza 63, 80-308 Gdańsk, Poland. <sup>3</sup>Ryvu Therapeutics, Leona Henryka Sternbacha 2, 30-394 Kraków, Poland. ✉email: natalia.maciejewska@pg.edu.pl

Chemical structure	Activity	Mechanism of action	References
<p><b>Metochalcone</b></p> 	Choleretic Diuretic	PCSK9 inhibitor	4
<p><b>Sofalcone</b></p> 	Anti-ulcer Mucoprotective	H2-receptor antagonist	5
<p><b>Isoliquiritigenin</b></p> 	Antioxidant Anti-inflammatory	EC 1.14.18.1 inhibitor NMDA receptor antagonist GABA-A benzodiazepine receptor positive allosteric modulator	6
<p><b>Xanthohumol</b></p> 	Anticancer Antioxidant Anti-inflammatory	Farnesoid X receptor agonist Inhibitor NFκB Inhibitor NRF2	7,8
<p><b>Hesperidin methylchalcone</b></p> 	Vascular protective Antioxidant Anti-inflammatory Neuroprotective	Inhibitor oxidative stress Inhibitor cytokine production Inhibitor NF-κB	9–11

**Table 1.** Chemical structures of approved and clinically tested chalcones.

antitumor properties, such as phenoxy moiety in the ortho position of the phenyl ring B<sup>21</sup>, methyl substitution in a position<sup>8</sup>, pyrazole hybrids<sup>22</sup>, and many others<sup>23</sup>.

Pyrazoles are heterocyclic compounds that possess two adjacent nitrogen atoms of the 5-membered ring of three carbon atoms. The pyrazole nucleus has diverse biological properties and therapeutic applications, such as analgesic, anticancer, anti-inflammatory, antimicrobial, antiviral, antidiabetic, anticonvulsant, antipyretic, and antidepressant properties<sup>24,25</sup>. Because many studies have reported the importance of the heterocyclic moiety of the pyrazole ring in medicinal chemistry, skeletons of pyrazoles are often modified to ameliorate their biological activity. Among others, pyrazoles derived from chalcones display an increase in the potency and spectrum of activity<sup>26</sup>.

On the basis of discussed studies and considering a constant need to develop new potent and selective anti-cancer compounds, we have designed and synthesized a series of derivatives of chalcone-derived pyrazoles with various combinations of substituents in the phenyl rings. Novel compounds were evaluated for their antitumor activity against various lung cancer cell lines, including studies on cytotoxic, antiproliferative, prooxidant, and proapoptotic effects. Among these compounds, **PCH-1** exhibited the strongest cytotoxic activity through interaction with tubulin, leading to cell cycle arrest and induction of apoptosis. To determine the molecular mechanism of action of these compounds, we performed molecular modeling studies, namely molecular docking. Our studies confirmed the potent interaction of **PCH-1** with the vinblastine binding site on tubulin. Overall, we have

Compound	R <sub>1</sub>	R <sub>2</sub>	R <sub>3</sub>	R <sub>4</sub>	R <sub>5</sub>	R <sub>6</sub>	R <sub>7</sub>	R <sub>8</sub>
PCH-1	H	O-CH <sub>2</sub> -O		H	OCH <sub>3</sub>	H	OCH <sub>3</sub>	H
PCH-2	H	OCH <sub>3</sub>	OCH <sub>3</sub>	OCH <sub>3</sub>	H	H	O-CH <sub>2</sub> -O	
PCH-3	H	H	CH <sub>3</sub>	H	H	H	O-CH <sub>2</sub> -O	
PCH-4	OCH <sub>3</sub>	H	H	H	H	H	O-CH <sub>2</sub> -O	
PCH-5	H	O-CH <sub>2</sub> -O		H	H	H	O-CH <sub>2</sub> -O	
PCH-6	H	H	OCF <sub>3</sub>	H	H	H	O-CH <sub>2</sub> -O	
PCH-7	H	H	OCH <sub>3</sub>	H	H	H	CH <sub>2</sub> -CH <sub>2</sub> -O	
PCH-8	H	H	OCH <sub>3</sub>	H	H	OCH <sub>3</sub>	O-CH <sub>2</sub> -O	
PCH-9	H	S-CH <sub>2</sub> -O		H	OCH <sub>3</sub>	H	OH	H

**Table 2.** Synthesized new chalcone-derived pyrazoles.

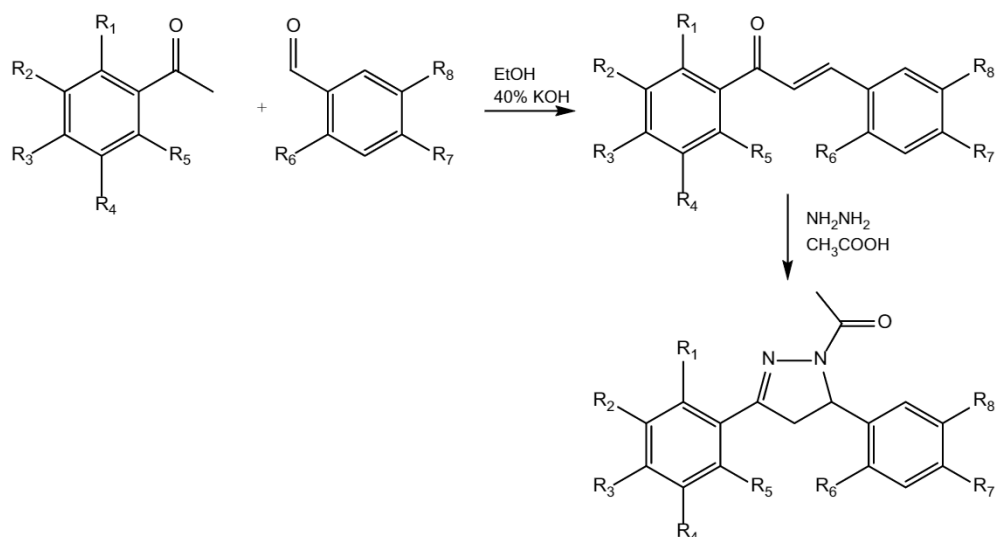


**Figure 1.** General synthetic pathway of the chalcone-derived pyrazoles.

demonstrated that **PCH-1** has a potent antitumor potential for the treatment of lung cancer and could be a lead for new drug development.

## Results

**Design of compounds.** The chalcone-derived pyrazoles were synthesized according to the protocols described by Yin Luo et al.<sup>27</sup> and are presented in Table 2 (Fig. 1).

Compounds PCH contain two differently substituted aromatic rings and *N*-acylated pyrazole ring. PCH-1, PCH-2, PCH-3, PCH-4, PCH-5, PCH-6, PCH-8 have at least one 1,3-benzodioxole moiety which is described as the structural element of compounds exhibiting an anticancer potential<sup>28</sup>. In PCH-7 and PCH-9 the oxygen atom in the benzodioxole ring is bioisosterically replaced by  $-CH_2-$  group and sulfur atom, respectively. PCH-1, PCH-2, PCH-4, PCH-7, PCH-8, and PCH-9 have from one to three methoxy groups substituting aromatic rings. In case of PCH-3 the methoxy group is changed into methyl group. Fluorine atoms have been incorporated into the methoxy group in PCH-6 derivative.

### **PCH-1** compound shows the potent cytotoxic effect towards NSCLC and non-toxic to normal cells.

All the synthesized chalcone-derived pyrazoles were evaluated for their antiproliferative activity against three human non-small cell lung cancer cell lines: A-549, H226, and H460, and a nonmalignant human embryonic kidney cell line HEK293. Cisplatin and 5-fluorouracil (5-FU) were used as a reference. Cells were exposed to a range of PCH concentrations (0.5–100  $\mu$ M) for 72 h and analyzed by 3-(4,5-dimethylthiazol-2-yl)-2,5-diphenyl-2H-tetrazolium bromide (MTT) assay. The results of the studies are expressed as the IC<sub>50</sub> concentration that inhibits 50% growth of cells. As depicted in Table 3, **PCH-1** was found to be the most potent cytotoxic compound against A-549 cells among all the tested pyrazoles, with the IC<sub>50</sub> value of  $4.32 \pm 0.28$   $\mu$ M. H226 and H460 cells showed similar sensitivity to **PCH-1** treatment, with IC<sub>50</sub> values of  $4.69 \pm 0.43$   $\mu$ M and  $8.40 \pm 1.10$   $\mu$ M, respectively. Other compounds exhibited moderate activity against cancer cells, besides **PCH-2**, **PCH-3**, **PCH-4**, **PCH-7**, and **PCH-8**, which were active only against H226 and H460 cells. Following treatment with **PCH-1**, the viability of all the tested cancer cell lines decreased in a concentration-dependent manner. In contrast, the

Compound	A-549	H226	H460	HEK293
PCH-1	4.32 ± 0.28	4.69 ± 0.43	8.40 ± 1.10	20.95 ± 2.34
PCH-2	> 100	40.46 ± 3.52	43.84 ± 1.12	> 100
PCH-3	> 100	86.70 ± 0.92	24.53 ± 1.74	> 100
PCH-4	> 100	86.70 ± 4.70	63.43 ± 3.34	> 100
PCH-5	60.89 ± 4.30	57.99 ± 2.56	38.84 ± 1.77	46.99 ± 3.18
PCH-6	21.46 ± 4.26	24.36 ± 2.13	18.12 ± 2.13	42.90 ± 1.23
PCH-7	> 100	41.49 ± 1.12	30.16 ± 2.14	> 100
PCH-8	> 100	61.11 ± 3.12	30.16 ± 2.14	> 100
PCH-9	79.46 ± 4.97	38.38 ± 3.53	43.77 ± 3.97	34.43 ± 2.01
Cisplatin	29.01 ± 0.12	17.47 ± 2.12	21.49 ± 1.87	28.45 ± 1.97
5-FU	8.12 ± 1.01	4.01 ± 0.76	4.08 ± 0.43	11.09 ± 1.53
Etoposide	0.54 ± 0.21	1.03 ± 0.16	0.05 ± 0.01	1.91 ± 0.97

**Table 3.** In vitro growth inhibitory activity of pyrazoles and reference compounds presented as an IC<sub>50</sub> ± SD (μM) value representing a concentration that inhibits 50% of cell growth.

nonmalignant human embryonic kidney cells (HEK293) exhibited less reduction of cell viability after **PCH-1** treatment. This finding indicates that compound **PCH-1** inhibited the cell viability of cancer cells without significantly affecting normal kidney cells. Additionally, **PCH-1** showed superior activity to the reference compound Cisplatin by approximately 6.7-fold, 3.7-fold, and 2.6-fold more for A-549, H226, and H460 cells, respectively.

The most potent compound **PCH-1** was selected to test its antiproliferative property by using a colony formation assay. As depicted in Fig. 2, **PCH-1** treatment reduced the number of colonies in all the tested cell lines in a dose-dependent manner.

**PCH-1 arrest cells in G<sub>2</sub>/M checkpoint.** Promising antiproliferative properties of **PCH-1** led us to further investigate the effect of this compound on cell cycle distribution. Therefore, cell cycle progression was analyzed by quantifying DNA content using flow cytometry. As shown in Fig. 3a,b, treatment of A-549, H226, and H460 cells with **PCH-1** after 24 h significantly (\*\*p < 0.001) induced cell cycle arrest in the G<sub>2</sub>/M phase, and this effect was followed by a decreasing trend at 48 h as compared to control. Concomitantly, we observed a significant increase in the sub-G<sub>1</sub> population of cells with the highest peak at 48 h after **PCH-1** treatment, thus suggesting apoptotic cell death. To thoroughly analyze the course of the cycle, A-549 cells were synchronized with a double-thymidine block in the G<sub>1</sub> phase and treated with IC<sub>90</sub> concentration of **PCH-1** for the indicated time. DNA content was quantified by the flow cytometric method and presented in Fig. 3c–e. Slight alterations of the division cycle were visible after 2 h of incubation with the compound. The prolonged exposure to **PCH-1** resulted in the accumulation of cells at the G<sub>2</sub>/M phase, resulting in a 50.12% increase in population as compared to that of the control. After 10 h of thymidine release, the DMSO control group showed a typical pattern of the cell cycle in the G<sub>1</sub>/G<sub>0</sub>, S, and G<sub>2</sub>/M phases. The results indicated that **PCH-1** arrests cells in the G<sub>2</sub>/M checkpoint and halts cell mitosis in a time-dependent manner, leading to the inhibition of the growth of A-549 cells.

**PCH-1 disrupt microtubule assembly.** To further evaluate whether the tubulin–microtubule system was the target site of **PCH-1**, in vitro microtubule polymerization assays were performed using the microtubule protein with Paclitaxel and Vincristine as a reference. Paclitaxel and Vincristine are antimetabolic drugs that have been commonly used in conventional chemotherapy for decades<sup>29</sup>. In 1979, it was shown that Paclitaxel accelerates the initiation of tubulin fiber polymerization and stabilizes the formed tubulin fibers in vitro, even in the absence of GTP or MAP in the solution<sup>30</sup>. Vincristine, on the other hand, binds to tubulin and inhibits its polymerization<sup>31</sup>. As shown in Fig. 4a, **PCH-1** remarkably reduced the total mass of tubulin polymer, without a significant increase in nucleation time. As expected, Paclitaxel accelerated the nucleation phase and increased the total mass of tubulin polymer, in contrast to Vincristine which extended the nucleation time and reduced the total mass of tubulin polymer compared to the vehicle. These results indicated that compound **PCH-1** interferes with microtubule polymerization by blocking microtubule assembly.

To confirm the influence of **PCH-1** on the organization of the tubulin cytoskeleton in A-549 cells, immunofluorescence was performed using antibodies for detecting β-tubulin and Aurora B. Aurora B is a protein kinase involved in the condensation and cohesion of chromosomes as well as in the process of attachment of tubulin spindles to the kinetochore and passing through the checkpoint of spindle assembly<sup>32</sup>. The expression of Aurora B is cell cycle-dependent and reaches a maximum at the G<sub>2</sub>/M transition, with the highest kinase activity during mitosis. Specifically, Aurora B localizes at the prophase in chromosomes, in the prometaphase and metaphase at centromeres, and is then transferred to the central mitotic spindle in the anaphase<sup>33,34</sup>. Visualization of the intracellular localization of Aurora B enables to determine whether the tubulin fibers forming the spindle are properly attached to the kinetochores and whether the cytokinesis process is proceeding properly.

A-549 cells after 6 h of exposure to the compounds showed a significantly increased fraction of mitotic cells. In the control group, usually 1 or 2 cells were seen dividing in several fields of view, while in the Paclitaxel, Vincristine, and **PCH-1** treatment groups, several mitotic cells could be seen in one field of view. As shown in Fig. 4b–d, mitosis is normal in control cells. A-549 cells treated with all compounds showed induction of various



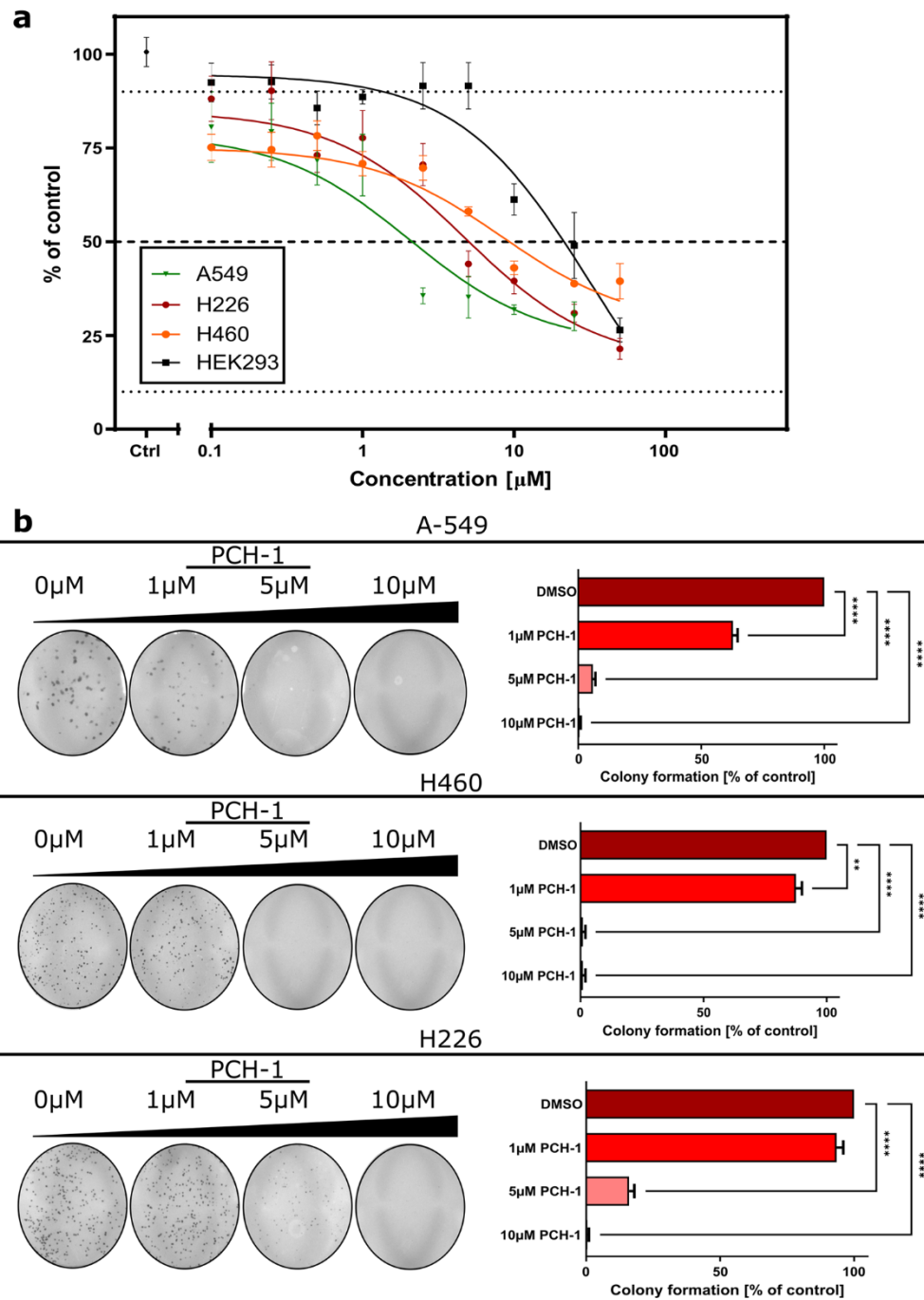


**Figure 2.** (a) Effect of compound PCH-1 on cell viability after 72 h incubation with compound. Results of percent viability vs concentration were plotted, and the IC<sub>50</sub> ± SEM was calculated for each cell line in triplicates by using GraphPad prism 9; (b) Representative photos of the colony formation assay are presented on the left panel and its quantification is depicted on the right panel. Data represent the mean ± SEM of three independent experiments. Statistical differences were analyzed by one-way ANOVA and post hoc Dunnett's test. \*\* p < 0.001, \*\*\*\* p < 0.00001.

mitotic alterations that occurred mainly at the metaphase and anaphase where they induced a strong centromeric localization of Aurora B. Multipolar mitotic cells and scattered metaphases were visible in the Paclitaxel-treated group and Vincristine-treated group, respectively (Fig. 4e–g). Chromosome scattering with irregular distribution was observed in the equatorial plane, which implied either the absence or irregular arrangement of the spindle. The morphological changes in spindle structure after PCH-1 treatment were nearly identical to those that occurred after Vincristine treatment and were the result of a prolonged metaphase arrest characterized by uncoordinated loss of chromatid cohesion (Fig. 4h–j).

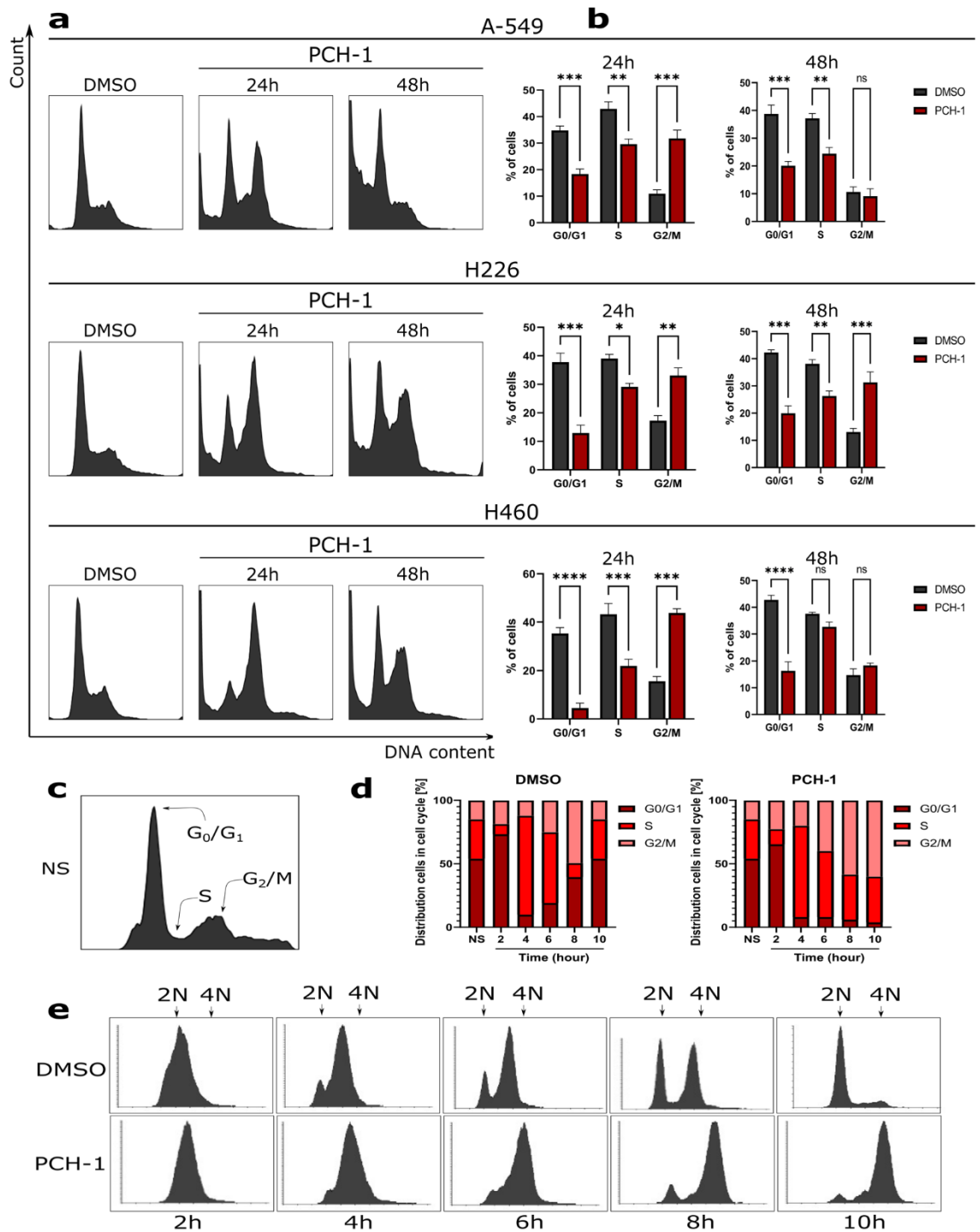


**Figure 3.** Cell cycle analysis of A-549, H226, and H460 cells after PCH-1 treatment. (a) Representative histograms after DNA staining; (b) Statistical analyses of histograms. Error bars represent the SEM of data obtained in  $n=3$  independent experiments. Statistical differences were analyzed with one-way ANOVA and post hoc Dunnet's test. \* $p < 0.01$ , \*\* $p < 0.001$ , \*\*\* $p < 0.0001$ , \*\*\*\* $p < 0.00001$  vs. vehicle; (c) Determination of cycle phases in unsynchronized cells; (d) The quantitation of the flow cytometric analysis in A-549 synchronized cells; (e) Representative histograms after flow cytometric analyses of cells synchronized in the G<sub>1</sub> phase after DMSO and PCH-1 treatment. 2N and 4N represent the DNA content of a cell in the G<sub>1</sub> (diploid), and G<sub>2</sub> phase (tetraploid), respectively.

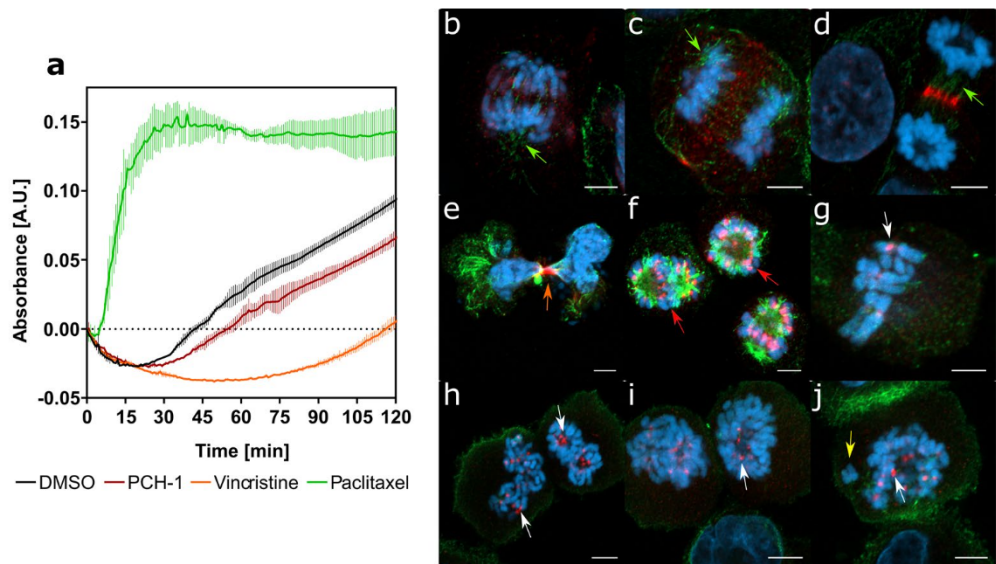


**Figure 4.** (a) Kinetic curves of a 120-min kinetic reaction of tubulin polymerization. Data represent the mean  $\pm$  SEM of two independent experiments. Representative microscopy images (b–j) presenting immunofluorescence of microtubule assembly and Aurora B in A-549 cells after 6 h of treatment with PCH-1. Scale bars = 5  $\mu$ m. DMSO, Vincristine, and Paclitaxel were used as reference compounds. The microtubule is depicted in green, Aurora B in red, and the nucleus is stained with DAPI (blue). (b–d) Mitosis in DMSO-treated cells; (e–f) Mitosis in Paclitaxel-treated cells; (g) Mitosis in Vincristine-treated cells; (h–j) Mitosis in PCH-1-treated cells. The arrows indicate a proper spindle assembly (green), a strong centromeric localization of Aurora B (white), chromosome scattering (yellow), improperly formed midbody (orange), multipolar spindle (red).

As shown in Fig. 5, A-549 cells after treatment with Paclitaxel passed the  $G_2/M$  checkpoint and entered mitosis, but its course was disturbed by the formation of a multipolar spindle. The strong accumulation of Aurora B on centrosomes indicates the incorrect attachment of microtubule fibers to the kinetochore and syntelic/monotelic chromosome orientation, which activates the spindle assembly checkpoint and mitotic arrest. Long-term exposure of cells to Paclitaxel leads to mitotic catastrophe, resulting in the formation of multinucleated polyploid cells. A similar cellular effect was observed after treatment of the cells with Vincristine and PCH-1. Figure 5 shows that A-549 cells exposed to Vincristine or PCH-1 passed the  $G_2/M$  checkpoint and entered mitosis; however, inhibition of tubulin polymerization blocked mitotic spindle formation. Potent accumulation of Aurora B on centromeres is caused by the lack of attachment of tubulin fibers to the kinetochore, which activates the checkpoint of the formation of the division spindle and leads to the arrest of cell proliferation in the mitotic phase. The consequence of this is a mitotic catastrophe and the formation of multinucleated polyploid cells.

**PCH-1 induce caspase-dependent apoptotic cell death.** To examine whether the effect of PCH-1 on reducing the viability of lung cancer cells was the result of inducing apoptotic cell death, A-549, H226, and H460 cells were treated with the compound for 6, 24, and 48 h, and analyzed by Annexin V/propidium iodide (PI) double staining using flow cytometry (Fig. S1 in supplementary information). After 6 h of incubation with PCH-1, the percent of live cells in all the tested cell lines significantly decreased and the fraction of Annexin V-positive cells concomitantly increased, thus confirming phosphatidylserine externalization and the ongoing process of apoptosis. At 24 h of treatment with the compound, a slight increase in both early (Annexin V(+)/PI(-)) and late (Annexin V(+)/PI(+)) apoptotic fractions was observed. Later exposure (48 h) to PCH-1 demonstrated a potent increase in the late apoptotic phase, from approximately 5% to 30–60%, depending on the cell line for vehicle and PCH-1-treated cells, respectively. Simultaneously, under the same conditions, a constant number of Annexin V(-)/PI(+) cells was observed for all cell lines. PI can enter only those cells with damaged plasma membrane, which enables to differentiate early apoptotic cells from late apoptotic and necrotic cells. Overall, biochemical changes involved in apoptotic cell death were prevailing, whereas necrotic changes were not observed. Furthermore, typical phenotypic features of cells undergoing apoptosis were visualized by fluorescent microscopy in Supplementary Fig. S2 and described in Supplementary Information.

To explain the type of cell death that cancer cells undergo after treatment with PCH-1, the ability of the compound to activate caspases 3–7 was determined by flow cytometry. As depicted in Supplementary Fig. S3 in Supplementary Information, after 6 h of treatment, PCH-1 activates executioner caspase-3/7 that executes apoptosis, as revealed by a 2.6-fold, 2.9-fold, and 3.15-fold increase in apoptosis for A-549, H226, and H460 cells, respectively, as compared to control. Later exposure to PCH-1 resulted in a massive increase in subpopulation cells with activated caspase 3/7, sustaining at a level greater than 5.8 times in A-549 cells and 4.7 times in H226 cells than in the control, while remaining approximately constant in H460 cells. The most pronounced activation of caspase 3 occurred equally in A-549 and H226 cell lines after 48 h of treatment and was sevenfold greater than that in the vehicle.

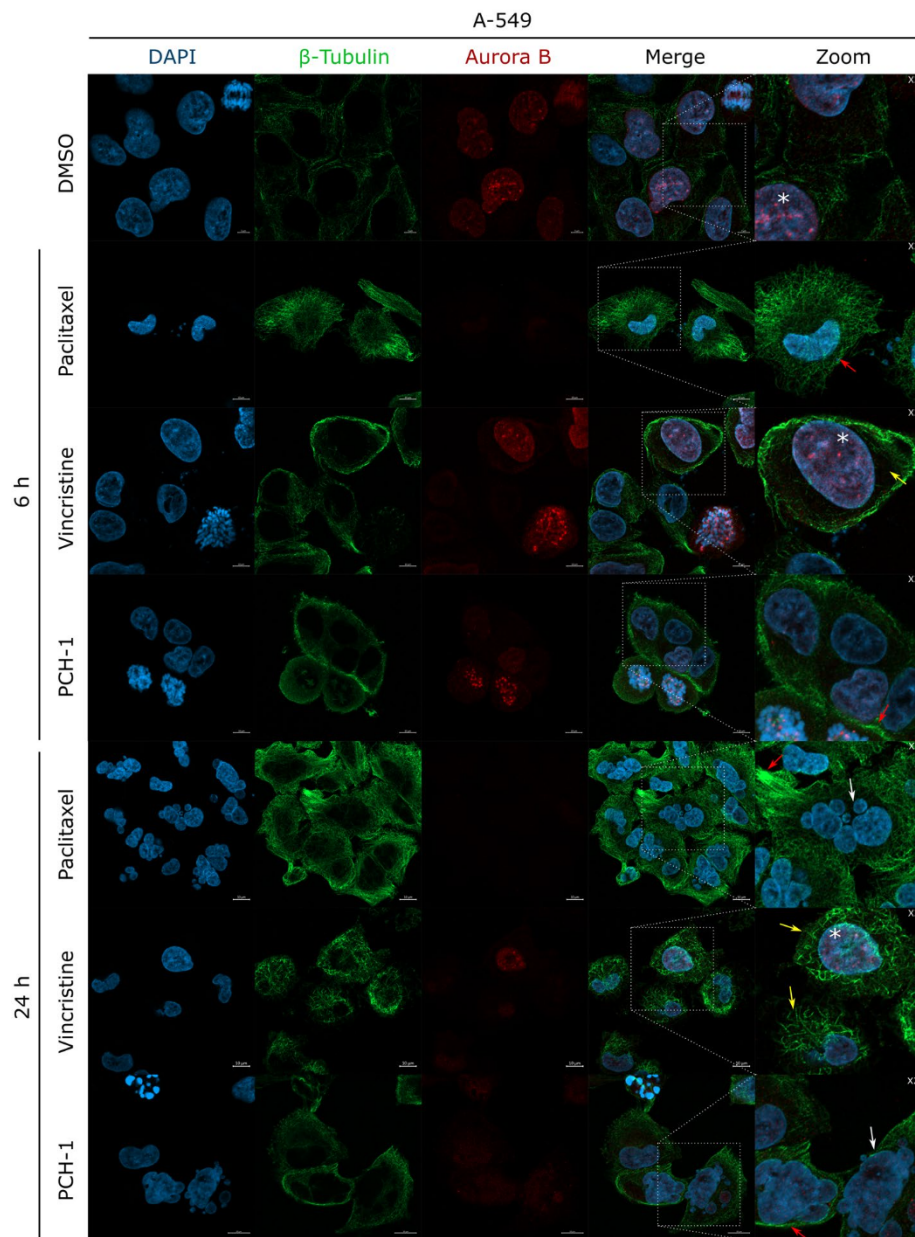


**Figure 5.** Representative microscopy images presenting immunofluorescence of microtubule assembly and Aurora B in A-549 cells at 6, and 24 h of treatment with **PCH-1**. The microtubule is depicted in green, Aurora B in red, and the nucleus is stained with DAPI (blue). Scale bars = 10  $\mu$ m. The arrows indicate a multinucleated nucleus (white), disturbed residual tubulin skeleton (yellow), coiled spiral aggregates of tubulin formation of rigid microtubule bundles (red). Asterisk marks cell nuclei in the G2 phase characterized by high Aurora expression.

**PCH-1 deregulates several apoptotic and EMT-related proteins.** To investigate the potential molecular mechanisms responsible for **PCH-1**-induced apoptosis in A-549 cells, we measured the expression of apoptosis-related proteins by western blot analysis. As shown in Fig. 6, **PCH-1** treatment downregulated the expression of full-length caspase 3, caspase 8, and caspase 9, accompanied by an increase in the levels of their cleaved forms. The activation of the caspase cascade by the test compound leads to proteolytic cleavage of poly(ADP-ribose) polymerase-1 (PARP-1), as revealed by a decrease in its full-length expression. Next, we determined the role of the antiapoptotic protein Bcl-2 as well as the proapoptotic proteins Bax and Bid in **PCH-1**-induced cell death in A-549 cells. As shown in Fig. 6, compared to the control cells, **PCH-1** treatment led to a significant increase in the Bax protein level (6 h, 24 h:  $**p < 0.001$ ; 48 h:  $*p < 0.01$ ), whereas the level of Bcl-2 was not changed. Additionally, we observed Bid cleavage (48 h:  $*p < 0.01$ ), which was noted as a reduction in full-length Bid protein.

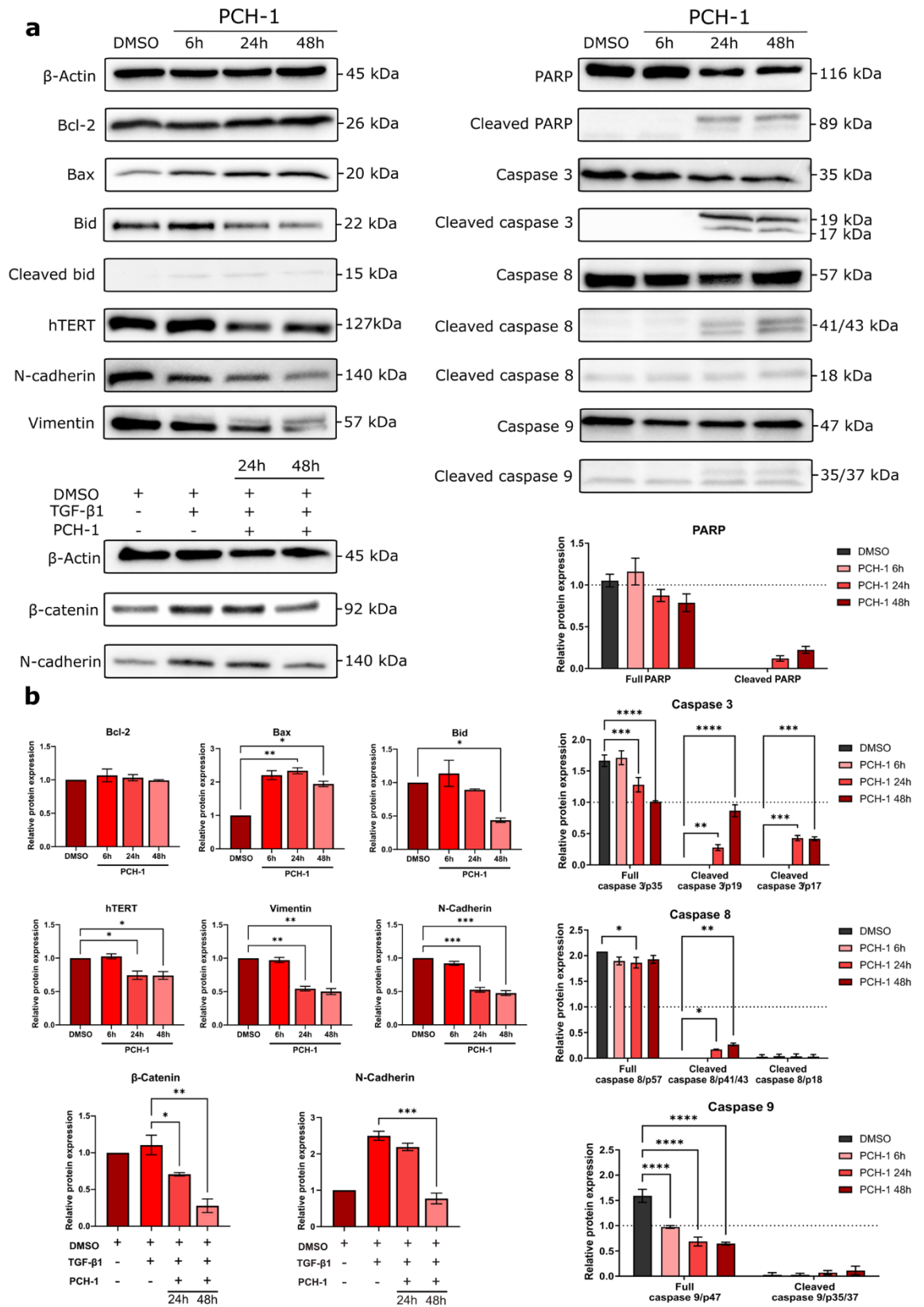


**Figure 6.** (a) Western blotting analysis showing the effects of PCH-1 on the expression of apoptotic, and EMT-related proteins in the A-549 cell line. Full length western blots were displayed in Supplementary Fig. S4 in Supplementary Information; (b) Density ratios of protein expression level after treatment with PCH-1 relative to β-Actin as a loading control. Data represent mean ± SEM of three independent experiments. Statistical differences were analyzed by one-way ANOVA and post hoc Dunnett's test. \*p < 0.05, \*\*p < 0.01, \*\*\*p < 0.001, \*\*\*\*p < 0.0001.

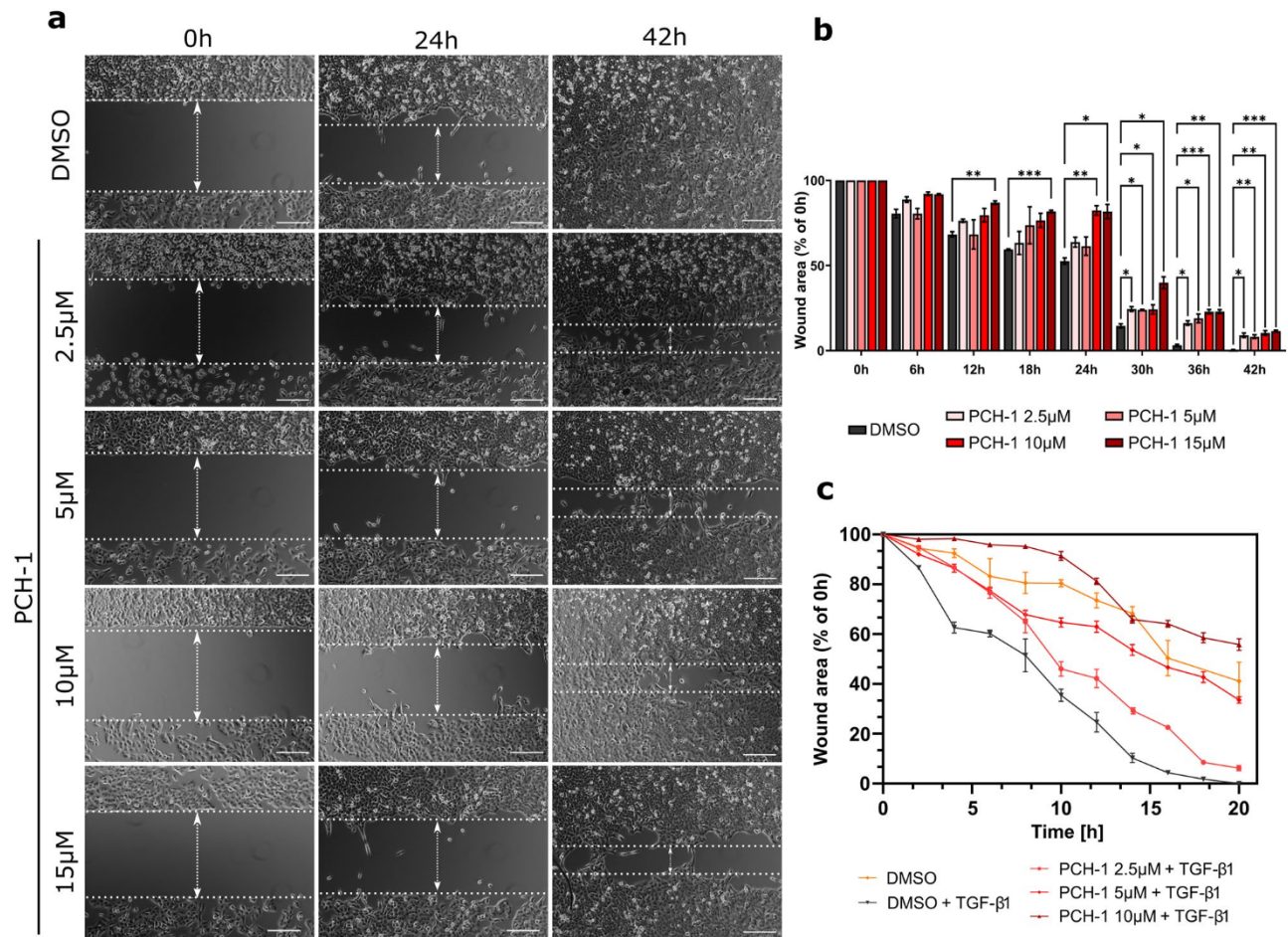


**Figure 7.** Analysis of cell migration by in vitro wound healing assay. (a) Time-lapse microscopy images after culture insert removal. Scale bars = 100 µm; (b) Quantification of the wound area after treatment A-549 cells with increasing concentrations of PCH-1. Data represent mean ± SEM of three independent experiments. Statistical differences were analyzed by one-way ANOVA and post hoc Dunnett's test. \*\* $p < 0.001$ , \*\*\* $p < 0.0001$ , \*\*\*\* $p < 0.00001$ ; (c) Quantification of wound area after treatment TGF-β1 stimulated A-549 cells with increasing concentrations of PCH-1.

Epithelial-mesenchymal transition (EMT) plays a crucial role in tumorigenesis by promoting cell motility, migration, and metastasis. Thus, we examined the expression of proteins involved in the EMT process by western blot assays. Figure 6 shows that compound PCH-1 dysregulated both biomarkers *N*-cadherin and vimentin of mesenchymal cells. The activity of *N*-cadherin in A-549 cells was reduced by 45% at 24 h ( $p = 0.0002$ ) and by 50% at 48 h ( $p = 0.0002$ ), while vimentin activity was reduced by 43% at 24 h ( $p = 0.005$ ) and by 46% at 48 h ( $p = 0.004$ ). Additional PCH-1 inhibited Transforming Growth Factor β1 (TGF-β1) induced mesenchymal-like phenotype in A-549 cells, indicating downstream of *N*-cadherin by 66% at 48 h ( $p = 0.0003$ ), and another EMT effector β-catenin, which was suppressed by 31% at 24 h ( $p = 0.0275$ ) and by 66% at 48 h ( $p = 0.0019$ ). Moreover, 24 and 48 h exposure to PCH-1 significantly decreased ( $p = 0.001$ ) the expression of the catalytic subunit of the telomerase reverse transcriptase hTERT, which is not only responsible for EMT but also plays an essential role in the maintenance of chromosomal telomere length, stemness, and resistance.

To further confirm the antimigratory potential of PCH-1, the wound healing assay was performed on A-549 cells. As shown in Fig. 7, cells in the DMSO control group gradually repopulated the wound area in a time-dependent manner. A similar effect was observed in groups treated with 2.5 µM and 5 µM PCH-1, except for 30–36 h, where the ability of cells to repopulate the wounded area was temporarily attenuated as compared to that in the vehicle. In contrast, 10 and 15 µM concentrations of PCH-1 significantly reduced the migration of the cells. This effect was retained during the entire exposure time, with the highest difference during 18–24 h compared to that in the control group. Finally, the anti-migratory properties of PCH-1 were studied by co-treatment A-549 cells with TGF-β1. As shown in Fig. 7c, and Supplementary Fig. S5 in Supplementary Information, TGF-β1 alone accelerated wound closure, whereas PCH-1 inhibited TGF-β1-induced cell motility, and as a result, the wound remained opened after 20 h of treatment with 5 µM and 10 µM of PCH-1. 2.5 µM of PCH-1 also resulted in a decrease in the rate of cell migration, but after 20 h of exposure, the wound closed similarly to the control-treated with TGF-β1 alone. A noteworthy aspect is that we did not observe detached cells at any point of treatment. Moreover, studied concentrations of PCH-1 were only slightly cytotoxic as evidenced by the IC<sub>50</sub> values determined after 24 and 48 h of treatments, which were  $41.27 \pm 0.75$  µM, and  $25.58 \pm 0.97$  µM,

Ligands	$\Delta G$ (kcal/mol)
PCH-1	-7.5
VLB	-7.2
VNC	-5.8

**Table 4.** Ligand–protein energies calculated with the Autodock Vina program.

respectively. This suggests that the observed antimigratory properties are not affected by the cytotoxic effect of the tested compound.

**PCH-1 induce intracellular oxidative stress.** The generation of intracellular reactive oxygen species (ROS) causes an imbalance of cellular redox homeostasis, followed by damage of cellular components and cell death. Therefore, compounds with the ability to produce high levels of ROS and/or inhibit antioxidant processes are often used in anticancer therapies<sup>35</sup>. In the present study, the effect of **PCH-1** on ROS generation in A-549 cells was investigated by flow cytometry. As an indicator of ROS generation, the fluorescent probe 2',7'-dichlorodihydrofluorescein diacetate (H2DCFDA) was used, which undergoes oxidation by ROS to form a highly fluorescent compound 2',7'-dichlorofluorescein (DCF). As shown in Supplementary Fig. S6 in Supplementary Information, compound **PCH-1** induced a massive amount of ROS in A-549 cells in a time-dependent manner. During 3, 6, and 24 h was observed accordingly a significant 15% (\*\*\*\* $p < 0.00001$ ), 56.9% (\*\*\*\* $p < 0.00001$ ), and 68.1% (\*\*\*\* $p < 0.00001$ ) increase of ROS towards vehicle control-treated cells. Moreover, the induction of ROS was equally high for **PCH-1** and the reference compound  $H_2O_2$  in all the tested time points.

**Molecular docking studies.** In addition to the abovementioned biological tests, a series of docking simulations were performed using the Autodock Vina program<sup>36</sup>. To estimate ligand–receptor affinity, an empirical scoring function inspired by the X-score function was used in Vina<sup>37</sup>. Docking was performed on 3 ligands, namely **PCH-1**, vinblastine (VLB), and vincristine (VNC), to investigate their binding mode in the vinblastine site of tubulin. The latter two ligands are already known for their effectiveness toward the tubulin target and served here as a reference<sup>31</sup>. Currently, there are a number of tubulin structures in the PDB database (such as 7DAD, 7DAE, 6KNZ, 6N47, and 6K9V). However, we decided that the most appropriate one for our study would be the 5JT2 structure from 2016 because it is a complex of protein with one of the ligands. Thus, we used the bound docking approach, for example, the structure of the target was used from the ligand–target complex. Both the receptor and the VLB ligand used in the docking simulation originated from the abovementioned 5JT2 PDB file<sup>38</sup>. The VNC ligand was derived from PDB 7A69<sup>39</sup>. **PCH-1** is a new molecule; therefore, its structure was built and optimized using the Biovia software<sup>40</sup>. The maximum energy difference between the worst and the best docking modes was set to 5 kcal/mol. The grid center of Vina docking was selected as the center of mass of the ligand VLB from 5JT2, which was obtained using the experimental pose. The grid size in docking was set to  $20 \text{ \AA} \times 20 \text{ \AA} \times 20 \text{ \AA}$ , which was adequate to cover the entire vinblastine site. Additionally, the rigid receptor and flexible ligands were parametrized by AutodockTools 1.5.6<sup>41</sup>. The parameterized systems were recorded in the PDBQT file. In particular, both receptor and ligand were presented using a united atom model, which involves the nonpolar hydrogen atoms. Atomic charges were estimated through the Gasteiger–Marsili method<sup>42</sup>.

The performed simulations were narrowed down to 10 best results based on the score function; after careful visual inspection, the best ones were selected based on their spatial arrangement and docking score (Table 4). The docking results indicate that **PCH-1** had scores similar to those of VLB, where the scores of VNC were lower by almost 2 kcal/mol, even with different spatial configurations. This finding agrees with our biological test results that **PCH-1** is biologically slightly more active than VLB or VNC.

These results were also visually checked by the VMD program<sup>43</sup>. Figure 8 was drawn using this program. Figure 8a shows the complete structure of tubulin in a complex with TTL together with the  $\alpha 1$ ,  $\alpha 2$ ,  $\beta 1$ , and  $\beta 2$  subunits. The additional box marked with dashed lines indicates the ligand docking site at the vinblastine site. Figure 8b–d are the magnifications of the mentioned place for each ligand. Each of them also shows the hydrogen bonds between the receptor amino acids and ligands; these bonds can hold the ligand in a permanent place and thus cause tubulin to malfunction. There was an apparent trend showing that the indole part attached to the heptylamine rings had a better score if it was located deeper at the vinblastine binding site of tubulin. This structure certainly influences the affinity of the ligand for the vinblastine site. It should be noted, however, that on the basis of molecular docking alone, it is difficult to conclude whether the proposed amino acids actually participate actively in the molecular mechanism of action. The main aim of performing molecular docking was to support biological data by checking whether the vinblastine binding site can be occupied by our ligands. More advanced molecular modeling methodology (thermodynamics study) could be used in future to further support our hypothesis about the binding site.

## Discussion

According to the World Health Organization (WHO), cancer is the leading cause of death worldwide and caused 10 million deaths in 2020, and lung cancer had the highest mortality rate and accounted for 1.8 million deaths<sup>44</sup>. The incidence of lung cancer is increasing dramatically each year, and this increase is associated with aging of the human population which has been exposed to several factors that promote mutations leading to cancer, such as smoking tobacco, unhealthy diet, or air pollution<sup>60</sup>. Treatment approaches for lung cancer mainly depend on

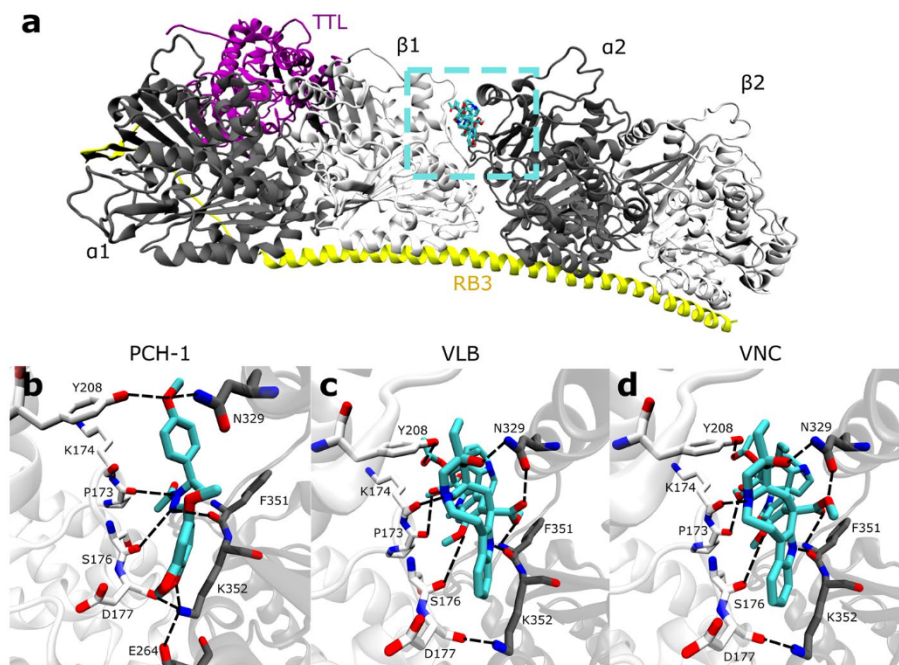


**Figure 8.** (a) Visualization of the complete tubulin protein in complex with TTL (purple) and RB3 (yellow);  $\alpha$  tubulin (dark gray) and  $\beta$  tubulin (light gray) subunits were taken from PDB 5JT2. Additionally, PCH-1, VLB, and VNC (cyan) ligands docked at the vinblastine site of tubulin are marked with dashed lines; (b–d) Visualization of ligands at the docking site of PCH-1/VLB/VNC ligands, respectively, shown as licorice, where the carbon atoms are stained with cyan, oxygen with red, and nitrogen with blue. Tubulin  $\beta 1$  and  $\alpha 2$  are displayed as light gray and dark gray bands, respectively. Our proposed receptor amino acids that may interact with the ligand are in the form of a stick and are labeled. The hydrogen bonds are underlined with black dashed lines.

tumor staging and type of cancer. Patients with small cell lung cancer show a good response to chemotherapy, while the progress in radiation therapy ensures their long-term survival<sup>45</sup>. Current pharmacological treatments for non-small cell lung cancer are not effective, but surgical resection offers substantial cure rates in early-stage cases. Patients with advanced, metastatic cancers are receiving combined chemotherapy and radiation<sup>46</sup>.

Many studies have proved that nitrogen-containing heterocyclic compounds such as pyrazole possess significant biological potency for cancer treatment<sup>47,48</sup>. In our present study, a series of pyrazoles derived from chalcones were reported based on the consideration of commonly used ring substitution modifications. Initially, the compounds were evaluated for cytotoxicity in the selected cell line models. Almost all derivatives exhibited moderate activity against all the three non-small cell lung cancer cell lines, except for the dimethoxy analogue **PCH-1**, which displayed potent cytotoxic properties and thus was chosen to evaluate its molecular mechanism of action. The substantial objective of cancer therapy is to kill cancer cells, but without affecting healthy cells. The toxicity studies on normal human embryonic kidney cells revealed that **PCH-1** is less toxic than the reference compound Cisplatin, and therefore, it is suitable for further evaluation of anticancer properties.

The determination of the mechanism responsible for cancer cell death is extremely important for drug efficacy and development. The antiproliferative effects of anticancer drugs are often linked with the suppression of the cell cycle. Studies on cell cycle distribution showed that **PCH-1** induces  $G_2/M$  cell cycle arrest after 24 h of incubation in all the tested cancer cell lines.

Antimitotic properties of chalcones are known from 1990 and are associated with the inhibition of microtubule assembly<sup>49</sup>. Many existing microtubule inhibitors are registered as drugs, but their clinical use is often limited due to the chemoresistance mechanisms<sup>50</sup>. **PCH-1** inhibited tubulin polymerization in the cell-free tubulin assembly assay, but the effect was less pronounced similar to that observed for the reference compounds. In cell-based assays, we observed similar depolymerization of the tubulin network and impaired spindle assembly in the test compound and Vincristine groups. These results were supported by molecular docking.

Current cancer chemotherapies mostly exert an antitumor effect by triggering apoptosis in cells<sup>51</sup>. Apoptosis, also known as programmed cell death, is a natural mechanism for the regulation of physiological growth and homeostasis. This process is characterized by several morphological and biochemical hallmarks, including chromatin condensation, cell shrinkage, and phosphatidylserine externalization. There are also many ways in which cells may undergo apoptosis. The two main pathways linked to the activation of apoptosis signal transduction are intrinsic and extrinsic pathways<sup>52</sup>. Microscopic observations and flow cytometry analysis revealed that **PCH-1** induces apoptosis in all the tested cancer cell lines in a time-dependent manner. Therefore, one of the assumptions of our studies was to obtain information about the exact mechanism by which **PCH-1** induces apoptosis. For this purpose, the A-549 cell line was selected as the most sensitive cell line to the test compound. Western blot



analyses revealed full activation of the initiation caspase-9 and execution caspase-3, with a significant increase in their cleaved forms in a time-dependent manner. Caspase-9 is activated by translocation from the cytosol into the intermembrane space and partially by recruitment into the Apaf-1 apoptosome complex following the efflux of cytochrome *c* from the mitochondria<sup>53</sup>. Once activated, caspase-9 cleaves and activates caspase-3 and caspase-7 to induce apoptosis<sup>54</sup>. Next, the activated caspases cleave cellular proteins such as nuclear enzyme PARP to dismantle the apoptotic cells<sup>55</sup>. Cleavage and inactivation of PARP by **PCH-1** lead to loss of genomic integrity, thereby depleting the cell of NAD and ATP and thus contributing to cell death. Moreover, the activation of caspase-8 was also observed in **PCH-1**-treated cells, which is closely related to apoptosis signaling by the extrinsic pathway<sup>56</sup>. Caspase-8 mediates the mitochondrial pathways through the cleavage of the proapoptotic Bcl-2 family members such as Bid to tBid. Subsequently, tBid switches the conformation of Bak, resulting in its oligomerization and allosteric activation and releasing cytochrome *c*<sup>57</sup>. **PCH-1** treatment leads to both cleavage of Bid and increased expression of Bax, thus suggesting the activation of cell surface death receptors and therefore the extrinsic apoptosis pathway.

Metastasis involves the spread of cancer cells from the primary tumor site to other tissues or organs of the body and is the major cause of cancer-related deaths<sup>58</sup>. One of the earliest events in cancer metastasis is EMT, a process that converts epithelial cells to mesenchymal cells that undergo cytoskeletal rearrangements to promote cancer motility and invasiveness<sup>59</sup>. Intermediate filaments (IFs) play an important role in EMT progression by maintaining cellular polarity and stiffness<sup>60</sup>. The most abundant member of the IF family is Vimentin (a type III protein) that is responsible for forming associated parallel arrays with microtubules and modulating prosurvival functions<sup>61</sup>. The disassembling of the microtubule network leads to a collapse of Vimentin IFs to the perinuclear region<sup>62</sup>. Recent studies have shown the significance of Vimentin in lung cancer, wherein a high expression of Vimentin was found to be related to a high frequency of metastases and therefore a poor prognosis in patients with resected non-small cell lung cancer<sup>63</sup>. On the basis of these findings, we decided to test the effect of **PCH-1** on the suppression of the EMT process. **PCH-1** effectively downregulated Vimentin and significantly promoted the suppression of another mesenchymal marker, *N*-cadherin, in A-549 cells. In order to show retrieving the epithelial phenotypes capacity by tested compound, A-549 cells were stimulated with well-known EMT inducer TGF- $\beta$ 1, and then exposed to **PCH-1**<sup>64</sup>. Treatment with TGF- $\beta$ 1 alone activated *N*-cadherin, and  $\beta$ -catenin, whereas co-treatment with **PCH-1** abrogated their expression. This suggests that **PCH-1** is a therapeutic agent for cancer treatment controlling TGF- $\beta$ 1-mediated EMT. Moreover, we studied the expression of telomerase reverse transcriptase, which plays a key role in ensuring chromosomal stability by maintaining telomere length, and therefore assert the uncontrolled proliferation of the cells<sup>65</sup>. Besides, telomerase exhibit many multiple non-canonical biological functions, like protecting mitochondrial DNA, regulating the expression of Wnt target genes (serving a critical role in tumorigenesis), and promoting EMT through the NF- $\kappa$ B signaling pathway<sup>66–68</sup>. Additionally, Liu et al. shows that depletion of hTERT leads to abolished TGF- $\beta$ 1 and  $\beta$ -catenin-mediated EMT.  $\beta$ -catenin in cooperation with hTERT regulates transcription of Vimentin, so deregulation of all those proteins leads to preventing cancer progression<sup>69</sup>. We demonstrated that **PCH-1** significantly decreased the level of hTERT, which suggests that it not only suppresses EMT but also inhibits tumor proliferation and induces cell mortality.

Microtubule dynamics are essential in the cell migration by providing protrusive and contractile forces, a front-rear polarity allowing movement of organelle and protein through the cells, and controlling signaling during motility<sup>70,71</sup>. Many microtubule-targeting agents inhibit cell migration, by preventing activation of Rac1/Cdc42<sup>72,73</sup>. During microtubule polymerization, Rac1 is activated in lamellipodia and stimulates actin stress fiber formation. Whereas, Cdc42 regulates polarization of cells, and proper orientation of the centrosome. Consequently, interference with microtubule dynamics inhibit Rac1 and Cdc42, and therefore decrease cell motility. **PCH-1** efficiently decreased cell migration in concentration-dependent manner in TGF- $\beta$ 1-stimulated, and unstimulated cells, which was observed under time-lapse microscopy by using a wound healing assay. However, the exact mechanism of inhibition cell migration by **PCH-1** should be further explored, such as confirming the involvement of Rac1 and Cdc42 in this process.

Several studies have shown that many compounds derived from chalcone possess oxidative properties<sup>74,75</sup>. Similar to its analogs, **PCH-1** robustly induces the generation of ROS in A-549 cells. This accumulation can activate both the intrinsic and extrinsic apoptotic cell death, by activating the downstream caspase cascades<sup>76</sup>.

In conclusion, this study provides evidence that **PCH-1** reduces cell viability and colony formation of non-small lung cancer cells in vitro. Our study demonstrated that **PCH-1** induces G<sub>2</sub>/M phase arrest by stabilizing tubulin polymers and cellular apoptosis through extrinsic and intrinsic pathways. In addition to its proapoptotic properties, **PCH-1** shows potent antimetastatic and prooxidant potential in A-549 cells. The molecular mechanism of action of this compound is shown in Fig. 9. On the basis of the presented findings, **PCH-1** is a promising antitumor compound that warrants further preclinical development.

## Methods

**Synthesis of the designed compounds.** Liquid chromatography-mass spectrometry (LCMS) spectra were registered on an LCMS IT-TOF (Shimadzu, Japan) with an electrospray ionization (ESI) source in the positive ion mode. <sup>1</sup>H-NMR spectra were acquired on a Bruker Avance III spectrometer at 500 MHz. The NMR data were processed and analyzed by TopSpin (Bruker, USA). Chemical shifts were expressed at  $\delta$  value to the internal standard (TMS). IR spectra were measured on an IF S66 spectrometer (Bruker, USA) in KBr pellets at an absorption range of 400–4000 cm<sup>-1</sup>. Thin layer chromatography (TLC) was performed on Merck Kieselgel 60 F254 aluminum plates and visualized with UV and iodine.

Each compound was synthesized in two stages: condensation of the appropriately substituted benzaldehydes and acetophenones, and reaction with hydrazine hydrate to yield chalcone-derived pyrazoles.

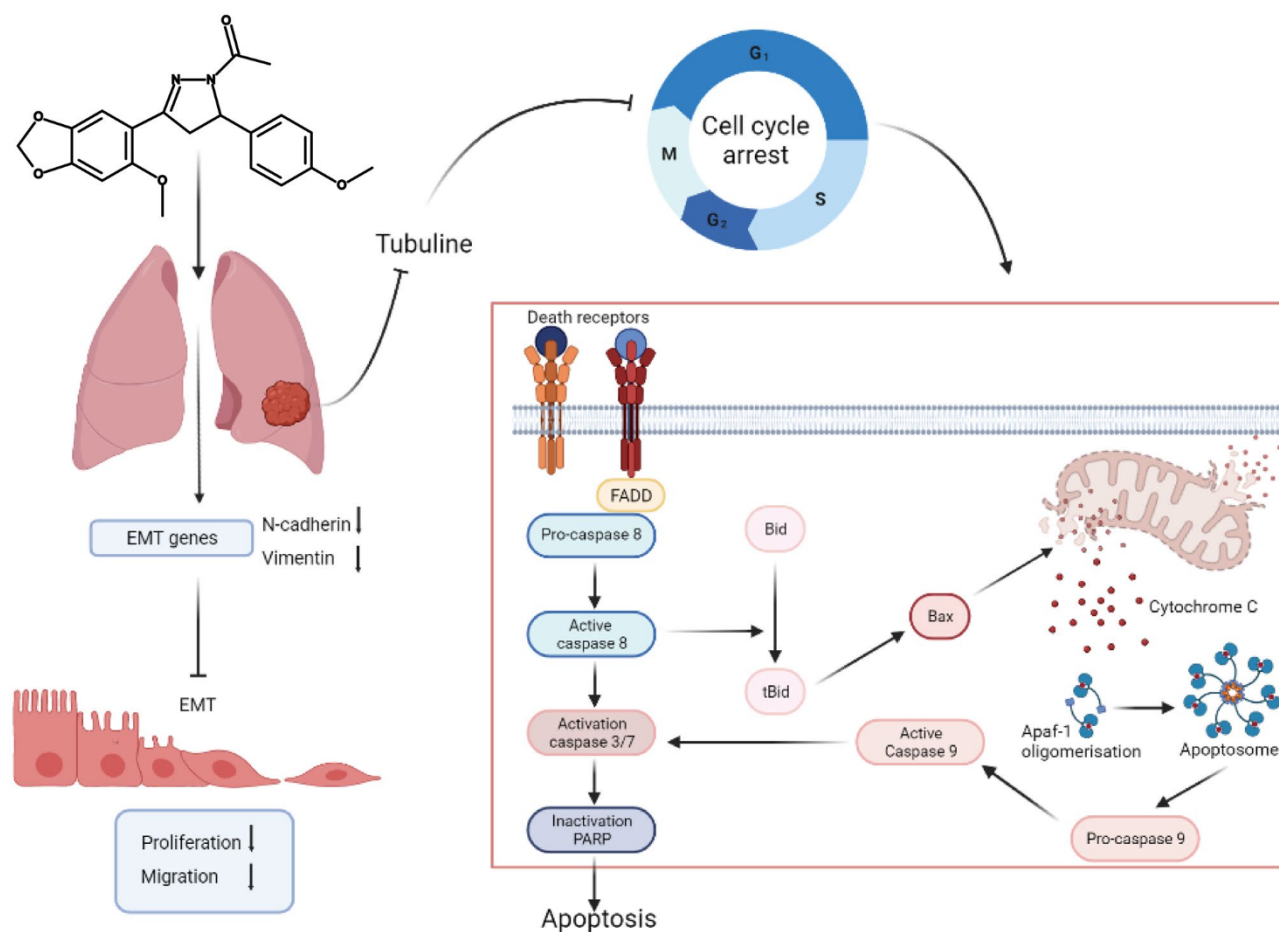


**Figure 9.** Molecular mechanism of action PCH-1 compound against lung cancer cells.

**General procedure for the synthesis of chalcones.** First, 10 mmol of the appropriately substituted benzaldehyde and acetophenone were dissolved in 20 ml of ethanol. The mixture was then stirred at 5 °C for few minutes. Next, 10 ml of 40% aqueous KOH was added, and the solution was stirred at room temperature (RT) for approximately 4 h. The formed precipitate was collected by filtration, characterized by HPLC and LCMS, and subjected to further reaction.

**General procedure for the synthesis of chalcone-derived pyrazoles.** Hydrazine hydrate (20 mmol) was added to a solution of chalcone (5 mmol) in acetic acid (10 ml). The reaction mixture was refluxed for approximately 2 h. The progress of the reaction was monitored by TLC. After the completion of the reaction, the mixture was cooled, adjusted to pH 7 with 10% Na<sub>2</sub>CO<sub>3</sub>, poured into crushed ice, and allowed to stand overnight at RT. The product was collected by filtration and purified by flash chromatography or reversed-phase high-performance liquid chromatography (RP-HPLC). The product was then characterized by LCMS, <sup>1</sup>H-NMR, and IR.

*1-[3-(6-methoxy-2H-1,3-benzodioxol-5-yl)-5-(4-methoxyphenyl)-4,5-dihydro-1H-pyrazol-1-yl]ethan-1-one (PCH-1).* ESI-MS: (*m/z*): 369.139 [M + H]<sup>+</sup>; <sup>1</sup>H-NMR (CDCl<sub>3</sub>, 500 MHz), δ (ppm): 2.39 (s, 3H), 3.30 (dd, *J*<sub>1</sub> = 3.77 Hz, *J*<sub>2</sub> = 3.77 Hz, 2H), 3.78 (s, 3H), 3.79 (s, 3H), 5.49 (dd, *J*<sub>1</sub> = 3.23 Hz, *J*<sub>2</sub> = 3.41 Hz, 1H), 6.00 (s, 2H), 6.54 (s, 1H), 6.85 (d, *J* = 8.26 Hz, 2H), 7.19 (d, *J* = 7.89 Hz, 2H), 7.48 (s, 1H); IR (KBr), ν (cm<sup>-1</sup>): 1650.92, 1468.94.

*1-[5-(2H-1,3-benzodioxol-5-yl)-3-(3,4,5-trimethoxyphenyl)-4,5-dihydro-1H-pyrazol-1-yl]ethan-1-one (PCH-2).* ESI-MS: (*m/z*): 399.125 [M + H]<sup>+</sup>; <sup>1</sup>H-NMR (CDCl<sub>3</sub>, 500 MHz), δ (ppm): 2.45 (s, 3H), 3.14 (dd, *J*<sub>1</sub> = 4.31 Hz, *J*<sub>2</sub> = 4.30 Hz, 1H), 3.73 (dd, *J*<sub>1</sub> = 11.84 Hz, *J*<sub>2</sub> = 11.85 Hz, 1H), 3.91 (s, 3H), 3.93 (s, 6H), 5.54 (dd, *J*<sub>1</sub> = 4.31 Hz, *J*<sub>2</sub> = 4.66 Hz, 1H), 5.94 (s, 2H), 6.73 (m, 3H), 6.97 (s, 2H); IR (KBr), ν (cm<sup>-1</sup>): 1665.00, 1417.26.

*1-[5-(2H-1,3-benzodioxol-5-yl)-3-(4-methylphenyl)-4,5-dihydro-1H-pyrazol-1-yl]ethan-1-one (PCH-3).* ESI-MS: (*m/z*): 323.098 [M + H]<sup>+</sup>; <sup>1</sup>H-NMR (CDCl<sub>3</sub>, 500 MHz), δ (ppm): 2.42 (s, 3H), 2.44 (s, 3H), 3.15 (d, *J* = 16.59 Hz, 1H), 3.73 (dd, *J*<sub>1</sub> = 10.78 Hz, *J*<sub>2</sub> = 11.19 Hz, 1H), 5.52 (d, *J* = 7.05 Hz, 1H), 5.94 (s, 2H), 6.70 (s, 1H), 6.75 (s, 2H), 7.25 (d, *J* = 7.46 Hz, 2H), 7.65 (d, *J* = 7.88 Hz, 2H); IR (KBr), ν (cm<sup>-1</sup>): 1649.10, 1443.97.

1-[5-(2H-1,3-benzodioxol-5-yl)-3-(2-methoxyphenyl)-4,5-dihydro-1H-pyrazol-1-yl]ethan-1-one (PCH-4). ESI-MS: (*m/z*): 339.101 [M + H]<sup>+</sup>; <sup>1</sup>H-NMR (CDCl<sub>3</sub>, 500 MHz), δ (ppm): 2.42 (s, 3H), 3.31 (dd, *J*<sub>1</sub> = 4.27 Hz, *J*<sub>2</sub> = 4.60 Hz, 1H), 3.85 (s, 3H), 3.86 (dd, *J*<sub>1</sub> = 11.50 Hz, *J*<sub>2</sub> = 11.83 Hz, 1H), 5.47 (dd, *J*<sub>1</sub> = 4.60 Hz, *J*<sub>2</sub> = 4.60 Hz, 1H), 5.93 (s, 2H), 6.73 (s, 1H), 6.76 (s, 2H), 6.96 (d, *J* = 8.21 Hz, 1H), 7.04 (t, *J*<sub>1</sub> = 7.56 Hz, *J*<sub>2</sub> = 7.32 Hz, 1H), 7.41 (m, 1H), 7.94 (dd, *J*<sub>1</sub> = 1.64 Hz, *J*<sub>2</sub> = 1.81 Hz, 1H); IR (KBr), ν (cm<sup>-1</sup>): 1659.49, 1419.84.

1-[3,5-bis(2H-1,3-benzodioxol-5-yl)-4,5-dihydro-1H-pyrazol-1-yl]ethan-1-one (PCH-5). ESI-MS: (*m/z*): 353.068 [M + H]<sup>+</sup>; <sup>1</sup>H-NMR (CDCl<sub>3</sub>, 500 MHz), δ (ppm): 2.42 (s, 3H), 3.09 (dd, *J*<sub>1</sub> = 4.61 Hz, *J*<sub>2</sub> = 4.23 Hz, 1H), 3.68 (dd, *J*<sub>1</sub> = 11.53 Hz, *J*<sub>2</sub> = 11.53 Hz, 1H), 5.51 (dd, *J*<sub>1</sub> = 4.62 Hz, *J*<sub>2</sub> = 4.23 Hz, 1H), 5.94 (s, 2H), 6.05 (s, 2H), 6.69 (s, 1H), 6.76 (m, 2H), 6.85 (d, *J* = 8.57 Hz, 1H), 7.11 (dd, *J*<sub>1</sub> = 1.54 Hz, *J*<sub>2</sub> = 1.54 Hz, 1H), 7.39 (d, *J* = 1.53 Hz, 1H); IR (KBr), ν (cm<sup>-1</sup>): 1653.92, 1458.82.

1-[5-(2H-1,3-benzodioxol-5-yl)-3-[4-(trifluoromethoxy)phenyl]-4,5-dihydro-1H-pyrazol-1-yl]ethan-1-one (PCH-6). ESI-MS: (*m/z*): 393.056 [M + H]<sup>+</sup>; <sup>1</sup>H-NMR (CDCl<sub>3</sub>, 500 MHz), δ (ppm): 2.44 (s, 3H), 3.14 (dd, *J*<sub>1</sub> = 4.40 Hz, *J*<sub>2</sub> = 4.83 Hz, 1H), 3.73 (dd, *J*<sub>1</sub> = 11.86 Hz, *J*<sub>2</sub> = 11.86 Hz, 1H), 5.55 (dd, *J*<sub>1</sub> = 4.40 Hz, *J*<sub>2</sub> = 4.39 Hz, 1H), 5.94 (s, 2H), 6.73 (m, 3H), 7.29 (d, *J* = 8.95 Hz, 2H), 7.79 (d, *J* = 8.63 Hz, 2H); IR (KBr), ν (cm<sup>-1</sup>): 1652.13, 1447.62.

1-[5-(2,3-dihydro-1-benzofuran-5-yl)-3-(4-methoxyphenyl)-4,5-dihydro-1H-pyrazol-1-yl]ethan-1-one (PCH-7). ESI-MS: (*m/z*): 337.108 [M + H]<sup>+</sup>; <sup>1</sup>H-NMR (CDCl<sub>3</sub>, 500 MHz), δ (ppm): 2.43 (s, 3H), 3.16 (m, 3H), 3.71 (dd, *J*<sub>1</sub> = 11.79 Hz, *J*<sub>2</sub> = 11.79 Hz, 1H), 3.88 (s, 3H), 4.55 (t, *J*<sub>1</sub> = 8.84 Hz, *J*<sub>2</sub> = 8.42 Hz, 2H), 5.53 (dd, *J*<sub>1</sub> = 4.42 Hz, *J*<sub>2</sub> = 4.21 Hz, 1H), 6.73 (d, *J* = 8.00 Hz, 1H), 6.96 (d, *J* = 8.85 Hz, 2H), 7.01 (dd, *J*<sub>1</sub> = 1.47 Hz, *J*<sub>2</sub> = 1.48 Hz, 1H), 7.07 (s, 3H), 7.72 (d, *J* = 8.85 Hz, 2H); IR (KBr), ν (cm<sup>-1</sup>): 1661.06, 1493.03.

1-[5-(6-methoxy-2H-1,3-benzodioxol-5-yl)-3-(4-methoxyphenyl)-4,5-dihydro-1H-pyrazol-1-yl]ethan-1-one (PCH-8). ESI-MS: (*m/z*): 369.092 [M + H]<sup>+</sup>; <sup>1</sup>H-NMR (CDCl<sub>3</sub>, 500 MHz), δ (ppm): 2.46 (s, 3H), 2.98 (dd, *J*<sub>1</sub> = 4.40 Hz, *J*<sub>2</sub> = 4.41 Hz, 1H), 3.67 (dd, *J*<sub>1</sub> = 11.64 Hz, *J*<sub>2</sub> = 11.63 Hz, 1H), 3.82 (s, 3H), 3.86 (s, 3H), 5.77 (dd, *J*<sub>1</sub> = 4.40 Hz, *J*<sub>2</sub> = 4.41 Hz, 1H), 5.88 (s, 2H), 6.54 (d, *J* = 5.66 Hz, 2H), 6.93 (d, *J* = 8.80 Hz, 2H), 7.68 (d, *J* = 8.80 Hz, 2H); IR (KBr), ν (cm<sup>-1</sup>): 1661.13, 1483.86.

1-[5-(4-hydroxyphenyl)-3-(6-methoxy-2H-1,3-benzoxathiol-5-yl)-4,5-dihydro-1H-pyrazol-1-yl]ethan-1-one (PCH-9). ESI-MS: (*m/z*): 371.045 [M + H]<sup>+</sup>; <sup>1</sup>H-NMR (CDCl<sub>3</sub>, 500 MHz), δ (ppm): 2.32 (s, 3H), 3.18 (dd, *J*<sub>1</sub> = 4.33 Hz, *J*<sub>2</sub> = 4.33 Hz, 1H), 3.69 (s, 3H), 3.73 (dd, *J*<sub>1</sub> = 7.11 Hz, *J*<sub>2</sub> = 8.39 Hz, 1H), 5.37 (dd, *J*<sub>1</sub> = 4.33 Hz, *J*<sub>2</sub> = 4.33 Hz, 1H), 5.67 (s, 2H), 6.42 (s, 1H), 6.55 (d, *J* = 8.66 Hz, 2H), 6.94 (d, *J* = 8.66 Hz, 2H), 7.69 (s, 1H); IR (KBr), ν (cm<sup>-1</sup>): 1638.59, 1468.15.

**Biological evaluation.** *Cell culture.* HEK293, A-549, H226, and H460 cells were obtained from the American Type Culture Collection (ATCC, USA) and cultured in DMEM (HEK293) or RPMI medium (Corning) supplemented with 10% fetal bovine serum (Corning), 2 mM L-glutamine (Sigma-Aldrich), and antibiotics (penicillin 62.6 µg/ml and streptomycin 40 µg/ml, Sigma-Aldrich). The cells were incubated in a humidified 5% CO<sub>2</sub> atmosphere at 37 °C and routinely screened for *Mycoplasma* contamination.

*Cell viability assay.* The cell viability assay was performed for A-549, H226, H460, and HEK293 cells after treatment with the test compounds by using the 3-(4,5-dimethylthiazol-2-yl)-2,5-diphenyltetrazolium bromide (MTT, Sigma-Aldrich) assay. Briefly, cells were seeded onto 96-well culture plates for attachment. After 24 h, triplicate wells were treated with DMSO (1%) and the agents. After 72 h of incubation at 37 °C in 5% CO<sub>2</sub>, the MTT solution (0.4 mg/ml) was added to each well. After 2–4 h of incubation, the medium was removed, and the formazan crystals were dissolved in 100 µl of DMSO. The absorption was measured at 450 nm with an ASYS UVM340 microplate reader (Biochrom Ltd.). The 50% inhibitory concentration (IC<sub>50</sub>) was defined as the concentration that reduced the absorbance of the DMSO-treated wells by 50% of the vehicle. The IC<sub>50</sub> values were generated from GraphPad Prism 9 software by plotting the survival curve as a function of dose from 3 independent experiments.

*Colony formation assay.* Cells were seeded onto 6-well plates (500 cells/well) and allowed to attach for 24 h in a fresh RPMI medium. Next, the cells were pretreated with DMSO (1%) solution of the examined compound (at the concentrations of 1, 5, and 10 µM) for 24 h. The medium containing compound was then changed, and the cells were cultured for additional 9 days. After incubation, the cells were washed twice with phosphate-buffered saline (PBS), fixed with 100% methanol for 30 min, and stained with 0.5% crystal violet for 15 min. The colonies were photographed and counted by ImageJ software.

*Morphology assessment.* Cells were seeded onto tissue culture plates with a glass slide and allowed to attach for 24 h. Next, the cells were treated for the indicated time with PCH-1 or DMSO. After incubation, the cells were rinsed with PBS, fixed in 3.7% paraformaldehyde (Sigma-Aldrich) for 10 min at RT and stained with 4',6-diamidino-2-phenylindole (DAPI, Sigma-Aldrich). The stained nuclei were visualized using a fluorescence microscope (Olympus BX60) with an appropriate filter.

*Analysis of cell cycle distribution.* Cells were seeded onto tissue culture plates and allowed to attach for 24 h. Unsynchronized cells were treated with PCH-1 or Etoposide at IC<sub>90</sub> concentration for 24 and 48 h, while syn-

chronized cells were treated with **PCH-1** or Etoposide at  $IC_{90}$  concentration for 2, 4, 6, 8, and 10 h. Synchronization of the cells was performed as described previously by Chen et al.<sup>77</sup>. Next, the cells were trypsinized, fixed in ice-cold 75% ethanol, and stored overnight at  $-20\text{ }^{\circ}\text{C}$ . After centrifugation, the cells were rinsed with PBS and stained with  $20\text{ }\mu\text{g}/\mu\text{l}$  PI (Sigma-Aldrich) and  $50\text{ }\mu\text{g}/\mu\text{l}$  RNaseA (Thermo Fisher) in PBS for 30 min at RT. The distribution of the cells in different phases of the cell cycle was determined by flow cytometry (Guava EasyCyte 8 cell sorter, Merck Millipore) and FlowJo software v10. Each experiment was repeated independently three times.

**HTS-tubulin polymerization assay biochem kit.** The assay was performed according to the manufacturer's instructions. Briefly, compounds were diluted in DMSO to a concentration of 2 mM and then in GTB buffer to a concentration of 50  $\mu\text{M}$ . In the wells of a 96-well plate (UV transparent, half surface wells) previously heated to  $37\text{ }^{\circ}\text{C}$ , 10  $\mu\text{l}$  of dilutions of the test compounds were placed in duplicate. The plate was incubated for 2 min at  $37\text{ }^{\circ}\text{C}$ , and 100  $\mu\text{l}$  of freshly prepared tubulin solution (4 mg/ml) in GTB-GTP buffer was then added. The plate was immediately placed in a Tecan SPARK 10 M plate reader, and the reaction kinetics were measured with the following settings: absorbance reading: 340 nm,  $37\text{ }^{\circ}\text{C}$ , interval: 45 s, number of cycles: 160.

**Immunofluorescence.** Cells were seeded onto tissue culture plates with a glass slide and allowed to attach for 24 h. After the incubation period, the cells were washed in PBS, fixed for 15 min at RT with 4% paraformaldehyde (Sigma-Aldrich) in PBS, and permeabilized for 15 min in 0.25% Triton-X100 (Sigma-Aldrich) in PBS. The cells were then washed twice with PBS, blocked with 3% bovine serum albumin (BSA, Sigma-Aldrich) in PBS for 1 h at RT, and incubated for 1 h at  $37\text{ }^{\circ}\text{C}$  in a humidified chamber with the following primary antibodies diluted in 3% BSA in PBS-T (PBS with 0.1% (v/v) Triton X-100): rabbit anti-Aurora B antibody (Abcam, ab2254) 1:500 and mouse anti-Tubulin 1:200 (Sigma-Aldrich, T8328). The slides were washed three times with PBS-T and incubated for 1 h at  $37\text{ }^{\circ}\text{C}$  in a humidified chamber with the following secondary antibodies diluted in 3% BSA in PBS-T: goat anti-mouse IgG antibody conjugated with Fluorochrome DyLight-488 (1:250, Thermo Fisher) and goat anti-rabbit IgG antibody conjugated to Alexa Fluor 594 (1:200, Jackson ImmunoResearch). The slides were then washed twice in PBS-T and stained with 0.25  $\mu\text{g}/\text{ml}$  DAPI. Images were acquired with an LSM 800 inverted laser scanning confocal microscope (Carl Zeiss) with an Airyscan detector using a  $\times 63$  1.4 NA Plan Apochromat objective (Carl Zeiss).

**Apoptosis and caspase 3/7 assay.** Cells were seeded onto tissue culture plates and allowed to attach for 24 h. Next, the cells were treated with **PCH-1** or Etoposide at  $IC_{90}$  concentration for 6, 24, and 48 h. After incubation, the cells were harvested by trypsinization, rinsed twice with PBS, and stained with Annexin V Alexa Fluor™ 488 conjugate (Thermo Fisher, #A13201) for apoptosis assay and with CellEvent™ Caspase-3/7 Green Flow Cytometry Assay Kit (Thermo Fisher, #C10427) for caspase-3/7 activation according to the manufacturer's protocols. The analysis was performed with Guava EasyCyte 8 cell sorter (Merck Millipore) and FlowJo software v10. Each experiment was repeated independently three times.

**Western blot.** Cells ( $1.5 \times 10^6$ ) were cultured in tissue culture plates for overnight attachment. The cells were then incubated with  $IC_{90}$  of **PCH-1** or 1% DMSO for 6, 24, and 48 h, or were co-treatment with 2.5 ng/ml TGF- $\beta 1$  (Sigma-Aldrich), and  $IC_{90}$  of PCH-1 or 1% DMSO for 24, and 48 h. Subsequently, the cells were collected and lysed in Laemmli buffer with a protease inhibitor cocktail (Roche) and phosphatase inhibitors [NaF (5 mM),  $\beta$ -glycerophosphate (5 mM), and  $\text{Na}_3\text{VO}_4$  (1 mM)]. The cells were then sonicated in triplicate (10 s, 30% amplitude) and centrifuged at  $16,000 \times g$  at  $12\text{ }^{\circ}\text{C}$  for 15 min. Protein concentrations were determined using the DC Protein Assay Kit (Bio-Rad). For determining total protein content, the cellular extract was separated by 10% or 12% sodium dodecyl sulfate–polyacrylamide gel electrophoresis (SDS-PAGE) and transferred onto a microporous polyvinylidene difluoride (PVDF) membrane (Bio-Rad). After blocking with 5% (w/v) BSA (Sigma-Aldrich) in  $1 \times$  TBST (pH 7.4 and 0.1% Tween-20) for 1 h, the membranes were incubated overnight with primary antibodies at  $4\text{ }^{\circ}\text{C}$ , followed by horseradish peroxidase-conjugated secondary antibodies for 1 h. All the used antibodies are listed in Table S1 in the supplementary information. The immunoreactive signals were detected using an enhanced chemiluminescence (ECL) detection reagent kit (Thermo Fisher) and a ChemiDoc XRS + Imaging System (Bio-Rad). The band intensity was measured using Image Lab 5.2 software (Bio-Rad).

**Wound healing migration assay.** To analyze cell motility, A-549 cells were seeded onto the Ibidi-silicone insert on a cover glass-bottom 24-well plate for live cell imaging and incubated for 24 h. Subsequently, the inserts were dislodged, the cellular debris was removed by washing with RPMI, and the cells were incubated with different concentrations of **PCH-1**, and/or 2.5 ng/ml TGF- $\beta 1$  (Sigma-Aldrich) in an imaging chamber (cellVivo incubation system, Olympus) at  $37\text{ }^{\circ}\text{C}$  with 5%  $\text{CO}_2$ . Images were captured every 10 min for 20 or 42 h under  $\times 10$  magnification using a fluorescence microscope (IX83 Inverted Microscope, Olympus) connected to an XC50 digital color camera (Olympus). The percentage of wound closure was quantified with ImageJ software.

**Intracellular ROS measurement.** For determination the ROS generation, cells were treated with  $IC_{90}$  of **PCH-1**,  $\text{H}_2\text{O}_2$ , or 1% DMSO for 3, 6, and 24 h. Next, a 1  $\mu\text{M}$  CM- $\text{H}_2\text{DCFDA}$  (#C6827; Thermo-Fisher) probe was added to the cells in each plate 30 min before the end of the drug treatment. After incubation cells were collected by trypsinization, stained with 7-Aminoactinomycin D (7-AAD, Sigma-Aldrich), and measured. The analysis was performed with Guava EasyCyte 8 cell sorter (Merck Millipore) and FlowJo software v10. Each experiment was repeated independently three times.

Received: 28 September 2021; Accepted: 23 February 2022

Published online: 08 March 2022

## References

- Rozmer, Z. & Perjési, P. Naturally occurring chalcones and their biological activities. *Phytochem. Rev.* **15**, 87–120 (2014).
- Tekale, S. *et al.* Biological role of chalcones in medicinal chemistry. *Vector-Borne Dis. Recent Dev. Epidemiol. Control.* <https://doi.org/10.5772/INTECHOPEN.91626> (2020).
- Salehi, B. *et al.* Pharmacological properties of chalcones: A review of preclinical including molecular mechanisms and clinical evidence. *Front. Pharmacol.* **11**, 2068 (2021).
- Sahu, N. K., Balbhadra, S. S., Choudhary, D. & Kohli, D. V. Exploring pharmacological significance of chalcone scaffold: A review. *Curr. Med. Chem.* **19**, 209–225 (2012).
- Higuchi, K. *et al.* Sofalcone, a gastroprotective drug, promotes gastric ulcer healing following eradication therapy for *Helicobacter pylori*: A randomized controlled comparative trial with cimetidine, an H<sub>2</sub>-receptor antagonist. *J. Gastroenterol. Hepatol.* **25**(Suppl 1), 155–160 (2010).
- Cho, S. *et al.* Isoliquiritigenin, a chalcone compound, is a positive allosteric modulator of GABAA receptors and shows hypnotic effects. *Biochem. Biophys. Res. Commun.* **413**, 637–642 (2011).
- Bradley, R. *et al.* Xanthohumol microbiome and signature in healthy adults (the XMaS trial): A phase I triple-masked, placebo-controlled clinical trial. *Trials* **21**, 1–14 (2020).
- Lust, S. *et al.* Xanthohumol kills B-chronic lymphocytic leukemia cells by an apoptotic mechanism. *Mol. Nutr. Food Res.* **49**, 844–850 (2005).
- Parhiz, H., Roohbakhsh, A., Soltani, F., Rezaee, R. & Iranshahi, M. Antioxidant and anti-inflammatory properties of the citrus flavonoids hesperidin and hesperetin: An updated review of their molecular mechanisms and experimental models. *Phytother. Res.* **29**, 323–331 (2015).
- Morand, C. *et al.* Hesperidin contributes to the vascular protective effects of orange juice: A randomized crossover study in healthy volunteers. *Am. J. Clin. Nutr.* **93**, 73–80 (2011).
- Martinez, R. M. *et al.* Hesperidin methyl chalcone inhibits oxidative stress and inflammation in a mouse model of ultraviolet B irradiation-induced skin damage. *J. Photochem. Photobiol. B.* **148**, 145–153 (2015).
- Zhou, K., Yang, S. & Li, S.-M. Naturally occurring prenylated chalcones from plants: Structural diversity, distribution, activities and biosynthesis. *Nat. Prod. Rep.* <https://doi.org/10.1039/D0NP00083C> (2021).
- Karthikeyan, C. *et al.* Advances in chalcones with anticancer activities. *Recent Pat. Anticancer. Drug Discov.* **10**, 97–115 (2015).
- Marquina, S. *et al.* Design, synthesis and QSAR study of 2'-hydroxy-4'-alkoxy chalcone derivatives that exert cytotoxic activity by the mitochondrial apoptotic pathway. *Bioorg. Med. Chem.* **27**, 43–54 (2019).
- Wang, G. *et al.* Synthesis, biological evaluation, and molecular modelling of new naphthalene-chalcone derivatives as potential anticancer agents on MCF-7 breast cancer cells by targeting tubulin colchicine binding site. *J. Enzyme Inhib. Med. Chem.* **35**, 139–144 (2019).
- Pawlak, A. *et al.* Chalcone methoxy derivatives exhibit antiproliferative and proapoptotic activity on canine lymphoma and leukemia cells. *Mol.* **25**, 4362 (2020).
- Barnes, N. G., Parker, A. W., Ahmed Mal Ullah, A. A., Ragazzon, P. A. & Hadfield, J. A. A 2-step synthesis of Combretastatin A-4 and derivatives as potent tubulin assembly inhibitors. *Bioorg. Med. Chem.* **28**, 115684 (2020).
- Kong, Y. *et al.* A boronic acid chalcone analog of combretastatin A-4 as a potent anti-proliferation agent. *Bioorg. Med. Chem.* **18**, 971–977 (2010).
- Lindamulage, I. K. *et al.* Novel quinolone chalcones targeting colchicine-binding pocket kill multidrug-resistant cancer cells by inhibiting tubulin activity and MRP1 function. *Sci. Rep.* **7**, 10298 (2017).
- Li, L. *et al.* Recent advances in trimethoxyphenyl (TMP) based tubulin inhibitors targeting the colchicine binding site. *Eur. J. Med. Chem.* **151**, 482–494 (2018).
- Zhang, H. *et al.* Design, synthesis and biological evaluation of novel chalcone derivatives as antitubulin agents. *Bioorg. Med. Chem.* **20**, 3212–3218 (2012).
- Chouiter, M. I. *et al.* New chalcone-type compounds and 2-pyrazoline derivatives: Synthesis and caspase-dependent anticancer activity. *Future Med. Chem.* **12**, 493–509 (2020).
- Ouyang, Y. *et al.* Chalcone derivatives: Role in anticancer therapy. *Biomolecules* <https://doi.org/10.3390/biom11060894> (2021).
- Faria, J. V. *et al.* Recently reported biological activities of pyrazole compounds. *Bioorg. Med. Chem.* **25**, 5891–5903 (2017).
- Naim, M. J., Alam, O., Nawaz, F., Alam, M. J. & Alam, P. Current status of pyrazole and its biological activities. *J. Pharm. Bioallied Sci.* **8**, 2 (2016).
- Monga, V. *et al.* Synthesis and evaluation of new chalcones, derived pyrazoline and cyclohexenone derivatives as potent antimicrobial, antitubercular and antileishmanial agents. *Med. Chem. Res.* **23**, 2019–2032 (2013).
- Luo, Y. *et al.* Synthesis, biological evaluation, 3D-QSAR studies of novel aryl-2H-pyrazole derivatives as telomerase inhibitors. *Bioorg. Med. Chem. Lett.* **23**, 1091–1095 (2013).
- Hassan, R. M., Abd-Allah, W. H., Salman, A. M., El-Azzouny, A. A. S. & Aboul-Enein, M. N. Design, synthesis and anticancer evaluation of novel 1,3-benzodioxoles and 1,4-benzodioxines. *Eur. J. Pharm. Sci.* **139**, 105045 (2019).
- Tsubaki, M. *et al.* Tamoxifen suppresses paclitaxel-, vincristine-, and bortezomib-induced neuropathy via inhibition of the protein kinase C/extracellular signal-regulated kinase pathway. *Tumour Biol.* <https://doi.org/10.1177/1010428318808670> (2018).
- Schiff, P. B., Fant, J. & Horwitz, S. B. Promotion of microtubule assembly in vitro by taxol. *Nature* **277**, 665–667 (1979).
- Lu, Y., Chen, J., Xiao, M., Li, W. & Miller, D. D. An overview of tubulin inhibitors that interact with the colchicine binding site. *Pharm. Res.* **29**, 2943 (2012).
- Hauf, S. *et al.* The small molecule Hesperadin reveals a role for Aurora B in correcting kinetochore-microtubule attachment and in maintaining the spindle assembly checkpoint. *J. Cell Biol.* **161**, 281–294 (2003).
- Krenn, V. & Musacchio, A. The Aurora B kinase in chromosome bi-orientation and spindle checkpoint signaling. *Front. Oncol.* **5**, 225 (2015).
- Fu, J., Bian, M., Jiang, Q. & Zhang, C. Roles of Aurora kinases in mitosis and tumorigenesis. *Mol. Cancer Res.* **5**, 1–10 (2007).
- Liu, J. & Wang, Z. Increased oxidative stress as a selective anticancer therapy. *Oxid. Med. Cell. Longev.* <https://doi.org/10.1155/2015/294303> (2015).
- Quiroga, R. & Villarreal, M. A. Vinardo: A scoring function based on Autodock Vina improves scoring, docking, and virtual screening. *PLoS ONE* <https://doi.org/10.1371/journal.pone.0155183> (2016).
- Wang, R., Lai, L. & Shaomeng, W. Further development and validation of empirical scoring functions for structure-based binding affinity prediction. *J. Comput. Aided. Mol. Des.* **16**, 11–26 (2002).
- Waight, A. B. *et al.* Structural basis of microtubule destabilization by potent auristatin anti-mitotics. *PLoS ONE* **11**, e0160890 (2016).

39. Nosol, K. *et al.* Cryo-EM structures reveal distinct mechanisms of inhibition of the human multidrug transporter ABCB1. *Proc. Natl. Acad. Sci.* **117**, 26245–26253 (2020).
40. Discovery Studio Visualizer, v19. 1.0, BIOVIA, Dassault Systemes. (2018).
41. Morris, G. M. *et al.* AutoDock4 and AutoDockTools4: Automated docking with selective receptor flexibility. *J. Comput. Chem.* **30**, 2785–2791 (2009).
42. Gasteiger, J. & Marsili, M. A new model for calculating atomic charges in molecules. *Tetrahedron Lett.* **19**, 3181–3184 (1978).
43. Humphrey, W., Dalke, A. & Schulten, K. V. M. D. Visual molecular dynamics. *J. Mol. Graph.* **14**, 33–38 (1996).
44. Cancer. [https://www.who.int/health-topics/cancer#tab=tab\\_1](https://www.who.int/health-topics/cancer#tab=tab_1) (2020).
45. Karim, S. M. & Zekri, J. Chemotherapy for small cell lung cancer: A comprehensive review. *Oncol. Rev.* **6**, 16–36 (2012).
46. Zappa, C. & Mousa, S. A. Non-small cell lung cancer: Current treatment and future advances. *Transl. Lung Cancer Res.* **5**, 288 (2016).
47. Martins, P. *et al.* Heterocyclic anticancer compounds: Recent advances and the paradigm shift towards the use of nanomedicine's tool box. *Molecules* **20**, 16852 (2015).
48. Lang, D. K., Kaur, R., Arora, R., Saini, B. & Arora, S. Nitrogen-containing heterocycles as anticancer agents: An overview. *Anticancer Agents Med. Chem.* **20**, 2150–2168 (2020).
49. Edwards, M. L., Stemerick, D. M. & Sunkara, P. S. Chalcones: A new class of antimitotic agents. *J. Med. Chem.* **33**, 1948–1954 (2002).
50. Perez, E. A. Microtubule inhibitors: Differentiating tubulin-inhibiting agents based on mechanisms of action, clinical activity, and resistance. *Mol. Cancer Ther.* **8**, 2086–2095 (2009).
51. Hassan, M., Watari, H., AbuAlmaaty, A., Ohba, Y. & Sakuragi, N. Apoptosis and molecular targeting therapy in cancer. *Biomed. Res. Int.* <https://doi.org/10.1155/2014/150845> (2014).
52. Fulda, S. & Debatin, K.-M. Extrinsic versus intrinsic apoptosis pathways in anticancer chemotherapy. *Oncogene* **25**, 4798–4811 (2006).
53. Chandra, D. & Tang, D. G. Mitochondrially localized active caspase-9 and caspase-3 result mostly from translocation from the cytosol and partly from caspase-mediated activation in the organelle: Lack of evidence for Apaf-1-mediated procaspase-9 activation in the mitochondria. *J. Biol. Chem.* **278**, 17408–17420 (2003).
54. Brentnall, M., Rodriguez-Menocal, L., De Guevara, R. L., Cepero, E. & Boise, L. H. Caspase-9, caspase-3 and caspase-7 have distinct roles during intrinsic apoptosis. *BMC Cell Biol.* **14**, 32 (2013).
55. Los, M. *et al.* Activation and caspase-mediated inhibition of PARP: A molecular switch between fibroblast necrosis and apoptosis in death receptor signaling. *Mol. Biol. Cell* **13**, 978 (2002).
56. Tummers, B. & Green, D. R. Caspase-8; regulating life and death. *Immunol. Rev.* **277**, 76 (2017).
57. Korsmeyer, S. J. *et al.* Pro-apoptotic cascade activates BID, which oligomerizes BAK or BAX into pores that result in the release of cytochrome c. *Cell Death Differ.* **7**, 1166–1173 (2000).
58. Pretzsch, E. *et al.* Mechanisms of metastasis in colorectal cancer and metastatic organotropism: Hematogenous versus peritoneal spread. *J. Oncol.* <https://doi.org/10.1155/2019/7407190> (2019).
59. Li, C. & Balazsi, G. A landscape view on the interplay between EMT and cancer metastasis. *NPJ Syst. Biol. Appl.* **4**, 1–9 (2018).
60. Wang, N. & Stamenović, D. Contribution of intermediate filaments to cell stiffness, stiffening, and growth. *Am. J. Physiol. Cell Physiol.* <https://doi.org/10.1152/ajpcell.2000.279.1.C188> (2000).
61. Strouhalova, K. *et al.* Vimentin intermediate filaments as potential target for cancer treatment. *Cancers (Basel)*. <https://doi.org/10.3390/cancers12010184> (2020).
62. Gurland, G. & Gundersen, G. G. Stable, detyrosinated microtubules function to localize vimentin intermediate filaments in fibroblasts. *J. Cell Biol.* **131**, 1275–1290 (1995).
63. Tadokoro, A. *et al.* Vimentin regulates invasiveness and is a poor prognostic marker in non-small cell lung cancer—PubMed. *Anticancer Res.* **36**, 1545–1551 (2016).
64. Xu, J., Lamouille, S. & Derynck, R. TGF- $\beta$ -induced epithelial to mesenchymal transition. *Cell Res.* **19**, 156–172 (2009).
65. Yuan, X., Larsson, C. & Xu, D. Mechanisms underlying the activation of TERT transcription and telomerase activity in human cancer: Old actors and new players. *Oncogene* **38**, 6172–6183 (2019).
66. Liu, Z. *et al.* Telomerase reverse transcriptase promotes epithelial–mesenchymal transition and stem cell-like traits in cancer cells. *Oncogene* **32**, 4203–4213 (2013).
67. Brabletz, T., Kalluri, R., Nieto, M. A. & Weinberg, R. A. EMT in cancer. *Nat. Rev. Cancer* **18**, 128–134 (2018).
68. Wu, Y. *et al.* Telomerase reverse transcriptase mediates EMT through NF- $\kappa$ B signaling in tongue squamous cell carcinoma. *Oncotarget* **8**, 85492 (2017).
69. Liu, Z. *et al.* Telomerase reverse transcriptase promotes epithelial–mesenchymal transition and stem cell-like traits in cancer cells. *Oncogene* **32**, 4203–4213 (2012).
70. Garcin, C. & Straube, A. Microtubules in cell migration. *Essays Biochem.* **63**, 509 (2019).
71. Etienne-Manneville, S. Actin and microtubules in cell motility: Which one is in control?. *Traffic* **5**, 470–477 (2004).
72. Wang, X., Decker, C. C., Zechner, L., Krstin, S. & Wink, M. In vitro wound healing of tumor cells: Inhibition of cell migration by selected cytotoxic alkaloids. *BMC Pharmacol. Toxicol.* **20**, 1–12 (2019).
73. Bijman, M. N. A., van Amerongen, G. P. N., Laurens, N., van Hinsbergh, V. W. M. & Boven, E. Microtubule-targeting agents inhibit angiogenesis at subtoxic concentrations, a process associated with inhibition of Rac1 and Cdc42 activity and changes in the endothelial cytoskeleton. *Mol. Cancer Ther.* **5**, 2348–2357 (2006).
74. Zhang, S. *et al.* A novel chalcone derivative S17 induces apoptosis through ROS dependent DR5 up-regulation in gastric cancer cells. *Sci. Rep.* **7**, 1–13 (2017).
75. Pandey, V., Tripathi, G., Kumar, D., Kumar, A. & Dubey, P. K. Novel 3,4-diarylpyrazole as prospective anti-cancerous agents. *Heliyon* **6**, e04397 (2020).
76. Redza-Dutordoir, M. & Averill-Bates, D. A. Activation of apoptosis signalling pathways by reactive oxygen species. *Biochim. Biophys. Acta Mol. Cell Res.* **1863**, 2977–2992 (2016).
77. Chen, G. & Deng, X. Cell synchronization by double thymidine block. *Bio-Protoc.* <https://doi.org/10.21769/BioProtoc.2994> (2018).

## Acknowledgements

This work was financially supported by a grant from the National Centre for Research and Development STRAT-EGMED3/306853/9/NCBR/2017, Warsaw, Poland. Figure 9 was created with BioRender.com.

## Author contributions

Conceptualization, N.M., methodology, N.M., M.O., J.J., M.D., M.S.; K.C.; validation: N.M., M.O., formal analysis, N.M., M.O., J.J.; writing—original draft preparation: N.M., M.O., J.J., M.D., E.W.; graphical conceptualization: N.M.; writing—review and editing: N.M., E.W., M.B.

### Competing interests

The authors declare no competing interests.

### Additional information

**Supplementary Information** The online version contains supplementary material available at <https://doi.org/10.1038/s41598-022-07691-6>.

**Correspondence** and requests for materials should be addressed to N.M.

**Reprints and permissions information** is available at [www.nature.com/reprints](http://www.nature.com/reprints).

**Publisher's note** Springer Nature remains neutral with regard to jurisdictional claims in published maps and institutional affiliations.



**Open Access** This article is licensed under a Creative Commons Attribution 4.0 International License, which permits use, sharing, adaptation, distribution and reproduction in any medium or format, as long as you give appropriate credit to the original author(s) and the source, provide a link to the Creative Commons licence, and indicate if changes were made. The images or other third party material in this article are included in the article's Creative Commons licence, unless indicated otherwise in a credit line to the material. If material is not included in the article's Creative Commons licence and your intended use is not permitted by statutory regulation or exceeds the permitted use, you will need to obtain permission directly from the copyright holder. To view a copy of this licence, visit <http://creativecommons.org/licenses/by/4.0/>.

© The Author(s) 2022





## *Supplementary Information*

### *Novel Chalcone-derived Pyrazoles as Potential Therapeutic Agents for the Treatment of Non-small Cell Lung Cancer*

Natalia Maciejewska<sup>1\*</sup>, Mateusz Olszewski<sup>1</sup>, Jakub Jurasz<sup>1</sup>, Marcin Serocki<sup>3</sup>, Maria Dzierzynska<sup>2</sup>, Katarzyna Cekala<sup>2</sup>, Ewa Wieczerzak<sup>2</sup>, Maciej Baginski<sup>1</sup>

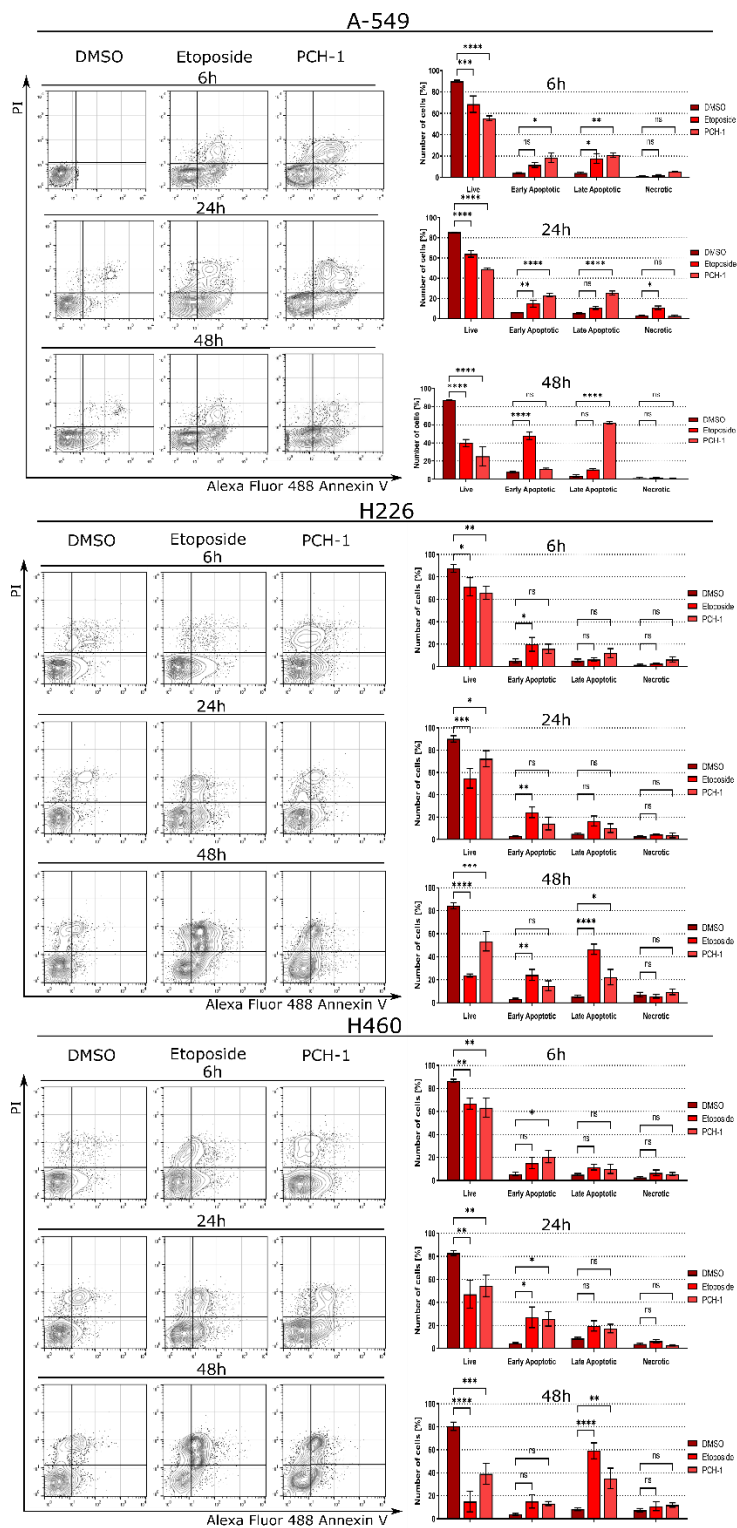
<sup>1</sup> Faculty of Chemistry, Gdansk University of Technology, Gabriela Narutowicza 11/12, 80-233 Gdansk, Poland

<sup>2</sup> Faculty of Chemistry, University of Gdansk, Wita Stwosza 63, 80-308 Gdansk, Poland

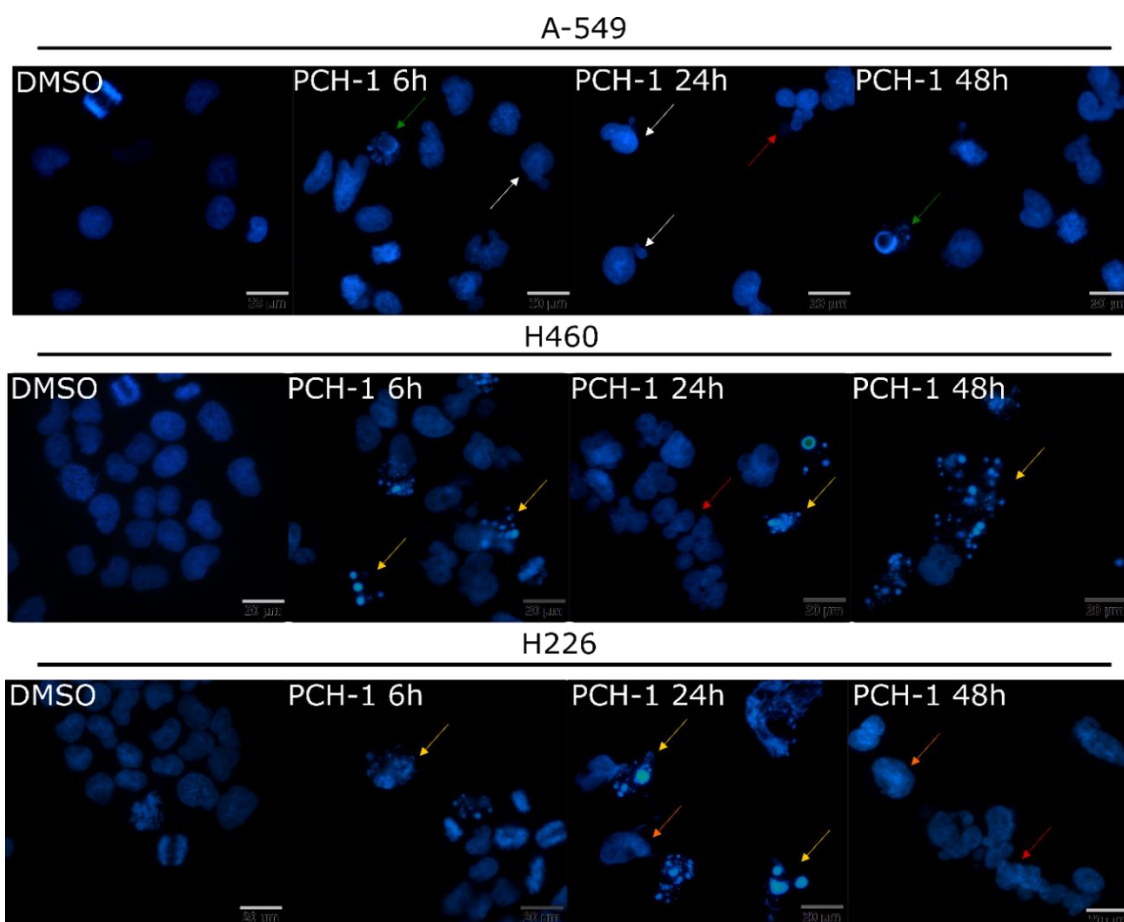
<sup>3</sup> Ryvu Therapeutics, Leona Henryka Sternbacha 2, 30-394 Krakow, Poland

\*Corresponding author: natalia.maciejewska@pg.edu.pl

## Biological evaluation



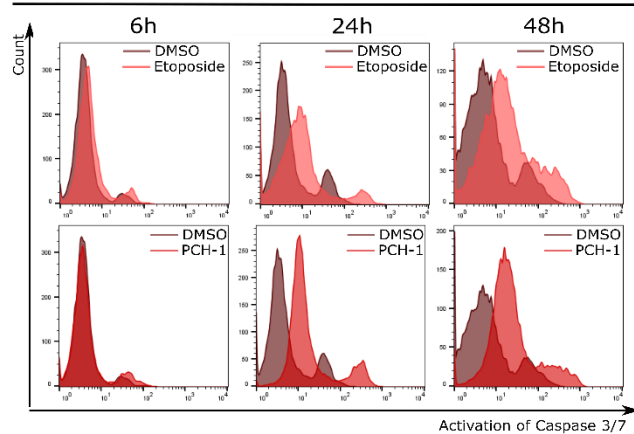
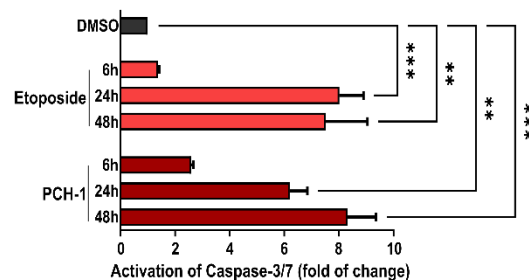
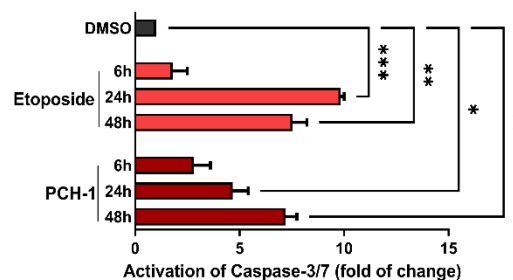
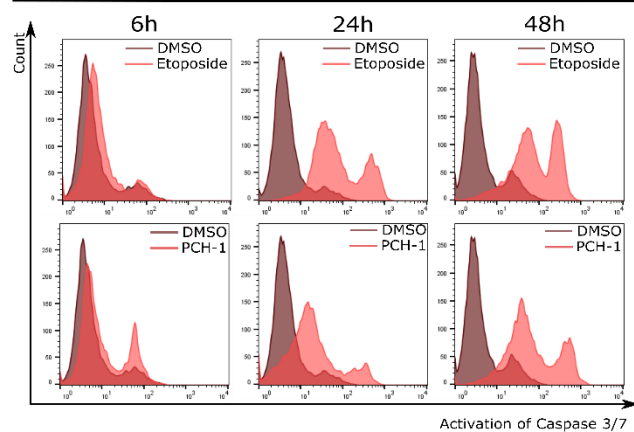
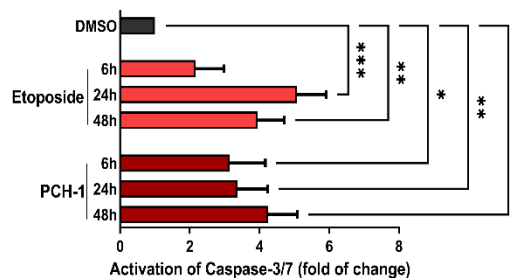
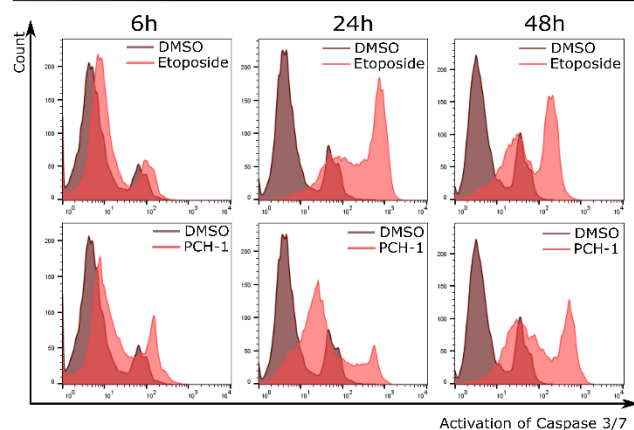
**Figure S1** Flow cytometric analyses of A-549, H226, and H460 cells after Alexa Fluor 488 Annexin V /PI staining. Representative dot-plots at 6, 24, and 48 h of treatment with **PCH-1**, Etoposide, or DMSO are presented on the left side. The quantitation of analysis is presented on a bar graph, on the right side. Error bars represent the SEM of data obtained in n=3 independent experiments. Statistical differences were analyzed with one-way ANOVA and post hoc Dunnett's test. <sup>ns</sup> p>0.05, \* p<0.01, \*\* p<0.001, \*\*\* p<0.0001, \*\*\*\* p<0.00001 vs. vehicle.



**Figure S2** Fluorescence images of A-549, H226, and H460 cells at 6, 24, and 48 h of treatment with **PCH-1** or DMSO. The cells were stained with DAPI and visualized by fluorescence microscopy, scale bar = 20  $\mu$ M. The arrows indicate cell blebbing (white), cell shrinkage (green), polyploid cells (red), apoptotic bodies (yellow), and chromatin condensation (orange).

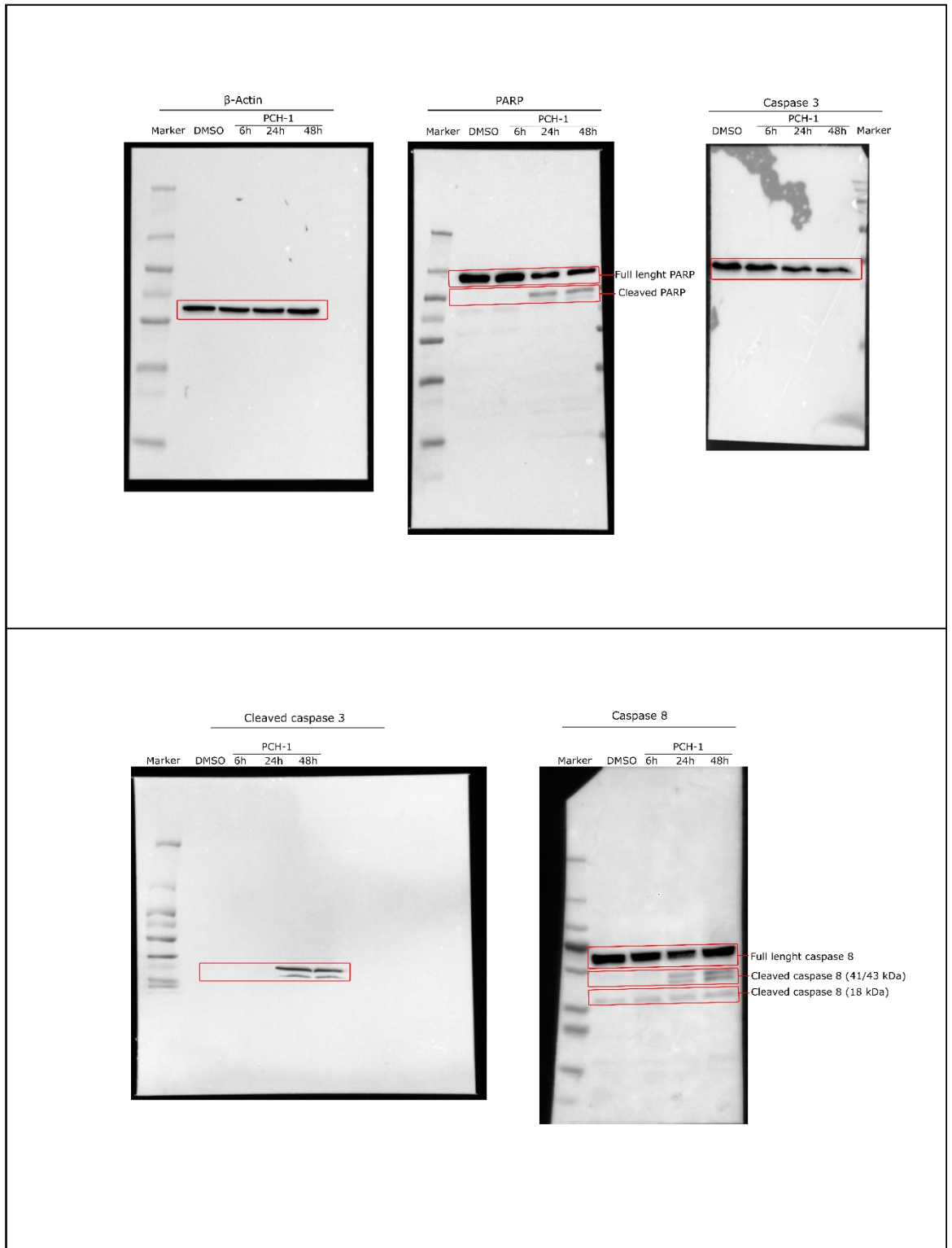
To confirm proapoptotic properties of investigated compound, A-549, H226, and H460 cells were treated with the **PCH-1** for 6, 24, and 48 h, and their nuclei were stained with DAPI and visualized by fluorescent microscopy. As depicted in **Figure S2**, **PCH-1** treatment exhibited typical phenotypic features of cells undergoing apoptosis, as evidenced by chromatin condensation, cell shrinkage, and membrane blebbing. Increasing the time of exposure to **PCH-1** triggered the formation of multinucleated polyploid cells, which is likely due to abnormalities of the spindle.



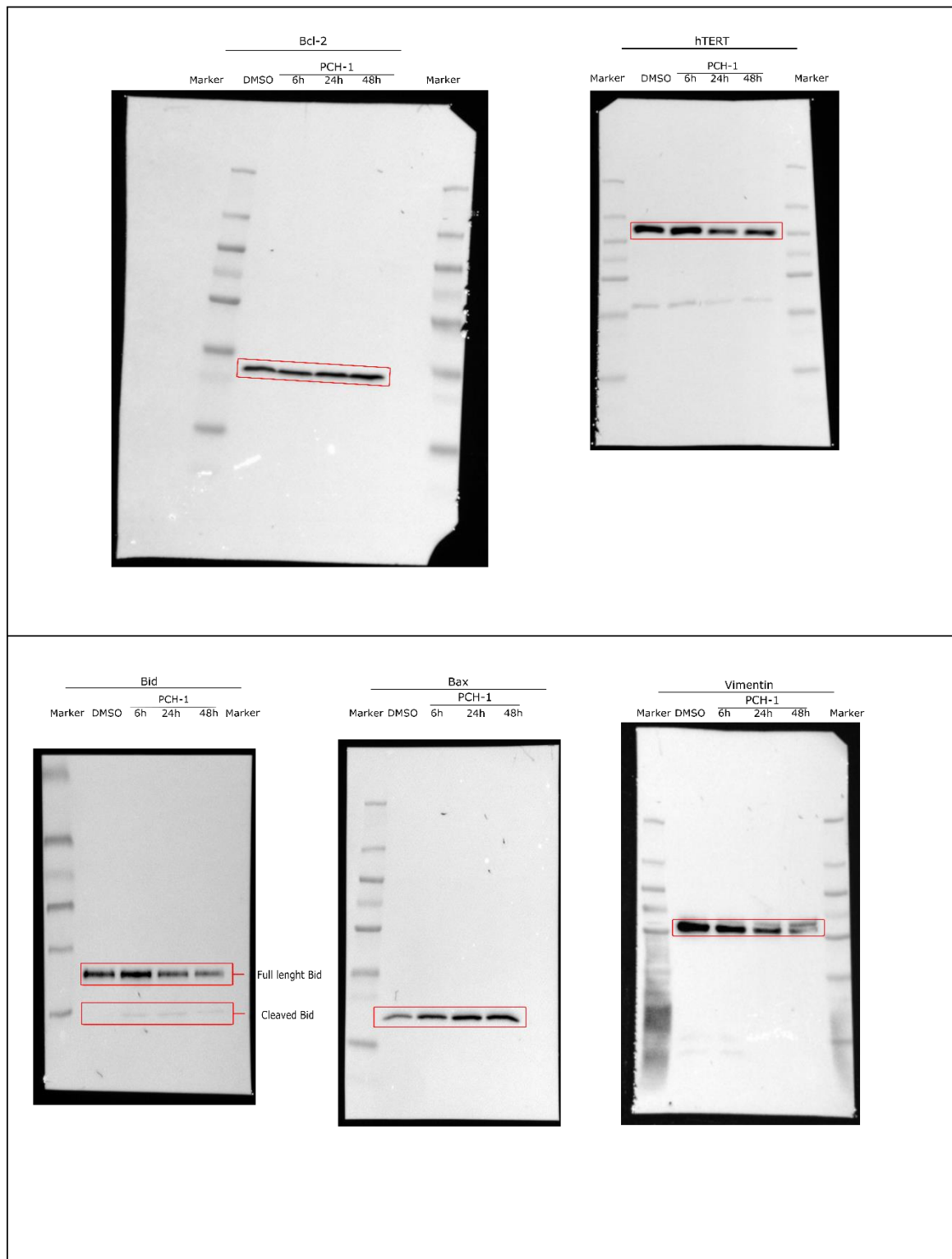
**a****b****H226****H460**

**Figure S3** Flow cytometric analyses of caspase-3/7 activation in A-549, H226, and H460 cell lines at 6, 24, and 48 h of treatment. **a.** Representative histograms; **b.** The quantitation of analysis is presented on a bar graph. Data represent mean  $\pm$  SEM of three independent experiments. Statistical differences were analyzed by one-way ANOVA and post hoc Dunnett's test. \*  $p < 0.01$ , \*\*  $p < 0.001$ , \*\*\*  $p < 0.0001$ .

**a**

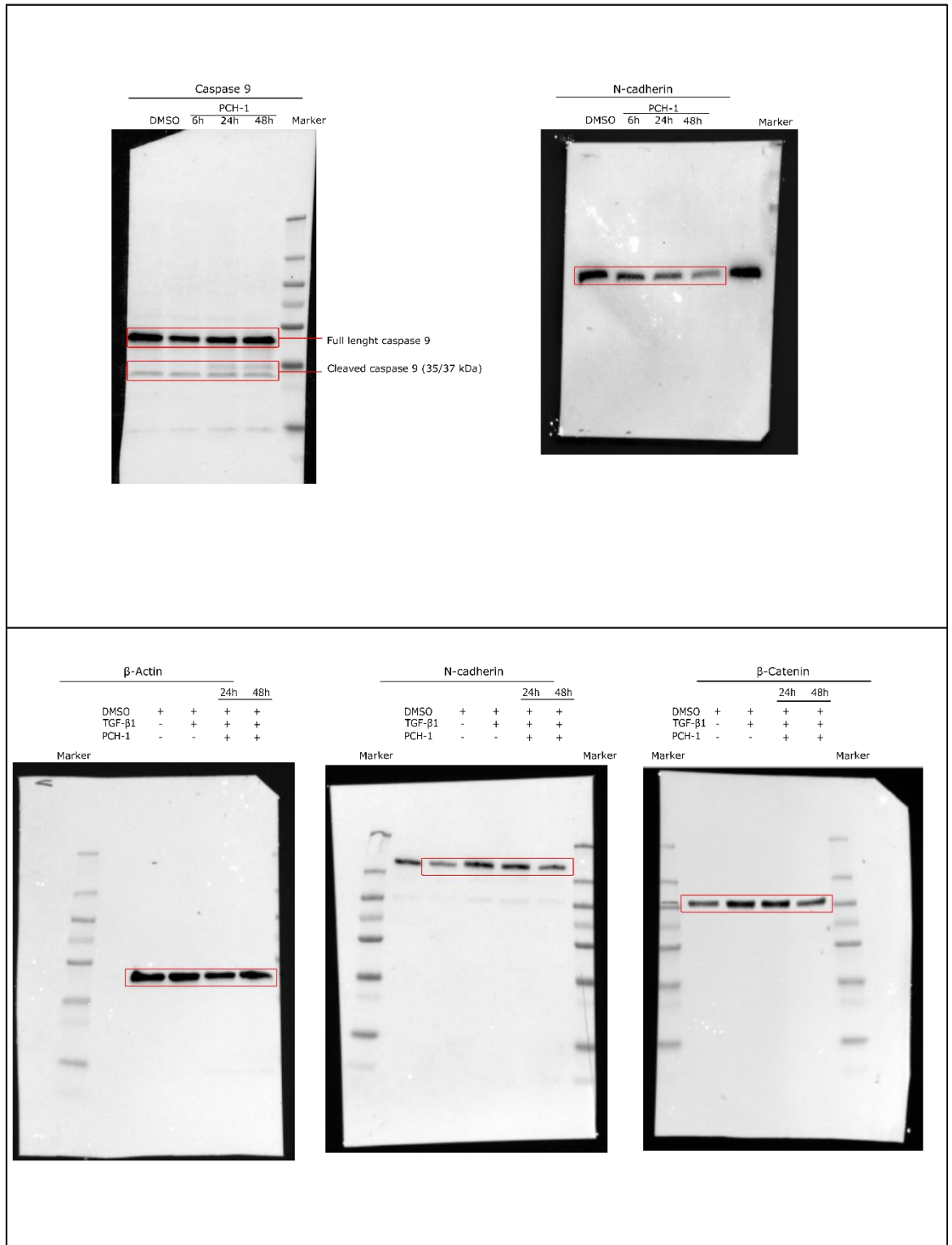


**Figure S4 a.** Full length western blot presented in **Figure 6** of the main article. Red boxes denote the cropped regions of the blots.

**b**

**Figure S4 b.** Full length western blot presented in **Figure 6** of the main article. Red boxes denote the cropped regions of the blots.



**C**

**Figure S4 c.** Full length western blot presented in **Figure 6** of the main article. Red boxes denote the cropped regions of the blots.

**d**

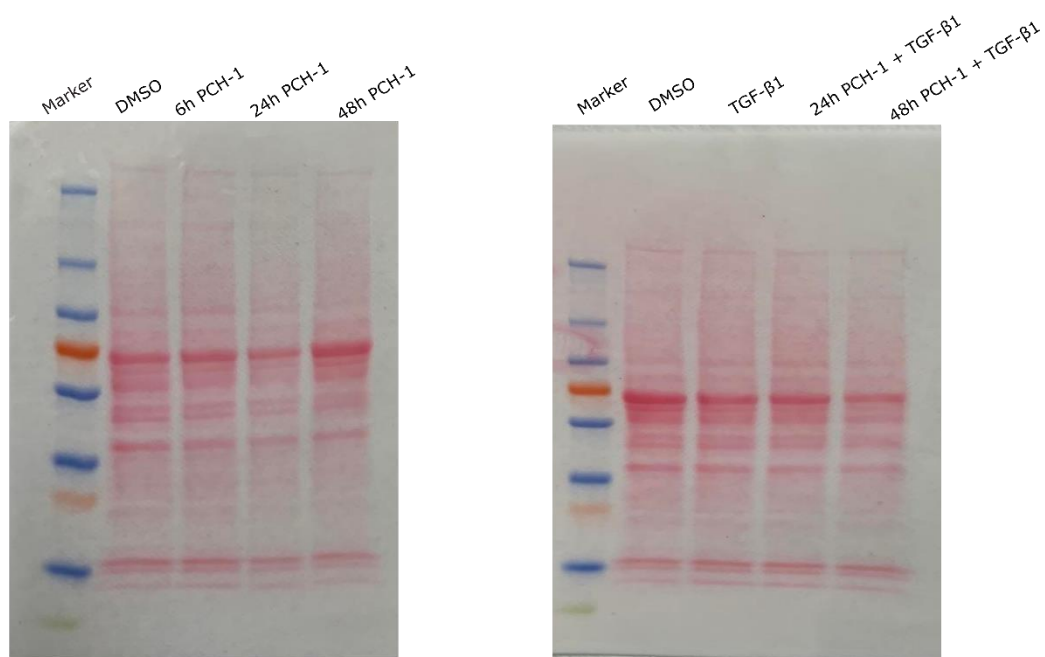


**Figure S4 d.** Representative images of a nitrocellulose membranes stained with Ponceau S dye for protein detection during western blot.



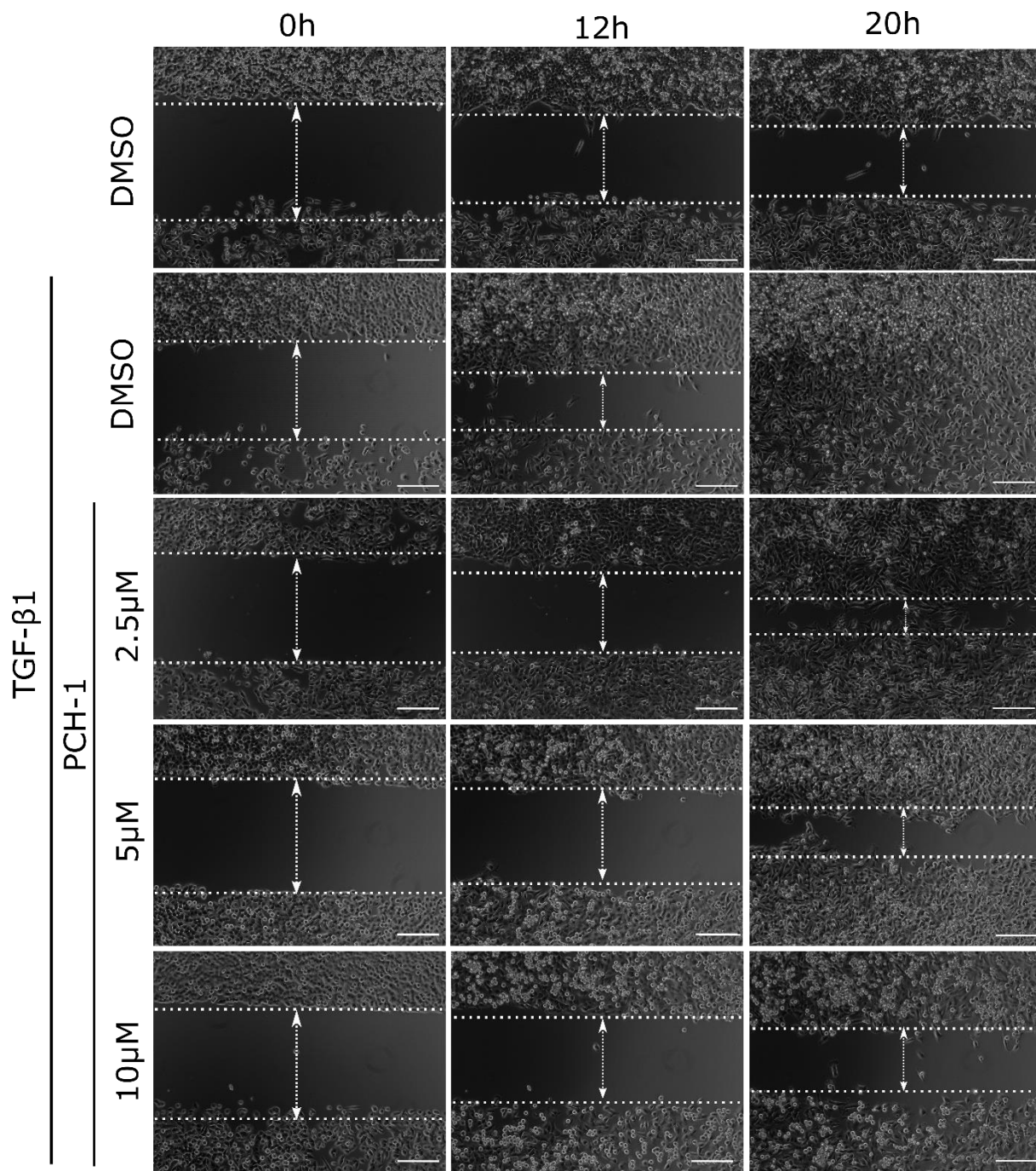


**Figure S5** Analysis of TGF- $\beta$ 1 stimulated and unstimulated A-549 cell migration after treatment with PCH-1 by *in vitro* wound healing assay presented as time-lapse microscopy images after culture insert removal. Scale bars = 100  $\mu$ m.

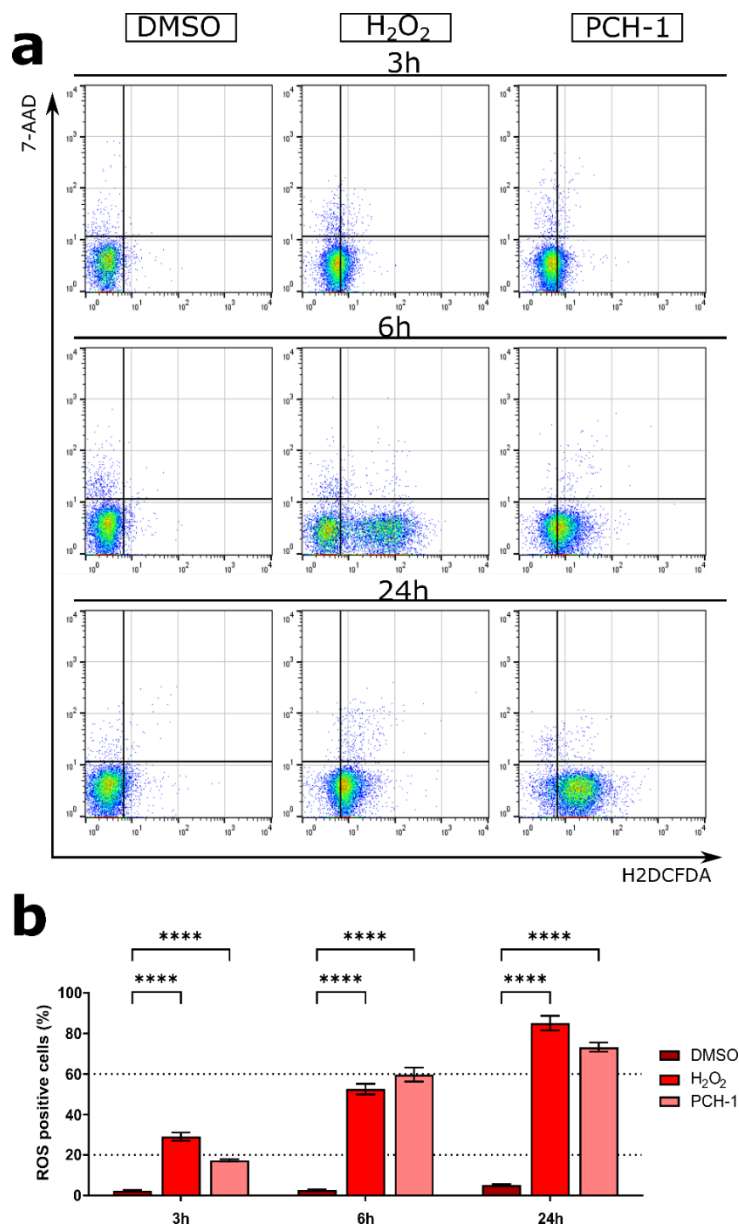


**Figure S6** Flow cytometry analyses of ROS level at 3, 6, and 24 h of treatment A-549 cells with **PCH-1**. **a**. Representative dot plots after labelling with H2DCFDA/7-AAD; **b**. The quantitation of the analysis is presented in a graph bar. Data represent the mean  $\pm$  SEM of three independent experiments. Statistical differences were analyzed by one-way ANOVA and post hoc Dunnett's test. \*\*  $p < 0.001$ , \*\*\*  $p < 0.0001$ , \*\*\*\*  $p < 0.00001$ .

## Methods

*Table S1* List of antibodies used in Western Blot

Antibody name	Company	Dilution
Anti-Caspase-3 (#9662)	Cell Signaling	1:1000
Anti-Cleavage caspase-3 (#9661)	Cell Signaling	1:1000
Anti-Caspase-9 (#9502)	Cell Signaling	1:1000
Anti-Caspase-8 (1C12) (#9746)	Cell Signaling	1:1000
Anti-PARP (#9542)	Cell Signaling	1:1000
Anti-Bcl-2 (#4223)	Cell Signaling	1:1000
Anti-BID (#2002)	Cell Signaling	1:1000
Anti-Bax (#2772)	Cell Signaling	1:1000
Anti-Telomerase reverse transcriptase antibody [Y182] (ab32020)	Cell Signaling	1:1000
Anti-Vimentin (#5741)	Cell Signaling	1:1000
Anti- $\beta$ -Catenin (#9562)	Cell Signaling	1:1000
Anti-N-cadherin (610920)	BD Transduction Laboratories	1:250
Anti-actin (sc-1616)	Santa Cruz	1:100
Anti-mouse-HRP (715-035-150)	Jacson ImmunoResearch Labs	1:10000
Anti-rabbit-HRP (711-035-152)	Jacson ImmunoResearch Labs	1:10000
Anti-goat-HRP (705-036-147)	Jacson ImmunoResearch Labs	1:10000